AD

AD661631

Preprints of Papers
To Be Presented
At The

UNGUIDED ROCKET BALLISTICS METEOROLOGY CONFERENCE

31 October -- 2 November 1967

ELMER J. TRAWLE
Conference Chairman

NEW MEXICO STATE UNIVERSITY

document has been approved
public release and sale; its
tion is unlimited.

ECOM
UNITED STATES ARMY ELECTRONICS COMMAND

DDC
RECEIVED
NOV 27 1967
C

Reproduced by the
CLEARINGHOUSE
for Federal Scientific & Technical
Information Springfield Va 22151

534

FOREWORD

This publication contains some of the papers to be presented at the Unguided Rocket Ballistics Meteorology Conference. Those not included here were not received by the Conference Chairman, E. J. Trawle, in time for publication. All papers are printed as received from the authors.

BLANK PAGE

CONTENTS

	Page
Empirical Determination of Drag by R. F. Filbin	1
Determination of the Sounding Rocket Configuration by George R. Conrad	41
Fin/Spin Stabilization of Unguided Launch Vehicles by A. T. Marriott and R. R. Brooks	65
New Low Cost Meteorological Rocket System for Temperature and Wind Measurement in the 75,000 to 200,000 Feet Altitude Region by Bruce Bollermann and Robert L. Walker	95
Sounding Rocket Performance Approximations by Wolfgang Schaechter	133
A Control System for Reducing the Dispersion of Multi-Stage Sounding Rockets by G. R. Conrad, H. R. Gleyre, J. Ottesen, and A. S. Hu	153
Results of Unguided Rocket Impact Predictions at WSMR by Gordon L. Dunaway	195
Recent Spectra of Atmospheric Turbulence by Niels E. Busch and Hans A. Panofsky	215
Wind Variability in Time and Space by M. Armendariz and V. D. Lang	259
Wind Profiles and Shear Derived from Smoke Trails by M. Armendariz, L. J. Rider, and G. C. Gill	285
Wind Speed Statistics Along a Hypothetical Missile Trajectory Downwind of a Sinusoidal Model Hill by Erich J. Plate, Paul Baer, and F. F. Yeh	297
Low Level Wind Study by M. D. Freeman	333
Wind Shear over Heterogeneous Terrain by E. Peterson and H. A. Panofsky	357

A Method to Compute the Effects of Wind on the Dispersion of a Vertically Launched Rocket by R. L. Ammons and C. P. Hoult 361

On Nonparametric Testing of the Nature of Certain Time Series by W. B. Miller and H. Rachele 391

A Technique for Predicting Nonlinear Wind Compensation of Ballistic Rocket Systems by G. G. Wilson 415

Project Twinkle by R. E. Gardner 431

Computer Applications to Wind Weighting and Their Limitations by Philip A. Sollow 449

Discrete Recursive Estimation; An Optimum Automated Data Processing Technique for Multi-Electronic Tracking Systems by Maceo T. Scott 491

Computation of Mean Wind Speed from Balloon Track by L. D. Duncan and B. F. Engebos 533

Blue Goose Wind Correction Analysis by Urban H. Dell. Lynch 539

Prelaunch Real-Time Impact Prediction System for the Aerobee 350 Rocket by H. Rachele and V. C. Cochran 605

Meteorological Requirements for the Aerobee - 350 by E. M. D'Arcy 617

Data Reduction Techniques for Use on Meteorological Data Above 30 Kilometers by E. P. Avara and B. T. Miers 627

EMPIRICAL DETERMINATION OF DRAG

R. F. Filbin

RAYTHEON COMPANY
Missile Systems Division
Bedford, Massachusetts

1. Introduction

During the development of the Ballistic Missile Target System a considerable effort was expended in attempts to determine the drag coefficients of gliding vehicles. Initially, it was expected that the drag coefficient would be calculated as:

$$C_D = \frac{2}{\rho V^2 S} (m \dot{V} + W \sin \gamma)$$

using values of V, $\dot{V}$, γ, and ρ provided by the missile range. It turned out that the velocity data, evaluated by differentiating radar position measurements, contained excessive scatter; and the acceleration data, obtained by differentiating the velocity data, contained so much scatter as to be useless.

During the BMTS Program it was noted that whenever range recovery crews were unable to locate an expended vehicle, a second search, guided by an extrapolation of radar position data, always resulted in vehicle recovery.

One BMTS flight was instrumented to provide independent measurements of missile position by radar and Dovap. This vehicle flew a ground range of nearly 100 nmi. Except for a short period near first stage burnout, the maximum difference in altitude and ground range at any time, as observed by the two instrumentation systems, was less than 0.02 percent. Velocity measurements of the two systems differed by as much as 20 percent.

It was concluded from the two observations (ability to extrapolate position data to impact and close agreement between independent measurements of position over a 100 mile trajectory) that the position measurements are very accurate and the procedure to be described was developed as a means of determining the drag of a ballistic vehicle on the basis of its position history and without prior knowledge of its velocity and acceleration.

2. Description of Procedure

2.1 Introduction

The observed trajectory is described by a sequence of points in the three dimensions of time, altitude, and ground range. For analysis, it is divided into segments on the basis of time. The drag coefficient, velocity, and acceleration at any instant are evaluated by computing a trajectory segment which matches the observed trajectory in the neighborhood of interest. The complete histories, from the time of motor burnout to the time when tracking is lost, are obtained as the computed histories in contiguous segments.

The task of computing trajectory segments which match the observed position history is quite simple, since preflight and flight test measurements provide accurate values for all but three of the variables in the equations of motion and even these are known with sufficient accuracy so that linear interpolation is appropriately used for their precise evaluation. It should be noted that general use of the word "interpolation" is made in this paper to indicate either interpolation or extrapolation.

The computed range, altitude, speed, and flight path angle at the end of any segment are functions only of:

a) Missile weight
b) Atmospheric properties (pressure, speed of sound, and wind velocity)
c) Vehicle position (altitude and range) at the start of the segment
d) Speed and flight path angle at the start of the segment
e) Vehicle drag coefficient

Vehicle weight is known by simply weighing each vehicle prior to launch and taking account of the propellant weight as determined by the rocket manufacturer. Atmospheric properties and the vehicle's position history are routinely and accurately measured by range personnel in support of each flight test. The only unknowns in the equations of motion are then the speed and flight path angle at the start of the segment and the vehicle drag coefficient. Approximate values for the initial speed and flight path angle can be computed from first differences in the observed position history and the approximate relation of drag coefficient as a function of Mach number is known from theoretical calculations which are necessarily made before each flight test for the purpose of impact prediction.

In the description which follows, the concept of a drag multiplier is introduced. The drag multiplier is a corrective coefficient which is applied to the assumed drag coefficient so that the product of the two is the actual drag coefficient used in the calculations. Later discussion may seem to refer to the drag coefficient as if it were a numerical constant but this is not the case. A curve displaying the usual variation with Mach number is assumed and the method provides a logical procedure for determining a sequence of corrective multipliers, each of which is appropriate to a small segment of the trajectory. In any segment, the correct multiplier is considered constant but the corrected drag coefficient is a function of Mach number.

The computer program which has been used for trajectory computations is a modified version of the TRAJ Program which was developed at White Sands Missile Range.[1] The modifications include

[1] Cochran, Vertis C.; D'Arcy, Edward M.; Ramirez, Florencio: Digital Computer Program for Five Degree of Freedom Trajectory ECOM-5036, Atmospheric Sciences Laboratory, White Sands Missile Range, New Mexico, March 1966

an additional item of input, missile range at the start of a segment, and seven additional items of output: ground range, height above sea level, total velocity, vehicle weight, drag coefficient, tangential acceleration, and normal acceleration. When a trajectory segment is computed which accurately matches the observed position history and satisfies certain tests for continuity with adjoining segments, then the histories of velocity, acceleration, and drag coefficient are read directly from the computer printout.

2.2 Description

A sequence of four steps is required to determine the drag coefficient and the velocity and acceleration histories. This sequence may need to be repeated one or more times depending on the accuracy of values used in the initial computations. The four steps are:

1) Divide the trajectory into segments on the basis of time.
2) Compute two paths between the initial and final points of each segment, one path for each of two initial velocities.
3) For each segment, determine, by linear interpolation, the characteristics of a third path which, in addition to passing through the initial and final points, passes very close to the observed midpoint of the segment.
4) Check for continuity.

The processes involved in carrying out the steps listed above are described in some detail below.

Step 1 (Figure 1)

An optimum basis for dividing the trajectory into segments has not yet been established, but two objectives of this task are readily identified and a degree of conflict between the objectives

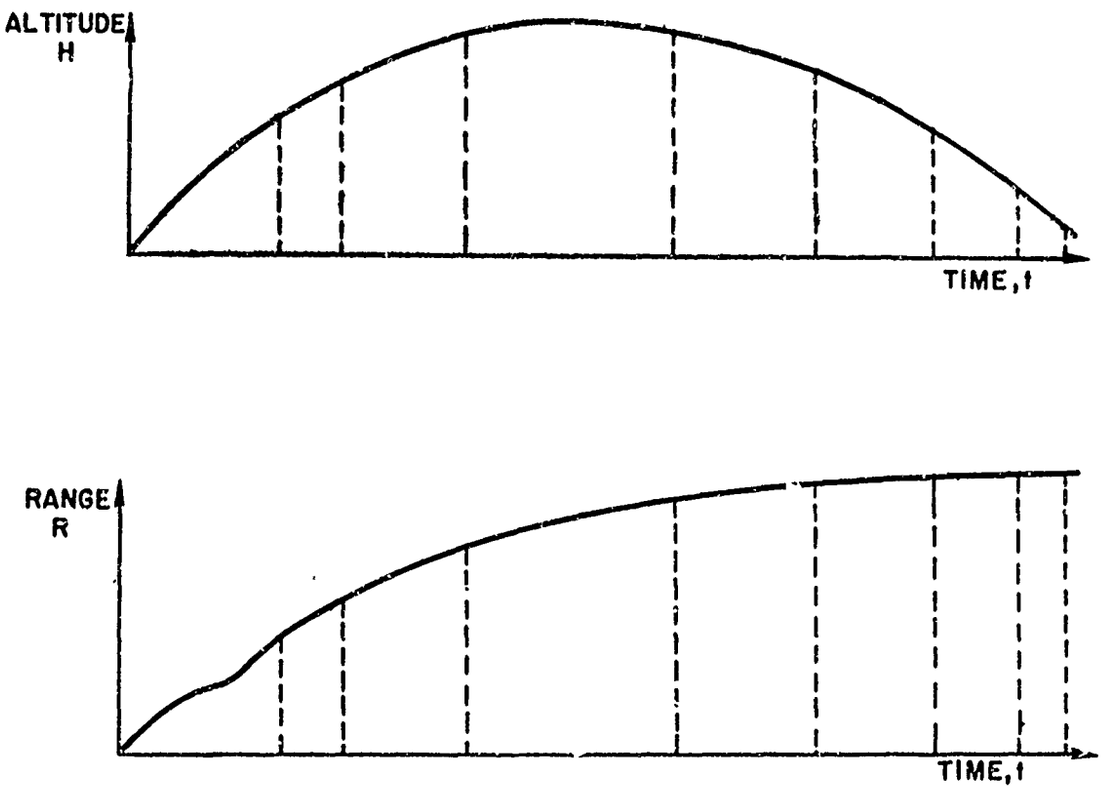

Figure 1 - Step 1 - Divide the Observed Trajectory into Segments on the Basis of Time

is apparent. First, it is desired that each segment be limited to a sufficiently small range of Mach numbers to assure the reasonableness of using a constant correction factor to the assumed drag curve. Second, it is desired that each segment cover a sufficiently long time period so that small errors in the position measurements will not be a cause for scatter or excessive uncertainty in the reduced velocity and acceleration histories.

Experience to date indicates that the segment lengths should range from about five to forty seconds, depending on altitude, as shown in Figure 1. In analyzing flights which go to very high altitudes, the entire high altitude portion should not be treated as one segment. The reason for this is that the angle-of-attack history in ascent may differ appreciably from that in descent with consequent effect on the total drag coefficient and the velocity and acceleration histories.

Step 2 (Figures 2 through 10)

To determine a path subject to the physical restraints governing ballistic flight and passing through the initial and final points of a segment, six intermediate steps are required. To compute a second path which also passes through the observed initial and final points of the segment, the same steps are repeated using a different value of initial flight speed.

1) (Figure 2)

Assume an initial value of flight speed (V_1), two values of initial flight path angle (γ_1 and γ_2), and two values of drag multiplier (D_1 and D_2). Compute four trajectory segments, one for each possible combination of drag multiplier and initial flight path angle. Typical histories of altitude versus range for the four trajectory computations are shown in Figure 2. For the cases p[illegible] the multiplier D_1 is less than the multiplier [illegible] and the computed distances travelled in the time period from t_1 to t_2 are greater with the multiplier D_1 than they are with D_2.

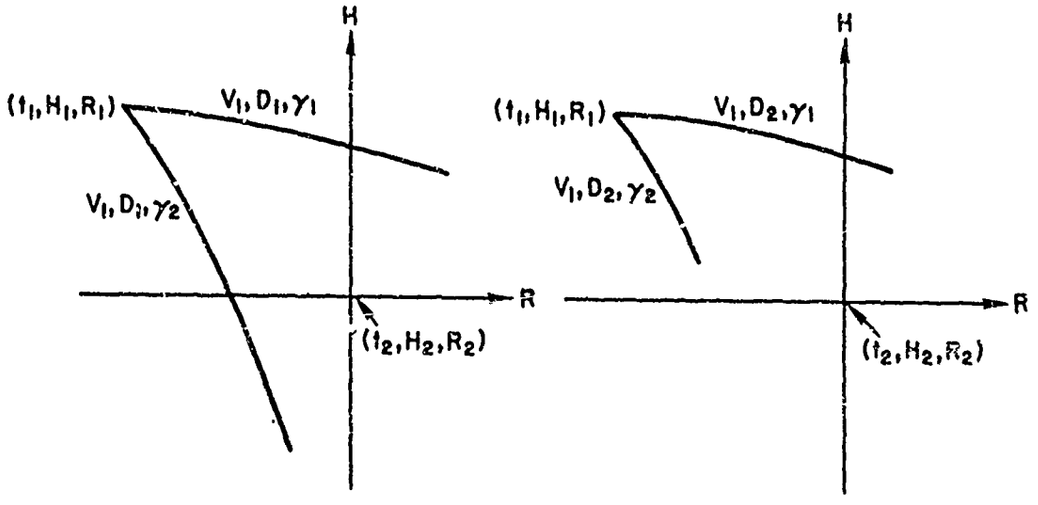

Figure 2 - Step 2(1) - Compute Four Trajectory Segments

2) (Figure 3)

As pictured in Figure 3, interpolate linearly with final altitude as the independent variable and initial flight path angle as the dependent variable to find γ_3. This is the flight path angle associated with V_1 and D_1 which, if linear interpolation is truly applicable, provides a match to the observed altitude at time t_2. Interpolate with range as the independent variable to find γ_4, also associated with V_1 and D_1, which provides a match to the observed range at t_2.

3) (Figure 4)

Repeat Step 2(2) for V_1 and D_2: find γ_5 which provides a match to the observed altitude at t_2, and find γ_6 which provides a match to the observed range at t_2. This procedure is pictured in Figure 4.

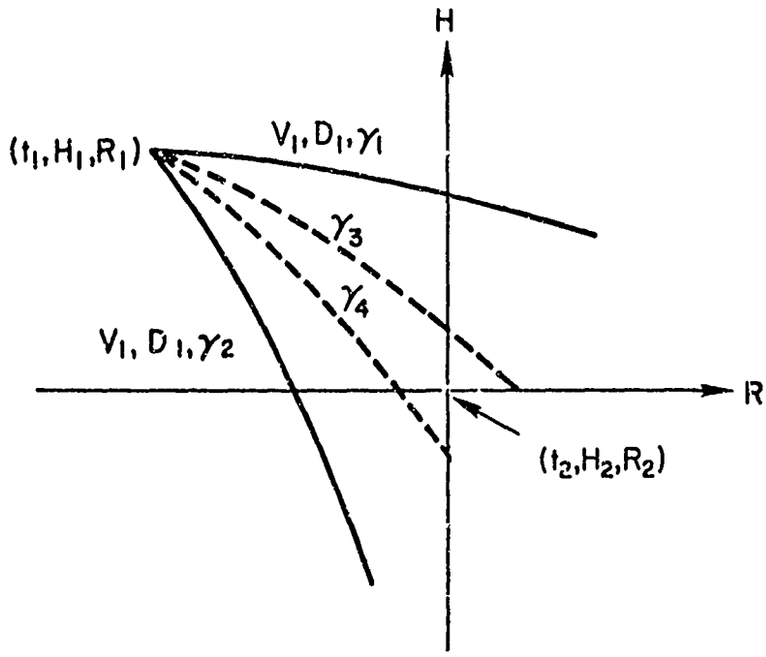

Figure 3 - Step 2(2) - Interpolate to Find the Flight Path Angles, γ_3 and γ_4, Associated with V_1 and D_1, which Provide Matching of Final Altitude and Final Range, Respectively

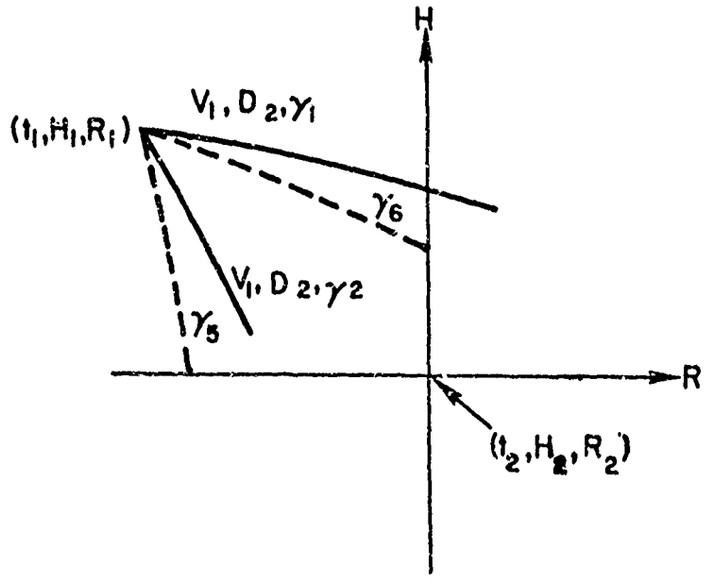

Figure 4 - Step 2(3) - Interpolate to Find the Flight Path Angles, γ_5 and γ_6, Associated with V_1 and D_2, which Provide Matching of Final Altitude and Final Range, Respectively

4) (Figure 5)

As pictured in Figure 5, consider the two combinations of drag multiplier and initial flight path angle which provide a match to the observed altitude at t_2, namely D_1, γ_3 and D_2, γ_5. Interpolate linearly with range as the independent variable and drag multiplier and flight path angle as dependent variables to find a combination of drag multiplier and flight path angle which, if linear interpolation is truly applicable, provides a match to the observed range at time t_2. Call this combination D_3, γ_7.

5) (Figure 6)

As pictured in Figure 6, consider the two combinations of drag multiplier and initial flight path angle which provide a match to the observed range at time t_2.

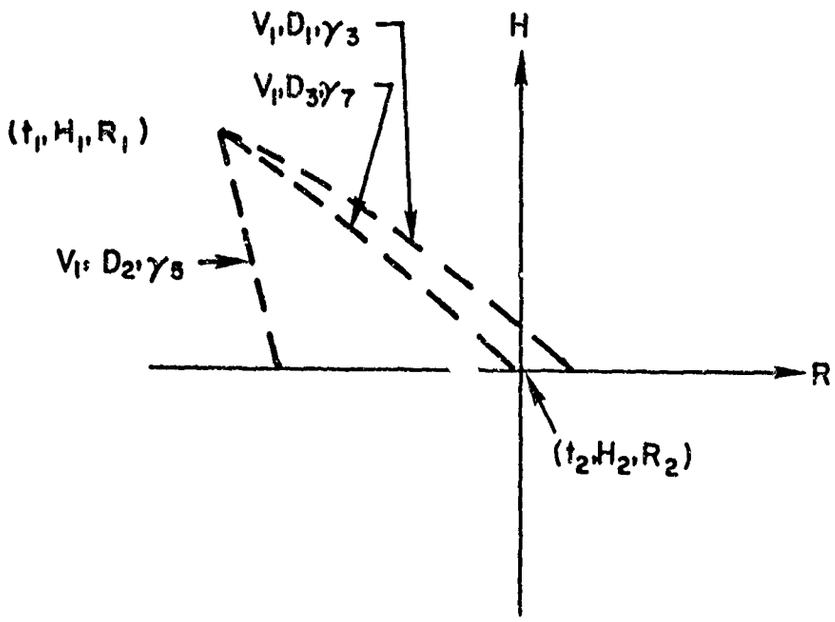

Figure 5 - Step 2(4) - Take the Two Combinations of Drag Multiplier and Flight Path Angle which Provide a Match to Final Altitude and Interpolate for Final Range

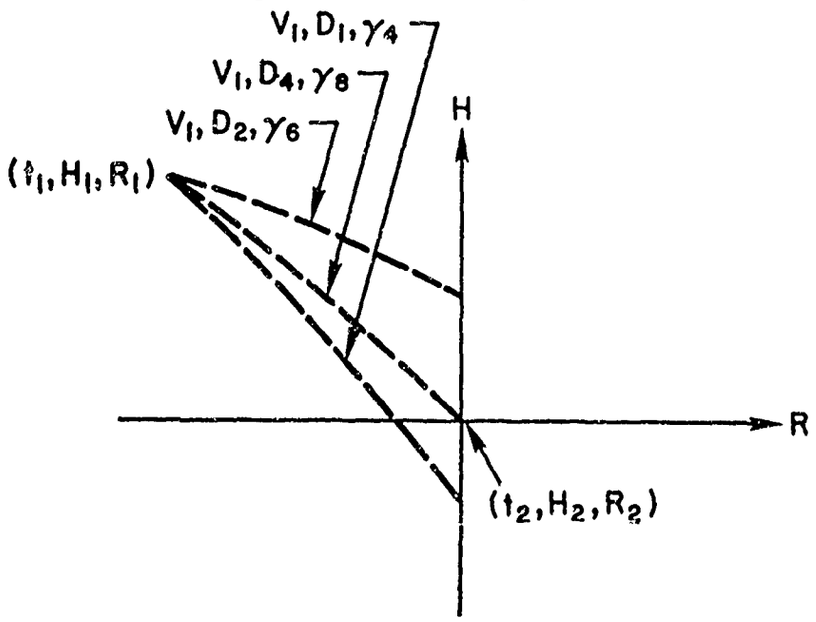

Figure 6 - Step 2(5) - Take the Two Combinations of Drag Multiplier and Flight Path Angle which Provide a Match to Final Range and Interpolate for Final Altitude

namely D_1, γ_4 and D_2, γ_6. Interpolate linearly with altitude as the independent variable and drag multiplier and initial flight path angle as dependent variables to determine a combination of multiplier and angle which provides a match to the observed altitude at t_2. Call this combination D_4, γ_8.

6) (Figure 7).

Verify that $D_3 = D_4$, $\gamma_7 = \gamma_8$, and that a computed trajectory segment which starts at (t_1, H_1, R_1) with initial speed V_1, flight path angle $\gamma_7 = \gamma_8$, and drag multiplier $D_3 = D_4$ does indeed terminate at the point (t_2, H_2, R_2). If the computed trajectory segment does not terminate at the point (t_2, H_2, R_2), then it is necessary to repeat all six of the steps listed in this section using a more appropriate choice of drag multipliers and initial flight path angles as indicated by results of the first iteration.

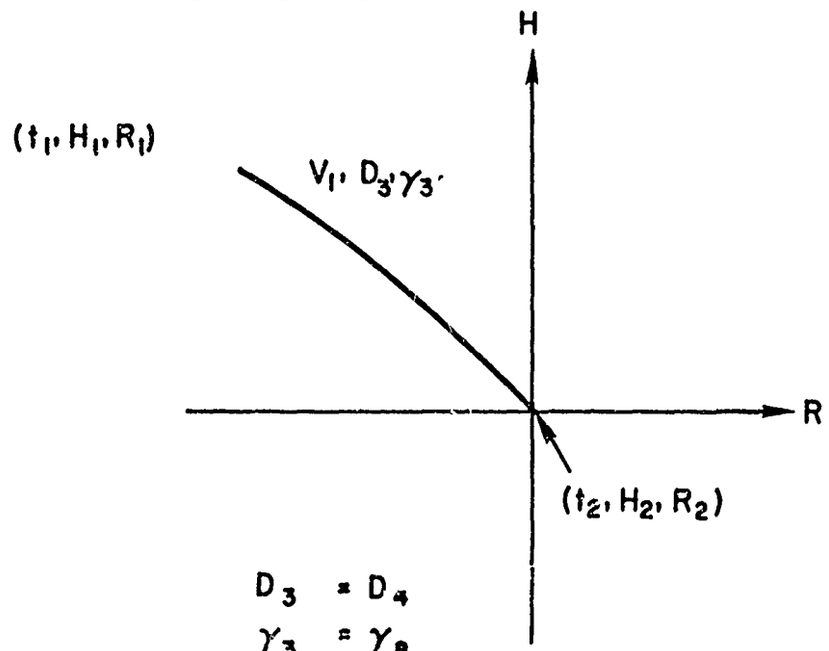

Figure 7 - Step 2 (6) - Compute a Path which Passes through the Initial and Final Points of the Segment

7) (Figure 8)

Compute a second path which also passes through the observed initial and final points of the segment by repeating steps 2 (1) through 2 (6) using a second estimate of initial speed. Associate with this path the symbols V_2, D'_3, γ'_7 for initial speed, drag multiplier, and initial flight path angle, respectively.

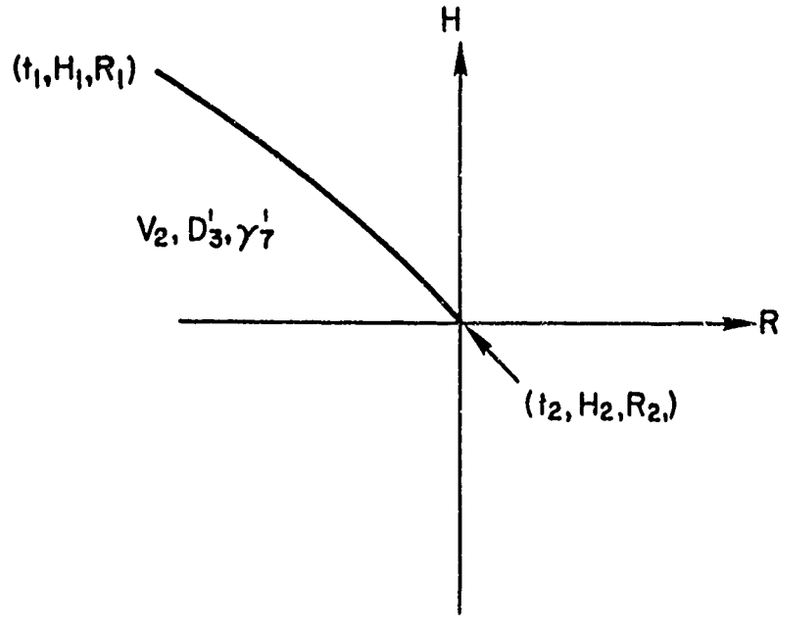

Figure 8 - Step 2 (7) - Compute a Second Path, Associated with a Second Estimate of Initial Speed, which also Passes through the Initial and Final Points of the Segment

At the conclusion of Step 2, two paths have been computed which pass through the observed initial and final points of a segment. The only differences in input for the two computations are the initial speed, initial flight path angle, and drag multiplier. Assume that one of the initial speeds used in computations is greater than the true speed at time t_1. Then the computed position history on this path provides an exact match to the observed position history only at time t_1 and t_2. At all intermediate values of time, the computed position history is always running ahead of the observed position history, as pictured in Figure 9. The discrepancy between the observed and the computed positions is greatest at, or nearly at, the midpoint of the segment. Similarly, assume that one of the initial speeds used in computations is less than the vehicle's actual speed at time t_1. Then, as pictured in Figure 10. the computed position history continually lags behind the observed position history and has a maximum error at, or nearly at, the timewise midpoint of the segment.

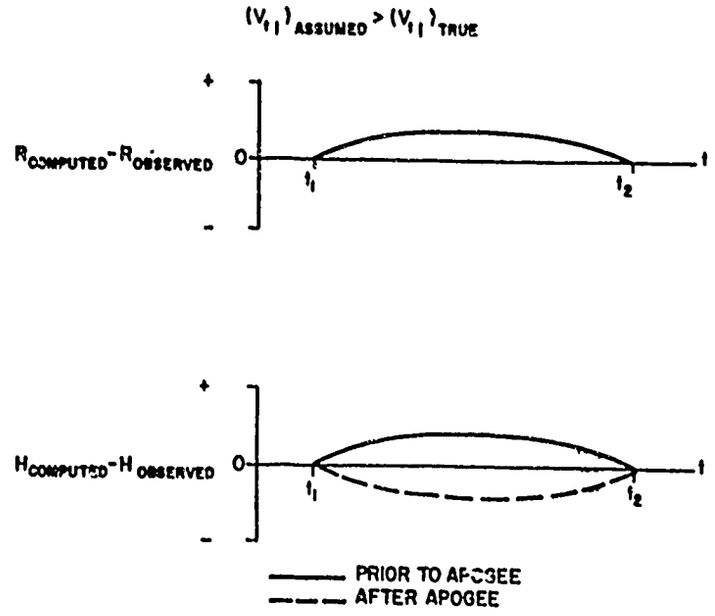

Figure 9 - Comparison of Computed and Observed Position Histories

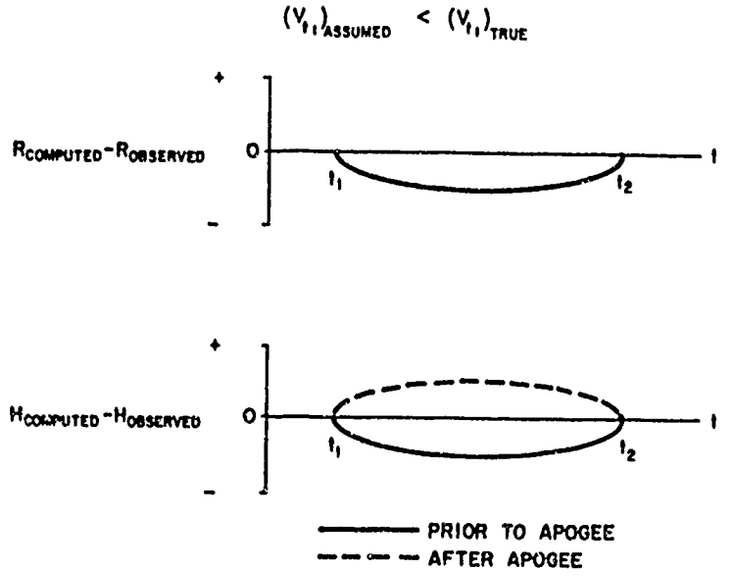

Figure 10 - Comparison of Computed and Observed Position Histories

Step 3 (a and b) (Figures 11 and 12)

The procedure for determining the characteristics of a path which, in addition to passing through the initial and final points of a segment, passes very close to the observed midpoint, is simply another exercise in linear interpolation. Denote by (t_M, H_M, R_M) the time and position coordinates on the observed trajectory where

$$t_M = \frac{1}{2} (t_1 + t_2)$$

Taking the two computed paths which pass through the observed initial and final points of the segment, interpolate as shown in Figure 11 with midpoint altitude as the independent variable to find the initial speed and the associated flight path angle and drag multiplier of a path which passes through the three points (t_1, H_1, R_1), (t_M, H_M, R_M, + δ), and (t_2, H_2, R_2). The term "δ" represents the slight range error that would occur at the midpoint attitude match. Interpolate again (Figure 12) with midpoint range as the independent variable to find the initial speed, flight path angle, and drag multiplier of a path which passes through the three points (t_1, H_1, R_1), (t_M, H_M, + ϵ, R_M), and (t_2, H_2, R_2). The term "ϵ" represents the small altitude error that would exist at the midpoint range match. Compare the two sets of answers thus obtained. Hopefully, the values of δ and ϵ are very near zero, with identical values being obtained for the two velocities. In practice a small discrepancy, in the order of ±3 fps, usually exists. This discrepancy is principally due to small errors in the observed position history.

If the two sets of data for initial speed, initial flight path angle, and drag multiplier determined by the interpolation described above are essentially identical, then the histories in this segment of flight speed, acceleration, and drag coefficient can be determined by computing a trajectory segment for which the initial speed, flight path angle, and drag multiplier are taken as the arithmetic mean of the values determined by interpolation.

If the two sets of data for initial speed, flight path angle, and drag multiplier as determined by the interpolation described in this section are not in satisfactory agreement, then the upper and lower bounds on the histories of flight speed, acceleration, and drag coefficient can be determined by making two computations, one for each set of values given by the interpolation.

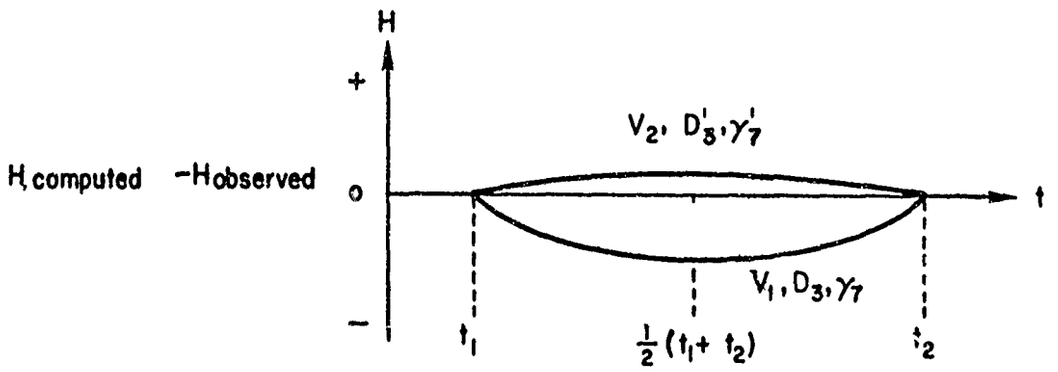

Figure 11 - Step 3(a) - Take the Two Computed Paths which Pass through the End Points of the Segment and Interpolate to Match Midpoint Altitude

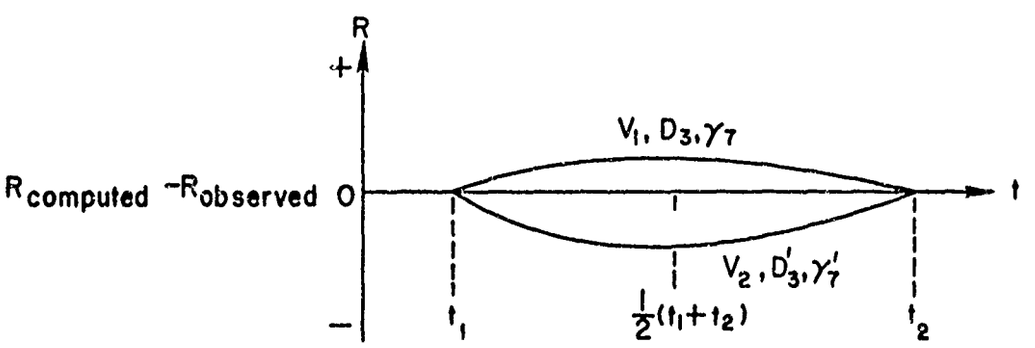

Figure 12 - Step 3(b) - Take the Two Computed Paths which Pass through the End Points of the Segment and Interpolate to Match Midpoint Range

Step 4 (Figure 13)

Having carried out Steps 2 and 3 for all of the segments which are to be analyzed, it is desirable to check for continuity. The initial speed in any segment should be equal to the computed final speed of the prior segment. The initial flight path angle for any segment should be equal to the computed flight path angle at the end of the previous segment. When these tests are satisfied, then it can truly be said that the histories of drag coefficient, velocity, and acceleration have been determined by computing trajectory segments which match the test vehicle's observed position history.

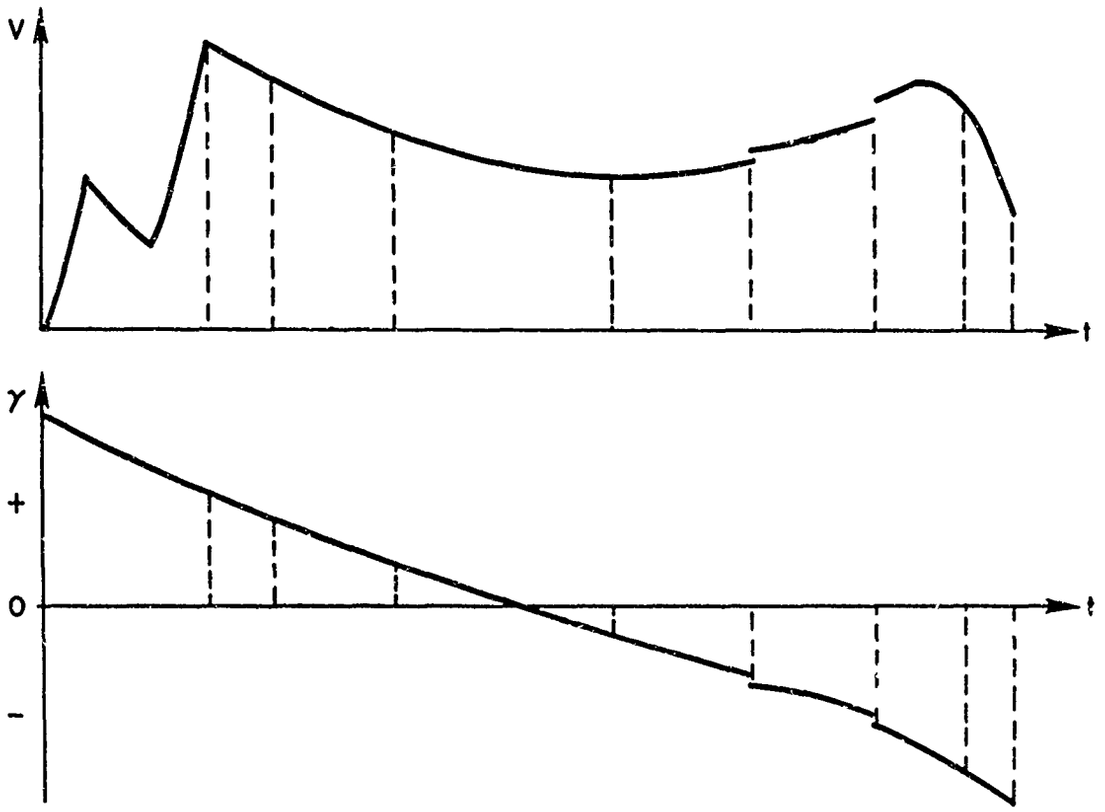

Figure 13 - Step 4 - Check for Continuity

3. Example of Procedure

To illustrate the procedure just described, it will be applied to the analysis of a portion of the trajectory flown by BMTS Round 15. This vehicle had a flight time of 272 seconds, covering a ground range of 100 nmi and reaching an apogee altitude of 250,000 feet. For the purpose of this example, we consider the portion of the trajectory shown in Figure 14. This covers the time period from 235.3 to 268.0 seconds after launch, altitudes from 118,000 to 19,000 feet, and a ground range of about 11 nmi.

Step 1

The portion of the trajectory selected for analysis was divided into four segments as shown in Figure 14. Coordinates of the observed initial and final points of each segment are listed in Table 1.

TABLE 1
TRAJECTORY COCRDINATES

Time (sec)	Altitude (feet)	Range (feet)
235.3	117,971	516,249
245.3	87,868	539,332
257.6	48,386	566,292
264.1	28,892	578,359
263.0	18,886	584,173

Step 2

To illustrate the several processes involved in determining two paths between the initial and final points of a segment we consider the time period from 257.6 to 264.1 seconds.

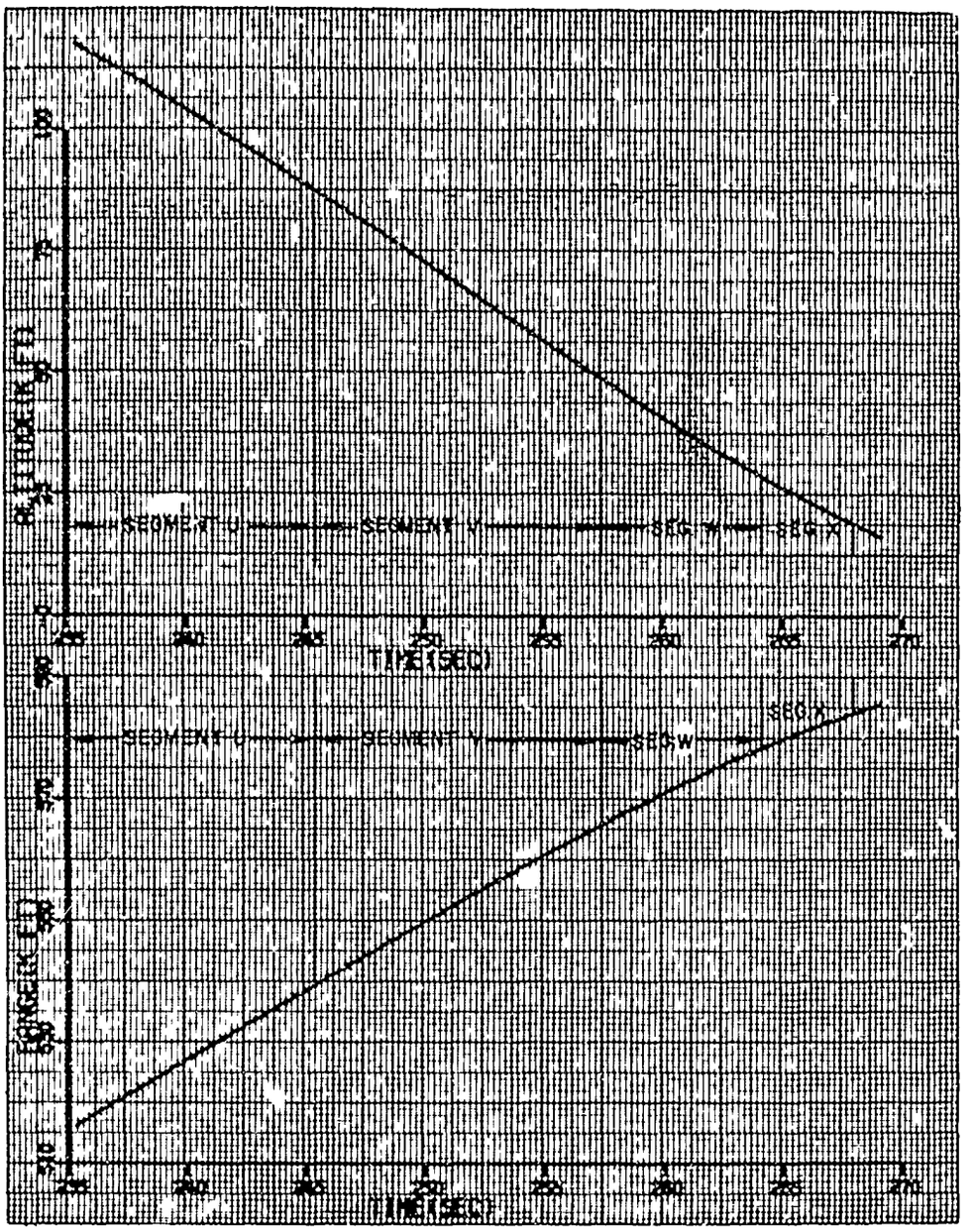

Figure 14 - BMTS Flight 15 Trajectory

Step 2(1)

An initial speed, two values of initial flight path angle, and two values of drag multiplier were assumed. Using these values, four trajectory segments were computed with results as shown in Table 2. The first column of this table refers to the trajectories shown in Figure 2.

TABLE 2

INITIAL COMPUTATIONS

V_1 = 3812 fps

Trajectory	Drag Multiplier	Initial Flight Path Angle (degrees)	Final Altitude (feet)	Final Range (feet)
V_1, D_1, γ_1	1.0	-56.3	28,892	578,873
V_1, D_1, γ_2	1.0	-59.3	28,277	577,858
V_1, D_2, γ_1	1.4	-56.3	29,509	578,472
V_1, D_2, γ_2	1.4	-59.3	28,918	577,486

Step 2(2)

Consider the trajectories associated with V_1 and D_1. Interpolate linearly to determine the flight path angle which would provide a computed trajectory segment terminating at the observed final altitude. Make a second interpolation to find the flight path angle giving the observed final range. These interpolations are shown in Figure 3 and in Table 3 where the observed final altitude and final range are underlined for clarity.

TABLE 3

DETERMINATION OF FLIGHT PATH ANGLES TO MATCH FINAL ALTITUDE AND RANGE, RESPECTIVELY
V_1 = 3812 fps D_1 = 1.0

Trajectory	Initial Flight Path Angle (degrees)	Final Altitude (feet)	Final Range (feet)
V_1, D_1, γ_1	-56.3	28,892	578,873
V_1, D_1, γ_3	-56.301	28,892	578,872
V_1, D_1, γ_4	-57.819	28,581	578,359
V_1, D_1, γ_2	-59.3	28,277	577,858

Step 2(3)

Interpolate to find the flight path angles associated with V_1 and D_2 which provide a match to the observed final altitude and final range, respectively. This step is illustrated in Figure 4 and Table 4.

TABLE 4

DETERMINATION OF FLIGHT PATH ANGLES TO MATCH FINAL ALTITUDE AND RANGE, RESPECTIVELY
V_1 = 3812 fps D_2 = 1.4

Trajectory	Initial Flight Path Angle (degrees)	Final Altitude (feet)	Final Range (feet)
V_1, D_2, γ_1	-56.3	29,509	578,472
V_1, D_2, γ_5	-59.435	28,892	577,442
V_1, D_2, γ_6	-56.644	29,441	578,359
V_1, D_2, γ_2	-59.3	28,918	577,486

Step 2(4)

Consider the two combinations of drag multiplier and flight path angle which provide a match to final altitude and interpolate for final range, as shown in Figure 5 and Table 5.

TABLE 5
DETERMINATION OF FLIGHT PATH ANGLE AND DRAG MULTIPLIER TO MATCH FINAL RANGE
V_1 = 3812 fps

Trajectory	Drag Multiplier	Initial Flight Path Angle (degrees)	Final Altitude (feet)	Final Range (feet)
V_1, D_1, γ_3	1.0	-56.301	28,892	578,872
V_1, D_3, γ_7	1.1436	-57.426	28,892	578,359
V_1, D_2, γ_5	1.4	-59.435	28,892	577,442

Step 2(5)

Consider the two combinations of drag multiplier and flight path angle which provide a match to final range and interpolate for final altitude, as shown in Figure 6 and Table 6.

TABLE 6
DETERMINATION OF FLIGHT PATH ANGLE AND DRAG MULTIPLIER TO MATCH FINAL ALTITUDE
V_1 = 3812 fps

Trajectory	Drag Multiplier	Initial Flight Path Angle (degrees)	Final Altitude (feet)	Final Range (feet)
V_1, D_1, γ_4	1.0	-57.819	28,581	578,359
V_1, D_4, γ_8	1.1447	-57.394	28,892	578,359
V_1, D_2, γ_6	1.4	-56.644	29,441	578,359

Step 2(6)

At this point it is necessary to verify that $D_3 = D_4$ and $\gamma_7 = \gamma_8$. Comparing entries in Tables 5 and 6 the drag multipliers are seen to differ by 0.09 percent and the initial flight path angles by 0.032 degrees. A computed segment using the values of drag multiplier and flight path angle given in Table 5 was found to terminate eight feet low in altitude and seven feet short in range. A computation with the values shown in Table 6 ended one foot high in altitude and three feet long in range. As percentages of the observed altitude change in this segment, more than 19,000 feet, and the observed change in ground range, almost 2 nmi, these are very small errors. However, for the purpose of demonstrating the appropriateness of linear interpolation in this procedure, the errors were considered excessive and a second iteration was carried out using a more appropriate selection of drag multipliers and flight path angles as indicated by the interpolations in Tables 5 and 6. Results of the second iteration are shown in the second part of Table 7; the first part of this table will be recognized as a summary of data previously shown in Tables 2 through 5.

The second iteration to determine the combination of drag multiplier and initial flight path angle which, together with the assumed initial speed of 3812 fps, provide an accurate match to the final coordinates of the segment, resulted in a discrepancy of only 0.02 percent in drag multiplier and no difference in the two values for initial flight path angle. The two drag multipliers were simply averaged and it was verified that the combination

$$V_1 = 3812 \text{ fps}, \; D_3 = D_4 = 1.1442, \; \gamma_7 = \gamma_8 = -57.401 \text{ deg}$$

does indeed provide a precise match to the observed time, altitude, and range coordinates of the segment end point. This is shown in Figure 15 where

TABLE 7

INTERPOLATIONS TO MATCH ENDPOINT COORDINATES

V_1 = 3812 fps

Drag Multiplier	Initial Flight Path Angle (degrees)	Final Flight Path Angle (degrees)	Final Speed (fps)	Final Altitude (ft MSL)	Final Range (feet)
FIRST ITERATION					
1.0000	-56.300	-58.117	3258.	28892.	578873.
	-56.301	-58.118	3258.	28892.	578872.
	-57.819	-59.562	3256.	28581.	578359.
1.0000	-59.300	-60.971	3254.	28277.	577858.
1.4000	-56.300	-58.178	3032.	29509.	578472.
	-59.435	-61.156	3025.	28892.	577442.
	-56.644	-58.505	3031.	29441.	578359.
1.4000	-59.300	-61.028	3025.	28918.	577486.
1.0000	-56.301	-58.118	3258.	28892.	578872.
1.1436	-57.426	-59.208	3174.	28892.	578359.
1.4000	-59.435	-61.156.	3025.	28892.	577442.
1.0000	-57.819	-59.562	3256.	28581.	578359.
1.1447	-57.394	-59.180	3175.	28892.	578359.
1.4000	-56.644	-58.505	3031.	29441.	578359.
SECOND ITERATION					
1.1300	-57.360	-59.145	3179.	28877.	578388.
	-57.287	-59.076	3179.	28892.	578412.
	-57.443	-59.225	3179.	28861.	578359.
1.1300	-57.460	-59.240	3179.	28858.	578354.
1.1500	-57.360	-59.148	3168.	28910.	578367.
	-57.448	-59.232	3168.	28892.	578338.
	-57.384	-59.171	3168.	28905.	578359.
1.1500	-57.460	-59.243	3168.	28889.	578334.
1.1300	-57.287	-59.076	3179.	28892.	578412.
1.1443	-57.401	-59.187	3171.	28892.	578359.
1.1500	-57.448	-59.232	3168.	28892.	578338.
1.1300	-57.443	-59.225	3179.	28861.	578359.
1.1441	-57.401	-59.187	3171.	28892.	578359.
1.1500	-57.384	-59.171	3168.	28905.	578359.

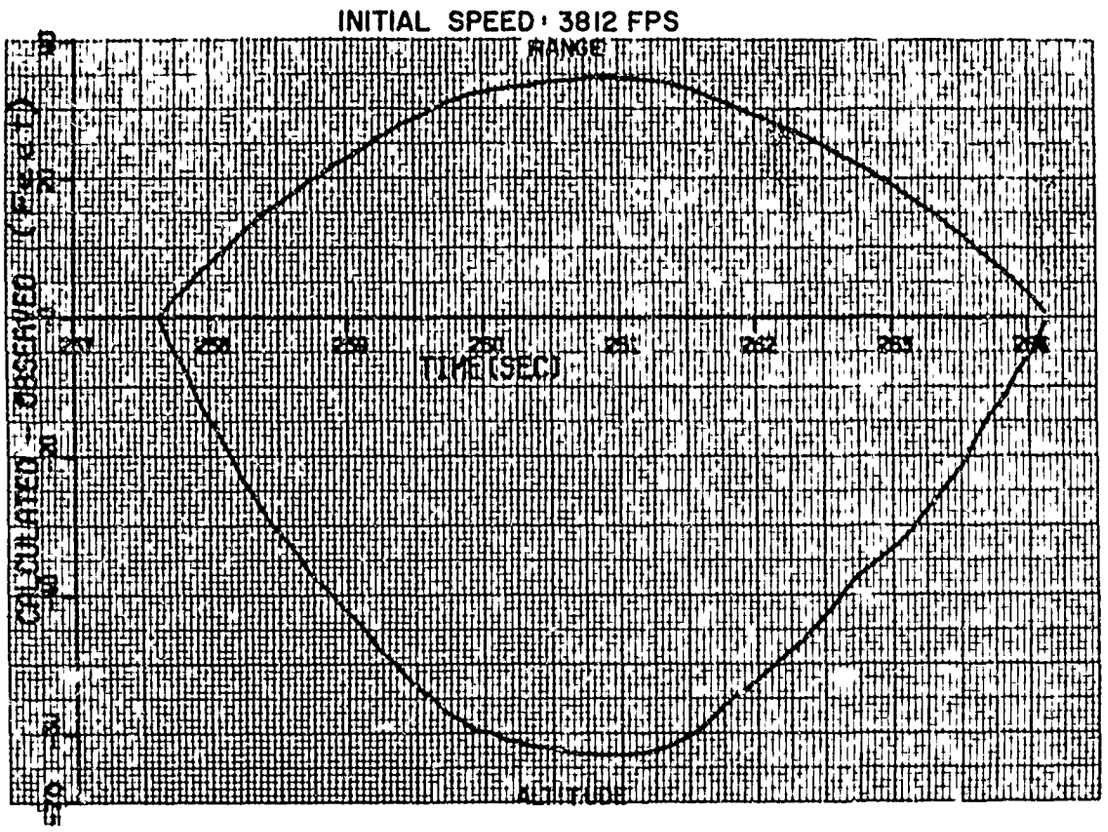

Figure 15 - Comparison of Computed (calculated) and Observed Position Histories

the differences between the observed and computed altitude and between the observed and computed range in this segment are plotted as functions of time. It is seen that the computed position history runs continually ahead of the observed position history. This clearly shows that the assumed initial speed of 3812 fps is greater than the vehicle's actual speed at the initial point of the segment.

Step 2(7)

To compute a second path between the observed initial and final points of the segment, an initial flight speed of 3782 fps was assumed. The computations which were made to determine the correct combination of drag multiplier and initial flight path angle associated with this initial speed are summarized in Table 8. Again, the initial choice of multipliers and flight path angles was quite different from the interpolated results and a second iteration was carried out using a more appropriate range of these variables.

Step 3

The two computed paths which pass through the segment end points were studied at the midpoint value of time, 260.8 seconds. Linear interpolations were made to find the values of initial speed, flight path angle, and drag multiplier that would match the midpoint altitude and midpoint range, respectively. These interpolations are pictured in Figures 11 and 12, respectively, and numerical values are shown in Table 9 where the observed midpoint altitude and midpoint range are underlined for clarity.

TABLE 8

INTERPOLATIONS TO MATCH ENDPOINT COORDINATES

V_2 = 3782 fps

Drag Multiplier	Initial Flight Path Angle (degrees)	Final Flight Path Angle (degrees)	Final Speed (fps)	Final Altitude (ft MSL)	Final Range (feet)
FIRST ITERATION					
0.6000	-56.300	-58.068	3495.	28369.	579211.
	-53.842	-55.727	3496.	28892.	580062.
	-58.760	-60.412	3494.	27845.	578359.
0.6000	-59.300	-60.926	3494.	27730.	578172.
1.0000	-56.300	-58.129	3238.	29030.	578780.
	-56.981	-58.777	3238.	28892.	578552.
	-57.554	-59.322	3237.	28775.	578359.
1.0000	-59.300	-60.983	3234.	28420.	577773.
0.6000	-53.842	-55.727	3496.	28892.	580062.
1.0510	-57.381	-59.166	3205.	28892.	578359.
1.0000	-56.981	-58.777	3238.	28892.	578552.
0.6000	-58.760	-60.412	3494.	27845.	578359.
1.0502	-57.403	-59.186	3204.	28892.	578359.
1.0000	-57.554	-59.322	3237.	28775.	578359.
SECOND ITERATION					
1.0400	-57.340	-59.125	3213.	28877.	578395.
	-57.267	-59.056	3213.	28892.	578419.
	-57.446	-59.226	3213.	28855.	578359.
1.0400	-57.440	-59.220	3213.	28856.	578361.
1.0600	-57.340	-59.128	3201.	28908.	578375
	-57.423	-59.207	3201.	28892.	578347
	-57.386	-59.172	3201.	28899.	578359.
1.0600	-57.440	-59.223	3201.	28888.	578342.
1.0400	-57.267	-59.056	3213.	28892.	578419.
1.0566	-57.396	-59.181	3203.	28892.	578359.
1.0600	-57.423	-59.207	3201.	28892.	578347.
1.0400	-57.446	-59.226	3213.	28855.	578359.
1.0567	-57.396	-59.181	3203.	28892.	578359.
1.0600	-57.386	-59.172	3201.	28899.	578359.

TABLE 9

DETERMINATION OF INITIAL SPEED, FLIGHT PATH ANGLE, AND DRAG MULTIPLIER TO MATCH MIDPOINT ALTITUDE AND RANGE, RESPECTIVELY

Trajectory	Initial Speed	Drag Multiplier	Initial Flight Path Angle	Midpoint Altitude	Midpoint Range
V_1, D_3, γ_7	3812	1.1442	-57.401	38,386	572,586
	3768.0	1.0172	-57.394	38,449	572,547
	3774.2	1.0332	-57.395	38,441	572,552
V_2, D_3', γ_7'	3782	1.0566	-57.396	38,429	572,559

The results given in Table 9 indicate that both of the initial speeds assumed for this example are too high. Are the extrapolations in Table 9 valid? To answer this question, Step 2 was repeated, using as new estimates of initial speed, the extrapolated values in Table 9. Results of the second iteration through Steps 2 and 3 are summarized in Table 10. The second iteration provides a more accurate set of values but the improvement is everywhere less than 0.22 percent.

The two sets of answers in Table 10 are not identical: if one selects the combination of speed, multiplier and angle which provides an exact match to the observed end points and to the midpoint altitude, then an error of 5 feet in midpoint range must be accepted. If one selects the combination of speed, multiplier, and angle which provides an exact match to the midpoint range, then an error of 8 feet in midpoint altitude must be accepted. These position errors are considered indicative of the accuracy of position measurements in this segment. The interpolated values for initial speed, 3769.0 and 3774.3 fps, indicate probable upper and lower bounds of the vehicle's actual speed at time 257.6 seconds.

TABLE 10

INTERPOLATION TO MATCH MIDPOINT COORDINATES

First Iteration				
Initial Speed	Drag Multiplier	Initial Flight Path Angle	Midpoint Altitude	Midpoint Range
3782	1.0566	-57.396	38,429	572,559
3768.0	1.0172	-57.394	38,449	572,547
3774.2	1.0332	-57.395	38,441	572,552
3812	1.1442	-57.401	38,386	572,586
Second Iteration				
Initial Speed	Drag Multiplier	Initial Flight Path Angle	Midpoint Altitude	Midpoint Range
3768.0	1.0169	-57.394	38,450	572,546
3769.0	1.0194	-57.394	38,449	572,547
3774.3	1.0350	-57.395	38,441	572,552
3774.2	1.0348	-57.395	38,441	572,552

An initial speed in the range 3769 to 3774 fps was arbitrarily selected, the associated drag multiplier and initial flight path angle were determined by linear interpolation between values listed in Table 10, and a trajectory segment was computed with

$$V = 3770 \text{ fps} \qquad \gamma = -57.394 \text{ deg}, \qquad D = 1.0224$$

The differences between the computed and observed altitude and between computed and observed range are shown in Figure 16. Nowhere does the computed altitude or range deviate from the measured value by more than five feet. A comparison of Figure 16 with Figure 15 shows the improvement gained. yet the initial speed for the computations associated with Figure 15 was chosen less than the speed determined at the missile range from Dovap data.

INITIAL SPEED = 3770 fps

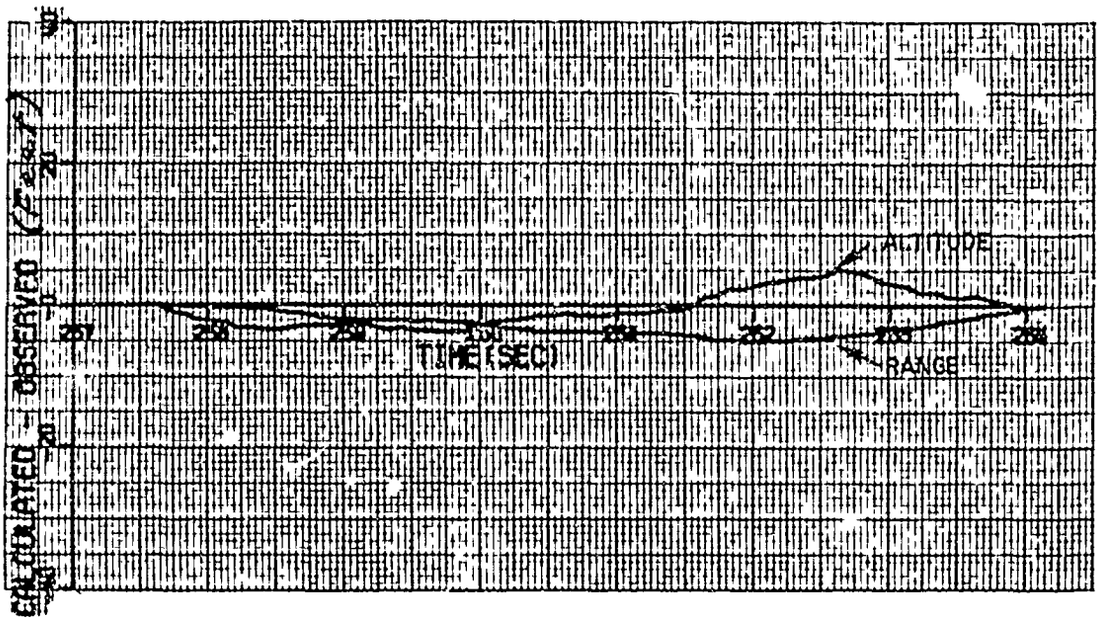

Figure 16 - Comparison of Computed (calculated) and Observed Position Histories

Step 4

After Steps 2 and 3 have been carried out for each of the segments to be analyzed, the results can be arranged in a format to facilitate checking for continuity. One such arrangement is shown in Table 11.

TABLE 11
CHECK FOR CONTINUITY

Segment	Trajectory Matches Endpoints and	Initial Speed	Final Speed
U	midpoint altitude midpoint range	3691 3697	3888 3879
V	midpoint altitude midpoint range	3879 3885	3770 3760
W	midpoint altitude midpoint range	3769 3774	3217 3212
X	midpoint altitude midpoint range	3200 3215	2725 2712

The final velocity of each segment should be equal to the initial velocity of the succeeding segment. The range of uncertainty indicated in Table 11 is very small, never more than 0.5 percent of the lower probable value. With such small differences, it is probably not possible to achieve increased accuracy by selecting a path on which the computed speed at the end of one segment is exactly equal to the initial speed of the succeeding segment. However, if Table 11 were to show any appreciable discrepancies, as it would if there were significant scatter in the position measurements, then the path of continuous flight speeds would provide a reasonable determination of the actual history.

The drag which had been used for the initial trajectory matching was modified in the following way:

a. A path of continuous flight speeds through the four segments under study was selected.

b. The drag multipliers associated with this path were plotted as functions of Mach number and a smooth curve was faired through the points.

c. Each entry in the original drag table was multiplied by the appropriate correction factor.

The correction factors determined in this way ranged from 1.01 at Mach number 4.0 to 1.08 at Mach 2.6. The drag coefficient determined by this procedure is shown in Figure 17. The extent to which this single-valued curve fits the observed position history will be considered in the following section.

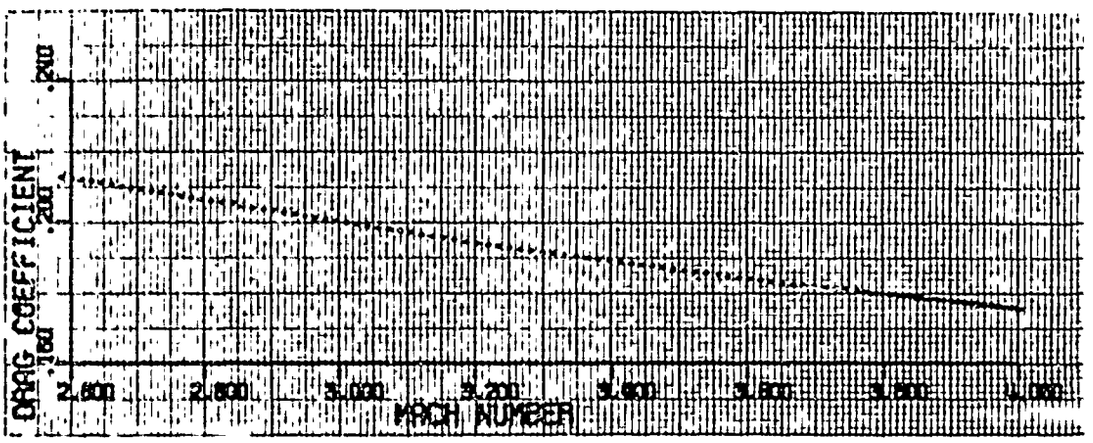

Figure 17 - Drag Coefficient vs Mach Number

4. Comparison with Dovap and Radar Tracking Data

The corrected drag curve was used to compute four trajectory segments which closely match the measured position history in the time period under consideration. Adequacy of the matching achieved is shown in Figure 18 in which the computed position history is compared with that measured by Dovap. The maximum difference is 15 feet, a very small part of the measured position change which exceeds 120,000 feet in this time interval.

The computed history of flight speed is compared in Figure 19, with the flight speed determined by Dovap. The Dovap speed history is continuous but ranges from 45 to 30 fps greater than the computed speed. Since the computed speed does indeed match the position history, the speed reported by Dovap must be considered excessive with an average error in this interval of about 1 percent. Errors of this magnitude are, of course, not important for the purpose of practical determination of vehicle drag coefficient.

The computed history of flight speed is compared in Figure 20 with the speed determined at the missile range by numerical differentiation of radar position data. The radar speed is reasonably continuous only in the period from 258 to 266 seconds, less than 25 percent of the interval chosen for study. Where the radar speed is continuous, it displays an average error of only 1.5 percent, which is certainly accurate enough for most practical purposes. However, where there is considerable scatter in the reported flight speed, any automatic procedure of data processing would indicate that very large positive and negative accelerations are occurring and a determination of drag coefficient could not be made.

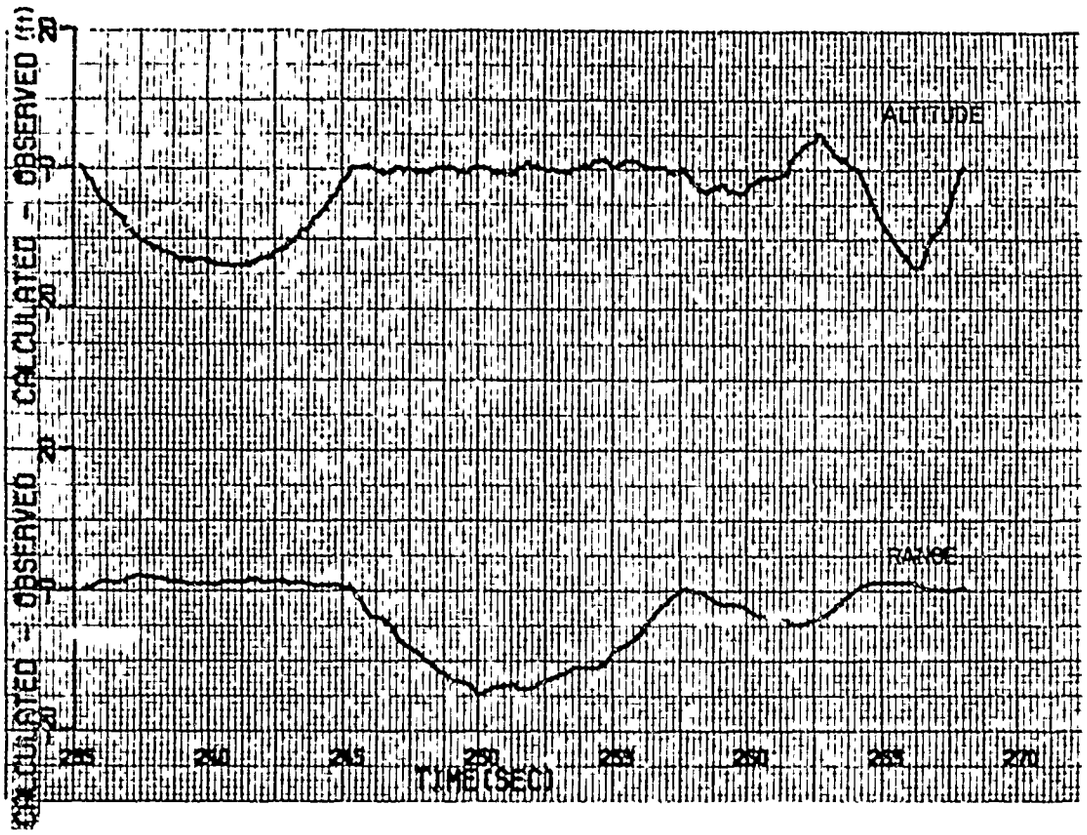

Figure 18 - Comparison of Computed (calculated) and Doyap (observed) Position Data

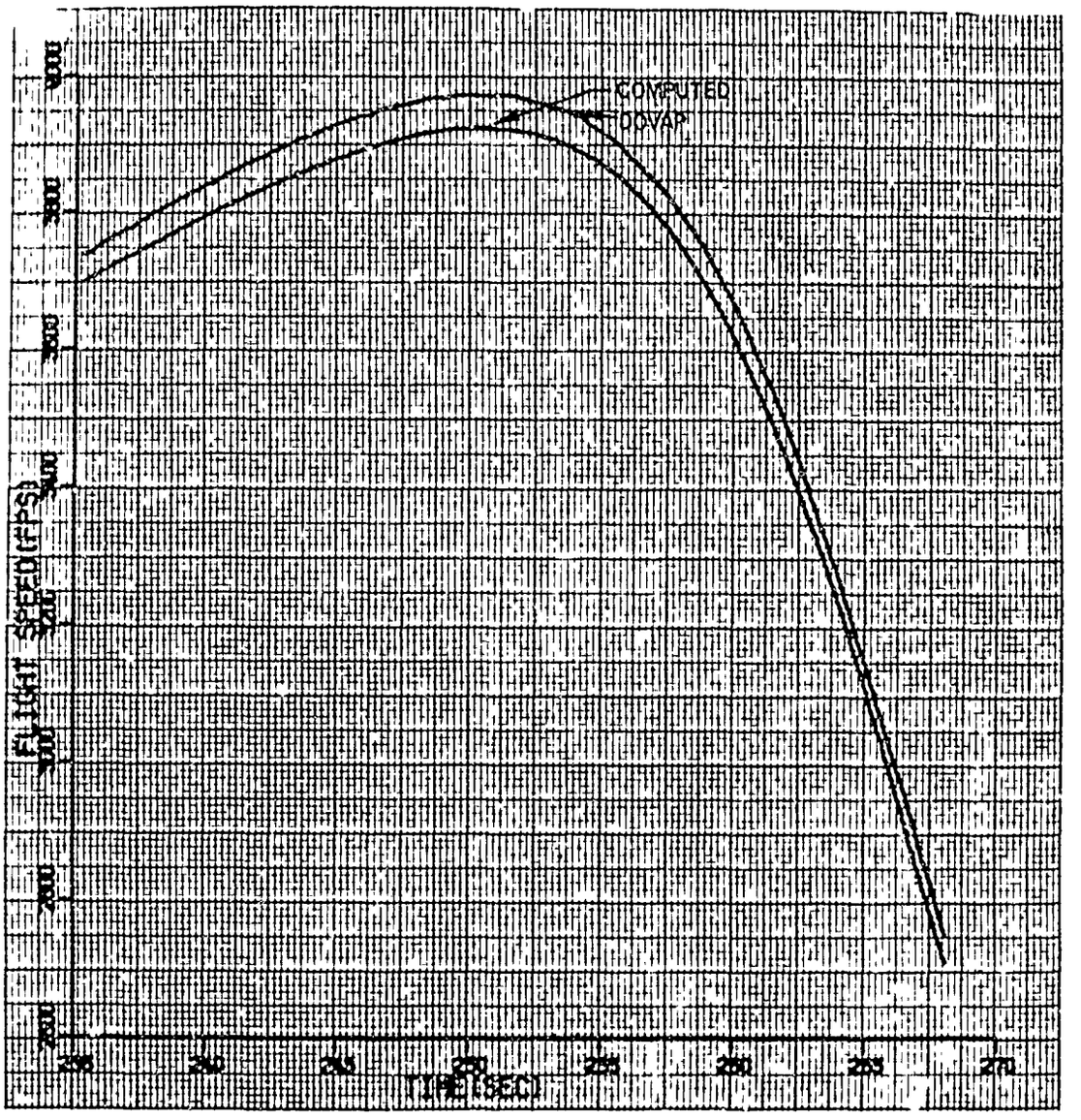

Figure 19 - Flight Speed vs Time
Computed and Measured by Dovap

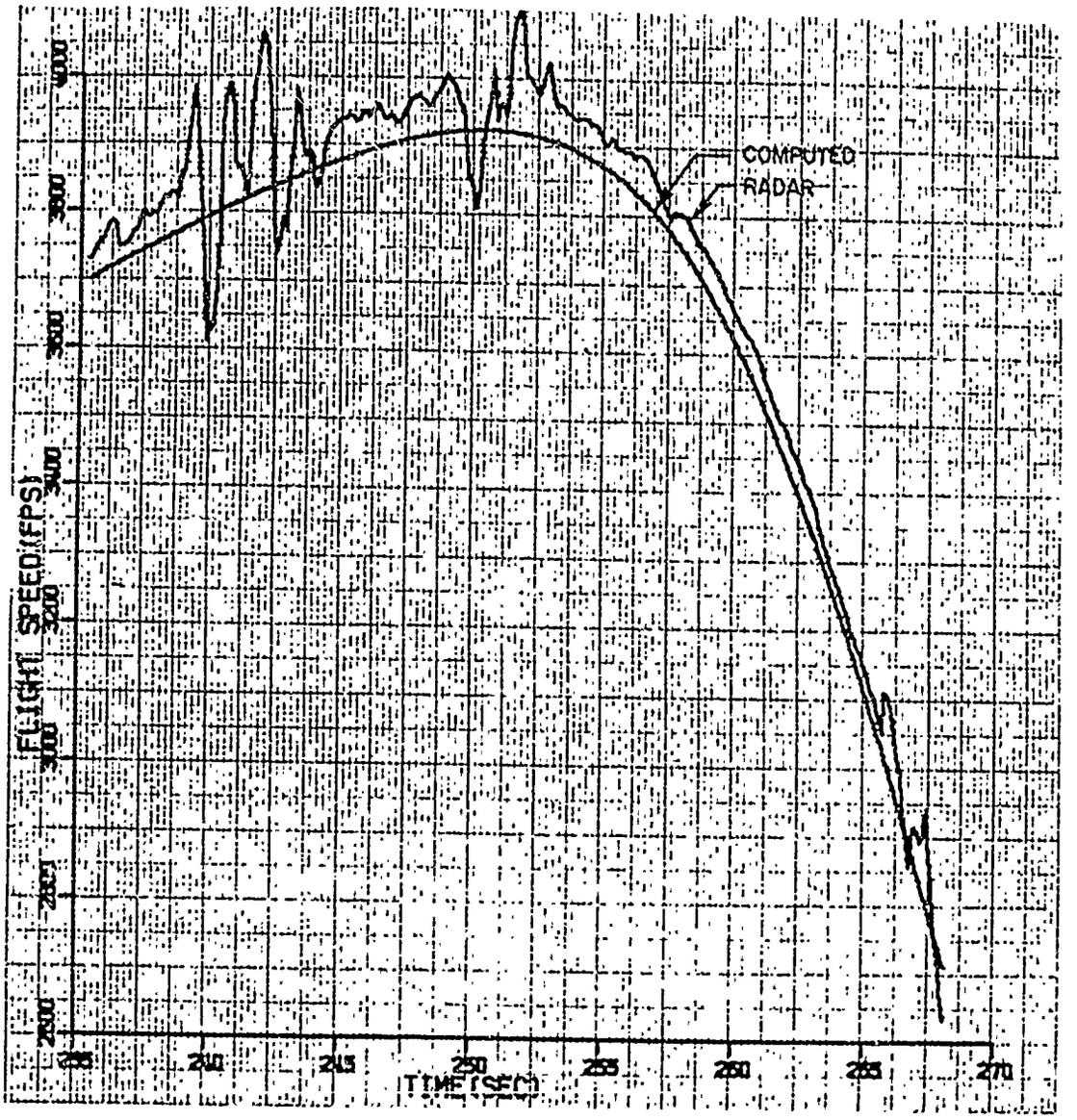

Figure 20 - Flight Speed vs Time
Computed and Measured by Radar

5. Conclusions

A procedure has been described which utilizes position measurements, the flight test data most frequently and most accurately obtained at the missile range, and permits determination of velocity histories to a greater accuracy than is presently obtained by either direct measurement or numerical differentiation of position data. Simultaneously, the procedure provides highly accurate records of vehicle acceleration and drag.

BLANK PAGE

DETERMINATION OF THE SOUNDING ROCKET CONFIGURATION

by

George R. Conrad

The design of a sounding rocket to accomplish a specific mission or series of missions may be quite simple and straightforward or agonizingly complex. To stretch a point, the selection of an existing vehicle design for a new application constitutes "determination of a configuration." This may not involve a process of design in the usual sense, but rather a thorough survey and assessment of available hardware and technology. Such action is as much to be applauded as the development of a new vehicle, if wisely implemented, since major economies can be thus achieved.

This paper addresses the problem of new vehicle design, which is the other extreme in determining a configuration.

The design of a new rocket vehicle is an iterative process, because of the broad variety of influencing factors, many of which are interdependent. Quite often, the originator of the mission requirements has only gross knowledge of these requirements, such as estimates of the payload weight and performance ranges. These are the crucial inputs to initiation of a vehicle design.

The following discussion of the design process assumes that the sounding rocket is characterized as a ballistic vehicle, i.e., the flight path is controlled only by launcher aim, and the flight paths are to be of the near-vertical type. The design will be discussed in four steps, largely serial in nature but not exclusively so; these are: (I) Vehicle "Sizing", (II) Configuration Selection, (III) Detail Design, and (IV) Testing.

I. Vehicle "Sizing"

With the minimum input information available, a first approximation of the vehicle size can be determined by utilization of the impulse-momentum equation which yields the well known vacuum velocity relationship:

$$\Delta V = I_{sp} g \ln \frac{Mg}{Mo} \tag{1}$$

where, ΔV = velocity increment in vacuum, no gravity field

g = acceleration due to gravity at earth surface

I_{sp} = propellant specific impulse

Mg = vehicle gross weight

Mo = vehicle burnout weight

and

$$Mg = \bar{M} + Mm + M_T \tag{2}$$

$$Mo = Mg - M_p \tag{3}$$

with

M_p = propellant weight

$\bar{M}$ = payload weight

M_T = loaded motor weight

M_m = miscellaneous inert weight

$\frac{M_p}{M_T} = \xi$ = motor mass fraction

Equation (1) can be employed after the performance requirements, usually expressed in terms of zenith altitude and/or time interval above some altitude, have been converted to burnout velocity by means of the simple uniform acceleration equations for translational motion. It should be emphasized at this point that although many simplifying assumptions are made, such as constant gravity after burnout, constant rocket exhaust velocity, no aerodynamic drag and no gravity loss during burning, the simple equations presented are most useful as a starting point.

These relations permit use of two powerful descriptive parameters for any propulsion unit, the specific impulse I_{sp} and the mass fraction ξ. Current technology has yielded I_{sp} values of 290 $\frac{\#\text{-sec}}{\#}$ for solid propulsion units, and greater than 300 $\frac{\#\text{-sec}}{\#}$ for liquid units. These are the exception rather than the rule, however, and for most motors suitable for sounding rocket applications an I_{sp} of 200-220 is suggested as more representative. Mass fraction values in excess of 0.90 have been achieved, but again, for sounding rockets, values of the order of 0.7 are more realistic. The use of advanced "state of the art" values at this point will tend to restrict the choice of available propulsion units, and leave insufficient margin to cope with the toll in performance from drag and gravity losses.

The value of the payload weight $\overline{M}$ should be large enough to include ancillary items which are often not included in the initial payload weight figure, e.g., tracking aids, safety command receivers, programmers. The miscellaneous weight M_m is included to account for such inert weight items as fin assemblies and payload airframe components. The miscellaneous weight can vary greatly, depending on the mission, but a value of 25 to 30% of the loaded motor weight is representative.

The "sizing" process can usually be accomplished by manual computations, and initially should assume a single stage rocket. At this point "real" motor performance characteristics must be compared against the first "sizing" approximation. There may be a severe discrepancy between computed and practical motor properties, indicating a need for a multi-stage rocket design.

Equation (1) can still be used for this purpose, by expanding it to yield discreet terms for each stage as shown:

$$\Delta V = I_{sp_1} g \ln \frac{M_{g1}}{Mo_1} + I_{sp_2} g \ln \frac{M_{g2}}{Mo_2}$$

$$+ \cdots\cdots\cdots + I_{sp_n} g \ln \frac{M_{gn}}{M_{on}}, \qquad (4)$$

where the weight values used properly describe the sums of all stages making up the vehicle at any point in time. For multi-stage rockets, equation (4) has been utilized to develop criteria for the optimum weight for each stage. Typical of these optimization techniques is one published by Weisbord, (Ref. 1) wherein the partial derivatives from Equation (4),

$$\frac{\partial M_{g1}}{\partial M_{g2}} = 0, \qquad \frac{\partial M_{g1}}{\partial M_{g3}} = 0, \text{ etc,}$$

are obtained and further manipulations are performed to yield a series of relationships for $\left(\frac{\bar{M}}{M_{gn}}\right)_{(max)}$ and $\left(\frac{M_{gn}}{M_{g\ n-1}}\right)_{(max)}$ etc. Iterative solutions for these ratios ultimately define the optimum weight for each stage. The complete sequence can be found in (Ref. I) but it is sufficient to point out here that the technique can be applied for any number of propulsion stages, if $\bar{M}$ and the M_m, ξ, and I_{sp} are known or chosen for each stage. This provides a useful test of the preliminary "sizing" results for a multi-stage approach.

After cursory comparison of the results of the "sizing" computations against some typical "real" motors, the next step can proceed.

II. Configuration Selection

A. Propulsion Considerations

Following the "sizing" phase, it is usually possible to synthesize several candidate propulsion combinations after study of existing motor designs. If existing motor designs do not fit the need in either single-stage or conventional tandem multi-stage form, consideration of clustered motors to form particular stages can be considered, for either simultaneous burn or "ripple-fire" modes.

It may even be necessary to initiate development of a new propulsion unit if a satisfactory combination of existing motors cannot be achieved.

The synthesis process is an extremely important one requiring additional knowledge of mission requirements. Among these are:

1. Number of vehicles to be built
2. Flight path dispersion limits
3. Payload environmental limits
4. Minimum payload packaging cross-sectional area
5. Launch site location/s

In selecting candidate propulsion combinations, the influence of motor characteristics on the overall vehicle must be weighed. Table I shows some of the more important interactions.

Most sounding rocket vehicles currently being employed have a high slenderness ratio. The most obvious reason for using this shape is its low drag. Another advantage is the ability of a small-diameter motor case to sustain the high combustion chamber pressures associated with relatively short-burn time motors.

The high slenderness ratio configuration suffers from a lack of structural stiffness, and this has been a source of many in-flight mission failures. This configuration also requires high-density payload packaging, which compromises accessibility and increases fabrication and assembly costs.

The introduction of solid state electronic circuitry has alleviated this problem greatly in recent years and it is thus not as important a consideration as formerly, if the payload is primarily electronic in nature. On balance, configurations or individual stages with major portions of the flight path within the lower, denser part of the atmosphere should possess a high slenderness ratio, while those operating almost or entirely exo-atmospheric should have a low slenderness ratio. The latter is particularly important for missions where attitude stability is important, since the low slenderness ratio offers a more favorable moment of inertia ratio for spin stabilization.

TABLE I

Motor Property	Influence on Vehicle Performance & Environment
Thrust vs. Time Profile	Vehicle vibration
	Longitudinal acceleration profile
	Wind Sensitivity and Dispersion
	Aerodynamic heating
	Structural Integrity
	Vehicle Drag
Slenderness Ratio	Structural Integrity
	Payload Packaging density
	Vehicle Drag
	Exo-atmospheric attitude stability
Motor Mechanical Design	Vehicle Dispersion
	Structural Integrity
	Cost
	Reliability
Propellant-Type	Ease of Ignition
	Storage and operating Temperature Limits
	Handling Safety

The thrust vs. time profile is one of the most critical motor properties affecting the vehicle design. Recognizing that a long burn time is desirable to hold acceleration, dynamic pressure, and aerodynamic heating to a minimum, and that a high burn rate is desirable early in flight to reduce wind sensitivity, an idealized thrust vs. time profile is depicted in Figure I(a) for a single stage vehicle. The profile is generally regressive, and is typical of several of the newer rocket motors designed for sounding applications. This is a more difficult and expensive motor design to achieve, however, because grain configurations are more complex and additional case insulation is usually required, compared to the progressive-type profile.

Figure 1(b) shows how a reasonable approximation of the regressive profile can be achieved by staging near neutral, slightly progressive motors.

The neutral and progressive thrust profiles have been used widely for sounding rockets, in single and multi-stage configurations. A special example of the neutral thrust profile is the end-burning grain design, which offers a burn time 4 to 5 times greater than the more popular internal burning type. The end burner represents a concerted assault upon the severe heating and acceleration environment produced by the short-burn motor.

Although a few end-burning designs have been successfully developed, e.g. Arcas and Iris, this type has not been widely used because of extreme wind sensitivity, and difficulty in achieving adequate motor case insulation.

The progressive thrust profile is the easiest for the motor designer to achieve, and is the least expensive. There are consequently more of these to choose from among existing designs.

The liquid propellant engines are characterized by neutral thrust-time profiles, although there has been progress achieved in throttleable and re-startable engines. The sounding rocket designer rarely chooses the liquid engine, because it is more complex in design and construction, with greater attendant cost and more complexity in launch operations.

TYPICAL SOLID PROPELLANT MOTOR THRUST-TIME PROFILES

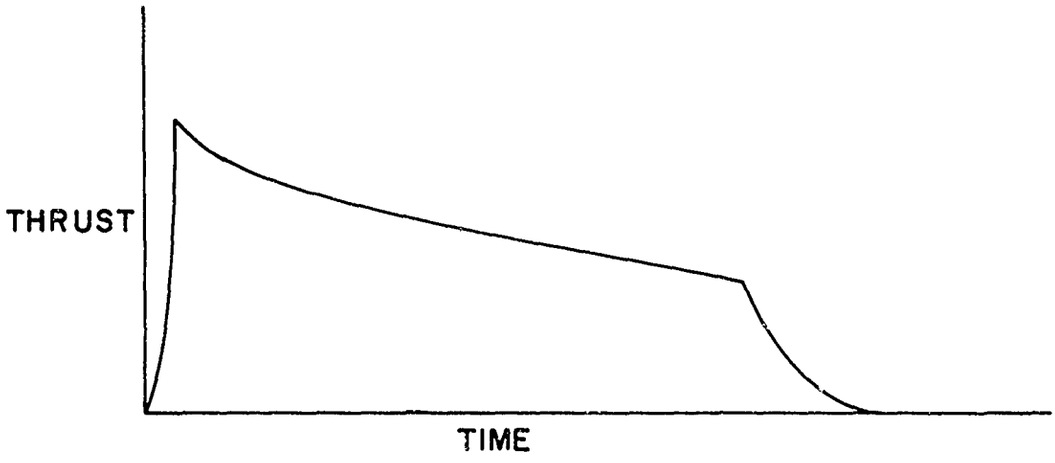

FIG. Ia REGRESSIVE THRUST PROFILE

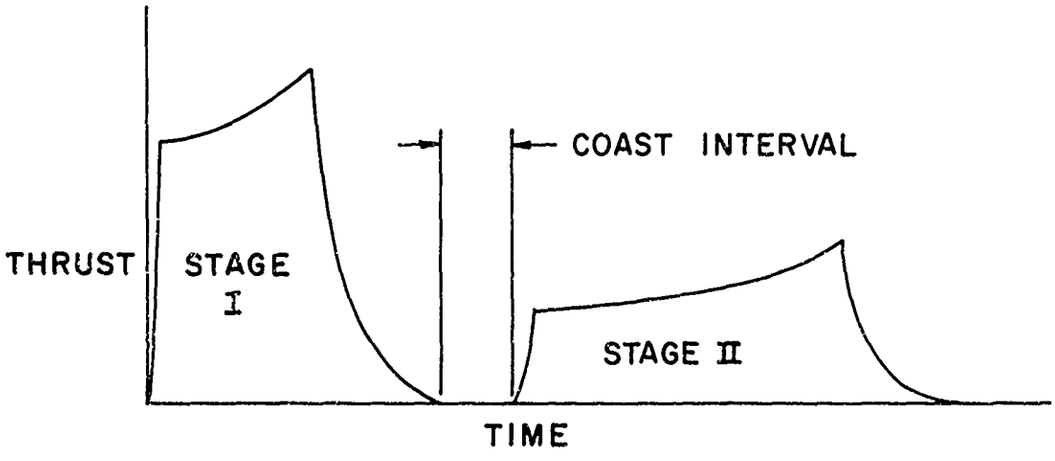

FIG. Ib STAGING WITH PROGRESSIVE THRUST PROFILE

The motor mechanical design is of significance for the more obvious reasons of fabrication cost, structural strength, and reliability. These criteria can be best achieved by a simple design with a minimum number of parts, and avoiding the obsession of mass fraction ξ. Although ξ is an important parameter in achieving high performance, it is better to be able to achieve slightly inferior performance consistently through conservative structural design, than to achieve occasional optimum performance amid a large number of catastrophic failures. Fortunately, nearly every propulsion unit now available has avoided this pitfall.

Thrust misalignment is one of the prime sources of ballistic vehicle dispersion and it is extremely important that manufacturing tolerances be controlled to assure a straight motor case, a concentric propellant grain, minimum "run-out" on payload and fin attachment surfaces, and a concentric, properly aligned nozzle. There is a practical "point of no return" in controlling these tolerances because of cost considerations, but before any propulsion unit is selected as a candidate these tolerances should be thoroughly examined.

The type of propellant used in a motor design strongly influences storage and operating temperature limits. A few formulations cannot withstand low-temperature conditioning, because of grain embrittlement resulting in cracks. Others become a safety hazard at high temperature. Some propellants are susceptible to excessive structural deformation and fracture in a high-acceleration environment.

In addition to the many points noted above, consideration should be given to the motor nozzle design, to assure that; (1) The nozzle will not operate in the over-expanded mode for the intended altitude range, since this severely compromises delivered impulse, and (2) The nozzle operates sufficiently close to optimum expansion at high altitudes to realize the additional impluse

to be gained. It is often worthwhile to develop a new nozzle for an existing motor design to achieve this extra performance. There is still another consideration here: Upper stage motors burning at very high altitudes near the upper edge of the atmosphere generate a spreading plume which can cause air flow separation in the vicinity of the stabilizing fins or flared skirt, diminishing their effectiveness with resulting vehicle instability. Operating at or near-optimum nozzle expansion minimizes this problem.

B. Point-Mass Trajectories

After motors have been selected for one or more candidate configurations, point-mass trajectories can be computed to verify that the "real" motors operating in the presence of drag and gravity still yield the required performance. The weight estimates should be revised to reflect the actual weights of the motors selected, and a weight vs. time profile must be computed. The loss in weight during motor burning can be grossly estimated by assuming a constant mass flow rate, or more precisely by assuming $\dot{M}_p = K \times \text{Thrust}$, where

$$K = \frac{\text{Propellant weight}}{\text{Total impulse}}$$

A plot of the vehicle drag coeeifient as a function of Mach Number can be obtained by examining the available literature describing vehicles of similar shape. It is not too important at this point that the match be precise.

The following relationship can be written for the "Point-Mass" trajectory computation:

$$\frac{W(t)\,\ddot{\vec{R}}}{g} = \vec{T}(t) - \vec{D}(M) - \vec{W}(t)$$

$$\ddot{\vec{R}} = \frac{g}{W(t)} \left[\frac{\vec{T}(t) - \vec{C}_D(M)\,\rho(Z)\,\dot{R}^2}{2} \right] - g \qquad (5)$$

where: $\vec{W}$ (t) = vehicle weight as a function of time

$\vec{T}$ (t) = thrust as a function of time

ρ (z) = atmospheric density as a function of altitude, standard atmosphere

C_D (M) = vehicle "zero lift" drag coefficient as a function of Mach Number

$\vec{R}$ = radius vector

This non-linear differential equation assumes the vehicle is always aligned tangent to the flight path. The equation cannot be solved in closed form but is amenable to numerical integration techniques, especially on a digital computer. Input consists of weight, drag, thrust, and density in table form, and outputs are altitude, range, velocity, acceleration and dynamic pressure, as a function of time of flight. Mach Number can also be computed if a table of sonic speed vs. altitude is added to the input. These outputs provide a good performance assessment of the candidate configurations, so that some may be eliminated and/or additional ones tried. The outputs are also useful for the first aerodynamic analyses to follow.

C. Preliminary Aerodynamic Design

For each of the configurations surviving the point-mass trajectory check, it is necessary to accomplish preliminary design of the nose shape, interstage structures, and vehicle stabilizing surfaces. By implementing vehicle layout or inboard profile drawings, an intuitive judgement of structural weights of these components can be made, as well as their "station" locations. These weight estimates are only slightly better than those used for the "point-mass" trajectories, but are adequate for initial vehicle center of gravity computations.

With the center of gravity history available and a nose shape selected, it is possible to "size" the stabilizing surfaces by conducting a vehicle longitudinal static stability analysis. When this is accomplished the configuration is sufficiently defined to make drag computations.

There a · four major considerations in selecting a nose shape. These are; (1) Minimum Drag/Maximum Packaging volume ratio, (2) Cost of Fabrication, (3) Aerodynamic Heating, and (4) Lift Characteristics.

The importance of a low-drag nose shape varies, depending upon the altitude regime. A space probe vehicle designed for a zenith altitude of 500 miles or more is likely to ascend through the atmosphere slowly, achieving the high required burnout velocity by exo-atmospheric burning of upper stages. In this instance the nose shape is of minor consequence and is likely to be a simple, relatively blunt conical shape. The majority of sounding rockets utilize intra-atmospheric thrust phases, and here the nose drag is extremely important, since it produces nearly all of the vehicle wave drag, which constitutes about a third or more of the total drag. The primary consideration is a slender shape whether it be conical or ogival, as seen in Figure 2, which depicts cone drag as a function of slenderness ratio. The ogival shape offers superior packaging volume, while the cone is less expensive to fabricate. The slenderness ratio also is the predominant parameter affecting aerodynamic heating and nose lift. Fortunately a low-drag shape creates the least wall heating and the lowest nose lift, a favorable trend since nose lift is de-stabilizing.

After selection of the nose shape the vehicle static stability margin (distance between center of gravity and center of pressure) criteria must be chosen. It is assumed at this point that aerodynamic stabilization will be employed. There is another means of achieving stability, gyroscopic stability by means of high spin rates. With a ballistic vehicle, an exo-atmospheric thrusting stage must rely on gyro stability, but for flight in the lower atmosphere this approach is seldom attempted since the required spin rates to assure adequate gyro "stiffness" against aerodynamically-induced perturbations are impractically high.

The static stability margin is an extremely important parameter since it is a measure of the restoring moment created as a function of angle

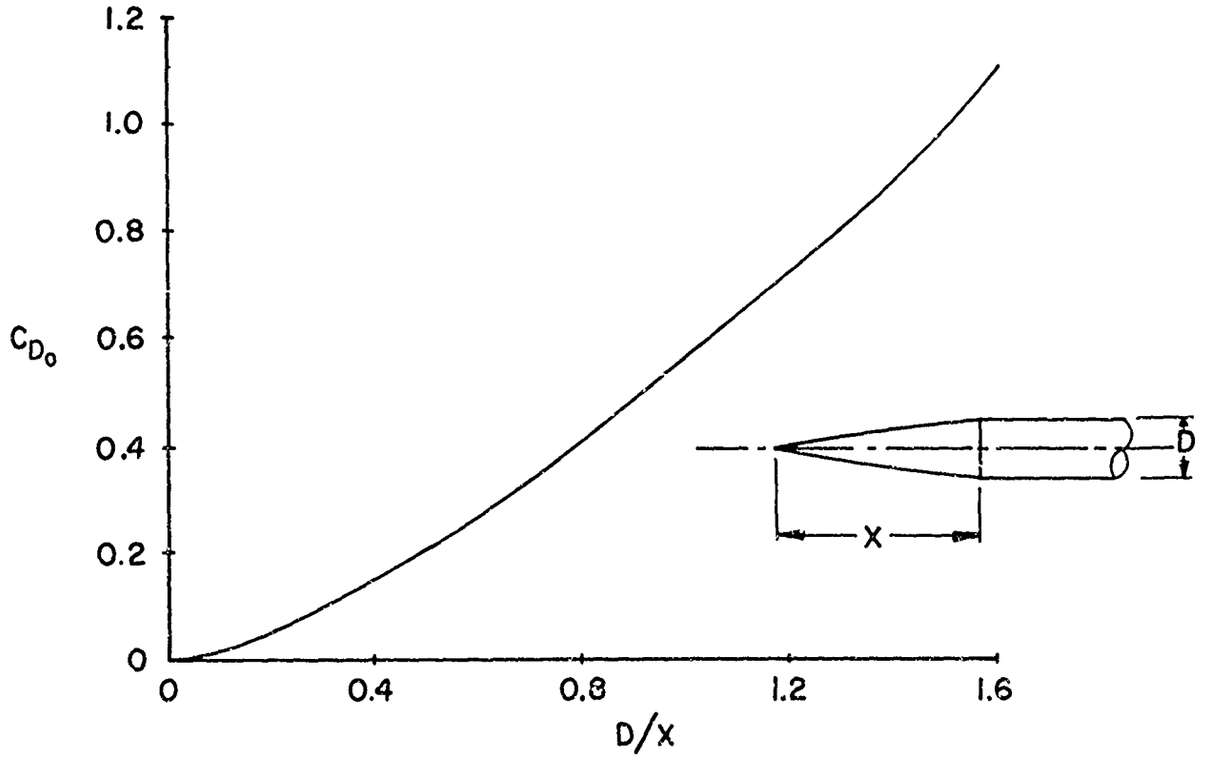

FIG. 2. CONICAL FOREBODY DRAG AS A FUNCTION OF SLENDERNESS PARAMETER, D/X AT M = 2. (FROM REF 2)

of attack. For most flight conditions this is the predominant stabilizing moment. The static stability margin determines the vehicle trim angle of attack as a result of perturbations, such as thrust and aerodynamic misalignments. The vehicle natural pitch frequency, or response time, is a function of the stability margin. An interesting case to consider is neutral stability, with the center of gravity and center of pressure coincident.

In this situation, if only aerodynamic perturbations were present the vehicle would not rotate about its C.G. since there would be no turning moment, and it would be almost insensitive to winds, i.e., no weather-cocking, only drift. This is an academic situation, since a neutrally stable rocket cannot be practically achieved, due to the movement of both C. G. and C. P. over the flight path, and furthermore the vehicle would be extremely vulnerable to rotation from thrust misalignment. A large stability margin is desirable since it produces minimum trim angles, with lower drag and structural loads, and minimizes dispersion from thrust misalignment. On the other hand, a large margin causes the vehicle to be extremely wind-sensitive at launch when vehicle velocity is low. For most configurations, the margin decreases with increasing Mach No. (Figure 3), and a range from about 1.5 to 3.0 calibers (body diameters) is usually employed.

Using this as a criterion, the required fin or stabilizing skirt configuration for each stage is established by the following equation:

$$X_{\substack{C.P. \\ Veh.}} = \frac{(A\, C_{N_\alpha}\, X_{C.P.})_{Nose} + (A\, C_{N_\alpha}\, X_{C.P.})_{Boattail} + (A\, C_{N\alpha}\, X_{C.P.})_{fins}}{A\, C_{N\alpha\ nose} + A\, C_{N_\alpha\ Boattail} + A\, C_{N\alpha\ fins}} \quad (6)$$

where: $X_{C.P.}$ = center of pressure location from some reference datum

$C_{N\alpha} = \frac{dC_N}{d\alpha}$ = normal force coefficient derivative

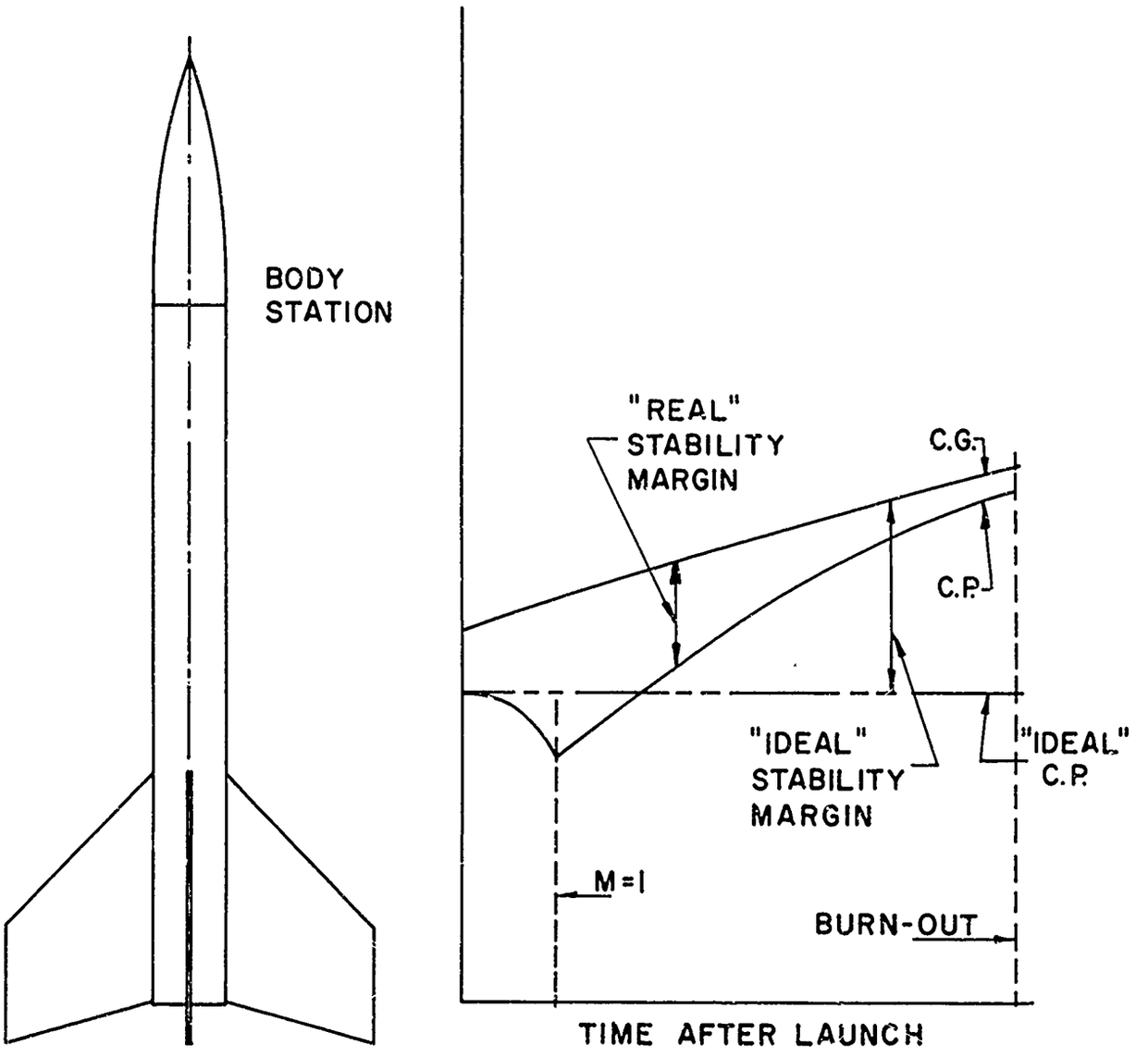

FIG. 3 VEHICLE STABILITY MARGIN VARIATION

This relationship essentially sums all of the contributing aerodynamic moments acting on the vehicle as a consequence of angle of attack, and is analogous to the determination of the vehicle center of gravity by summing first moments of masses. For a multi-stage configuration, the final stage stabilizing surfaces should be sized first, then those on the lower stages. Generally the vehicle center of pressure is determined only as a function of Mach No., since angle of attack is usually constrained to a range where the $C_{N_{\alpha}}$'s can be considered constant. This is not always so, and in the event subsequent flight simulation procedures show large angle of attack, the influence on center of pressure location must be recognized. The reference areas A_{nose} and $A_{interstage}$ are already known, as are $C_{N\alpha}$ nose, $C_{N\alpha}$ boattail, C.P. nose, C. P. boattail, and the desired $X_{C.P.}$ for the vehicle. From the vehicle layout drawing, an approximate location for $X_{C.P.\ fin}$ can be defined. Thus it remains only to solve for the quantity $\left[A_{fin}\ C_{N\alpha\ fin}\right]$ for the highest Mach No. value to be encountered. Since any fin configuration loses effectiveness with increasing Mach No., (for $M > 1$) a fin thus "sized" will usually be adequate for the entire flight regime. The solution should be checked over the entire Mach No. range to verify adequacy and also provide necessary information on the center of pressure movement. This done, it is now possible to adjust values of A_{fin} and $C_{N\alpha\ fin}$ by selecting a particular fin planform shape and airfoil. The value $C_{N\alpha\ fin}$ is really more properly written to include fin - body interference effects, such as:

$$C_{N\alpha\ Fin\ Total} = C_{N\alpha\ Fin}\ (K_{B/W} + K_{W/B})$$

where $C_{N\alpha\ Fin}$ = normal force coefficient, fin alone

$K_{B/F}$ = interference factor, body on fin

$K_{F/B}$ = interference factor, fin on body

Although $K_{F/B}$ is really a body lift influence, the various treatments in the literature normalize the factor for expression in terms of fin lift. It is beyond the scope of this paper to discuss interference factors in detail, but they do significantly affect the total lift generated by the fin presence and must be accurately assessed, since they often increase $C_{N\alpha\ Fin}$ by a factor of 2.0 or more.

The selection of a fin planform and airfoil is generally determined by considerations of strength, drag, and fabrication cost. The details of these trade-offs are too extensive to discuss here, except to say that for sounding vehicles, good structural rigidity and low manufacturing cost usually are most important.

After the fin configuration and size have been selected, it is now possible to compute the total vehicle drag coefficient, C_{Do}, again as a function of Mach No. and possibly Reynolds No., but ignoring induced drag due to angle of attack, on the assumption that it is constrained to small angles.

The vehicle drag coefficient is computed by summing the wave, friction, and base drag coefficients as shown below:

$$C_{Do}\ A_{Veh} = C_{DW\ Nose}\ A_{Nose} + C_{DW\ Fins}\ A_{Fins} + \left[C_{Df}\ A_{Wetted}\right]_{Veh.} + \left[C_{DB}\ A_{Base}\right]_{Veh.} \quad (7)$$

where:

C_{Do} = vehicle zero-lift drag coefficient, f (M, R.N.)

A_{Veh} = vehicle reference area

$C_{DW\ nose}$ = nose wave or form drag coefficient, f (M)

A_{nose} = reference area associated with $C_{DW\ nose}$

$C_{DW\ Fins}$ = fin wave or form drag coefficient, f (M)

A_{Fins} = reference area associated with $C_{DW\ Fins}$

C_{Df} = vehicle friction drag coefficient, f (M,R.N.)

A_{Wetted} = vehicle wetted area

C_{DB} = base drag coefficient, f (M)

A_{Base} = vehicle base area

Eq. (7) is written to show the importance of matching various drag coefficients with the proper reference area. No drag coefficient data should be used unless this is done. This may seem trivial, but this has been a source of costly errors and confusion to the point where drag data is increasingly being expressed as C_DA, rather than C_D only. Hopefully this will become standardized nomenclature,

The drag coefficients can be computed by a variety of methods, some theoretical, others empirical. If conventional, widely used shapes are involved, a search of the literature is likely to yield applicable test data.

Refinements in analysis and detail design can progress either before or after the final configuration choice is made. At this point fairly good parametric performance data is available on each candidate configuration from point-mass trajectories, and the aerodynamic analyses just described may have contributed additional data to narrow the choice, e.g., the fin "sizing" procedure may have revealed that one of the vehicle designs requires impractically large stabilizing fins. If it is still not evident that one configuration is superior to the others, it may be necessary to repeat the "point mass" trajectory simulations using the computed drag vs. Mach No. data and thus obtain more precise performance data, or, begin assessing dispersion characteristics by determining the sensitivity to drag and motor impulse uncertainties. At any rate the determination of the configuration has progressed to Step 3, Detail Design, with implications of further sophistication in analysis.

III. Detail Design and Analysis

A. Dispersion and Vehicle Dynamics Analysis

It will be assumed at this point that the final configuration selection has been made. The vehicle shape and dimensions are now largely defined as a result of the analyses already performed. The design must now be explored in depth to assure that dispersion and wind sensitivity will be within acceptable limits, and that no dangerous dynamic instability conditions will occur.

In order to accomplish these studies, it is necessary to complete detail design of the various vehicle components accompanied by detailed structural analysis, so that sufficiently accurate weight, center-of-gravity and moment of inertia tables can be generated.

Further refinement in the aerodynamic coefficients beyond that achievable by the previously described analyses is desirable, but should be achieved through wind tunnel testing. It is appropriate here to comment that the most valuable data to be gained by tunnel testing are the dynamic stability derivatives, such as the damping coefficient C_{mq} and the Magnus moment coefficient $C_{mp\alpha}$. These are admittedly difficult to obtain in the tunnel, yet they are far less amenable to computation. On the other hand, if the vehicle configuration is made up of such well-defined components as a cone or ogive-cylinder, cone frustum interstage and conventional fin planform and airfoil shapes, the linear aerodynamic theories yield drag and normal force coefficients and center-of-pressure locations to about 10 percent accuracy, and furthermore there is an abundance of this test data published. Wind tunnel testing to refine this data may not be justified because of the high cost.

With a complete, accurate description of the vehicle available, the more comprehensive flight simulation techniques can now be effectively applied to assess dispersion and vehicle dynamic behavior. An example of a simulation mathematical model for such study is one heavily used by the Physical Science Laboratory and probably many other organizations, as shown by the equations below:

$$\dot{U} = \frac{1}{M}\left[T - qd^2\left(C_D \cos\alpha - C_{L\alpha}\sin^2\alpha\right) - qd^2 C_{L\alpha F}\delta_F \sin\phi \sin\alpha\right] - g_o\left(\frac{R_o}{R_o+Z}\right)^2 \cos\beta - \dot{\beta}W \tag{7}$$

$$\dot{W} = \frac{1}{M}\left[T\,\delta_T \sin\phi + qd^2 C_{L\alpha F}\delta_F \sin\phi\cos\alpha - qd^2\left(C_D \sin\alpha + C_{L\alpha}\cos\alpha\sin\alpha\right)\right] - g_o\left(\frac{R_o}{R_o+Z}\right)^2 \sin\beta + \dot{\beta}U \tag{8}$$

$$\ddot{\beta} = \frac{1}{I}\left[T\,\delta_T\,R_T \sin\phi - \left(\frac{I}{M} - R_E\,R_T\right)\ddot{\beta}_M - qd^2\,C_{L\alpha}\,R_D^2\,\frac{\dot{\beta}}{V_R}\right.$$

$$- qd^2\,(C_D \sin\alpha + C_{L\alpha} \sin\alpha\cos\alpha)\,R_p$$

$$\left. + qd^2\,(C_{L\alpha F}\,\delta_F \sin\phi\cos\alpha)\,R_F\right] \qquad (9)$$

Ancillary relationships and a complete nomenclature fully describing terms can be found in Ref. 3, and the more important parameters are shown in Figure 4.

These are three-degree-of-freedom equations of motion for a rigid body vehicle with inertia in a "flat earth" gravity field, constraining motion to translation and rotation in the vertical (pitch) plane only. This model certainly has limitations, in that there is little capability to examine vehicle roll-pitch or yaw type cross-coupling dynamics. But for symmetrical vehicles designed for near-vertical trajectories, the model is a powerful tool for dispersion and wind response studies. The six-degree-of-freedom model is required for complete analysis, but its use should be reserved for studies where it is essential, since it is more expensive to apply.

It is beyond the scope of this paper to discuss these analyses in detail, but it is appropriate to comment on the influence the results can exert upon the vehicle configuration. There may be changes in stability margin indicated, which might be implemented by revising fin design. The desired vehicle spin profile becomes evident, and the technique for achieving spin can be chosen. Certain flight event times and associated tolerances can be established, notably those associated with coasting intervals. The vehicle natural pitch-yaw frequencies are now established and can be compared with body bending frequencies. This check might lead to changes in structural stiffness requirements. The type of launcher to be used becomes evident, whether it be zero-length, finite length, or finite length with simultaneous launch lug release.

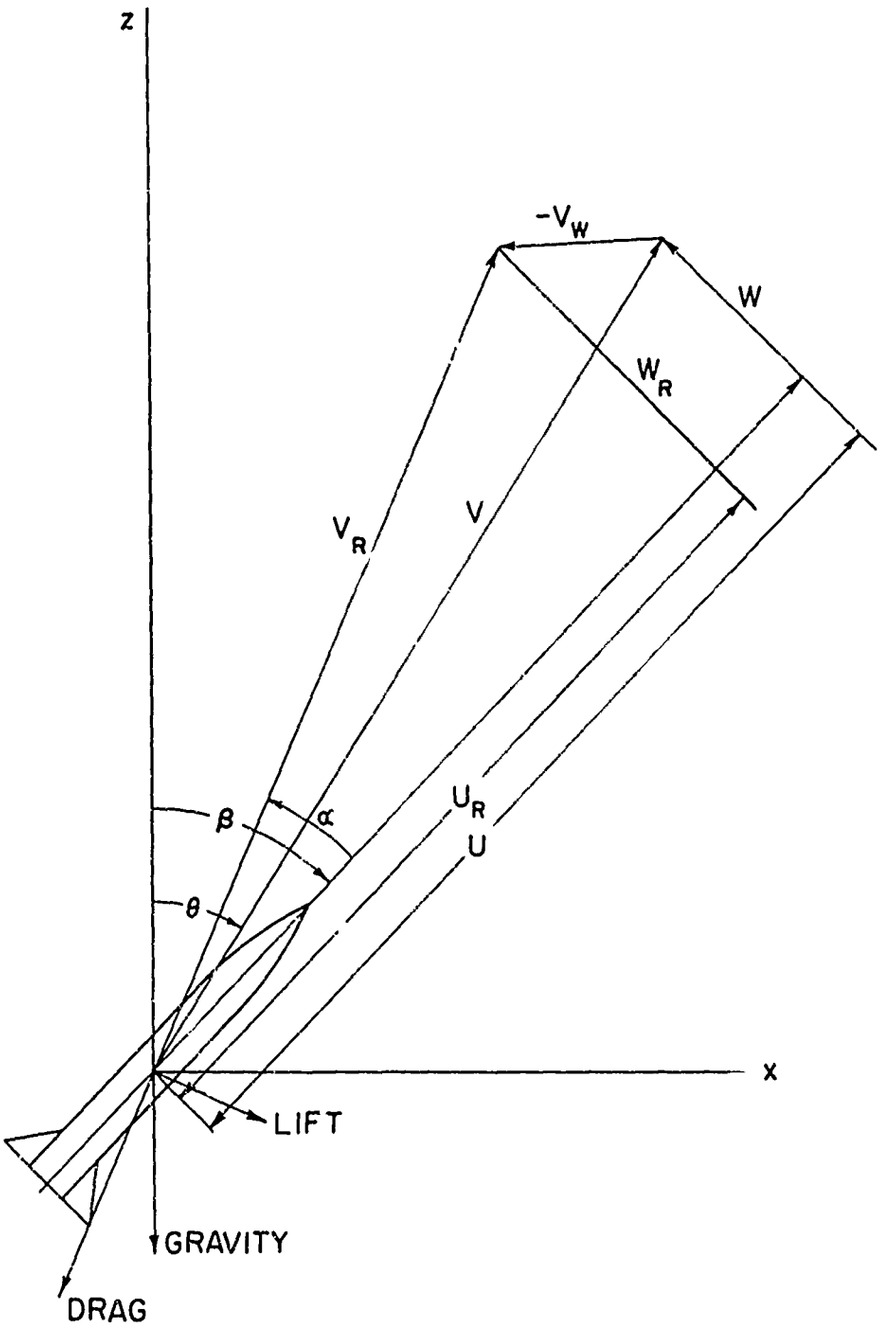

FIGURE 4-PITCH PLANE
VEHICLE DYNAMICS PARAMETERS

At this stage in the design process, the conduct of all studies, from the simple point-mass trajectory computations to the complex six-degree-of-freedom dynamics analyses, if done on a parametric basis, has yielded a comprehensive picture of the interaction of each vehicle characteristic on another, and the key task of the designer is to "juggle" these parameters within the practical ranges available to achieve the design objectives. This done, the final phase, testing, may be implemented.

IV. Testing:

The testing of a new configuration consists of both pre-flight ground testing and flight testing; and the pre-flight testing may be initiated during the detail design phase, as an aid in making design decisions. This testing should be as comprehensive as is practical, with a view toward verifying proper function, such as the "cleanliness" of stage separations, activation of pyrotechnic devices for nose jettison, de-spin systems, etc. Structural integrity must be demonstrated under static and dynamic loading conditions, notably vibration, and other environmental qualification testing, such as for aerodynamic heating, must be accomplished. These tests very often pinpoint the need for redesign, and serve to illustrate the limitations in analytical approaches.

The final "proof of the pudding", flight testing, follows the pre-flight test phase, and must be supported by thorough planning, especially in the areas of the objectives of each flight test, and the instrumentation required to support those objectives. In most sounding rockets programs, few prototype vehicles are available for flight evaluation. Very often the first flight vehicle is committed to a primary operational mission objective. These circumstances emphasize the need for good test planning. One favorable aspect in regard to flight testing is that advances in flight simulation technology have reduced the uncertainties facing the designer at the onset of flight testing, and this advantage should be exploited to the fullest extent.

V. Conclusion:

The determination of the sounding rocket configuration, is, on the one hand, a less risky procedure today because of the powerful flight simulation techniques now available. Yet improved flight instrumentation, both in on-board sensors and ground tracking facilities, have brought to the vehicle engineer's attention a host of anomalies, particularly in vehicle dynamics, which challenge the capabilities of flight simulation. Furthermore, the mission of the sounding rocket grows more demanding, in terms of more precise trajectory prediction and attitude stabilization requirements, and, of course, greater performance.

These trends assure a need for continuing and intensified effort on the part of the rocket vehicle designer to be thorough and resourceful in evolving new sounding rocket vehicle designs. It is also incumbent upon the sounding rocket user to recognize these vehicles for what they are, a fairly complex flying machine, not necessarily a simple, inexpensive item of ordnance.

LIST OF REFERENCES

1. Wiesbord, Leon, "A Generalized Optimization Procedure for N-Staged Missiles." Jet Propulsion, March 1958.
2. Hoerner, Sigurd F., "Aerodynamic Drag." Self Published, 1950.
3. Guard, K., Ottesen, J., Seagraves, E., "Speedball II Dispersion Analysis for Launchings at WSMR." Physical Science Laboratory, NMSU Report, 25 October 1961.

FIN/SPIN STABILIZATION OF UNGUIDED LAUNCH VEHICLES

BY

A. T. MARRIOTT and R. R. BROOKS

ATLANTIC RESEARCH CORPORATION
Missile Systems Division
Costa Mesa, California

ABSTRACT

The design and development of system concepts which utilize an unguided boost phase and a partially guided reentry phase during long range overland flights require that special considerations be given to accuracy and safety. Discussed in this paper are design techniques utilized during the early design phase of an improved Athena vehicle to insure system accuracy and safety. These include the aerodynamic/spin stabilization techniques used to provide the optimum dispersion/stability characteristics during boost within the constraints established by other design considerations. Also included are the spin stabilization techniques used during the exoatmospheric portion of flight. The effect of spin on stage separation dynamics is also discussed.

INTRODUCTION

The primary objective of the Advanced Ballistic Reentry Systems (ABRES) Program, which is under the jurisdiction of the Space and Missile Systems Organization of the United States Air Force, is the investigation of reentry systems concepts concerned with advanced payload technology. Prior to the Athena Program, the testing capability of the ABRES Program was limited to full scale overwater testing. Several of the disadvantages associated with the full scale overwater testing are:

1. There is a limited amount of instrumentation available at sea.
2. The use of full scale prototype launch vehicles is expensive.
3. The range of reentry performance (Velocity-Gamma Envelope) is limited.

To alleviate these disadvantages the Athena Program was conceived. Through the Athena Program subscale reentry system tests could be conducted overland with the following advantages:

1. The vast amount of instrumentation available at the White Sands Missile Range could be utilized.
2. An inexpensive but reliable launch system could be provided.
3. A wide range of reentry performance (Velocity-Gamma Envelope) is available.

With the introduction of the Athena Program the capability of the ABRES Program is now expanded to include testing of:

1. Heavy full scale payloads over a limited performance range.
2. Light subscale payloads over a wide performance range.

It is seen, however, that a gap still exists within the testing capability of the ARRES Program. This gap is the capability to test heavy payloads over a wide performance range. In order to bridge this gap the Missile Systems Division of Atlantic Research Corporation has investigated an Athena configuration having improved performance. The objective of this improved Athena, which has been given the designation of Athena H, is to provide the testing capability of heavy payloads over a wide performance range.

The flight plan of Athena H will be quite similar to that of Athena. Athena H flights will consist of overland trajectories from Green River, Utah, to White Sands, New Mexico. Since, like the Athena, this trajectory brings the vehicle in the vicinity of populated areas, consideration of reliability, accuracy and safety during the preliminary design phase, are all important. However, in order to keep the Athena H airborne systems as simple and straightforward as possible, the use of a complex boost guidance system is rejected. Instead, the rather simple yet proven concept of a spin stabilized wind compensate vehicle which has achieved an outstanding success record with the Athena Program will be utilized. Accomplishment of these overland flights with an unguided booster requires that particular attention be given to the dispersion as well as to stability characteristics of the Athena H. The fin design during boost and the spin characteristics during exoatmospheric flights are, therefore, extremely important to provide both the necessary dispersion and stability characteristics.

FIN STABILIZATION DURING BOOST

During boost, the fin design of Athena H must provide adequate stability throughout the boost phase and yet not permit excessive stability at launch. A low margin of stability at launch is necessary for acceptable dispersion characteristics resulting from wind measurement error. At launch when the vehicle is more susceptible to winds, a stable vehicle tends to repoint into the wind. The greater the stability, the greater this repointing tendency and the greater the scatter of impact due to wind measurement variations. Therefore, the fin design must be such to provide little stability at launch to minimize this repointing influence. Also, a stable platform throughout boost is necessary to provide proper functioning of all events. With a fin arrangement similar to Athena, which has a two stage boost, accomplishment of these two requirements is difficult, as can be illustrated by Figure 1. An attempt to obtain sufficient stability at the higher Mach numbers results in excessive stability at launch. An acceptable level of stability at launch results in the vehicle becoming unstable at higher Mach numbers. It is seen, therefore, that the fin configuration for Athena H application must be highly effective at high Mach numbers and relatively ineffective at the low Mach numbers. The fin, however, must also provide the desired spin characteristics. A spinning motion is imparted to the Athena H during boost in order to minimize impact dispersions resulting from thrust misalignment and rail tipoff. The spin rate must be sufficient to provide acceptable dispersion characteristics; yet it cannot exceed the tolerance level of system components. Care must be taken also to avoid

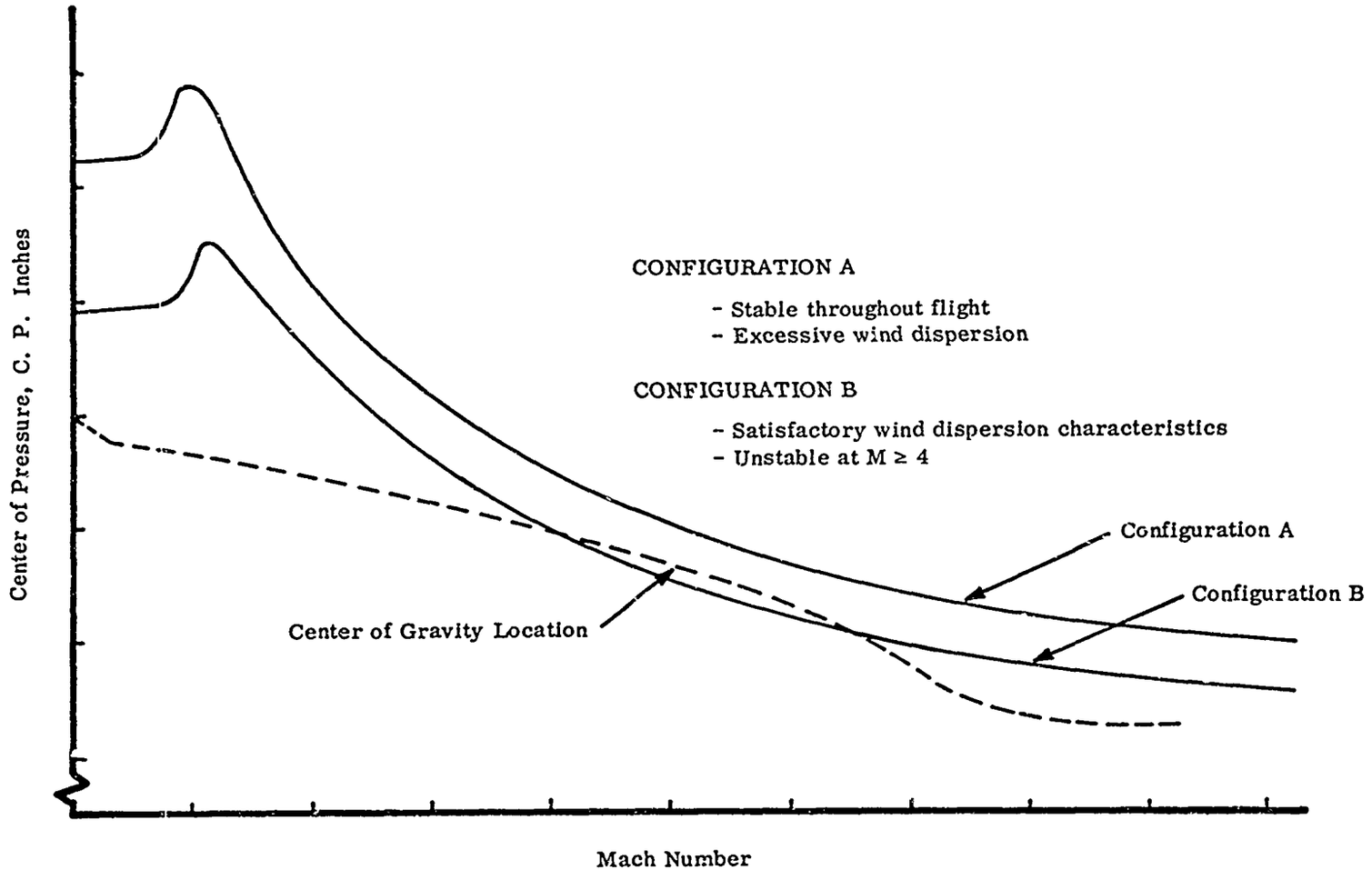

Figure 1. Static Margin Effects On Stability And Dispersion

coupling of the spin rate with the aerodynamic natural frequency of the vehicle.

Having established these various design requirements and constraints, the fin configuration can be selected which is most suitable for application to Athena H. The first step in selecting the fin is to establish the best airfoil section and size of fin for adequate stability throughout boost. This is done by comparing the weight and drag characteristics to obtain the maximum performance capability. Consideration is also given at this time to design compatibility. The establishment of the fin size is shown on Figure 2. Having established the fin size for adequate stability and the airfoil section for best performance and design compatibility, the effect of fin planform on dispersion, spin rate profile and pitch natural frequency is determined. The fin planform is then selected which provides the least dispersion, does not exceed the maximum allowable spin rate and does not allow a spin of the same frequency as the aerodynamics natural frequency. The influence of fin planform on dispersion is shown on Figure 3 and indicates the desired planform. The selected fin planform is then investigated for the effects on the aerodynamic spin profile during boost. Studies have shown that the realtively poor initial spin acceleration provided by the fin, necessitates that the initial aerodynamic spin be supplemented by spin motors to provide acceptable impact dispersion. A typical aerodynamic spin profile supplement by spin motors is shown on Figure 4.

The results of these various studies define the aerodynamic configuration most suitable for Athena H application. The optimum aerodynamic configuration

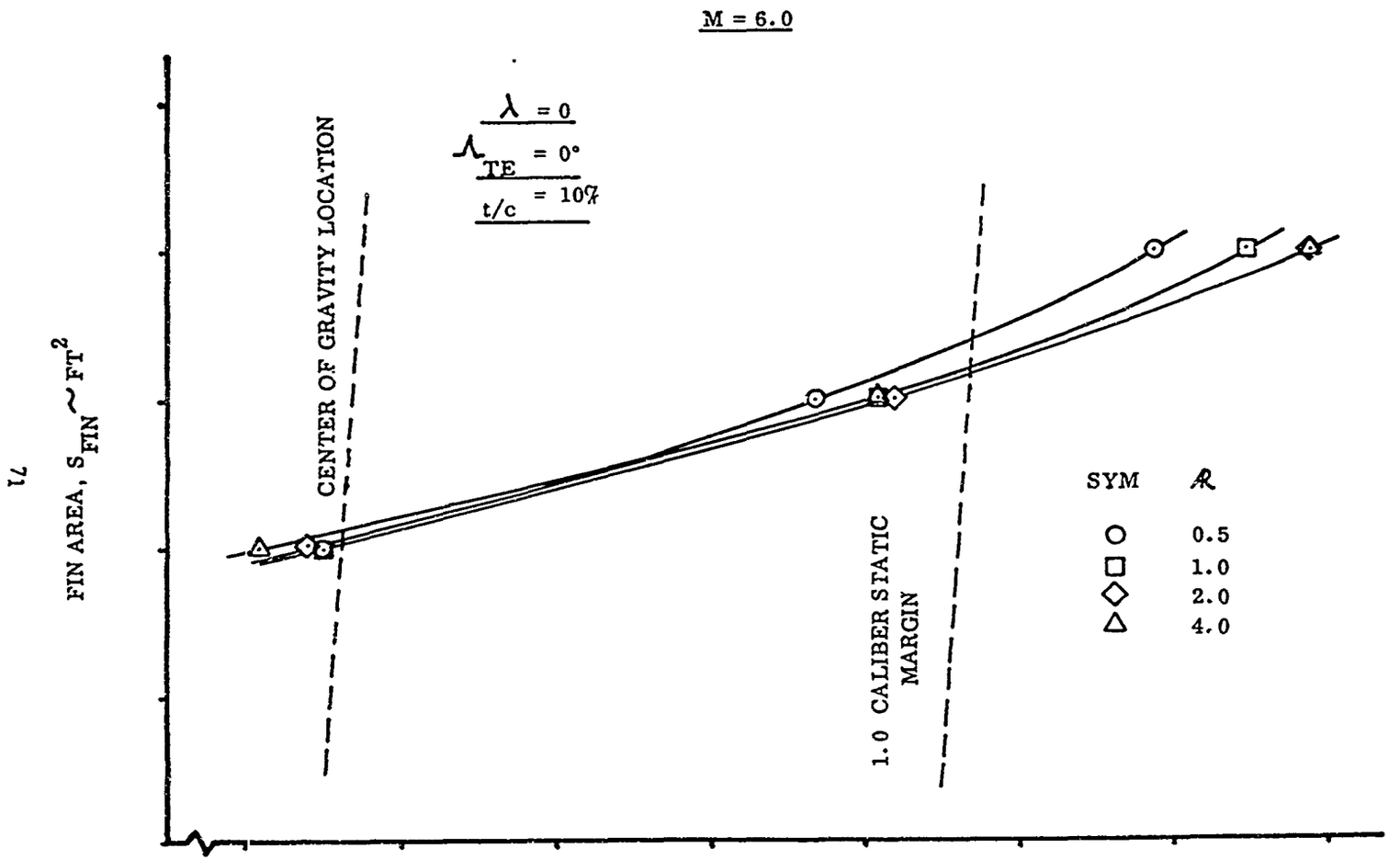

Figure 2. Effect of Fin Size on Stability

M = O

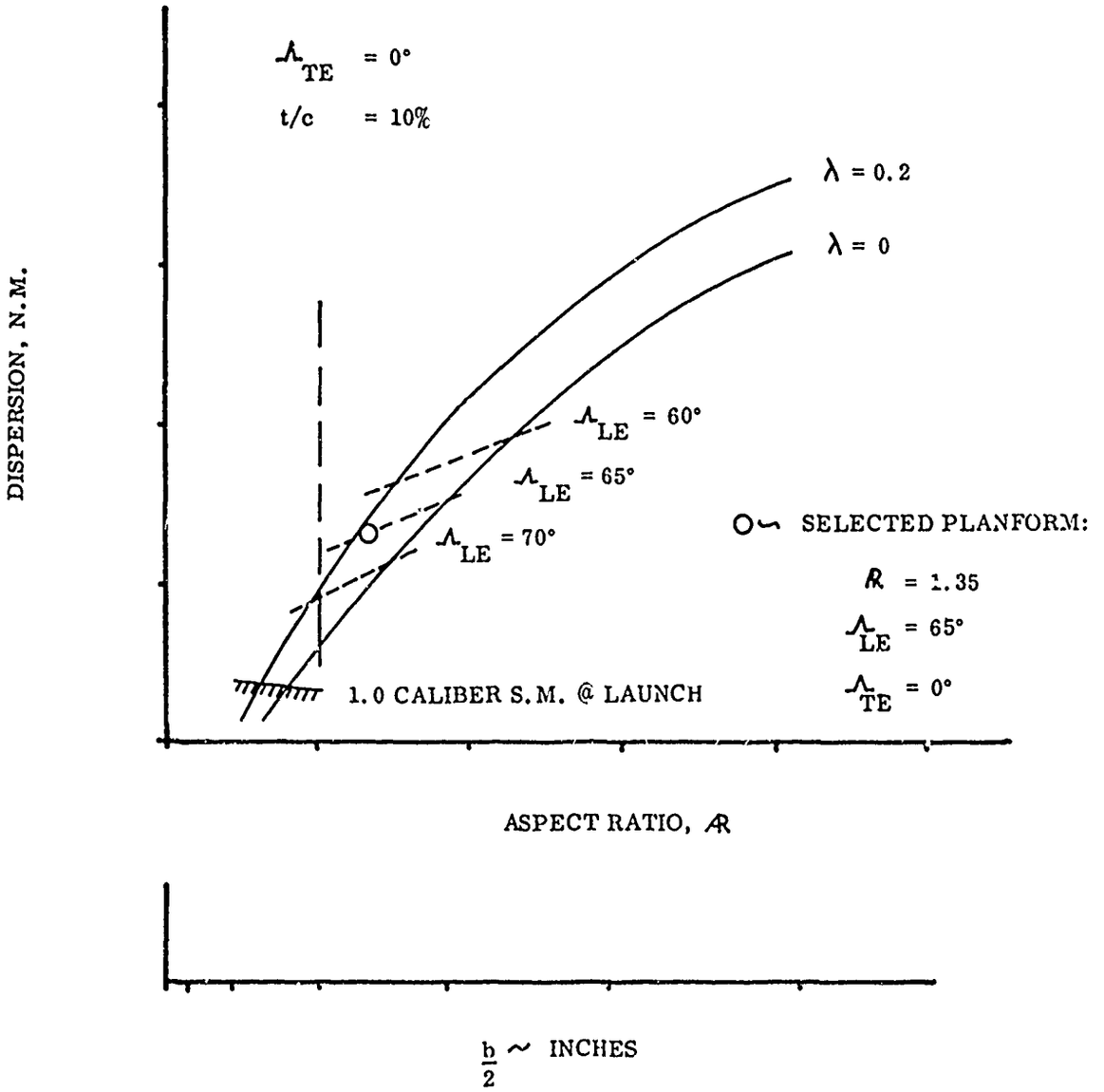

Figure 3. Effect of Fin Planform on Dispersion

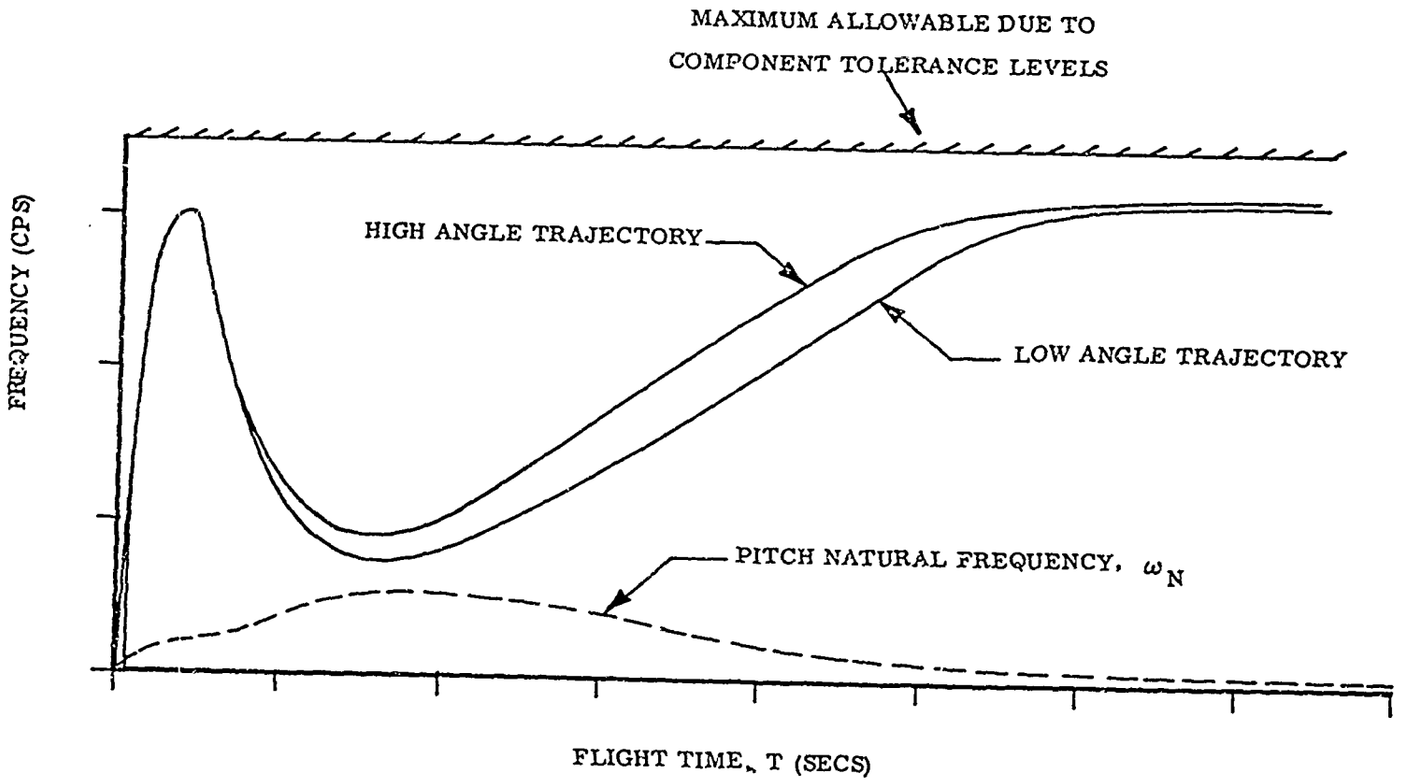

Figure 4. Vehicle Roll Rate and Natural Pitching Frequency Versus Flight Time

selection criteria was the requirement for adequate aerodynamic stability throughout boost and the requirement that the dispersion characteristics be compatible with existing impact areas. The constraints placed upon the aerodynamic configuration selection criteria were the effects on the performance capabilities, the spin requirements during boost and avoidance of the spin rate during boost coinciding with the aerodynamic natural frequency.

Having satisfied ourselves with the aerodynamic characteristics during boost, the spin characteristics during exoatmospheric flight was then investigated.

EXOATMOSPHERIC SPIN STABILIZATION

The second part of this paper is concerned with the exoatmospheric and reentry parts of the Athena H mission, where spin stabilization is employed to allow delivery of a payload within a fixed impact dispersion area without terminal guidance. It will discuss the means by which spin stabilization is achieved and consider some of the problems associated with a spinning vehicle having separating stages upon reentry.

In order to better understand the following discussion, a brief description of the portion of the flight after booster release is helpful. Figure 5 shows a typical trajectory and notes pertinent events from launch to impact. Shortly after the booster is ejected, the velocity package (final stages plus payload) is despun with yo-yo's to a near zero spin rate. The attitude control system is then activated and roll arrest and attitude acquisition accomplished. The heat shield fairing is released. The vehicle is then pitched over to its predetermined final pointing position. Based upon radar data acquired at a time after velocity package separation, corrections are computed and transmitted to the attitude controller and the vehicle is brought to its final corrected pointing. It is then spin stabilized using six spin motors which provide a spin rate of 4 cps. The attitude control system is ejected after which the final stages are burned and the payload separated as shown in the illustration. Impact of the payload will be within a dispersion area approximately 420 nautical miles down range of the launch point.

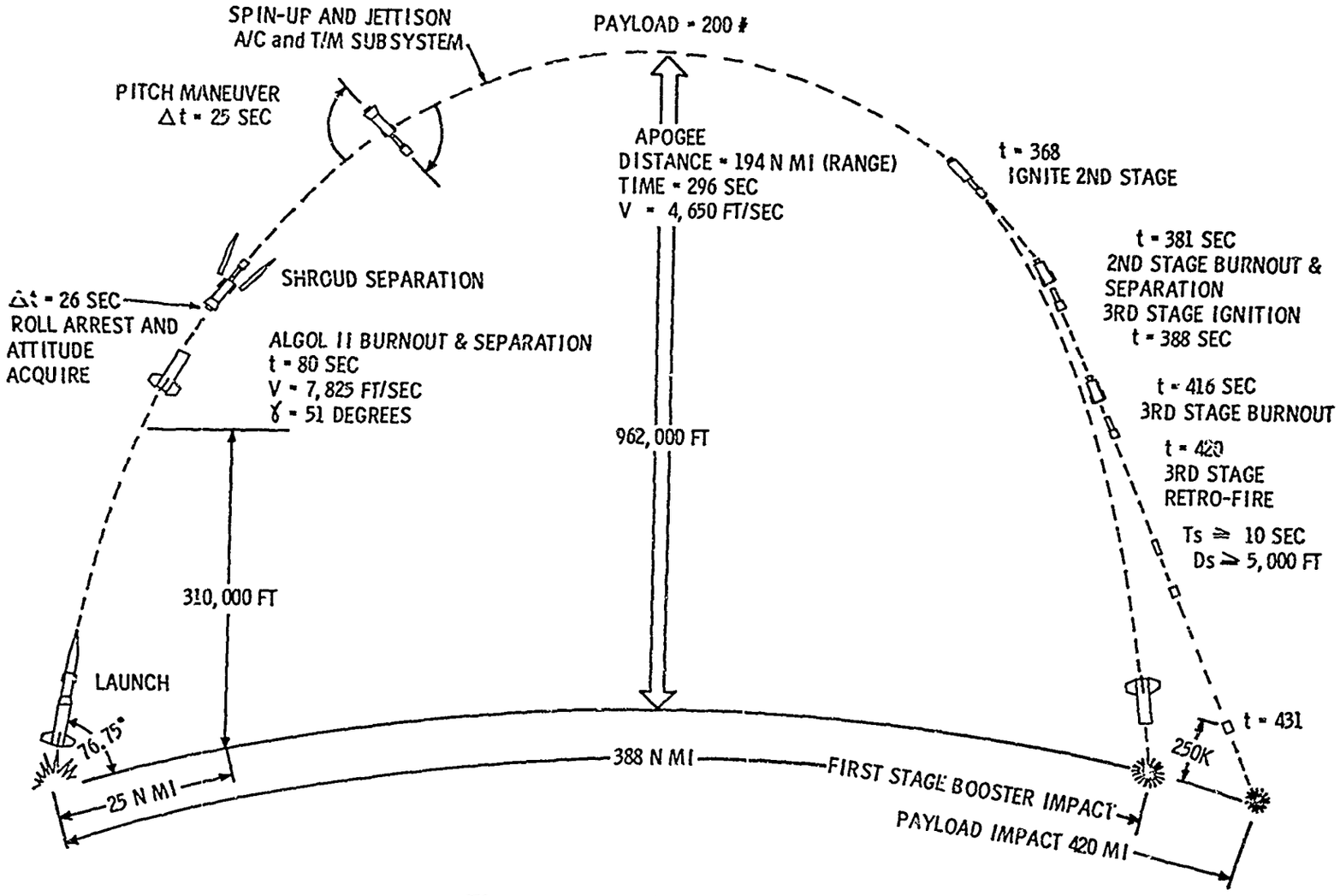

Figure 5. Typical Trajectory Profile

The improved Athena vehicle is designed to deliver instrumented payloads under simulated ICBM/IRBM reentry conditions. By the nature of its test area and the type of payloads flown, certain restrictions are placed on allowable dispersions as well as vehicle induced rates that may affect payload dyhamics. Because its final stages are unguided, spin stabilization is essential to keep the dispersions within prescribed bounds and to ensure that the vehicle attitude is maintained as desired for the particular payload being flown.

Spin stabilization employs the well known gyroscopic principal that a body spinning about a principal axis in space will endeavor to retain its initial attitude in an inertial frame of reference. The resistance offered by a spinning body to an attitude change resulting from a disturbing moment is proportional to the square of the spin rate. This would suggest then that as high a spin rate as possible would be desirable. In rockets, structural considerations of motors or other components usually limit spin rates to something less than 10 cps. The Athena H final stages are spun at 4 cps.

With this cursory background, it is now possible to consider some of the problems and aspects of designing a spin-stabilized reentry vehicle as represented by an advanced version of the Athena missile.

Error Sources For A Spinning Vehicle With Separating Stages

Associated with a spinning body in space, and in particular with one which has components separating [illegible], are several sources of disturbances that can induce undesirable [illegible]nd attitude motion. Each of these must

be identified and considered in the preliminary design stages of a missile since they will ultimately affect the payload carrying characteristics and the dispersions in both flight parameters and range impact.

In the initial definition phase of the improved Athena, the following error sources were considered and investigated:

1. Attitude control system errors.
2. Spin motor disturbances.
3. Thrust misalignment of major stage motors.
4. Dynamic unbalance due to balancing tolerances.
5. Principal axis misalignment due to vehicle manufacturing tolerances.
6. Separation mechanism induced motion (initial rates).

Figure 6 shows how these errors combine to produce rates and attitude motion at payload release. Jet damping effects are noted and were also considered in the analysis. The magnitude of each error must be determined analytically or by measurement and a two sigma (standard deviation) value assigned to it. This portion of the study constitutes a topic for discussion in itself and will not be pursued here; only the qualitative results in terms of the effect of the errors on the dynamics will be presented.

Analysis And Equations of Motion

The method of analysis used to investigate the effects of the discussed errors was to program the equations of rotational, rigid body, motion (Euler's Dynamical Equations) on an analog computer and to consider each error on an individual basis in terms of the rates and attitude motion it produced. The results were then statistically combined to produce the total effect at payload release.

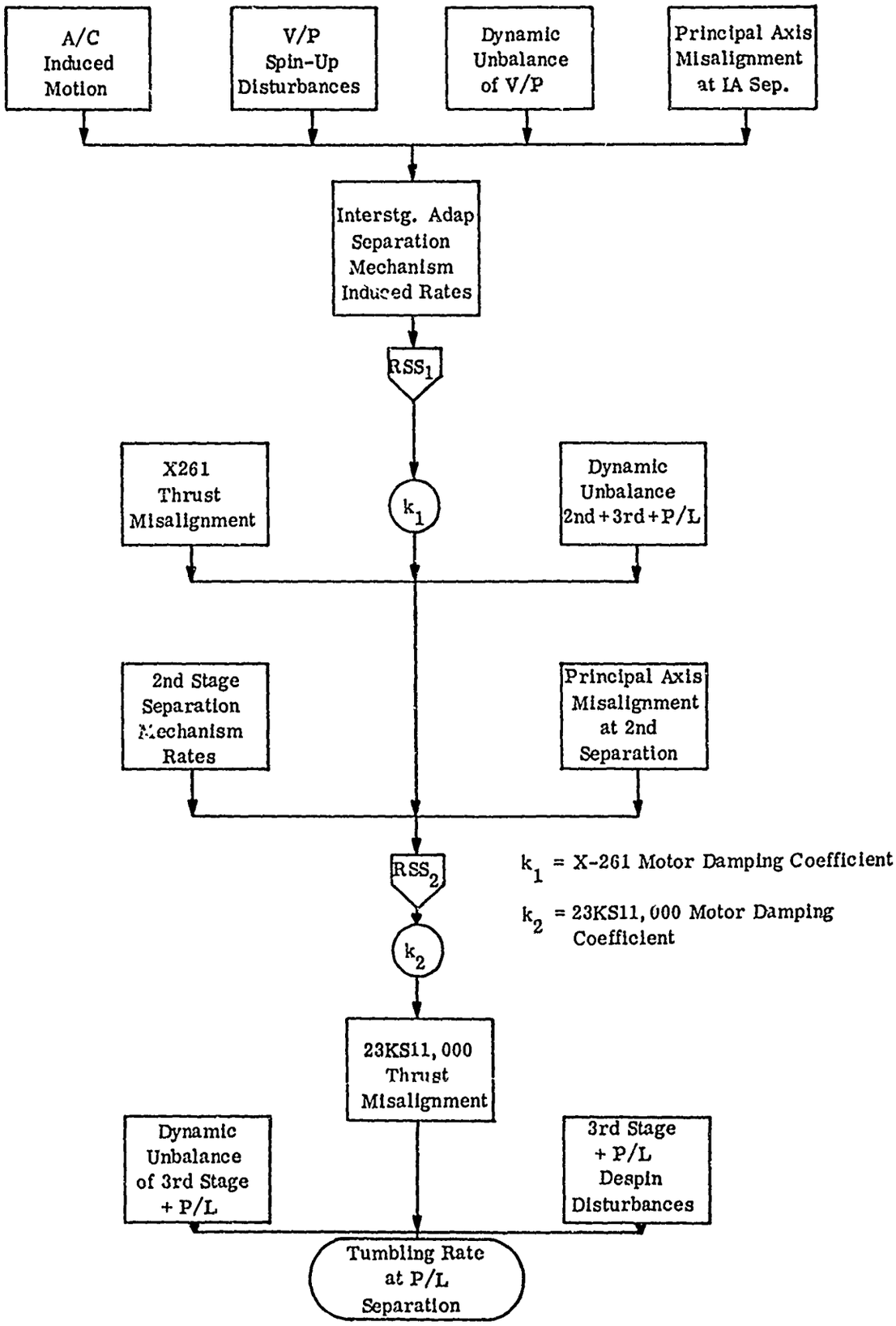

Figure 6. Factors Contributing to Rates and Attitude Error at Payload Release

The equations of motion used to describe the rotational motion of a spinning body in exoatmospheric space were as follows:

$$\dot{p} = \frac{M_x(t)}{I_x}$$

$$\dot{q} = \frac{M_y}{I_y} + \frac{(I_y - I_x)}{I_y} pr - kq$$

$$\dot{r} = \frac{M_z}{I_y} - \frac{(I_y - I_x)}{I_y} pq - kr$$

These equations describe the rate of change of the body rates, p, q, r, in a body-fixed rotating coordinate system, x, y, z, in terms of the components of a body-attached moment, M_x, M_y, M_z. I_x and I_y are moments of inertia and k is the jet damping coefficient for a thrusting vehicle. The rolling moment was programmed as a function of time to allow spin and despin simulations. The assumptions of mass symmetry and that principal axes are coincident with the reference axes have been made.

In order to consider the spatial motion of the vehicle, the above equations must be related to a set of inertial axes. This is accomplished through the following transformation.

$$\dot{\phi} = p$$

$$\dot{\theta} = q \cos \phi - r \sin \phi$$

$$\dot{\psi} = q \sin \phi + r \cos \phi$$

The angles, ϕ , θ and ψ are Euler angles describing the rotations required to go from the inertial axes system to the body axes coordinate

system. Figure 7 shows that two coordinate systems and the Euler angle rotations. The analog output data in all cases were phase plots of $\dot{\theta}$ versus $\dot{\psi}$ and θ versus ψ. The latter relationship can be thought of as the motion of the missile in space as depicted by a projection of its longitudinal axis onto a normal plane, and initially coincident with its equivalent inertial axis.

Discussion of Results

Having defined the error sources in general and the method of analysis used to study their effect on vehicle motion, we can now consider in more detail each error and the results obtained on the analog computer.

Attitude controller errors are the result of two factors; the limit cycle motion before ignition of the second stage motor and the fact that attitude controller jets are activated for a short time during the spin-up of the velocity package. Only the latter error was found to be significant and its magnitude dictated the allowable time delay before attitude controller jet deactivation. Figures 8 and 9 show the effect of this error on vehicle rates and attitude. The figures show the effect of the increasing spin rate and reflect a constant moment in the pitch plane for the duration of the jet activation as well as a moment due to thrust unbalance in the spin motors which is discussed next.

The spin-up and despin operations introduce errors because of motor tolerances. For example, in a system of motors mounted around the periphery of the vehicle, a deviation in thrust of any motor will produce a moment which results in adverse attitude motion. For the motors used in the spin

NOTE:
- x y z = Body axes
- X Y Z = Inertial axes
- $\psi\ \theta\ \phi$ = Euler angles in order of rotation
- x - axis is oriented along the axis of symmetry of the vehicle — positive forward
- p, q, r - Body rates
- $\dot{\phi}$, $\dot{\theta}$, $\dot{\psi}$ - Inertial rates

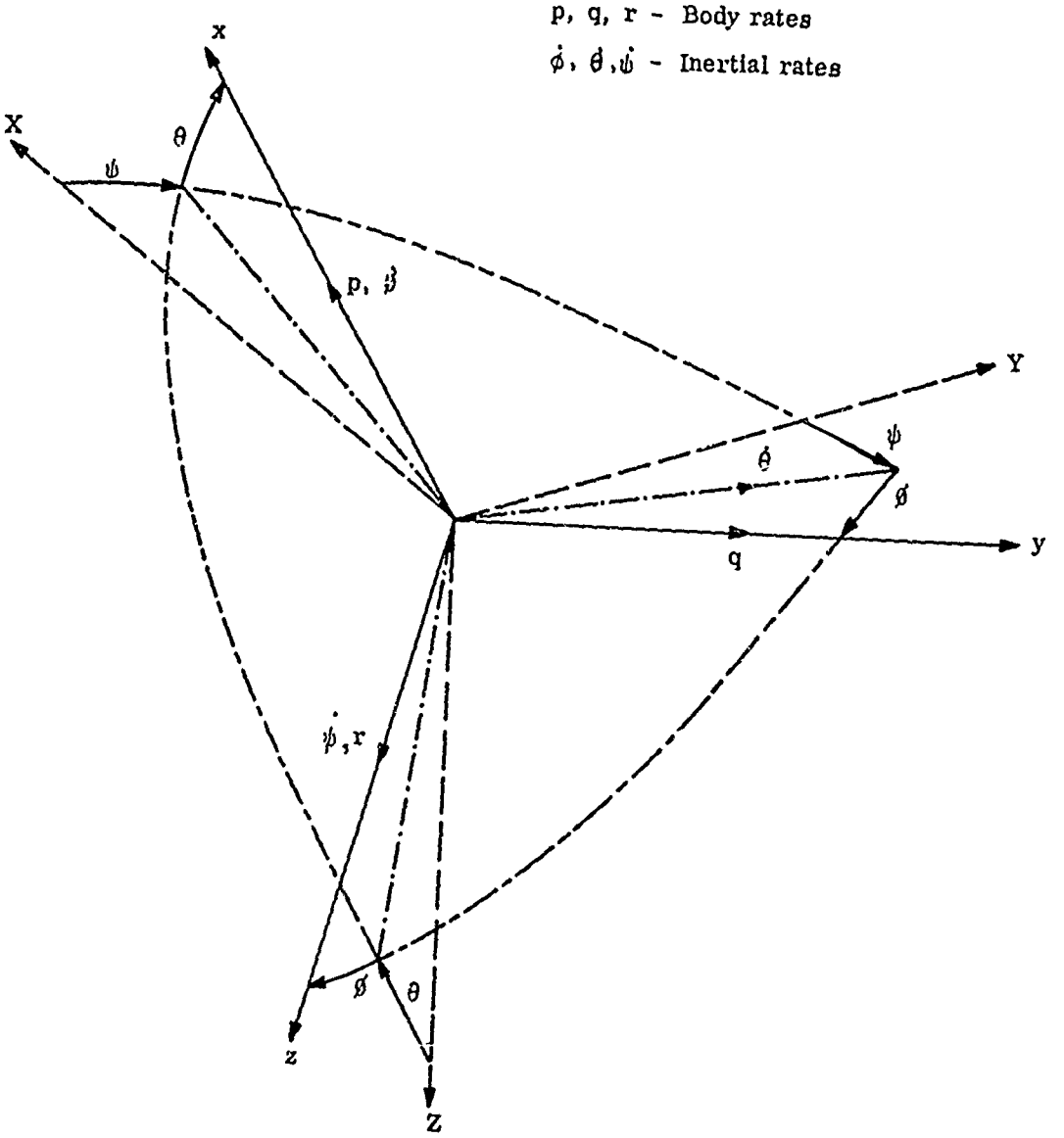

Figure 7. Coordinate System Description

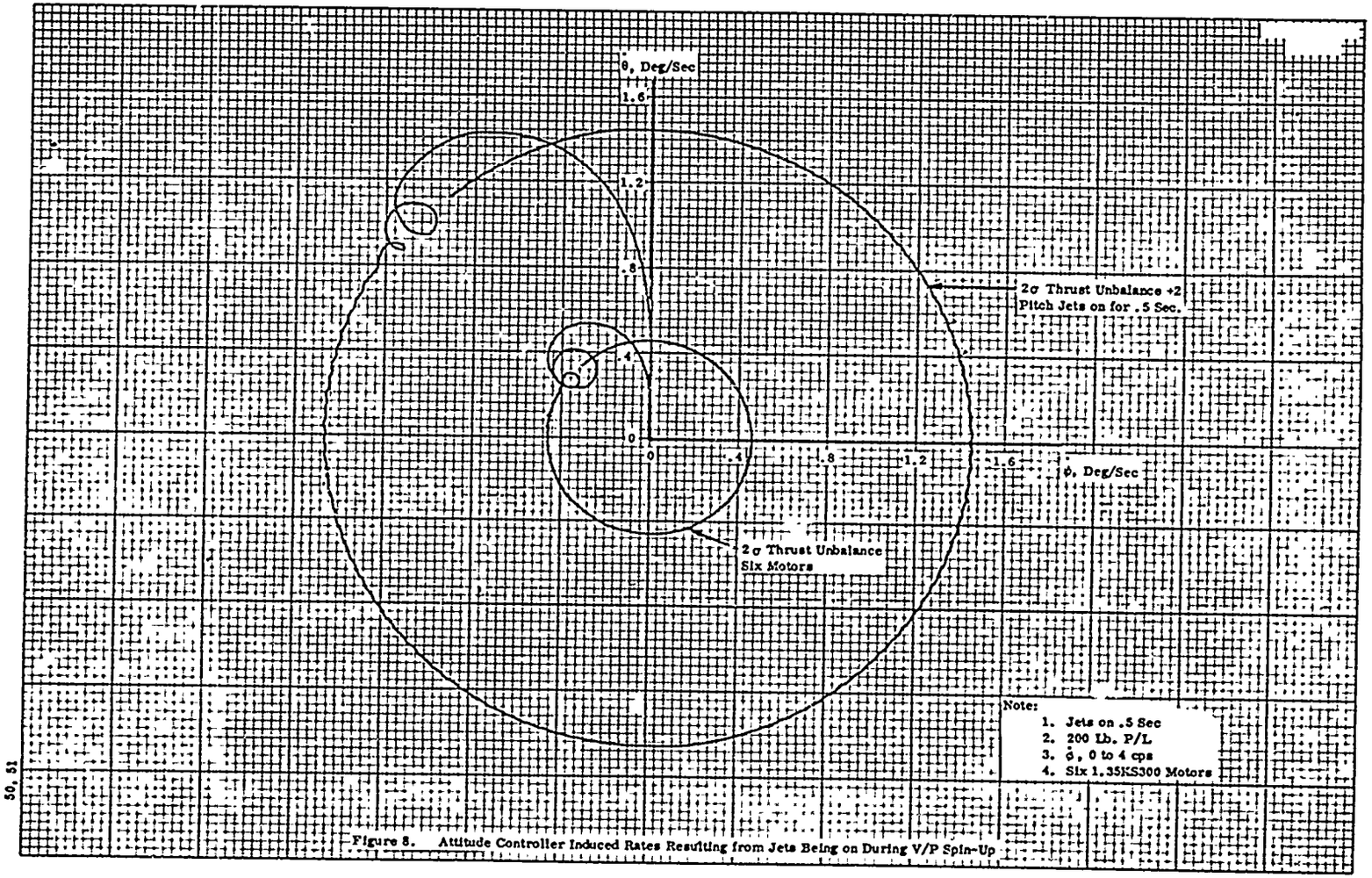

Figure 8. Attitude Controller Induced Rates Resulting from Jets Being on During V/P Spin-Up

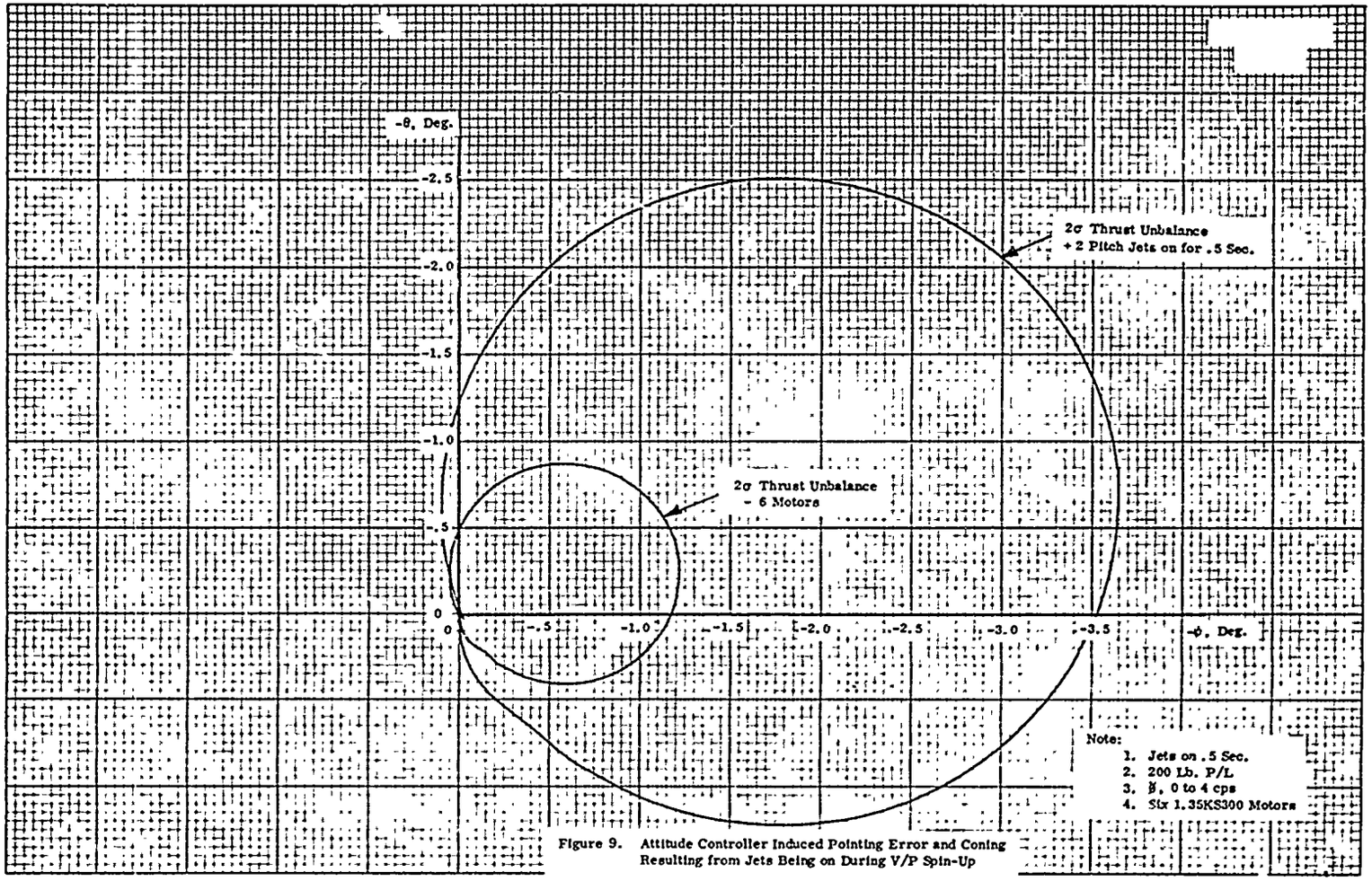

Figure 9. Attitude Controller Induced Pointing Error and Coning Resulting from Jets Being on During V/P Spin-Up

maneuvers, standard deviations in motor parameters were determined from recent test data and used in the analysis. Figures 8 and 9 also show the results of a 2-sigma thrust unbalance in the spin motor system in terms of rates and attitude motion, respectively.

Dynamic unbalance and principal axis misalignment are essentially the same thing; however, for purposes of discussion they are treated separately. Dynamic unbalance results when the vehicle is spun about an axis not coincident with its principal axis and as a result a moment is created about the vehicle cg proportional to the amount of unbalance (or equivalently, the angle between the spin axis and the principal axis). In the Athena H dynamic analysis, mass unbalance was considered to be the result of dynamic balancing tolerances which are the limits imposed on the balancing of the various stages. Principal axis misalignment results when vehicle tolerances accumulate during the build-up of stages. In both instances, the attitude rate may be obtained by:

$$\dot{\xi} = (\dot{\theta}^2 + \dot{\psi}^2)^{1/2} = \frac{2M}{(I_y - I_x)\dot{\phi}} \sin \frac{(I_y - I_x)\dot{\phi}}{2I_y} t$$

where M represents the moment due to mass unbalance or principal axis misalignment. Thus the attitude rate is directly proportional to the spin rate, since the moment is a function of the square of the spin rate. It is of interest to note that the attitude motion is not a function of the spin rate in this case as can be seen by the relationship between attitude rate and coning angle. That is,

$$\lambda \simeq \frac{\dot{\xi}}{\frac{I_x}{I_y}\dot{\phi}}$$

Therefore, one can conclude that spin stabilization is not a consideration in the attitude errors introduced by mass unbalance and principal axis misalignment.

Figures 10 and 11 are examples of analog traces for mass unbalance showing rates and attitude motion, respectively.

Thrust misalignment is the result of both motor manufacturing tolerances and vehicle alignment causing the thrust axis to be displaced from the vehicle center of gravity. Jet damping has the effect of reducing the rates and attitude motion that thrust misalignment produces. Figures 12 and 13 are typical analog plots showing the effect of thrust misalignment on attitude rates and attitude motion.

Finally, rates are produced by the separation mechanisms themselves and one of the primary objectives of the preliminary design phase of the Athena H was to determine criteria for the design of the various separation mechanisms such that a specified rate at payload release would not be exceeded. Moments created by separation mechanisms are generally of such short duration that they can be considered as impulses which produce initial rates. Spring systems introduce errors becuase of the variation in the spring rates. Figures 14 and 15 show initial rates and the coning angles produced by them. Of interest in these figures is the effect of jet damping. It is seen that the damping has the effect of reducing both rates and coning angle, λ, but not pointing error, η. This factor is significant from the point-of-view of dispersion, as it is the pointing error that is primarily

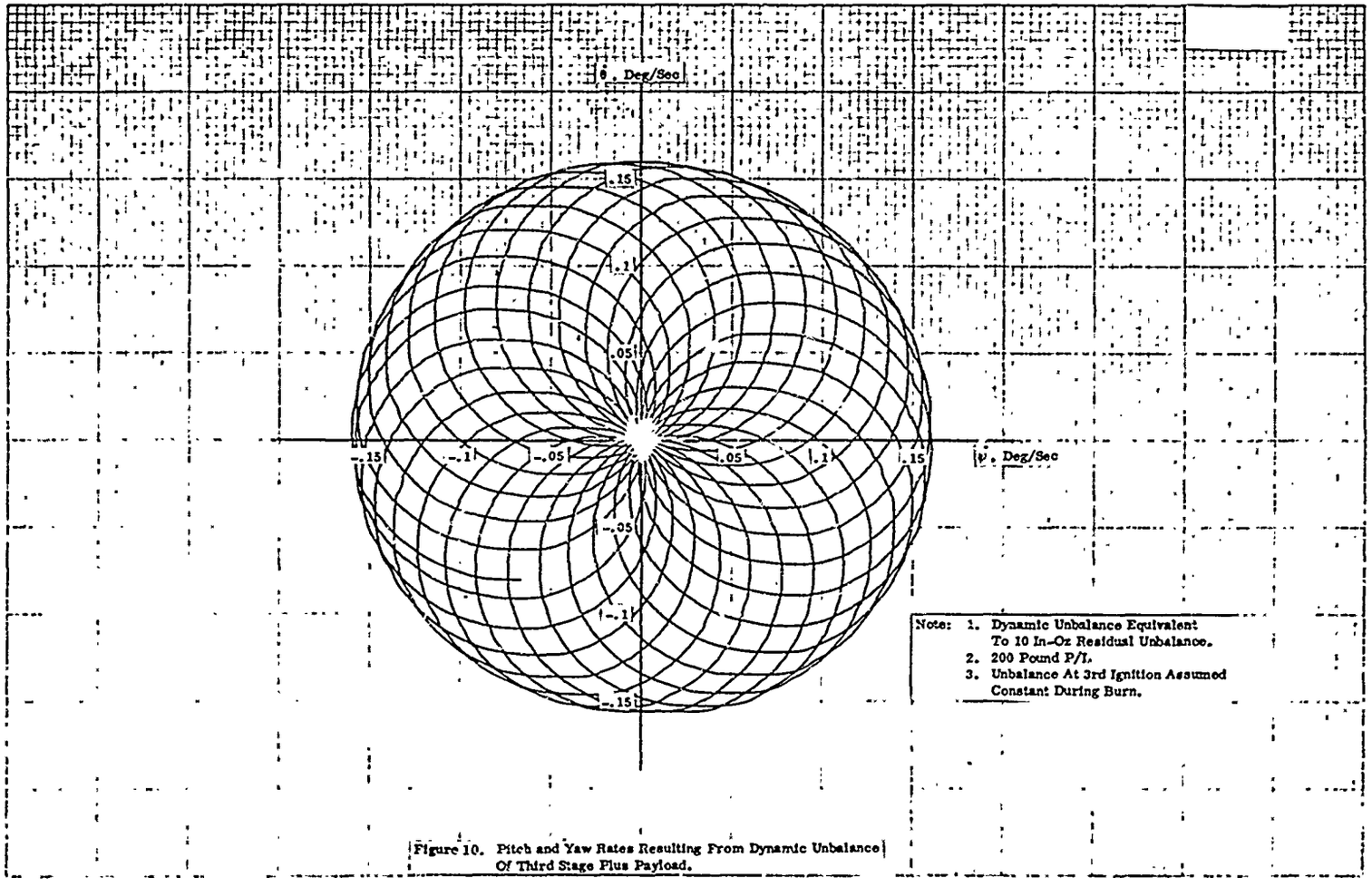

Figure 10. Pitch and Yaw Rates Resulting From Dynamic Unbalance Of Third Stage Plus Payload.

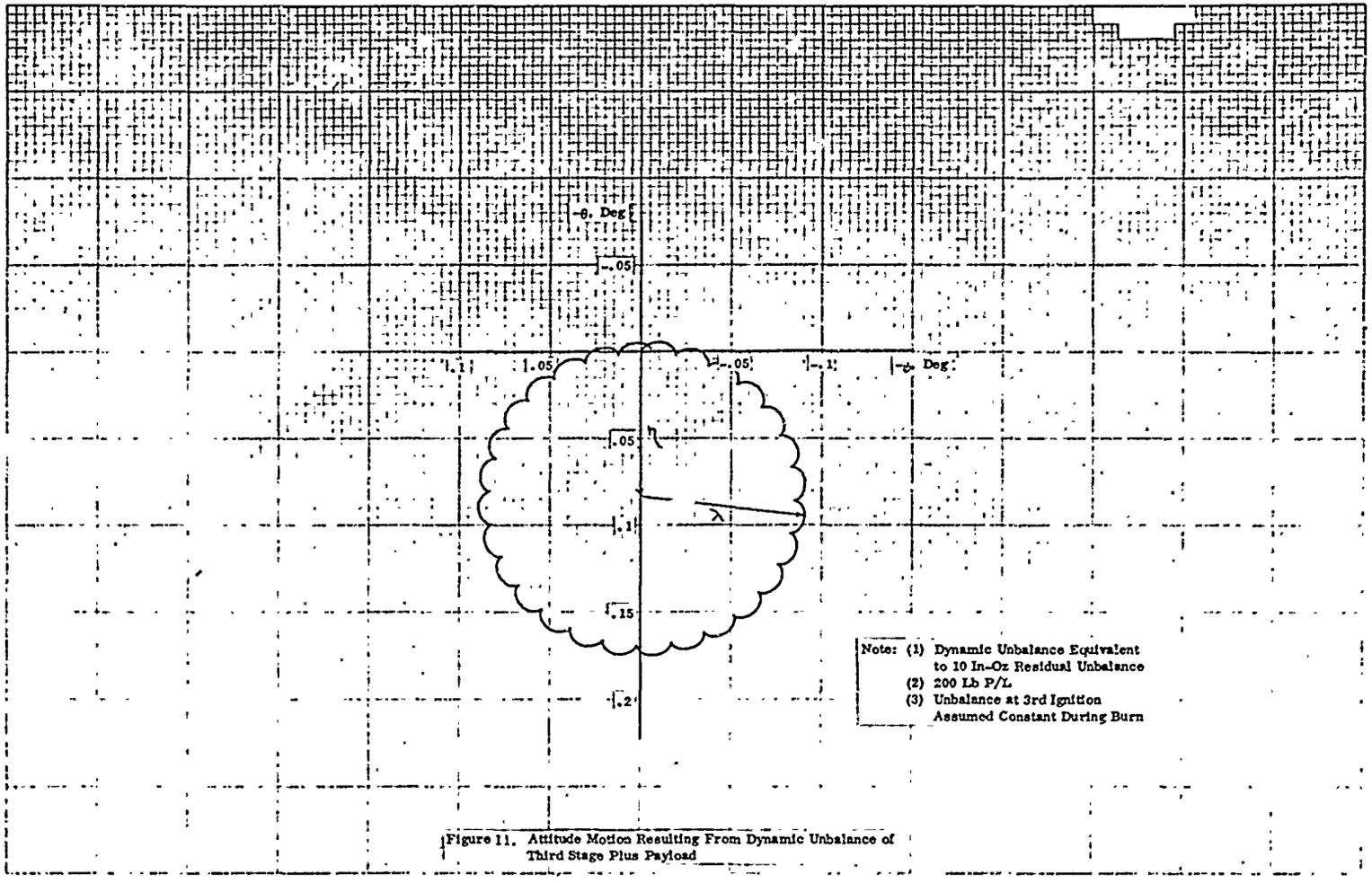

Figure 11. Attitude Motion Resulting From Dynamic Unbalance of Third Stage Plus Payload

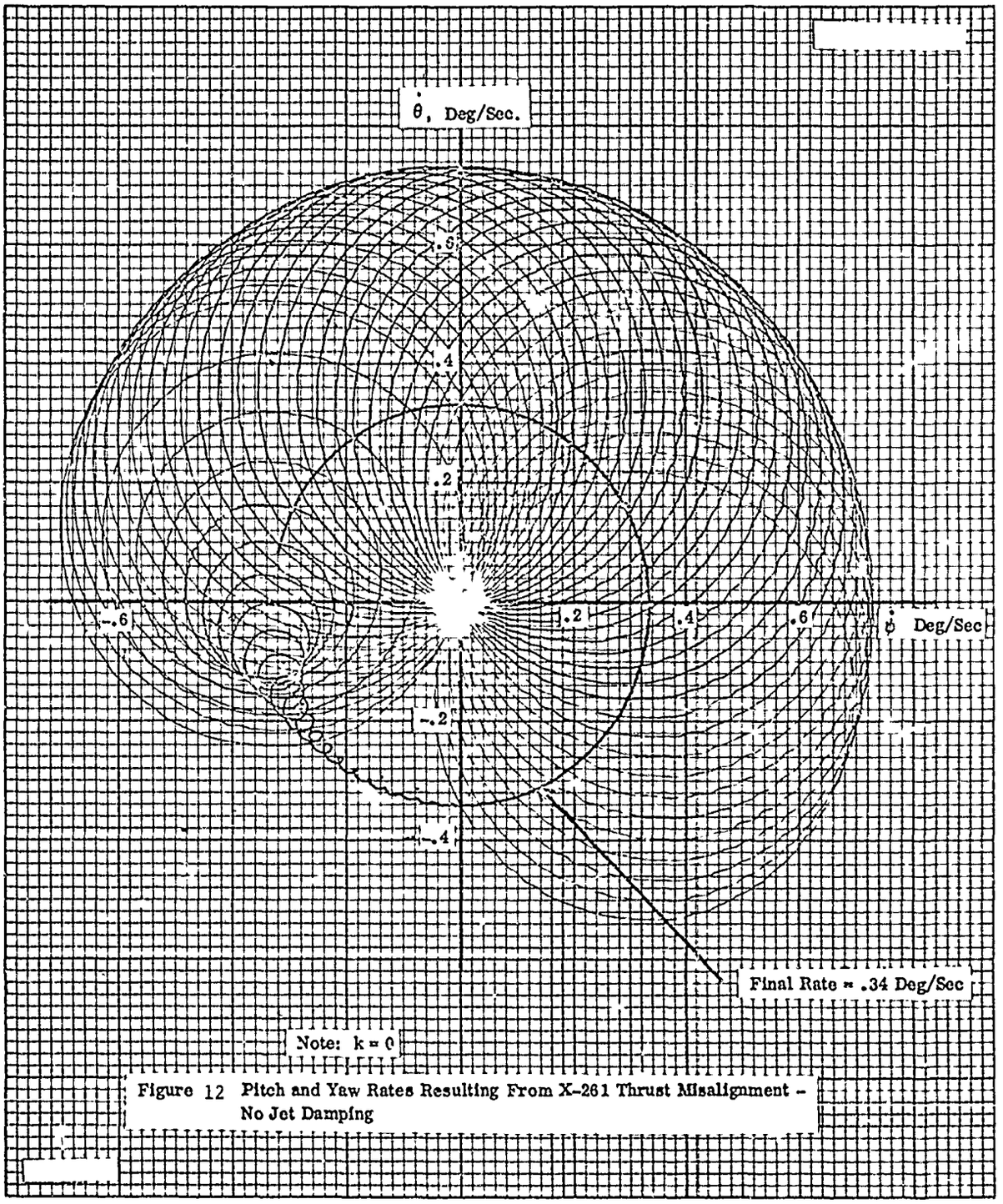

Figure 12 Pitch and Yaw Rates Resulting From X-261 Thrust Misalignment – No Jet Damping

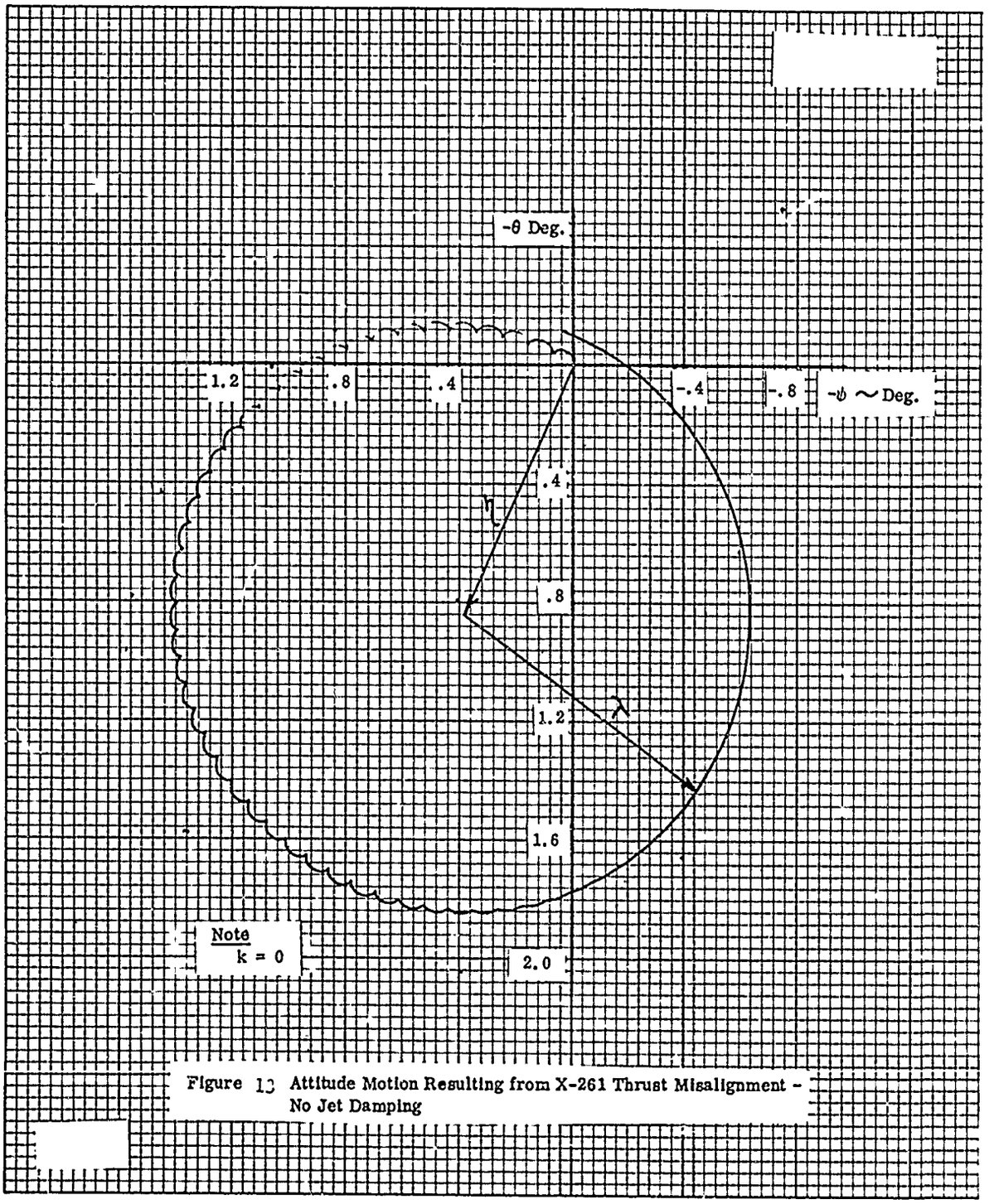

Figure 13 Attitude Motion Resulting from X-261 Thrust Misalignment – No Jet Damping

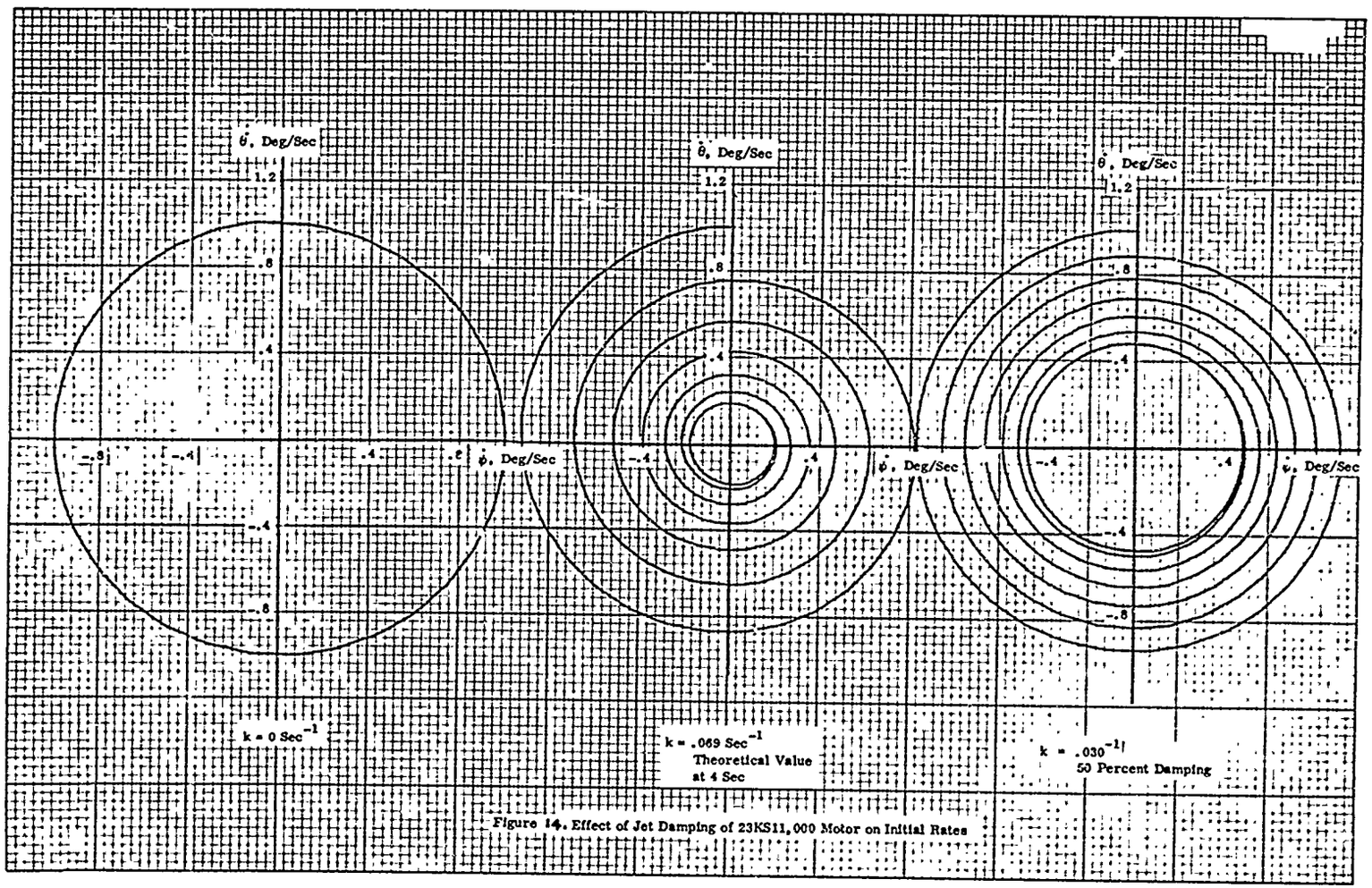

Figure 14. Effect of Jet Damping of 23KS11,000 Motor on Initial Rates

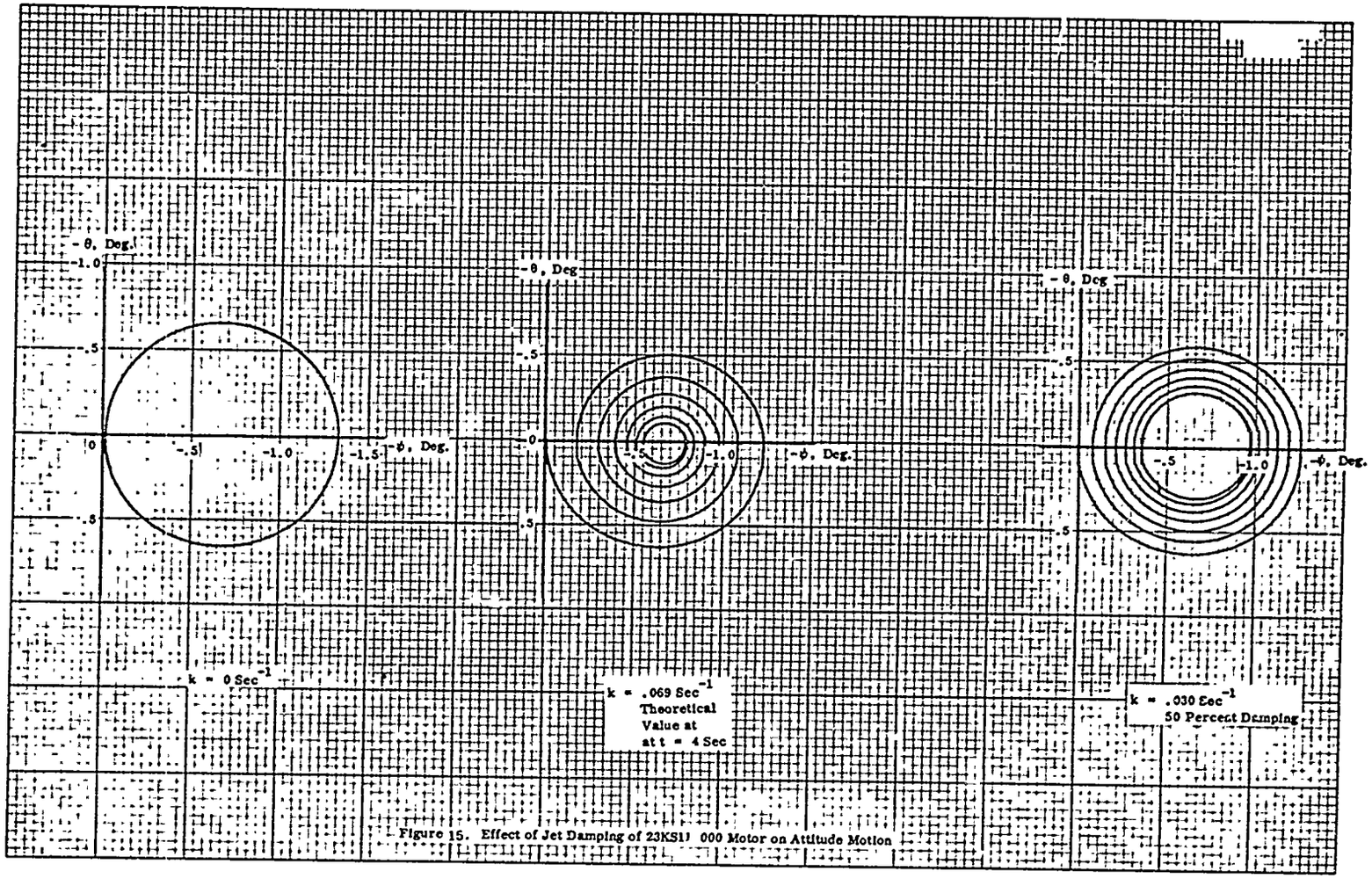

Figure 15. Effect of Jet Damping of 23KS1J 000 Motor on Attitude Motion

responsible for deviation in the flight path angle and thus impact in a thrusting vehicle.

Using the above approach, each error was analyzed in terms of rates and attitude motion. The results were then statistically combined in a root-sum-square fashion to produce the total 2-sigma error in rate at payload release. Attitude errors were used in a dispersion analysis to predict expected deviation of flight parameters and impact of stages and payload.

CONCLUSIONS

In this brief discussion we have attempted to illustrate the methods used to stabilize an essentially unguided launch vehicle as exemplified by an improved version of the Athena missile. Some of the problems of fin stabilization in the atmosphere and spin stabilization during atmospheric exit and reentry have been discussed. The initial identification of the Athena H has been completed and by making use of the methods described in this report we have successfully defined a vehicle that meets all constraints placed upon the dispersion of stages and payload in terms of impact, performance and dynamics.

NEW LOW COST METEOROLOGICAL ROCKET SYSTEM FOR TEMPERATURE AND WIND MEASUREMENT IN THE 75,000 TO 200,000 FEET ALTITUDE REGION

By Bruce Bollermann and Robert L. Walker
Space Data Corporation
Phoenix, Arizona

ABSTRACT

An instrumented dart system, which can be used as the upper stage of the Loki Dart meteorological rocket vehicle, has been designed to m asure vertical profiles of temperature and winds between 75,000 feet and 200,000 feet altitudes. The components of the instrumented dart include the dart assembly, time delay and payload expulsion system, telemetry system, temperature sensor, and parachute. The telemetry system is designed to be compatible with the Rawin Set AN/GMD-1B and associated equipment.

Flight tests of the system, which were conducted at the White Sands Missile Range and the Air Force Eastern Test Range, have demonstrated the feasibility of the system for measurement of upper atmosphere winds and temperatures. An error analysis for temperatue and wind measurements indicate that appreciable improvements can be obtained by reducing the descent rate of the parachute-sonde system.

INTRODUCTION

With the increased tempo of nuclear testing during operations Castle and Redwing in the Central Pacific in 1954 to 1956, the requirement for a wind-sensing meteorological rocket system was generated. The rocket system utilized was the Loki, which was originally

developed by the Jet Propulsion Lab. for the U.S. Army Ordnance Corp. as an anti-aircraft rocket. The Loki system utilized a small, high thrust, short duration rocket motor with a high ballistic coefficient, coasting dart vehicle. After rocket motor burn out, the dart vehicle coasted to an altitude of approximately 100,000 feet and ejected a cloud of radar-reflective, wind-sensitive chaff. This chaff cloud was radar tracked during its descent to determine the upper-altitude winds. At a later date, the same rocket motor hardware was loaded with a higher energy propellant, and the propellant grain port diameter was reduced to increase propellant volume. These two changes increased the total impulse from 2,660 lb-seconds to 3760 lb-seconds. In addition the burning time was increased from 0.80 seconds to 1.86 seconds. With these changes, apogee altitude was increased to approximately 200,000 feet. This latter system, with a chaff payload, has been a mainstay of the Meteorological Rocket Network. More recently a number of companies have further increased the total impulse of the Loki rocket motor to slightly over 4,000 lb-seconds by further reducing the port diameter and increasing the propellant density. With this latest increase in propellant weight, apogee altitude for the standard chaff dart is increased to about 230,000 feet from an 85° sea level launch. The Robin inflatable sphere has also been successfully deployed at altitudes of 205,000 feet from a 1.500 inch dart and 230,000 feet from a 1.375 inch dart. Only recently, however, have temperature measuring parachute-sonde systems been successfully flown with this basic system.

The goal of an instrumented dart program, which Space Data Corporation has conducted for the Aerospace Instrumentation Laboratory of Air Force Cambridge Research Laboratories [Walker, ref. 1], with additional support and cooperation by the Electronics Research and Development Activity at White Sands Missile Range, has been the development of a minimum cost rocketsonde system which is specialized to make routine wind and temperature measurements to altitudes of 200,000 feet. In addition to minimum cost, an all-weather launch capability and minimum impact dispersion are further advantages of the system.

REQUIREMENTS

Although the high-altitude research meteorologist would like to measure a variety of parameters, such as ozone and electron density, on a research basis, the requirements for routine high-altitude meteorological measurements appear to be limited to those of Table 1. These requirements differ only slightly from agency-to-agency, and it appears that a rocketborne parachute-sonde descent system which employs a temperature sensing element can satisfy most of the operational requirements. Though density is generally required, a reasonably accurate density profile can be calculated from the measured temperatures with a combination of the equation-of-state for an ideal gas and the hydrostatic equation. The bead thermistor which is used for the temperature measurements is both small and inexpensive. It seems to be ideally compatible with the small inexpensive rocket system. For the next few years, at least, it is expected that the thermistor will be used for operational data instead of more cumbersome and expensive sensor instrumentation, designed to measure either density or pressure directly. The Robin inflatable sphere is certainly a candidate for the direct measurement of density, and it is quite inexpensive. The sphere is a passive sensor which relies on a fairly high-precision radar track to determine its fall velocity and acceleration from which atmospheric density may be calculated through the appropriate drag equations. A Loki Dart Robin system has been successfully developed and flight tested under a previous AFCRL program [Watson, ref. 2]. The Robin payload could easily be interchanged with the parachute-sonde in the current loki dart vehicle whenever direct density measurements are required.

TABLE 1

MEASUREMENT REQUIREMENTS FOR ROUTINE METEOROLOGICAL SUPPORT AND OPERATIONS

Parameter	Wind	Temperature	Density
Altitude	80,000 - 200,000 Ft.	80,000 - 200,000 Ft.	80,000 - 200,000 Ft.
Accuracy, rms	3 - 10 ft/sec	1 - 2°C	2 - 3%

The logistics requirements for a routine meteorological rocket system are that the system must be capable of being launched by a minimum crew of two men and with ground winds up to thirty-five knots. The system must be simple to launch by relatively untrained personnel and must have the capability for mobility. A most important consideration is that the system be extremely low in cost. This latter requirement is perhaps the most important for a routine meteorological rocket system.

INSTRUMENTED DART SYSTEM

System Design and Operation.

The design and flight tests of an instrumented dart system compatible with the Loki rocket motor has been completed by Space Data Corporation for the Aerospace Instrumentation Laboratory, Air Force Cambridge Research Laboratories, Bedford, Massachusetts. The instrumented dart system includes the dart assembly, parachute and instrument package with temperature sensor. The instrument package transmits temperature data using a standard 10-mil bead thermistor as the sensor. The transmitted signal is adjustable between 1660 and 1700 mc and is compatible with the Rawin Set AN/GMD-1B and associated equipment such as the radiosonde recorder AN/TMQ-5C. The capability of the system to eject its payload at an altitude in excess of 200,000 feet and transmit temperature data from that height to 75,000 feet or less has been demonstrated. The instrument package descends by parachute over this altitude region in approximately 20 minutes, and the parachute is radar reflective for S-Band and/or C-Band radar tracking.

The vehicle as shown in Figure 1 is a two-stage system with the first stage being a Loki rocket motor, and the second stage an inert dart with a high ballistic coefficient. The dart houses the payload. The Loki booster is a short burning, high thrust unit with a burning time of approximately 1.8 seconds. The operation of the system is shown in Figure 2. The vehicle is launched from a spiral tube at the desired elevation and azimuth setting. The booster burns out at approximately 5,000 feet altitude at which time dart separation occurs.

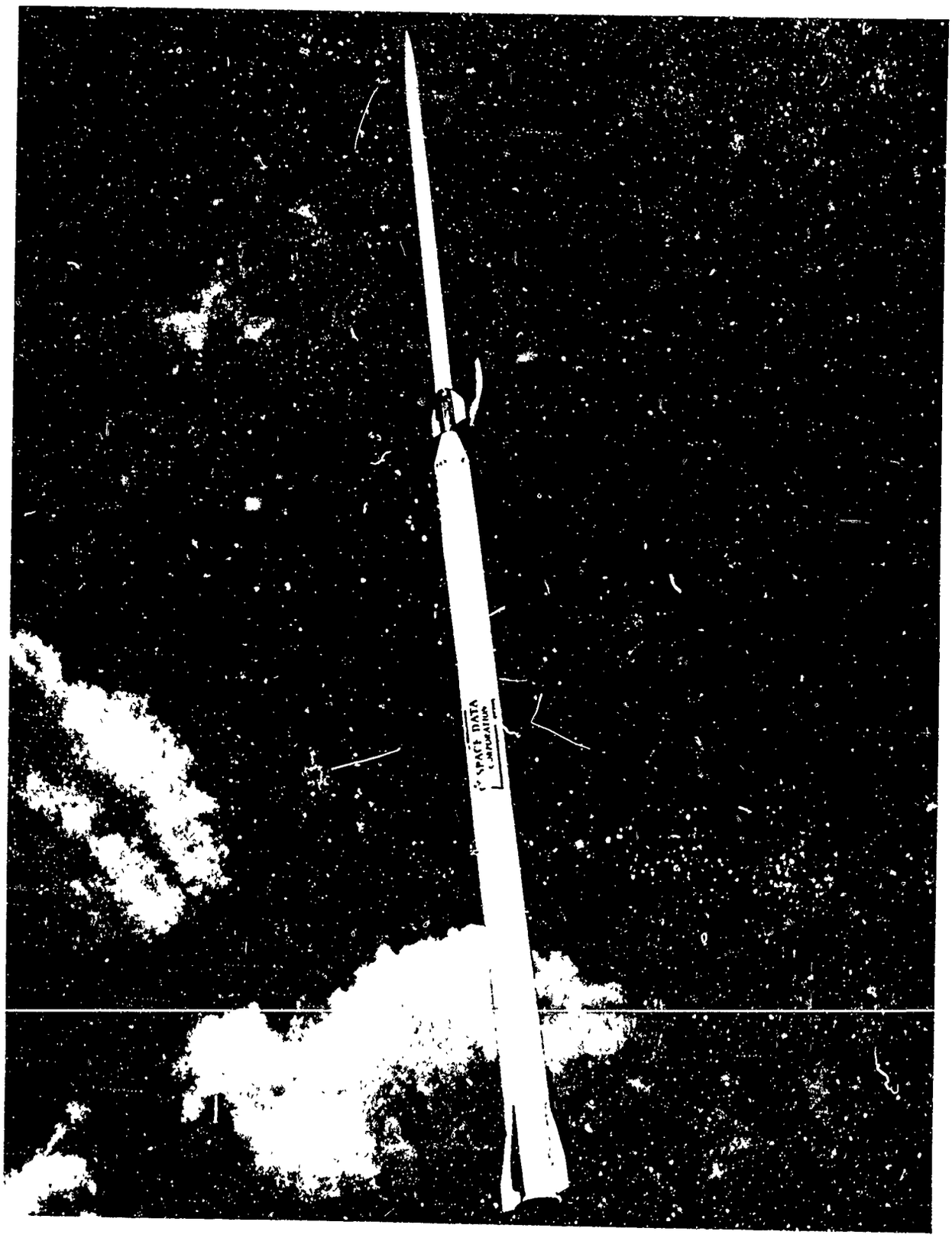

FIG. 1 LOKI - DART VEHICLE

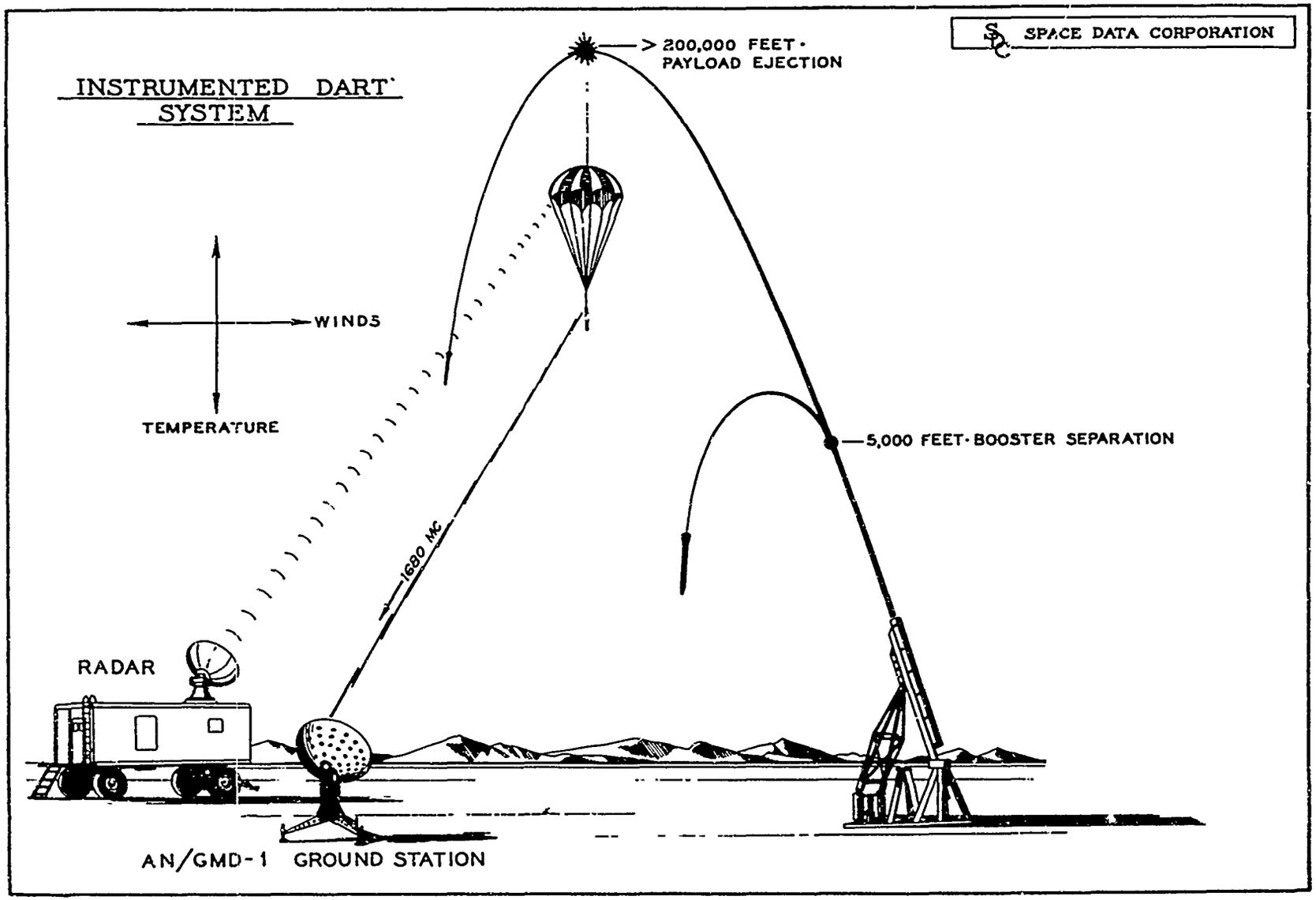
SPACE DATA CORPORATION
INSTRUMENTED DART SYSTEM
> 200,000 FEET · PAYLOAD EJECTION
WINDS
TEMPERATURE
5,000 FEET · BOOSTER SEPARATION
1680 MC
RADAR
AN/GMD-1 GROUND STATION

FIGURE 2

The dart coasts to apogee and ejects the payload. Upon ejection of the payload, the parachute inflates, resulting in a controlled fall rate for the parachute-instrument package combination. The standard GMD-1B receives the telemetered temperature data and records the data on the AN/TMQ-5C recorder without any modifications to either the receiver or the recorder. The parachute is 50% silvered to provide a radar-reflecting target which allows the radar to track the motion of the parachute and provide the altitude time history required for the temperature measurement and the horizontal motion for the wind data.

The instrumented dart system as shown in Figure 3 is made up of the following major dart components:

a. dart ogive

b. dart body

c. dart tail assembly

d. delay and expulsion charge

e. parachute

f. instrument package with temperature sensor

The configuration of the dart assembly is shown in Figure 4. The tail assembly of the dart is designed to be compatible with the Loki rocket motor forward closure. The overall aerodynamic configuration of the system is designed to give the vehicle the required aerodynamic stability necessary for reliable performance both during the boost phase and while the dart is coasting to altitude. The payload ejection is timed by a pyrotechnic time delay which is initiated at launch. The time delay is selected such that the ejection occurs at apogee. The time delay ignites the expulsion charge which expels the payload and parachute system as shown in Figure 5. At this point the parachute inflates giving the instrument package a controlled fall rate, necessary for the temperature and wind measurement.

One important feature that is incorporated in the design is for the vehicle to have an uptrack capability for the GMD, so the signal is being received at the time of ejection.

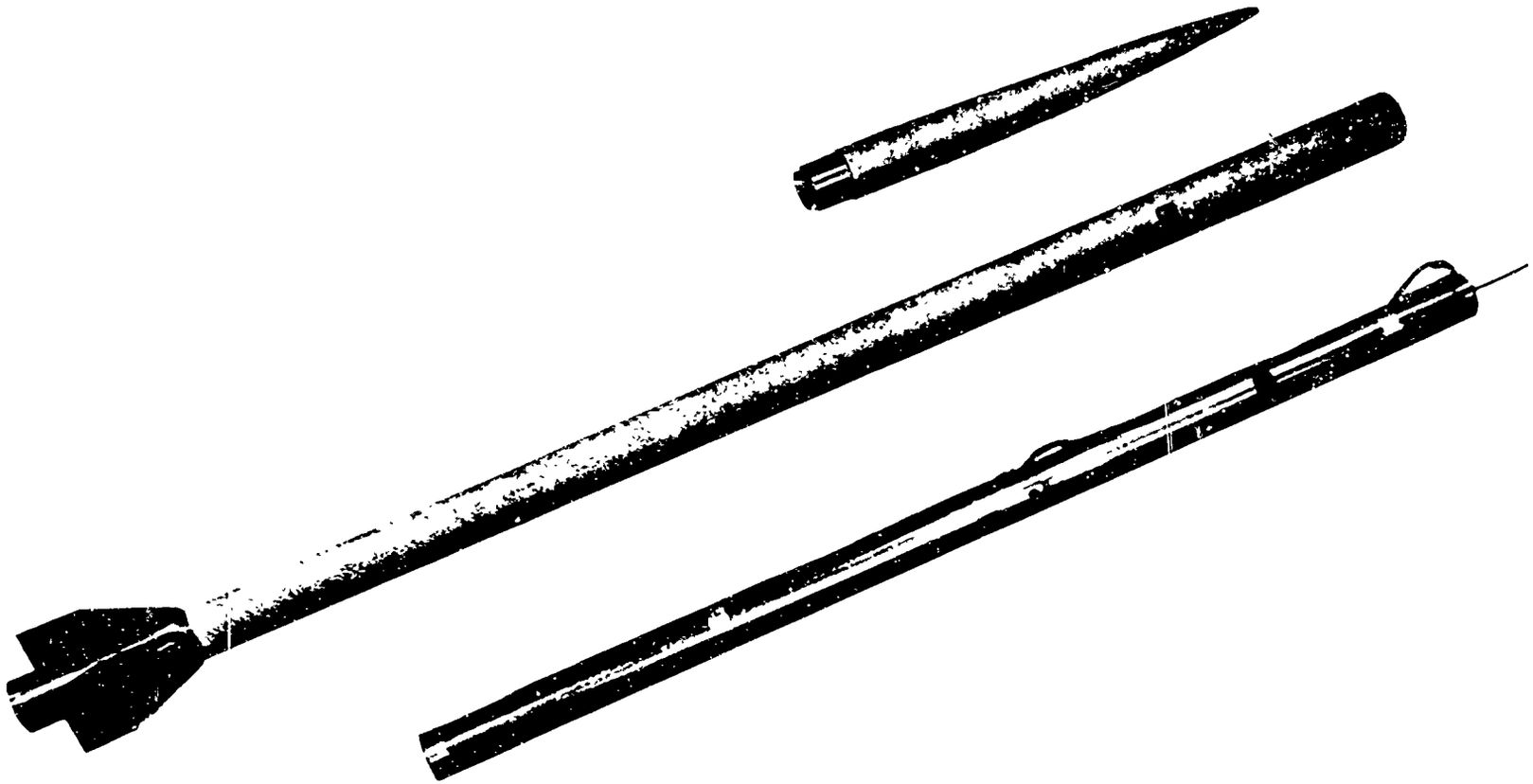

FIG. 3 INSTRUMENTED DART COMPONENTS

SPACE DATA CORPORATION

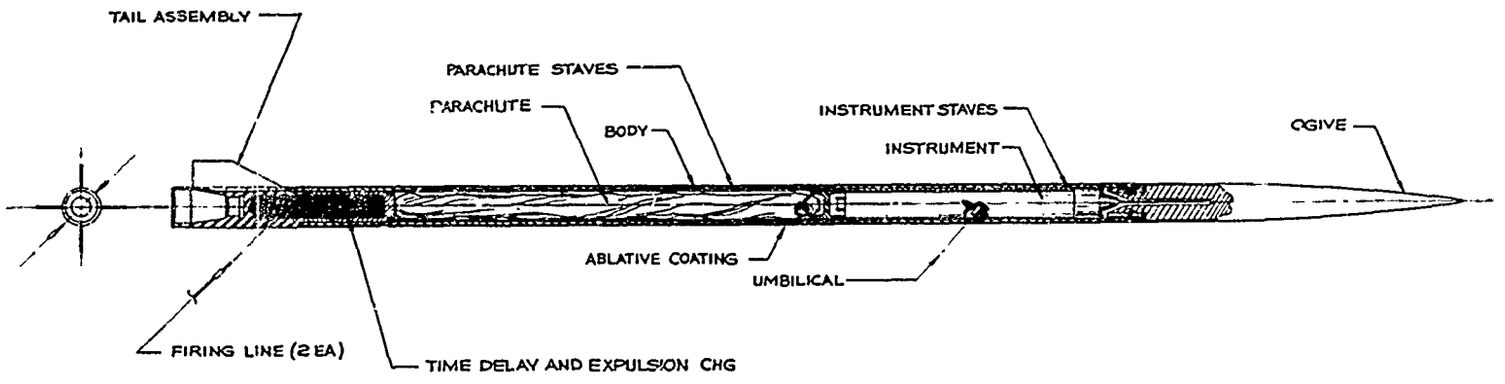

DART ASSEMBLY

FIGURE 4

SPACE DATA CORPORATION

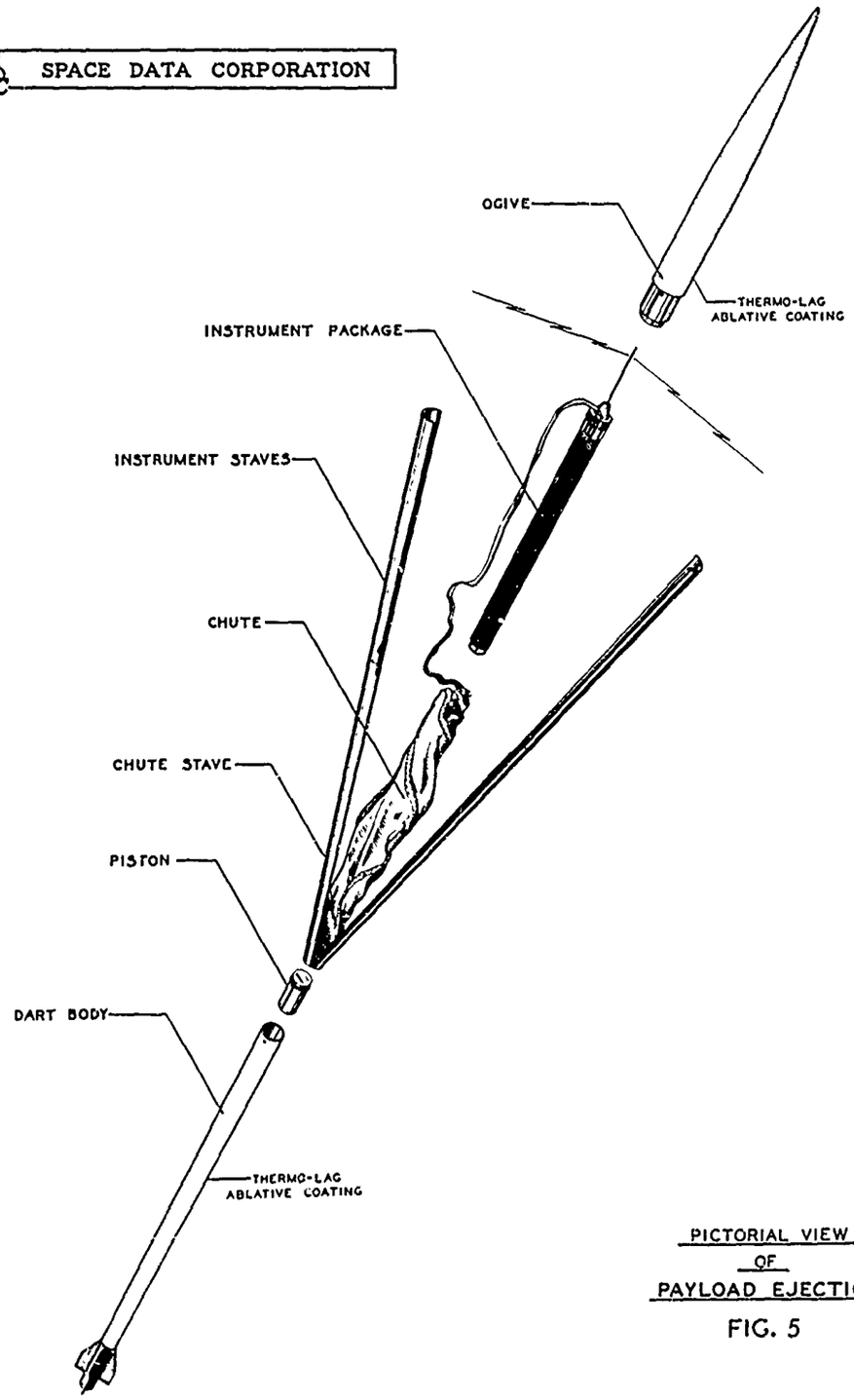

PICTORIAL VIEW
OF
PAYLOAD EJECTION

FIG. 5

This allows the GMD to track the signal on the say to apogee, eliminating any delay in acquiring the instrument, both in position and frequency at ejection. Ability to track the signal prior to ejection can save several minutes of data which may be lost if it is necessary to acquire the signal after ejection. Also the capability of the instrument to transmit, while it is in the dart, facilitates the prelaunch checkout. The instrument can be switched on remotely prior to launch and acquired by the GMD to verify that the instrument is operating properly.

Another important feature of the design of this system is the method of controlling the heat transfer to the instrument package from aerodynamic heating. The concept of the boosted dart system is to obtain a high velocity in as short a time period as possible, separate the booster and allow the dart to coast to altitude. This technique is employed to limit wind-sensitivity for minimum impact dispersion. These high velocities in the dense portion of the atmosphere cause aerodynamic heating to be relatively severe. Two basic techniques were used to control the aerodynamic heating: (1) Internal insulation of the payload by using a material having a low coefficient of heat transfer or an air gap and (2) use of an externally applied ablative material called Thermolag. The Thermolag is sprayed on the exterior of the dart so that the dart body will not reach a temperature in excess of the ablation temperature of the Thermolag. Figure 6 shows a comparison between the skin temperature of the dart with and without the Thermolag coating.

Altitude capability of this system is largely dependent on the type of Loki motor used. The Loki motor used for the White Sands tests and some of the later tests at the Air Force Eastern Test Range is a higher performance version of the Loki II-A and is known as the Judi rocket motor or SDC Loki rocket motor. The nominal altitude capability of the system using this motor is shown in Figure 7.

The older Loki motor design which was used at the AFETR is designated Rocket Motor MX-3290-FMQ-6 and is basically the same motor as the original Loki II-A. The altitude that is achieved by using this motor is nominally 170,000 feet when launched from sea level.

FIGURE 6

DART WALL TEMPERATURES DUE TO AERODYNAMIC HEATING

1-3/8", 9.5 LB. DART
LAUNCH ALTITUDE = 0 FT., Q.E. = 84°

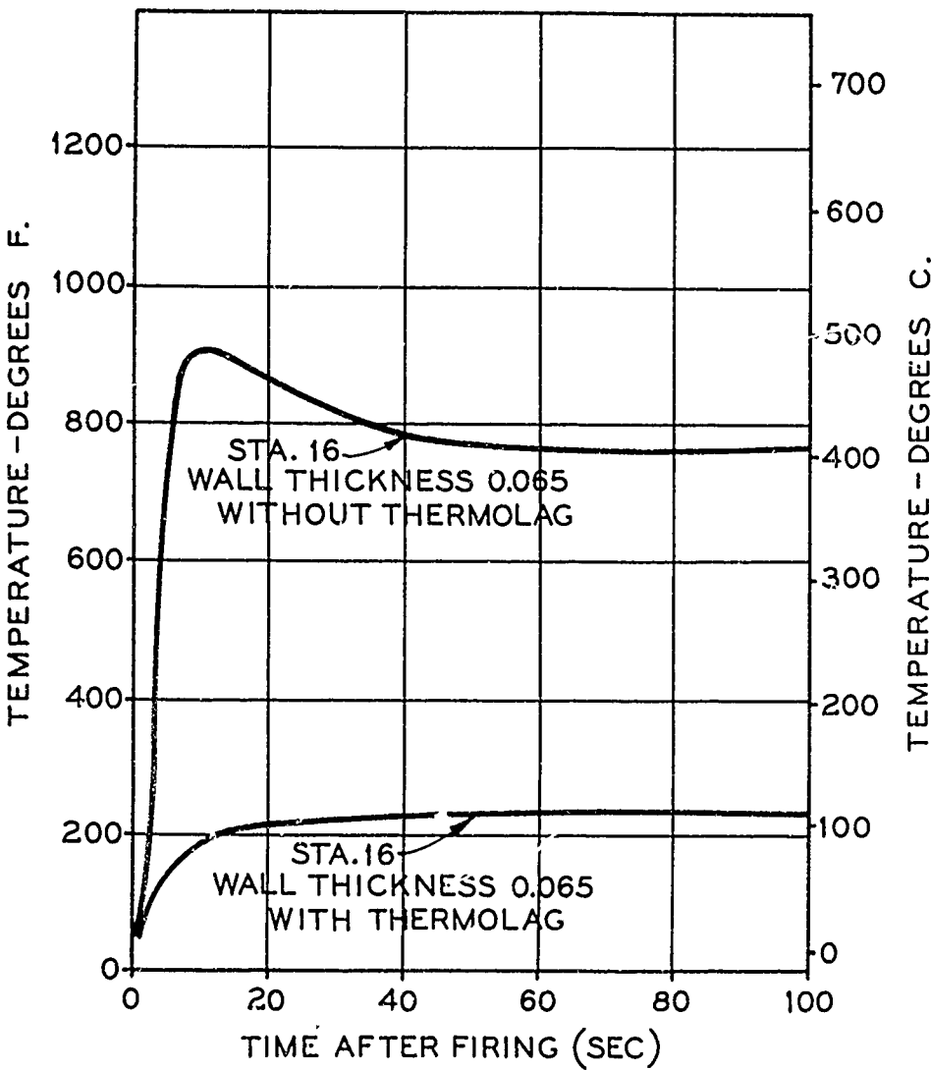

FIGURE 7 APOGEE PERFORMANCE FOR THE LOKI INSTRUMENTED DART WITH THERMOLAG

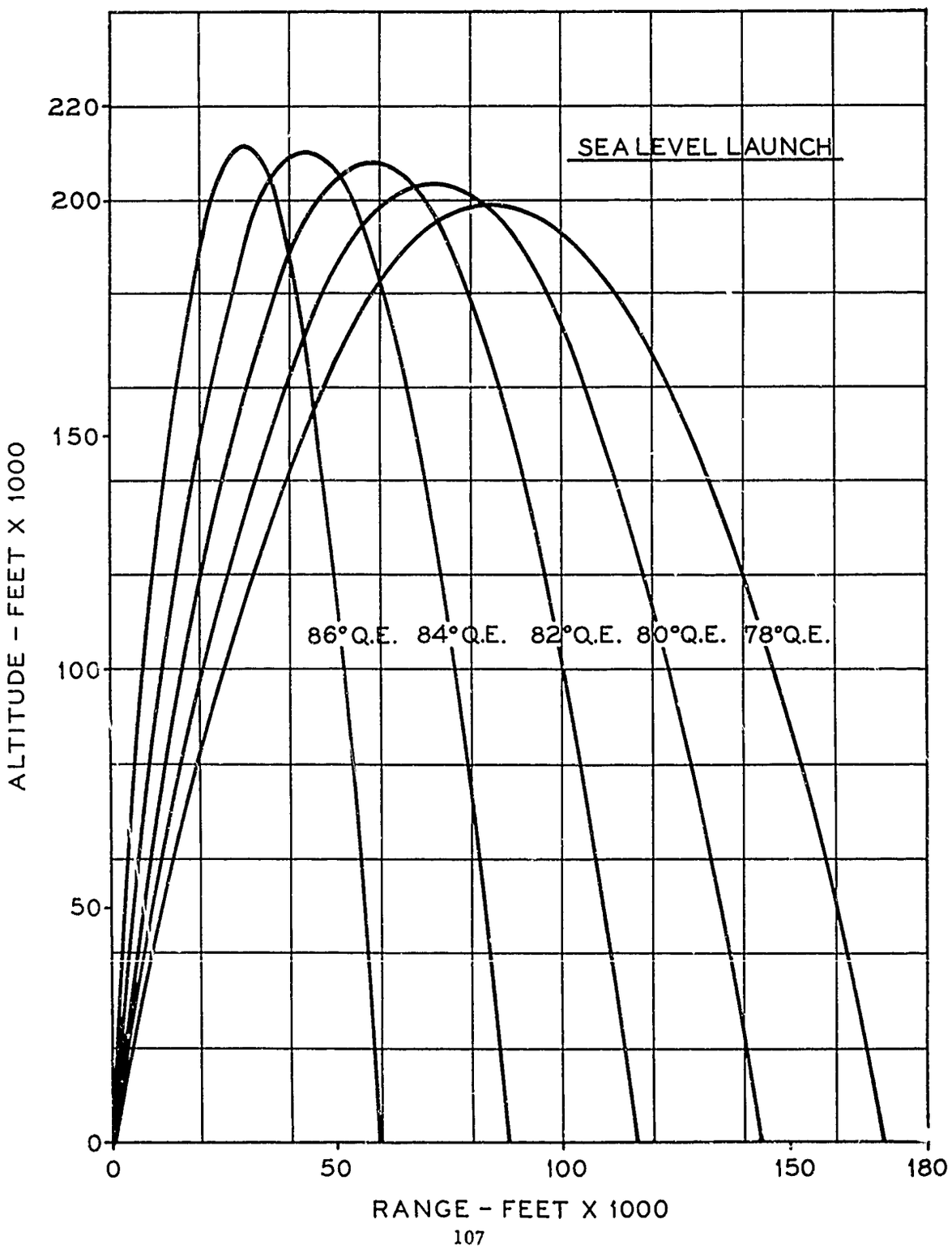

Therefore, the higher performance Loki motor is required for the system to make measurements to 200,000 feet. Table 2 presents a comparison of rocket motor characteristics and performance.

TABLE 2

ROCKET MOTOR CHARACTERISTICS AND PERFORMANCE

Characteristics	Loki #1.9 KS 2000 or Hasp #MK32 Mod 0	Judi 1.9 KS 2150 or SDC P/N 250-10
Length (inches)	66.0	66.0
Diameter (inches)	3.13	3.13
Inert Weight (pounds)	6.45	5.80
Propellant Weight (pounds)	16.88	18.15
Mass Fraction	0.724	0.758
Grain Port Diameter (inches), Tapered	1.004-1.583	0.996-1.297
Throat Area (inches^2)	0.983	1.41
Performance		
Apogee Altitude (Feet) (85° QE, Sea Level Launch, 1.375"/9.8 lb Dart)	170,000	205,000
Total Impulse (lbf-sec)	3760	4063
Action Time (seconds)	1.90	1.89
Average Thrust (lbf)	1980	2150
Average Chamber Pressure (psia)	1340	1100
Specific Impulse (seconds)	223	224

Parachute.

Prior to the beginning of the development program, three different types of parachutes had been flown in the Loki system. These three types were as follows: (1) 6 ft square-flat-silk parachute, (2) 7.6 ft flat-circular-silk parachute, (3) 5 ft silk baseball type parachute. Of the three parachutes, the first two gave an acceptable fall rate. The baseball type has

a fall rate which was too high. This fall rate could have been decreased by increasing the size of the parachute, however, the volume limitations in the dart made any increase in packaging requirements for the larger parachute size objectionable. From a limited number of flight tests it appeared that the 7.6 foot chute had slightly better opening characteristics at high altitude than the square chute; therefore, the 7.6 foot circular parachute was selected.

The 7.6 foot parachute weighs approximately 3.6 ounces, with alternate panels of the silk forming the parachute canopy being metalized to make the parachute radar reflective and suitable to be tracked by an S and/or C Band rada. Figure 8 shows the parachute and the method of canopy construction.

Instrument Electronic Design.

The electronic package is a hybrid solid state and vacuum tube device, powered by nickel-cadmium batteries. The vacuum tube is a cavity oscillator triode similar to that which has been used for rocket and balloon borne packages for a number of years. The modulation circuit, reference circuit and DC to DC converter utilize solid state devices. The sensor is a bead thermistor of approximately 0.010-inch diameter with leads of 0.001 inch diameter platinum-iridium wire. The sensor is coated to reduce solar absorption. The methods used to expose the sensor to the environment are discussed in the mechanical system description which follows. The sensor used has a resistance range of 60K ohms to 3 megohms in the region of data acquisition.

The thermistor, which has a negative temperature coefficient of resistance of approximately 4%/°C, is a component in a pulse generating circuit whose rate is a function of its resistance. The pulses from this circuit are applied to the cavity oscillator in such a way as to terminate the carrier for the duration of the pulse, thus allowing the ground equipment to receive the data as described in the following section. In order to detect any drift in pulse frequency due to environmental effects on the airborne circuitry, a known resistance value is periodically switched into the circuit. Comparison of the pulse rate observed with that obtained during a preflight calibration allows corrections to be made if any drift is present.

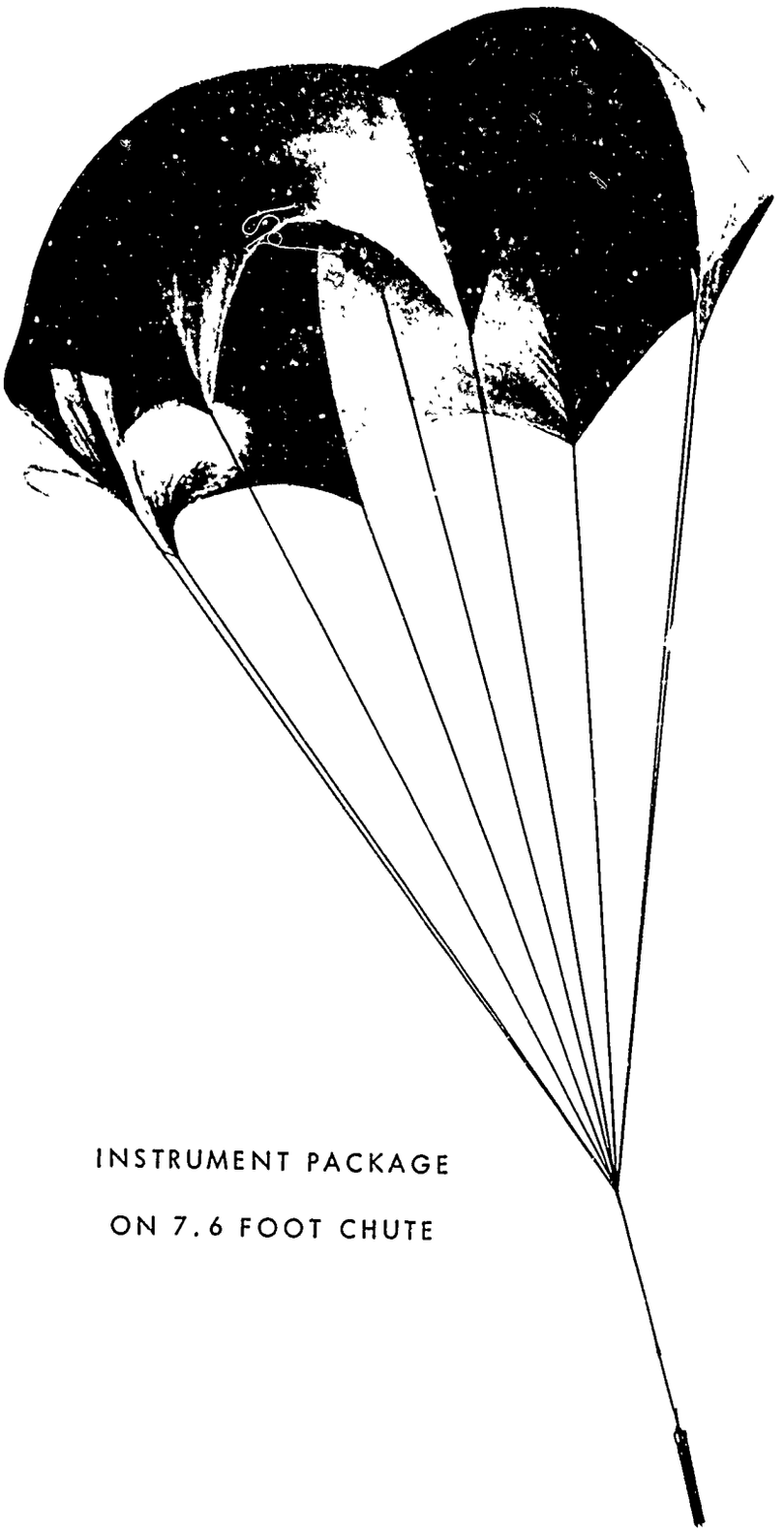

INSTRUMENT PACKAGE

ON 7.6 FOOT CHUTE

FIGURE 8

This reference period was 2 to 3 seconds approximately 3 times per minute on the early units, but has been extended to 6 to 7 seconds every 1-1/2 minutes on recent systems. The cavity oscillator triode provides the 1680 mc carrier frequency upon which the data pulses are imposed. It is transmitted using a linear asymmetric dipole antenna, which provides excellent coverage. In addition, provision is made to utilize the dart ogive and case as an antenna to allow the dart system to be tracked during the flight prior to ejection of the instrument. The power supply for this instrument consists of a nickel-cadmium battery pack which supplied 6 volts DC and a DC to DC convertor which supplied approximately 95 volts DC for the tube plate voltage. Nickel-cadmium batteries are used because they are rechargeable, have a long shelf life and possess good voltage discharge characteristics.

Instrument Mechanical Design.

The instrument is 11.125 inches in length and 1.1 inch in diameter, with the antenna at the forward end. The electronic system and batteries are enclosed in a thin phenolic-fiberglass tube, and all voids are filled with an encapsulation compound.

At the start of the development program it was considered necessary to suspend the instrument with the antenna pointed downward. Therefore, the instrument was suspended from the aft end, and the sensor was mounted on an arm. This arm was spring loaded and extended perpendicular to the instrument body when the staves were removed. As the program progressed, it was found that it would be desirable to suspend the instrument such that the sensor would be first in the air flow pattern. This was accomplished by suspending the instrument with the antenna pointing upward and the sensor pointing downward. The sensor was protected by a wire guard and the suspension harness extended the length of the instrument. Flight tests proved that this did not significantly affect the RF signal received at the ground station. Since that time, minor design changes have been accomplished. Notably, the wire thermistor guard was eliminated, the suspension line was looped as near as practical to the antenna, and a thin-film mylar thermistor mount has been flight tested. These changes, though minor, have significantly improved the quality of the data obtained. Figure 9 shows the sonde suspended from the parachute load line and the conventional post method of

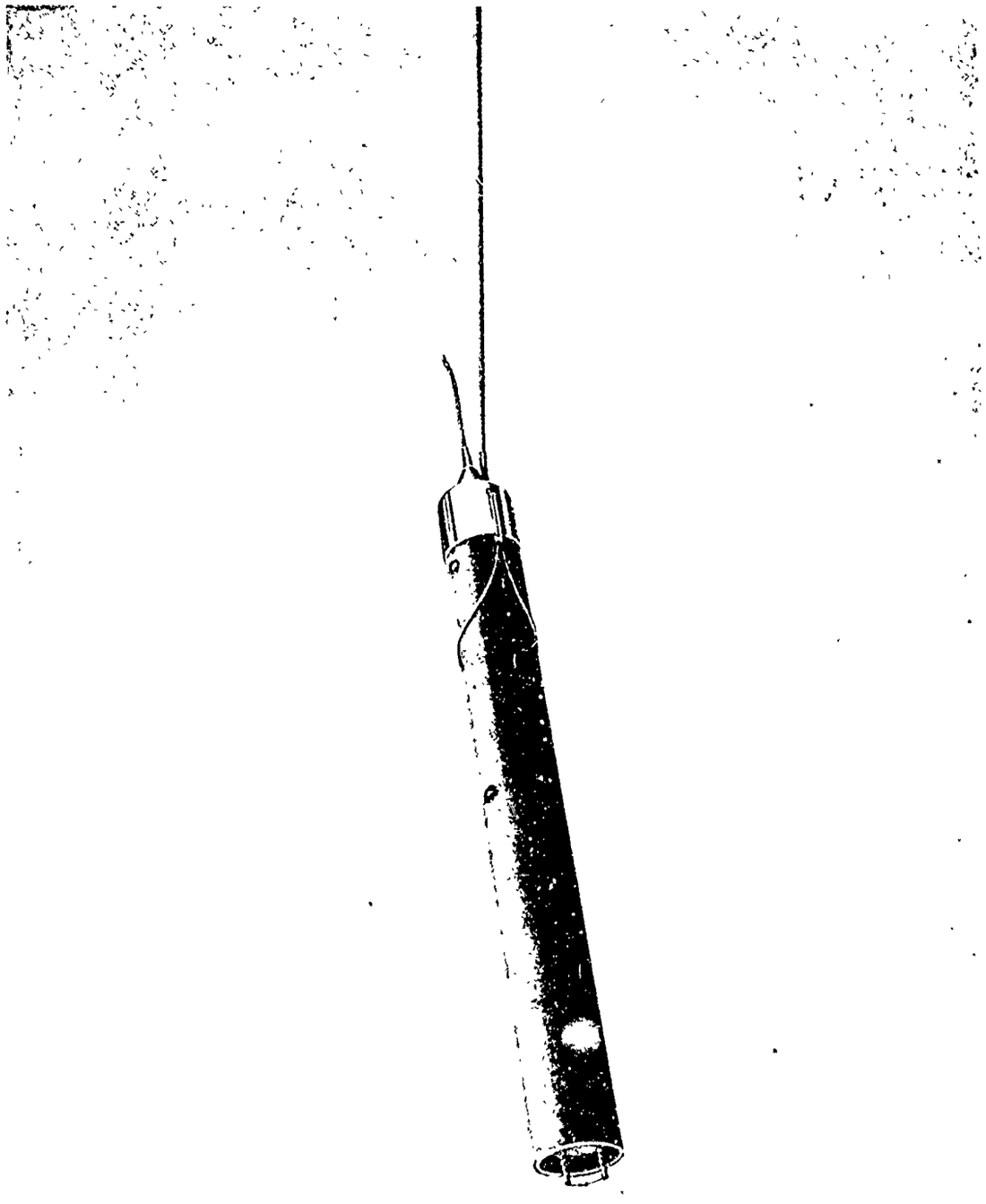

FIG. 9 INSTRUMENT & PARACHUTE SUSPENSION SYSTEM

thermistor mounting which will be further discussed in the following temperature measurement section.

Ground System Instrumentation.

The data sensing and telemetry system incorporated by the dart vehicle utilizes the standard Ground Meteorological Detection (GMD) system for data receiption and print out. Any version of the GMD up through the GMD/4, may be used to handle the dart information. The GMD/1 ground equipment consists of a tracking dish antenna and receiver unit, a control recorder unit and a TMQ/5 chart recorder. Other versions of the system contain various auxillary equipment such as ranging transmitter and various automatic data equipment. The antenna and receiver unit consists of a seven foot diameter dish, mounted on a pedestal which contains the receiver and antenna motor controls. The dish may be operated in either automatic or manual track made locally at the pedestal or from controls on the recorder, which is usually remote from the pedestal. The receiver covers a band from 1655 mc to 1705 mc and will operate in either AM or FM mode. AM mode is utilized by the current dart system. The modulation type, when viewed from the carrier, is PDM-AM in that the intelligence is impressed upon the carrier in the form of negative pulses of sufficient magnitude to exceed 100% AM and hence terminate the carrier for the duration of each pulse. The repetition of the carrier terminating pulses contains the data. This technique results in pulses of carrier frequency energy of varying duration as a function of the data transmitted. The incoming signal is mixed with the local oscillation frequency in a wave guide, and a 30 mc IF is detected in the receiver which reconstructs the chain of pulses originally impressed upon the carrier. These pulses are then differentiated and the resulting positive pulse from the trailing edge is used to trigger a multivibrator, which results in a new pulse of constant amplitude and duration. The trigger level of this multivibrator is adjustable so that "grass" may be excluded from the resultant pulse train. These pulses are then transferred over a line, via the control recorder, to the TMQ/5 unit where they trigger a univibrator which results in a train of pulses of very constant amplitude and duration. These

pulses are fed into a self-balancing servosystem which positions a pen on a strip chart recorder. The recorder pin is displaced as a function of pulse repetition frequency and can accommodate rates up to 200 pps. Various auxiliary amplifier systems have been used to enhance the incoming signal and, of these, the parametric amplifier seems to be the most satisfactory.

Instrumented Dart System Data.

The major dimensions of the vehicle system are indicated in Figure 10, and a summary of the main system parameters are listed in Table 3. Since the beginning of the instrumented dart development program, there have been more than 50 successful flights in which both temperature and winds have been measured.

TABLE 3

SUMMARY OF SYSTEM PARAMETERS

WEIGHTS	
Dart Hardware	8.60 Lbs.
Parachute	.25 Lbs. (4 Ounces)
Instrument	.75 Lbs. (12 Ounces)
Expulsion Charge	.01 Lbs. (5 Grams)
Miscellaneous	.19 Lbs.
COMPLETE DART SYSTEM	9.8 Lbs.
Loki Rocket Motor	24.2 Lbs.
VEHICLE LAUNCH WEIGHT	34.0 Lbs.
PAYLOAD EJECTION TIME	100 Sec.
INSTRUMENT INFORMATION (Datasonde)	
Power Output	600-850 Milliwatts
Modulation	PDMAM
Pulse Repetition Rate	10-200 Pulses Per Second
Polarity of Modulation	Negative
Time Reference is Transmitted	5-7 Seconds
Time Temperature is Transmitted	50-90 Seconds
Frequency	1660-1700 mc.
Reference Switching	Relay
Batteries	Nickel Cadmium
Operating Time	40-50 Minutes
Length	11.125 Inches
Diameter	1.1 Inches
Thermistor	10 Mil Coated Bead

SPACE DATA CORPORATION
PHOENIX, ARIZONA

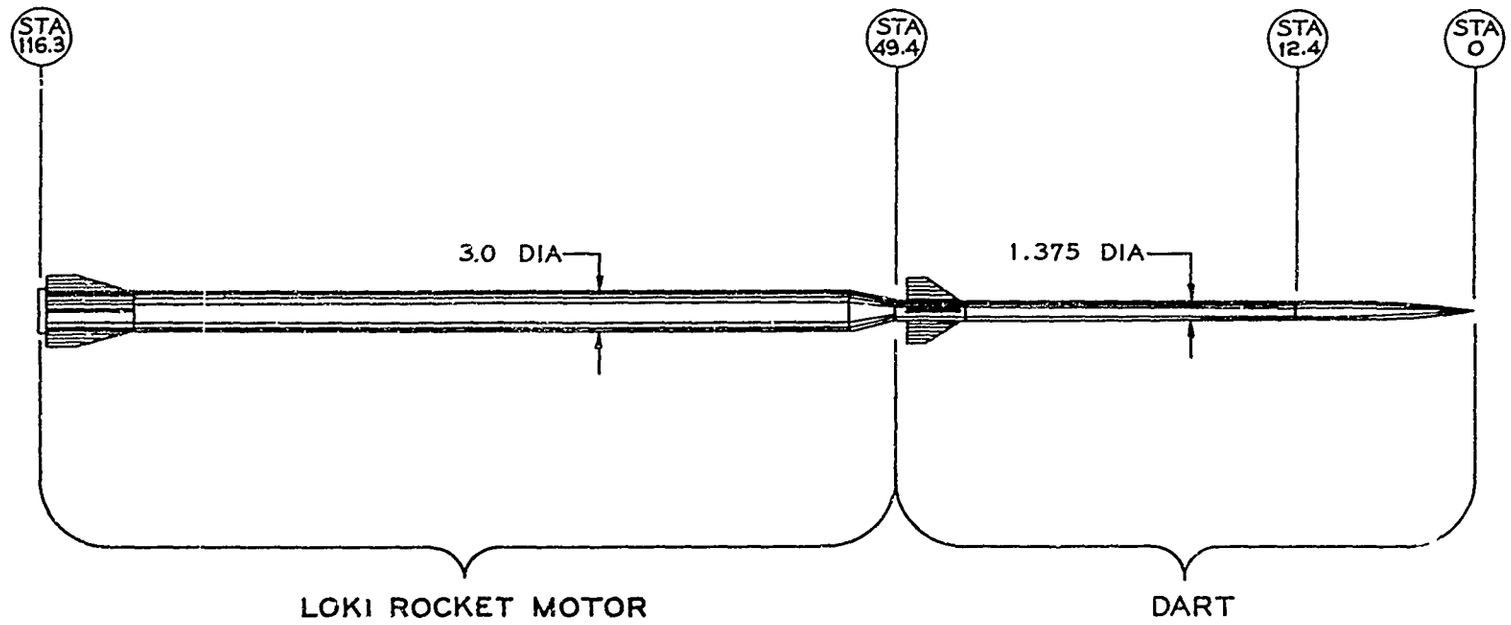

VEHICLE CONFIGURATION

FIGURE 10

ATMOSPHERIC TEMPERATURE MEASUREMENT

Prior to the development of a thin-film Mylar mount for the bead thermistor, there was considerable error in the measurement of atmospheric temperatures with the meteorological rocketsonde systems in the stratopause and lower mesophere regions. The thermistor and its mounting fixtures become relatively warm (40°C to 50°C) during their residence in the vehicle prior to launch and during rocket ascent. The main source of heating with the Arcas* system is the power output from the cavity-oscillator transmitter tube. In the case of the dartsonde, aerodynamic heating provides the main source of heat for the temperature rise. At apogee the instruments are ejected into the relatively cold atmosphere (-20°C to -30°C), and heat must be lost from the thermistor-mount combination before ambient air temperatures can be adequately measured. The rate of heat loss is related to the thermal time constant of the sensing system which includes both the basic characteristics of the thermistor and its mounting fixture. The thin-film Mylar mount, as indicated in Figure 11, was developed by [Drews, ref. 3] to reduce the thermal mass to which the thermistor lead wires are mounted, and hence reduce the thermal time constant and conduction errors of the measurement system.

A comparison of the response time and the heat loss curve between the old mounting post arrangement, and the new thin-film Mylar mount is presented for two instrumented dart,** Datasonde, flights in Figure 12. For the mounting post arrangement, an elapsed time of approximately 70 seconds occured between apogee ejection, at a system temperature of 48°C, to equilibrium with the atmosphere at approximately 0°C. Apogee for this flight occured at 203,000 feet, and sensor equilibrium with the atmosphere occured at 180,000 feet. For the thin-film Mylar mount only 35 seconds were necessary for the temperature sensor to reach

---

* A relatively large 4.5-inch diameter meteorological rocket employing a long burning time propellant grain and relatively large temperature measuring sondes, i.e. Arcasonde, Delta Sonde.

** Space Data Corporation dart instrument.

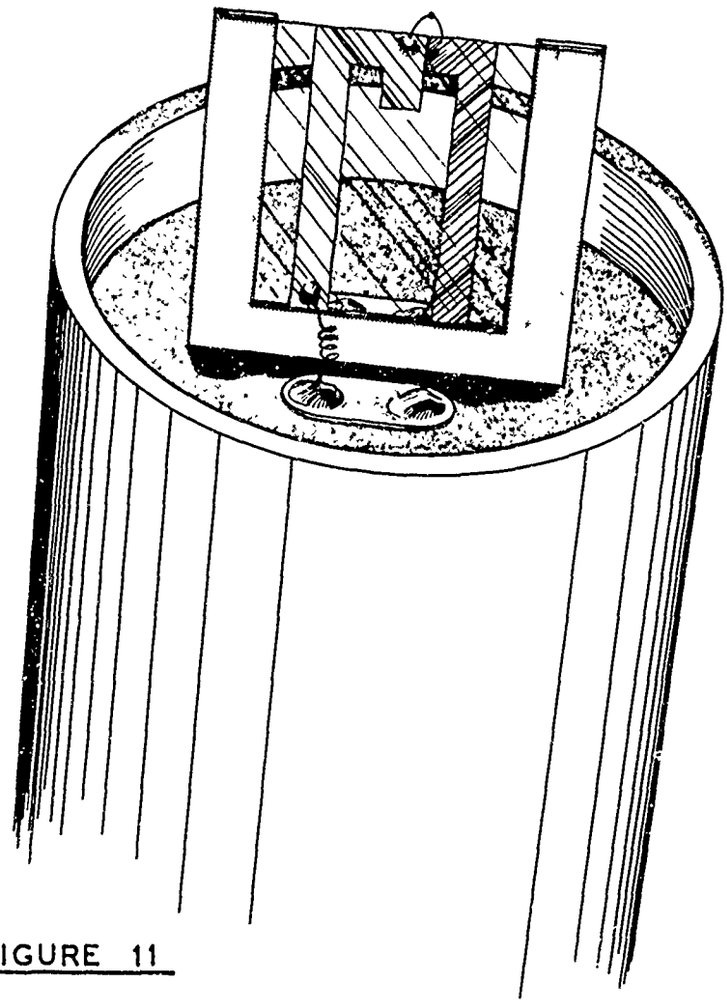

FIGURE 11

THIN FILM THERMISTOR MOUNT

FIG. 12 DATASONDE THERMISTOR TEMPERATURE VS. TIME

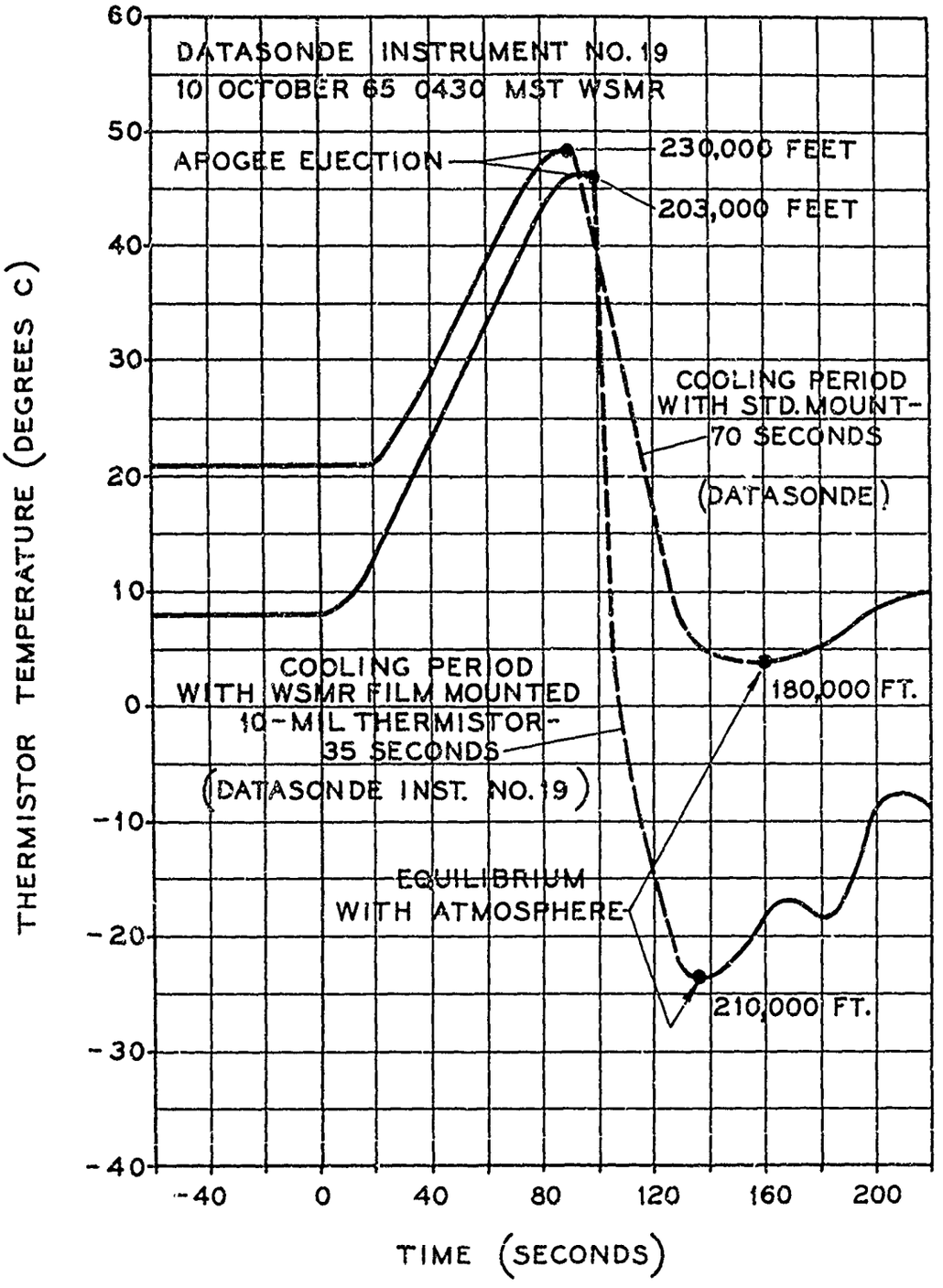

equilibrium with the atmosphere, at a temperature level of -23°C, at 210,000 feet. Apogee for this flight occured at 230,000 feet, and ejection temperature was 46°C. Thus it can be seen that by utilizing a thin-film Mylar mount with the Datasonde instrument, the response characteristics of the sensing system are significantly improved, and more accurate temperatures can be obtained at higher altitudes.

The times for the 10-mil bead thermistor to reach equilibrium with the atmosphere from payload ejection, at approximately 210,000 feet, for both the Datasonde and Arcasonde instruments, with both the older post mounting arrangements and the newer thin-film Mylar mount arrangements, are presented from typical flight data in Table 4. These data indicate that the temperature sensing response time is primarily a function of the thermistor mounting arrangement rather than the particular telemetry instrument employed. Not only do these sensor response characteristics influence the maximum altitude to which temperature data can be measured, but they also influence the accuracy of the temperature measurements throughout the sounding, at least to altitudes in excess of 150,000 feet. Sensor lag error due to slow response characteristics has proven to be a significant source of temperature measurement error down to a level of 190,000 feet even with the faster response thin-film Mylar mount.

An envelope of atmospheric temperatures obtained with the Datasonde instruments during the development program is presented in Figure 13 along with average profiles obtained with the Arcasonde 1 and 1A instruments. The Arcasonde 1 instrument employed rather heavy wire mounting posts, and it can be noticed that on the average the temperatures derived with this instrument were considerably warmer than for the other two sondes. All of the Datasonde flights presented in this figure employed plastic mounting posts which evidently did not permit as much heat transfer through the lead wires to the bead thermistor as with the heavy wire mounting posts. This is indicated by the fact that the average Datasonde temperatures ran about 8°C cooler in the stratopause, and above, than the comparable Arcasonde 1 temperatures. These Datasonde temperatures, however, can not be considered

very accurate above the stratopause since they are considerably warmer than those temperatures for the Arcasonde 1A which employs the thin-film Mylar mount. Most of the temperature profiles in Figure 13 were taken at the Eastern Test Range.

TABLE 4

TIME FOR TEMPERATURE SENSOR TO REACH EQUILIBRIUM WITH THE ATMOSPHERE FROM PAYLOAD EJECTION AT ABOUT 210,000 FEET

Instrument	Post Mount (Seconds)	Film Mount (Seconds)
Datasonde	70	35
Arcasonde	80	40

At the conclusion of the instrumented dart development program, personnel from the White Sands Missile Range flew a thin-film mounted 10-mil bead thermistor with the Datasonde system. The temperature profile from this flight is presented in Figure 14. It should be noted that the dashed line at the top of the profile represents the thermistor heat loss or cooling curve and cannot be considered to be indicative of atmospheric temperature. As a general rule, atmospheric temperatures are reported only after the heat loss or cooling curve experiences a reversal which indicates that the sensor has started to respond to the atmospheric temperature profile. Such a reversal for this flight occured at an altitude of 210,000 feet and a temperature of -24.5°C. For comparative purposes the temperature profile for an Arcasonde 1A flight is also included. Both of these temperature profiles are to the highest altitude yet obtained for either of the two systems.

Although the temperature profiles shown in Figure 14 indicate a significant improvement in temperature data over the older post-mounted systems, the fact that a reversal in temperature from the heat loss curve has occured does not indicate the accuracy of the temperature profile obtained from this reversal point on down throughout the sounding.

Temperatures obtained at the 200,000 feet level with the thin-film mounts are approximately 30° to 40°C colder than those obtained with the post mounting arrangements. However, even these colder temperatures may be significantly warmer than the atmosphere at this level. Although the sources of error in these data are due to aerodynamic heating, sensor lag or response time, condutction effects and solar radiation, the major source of temperature error at this level appears to be due to aerodynamic heating.

The boundary layer recovery temperature increase, above the ambient, can be estimated by the equation -

$$\Delta T_r = T_a \frac{\gamma - 1}{2} (Pr) \tfrac{1}{2} M^2$$

Where T_r = recovery temperature of the boundary layer, °K

T_a = ambient atmospheric temperature, °K

γ = ratio of specific heats, cp/cv for air at 200,000 feet, 1.401

P_r = Prandtl number for air at 200,000 feet, 0.731

M = Mach number

Boundary layer temperature increase at an altitude of 200,000 feet is plotted against sensor velocity in Figure 15. The velocity of the system which causes the boundary layer temperature to increase is not only descent velocity of the parachute-sonde system, but the total velocity. Figure 16 presents the horizontal component of the vehicle velocity at apogee for both the Arcas and the Dart system for various sea level launch angles. For a launch angle of 84°, the Arcas horizontal velocity at apogee is 775 feet per second, and the dart velocity is 415 feet per second. The difference in these apogee horizontal velocities is due to the greater gravity turn experienced by the longer burning-time Arcas vehicle. When these velocity data are related back to Figure 15, it appears that upon payload ejection, the thermistor boundary-layer temperature increase for the Arcas system is greater than 20°C, and for the Dart system is approximately 7°C.

Aerodynamic heating and sensor response lag temperature measurement errors have been

FIGURE 13 ROCKETSONDE TEMPERATURE PROFILES

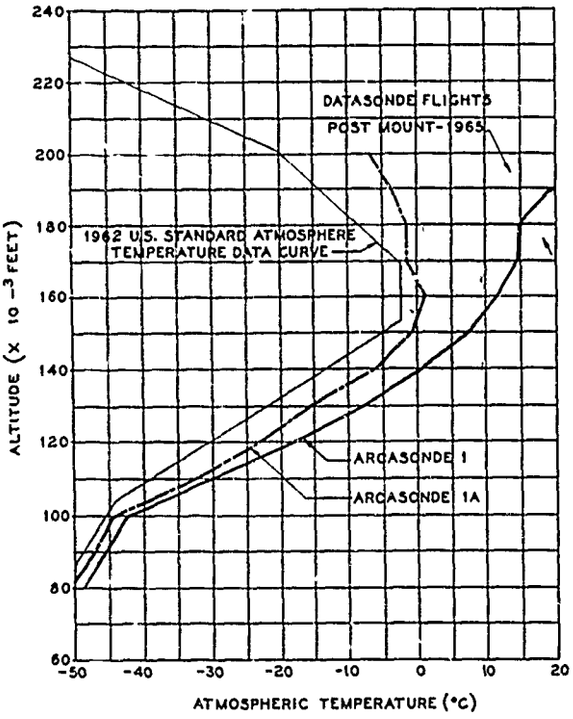

FIGURE 14

DATASONDE TEMPERATURE MEASUREMENT OF THE ATMOSPHERE

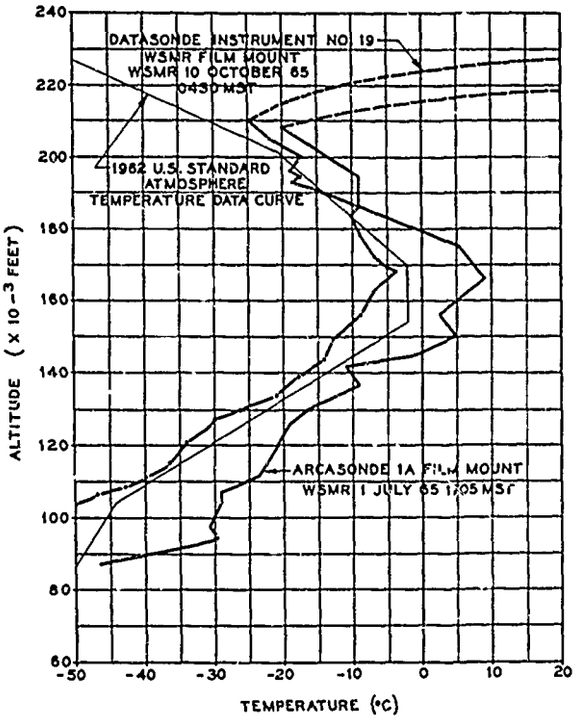

FIGURE 15 AERODYNAMIC HEATING EFFECT

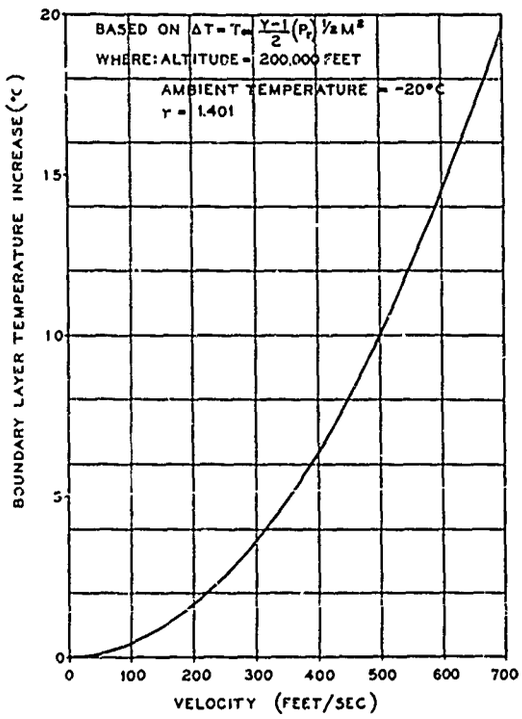

FIGURE 16 HORIZONTAL COMPONENT OF VELOCITY AT APOGEE

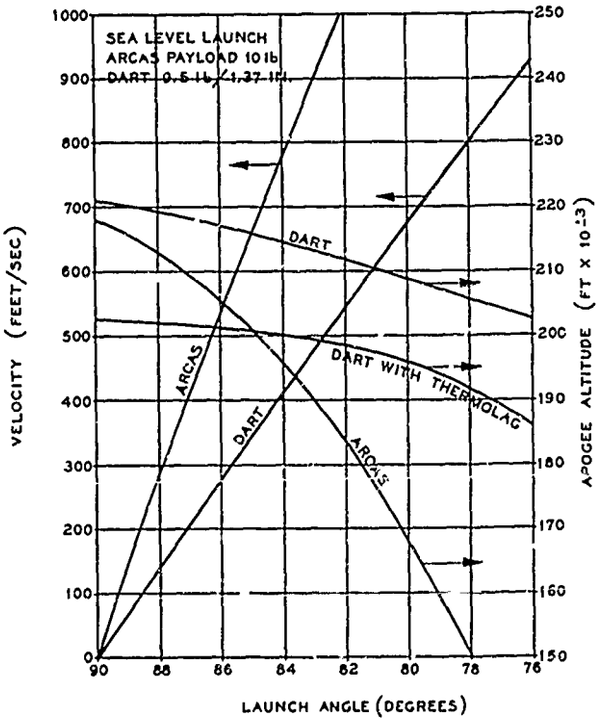

estimated for the instrumented dart system with the results presented in Figure 17. The 1962 U.S. Standard Atmosphere temperature was used as an ambient temperature model, and a parachute-sonde trajectory, aerodynamic heating and sensor lag computer program was devised to simulate a typical 215,000-feet deployment. The standard 7.6-feet diameter parachute, and a thin-film thermistor mount were assumed. Thermistor time constant values were taken from a report by [Wagner, ref. 4].

These data indicate an appreciable aerodynamic heating effect above 180,000 feet. Since the thermistor can do no better than measure the temperature of the air immediately surrounding it, i.e. the boundary layer temperature, the aerodynamic heating presents a measurement accuracy limit. The temperature measurement error resulting from sensor response lag can be estimated as the difference in temperature between the boundary layer and the thermistor from Figure 17.

Estimates for temperature measurement error due to solar radiation and thermistor lead conduction made by [Wagner, ref. 4; Barr, ref. 5; and Drews, ref. 3] indicate that both solar radiation, and the thin-film mount conduction errors are each less than 1°C at an altitude of 200,000 feet. An estimate of the total measurement error for a 215,000 feet deployment of the current instrumented dart system with a thin-film mount at an altitude of 200,000 feet is as follows:

Aerodynamic Boundary Layer Heating	+ 10.0°C
Sensor Response Lag	- 5.0°C
Solar and IR Radiation	$\leq$ + 1.0°C
Thermistor Lead Conduction & Internal Power	$\leq \pm$ 1.0°C
Total Error	6.0°C $\pm$ 1.0°C

It is obvious from the above data that the greatest improvement in temperature measurement accuracy can be obtained by decreasing the descent velocity of the parachute-sonde system. Not only is the aerodynamic heating proportional to the square of the descent velocity, but

the sensor lag error should also be improved with a more slowly falling system. By reducing the descent velocity of the system to 75% of its current value, an improvement of about 50% in the temperature measurement accuracy at 200,000-feet should be realized

WIND MEASUREMENT AND PARACHUTE DATA

The instrumented dart parachute is used for wind measurement and to lower the temperature-measuring sonde through the atmosphere at a sufficiently slow velocity for adequate temperature measurements. The descent rate of the parachute is of prime importance since both wind measurement errors and temperature measurement errors due to aerodynamic heating are directly related to the square of the descent velocity of the parachute-sonde system. Figure 18 presents the altitude versus time descent profile for various ejection altitudes. The descent rates of the parachute-sonde system is presented in Figure 19 for various ejection altitudes.

To attain the indicated fall rates and descent times, the parachute must deploy properly and fully inflate to take advantage of its shape and fabric area. For a limited number of instrumented dart flights, the 7.6-foot diameter flat-circular parachute has exhibited a certain amount of instability in its descent rate at altitudes above 170,000 feet. A possible explanation for this erratic behavior may be explained on the basis of the dynamic pressure at deployment. Figure 20 shows the dynamic pressure at apogee for various launch angles for both the Arcas and the Dart systems. Since the component of horizontal velocity at apogee for the Arcas vehicle is significantly greater than that for the Dart system, the dynamic pressure available for full parachute deployment with the Arcas system is generally greater than that for the Dart system. [Knacke, ref. 6] states that a minimum dynamic pressure of 0.03 to 0.07 lbf/ft^2, depending on parachute design, is required to create a sufficient pressure differential from the inside to the outside of the parachute for full inflation. This may indicate that for a higher degree of reliability in achieving full deployment of dart parachutes, a positive inflation aid such as an inflatable torus ring may be required. These dynamic pressure data at apogee or deployment also indicate that the dart parachutes

FIGURE 17 ESTIMATED BOUNDARY LAYER RECOVERY AND THERMISTOR RESPONSE LAG TEMPERATURE FOR A 215 000 FEET INSTRUMENTED DART DEPLOYMENT

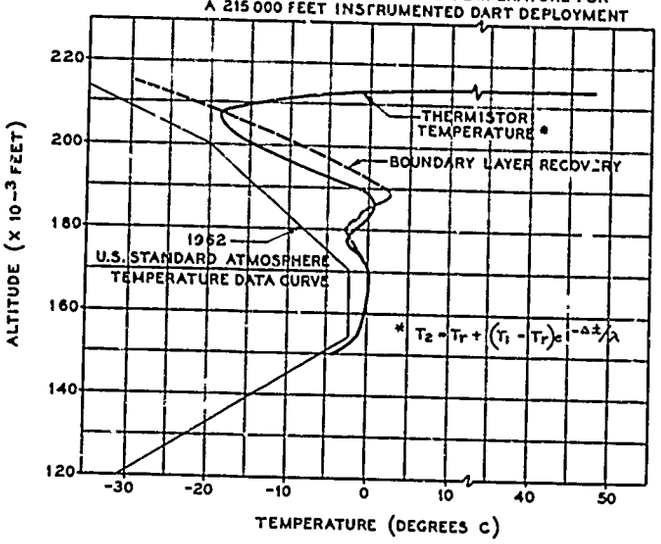

FIGURE 18 PARACHUTE-SONDE DESCENT TIME

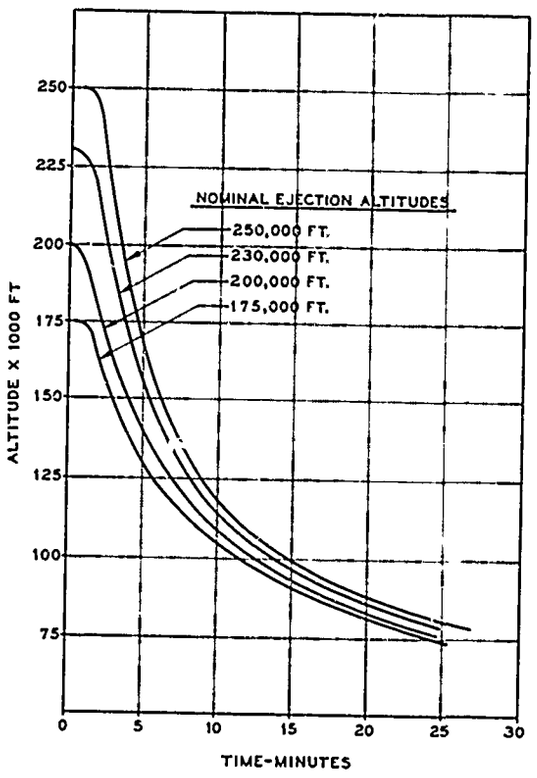

FIGURE 19 PARACHUTE-SONDE DESCENT VELOCITY

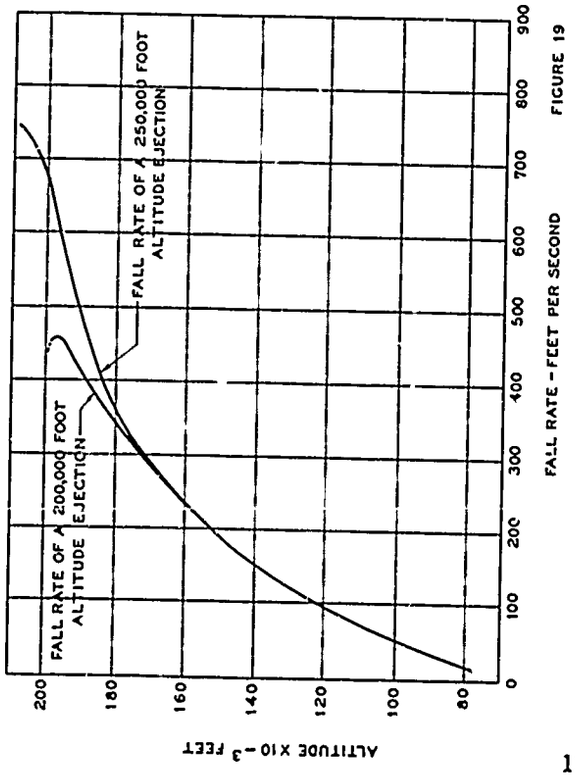

FIGURE 20 DYNAMIC PRESSURE AT APOGEE

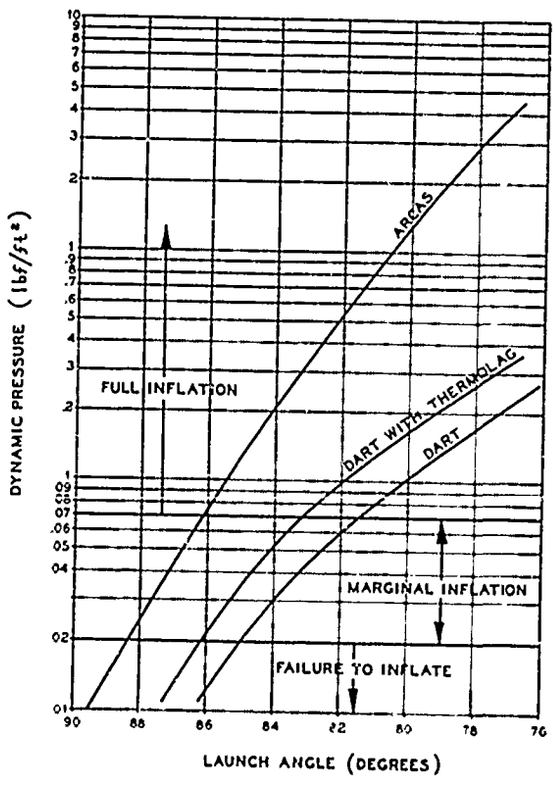

may be constructed from relatively lighter-weight materials than for the Arcas system; for the opening shock should be significantly less. By reducing parachute weight, the ballistic coefficient or weight-to-drag-ratio for the descending system can be improved to give slower descent profiles which are so important for more accurate wind and temperature measurements at the 200,000 feet altitude levels.

Wind measurement requirements for routine meteorological support and operations have generally been stated as an rms error of 3 ft/sec at 80,000 feet to an rms error of 10 ft/sec at 200,000 feet. The wind measurement error is a function of the vertical gradient of the wind or wind shear, rather than the absolute wind velocity, and the descent rate of the parachute as given by the approximate expression by [Leviton, ref 7] .

$$E \doteq \frac{s}{g} \times V_z^2$$

Where E = wind speed lag error, ft/sec

s = wind shear, sec^{-1}

V_z = vertical descent velocity, ft/sec

Therefore, a wind shear value must be specified in addition to the measurement error for a meaningful parachute design criterion. Since the wind measurement error is a function of the square of the descent velocity, and the descent velocity is much greater at the 200,000-feet level than below, it is assumed that the wind measurement requirements can be met throughout the descent with a system which can satisfy the requirements at 200,000-feet.

A review of chaff-derived winds obtained at the 200,000-feet level revealed that the 90% wind shear level through a 1,000-feet altitude layer for annual data over the United States is about 20 ft/sec per 1,000 feet or 0.020 sec^{-1}. With the 200,000 feet altitude wind shear specified as 0.020 sec^{-1}, Table 5 has been constructed to indicate the descent system velocities and ballistic coefficients required to satisfy various wind measurement error requirements. Table 6 presents the parachute descent system data for both the

Arcas 15-feet diameter parachute - Arcasonde 1A system, and the Dart 7.6-feet diameter parachute - Datasonde system. From these data one can determine that both systems need significant improvement to meet the 10 ft/sec measuring error requirement. The Arcas system ballistic coefficient of 0.0655 lbf/ft^2 will permit a lag error of more than 130 ft/sec under a 0.020 sec^{-1} shear at 200,000-feet. The dart system is only slightly better with a ballistic coefficient of 0.0603 lbf/ft^2. This system will permit a 120 ft/sec lag error.

TABLE 5

DESCENT SYSTEM VELOCITIES AND BALLISTIC COEFFICIENTS REQUIRED FOR VARIOUS WIND MEASUREMENT ERRORS BASED ON AN ALTITUDE OF 200,000-FEET AND A WIND SHEAR OF 0.020 SECONDS^{-1}

Wind Measurement Error, E	Descent Velocity, V_z	Ballistic Coefficient W/C_DS
10 ft/sec	127 ft/sec	0.005 lbf/ft^2
20	180	.010
30	221	.015
40	254	.020
50	285	.025
60	312	.030
70	335	.035
80	358	.040
90	380	.045
100	401	.050
110	420	.055
120	439	.060
130	457	.065
140	475	.070
150	491	.075

Since the wind measurement error under consideration is essentially a response lag or systematic error, rather than a purely random error, it appears appropriate to use more than a 1-sigma (standard deviation), rms, error criterion for systems design. This is especially true if the random errors due to radar tracking and parachute oscillations are small with respect to the $\pm$ 10 ft/sec, rms, accuracy requirement. Perhaps a realistic requirement would be for a 2.5 -sigma allowance of 25 ft/sec in the response lag error. For such a

criterion, a descent rate of 201 ft/sec at 200,000-feet and a ballistic coefficient of 0.0125 lbf/ft^2 would be required.

TABLE 6

DESCENT SYSTEM DATA

	Arcas	Dart
Parachute Type	15' Hemispherical	7.6' Flat-Circular
Flying Diameter, ft	15	5.7
Flying Area, S, ft^2	177	25.5
Parachute Weight, lb	2.62	0.225
Payload Weight, lb	4.65	0.788
Total Weight, W, lb	7.27	1.013
Drag Coefficient, C_D (on flying area, S)	0.624	0.660
Ballistic Coefficient, W/C_DS	0.0655	0.0603
Payload	Arcasonde 1A	Datasonde

Three ways to reduce the ballistic coefficient of the current systems are to: (1) improve the drag coefficient (based on fabric area and packaging volume requirements), (2) reduce the overall weight of the system, and (3) increase the fabric area or parachute size. Most probably the drag coefficient based on fabric area cannot be greatly improved over current systems, providing full inflation is currently being achieved. A weight reduction of the overall system can be achieved in the case of the Arcas by reducing the weight of the instrument. Since the dynamic pressure at apogee is appreciable with the Arcas, reducing parachute weight and, thereby, strength may not be advisable. The weight of the Datasonde dart instrument is already minimum for the desired power supply operating time. However, the dynamic pressure at apogee is so low with the dart system that a lighter-weight parachute fabric may be employed. An increase in the fabric area and

parachute size is the most likely improvement for both systems up to the size where deployment may become a problem. However, if one follows the general rule that the parachute weight should never be heavier than the payload for stability, a limitation on the improvement of the ballistic coefficient for the Arcas system is approximately 0.0475 lbf/ft^2, and for the dart system is 0.0268 lbf/ft^2. These data are based upon maintaining the same fabric strength and density as is currently employed. The increased size of the instrumented dart parachute to achieve this reduced ballistic coefficient would have a flying area of 89 ft^2, a flying diameter of 10.7-feet and a flat diameter of 14.2-feet. Its weight would equal that of the instrument payload which is 0.788 lb. This system should have a descent rate of 294 ft/sec at 200,000-feet and be capable of measuring a 0.020 sec^{-1} wind shear at this level with an accuracy of 54 ft/sec.

An additional benefit from reducing the parachute descent rate as suggested above would be the reduction of the aerodynamic heating error of the temperature sensor from a +7.7°C error to a +3.5°C error at 200,000-feet. The sensor lag error would also be improved.

[Ammons, ref. 8] estimates that for the 15-feet diameter hemispherical parachute, used with the Arcas, the instantaneous horizontal velocity due to parachute oscillations follows approximately a sinusoidal pattern with a maximum amplitude of about 50 ft/sec at an altitude of 200,000-feet. The period of this pattern at 200,000-feet appears to be about 2,700 ft. in altitude or 6.3 seconds. This pattern may be assumed to represent a theoretical wind measurement error due to parachute oscillation. However, when this velocity pattern is integrated to estimate a displacement pattern, a maximum displacement of only 50 ft is found. Since the period of parachute oscillations, in the high altitudes at least, appears to be proportional to the square root of shroud line length, the estimated period for the dart parachute is $\sqrt{\frac{8}{28}} \times 6.3$ seconds or 3.4 seconds. If the same horizontal velocity maximum is assumed for the 7.6-feet diameter dart parachute as for the 15-feet diameter parachute, with the

period reduced to 3. seconds, a maximum horizontal displacement due to parachute oscillation at 200,000-feet is only 26.3-feet. This is equivalent to a radar look-angle displacement of 0.115 mils. FPS-16 radar rms accuracy is ± 0.14 mils in angular measurement and ± 45 ft in slant range. Other less precise radar have rms accuracies of about ± 2 mils and ± 120 ft, respectively. It appears that although oscillations of the dart parachute may lead to instantaneous velocities which might theoretically be interpreted as wind error, these velocities do not cause sufficient horizontal displacements to be detected by radar.

CONCLUSIONS

The flight tests of the Loki instrumented dart, Datasonde, system which have been conducted to date have demonstrated that the system is compatible with the standard AN/GMD-1B ground equipment and is feasible for temperature and wind measurements between 75,000-feet and 200,000-feet altitudes. The measurement accuracies of this system are consistent with the current state-of-the-art when the thin-film thermistor mount is employed. Reasonable temperatures have been measured to an altitude of 215,000-feet. A further improvement in both the wind and temperature measurement accuracies can be made by reducing the descent rate of the parachute-sonde system.

The reliability of the system is adequate for operational use and no special skills or techniques are required for launching or data acquisition. The primary advantages of the system are: (1) comparatively low cost, (2) minimum of handling effort by weather station launch crews, and (3) much lower wind sensitivity than most other meteorological rockets. Of the three advantages listed above the one of primary importance is that the miniaturized system provides essentially the same data obtained with much larger meteorological rocket systems at less than half the cost.

The system can be easily handled by one person, and a launch crew of two people is sufficient to perform all launching functions.

The Loki Dart vehicle system has been fired in winds in excess of 40 knots with

minimum launcher corrections, and many ranges do not require launcher corrections for winds less than 20 knots. Therefore, very little effort need be expended in determining launcher corrections due to winds.

ACKNOWLEDGEMENTS

The authors wish to express their appreciation to the Aerospace Instrumentation Laboratory, Air Force Cambridge Research Laboratories; Electronics Research and Development Activity, White Sands Missile Range; U.S.A.F., Detachment 11, 6th Weather Wing, Air Weather Service; and Pan American World Airways, U. S. Eastern Test Range for their support and cooperation in the development and flight testing of the instrumented dart system.

REFERENCES

1. Walker, R. L., Design, development and flight test results of the Loki instrumented dart system. Final Report for Contract AF19(628)4164 by Space Data Corporation, October, 1965.

2. Watson, C. W., Judi-Robin Balloon Dart Sounding Vehicle Final Report for CRL Contract No. AF 19(628)2805 by Rocker Power, Inc., May, 1964.

3. Drews, W. A., Unpublished data from a NASA Langley Research Center contract performed by Atlantic Research Corporation.

4. Wagner, N. K., 1 July 1963 Theorerical accuracy of the meteorological rocketsonde thermistor. Report 7-23 contract DA-23-072-ORD-1564, Electrical Engineering Labs., University of Texas.

5. Barr, W. C., Theoretical considerations in the design of atmospheric temperature sensing elements, USASRDL, TR2138, AD 241876,36.

6. Knacke, T.W., High Altitude Parachute Recovery of Data and Instrumentation, Technical Data Digest, V17, No. 7, July 1952, pages 25 to 29.

7. Leviton, R. and Lalley, V.E., Accuracy of wind determination from the track of a falling object, AF Surveys in Geophysics, U. S. AFCRL No. 93, AD146858.

8. Ammons, R. L., A digital computer simulation of high-altitude parachute response to wind gradients. NASA, Langley Research Center, Contract NAS-1-4537, performed by Thiokol Chemical Corporation, 1965.

SOUNDING ROCKET PERFORMANCE APPROXIMATIONS

Wolfgang Schaechter, Thiokol Chemical Corporation, Astro-Met Division, Ogden, Utah

ABSTRACT

After reviewing the tremendous amount of computations work completed for the preparation of a sounding rocket vehicle handbook, we wondered if, empirically derived, closed-form approximations of the variation of some of the performance parameters could be found which might cut down the computing load on similar efforts. Apparently, accurate closed-form performance approximations can be developed, not only for the vehicle system considered in the original effort, but for other sounding rockets with widely differing payload and altitude capabilities.

Sine functions were found that predict the variation of a sounding rocket's apogee altitude with launch elevation angle (in a range of 70-90 Degrees) to within 1.0 Percent of the value calculated with a digital computer trajectory program. Cosine functions were developed that predict impact range as a function of launch elevation angle to within 1.0 Percent of the electronically computed value. Similar trigonometric expressions accurately described the variation of apogee and impact time, and range derivatives, with elevation angle. The ratio of impact range to apogee altitude was found to be proportional to a Cotangent function of the launch elevation angle. These approximations were applicable to vehicles having apogee altitude capabilities from 60,000 to at least 6,000,000 Feet. Simple (computer) time-saving relationships were also verified for wind weighting data.

By the use of approximations it would, first of all, be possible to save considerable computer time. In addition, once the basic performance parameters have been electronically computed, data points not covered by the original computer runs could be rapidly and accurately determined with the approximation formulas.

Attempts were made to correlate the approximation formulas with the physical performance characteristics of the various sounding rocket systems to which they apply. These attempts were not too successful. We, therefore, have no clear theoretically founded understanding of why the closed-form approximations apply to the data with such high accuracy. However, the relationships are apparently valid so that they can be used with a considerable degree of confidence.

I. INTRODUCTION

The proliferation of digital computers has certainly been a blessing to those of us who need to calculate the flight performance and behavior of sounding rocket vehicles. Computers are, today, readily available to almost everyone in the sounding rocket field, and each new generation of data processing machinery is faster and cheaper than the preceeding one. Furthermore, data communications systems give us rapid telephone line access to large machines. Why then bother with performance approximations?

There are a number of reasons why one would be interested in performance approximations. First, no matter how fast and cheap, electronic data processing costs money. For instance, at $3.00 per minute for an IBM 7040 computer, a 300-500 Second flight time point-mass trajectory simulation can cost as much as $10.00. Second, the turnaround time between input and output is an indirect cost that adds to the first $10.00.

Furthermore, it is often the case that a whole trajectory simulation is required to furnish an accurate value of "end-point data" such as apogee altitude, impact range, apogee and impact time, and similar variables. It would be very convenient if some of these parameters could be obtained, with reasonable accuracy, from closed-form equations. The performance approximation formulas, described in this paper, are aimed at providing this type of convenience.

The approximation formulas are almost entirely based on and derived from empirical data. For example, to describe the variation of apogee altitude with launch elevation angle with a formula a series of computer runs are needed to empirically describe this relationship. From the computer data it is then possible to obtain the constants and exponents that make up the performance approximation formula. Therefore, these relationships augment, but, do not

replace, the electronic computer.

The approximation formulas can best be used for the following:

1. To reduce the matrix of trajectory variables that have to be considered in a parametric performance study. For example, to obtain enough data to fill an apogee altitude vs. launch elevation angle and payload weight grid m (payloads) times n (launch elevation angles) trajectories now have to be computed. If there are four payloads at five launch elevation angles, this comes to 20 runs. Using the empirical performance approximations we can cut these 20 runs down to eight. Then the remaining 12 data points are obtained (in no more than 15 minutes) with a desk calculator - to within 1.0 Percent of the electronically computed values.

2. Additional data points, not covered by the original parametric study, can be readily calculated with the formulas.

3. Range derivatives (derivatives of impact range with respect to launch elevation angle) can be directly obtained with a desk calculator.

4. The number of six-degree-of-freedom rigid body simulations required for the determination of unit wind effects can be reduced considerably. Range- and cross-wind effects for a variety of payload weights and launch elevation angles can be determined with no more than three rigid body simulations and a few point-mass trajectories.

There are a number of applications that these performance approximations are not suitable for. These are:

1. The performance approximations do not replace basic parametric studies conducted on a computer; although their scope can be significantly reduced, these must still be performed.

2. Most of the empirical relationships we have developed describe the variation of performance parameters only with launch elevation angle; they do not describe the parameter's variation with payload weight.

3. The empirical relationships will not replace an electronic computer in producing a continuous record of time, velocity, altitude, elevation, range, etc. Although performance approximations could possibly be developed for these parameters, such an application would compete with the computer in the repetitive aspects of the task - where the computer is an undisputed champion.

4. For some vehicles, the empirical relationships don't apply to certain parameters with sufficient accuracy to be really practical. For some other vehicles, the relationships may not work at all. We have, to date, identified only one sounding rocket vehicle in which the approximations give answers with relatively poor accuracy. However, there are undoubtedly others for which this is the case. The approximations are, therefore, not universally applicable.

We found the empirical approximations to be a very useful tool, despite these limitations. Even while developing them we have already used them extensively to provide quick- and accurate - answers to pressing problems.

II. ANALYSIS

Empirically derived relationships have been developed for the variation, with launch elevation angle of apogee altitude, apogee time, the ratio of impact range to apogee altitude, impact range, impact time, and range derivatives. The relationships for these performance parameters give answers that, in almost all cases, are within 1.0 Percent of the values obtained from a trajectory simulation on an electronic data processing machine. The approximations were shown to apply, with the aforementioned 1.0 Percent accuracy, to a wide variety of vehicles with peak altitude capabilities from 60,000 to 6,000,000 Feet.

In addition, a relationship of unit wind effects to apogee altitude, previously suggested by another author, has been examined and found to apply very well to actual data. Suggestions regarding the most advantageous use of this relationship are made.

To test and demonstrate the application of the empirically derived performance approximations we selected nine different sounding rocket configurations. These nine were chosen because they represent distinct atmospheric regimes spanning two orders of magnitude of altitude, from a low of only 60,000 Feet to a high of 6,000,000 Feet. The vehicles, their altitude regimes, their payloads, and the sources from which the data were obtained, are listed below:

Vehicle	Apogee Altitude Regime (Feet)	Payload weight (Pounds)	Data Source (Reference)
NIKE-DART (Unignited Tomahawk Upper Stage)	60,000-65,000	710	1
NIKE-NIKE-NIKE-CREE III	130,000-180,000	298	2
ARCAS-ROBIN	215,000-260,000	8.5	3
D-REGION TOMAHAWK	365,000-420,000	80	4
NIRO	550,000-780,000	80	5
NIKE-TOMAHAWK	900,000-1,050,000	140	1
NIKE-SANDHAWK	1,000,000-1,170,000	250	6
SANDHAWK-TOMAHAWK	2,100,000-2,500,000	100	6
ASTROBEE 1500	4,000,000-6,000,000	200	7

(References are listed at the end of the paper.)

Each of the performance approximation formulas will be presented in the following format:

1. What is the closed-form approximation formula for a particular parameter?
2. How well does the formula work?
3. What, if any, theoretical correlation does the approximation formula have?

A. APOGEE ALTITUDE vs. LAUNCH ELEVATION ANGLE

Apogee altitude is perhaps the single most important performance parameter in sounding rockets. In addition to being of primary importance to the experimenter, it is also of great interest to range safety personnel.

1. The Approximation Formula. A simple relationship describes the variation of apogee altitude with launch elevation angle for a wide variety of rockets. In equation form:

$$\text{Apogee Altitude} = A_k \cdot \text{Sin}^n\theta \qquad \text{----1}$$

where,

$$A_k = (\text{Apogee Altitude}/\text{Sin}^n\theta)_{\theta = \theta_k} \qquad \text{----2}$$

in which θ_k is some reference launch elevation angle. Experience indicates that, in most cases, the highest formula accuracy is obtained when the reference launch elevation angle is taken near the midpoint of the elevation range considered for the particular vehicle. Thus, if the potential range is 75-86 Degrees elevation, 80 Degrees is the best reference angle. However, for some vehicles, the approximation formula works best when either the maximum or the minimum elevation angle is used as the reference point.

We found that the Sinθ exponent (n) varies with the sounding rocket configuration, and cannot be directly correlated with any of the vehicle characteristics we have, thus far, examined. Therefore, an easy way of determining the exponent (using a graph presented in the paper) is described in the Appendix.

2. Approximation Formula Results. Table 1 shows the results of the apogee altitude approximation formula applied to nine different sounding rocket configurations.

TABLE 1. APOGEE ALTITUDE vs. LAUNCH ELEVATION ANGLE

Approximation Formula: Apogee Altitude = $A_k \cdot \text{Sin}^n\theta$.

$A_k = (\text{Apogee Altitude}/\text{Sin}^n\theta)_{\theta = \theta_k}$

Vehicle	Launch Elevation Angle (Degrees)	$\text{Sin}^n\theta$ Exponent	Apogee Altitude (Feet) Computed	Apogee Altitude (Feet) Predicted	Error (Percent)
NIKE-DART (Unignited Tomahawk Upper Stage)	75	n = 3	60,165	59,862	0.4
	80*		63,386		
	86		65,870	[illegible]	0.3
NIKE-NIKE-NIKE CREE III	75	n = 4	133,100	133,800	0.5
	80*		156,200		
	88		176,300	175,700	0.3
ARCAS-ROBIN	80	n = 13	233,400	234,000	0.3
	85*		248,700		
	88		259,000	259,000	0
D-REGION TOMAHAWK	75	n = 4.5	365,700	365,700	0
	80*		399,000		
	85		420,000	420,500	1
NIRO	76	n = 6	652,000	656,500	0.6
	80*		715,640	"	"
	88		778,800	781,500	0.3
NIKE-TOMAHAWK	75	n = 5	912,770	907,630	0.6
	80*		999,820	"	"
	86		1,061,660	1,066,310	0.4
NIKE-SANDHAWK	75	n = 5	1,005,830	1,000,630	0.5
	80*		1,102,060	"	"
	85		1,162,760	1,167,500	0.4
SANDHAWK-TOMAHAWK	75	n = 6	2,096,830	2,086,500	0.4
	80*		2,346,000	"	"
	85		2,504,160	2,513,700	0.3
ASTROBEE 1500	70	n = 6.5	2,970,000	2,943,000	0.7
	80*		5,348,000	"	"
	88		5,905,800	5,884,800	0.4

* Indicates θ_k

Starting at the low end of the altitude scale, we have a vehicle consisting of a Nike booster and an unignited Tomahawk upper stage, the Nike-Dart. (This configuration can only be realized in case of an upper stage ignition failure on a standard Nike-Tomahawk vehicle.) Using an exponent of 3.0, the approximation formula predicts the variation of apogee altitude with launch elevation angle with at most a 0.6 Percent difference from that calculated with an electronic data processing machine.

At the other altitude extreme, the Astrobee 1500 is capable of carrying a 200 Pound payload to an altitude of almost 6,000,000 Feet. The formula, with a Sinθ exponent of 6.5, approximates the function apogee altitude vs. launch elevation angle with a maximum of 0.7 Percent error over a 70-88 Degrees elevation angle range.

This correspondence of apogee altitude vs. launch elevation angle to the Sine functions is illustrated in Figure 1. To show the relationship more clearly, we form the ratio of apogee altitude at any

angle to apogee altitude at some reference launch elevation angle. This has been done for two of the vehicles described in Table 1, the Nike-Dart and the Astrobee 1500.

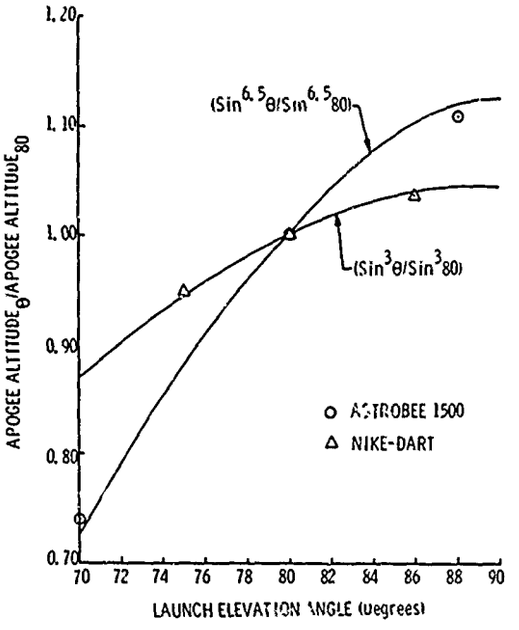

FIGURE 1. NON-DIMENSIONALIZED APOGEE ALTITUDE VS. LAUNCH ELEVATION ANGLE

A close look at the Sin$^{6.5}\theta$ curve and the Astrobee 1500 computed data shows that even better agreement would have been possible with a Sinθ function exponent slightly less than 6.5.

The empirically derived equations for apogee altitude vs, launch elevation angle can usually be applied, without modification, to the whole range of payload weights normally carried by the particular vehicle. Therefore, if a Sinθ exponent of 5.0 and a reference elevation angle of 80 Degrees works well for the Nike-Tomahawk, carrying a 140 Pounds payload (the example shown in Table 1), it also applies to the minimum weight of 60 Pounds, and the larger payload of 260 Pounds (see Table 2).

TABLE 2. APOGEE ALTITUDE vs. LAUNCH ELEVATION ANGLE FOR THREE NIKE-TOMAHAWK PAYLOADS

Payload	Launch Elevation Angle (Degrees)	Sin$^n\theta$ Exponent	Apogee Altitude (Nautical Miles)	
[illegible]	75	[illegible]	[illegible]	[illegible]
	80	[illegible]	[illegible]	
	90		[illegible]	
[illegible]	[illegible]	[illegible]	[illegible]	[illegible]
	80	[illegible]	[illegible]	
	90		[illegible]	
[illegible]	75	[illegible]	[illegible]	[illegible]
	80	[illegible]	[illegible]	
	90		[illegible]	

For the 60 Pound payload the Sin$^5\theta$ curve answers differ by a maximum of only 0.2 Percent from computer results. At 260 Pounds, the approximation formula results in only 0.9 Percent error. Therefore, once the variation of a vehicle's apogee altitude with launch elevation angle has been characterized for any given payload, this empirically derived relationship applies, as well, to other payloads that may be carried by that vehicle. (This tendency, of a vehicle to be characterized by one exponent, was verified on a number of other sounding rockets for which data was available.)

The approximation formula does not always work satisfactorily. The empirical formulas did not apply to one vehicle, the Argo-D4, or Javelin, (Reference 8) nearly as well as to the others. Table 3 shows the results of the attempt to fit Equation 1 to the data for this system.

TABLE 3. APOGEE ALTITUDE vs. LAUNCH ELEVATION ANGLE FOR THE JAVELIN (ARGO D-4)

Vehicle	Launch Elevation Angle (Degrees)	Sin$^n\theta$ Exponent	Apogee Altitude (Nautical Miles)		Error (Percent)
			Computed	Predicted	
JAVELIN	[illegible]	[illegible]	[illegible]		
	[illegible]		[illegible]	[illegible]	[illegible]
	[illegible]		[illegible]	[illegible]	[illegible]

The minimum error, for the Javelin, is 1.5 Percent, twice the largest maximum error observed for any of the vehicles listed in Table 1. The maximum error is 2.4 Percent.

After considerable soul searching on the subject we did not come up with any reasonable explanations for the ineffectiveness of the approximation formula for this vehicle. Altitude was obviously not the reason; the Sandhawk-Tomahawk goes almost as high, and the Astrobee 1500 much higher. The number of stages seems to have little bearing on the problem; the Nike-Nike-Nike-Cree III has three stages and yet the approximation formula works quite well. Exoatmospheric flight was not the cause either; the Astrobee 1500 upper stage ignites at 200,000 Feet and burns out at well over 500,000 Feet. The extensive stage III/IV coasting period might be one source of the problem; this is the only item that was significantly different from the trajectories of the other vehicles.

There is, therefore, at least one vehicle system, and undoubtedly a number of others, to which these empirically derived relationships do not apply with a high degree of accuracy. If a 2-3 Percent accuracy is acceptable, Equation 1 could still be used for the Javelin. However, at that level of

accuracy, there would probably be a tendency to make a computer run anyway, "just to be sure". This would reduce the usefulness of the approximation formula considerably.

3. Correlation of the Approximation Formula with Theory. The theoretical basis for the empirical characterization of the apogee altitude vs. launch elevation angle relationship is vague, at best. A tenuous link to theory is provided by the simplified case of a vacuum trajectory of a point-mass over a flat, non-rotating earth, with constant gravitational attraction. In these circumstances apogee altitude is related to the Sine function as follows:

$$\text{Apogee Altitude} = H_{bo} + \frac{(V_{bo})^2 \text{Sin}^2\theta_{bo}}{2g} \qquad ----3$$

where H_{bo}, V_{bo}, and θ_{bo}, are, respectively, the altitude, velocity, and flight path angle (above the horizontal) of the final propulsive stage.

Experience indicates that two terms in Equation 3, H_{bo} and V_{bo}, do not vary substantially with launch elevation angle. For example, in the high flying Astrobee 1500 the final stage burnout altitude varies from 420,000 to 525,000 Feet, at the launch elevation angles of 70 and 88 Degrees, respectively. For the same vehicle, the burnout velocity is even less affected by launch elevation angle; 17,400 Feet/Second at 70 Degrees, and 17,500 Feet/Second at 88 Degrees.

This illustrates that, even in the non-idealized, "real-life" world, apogee altitude is primarily dependent on some function of the Sine. Intuitively, this makes sense; apogee altitude is maximum when the flight path or launch elevation angle is 90 Degrees, which corresponds to the maximum value of the Sine function. What is not clear, is why the various sounding rocket vehicles have apogee altitude curves that so closely follow the function of Sinθ to higher exponents.

The shapes of the Sine functions, to various exponents (1, 2, 3, 5, 10, 15, and 20), are shown in Figure 2, below. As the Sinθ exponent increases, the curves become steeper as the angle θ approaches 90 Degrees.

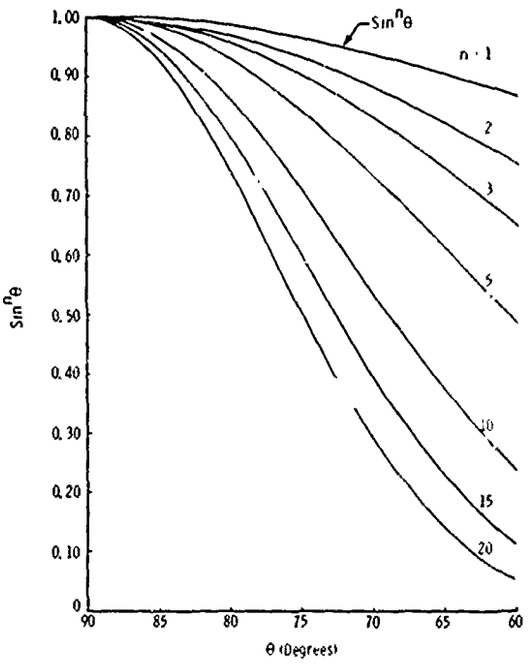

FIGURE 2. THE FUNCTION Sin$^n\theta$ vs. θ

The increasing steepness corresponds to a greater sensitivity of apogee altitude to launch elevation angle. A strong variation of apogee with elevation angle indicates either a drag sensitive configuration, or a high altitude capability rocket, or a combination of both. Therefore, one would expect these types of vehicles to have high Sinθ exponents, and they do.

However, these are not the only variables that affect the shape of the apogee altitude vs. launch elevation angle curve for a sounding rocket vehicle. At least the following factors are involved:

- Ballistic coefficient (W/C_DA)
- Specific impulse of the propulsive stages
- Burn time of the propulsive stages
- Coasting time between stages
- Number of propulsive stages
- Final stage burnout altitude

It is difficult to understand the simulataneous effect of all of these factors on the variation of apogee altitude with launch elevation angle, for a particular sounding rocket. We do know that their

combined effects can be empirically represented by a Sine function (of the elevation angle) to various exponential powers. After an extensive search for some kind of a relationship between the Sinθ exponent and the factors mentioned above, we were unable to find any explicit mathematical connection between them.

Summing up for variation of apogee altitude with launch elevation angle, this relationship was accurately approximated by the function $Sin^n\theta$, where the exponent (n) was empirically determined for a particular sounding rocket vehicle. The empirically derived approximation gave answers that were usually within 1.0 Percent of those obtained in a trajectory simulation on an electronic computer. With the exception that the Sine of the launch elevation angle correctly describes the maximum of apogee altitude to be at 90 Degrees, the theoretical reasons for this function closely approximating the actual physical relationship (between apogee altitude and launch elevation angle), are not clear.

B. APOGEE TIME vs. LAUNCH ELEVATION ANGLE.

To develop an approximate relationship of apogee time to launch elevation angle we tried the same type of Sine function that worked well for apogee altitude. The results of this approach were very encouraging.

1. The Approximation Formula. The following empirical relationship described the variation of apogee time with launch elevation angle:

$$\text{Apogee Time} = B_k \cdot Sin^n\theta \qquad ----4$$

where,

$$B_k = (\text{Apogee Time}/Sin^n\theta)_{\theta = \theta_k} \qquad ----5$$

in which θ_k is the reference launch elevation angle, and n, the empirically determined exponent of the Sin function.

2. Approximation Formula Results. Table 4 shows the results of applying the approximation formula to the seven sounding rocket vehicles for which apogee time data were available. (Apogee time information was not given for either the Nike-Nike-Nike-Cree III, or the Astrobee 1500, References 2 and 7.)

TABLE 4. APOGEE TIME vs. LAUNCH ELEVATION ANGLE

Approximation Formula: Apogee Time = $B_k \cdot Sin^n\theta$:

$B_k = (\text{Apogee Time}/Sin^n\theta)_{\theta = \theta_k}$

Vehicle	Launch Elevation Angle (Degrees)	$Sin^n\theta$ Exponent	Apogee Time (Seconds) Computed	Apogee Time (Seconds) Predicted	Error (Percent)
NIKE-DART (Unguided Tomahawk Upper Stage)	75		61.9	61.9	0.0
	80*	n = 1.5	63.7	"	"
	86		65	64.8	0.2
ARCAS-ROBIN	80		130	129.9	0.1
	83*	n = 0.5	140	"	"
	88		143	142.9	0.1
D-REGION TOMAHAWK	75		155.1	154.7	0.3
	78		159.8	159.7	0.1
	80*	n = 2.5	162.4	"	"
	82		164.5	164.7	0.1
	85		166.8	166.5	0.2
NIRO	76		211.7	211.4	0.1
	80*	n = 3	221	"	"
	84		227	227.7	0.3
	88		229.8	231	0.5
NIKE-TOMAHAWK	75		259	258.7	0.1
	80*	n = 2.5	271.5	"	"
	86		280.1	280.4	0.1
NIKE-SAROMAN	75		269.9	269.8	0.0
	80*	n = 2.5	283.1	"	"
	85		291.3	291.4	0.1
SARONAVE-TOMAHAWK	75		406.5	408.5	0.5
	80*	n = 3	433	"	"
	85		449.6	448.2	0.3

* Indicates θ_k

In Table 4 the maximum error, defined as the difference between results predicted by the formula and those obtained from digital computer trajectory simulations, is only one-half of one Percent for any of the vehicles examined. Errors of 0.1 and 0.2 Percent are common.

Therefore, the empirically derived formula for the relationship of apogee time to launch elevation angle produces very high quality approximations, in this application. Furthermore, as was the case for apogee altitude vs. launch elevation angle, the approximation formula can be directly applied to a wide variety of payloads in any given sounding rocket. Once that vehicle system has been characterized by a Sinθ exponent, the value of n remains unchanged for all payload weights carried by that system.

3. Correlation of the Approximation Formula with Theory. The development of an apogee time vs. launch elevation angle formula was based on the intuitive feeling that altitude and time should be similarly related to elevation angle. It soon became obvious that apogee altitude and time were indeed related, and in a most straightforward way.

Consider the vacuum trajectory of a point-mass, launched vertically, from sea level, over a flat earth, with a constant gravity field. If the vehicle reaches an apogee altitude H_{max}, in time t_{apogee}, these parameters are related by:

$$H_{max} = (g/2)\ (t_{apogee})^2 \qquad \text{----6}$$

Rearranging Equation 6, the time required, to get to apogee, becomes:

$$t_{apogee} = (2 \cdot H_{max}/g)^{\frac{1}{2}} \qquad \text{----7}$$

which means that apogee time is proportional to the square root of apogee altitude.

This was immediately verified by the Sinθ exponents found to best approximate apogee time vs. launch elevation angle; in every case, the best value of the Sinθ exponent for apogee time was nearly half of the best exponent found for apogee altitude. In fact, the empirically derived relationship for apogee time applied to the data with even higher accuracy than did the approximation for apogee altitude.

This relationship, between apogee altitude and time, reflects the behavior of these parameters in an idealized drag-free, constant-gravity environment. Yet, this idealized environment is not encountered by any of the vehicles examined in this paper. Drag losses are certainly significant in the flight of the Nike-Dart. This vehicle, which has a burnout velocity of almost 3000 Feet/Second, is sufficiently retarded by aerodynamic drag to reach less than half of its in-vaccuo apogee altitude. The assumption of constant gravity obviously does not apply to the Astrobee 1500 where the gravitational acceleration, at apogee, is approximately 88 Percent of the sea level value.

Therefore, it seems remarkable that the relationship between apogee altitude and apogee time in the "real world" so closely resembles the variation of these parameters in an idealized (constant-gravity, zero-drag) environment.

C. THE RATIO OF IMPACT RANGE TO APOGEE ALTITUDE.

In a 1963 paper Hoult(Reference 9) postulated that a simple approximate relationship exists between the ratio of impact range to apogee altitude and the launch elevation angle. If this were true, this ratio could be used to obtain impact range as a by-product of the empirically derived relationship of apogee altitude vs. launch elevation angle. Hoult thought that the following was a good approximation:

$$\frac{\text{Impact Range}}{\text{Apogee Altitude}} = 4\ \text{Cotan}\theta \qquad \text{----8}$$

where θ is the launch elevation angle. This relationship did not quite hold in the simplified form he proposed. However, with a modification in the constant of Equation 8, reasonably good results were obtained.

1. The Approximation Formula. An empirically verified formula, for the ratio of impact range to apogee altitude as a function of launch elevation angle, is shown below:

$$\left(\frac{\text{Impact Range}}{\text{Apogee Altitude}}\right)_{\theta} = C_k \cdot \text{Cotan}\theta \qquad \text{----9}$$

where

$$C_k = \left(\frac{\text{Impact Range}}{\text{Apogee Altitude}}\right)_{\theta = 80°} / (\text{Cotan } 80°) \qquad \text{----10}$$

Equation 8 differs from Equation 9 in that a constant in the latter is empirically determined at some reference launch elevation angle.

2. Approximation Formula Results. Equation 9 was applied to eight sounding rockets for which we had apogee altitude and impact range data. Table 5 shows the results.

TABLE 5. IMPACT RANGE/APOGEE ALTITUDE vs. LAUNCH ELEVATION ANGLE

Approximation Formula $\left(\frac{\text{Impact Range}}{\text{Apogee Altitude}}\right)_{\theta} = C_k \cdot \text{Cotan}\theta$

$$C_k = \left(\frac{\text{Impact Range}}{\text{Apogee Altitude}}\right)_{\theta = 80°} / (\text{Cotan } 80°)$$

Vehicle	Launch Elevation Angle (Degrees)	Impact Range/Apogee Altitude Computed	Impact Range/Apogee Altitude Predicted	Error (Percent)
NIKE-DART (Unignited Tomahawk Upper Stage)	75	1.019	1.029	1.0
	80	0.677		
	86	0.270	[illegible]	[illegible]
NIKE NIKE NIKE CREE III	75	1.26[illegible]	1.3[illegible]4	[illegible]
	80	0.891	[illegible]	
	85	0.442	[illegible]	[illegible]
ARCAS ROBIN	80	1.304		
	85	0.667	[illegible]	[illegible]
	88	0.264	[illegible]	[illegible]
U REGION TOMAHAWK	75	1.22[illegible]	1.[illegible]	[illegible]
	80	0.808		
	85	0.401	[illegible]	
NIBO	76	1.453	[illegible]	[illegible]
	80	1.015		
	84	0.599	[illegible]	[illegible]
	88	0.198	[illegible]	[illegible]
NIKE TOMAHAWK	75	1.440	[illegible]	[illegible]
	80	0.943		
	83	[illegible]	[illegible]	[illegible]
	86	[illegible]	[illegible]	[illegible]
NIKE SANDHAWK	75	1.425	[illegible]	
	80	[illegible]		
	85	[illegible]	[illegible]	[illegible]
SANDHAWK TOMAHAWK	75	1.657	[illegible]	
	80	1.081		
	85	[illegible]	[illegible]	[illegible]

It is evident that this formula is less accurate at predicting the variation of actual data than some of the approximations previously developed. Errors as large as 7.0 Percent, between electronically computed and predicted values, are found. However, the relationship is acceptable for rough-order-of magnitude answers.

3. Correlation of the Approximation Formula with Theory. The theoretical basis of the approximation formula is established in the previously mentioned Reference 9. Briefly, the relationship would apply exactly to a vehicle in a parabolic vacuum trajectory over a flat earth, with a constant gravity field. In such an idealized environment we have for impact range:

$$\text{Impact Range} = (2V_o^2 \text{Sin}\theta\text{Cos}\theta)/g \qquad \text{----11}$$

and apogee altitude:

$$\text{Apogee Altitude} = (V_o^2 \text{Sin}^2\theta)/(2g) \qquad \text{----12}$$

Dividing Equation 12 into Equation 11 gives:

$$\frac{\text{Impact Range}}{\text{Apogee Altitude}} = 4\ \text{Cotan}\theta$$

previously indicated as Equation 8.

D. IMPACT RANGE vs. LAUNCH ELEVATION ANGLE.

Impact range is, like apogee altitude, one of the important performance variables in a sounding rocket. Range is extremely sensitive to launch elevation angle; for the vehicles considered in this paper this parameter varies by more than two orders of magnitude.

1. The Approximation Formula. If the Cotangent of the launch elevation angle expresses a functional relationship between impact range and apogee altitude, then we can perhaps extract range from Equation 8 as follows:

$$\text{Impact Range} = K_1 \cdot \text{Apogee Altitude} \cdot \text{Cotan}\theta \qquad \text{----13}$$

where K_1 is a constant. Section A. shows that apogee altitude is a function of launch elevation angle, so that Equation 13 can be rewritten as:

$$\text{Impact Range} = K_2 \cdot \text{Sin}^n\theta \cdot \text{Cotan}\theta \qquad \text{----14}$$

where K_2 is another constant. Since the Cotangent equals the ratio Cosθ/Sinθ, Equation 14 becomes:

$$\text{Impact Range} = K_2 \cdot \text{Sin}^{n-1}\theta \cdot \text{Cos}\theta \qquad \text{----15}$$

As the elevation angle increases Cosθ approaches zero, reflecting the physical fact that impact range is essentially zero when the launch elevation angle is 90 Degrees.

2. Approximation Formula Results. The results of applying Equation 15 to eight different sounding rocket vehicles are shown in Table 6.

TABLE 6. IMPACT RANGE vs. LAUNCH ELEVATION ANGLE

Approximation Formula: Impact Range = $D_k \cdot \text{Sin}^n\theta \cdot \text{Cos}\theta$

$D_k = (\text{Impact Range}/\text{Sin}^n\theta \cdot \text{Cos}\theta)_{\theta = \theta_k}$

Vehicle	Launch Elevation Angle (Degrees)	Sine^n θ Exponent n	Impact Range (Feet) Computed	Impact Range (Feet) Predicted	Error Percent
NIKE HART (Instrumented Tomahawk Upper Stages)	75	n = 3	43,209	43,654	1.0
	80*		44,654		
	88		38,677	38,681	0.0
NIKE NIKE NIKE CAGE III	75	n = 11	142,200	142,304	0.1
	80*		138,491		
	85		78,491	77,894	0.8
ARCAS ROBIN	80	n = 33	272,820	272,744	0.1
	85*		248,228		
	88		88,246	87,243	1.2
0 REGION TOMAHAWK	75	n = 3.5	668,300	668,844	0.1
	80*		622,290		
	85		348,490	348,540	0.0
NIKE	75	n = 3.5	853,080	854,...	0.1
	80*		652,080		
	88		338,340	338,...	0.2
NIKE TOMAHAWK	75	n = 3.5	1,335,...	1,336,...	0.1
	80*		963,820		
	86		544,...	547,...	0.6
NIKE SANDHAWK	75	n = 3.5	1,635,...	1,...	0.1
	80*		1,029,18		
	85		537,...	538,...	0.1
SANDHAWK TOMAHAWK	75	n = 4	3,...	3,...	0.2
	80*		2,...	2,...	0.1
	85		1,337,...	1,...	0.1

* Indicates θ_k

The values of impact range, predicted by the approximation formula, are, generally, quite accurate. Differences between (electronically) computed and predicted range vary from a high of 1.7 Percent for the Arcas-Robin to a low of essentially zero for several vehicles. The 1.7 Percent error in the Arcas-Robin occurred at 88 Degrees elevation angle; at 80 Degrees the computed/predicted difference, for this vehicle, was 0.1 Percent. Of the remaining seven vehicles, five had maximum errors of less than 0.5 Percent.

3. Correlation of the Approximation Formula with Theory. The formula for the relationship between impact range and launch elevation angle is derived from the approximate proportionality of the range/apogee ratio to the Cotangent of the elevation angle. Since, empirically, apogee altitude vs. launch elevation angle is proportional to a Sine function, we can relate impact range to launch elevation as demonstrated in Equations 13, 14 and 15, above.

According to Equation 15, the Sinθ exponent for impact range should be one less than the value of n for apogee altitude. However, a review of the Sinθ exponents that gave the best results in Table 6 (Impact Range) shows that these are not always one less than the "n" values that produced the best answers in Table 1 (Apogee Altitude). This indicates that the Cotanθ link, between impact range and apogee altitude, does not reflect the physical data in the same way as either of the empirical relationships for apogee or range as functions of launch elevation angle.

Thus, we have again an empirical formula, partly derived from vacuum, constant-gravity considerations, that accurately describes the variation of impact range with launch elevation angle, for a wide variety of sounding rocket vehicles that fly neither in a vacuum, nor in a constant gravity field.

E. IMPACT TIME vs. LAUNCH ELEVATION ANGLE.

Impact time, or total time of flight, is another parameter routinely computed in sounding rocket performance. The variation of impact time with launch elevation angle was empirically approximated by the same type of equation used to describe the apogee time function.

1. The Approximation Formula. The following formula accurately approximates the relationship of impact time to launch elevation angle:

$$\text{Impact Time} = E_k \cdot \text{Sin}^n\theta \qquad \text{----16}$$

where

$$E_k = (\text{Impact Time}/\text{Sin}^n\theta)_{\theta = \theta_k} \qquad \text{----17}$$

Equation 16 is similar to Equation 4, developed for apogee time.

2. Approximation Formula Results. Table 7 shows the results of applying an empirically derived approximation formula to the function impact time vs. launch elevation angle.

TABLE 7. IMPACT TIME vs. LAUNCH ELEVATION ANGLE

Approximation Formula: $\text{Impact Time} = E_k \cdot \text{Sin}^n\theta$

$E_k = (\text{Impact Time}/\text{Sin}^n\theta)_{\theta = \theta_k}$

Vehicle	Launch Elevation Angle (Degrees)	$\text{Sin}^n\theta$ Exponent	Impact Time (Seconds) Computed	Impact Time (Seconds) Predicted	Error (Percent)
NIKE GART (Originator) Tomahawk (Upper Stage)	75		[illegible]	[illegible]	[illegible]
	80*	n = 1.5	[illegible]		[illegible]
	85		[illegible]	[illegible]	
ARCAS ROBIN	80		[illegible]	[illegible]	[illegible]
	85*	n = 4	[illegible]		
	88		[illegible]	[illegible]	[illegible]
[illegible] REGION TOMAHAWK	[illegible]		[illegible]	[illegible]	[illegible]
	80*	n = 2	[illegible]		
	85		[illegible]	[illegible]	
NIRO	[illegible]		[illegible]	[illegible]	
	84*	n = 2.5	[illegible]		
	88		[illegible]	[illegible]	[illegible]
NIKE TOMAHAWK	75		[illegible]	[illegible]	[illegible]
	80*	n = 2.5	[illegible]		
	86		[illegible]	[illegible]	[illegible]
NIKE-SANDHAWK	75		[illegible]	[illegible]	
	80*	n = 2.5	[illegible]		
	85		[illegible]	[illegible]	[illegible]
SANDHAWK TOMAHAWK	75		[illegible]	[illegible]	[illegible]
	80*	n = 3.5	[illegible]		
	85		[illegible]	[illegible]	[illegible]

* Indicates θ_k

Excellent approximations were obtained by using the $\text{Sin}^n\theta$ function. The maximum difference between the electronically computed and predicted results was 0.7 Percent, for the Arcas-Robin at 80 Degrees launch elevation angle. The best results were obtained for the Nike-Sandhawk, where the approximation formula predicted impact time to within less than 0.1 Percent of the actual data, at the extremes of the elevation angles considered.

3. Correlation of the Approximation Formula with Theory. The total time of flight (or the impact time) of a point-mass in a zero-drag, constant-gravity environment is exactly twice the time required to reach apogee. Under these conditions, a linear relationship should exist between the impact and apogee times.

The sounding rocket vehicles considered in this study do not, however, fly in a drag-free constant-gravity environment. Therefore, one would expect some differences between the relationships of the apogee and impact times to launch elevation angle. This is verified by the fact that the $\text{Sin}\theta$ exponents which best fit the formulas for impact time (Table 7), differ from those which are most effective for the apogee time (Table 4) approximation.

It is true, for a great many sounding rockets, that the total time of flight is nearly twice that required to reach apogee. This holds especially for vehicles with high ballistic coefficients (W/C_DA), and burn times that are short, compared to the time required to reach apogee. Vehicles with long burn times and high ballistic coefficients will take longer to rise to apogee than they will to fall from apogee to impact. Conversely, vehicles with long burn times and small ballistic coefficients will take significantly longer from apogee to impact, because of their deceleration by aerodynamic drag. Launch elevation angle also influences sounding rocket flight time. As the elevation angle is increased, drag losses approach a minimum since the vehicle leaves the retarding atmosphere more quickly at the higher angles.

The different combinations of burn time, ballistic coefficient, and launch elevation angle all interact to affect the total time of flight of a sounding rocket. The $\text{Sin}^n\theta$ function accurately describes this interaction for all of the vehicles examined. These include sounding rocket configurations with high ballistic coefficients and short burn times, low ballistic coefficients and long burn times, and combinations of the previous two.

F. RANGE DERIVATIVES vs. LAUNCH ELEVATION ANGLE.

Approximations for the function impact range vs. launch elevation angle are, in themselves, useful in a number of ways. In addition, the approximation formulas can be mathematically manipulated to yield some useful by-products. For example, differentiating the equation for impact range vs. launch elevation angle yields the range derivative, $dR/d\theta$, the rate of change of range with respect to elevation angle. This parameter is required to compensate the launcher elevation setting for wind effects.

To illustrate the method by which range derivatives are obtained, we used the Nike-Tomahawk data from Table 6. For this vehicle, the empirically derived approximate relationship of impact range to launch elevation angle is:

$$\text{Impact Range} = D_k \cdot \text{Sin}^n\theta \cdot \text{Cos}\theta \qquad \text{----18}$$

where $n = 3.5$ and $D_k = 5{,}734{,}512$ Feet. Substituting these constants,

$$\text{Impact Range (Feet)} = 5{,}734{,}512(\text{Sin}^{3.5}\theta \cdot \text{Cos}\theta) \qquad \text{----19}$$

Differentiation of Equation 19 with respect to the launch elevation angle (θ) gives:

$$dR/d\theta(\text{Feet/Degree}) =$$

$$= 5{,}734{,}512\ (3.5 \cdot \text{Sin}^{2.5}\theta \cdot \text{Cos}\theta - \text{Sin}^{4.5}\theta) \qquad \text{----20}$$

Equation 20 for $dR/d\theta$ was evaluated at 75, 80 and 86 Degrees launch elevation angle, and the data is compared below with the digital computer results from Reference 1.

Launch Elevation Angle (Degrees)	Range Derivative, $dR/d\theta$ (Feet/Degree)	
	Computed	Predicted
75	-64,000	-64,100
80	-83,200	-83,250
86	-97,300	-97,300

The maximum difference between the electronically computed and predicted results is one-sixth of one Percent.

The empirically derived data could be obtained with a Sine table and a desk calculator; the computed results involved an electronic data processing machine and a desk calculator. The data processing machine was used to determine the least-squares coefficients of an equation for range vs. launch elevation angle. The curve-fit equation was then differentiated to determine the range derivatives.

There is no question that it would be simpler and more convenient to use the empirically derived impact range vs. launch elevation angle equation; the sacrifice in the accuracy of the results is nearly negligible.

G. UNIT WIND EFFECTS vs. APOGEE ALTITUDE.

In a paper presented to this conference last year, Hoult (Reference 10) stated that "the unit wind effect. . . .(was) proportional to peak altitude". In that paper his analysis was based on a simplified model of vehicle flight in a zero-drag constant-gravity environment. We checked this simplification against six-degree-of-freedom unit wind data, computed for several different sounding rocket vehicles. The linear relationship between unit wind effect and apogee altitude accurately described the behavior of the data.

As an example, unit range- and cross-wind effects were computed, at one payload weight and four launch elevation angles, for a NASA/Nike-Tomahawk sounding rocket configuration, serial NASA 18.46. This vehicle will carry a payload weighing 210 Pounds. The unit wind effects, computed with a six-degree-of-freedom (6-D) trajectory program, are shown in Figure 3.

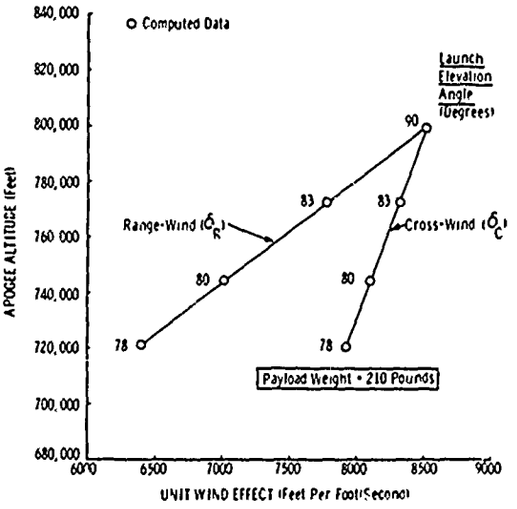

FIGURE 3. UNIT WIND EFFECTS (FOR NASA 18.46) COMPUTED WITH SIX-DEGREE-OF-FREEDOM TRAJECTORY PROGRAM

The 6-D data points are the dots inside the circles in Figure 3. It is immediately obvious that the 80 and 83 Degrees data points, for both range-and cross-wind are superfluous; the line, between 78 and 90 Degrees, is straight. Note that when the launch elevation angle is 90 Degrees unit range- and cross-winds are (by definition) identical. Therefore, only five rigid body trajectory simulations are required to construct the lines in Figure 3; three runs at 78 Degrees launch elevation angle, and two at 90 Degrees.

The proportionality of unit wind effects to apogee altitude is a very useful relationship. First, it eliminates about 75 Percent of the 6-D trajectory simulations needed to generate a matrix of unit wind effects vs. payload weight and launch elevation angle. Second, a last minute change in payload weight, or launch elevation angle no longer requires a recomputation of unit wind effects. Unit winds, for the new payload or elevation angle, can be quickly and accurately determined from graphs of the existing data. Therefore, both convenience and economy indicate that we should take full advantage of the unit wind effect/apogee altitude relationship. The method for doing so is explained below.

1. Six-Degree-of-Freedom Data. In Figure 3 it was evident that 6-D computed unit wind effects are required only at the "anchor-points" of the unit wind vs. apogee altitude lines. Our example shows these at 90 and 78 Degrees launch elevation angle. These points provide enough data to handle any wind compensations for one payload weight (210 Pounds).

Now unit wind effects are apparently linearly proportional to apogee altitude, for any given payload weight. One would expect a similar relationship to hold, at any given launch elevation angle, for different payload weights. A line of unit wind effects vs. apogee altitude, at one launch elevation angle is, therefore, needed. Logically this line should be at 90 Degrees. Because of the linearity of the unit wind/apogee altitude function only two 90 Degree data points are required. In the example, one of these has already been computed for 210 Pounds payload weight (see Figure 3). A second point, at 200 Pounds and 90 Degrees launch elevation angle, is added in Figure 4.

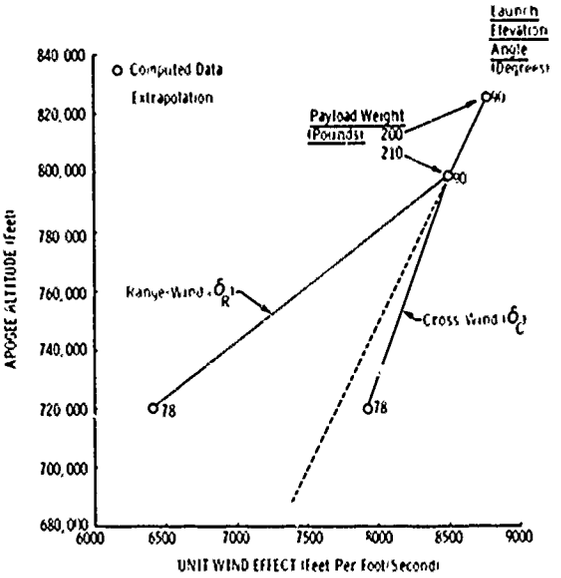

FIGURE 4. UNIT WIND EFFECTS (FOR NASA 18.46) AT 78 AND 90 DEGREES LAUNCH ELEVATION ANGLE

The line of apogee altitude vs. unit wind effects at 90 Degrees launch elevation angle (Figure 4) is highly important. It contains the "anchor-points" for range and cross unit wind effects for the different payloads, at 90 Degrees elevation angle, where the range and cross unit wind effects are equal. Thus, knowing apogee altitude at 90 Degrees for any payload, we can immediately obtain the corresponding unit wind effect.

2. Three-Degree-of-Freedom Data. To complete the set of unit wind data, a curve of apogee altitude vs. payload weight - at 90 Degrees launch elevation angle is needed. Such a curve, easily obtained with three point-mass (3-D) trajectory simulations, is shown (on the next page) for the NASA 18.46 configuration (Figure 5).

Once the apogee altitude, for any payload weight at 90 Degrees launch elevation angle, is known (from Figure 5), the corresponding unit wind effect, at 90 Degrees elevation, can be found in Figure 4.

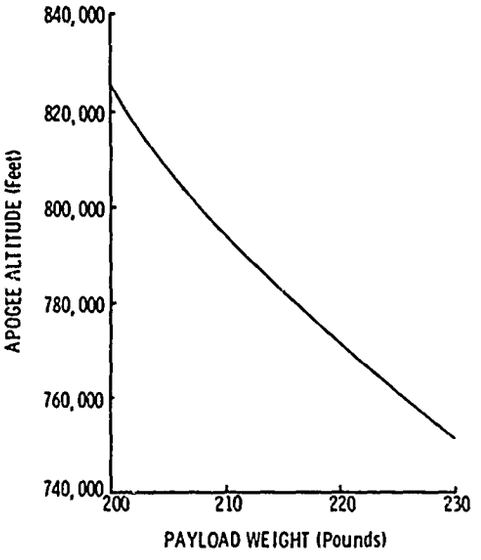

FIGURE 5. APOGEE ALTITUDE (FOR NASA 18.46) VS. PAYLOAD WEIGHT, AT 90 DEGREES LAUNCH ELEVATION ANGLE

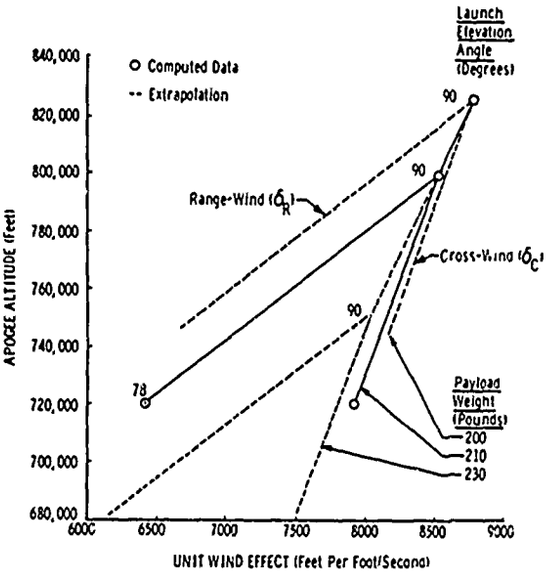

FIGURE 6. UNIT WIND EFFECTS (FOR NASA 18.46) AT 78 AND 90 DEGREES LAUNCH ELEVATION ANGLE FOR PAYLOAD WEIGHTS OF 200-230 POUNDS

3. Unit Wind Effects Matrix. The seven 6-D trajectory simulations and the three 3-D runs have provided enough data to fill in a complete unit wind effects vs. launch elevation angle and payload weight matrix for NASA 18.46.

The 6-D trajectories established the slopes of the range and cross unit wind effect vs. apogee altitude lines, at one payload weight. They also fixed the slope of the unit wind effect vs. apogee altitude line, at 90 Degrees launch elevation angle. The 3-D trajectory curve of apogee altitude vs. payload weight provided the intercepts, for different vehicle payloads, on the unit wind effect vs. apogee altitude line at 90 Degrees elevation angle.

Once these slopes have been established, the range and cross unit winds are determined by drawing lines parallel to the original (computed) unit wind effect vs. apogee altitude curves. This process is illustrated in Figure 6.

The solid line and circles in Figure 6 represent the data obtained by six-degree-of-freedom trajectory simulations. All of the rest of the information, shown on that graph as dashed lines, can be obtained from these 6-D points and the curve of apogee altitude vs. payload weight (at 90 Degrees launch elevation angle).

From this information unit range- and cross-wind effects can be determined for any combination of launch elevation angles and/or payload weights, considered for the vehicle.

Impressive savings in computer time are possible by this method. Previously, for a three payload weight by a three launch elevation angle matrix of unit wind effects, 27 six-degree-of-freedom trajectory simulations were required. This took about one hour of (7040) computer time. Using the method described above, a much more comprehensive set of unit wind data could be obtained with just seven 6-D simulations and three 3-D trajectories. Less than 20 minutes of computer time would have been required to calculate all of the necessary data.

III. CONCLUSIONS

A number of empirically derived approximations were developed that accurately describe the variation, with launch elevation angle, of several important sounding rocket performance parameters. In addition, a straightforward relationship between unit wind effects and apogee altitude, proposed by another author, was verified, and methods for its useful employment were demonstrated.

Specifically, we found that:

- The variation of apogee altitude with launch elevation angle can be accurately approximated by the function $Sin^n\theta$, where θ is the elevation angle, and n an exponent characteristic of each specific vehicle.

- Apogee time vs. launch elevation angle also follows the function $Sin^n\theta$. Significantly, the exponent n is exactly one-half the value used in the empirical approximation for apogee altitude.

- The ratio of impact range to apogee altitude is proportional to the Cotangent of θ. The accuracy of this approximation is not as high as those developed for other parameters.

- Impact range vs. launch elevation angle is accurately expressed by a function $Sin^n\theta \cdot Cos\theta$.

- Impact time vs. launch elevation angle can be approximated by a $Sin^n\theta$ function.

- The variation of range derivatives as a function of launch elevation angle can be directly extracted from the impact range vs. launch elevation angle approximation by simple differentiation.

- Unit wind effects are linearly proportional to apogee altitude. This relationship holds for both range- and cross-winds over a wide span of launch elevation angles.

With exception of the impact range/apogee altitude variation, the empirically derived approximations, for the functions described above, generally hold to within 1.0 Percent of the values obtained by trajectory simulations on digital computers. Therefore, the approximations will give answers of sufficiently high accuracy to significantly reduce the need for digital computer trajectory simulations.

The correlation with theory of most of the empirically derived relationships is vague. For example, we were not able to find any explicit link between apogee altitude vs. launch elevation angle and the Sine function. Some of the approximations can be at least crudely justified on the basis of flat-earth, zero-drag, constant-gravity considerations.

In this vein, it does make sense that apogee time is directly proportional to the square root of apogee altitude, and that a range/apogee ratio is roughly proportional to the Cotangent of the launch elevation angle - if the sounding rockets are flying in a zero-drag constant-gravity environment. However, the approximations are accurate when applied both to vehicles that traverse only the lower atmosphere (and are thus strongly affected by drag), and to sounding rockets that go to altitudes approaching one-third of the earth's radius (in trajectories where gravity cannot, by any stretch of the imagination, be considered constant).

The sounding rocket performance approximations described in this paper are, very probably, only a small fraction of those that can be developed. For instance, there are undoubtedly ways of predicting the variation of some performance parameters as a function of payload weight. Such a relationship would, possibly, involve a more sophisticated approach than the one we have taken. However, parameters such as range at apogee, time above a certain altitude, and others, would probably follow familiar trigonometric functions similar to those used in this paper.

ACKNOWLEDGMENT

The author is sincerely grateful to Messrs. Michael B. Harris and David T. Halversen of Astro-Met's Analysis Department for their help in the preparation of this paper. Special thanks are also due Mr. Fred B. Schow for his assistance in the development of the approximation for apogee altitude vs. launch elevation angle.

APPENDIX

The primary function of this paper is utilitarian; it presents some useful relationships for the empirical approximation of a number of important sounding rocket vehicle performance parameters. To enhance this utility we have included several graphs in this Appendix to simplify the task of determining the exponents for the various approximation formulas presented in the previous sections. The use of these graphs is explained below.

A.1. APOGEE ALTITUDE vs. LAUNCH ELEVATION ANGLE.

It was shown in Section II.A. that apogee altitude depends on the $\mathrm{Sin}^n\theta$, where θ is the launch elevation angle, and n is empirically determined. Since the various sounding rockets have different exponents a graph was constructed to simplify the determination of n.

To find the correct $\mathrm{Sin}^n\theta$ exponent, data from several trajectory simulation runs, at one payload weight and various launch elevation angles, are needed. Using that information, divide the apogee altitude at any elevation angle by that at 80 Degrees. Then, recalling (a slightly rearranged) Equation 1, we have:

$$\frac{\text{Apogee Altitude}_{\theta}}{\text{Apogee Altitude}_{80}} = \frac{\mathrm{Sin}^n\theta}{\mathrm{Sin}^n 80}$$

The result is equal to the ratio of the Sines - to some exponent. To determine the exponent, turn to Figure A.1 which contains the function $\mathrm{Sin}^n\theta/\mathrm{Sin}^n 80$, for n = 1-15, and θ = 75-90 Degrees. The value on the ordinate ($\text{Apogee Altitude}_{\theta}/\text{Apogee Altitude}_{80}$) will intersect one of the $\mathrm{Sin}^n\theta/\mathrm{Sin}^n 80$ curves at the angle θ at which the ratio was originally formed. That Sine curve, and that exponent, represent the variation of apogee altitude with launch elevation angle for the particular sounding rocket configuration.

A.2. APOGEE TIME vs. LAUNCH ELEVATION ANGLE.

To establish the exponent of this function we have provided Figure A.2. In that illustration, the ratio $\mathrm{Sin}^n\theta/\mathrm{Sin}^n 80$ is expanded to include exponents from 1.0 to 5.0, in increments of 0.5.

As in A.1 above, to find the $\mathrm{Sin}^n\theta$ exponent for the function apogee time vs. launch elevation angle, first form the ratio of apogee time at some elevation angle (θ) to that at 80 Degrees. The intersection of that ratio (along the ordinate) with the launch elevation angle at which it was formed (along the abcissa) will determine the $\mathrm{Sin}^n\theta$ curve that best fits the particular vehicle.

The same technique can be used to find the best exponent for the function impact time vs. launch elevation angle, where Figure A.2 is also applicable.

A.3. IMPACT RANGE vs. LAUNCH ELEVATION ANGLE.

This relationship is a function of $\mathrm{Sin}^n\theta \cdot \mathrm{Cos}\theta$. $\mathrm{Sin}^n\theta \cdot \mathrm{Cos}\theta / \mathrm{Sin}^n 80 \cdot \mathrm{Cos}80$ curves are given for exponents n = 1, 3, 5, 10, and 15, at launch elevation angles of 80-90 Degrees (Figure A.3). Figure A.4 shows this ratio (same exponents) at launch elevation angles of 75-80 Degrees.

To find the best $\mathrm{Sin}^n\theta$ exponent the ratio of impact range at some elevation angle (θ) to that at 80 Degrees is determined. Locate that point on Figure A. 3 or A.4. The exponent of the nearest $\mathrm{Sin}^n\theta \cdot \mathrm{Cos}\theta$ curve can be used for this vehicle.

NOTE: FIGURE A.1 - A.4 ARE ALL BASED ON A REFERENCE LAUNCH ELEVATION ANGLE OF 80 DEGREES. FOR SOME VEHICLES THE APPROXIMATION FORMULAS WORK BEST WITH REFERENCE ELEVATION ANGLES OTHER THAN 80 DEGREES. THEREFORE, FIGURES A.1 - A.4 CANNOT BE USED FOR THOSE SOUNDING ROCKETS.

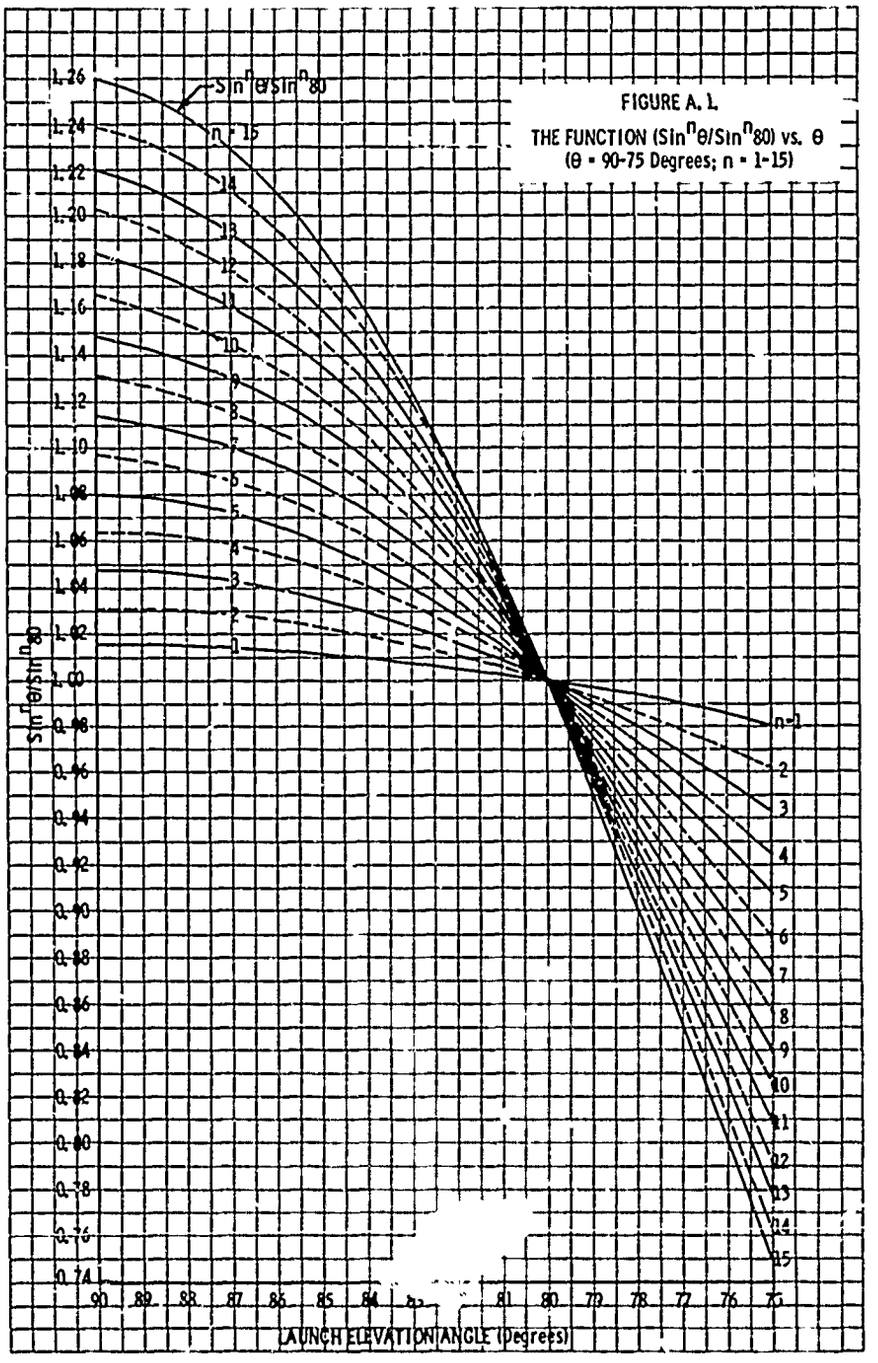
FIGURE A. 1.
THE FUNCTION (Sin^{n}θ/Sin^{n}80) vs. θ
(θ = 90-75 Degrees; n = 1-15)
Sin^{n}θ/Sin^{n}80
n = 15
14
13
12
11
10
9
8
7
6
5
4
3
2
1
n=1
2
3
4
5
6
7
8
9
10
11
12
13
14
15
1.26
1.24
1.22
1.20
1.18
1.16
1.14
1.12
1.10
1.08
1.06
1.04
1.02
1.00
0.98
0.96
0.94
0.92
0.90
0.88
0.86
0.84
0.82
0.80
0.78
0.76
0.74
Sin^{n}θ/Sin^{n}80
90 89 88 87 86 85 84 83 82 81 80 79 78 77 76 75
LAUNCH ELEVATION ANGLE (Degrees)

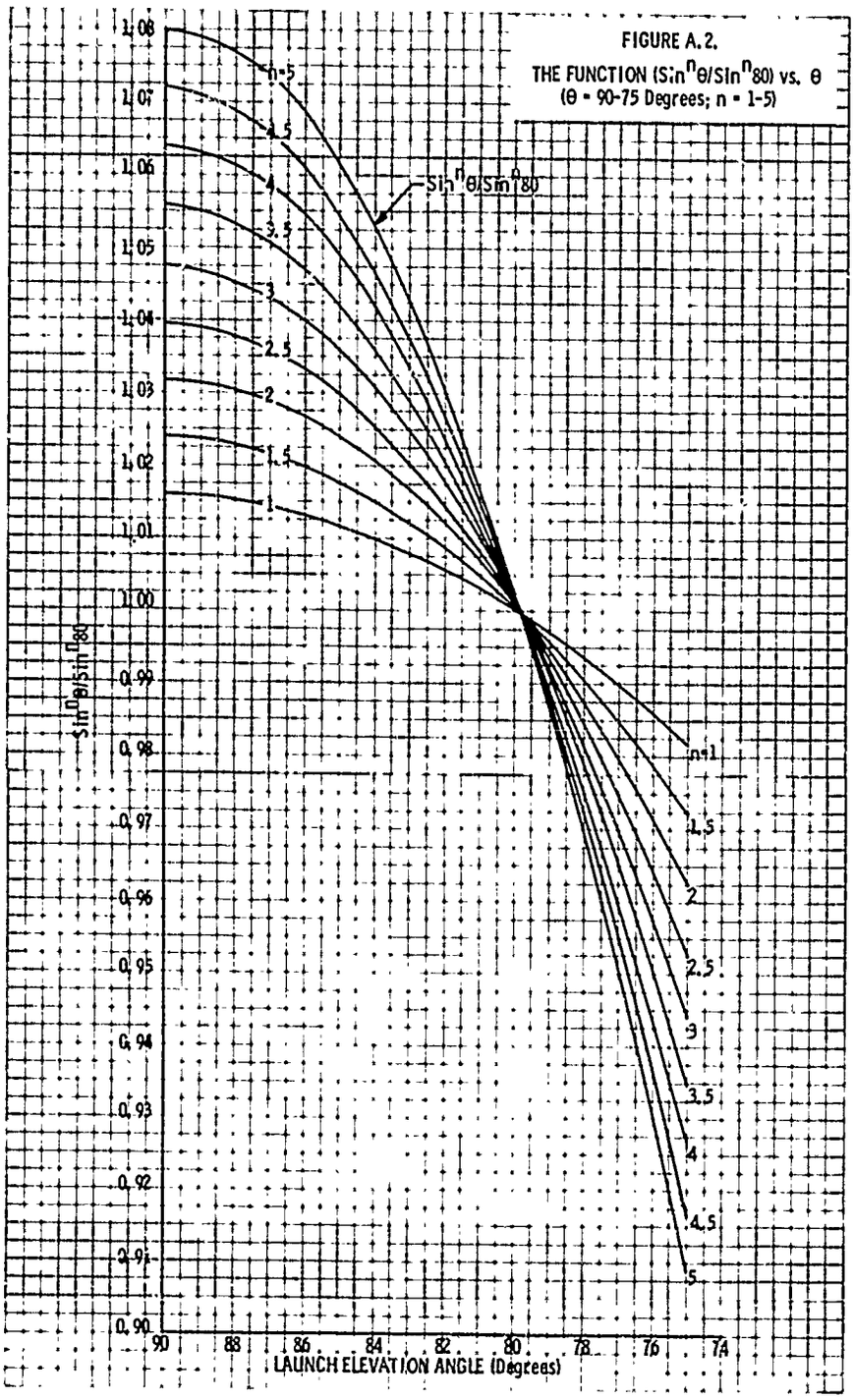
FIGURE A.2.
THE FUNCTION ($Sin^n\theta/Sin^n80$) vs. θ
(θ = 90-75 Degrees; n = 1-5)
$Sin^n\theta/Sin^n80$
n=5
4.5
4
3.5
3
2.5
2
1.5
1
n=1
1.5
2
2.5
3
3.5
4
4.5
5
1.08
1.07
1.06
1.05
1.04
1.03
1.02
1.01
1.00
0.99
0.98
0.97
0.96
0.95
0.94
0.93
0.92
0.91
0.90
90
88
86
84
82
80
78
76
74
LAUNCH ELEVATION ANGLE (Degrees)

16

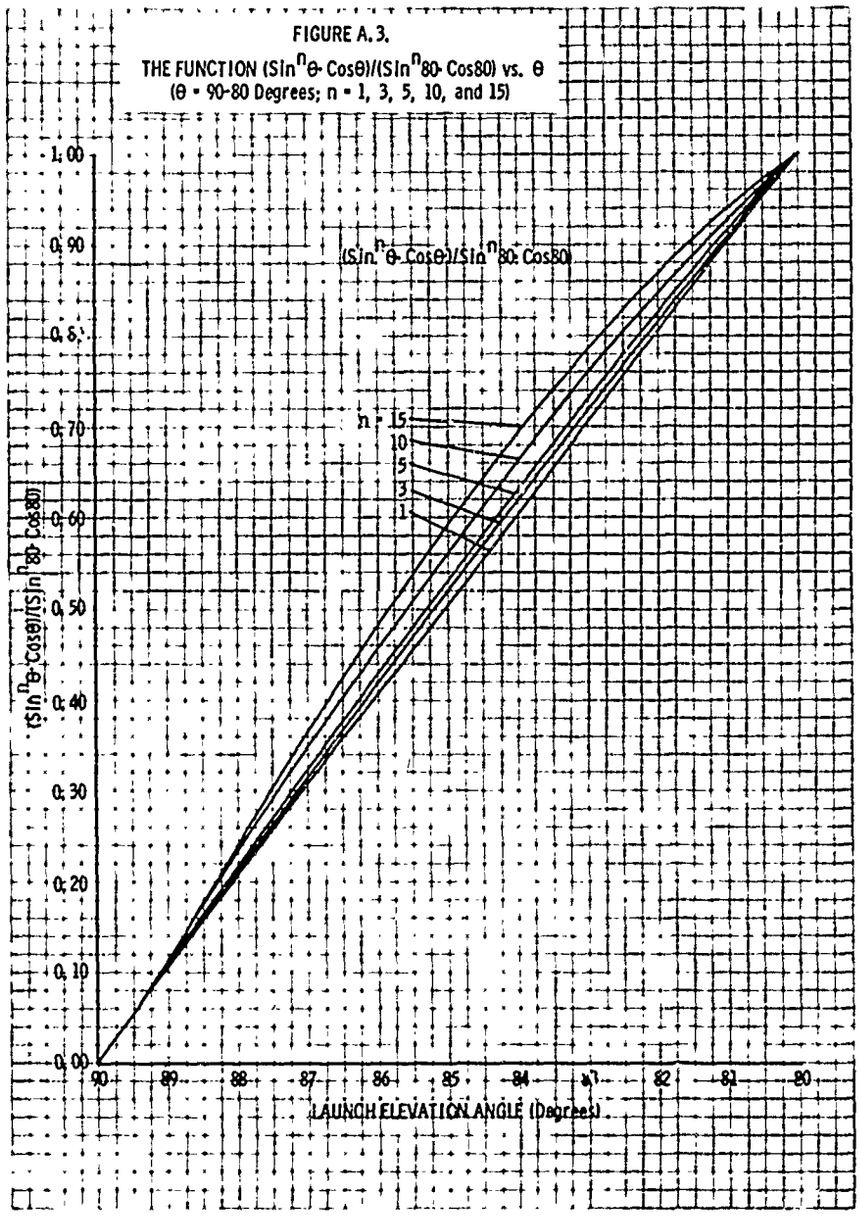
FIGURE A.3.
THE FUNCTION (SIn^{n}θ- Cosθ)/(SIn^{n}80- Cos80) vs. θ
(θ = 90-80 Degrees; n = 1, 3, 5, 10, and 15)
(SIn^{n}θ- Cosθ)/SIn^{n}80- Cos80)
n = 15
10
5
3
1
(SIn^{n}θ- Cosθ)/(SIn^{n}80- Cos80)
1.00
0.90
0.80
0.70
0.60
0.50
0.40
0.30
0.20
0.10
0.00
90
89
88
87
86
85
84
83
82
81
80
LAUNCH ELEVATION ANGLE (Degrees)

17

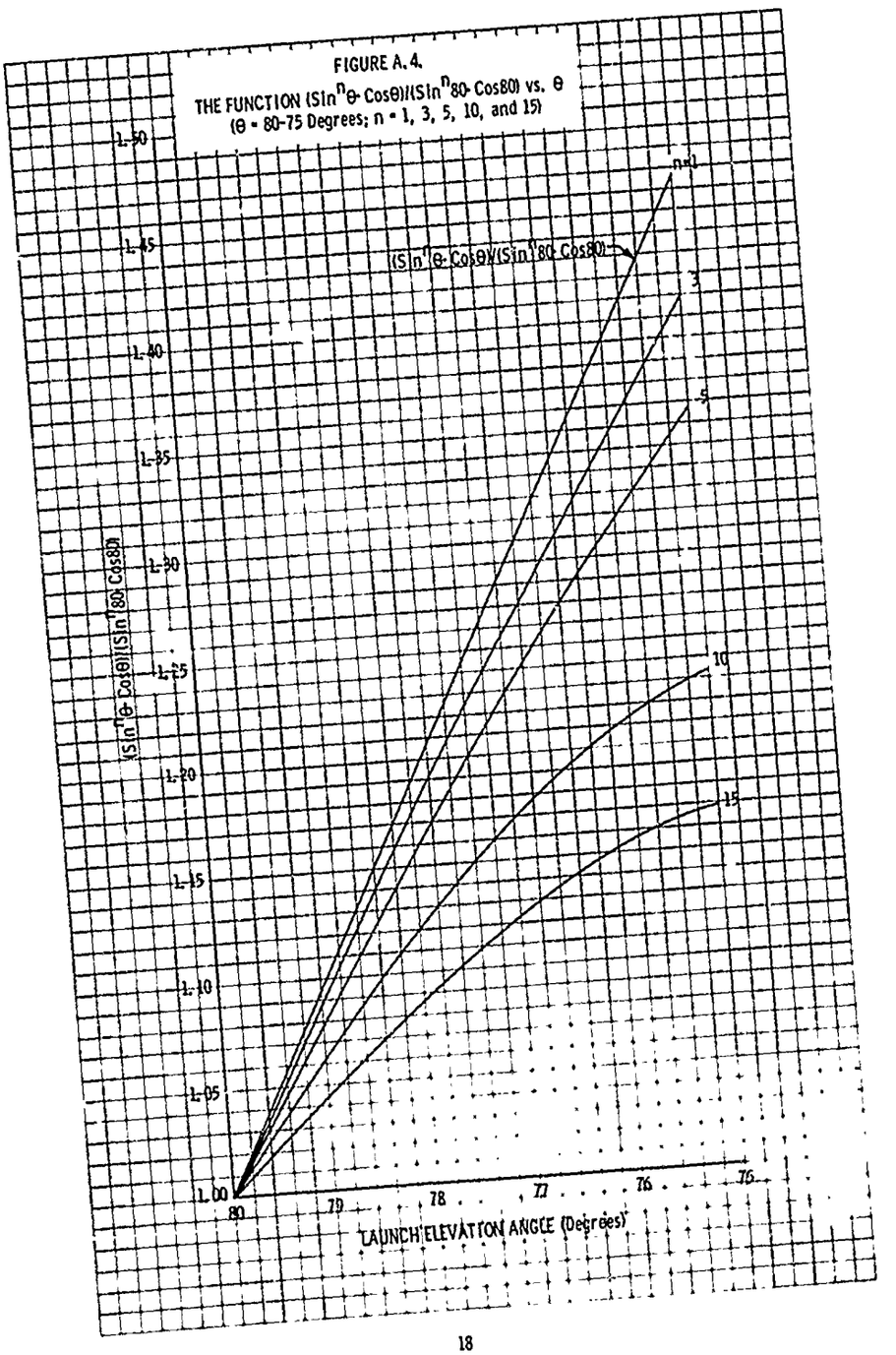
FIGURE A.4.
THE FUNCTION (Sin^{n}θ-Cosθ)/(Sin^{n}80-Cos80) vs. θ
(θ = 80-75 Degrees; n = 1, 3, 5, 10, and 15)
(Sin^{n}θ-Cosθ)/(Sin^{n}80-Cos80)
n=1
3
5
10
15
1.50
1.45
1.40
1.35
1.30
1.25
1.20
1.15
1.10
1.05
1.00
80
79
78
77
76
75
LAUNCH ELEVATION ANGLE (Degrees)

REFERENCES

1. NASA NIKE-TOMAHAWK HANDBOOK; Thiokol Chemical Corporation, Astro-Met Division; Ogden, Utah; December 1966

2. Baldwin, Robert M.; DISPERSION STUDY FOR THE NIKE-NIKE-NIKE-CREE III; Report No. APGC AIDR 63-35; Air Proving Ground Center, Air Force Systems Command, United States Air Force, Eglin Air Force Base, Florida; May 1963

3. Bradford, W. C. and Myers, P. W.; THEORETICAL AND EXPERIMENTAL DISPERSIONS FOR THE ARCAS ROBIN ROCKET; Technical Documentary Report No. APGC-TDR-61-62; Air Proving Ground Center, Air Force Systems Command, United States Air Force, Eglin Air Force Base, Florida; December 1961

4. RANGE-SAFETY DATA FOR THE D-REGION TOMAHAWK; Thiokol Chemical Corporation, Astro-Met Division; Ogden, Utah; To be published September 1967.

5. Taylor, J. P. and Olson, A. M.; AERODYNAMIC AND FLIGHT PERFORMANCE ANALYSIS FOR THE NIRO SOUNDING ROCKET; Appendix A to Scientific Report SGC 916 FR-1; Space-General Corporation, El Monte, California; March 1966

6. FLIGHT PERFORMANCE OF THE SANDHAWK VEHICLE FAMILY; Thiokol Chemical Corporation, Astro-Met Division, Ogden, Utah; June 1967

7. PERFORMANCE SUMMARY FOR THE ASTROBEE 1500 SOUNDING ROCKET VEHICLE; Report No. AST/EIR-00.91; Astronautics Division of Chance Vought Corporation, a Division of Ling-Temco-Vought Incorporated; March 1963

8. Sollow, P. A.; JAVELIN WIND WEIGHTING AND DISPERSION ANALYSIS; Report No. 358 FR-3-2; Space-General Corporation, El Monte, California; April 1964

9. Hoult, C. P.; SOUNDING ROCKET DISPERSION SCALING LAWS AND THEIR APPLICATION TO THE DETERMINATION OF THE LAUNCH WINDOW FOR JAVELIN OPERATIONS AT FORT CHURCHILL; Tech Data No. 63-3; Air Force Cambridge Research Laboratories, Bedford, Mass.; March 1963

10. Hoult, C. P.; A SIMPLIFIED BALLISTIC MODEL FOR SOUNDING ROCKETS; Unguided Rocket Ballistics Conference, Preprint of Papers, Page 9, f.f.; ECOM, United States Army Electronics Command; September 1966

BLANK PAGE

A CONTROL SYSTEM FOR REDUCING THE DISPERSION OF MULTI-STAGE SOUNDING ROCKETS *

by

G. R. Conrad
H. R. Gleyre
J. Ottesen
A. S. Hu

INTRODUCTION:

Those active in the sounding rocket community, notably vehicle designers, users, ballisticians and flight safety officers, have been confronted with the problem of flight path dispersion throughout the history of sounding rocket utilization. The problem is most serious with vehicles achieving zenith altitudes of 100 miles or more; and the evolution of vehicle design toward higher performance, coupled with more stringent requirements for trajectory precision imposed by the user, have aggravated the problem.

Two characteristics of the sounding rocket contribute to high dispersion. The most obvious of these is the ballistic flight mode; and the other is the near-vertical flight path, which maximizes the time of flight, thus amplifying rather small velocity errors to cause large impact point displacements.

The examination of trajectory data from a large number of Nike-Apache firings by PSL has shown that in nearly every instance the vehicle became essentially committed to its ultimate flight path direction by the time of booster burnout. The study of Nike-Apache dispersion by means of flight simulation has supported the findings from flight data. Table I shows a breakdown of Nike-Apache dispersion estimates achieved by flight simulation. Note that the three largest contributors are booster thrust misalignment, launcher-induced tip-off and uncertainties in the wind field. Note from Figure 1, the vehicle wind-weighting curve, that 90% of the wind effect is incurred by booster burnout, assuming a uniform wind velocity profile as a function of altitude. The Nike-Apache is not unique in this regard, in that many other sounding rockets exhibit similar behavior.

*The effort described herein is supported by U.S. Army, Redstone Arsenal Contract #DAAG 43-67-C-0016, and by Bell Telephone Laboratories Subcontracts #232136 and #601720.

TABLE I
NIKE — APACHE
DISPERSION
Analysis Results

Dispersion Source	Estimated 3 σ Value	Range Effect (Naut. Mi.)	Cross-Range Effect (Naut. Mi.)
Thrust Misalignment			
First Stage	0.1 deg.	12.185	12.185
Second Stage	0.1 deg.	0.156	0.156
Fin Misalignment			
First Stage	0.1 deg.	1.644	1.644
Second Stage	0.1 deg.	0.337	0.377
Thrust Variation	1%	1.356	None
Drag Variation	5%	1.252	None
Launch Tip-Off Effect			
Pitch	7.5 deg/sec.	15.682	None
Yaw	7.5 deg/sec.	None	15.682
Wind Uncertainty	5 ft/sec.	9.60	9.60
Second Stage Ignition Time Variation	2 sec.	1.913	None
R. S. S. Total		22.28 N. M.	22.12 N. M.

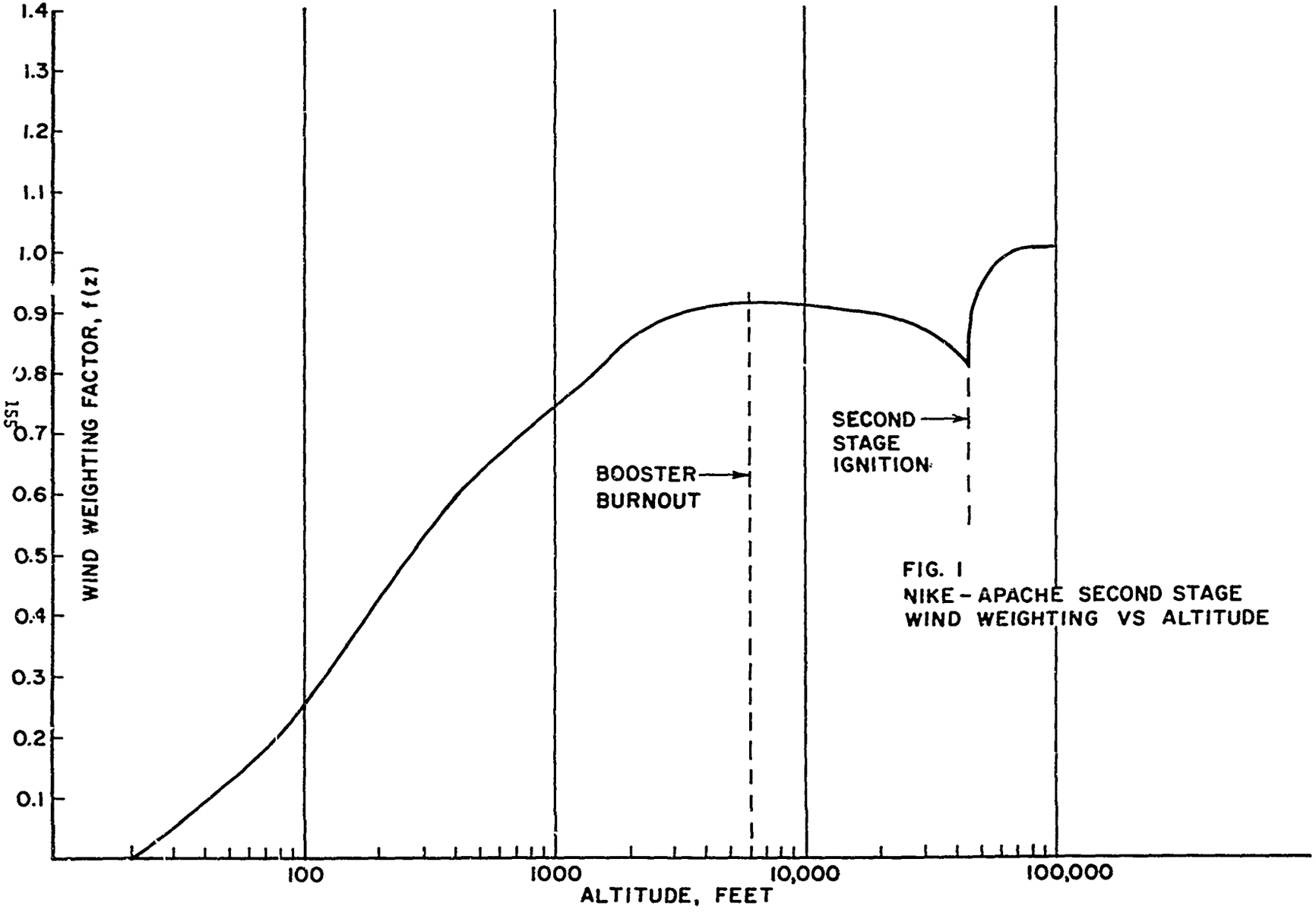

FIG. 1
NIKE - APACHE SECOND STAGE
WIND WEIGHTING VS ALTITUDE

The potent influence of these three dispersion contributors, has been widely recognized; and a substantial effort has been exerted continuously by many agencies and individuals to eliminate or minimize these uncertainties. The problem of wind uncertainty is being dealt with by the development of semi and fully automated wind measurement and compensation computation systems to yield more accurate and timely data. More comprehensive mathematical models of vehicle behavior are now available for predicting the response of a vehicle to a wind profile. Thrust misalignment is being controlled by more precision in the manufacture of rocket motors and payload components; and its effect is minimized by the development of adequate vehicle spin rates early in flight, sometimes even on the launcher. The evolution of the simultaneous lug-release finite-length launch rail has been effective in reducing launch tip-off.

All of these approaches have produced improvement, and more can be expected, yet the best of these in aggregate have produced reductions of the order of about 20%. When the Physical Science Laboratory was recently confronted with a Nike-Apache mission requirement for a near-vertical trajectory achieving a zenith altitude of the order of 800K ft. and a second stage/payload impact accuracy of 5 - 10 nautical miles radius on a 3σ confidence basis, it was concluded that some form of guidance and control was essential.

This conclusion was not made lightly, since the addition of guidance and control to a sounding rocket poses a number of disadvantages, such as increased cost and complexity, compromises in performance and new flight safety problems. With these constraints in mind, a variety of approaches were studied, culminating in the selection of a Coast Phase Control System, hereafter referred to as the CPCS. The other systems studied and the reasons for selection of the CPCS will be discussed in a following section. At this point, a brief description of the CPCS is in order.

Figure 2 shows the CPCS general arrangement, in a module located between the head end of the M-5 booster and the aft end of the Apache second stage. The aft end of the module seats in a socket forming the forward end of the interstage

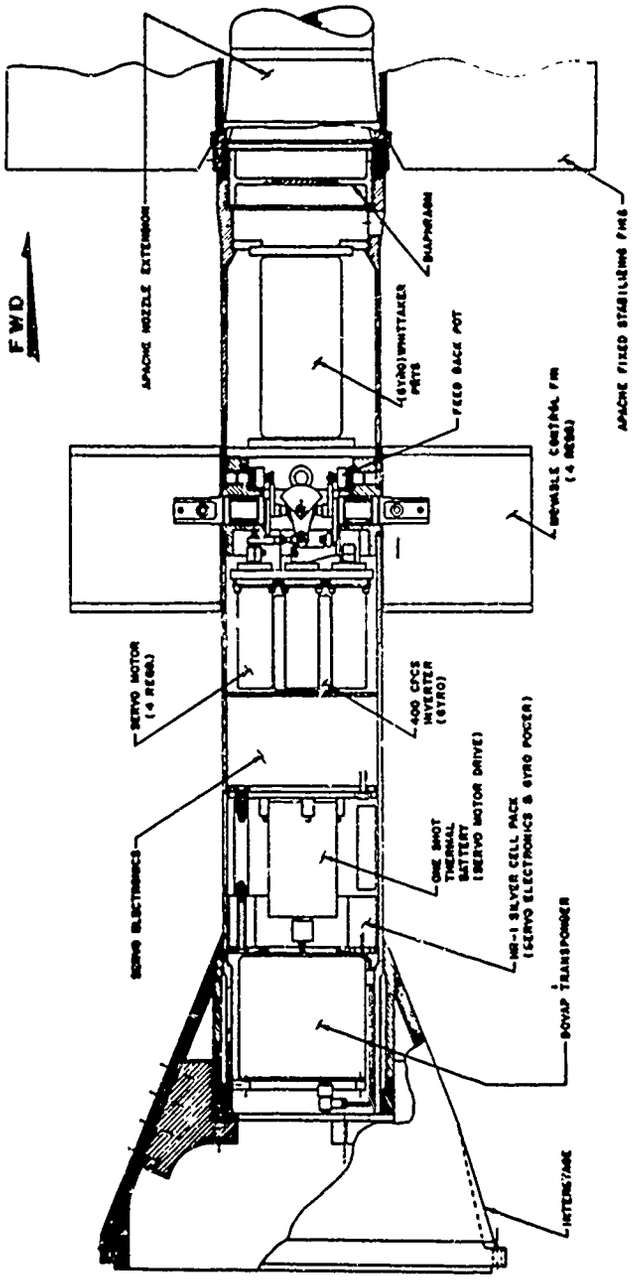

FIG 2 CPCS INBOARD PROFILE

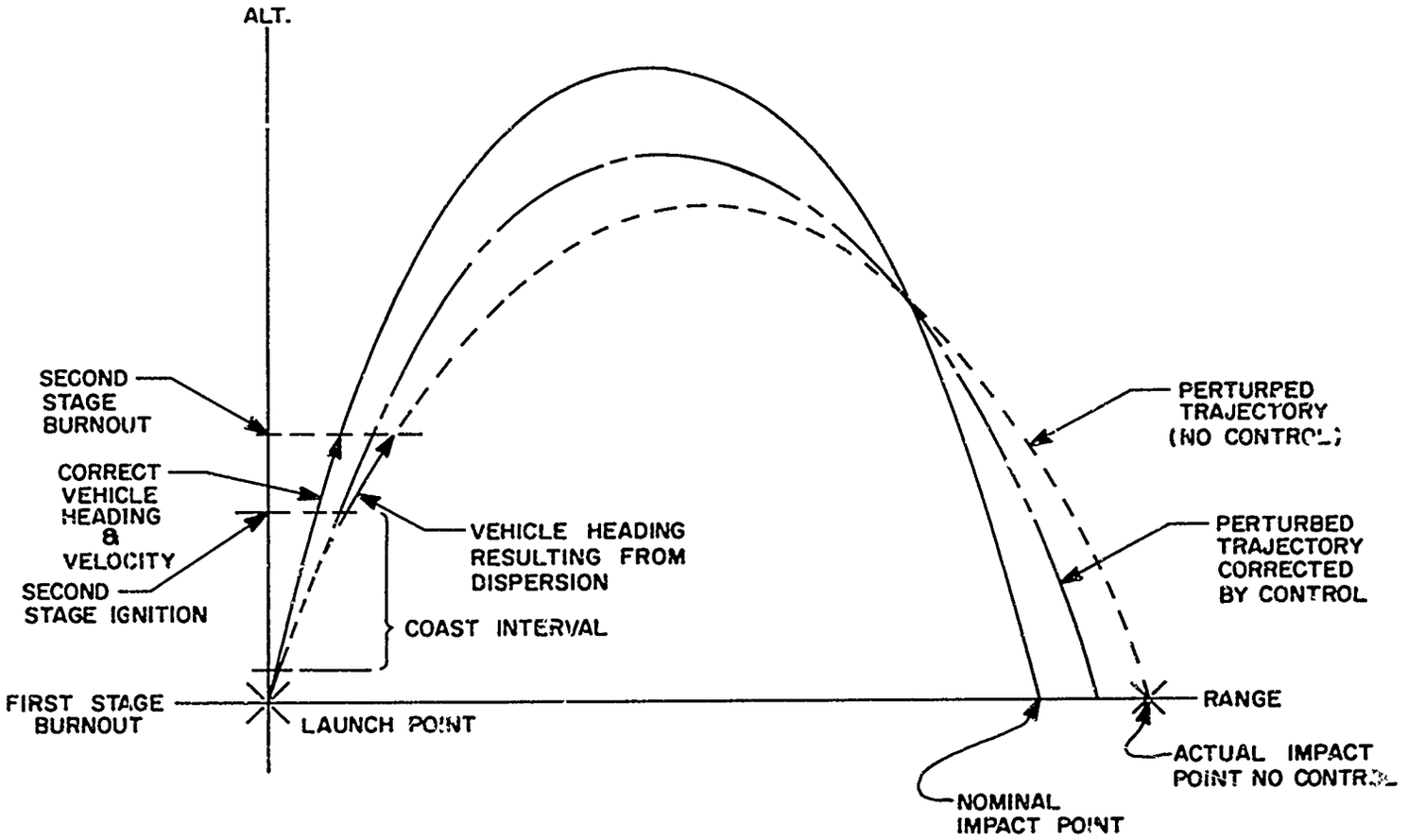

FIGURE 3

NIKE-APACHE DISPERSION REDUCTION BY CORRECTION OF SECOND STAGE HEADING DURING COAST INTERVAL

adapter, allowing the booster to separate by differential drag at burnout. The forward end of the module is positively attached to the aft end of the Apache by a threaded blast diaphragm, which shatters upon ignition of the second stage, jettisoning the module. Aft of the blast diaphragm is the gyro housing, mounting a three-axis free gyro set which constitutes the attitude reference. At the center of the module are mounted four moveable rectangular fin panels, with the hubs, support bearings, lever linkages, and feedback potentiometers. Aft of this space there are four D-C servo motor-gear head assemblies, mounted with the shaft axes parallel to the vehicle longitudinal axis, each driving one moveable fin. An electronics sub-assembly consisting of servo-amplifiers, compensation networks, and bias voltage circuits is mounted behind the servo-motors. Located near the rear of the module is a primary power supply, consisting of a "one-shot" high-current thermal battery for servo motor and second-stage ignition power and a separate silver-zinc battery supply for other module power requirements. The most rearward compartment of the module contains a flight safety command receiver device and/or a module recovery parachute.

The module functions to accomplish a course correction maneuver during the interval between booster burnout and second stage ignition, so that the vehicle velocity vector and body axis are restored to the orientation required for the desired nominal trajectory, as shown in Figure 3. The result is a trajectory parallel to the intended nominal path but displaced by the dispersion accumulated prior to and during the course correction maneuver. The source of the error information is the attitude reference in the module, wherein the desired vehicle attitude at second-stage ignition is preset prior to launch by uncaging the gyros a few seconds prior to launch, and inserting bias voltages in the pitch and yaw servo loops which are equivalent to the difference between the launch attitude and the required attitude at second stage ignition. The vehicle roll control loop is active from launch, maintaining the "on-launcher" vehicle roll attitude. The pitch and yaw control loops are activated after booster separation.

With this introductory description it is now appropriate to discuss the various details of system selection, design, operation, and performance.

DISCUSSION OF GUIDANCE PHILOSOPHY:

The application of guidance principles to reduce dispersion is implicit in the launching of "unguided" sounding rockets. Historically, the advent of high altitude rockets required the development of techniques to predict the deterministic effects of perturbing influences such as wind, on trajectories. These techniques and their applications are the elements of guidance procedures in that they are used to adjust launcher settings to obtain desired results such as impact at a target point.

The CPCS guidance principle is a simple extension of aiming to an in-flight phase by means of an attitude control system. After activation, this system acts as a nulling device to force rocket attitude to a preset value, thereby removing the directional dispersion accrued prior to activation. The system can also be used to "shape" the trajectory.

It should be noted that there is no on-board guidance function. The guidance function is a procedure applied, like those which adjust launcher settings, prior to the fact of firing, in order to establish what conditions the control system is to achieve.

Choice of the Control Phase

A normal Nike Apache flight consists of four or five phases:

1. Nike Boost (0 - 3.3 sec.).
2. Apache Pre-ignition Coast (3.3 - 23 sec.).
3. Apache Burn (23 - 29.4 sec.).
4. Apache Coast (29.4 sec. -).
5. Afterbody Coast (payload separation).

Control could be implemented in any phase or combination of phases of the upleg trajectory. However, the intent is to utilize attitude control to produce alterations of the flight path, which requires the existence or generation of appreciable reactive force during the control phase. Thus, attitude control after phase 3 will not have much effect on the trajectory itself. Control in a combination of phases generally requires a more complex control system than a single phase because of the requirement of variable gain constants and compensation.

Since the major source of dispersion is in the first phase, an obvious choice would be to implement control during boost to counter perturbations while they occur. There are, however, considerations that make this approach unattractive. A rapid response system would be required, due to the short time interval of 3.3 sec. Such a system would have to utilize some type of thrust vector direction, or thrust force generation. Although this is technically feasible, it would require extensive modifications of the booster, incurring a high unit cost.

Implementation of control into the Apache burn phase (phase 3) has at the outset the serious disadvantage of a heavy payload capacity penalty. It has been estimated that a cold-gas reaction control system for this phase would weigh at least 26 pounds. The system would also require a nitrogen tank having a 10 inch diameter, which is a prohibitive size for the Apache. Another system, utilizing "hot gas" reaction control, where the gas is bled from the Apache, has even greater liabilities. The design of valving mechanisms to handle the gas without leakage or crippling erosion is a formidable task. The final disadvantage is that this system could provide control only during burn, necessitating the use of a roll-free attitude reference system, which is more expensive than the simpler gyro set used in the CPCS.

The pre-ignition coast phase (phase 2), is the most attractive choice for control. A control module inserted between the booster and second stage, and attached to the second stage aft end, requires little modification of the existing hardware, and does not impose a severe payload weight penalty. The system will utilize existing aerodynamic forces for attitude control and flight path correction. Dispersion and normal wind response are allowed to take place in the boost phase. After separation, the activated control system effectively removes the directional dispersion and, if required, would perform to make other attitude and flight path alterations.

The Inertial Reference System and Coordinates

The extension of aiming via attitude control requires a coexistent extension of reference, which, in the CPCS, will be supplied by the Whittaker PRYS (Pitch-Roll-Yaw-Sensor). Other methods of attitude sensing, such as a solar sensor-magnetometer system do not offer the advantage of direct measurement, and are affected by environmental factors outside of the rocket. On the other hand, a gyroscopic reference is subject mainly to an internal environment that causes drift, which in turn, causes attitude measurement errors.

Associated with the reference system is a coordinate system defined by the gyro arrangement (fig. 4). Pitch and yaw angles lay in orthogonal planes whose orientation with respect to the reference coordinates is the roll angle (fig. 4a). It should be noted that the angles are not an Euler sequence. Appendix I contains transformations used in simulation of CPCS trajectories.

Because the PRYS does not have full rotational freedom of roll ($\pm 60^{\circ}$), it will be necessary to control roll during boost as well as in the control phase. Although this requires an element of control in a combination of phases, no changes of gain or compensation will be required.

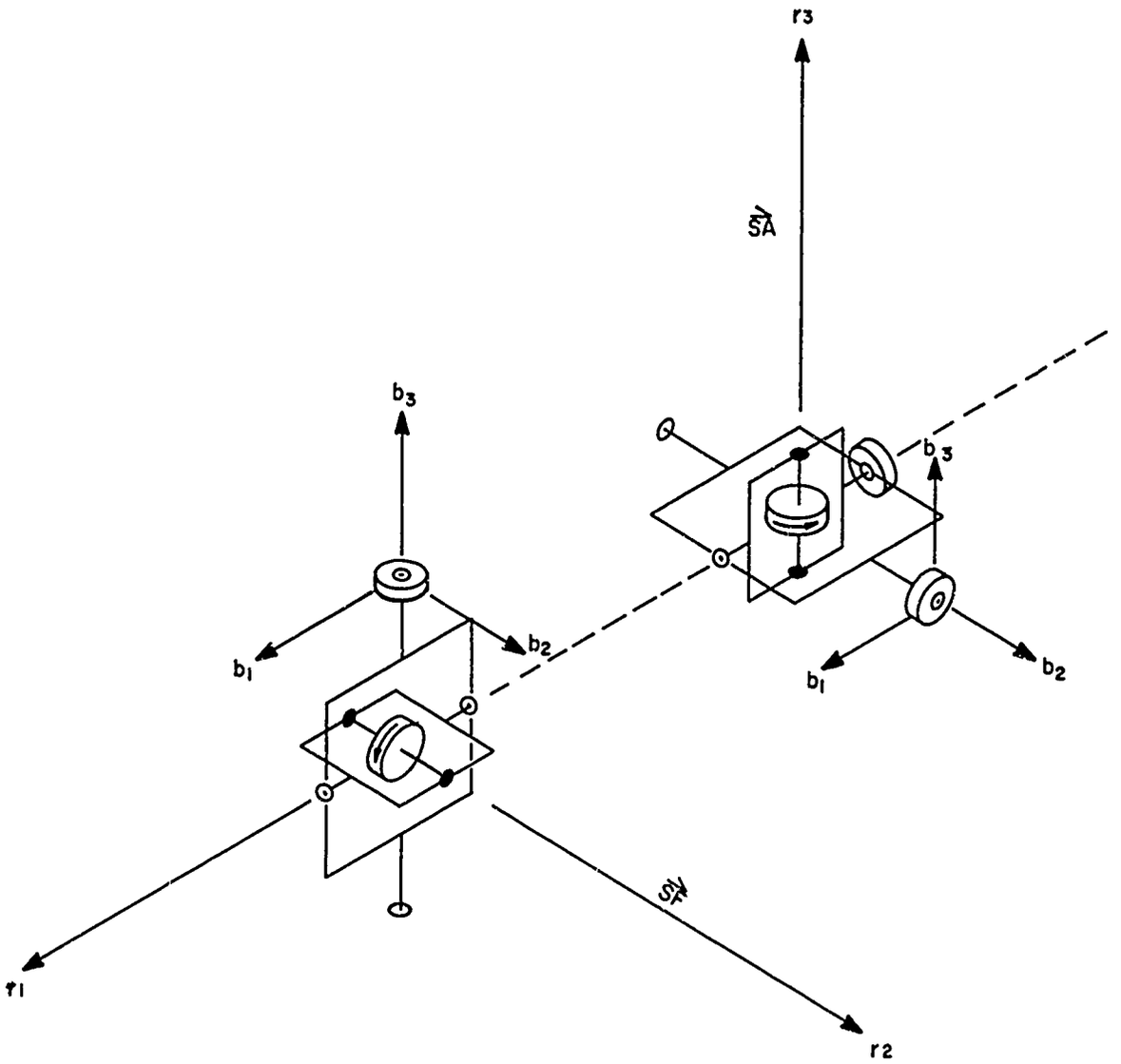

FIG. 4

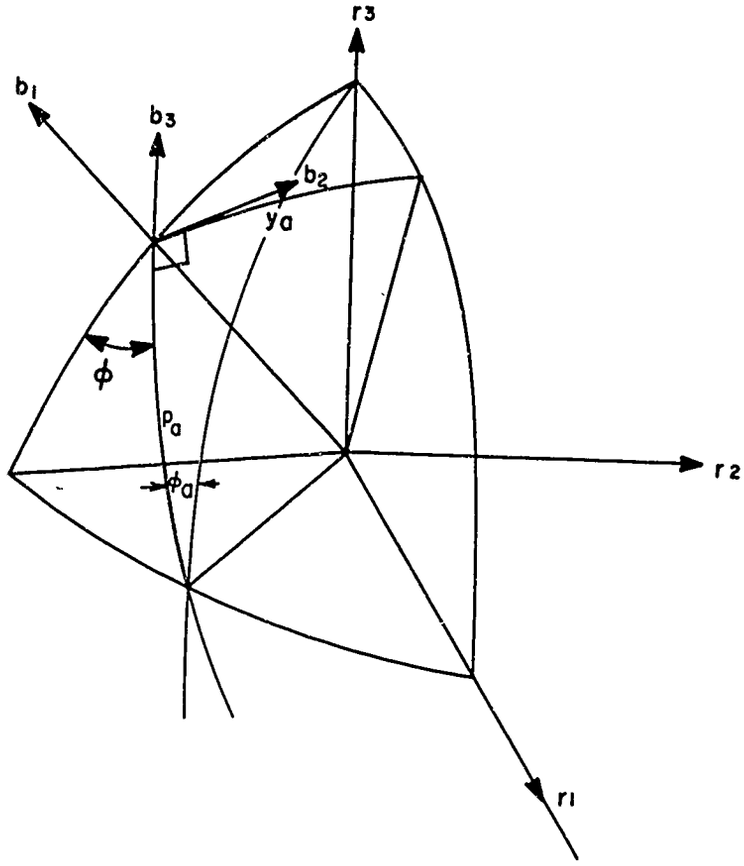
r3
b1
b3
b2
ya
ϕ
pa
ϕa
r2
r1

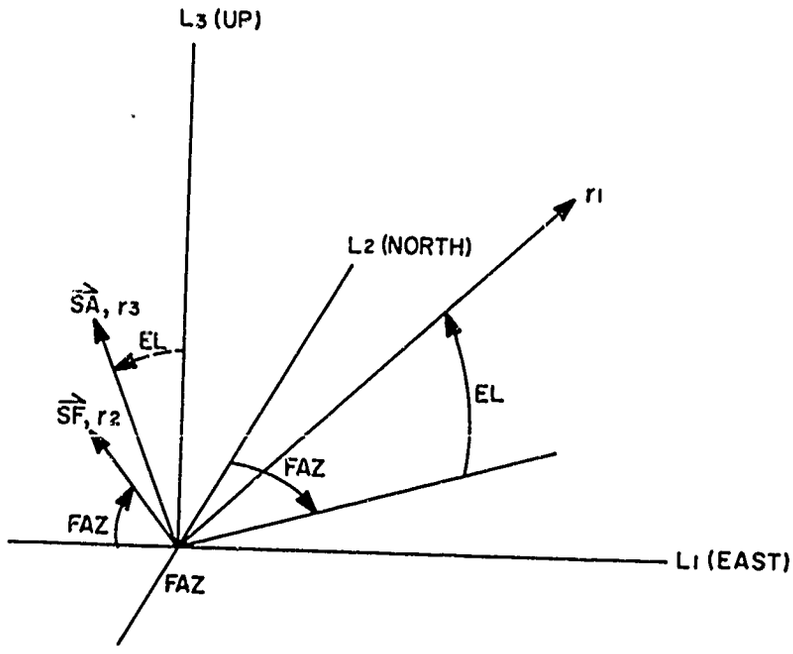
L3 (UP)
r1
L2 (NORTH)
SA, r3
EL
SF, r2
EL
FAZ
FAZ
FAZ
L1 (EAST)

FIG. 4a

Requirement for Bias Insertion

The attitude reference orientation will be that of the system at gyro uncage time. Because it will not generally be desirable to force attitude to this particular orientation, it is required that an attitude programmer be carried on-board that will electronically provide signals corresponding to a desired attitude in terms of pitch and yaw angles. The setting of the programmer is referred to as "bias insertion". Since the desire is also to allow the normal boost-phase wind response as a non-dispersion effect, the bias settings will be modified accordingly. It should be obvious too, that changes to launcher settings will generally require corresponding changes in bias settings.

The processes involved in determination of launcher and bias settings amount to the solution of "guidance equations", which will utilize multiple wind weighting by standard methods, and pre-computed ballistic tables. Multiple weighting is required to determine the boost phase wind response and the effects of upper winds on the burning second stage separately.

Sources of Error

The primary errors in the Nike Apache CPCS trajectory will be caused by attitude measurement. In practice no gimbal system can completely isolate a gyro from outside rotations. Torques are communicated to the gyro by friction and other causes, so that the spin axis is not really fixed in space. Over a sufficiently long time period then, the PRYS gyro spin axes will tend to drift away from their initial orthogonality. The PRYS 3σ drift per gyro is about 0.5° from uncage to control termination. This amounts to roughly a total 3σ error in attitude of 0.7°, with associated range and cross range impact components of about 6.5 n. miles, which dominates the predicted 3σ impact dispersion (9.7 n. mi.).

Thus, the CPCS will operate to remove almost completely the dispersion originating during boost and replace it with a smaller dispersion of its own.

CPCS Flight Path Behavior

As was mentioned previously, the CPCS acts to null attitude errors. The nulling rate is proportional to the error magnitude so that the attitude tends to approach desired attitude exponentially. Flight path direction also tends to approach desired attitude but lags rocket attitude. Figure 5 shows typical rocket and flight path response in terms of elevation and azimuth, and figure 6 shows the hypothetical ground track. These plots demonstrate the "dog-leg" capability of the CPCS in a situation where safe booster impact and avoidance of over-flight of a forbidden area can be achieved simultaneously with second stage impact at a desired target point. The flight path angle change in the example trajectory is approximately 13°. Use of the CPCS for course correction alone will involve flight path changes of about 3° (3σ).

AERODYNAMIC AND MECHANICAL DESIGN CONSIDERATIONS

Aerodynamic control was selected because of its design simplicity. During the portion of flight where control is to be exercised, aerodynamic surfaces are sufficiently effective to accomplish the required flight path corrections. Control system components are largely "off-the-shelf" type. Components which must be designed and built can be available within reasonable lead times. Aerodynamic parameter values can be predicted close enough for preliminary design from correlation of published results of numerous wind tunnel tests and theoretical studies. For accurate values, however, wind tunnel tests of the specific configuration will be conducted in order to determine precisely the effect of the flow disturbances generated by the forward rocket stage, particularly, the stabilizing fins located just ahead of the control fins. Tests of wind tunnel models, for example, should show whether it is better to place the control fins in line with the stabilizing fins or off-set them 45 degrees for maximum effectiveness.

FIG. 5

NIKE APACHE CPCS FLIGHT PATH RESPONSE

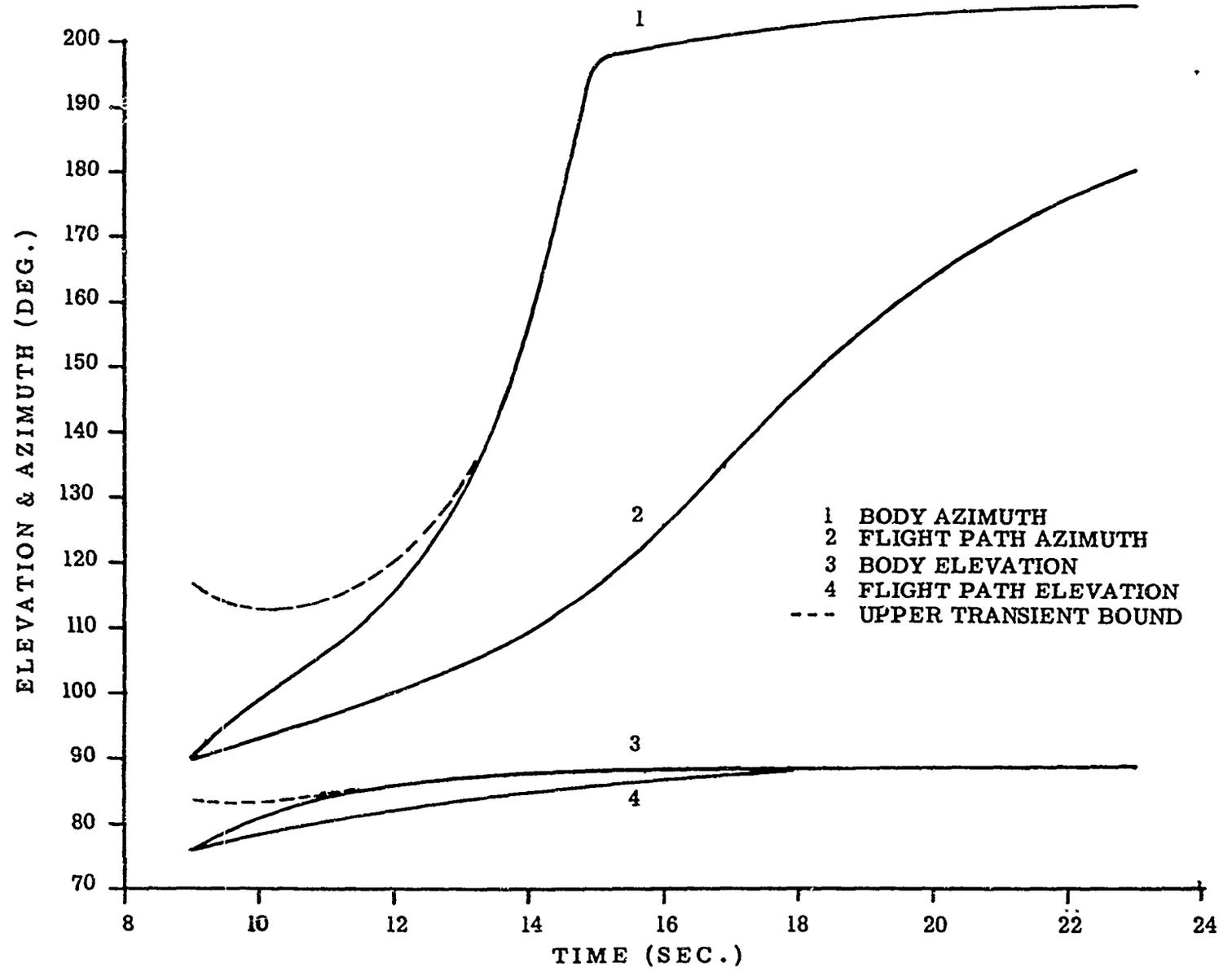

NIKE APACHE CPCS GROUND TRACK

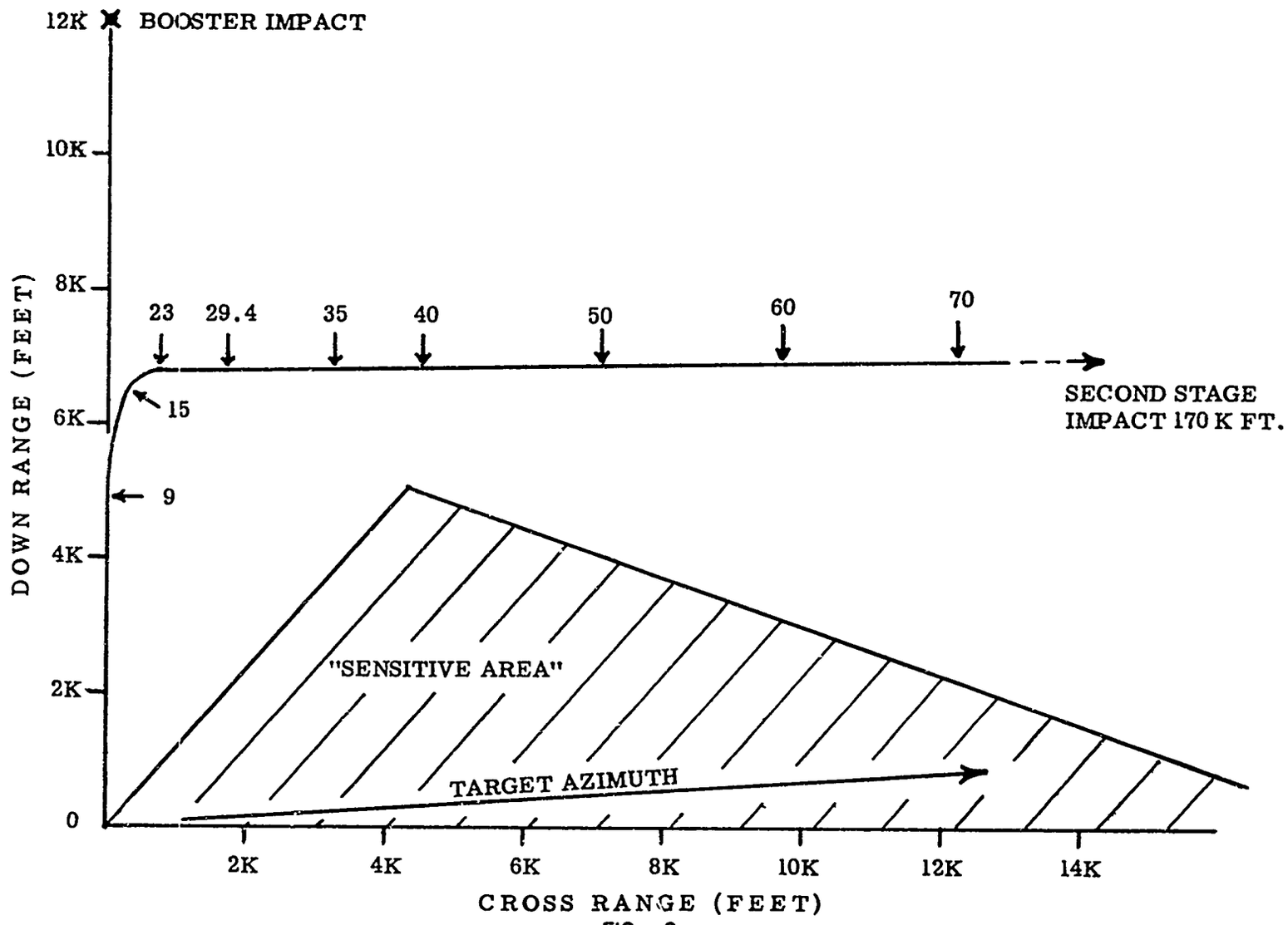

FIG. 6

For the present application on the Nike Apache rocket a preliminary aerodynamic analysis was made using Nike Apache wind tunnel force test data and modifying these to account for addition of the control module. An attempt was made to account for downwash effects in computing normal forces and moments. Accurate assessment of the maneuverability and dynamic behavior of the controlled vehicle will necessarily be dependent upon the wind tunnel test results. Figure 7 is an outline of the Nike Apache rocket with the control module.

Figures 8 through 17 show estimated static aerodynamic and performance parameters. Turning rates shown in figures 11 and 14 are of interest because from these, total flight path angle changes can be computed where a "dog-leg" trajectory is employed. "Dog-leg" trajectories, as suggested earlier, would be desirable in the case where the launch and payload impact areas are fixed, but flight over a particular area in between is prohibited. The control system is capable of up to a 180 degree flight path azimuth change during the initial coast phase of the second stage. Utilizing this capability it is possible to alter significantly the locations of the first and unignited second stage impact zones. Thus over-flight of certain areas near the launcher could be avoided.

The CPCS unit is attached to the APACHE motor (See Figure 2) by means of a threaded steel blowout diaphragm which, after completion of the control phase, is shattered by APACHE motor ignition allowing the unit to fall away from the second stage. The standard probe-type interstage was modified so that the aft 7 1/2 inches of the module can be inserted into a socket.

The control fin hinge line is placed just ahead of the most forward fin center-of-pressure location. The reason for placing the hinge line ahead of the c.p. was to enable the fin normal force to aid in returning the fin to a neutral position in the event of loss of fin control power.

The control housing consists of 2 sections of 3/16" thick 7075-T6 Aluminum

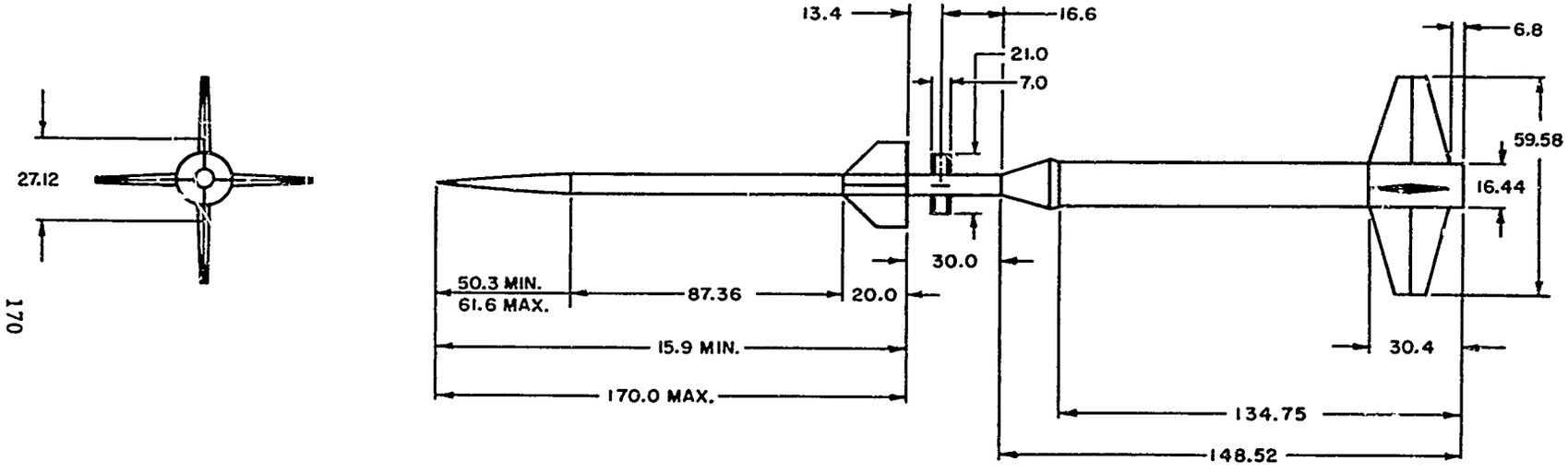

FIG. 7
NIKE-APACHE WITH CPCS
INBOARD PROFILE

STATIC LIFT & MOMENT COEFFICIENT SLOPES
NIKE-APACHE 2ND STAGE WITH CPCS

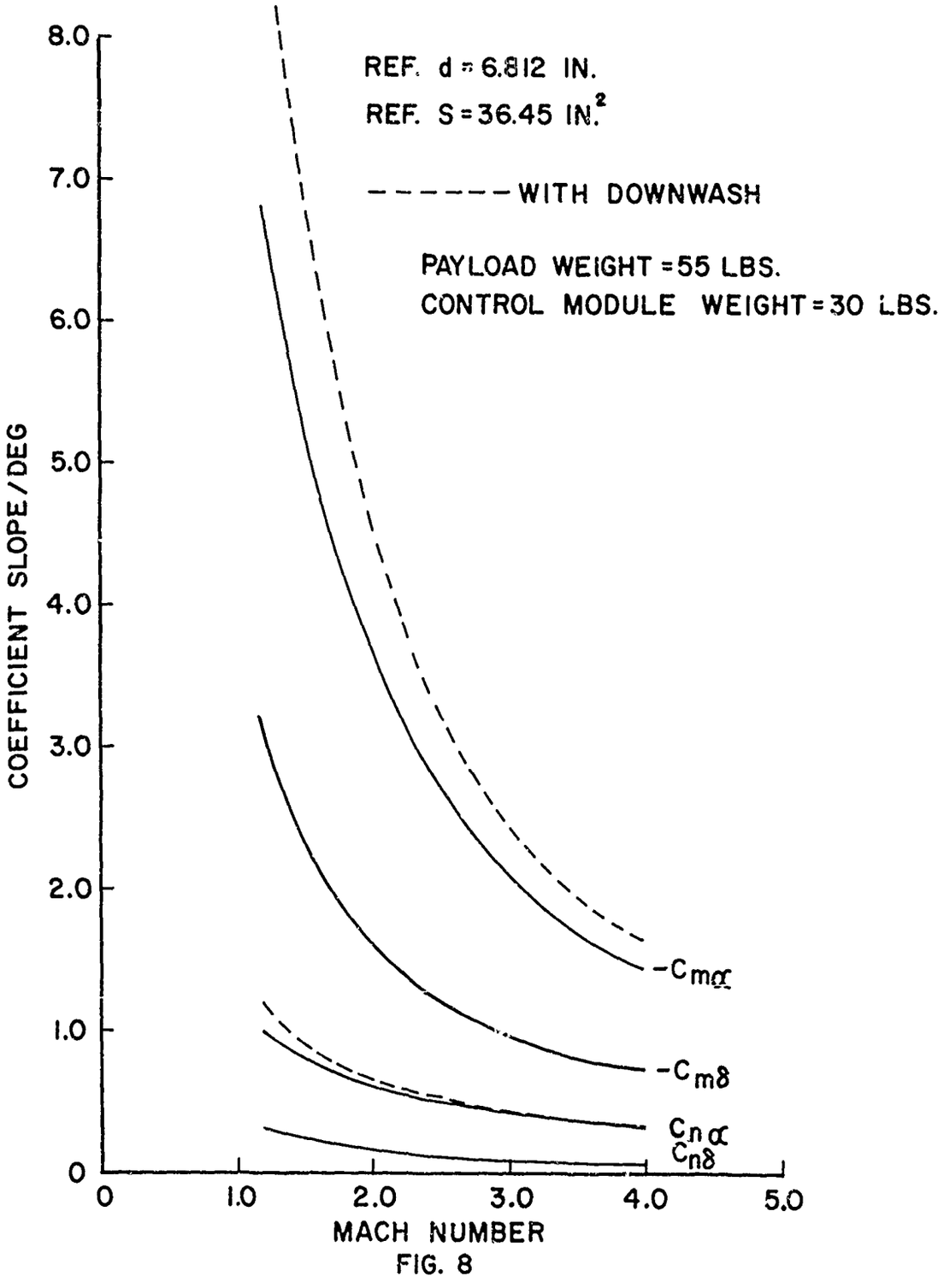

FIG. 8

TRIM ANGLE OF ATTACK
NIKE-APACHE WITH CPCS-1ST STG. BOOST
CONTROL DEFLECTION, $\delta_1 = 10$ DEG.

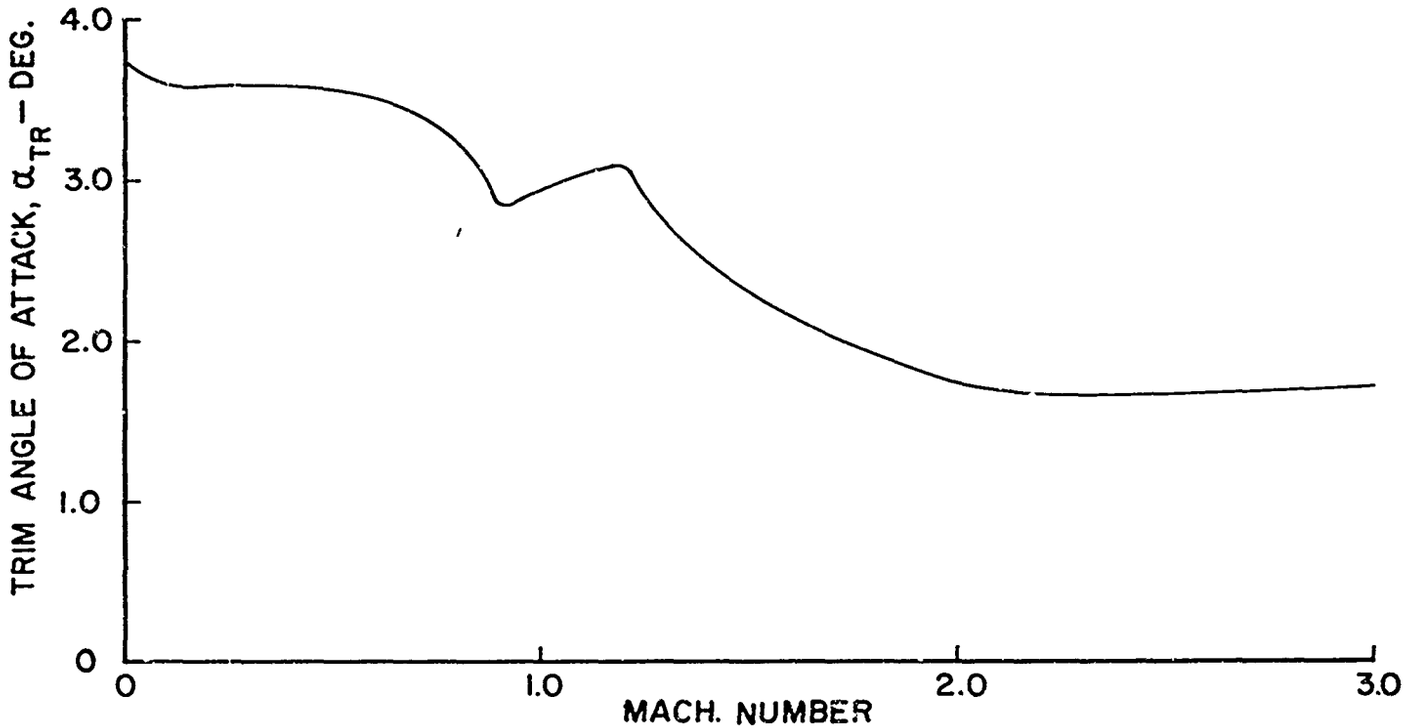

FIG. 9

SEA LEVEL
TURNING RATE FOR NIKE-APACHE
2ND STAGE WITH CPCS

LAUNCH QE=87 DEG.
QUAD. ANT.-PAYLOAD WT.=50 LBS.

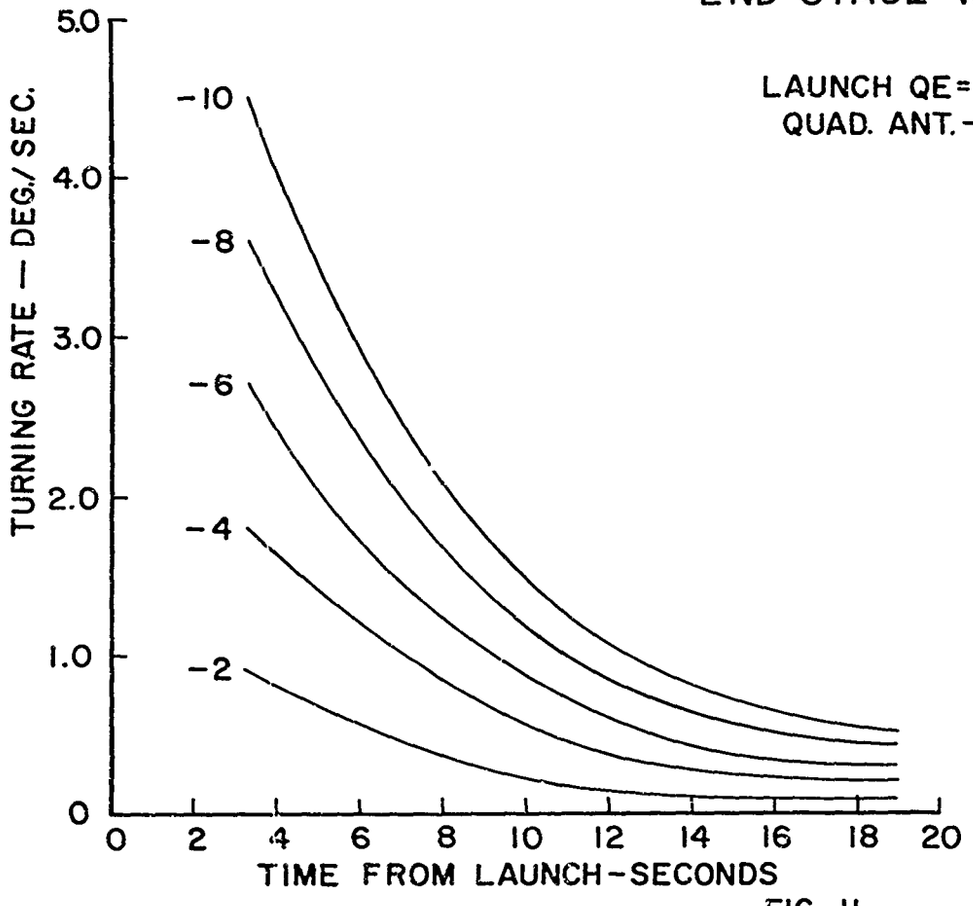

FIG. 11

SEA LEVEL
LOAD FACTOR, n, FOR
NIKE-APACHE 2ND STAGE
WITH CPCS

LAUNCH QE = 87 DEG.
QUAD. ANT. - PAYLOAD WT. = 50 LBS

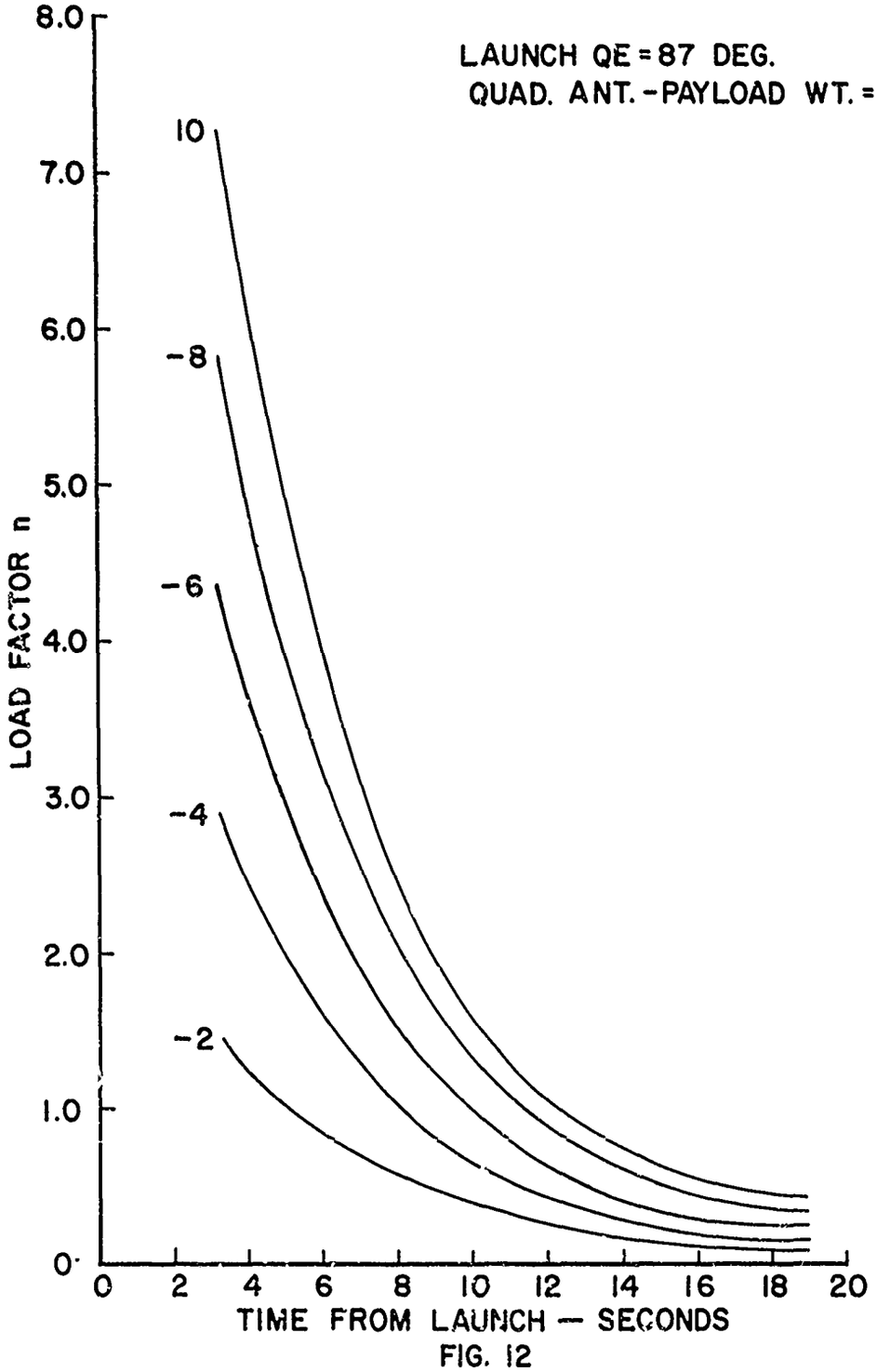

FIG. 12

4000 FT. LAUNCH
TRIM ANGLE OF ATTACK, α_{TR}, FOR NIKE-APACHE 2ND STAGE WITH CPCS

LAUNCH QE=87 DEG.
QUAD. ANT.-PAYLOAD WT.=50 LBS.

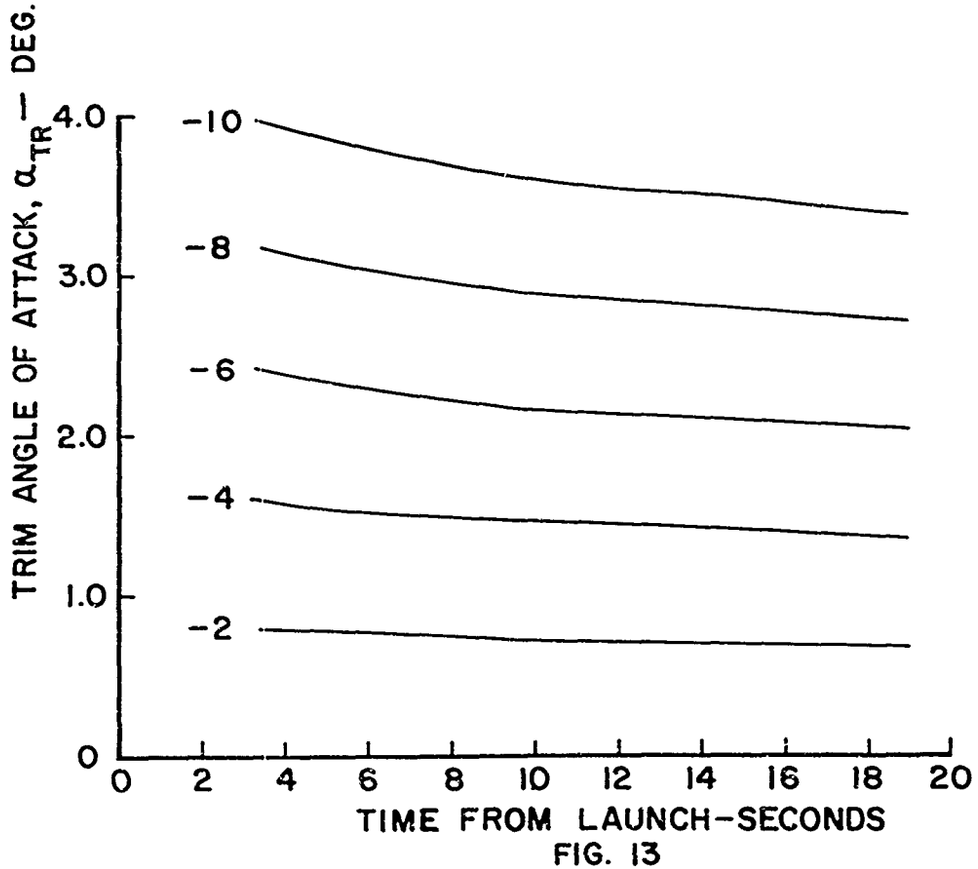

FIG. 13

4000 FT. LAUNCH
TURNING RATE FOR NIKE-APACHE STAGE WITH CPCS

LAUNCH QE = 87 DEG
QUAD. ANT.-PAYLOAD WT.= 50 LBS.

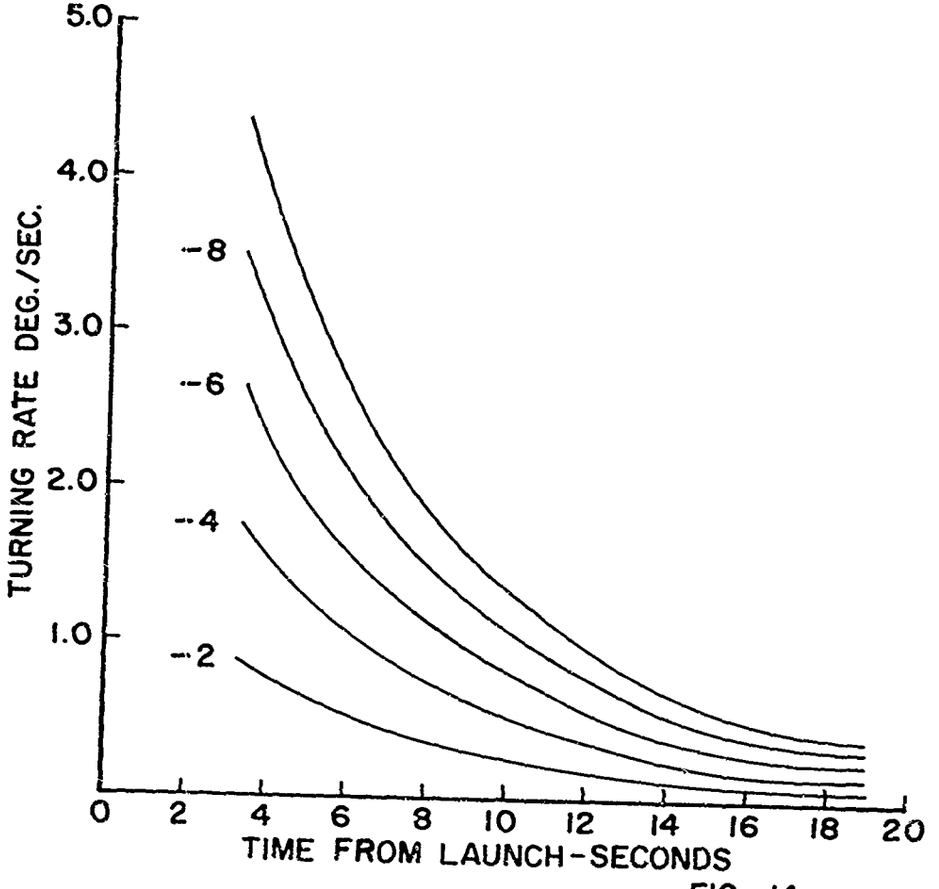

FIG. 14

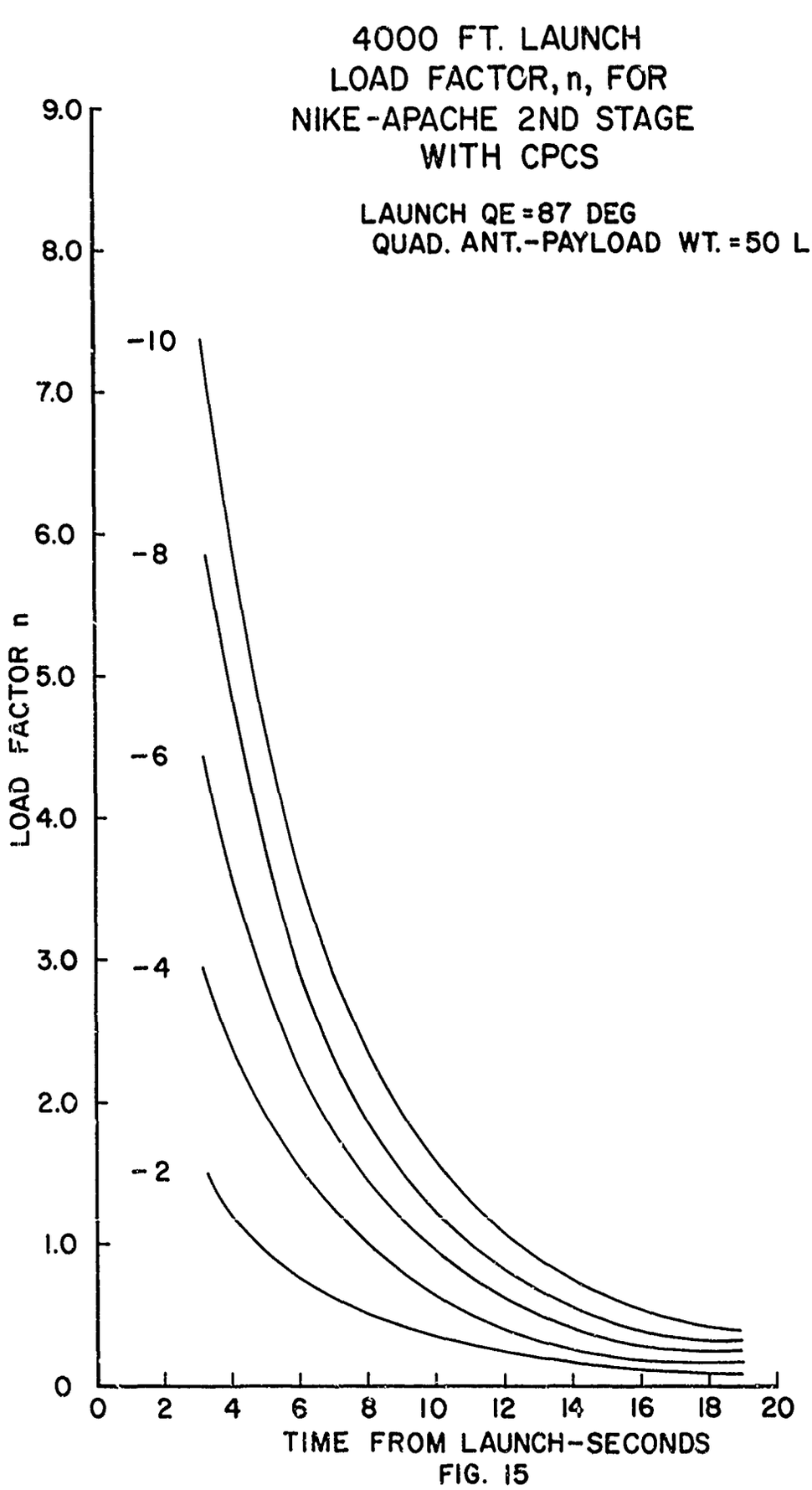
4000 FT. LAUNCH
LOAD FACTOR, n, FOR
NIKE-APACHE 2ND STAGE
WITH CPCS
LAUNCH QE = 87 DEG
QUAD. ANT.-PAYLOAD WT. = 50 LBS.
LOAD FACTOR n
9.0
8.0
7.0
6.0
5.0
4.0
3.0
2.0
1.0
0
-10
-8
-6
-4
-2
0 2 4 6 8 10 12 14 16 18 20
TIME FROM LAUNCH-SECONDS

FIG. 15

SEA LEVEL
TRIM ANGLE OF ATTACK, α_{TR},
FOR NIKE-APACHE 2ND STAGE
WITH CPCS

LAUNCH QE.=87 DEG.
QUAD. ANT.-PAYLOAD WT.=50 LBS.

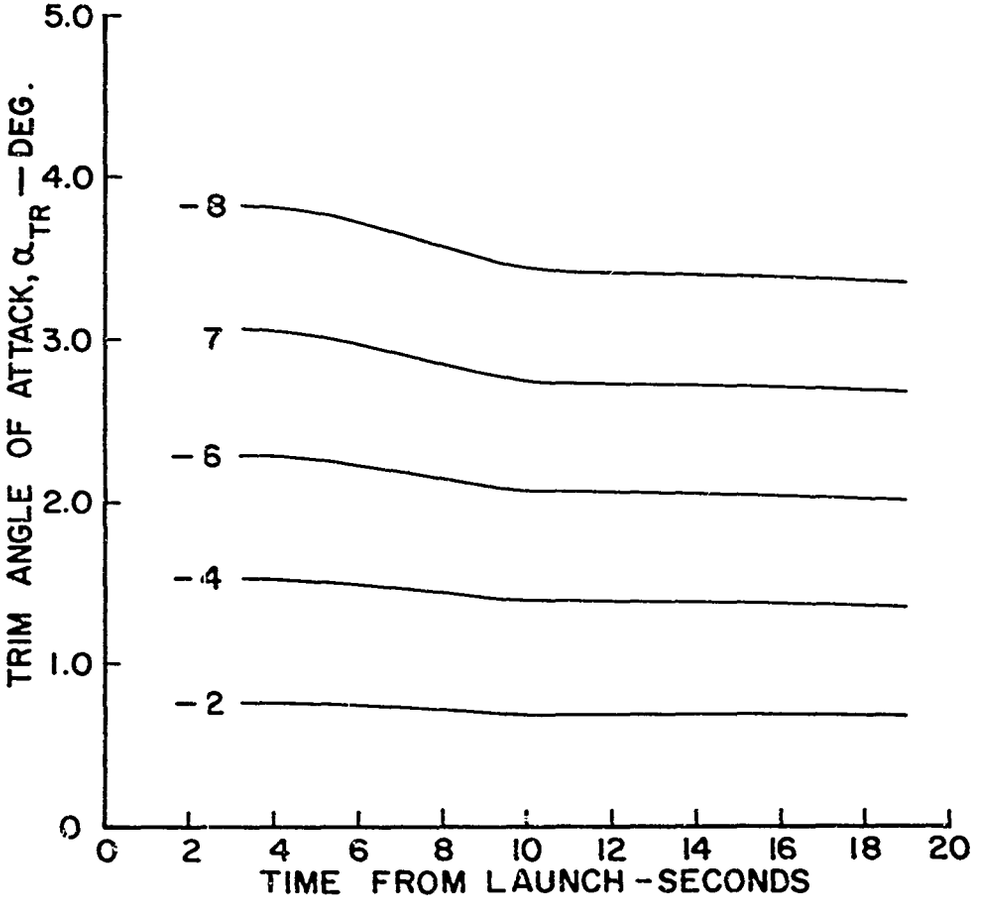

FIG. 16

PITCH FREQUENCY
NIKE-APACHE 2ND STAGE WITH CPCS

PAYLOAD=70 LBS.
I_y=1 55 SLUG-FT.^{2}

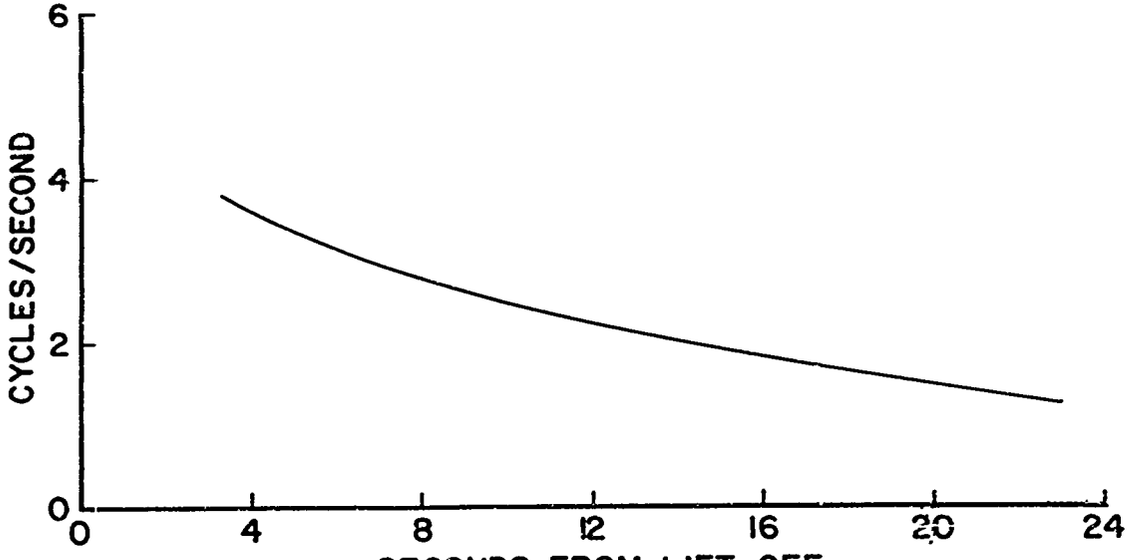

FIG. 17

Tubing. These sections are joined at the fin hub assembly by 2 peripheral screw joints. Each joint has 2 rows of 10-32 screws-each row containing 16 screws. Preliminary calculations show that flight moments in this area are large, necessitating this type of joint. Bending and vibration tests are being performed on a prototype unit to verify the results of the stress analysis. Also, functional tests have been conducted on the blowout diaphragm. These tests were in two series, separation by cold gas pressure at PSL and separation on APACHE and CAJUN static firings at Thiokol Chemical Corporation at Elkton, Maryland. These tests verified proper function of the diaphragm without significant tip-off effects.

CONTROL LOOP DESIGN COMPONENT SELECTION AND OPERATION

The CPCS functional diagram (Fig. 18) can be described as follows:

The system power is turned on. The bias programmers are set and the attitude reference is uncaged prior to launch. The roll axis control is operating through the boost phase. Upon booster separation, a delay timer is initiated by a booster pull plug, and after the prescribed delay time this timer will initiate the pitch and yaw control.

The control sequence is described for the pitch-roll control only, as the yaw-roll control is similar to the pitch-roll control. The gyros sense the rocket attitude, the pitch gimbal pot provides the electrical signal (voltage) which is proportional to the rocket pitch error angle, and the roll gimbal pot provides the electrical signal (voltage) which is proportional to the rocket roll error angle. These pitch and roll error signals pass through their individual compensation networks, where the signals are processed according to the loop response requirements.

The compensated pitch error voltage is compared with the programmed pitch bias voltage, and if the two voltages are equal, that is, the rocket pitch angle is the same as the bias programmed angle, then the difference signal will be zero and the rocket pitch angle will stay at this angle unless disturbed. Should the difference signal not be zero it will enter the pitch

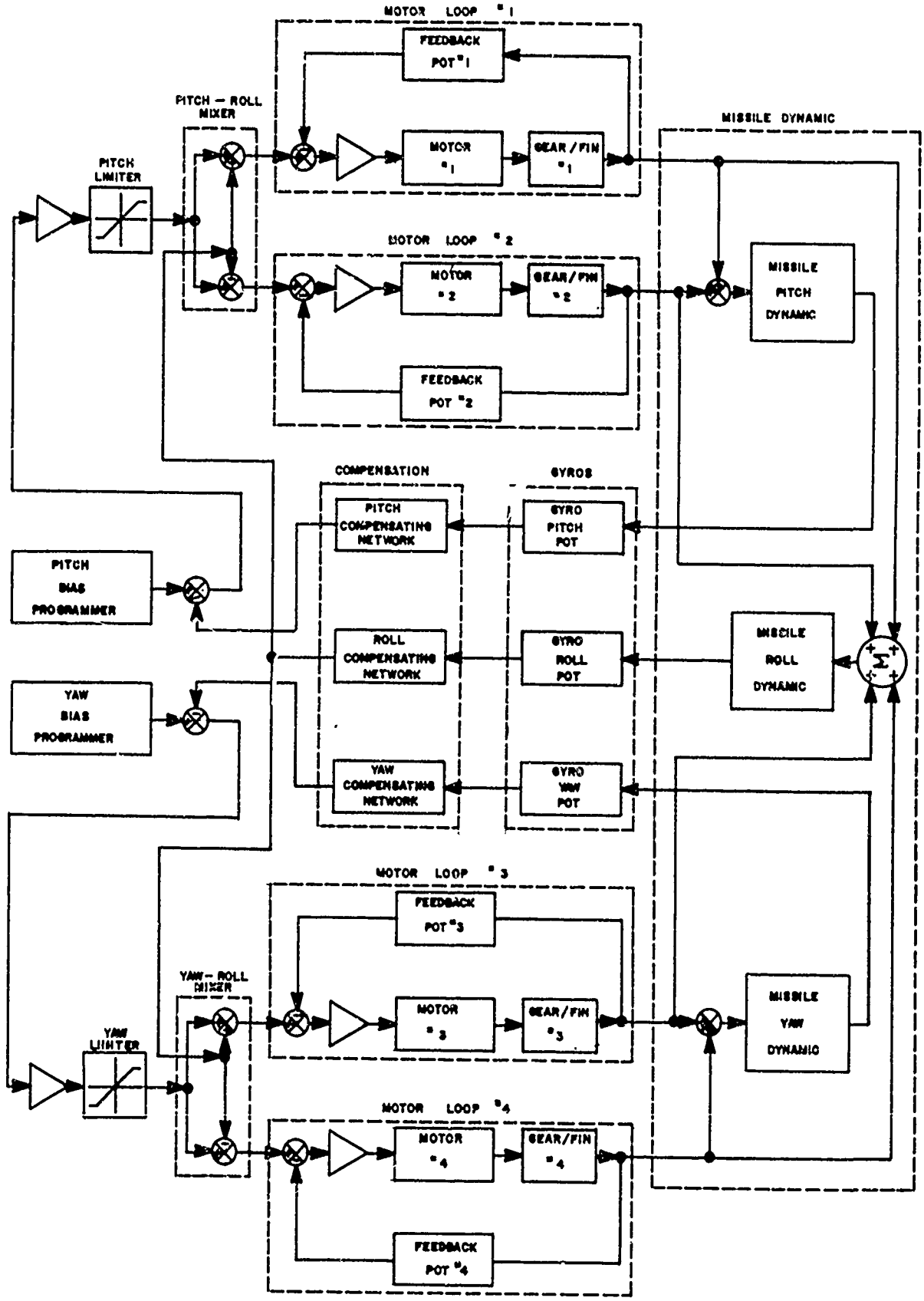

CPCS BLOCK DIAGRAM
FIG. 18
181

limiter through an amplifier, which is used for comparing the compensated pitch voltage and the pitch bias voltage, and for gain adjustment. The pitch limiter is a saturating device which limits the control signal and the fin displacement, to a certain range. When the actuating signal is saturated at this level, the fin stays at its maximum position (assuming roll error is zero).

The limited pitch signal and the compensated roll signal are then mixed, the mixed sum drives motor loop #1, and the mixed difference drives motor loop #2. These two fins are called the pitch-roll fins, and are oppositely located.

Fins number three and four control the rocket yaw and roll, thus providing the three-axis attitude control.

Choice of Main Power Drive Elements

Each motor loop consists of one mixer, summing the compensated pitch (or yaw), the compensated roll, and the fin position feedback signals. This mixed signal drives several stages of preamplifiers which in turn drive a power bridge amplifier; each power bridge amplifier consists of four power transistors connected as two complimentary amplifiers and are driven opposite. This provides the amplification and the polarity reversing of the drive power by using only one battery.

The Globe Model 1004108-8 D.C. permanent magnet motor with the Model 102A199 planetary gear is used to drive the control surface. The motor has a no-load speed of 10,000 rpm, a rated torque of 3.7 oz. in., and a stall torque of 27 oz. in. The gear has a ratio of 211 and the nominal efficiency of 81%.

Servo Loop Analysis and Compensation

The minor loop, i.e. the motor loop, with proper loop gain has a frequency response nearly flat up to 10 Hz, and + 3 db at 15 Hz. The resonant frequency is 30 Hz so the design bandwidth is wide enough to cover the rocket response, which has a natural frequency of 5 Hz in pitch and yaw. Thus no compensation is required for the motor loop.

The main loop, however, is a time variable system, because of the varying aerodynamic coefficients. The pitch (or yaw) transfer function of the rocket is a third order type 1 system, with two infinite zeros. The roll transfer function of the rocket is a second order type 1 system with two infinite zeros. The following table lists the average gain and Pole-zero pattern for various regions of the flight.

TABLE II

Region	Time (seconds)	Pitch or Yaw			Roll	
		Gain	Zero	Pole	Gain	Pole
1	3.5	441	-0.67	$0,-2 \pm J34$	4,980	0,-0.98
2	7	280	-0.45	$0,-1.5 \pm J28$	2,900	0,-0.66
3	11	160	-0.27	$0,-1 \pm J22$	1,700	0,-0.44
4	15	100	-0.16	$0,-0.7 \pm J17$	950	0,-0.28
5	20	50	-0.10	$0,-0.5 \pm J13$	400	0,-0.16

A lead network is used for the roll compensations, and two identical notch networks are used for the pitch and yaw compensation.

Choice of Attitude Reference Gyros

The attitude reference gyro package used for the CPCS Module is the PRYS (Pitch, Roll, and Yaw Sensor) Unit manufactured by the Whittaker Corporation. This unit uses dual two-degree-of-freedom gyros which are positioned in a tandem arrangement along the longitudinal axis of a single cylindrical housing. The two gyros can be mechanically constrained for mutually orthogonal gimbal alignment with respect to a fixed frame reference, through the insertion of an electrical command. The gyro can be uncaged and placed into attitude reference operation with the application of a momentary electrical command.

Some specifications are-Spin-Up Time, 5 Minutes; Power requirement, Single phase 115 volts, rms, 400 Hz, 15VA (a DC to AC inverter, Arnold Magnetics Model SKB-28-115-400-40, is used for this power inversion); caging, three amperes at 28 vdc; uncaging, 2 amperes at 28 vdc; pick-off potentiometer; rational freedom, 60 degrees, 3-axis; weight 5 pounds; size 3.53 in. diam. x 7.63 inches long.

Bias Circuits, Main Power Supplies

In order to reduce the gyro drift, the gyros should be uncaged as close to launch time as possible, but the final launcher setting for firing is not the attitude required for second stage pointing. (for wind compensation or for dog-leg maneuver). Because the gyros considered have only one caged position, this requires a remote bias setting device, so the actual final pointing angle can be set (or stored) remotely just prior to launch.

A series of binary coded resistors, i.e. R, 2R, ----nR, is connected in series, and each resistor can be shorted by a latching relay. A series of seven resistors are used here, assuming the increment is 0.25 degrees for R. Then a maximum bias of 37.5 degrees can be stored. One separated relay is used for the polarity selection.

A thermol battery is used to drive the four servo motors and to ignite the second stage. This battery is a "one-shot" device activated by initiation of a pyrotechnic charge, and delivers a high current for a short period. Activation is accomplished remotely just prior to launch. A separate silver-zinc battery pack is used to provide all other CPCS power.

FLIGHT SAFETY CONSIDERATIONS

The incorporation of control provides relief to the flight safety officer in that trajectories are more precise and impact dispersion is reduced, but a new safety problem, the consequence of a control system malfunction, is introduced.

The most damaging malfunction is a pitch or yaw "open loop" condition where a pair of control fins is deflected to a "hard-over" position. The result is a turning maneuver confined to one control plane, with the turning rate

decreasing as depicted in Figure 11 and 14, until the control fins become ineffective. The total change in flight path direction is dependent on two factors: (1) the time of malfunction occurrence, and (2) the maximum fin deflection permitted by the mechanical limits in the system.

If the control system is employed in a course-correction mode only, the required maneuverability is relatively small, in that flight path changes of the order of only 2 - 3 degrees are required (with respect to gyro co-ordinates.) In this instance fin deflections can be mechanically limited to small values, but the consequence of the malfunction is sufficient to cause severe dispersion of the second stage impact, worse than encountered with a ballistic vehicle, so that a means for denial of second stage ignition may be required. The unignited second stage impact dispersion will also be worse than with a ballistic vehicle, but not large enough to require further safety action.

If the control system is employed for trajectory "shaping," much larger maneuvers are required, so a large fin deflection is required. Here again it is necessary to have second stage ignition denial capability, and the unignited second stage impact dispersion will become dangerously large. It may be necessary to take additional action to shut down the control system as soon as the malfunction is detected, permitting the control fins to return to a neutral position.

For either control system application it is thus essential that an on-board malfunction detection and abort system, or a suitable ground tracking system and ground-to-vehicle command link, be incorporated.

If an "on-board" system could be devised, it would be preferred over the ground-based system since its reaction would be rapid and automatic. It could also be less expensive, on a unit cost basis. But such a system is difficult to achieve, especially one which functions reliably and independently of the control system, i.e., without utilizing elements of the system.

The latter approach, a ground-based tracking system which provides real-time vehicle trajectory data, plus a radio command link for transmitting abort and related instructions, has been selected for the CPCS-equipped Nike-Apache vehicles. Since the CPCS will function during the first 23 seconds of flight,

radar tracking systems have been ruled out for this application, since previous experience has shown that adequate radar track of the Nike-Apache is not generally established prior to 10 seconds after launch. A Doppler Velocity and Position (DOVAP) system operating in a single-station, real-time mode, has been selected because it can provide reliable tracking data from launch. Provisions for command transmissions are incorporated by means of sub-carrier channels on the "up-leg" R-F carrier frequency in the DOVAP system. A DOVAP transponder, modified to include command sub-carrier demodulators, is mounted in the aft end of the CPCS module.

Since the CPCS corrects not only the vehicle heading, but also the flight path direction, the safety officer can observe the DOVAP-derived trajectory on a plotting board and take safety action if the flight path passes outside a predetermined acceptable envelope The safety action will be a second stage ignition denial command, and possibly a CPCS shutdown command. CPCS shutdown can be accomplished by cutting servo motor battery power. Since the control fins are designed to maintain their centers-of-pressure always aft of the hinge line regardless of angle-of-attack or Mach Number, aerodynamic torque will drive the fins to a neutral position, although there is some time delay involved.

Although the Nike-Apache CPCS system will utilize the flight safety system just briefly described, there are other options available, depending upon the application. The other possible approaches are too varied to discuss here, but it is important to point out that flight safety considerations must receive adequate attention in a control system design of this type, as it must be with any other.

CONCLUSIONS

A description of the operation and performance of a control system for the Nike-Apache sounding rocket vehicle has been presented, and its capabilitities for reducing trajectory dispersion and/or "shaping" trajectories have been pointed out. The addition of this capability without compromising vehicle performance

significantly is possibly the most attractive feature of the CPCS. The adaptability of the concept to other multi-stage vehicles of similar design is also attractive.

The CPCS must, however, be considered as a halting, first step in sounding rocket vehicle control. Although a major effort was made to achieve low cost and simplicity of design, undoubtedly the application of additional effort in these areas can result in significant improvements. The availability of an effective, reliable, and economical control system for sounding rocket vehicles will do much to broaden their usefulness.

APPENDIX I PRYS ATTITUDE REFERENCE

It is the purpose here to define, for simulation applications, the "pitch", "roll" and "yaw" angles that the system measures, and the associated coordinate transformations which relate gyro attitudes to rocket attitude.

The theoretical principle applied states that the direction of the spin axis of a properly gimballed gyro remains fixed in space. In the particular case there are two gyros, with spin axes orthogonal, each isolated from external angular motion by two gimbals. Although the gyros are called "two-degree-of-freedom gyros", there is a third degree of rotational freedom about the spin axis of each gyro. The two spin axes define a space fixed coordinate system whose axes we shall define as:

$\vec{r}_2$ along the forward spin axis,

$\vec{r}_3$ along the aft spin axis,

and $\vec{r}_1$ along $\vec{r}_2 \times \vec{r}_3$

(See Fig. 4)

PRYS - NIKE APACHE RELATIVE ORIENTATION

The instrument is assumed to be mounted in the Nike Apache airframe, oriented FWD along the rocket FWD longitudinal axis, with the forward gyro spin axis in the horizontal plane and with the aft gyro spin axis in the vertical plane, each spin axis being orthogonal to the rocket longitudinal axis.

ANGLE DEFINITION AND SENSING

Gyro gimbal angles, measured by pickoffs, are "yaw", "pitch" and "roll". For sign convention consistent with simulation practice at PSL, we chose to take positive angles analogous to firing azimuth (positive clockwise from North), firing elevation (positive up from horizontal), and roll (positive clockwise, looking forward). Hence, "yaw" will be positive right (clockwise), "pitch" will be positive up and "roll" will be positive clockwise, looking forward.

COORDINATE TRANSFORMATIONS

Rocket attitude relative to the spin axes is obtained in terms of the relative angles between gimbals. The easiest method to obtain transformation is to associate with each gimbal ring a coordinate system, oriented with two axes in the plane of the gimbal, with one axis made collinear with the gimbal axis. Further, the choice of coordinate axes is made so that one axis of each coordinate system is collinear with its corresponding member in the next.

The transformation from gyro to rocket is the result of two rotations. For the forward gyro, we consider first a positive roll angle and then a positive yaw; the transformation from inner gimbal to outer gimbal amounts to a positive* rotation thru a roll angle, ϕ_1, while the transformation from outer gimbal to rocket is a negative* rotation thru the measured yaw angle, y_a. Thus, the transformation matrix is

$$\left[F\right] = \left[R_z(-y_a)\right] \left[R_x(\phi_1)\right],$$

$$\left[F\right] = \begin{pmatrix} \cos y_a & -\sin y_a & 0 \\ \sin y_a & \cos y_a & 0 \\ 0 & 0 & 1 \end{pmatrix} \cdot \begin{pmatrix} 1 & 0 & 0 \\ 0 & \cos \phi_1 & \sin \phi_1 \\ 0 & -\sin \phi_1 & \cos \phi_1 \end{pmatrix}.$$

For the aft gyro, the transformation from inner gimbal to outer gimbal is a positive rotation thru the measured roll angle, ϕ_a, while the transformation from outer gimbal to rocket is a negative rotation thru the measured pitch angle, p_a:

$$\left[A\right] = \left[R_y(-p_a)\right] \left[R_x(\phi_a)\right],$$

$$A = \begin{pmatrix} \cos p_a & 0 & \sin p_a \\ 0 & 1 & 0 \\ -\sin p_a & 0 & \cos p_a \end{pmatrix} \cdot \begin{pmatrix} 1 & 0 & 0 \\ 0 & \cos \phi_a & \sin \phi_a \\ 0 & -\sin \phi_a & \cos \phi_a \end{pmatrix}.$$

* A positive rotation is one in which the axes are rotated in the positive right hand sense.

SPIN-AXIS-RELATIVE ROCKET ATTITUDE

We consider a unit vector along the spin axis of the forward gyro; its components in the body system are:

$$\left(\vec{SF}\right)^b = \left[F\right]\begin{pmatrix}0\\1\\0\end{pmatrix}^r$$

$$\left(\vec{SF}\right)^b = \begin{pmatrix}-\sin y_a \cdot \cos \phi_1\\ \cos y_a \cdot \cos \phi_1\\ -\sin \phi_1\end{pmatrix}.$$

The unit vector along the aft gyro spin axis has its components in the body system given by

$$\left(\vec{SA}\right)^b = \left[A\right]\begin{pmatrix}0\\0\\1\end{pmatrix}^r$$

$$\left(\vec{SA}\right)^b = \begin{pmatrix}\sin p_a \cdot \cos \phi_a\\ \sin \phi_a\\ \cos p_a \cdot \cos \phi_a\end{pmatrix}.$$

Since the rocket attitude is computed in simulation and the orientations of gyro spin axes are assumed to be determined by launcher setting and known drift characteristics, the pitch, yaw and roll angles will be determined by:

$\left[a_{ij}\right]$, the transformation from ground reference system to rocket airframe,

and $\left(\vec{SF}\right)^L$, $\left(\vec{SA}\right)^L$, the spin axes components in the ground reference system.

Hence,

$$\left(\vec{SF}\right)^b = \left[a_{ij}\right] \left(\vec{SF}\right)^L ,$$

$$\left(\vec{SA}\right)^b = \left[a_{ij}\right] \left(\vec{SA}\right)^L ,$$

where

$$\left(\vec{SA}\right)^L = \begin{pmatrix}-\sin El \cdot \sin FAZ\\ -\sin El \cdot \cos FAZ\\ \cos El\end{pmatrix},$$

$$\left(\vec{SF}\right)^L = \begin{pmatrix} -\cos FAZ \\ \sin FAZ \\ 0 \end{pmatrix}$$

assuming no drift. Then the yaw, pitch, and roll angles are given by

$$y_a = -\text{Arc tan } \frac{-a_{11} \cos FAZ + a_{12} \sin FAZ}{-a_{21} \cos FAZ + a_{22} \sin FAZ} ,$$

$$p_a = \text{Arc tan } \frac{-a_{11} \sin El \sin FAZ - a_{12} \sin El \cos FAZ + a_{13} \cos El}{-a_{31} \sin El \sin FAZ - a_{32} \sin El \cos FAZ + a_{33} \cos El} ,$$

and $\emptyset_A = \text{Arc sin } (-a_{21} \sin El \sin FAZ - a_{22} \sin El \cos FAZ + a_{23} \cos El)$.

DESIRED ATTITUDE (CONTROL ATTITUDE)

In the CPCS application the goal is to drive, by means of aerodynamic control, the NikeApache to some desired attitude. The CPCS acts as a nulling device so that

$$\varepsilon_1 = ya - y_d \longrightarrow 0$$
$$\varepsilon_2 = pa - p_d \longrightarrow 0$$
$$\varepsilon_3 = \emptyset_a - \emptyset_d \longrightarrow 0$$

where ε_1, ε_2, ε_3 are attitude error signals, and y_d, p_d, $\emptyset_d$ are the desired yaw, pitch and roll angles.

The formulas of the preceding section can be used to calculate y_d, p_d and $\emptyset_d$, given any desired attitude in the ground reference system. However, in the CPCS application $\emptyset_d$ will be zero, which simplifies finding y_d and p_d.

Suppose that one had the desired attitude pointing angles (elevation and azimuth) in the ground reference system. Then the transformation to the rocket system is

$$\left(\vec{DA}\right)^b = \begin{pmatrix} \cos El & 0 & \sin El \\ 0 & 1 & 0 \\ -\sin El & 0 & \cos El \end{pmatrix} \begin{pmatrix} \sin FAZ \cos FAZ & 0 \\ -\cos FAZ \sin FAZ & 0 \\ 0 & 0 & 1 \end{pmatrix} \begin{pmatrix} \cos el \sin az \\ \cos el \cos az \\ \sin el \end{pmatrix}$$

With the roll angle set to zero, p_d and y_d are

$$p_d = \text{arc sin } (DA_3)$$

$$y_d = -\text{arc sin } (DA_2).$$

Figure a shows the geometry of the desired attitude.

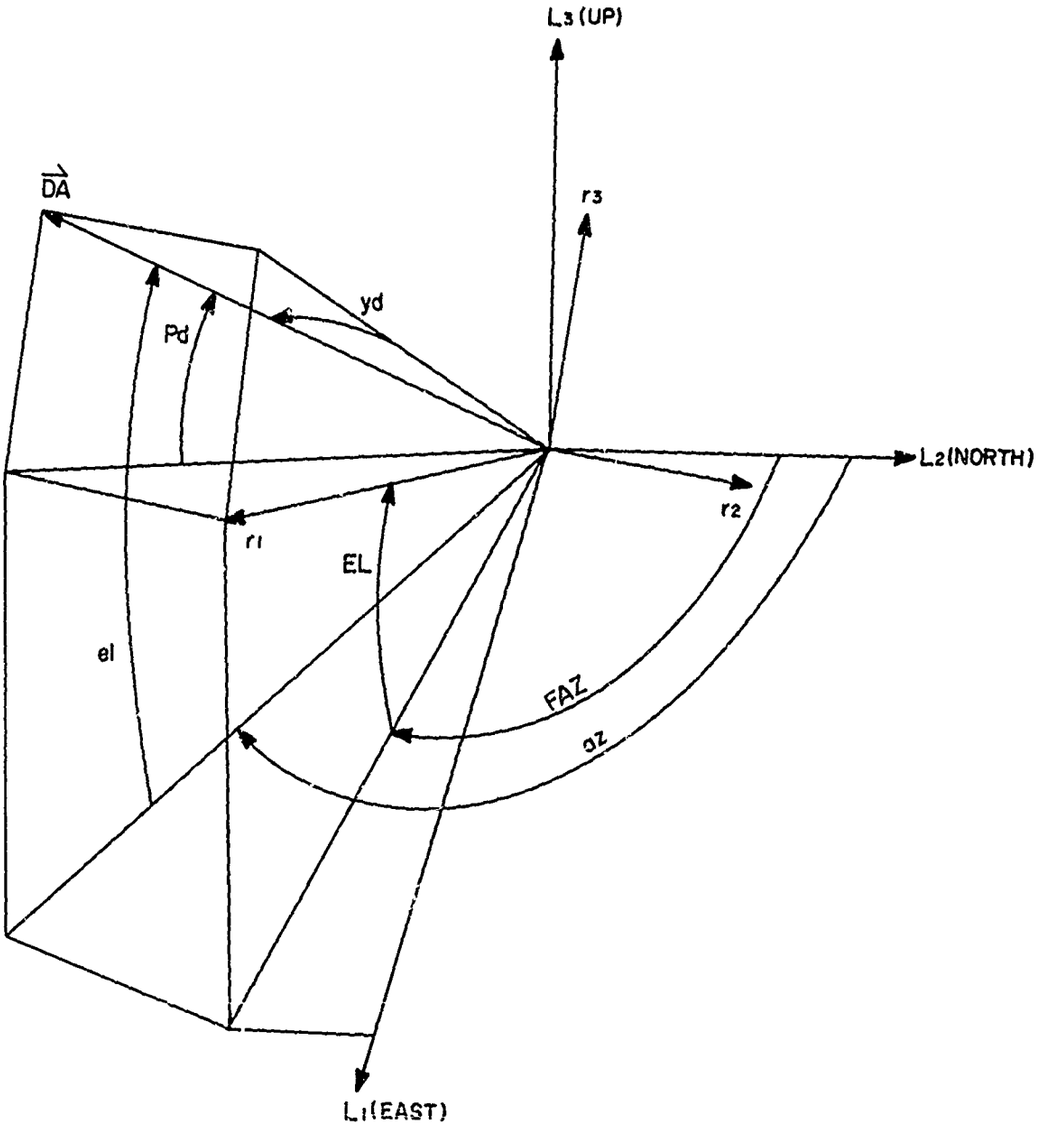

FIG. a

BLANK PAGE

RESULTS OF UNGUIDED ROCKET IMPACT PREDICTIONS AT WSMR

Gordon L. Dunaway
Atmospheric Sciences Office
White Sands Missile Range, New Mexico

ABSTRACT

An analysis is made of the impact dispersion of several types of unguided rockets fired at WSMR. The rockets considered are: Athena, Aerobee 150, Nike-Apache, Nike-Cajun, and Arcas.

Data is presented in graphical and tabular form.

INTRODUCTION

The Meteorological Support Division of the Atmospheric Sciences Office at White Sands Missile Range, New Mexico is responsible for providing "impact prediction" support for all unguided rockets fired on the range which are considered wind-sensitive enough that a compensation for the wind dispersion is necessary to insure safe, on-range impacts.

This report presents an analysis of impact prediction miss distances for several types of unguided rockets fired at WSMR. The analysis includes dispersions from: Athena, Aerobee 150, Nike-Cajun, Nike-Apache, and Arcas.

DISCUSSION

The "impact prediction" support provided by the Meteorological Support Division consists of the collection, reduction, and prediction of atmospheric parameters; and the application of these data to the theoretical trajectories of the given rockets in such a manner that the theoretical deviations in the rocket trajectories due to these parameters can be determined and compensated for in the form of appropriate launcher settings or new predicted impact locations.

Of the atmospheric arameters affecting the rocket trajectories, the wind is the most variable and has the most pronounced effect. Therefore, it is considered essential that wind measurements be taken as near firing time as possible-especially in the lower levels where its effect on the rocket trajectories is greatest-so that effective trajectory and impact predictions can be made.

The Ballistics Meteorologist in charge of the impact prediction support makes a careful analysis of the feasibility of obtaining the desired results based on the current meteorological situation and the characteristics of the rocket in question. Recommendations based on this analysis are given to the Missile Flight Surveillance Office and the Test Conductor to be used in determining if it is feasible to fire with the given conditions. Such aspects as total correction, variability, wind shear, surface wind gustiness and velocity, previous results under similar conditions, and the

probability of better or worse conditions in the near future are among the factors considered in this analysis.

In addition to the dispersion in rocket trajectories caused by atmospheric parameters, such factors as fin and thrust misalignments, variations in weights and motor performance, stability margins, and errors in launcher settings also make substantial contributions.

For this analysis, the actual dispersion-regardless of cause-is presented. Only cases where obvious rocket malfunctions occurred were excluded. The actual impacts were surveyed impacts where available; elsewhere radar or sound ranging impacts were used. For all cases, the "predicted impacts" were the predictions given to the Test Conductor prior to the firings, along with recommended launcher settings.

The Athena is a multi-stage rocket fired from Green River, Utah to WSMR. The first two stages are unguided and trajectory predictions and launcher settings are provided by the Meteorological Support Division.

A system composed of an IBM 7044 Computer at the Range Control Center building at WSMR, receiving wind data from the launch site at Green River via commercial data lines is used for these predictions. A program furnished by the research group of the Atmospheric Sciences Office reduces the wind data and applies it to a 5-D trajectory model and selects launcher settings by iterative techniques.

There are two basic types of Athena firings: the high-angle Athena, which has a nominal second stage impact some 445 miles from the launcher, near the west center of the missile range; and the low-angle Athena which has a nominal second stage impact 355 miles from the launcher, near Datil, New Mexico.

It was found that for the high-angle Athena, the average second stage miss distance for 49 cases was 15.2 miles with a standard error of estimate of 17.7 miles. The average north-south miss distance was 7.9 miles north with a standard error of estimate of 12.7 miles and the average east-west miss was 0.3 miles west with a standard error of estimate of 12.3 miles. For the low-angle Athena, the average miss distance for 18 cases was 9.9 miles with a standard error of estimate of 13.0 miles. The average north-south miss was 6.1 miles north with a standard error of estimate of 10.1 miles and the average east-west miss was 2.5 miles east with a standard error of estimate of 8.2 miles.

The Aerobee 150 is a single stage, boosted rocket which is launched from Launch Complex 35 on the south end of the missile range. The nominal impact area is some 50 miles from the launcher, near the center of the range. The ballistic wind technique is used to determine launcher settings for these firings.

It was found that for 94 cases, the average impact miss distance of the Aerobee 150 was 10.4 miles with a standard

error of estimate of 11.8 miles. The average north-south miss distance was 2.5 miles south with a standard error of estimate of 9.5 miles. The average east-west miss was 1.1 miles west with a standard error of estimate of 7.0 miles.

The Nike-Apache is a two-stage rocket composed of a Nike-M-5 booster and an Apache second stage. The thrust from the booster pushes the rocket to some 40 to 50 thousand feet where the second stage ignites and sends the rocket to a peak altitude of from 600,000 feet to 800,000 feet, carrying payloads of from 55 to 90 pounds. Nike-Apaches are fired from Launch Complex 33 on the south end of the range and from Sulf Site near the northwest-corner of the range.

It was found that for 98 cases, the average miss distance of the Nike-Apache was 13.2 miles with a standard error of estimate of 14.9 miles. The average north-south miss was 1.2 miles south with a standard error of estimate of 9.7 miles and the average east-west miss was 2.5 miles west with a standard error of estimate of 11.3 miles.

The Nike-Cajun is similar to the Nike-Apache but has a lower performance second-stage. It carries payloads of 55 to 110 pounds to altitudes of from 425,000 to 620,000 feet.

It was found that for 22 cases, the average miss distance of the Nike-Cajun was 6.7 miles with a standard error of estimate of 7.9miles. The average north-south miss was 0.3 miles south with a standard error of estimate of 6.4 miles and the average east-west miss was 1.2 miles east

with a standard error of estimate of 4.7 miles.

The Arcas is a meteorological rocket launched from a tube with a gas generator for a booster. It carries a 9 pound payload to approximately 250,000 feet.

It was found that for 73 cases, the average miss distance for the Arcas was 6.3 miles with a standard error of estimate of 7.2 miles. The average north-south miss was 0.9 miles south with a standard error of estimate of 5.5 miles and the average east-west miss was 1.4 miles west with a standard error of estimate of 4.7 miles.

CONCLUSIONS

Although the impact miss distances for the various types of unguided rockets fired at WSMR may seem large at a first glance, it should be noted that many of the rockets have been fired on the missile range with a very high percentage of successful results.

Since the dispersion depends on the overall rocket performance, as well as the wind, one must be careful in the selection of a vehicle where extreme accuracy is necessary.

The advent of more accurate wind measurements and forecasts, along with better design and quality control on the individual rockets, will result in more accurate trajectory and impact predictions.

ROCKET TYPE	NUMBER OF CASES	AVERAGE N-S MISS DIST MILES	S.S.E. OF N-S MISS DIST MILES	AVERAGE E-W MISS DIST MILES	S.S.E. OF E-W MISS DIST MILES	AVERAGE TOTAL MISS DIST MILES	S.S.E. OF TOTAL MISS DIST MILES
ATHENA (HIGH-ANGLE)	49	7.94 N	12.69	0.30 W	12.27	15.15	17.66
ATHENA (LOW-ANGLE)	18	6.11 N	10.11	2.54 E	8.24	9.89	13.02
AEROBEE-150	94	2.50 S	9.46	1.11 W	7.00	10.38	11.77
NIKE-APACHE	98	1.16 S	9.72	2.46 W	11.27	13.19	14.89
NIKE-CAJUN	22	0.25 S	6.35	1.21 E	4.66	6.74	7.88
ARCAS	73	0.87 S	5.49	1.39 W	4.69	6.32	7.22

TABLE I. SUMMARY OF IMPACT MISS DISTANCES FOR INDICATED UNGUIDED ROCKETS FIRED AT WSMR.

NOTE: ALL DISTANCES ARE STATUTE MILES.

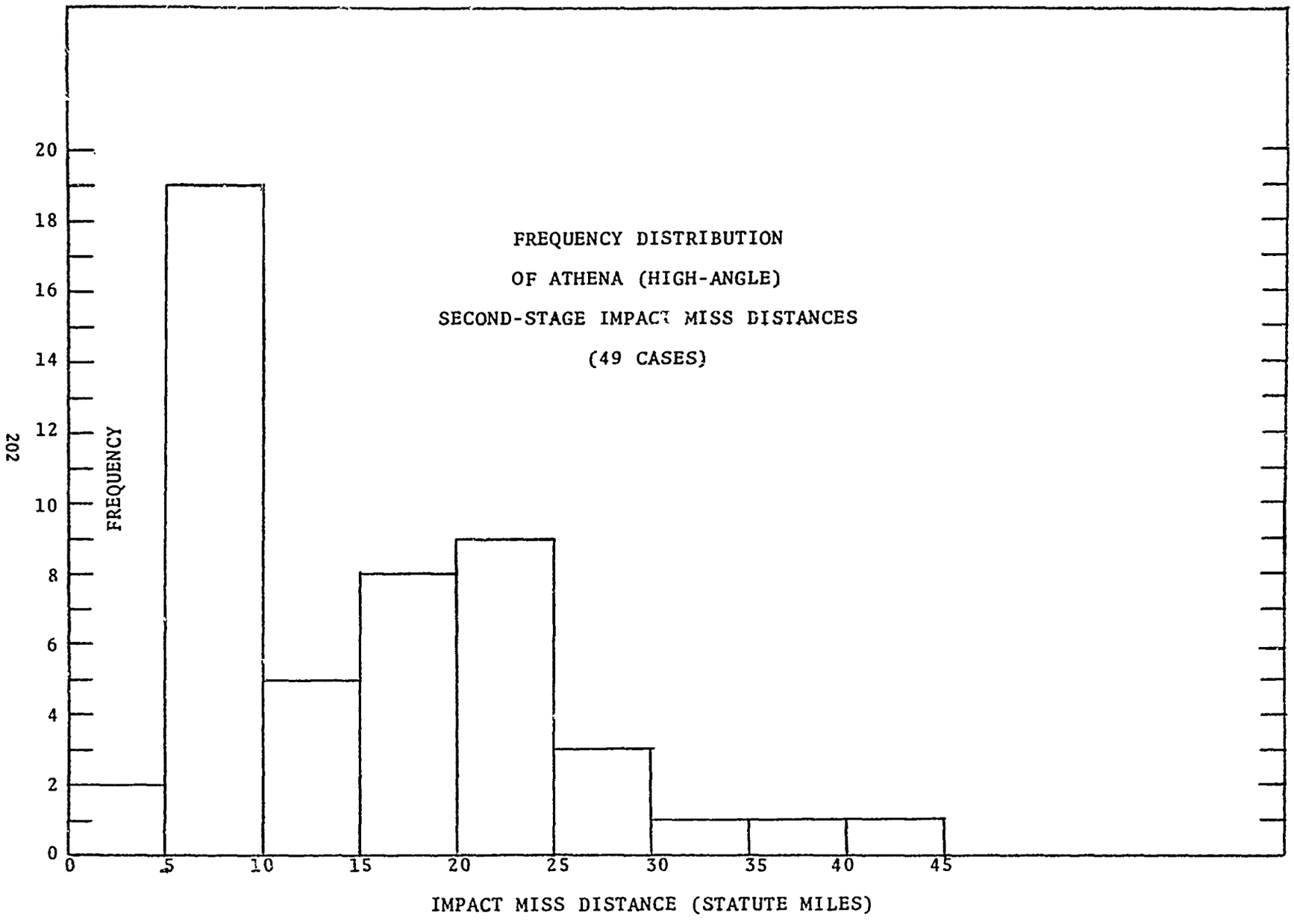
FREQUENCY DISTRIBUTION
OF ATHENA (HIGH-ANGLE)
SECOND-STAGE IMPACT MISS DISTANCES
(49 CASES)
FREQUENCY
202
0
2
4
6
8
10
12
14
16
18
20
0
5
10
15
20
25
30
35
40
45
IMPACT MISS DISTANCE (STATUTE MILES)

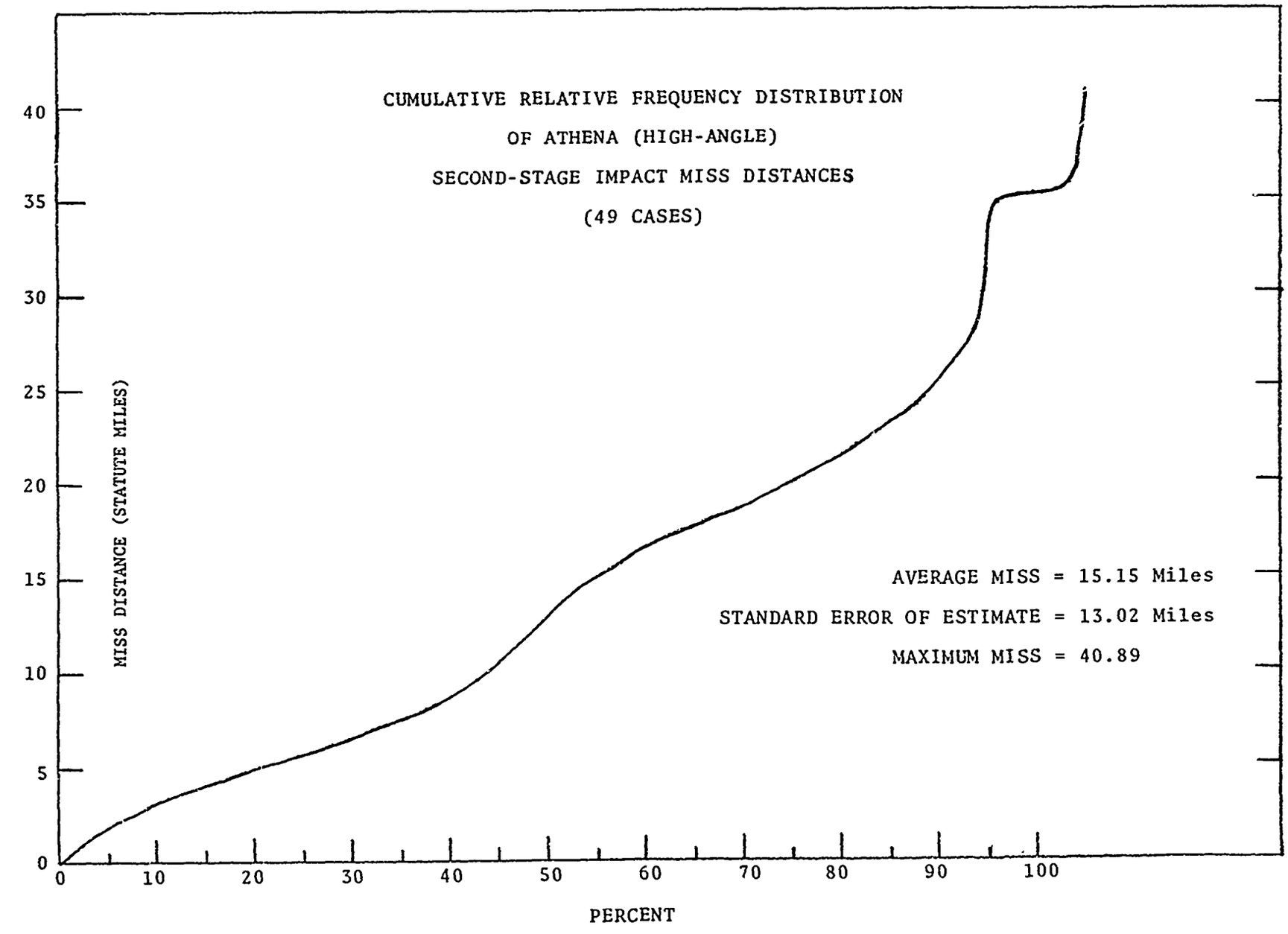
CUMULATIVE RELATIVE FREQUENCY DISTRIBUTION
OF ATHENA (HIGH-ANGLE)
SECOND-STAGE IMPACT MISS DISTANCES
(49 CASES)
MISS DISTANCE (STATUTE MILES)
0
5
10
15
20
25
30
35
40
0
10
20
30
40
50
60
70
80
90
100
PERCENT
AVERAGE MISS = 15.15 Miles
STANDARD ERROR OF ESTIMATE = 13.02 Miles
MAXIMUM MISS = 40.89

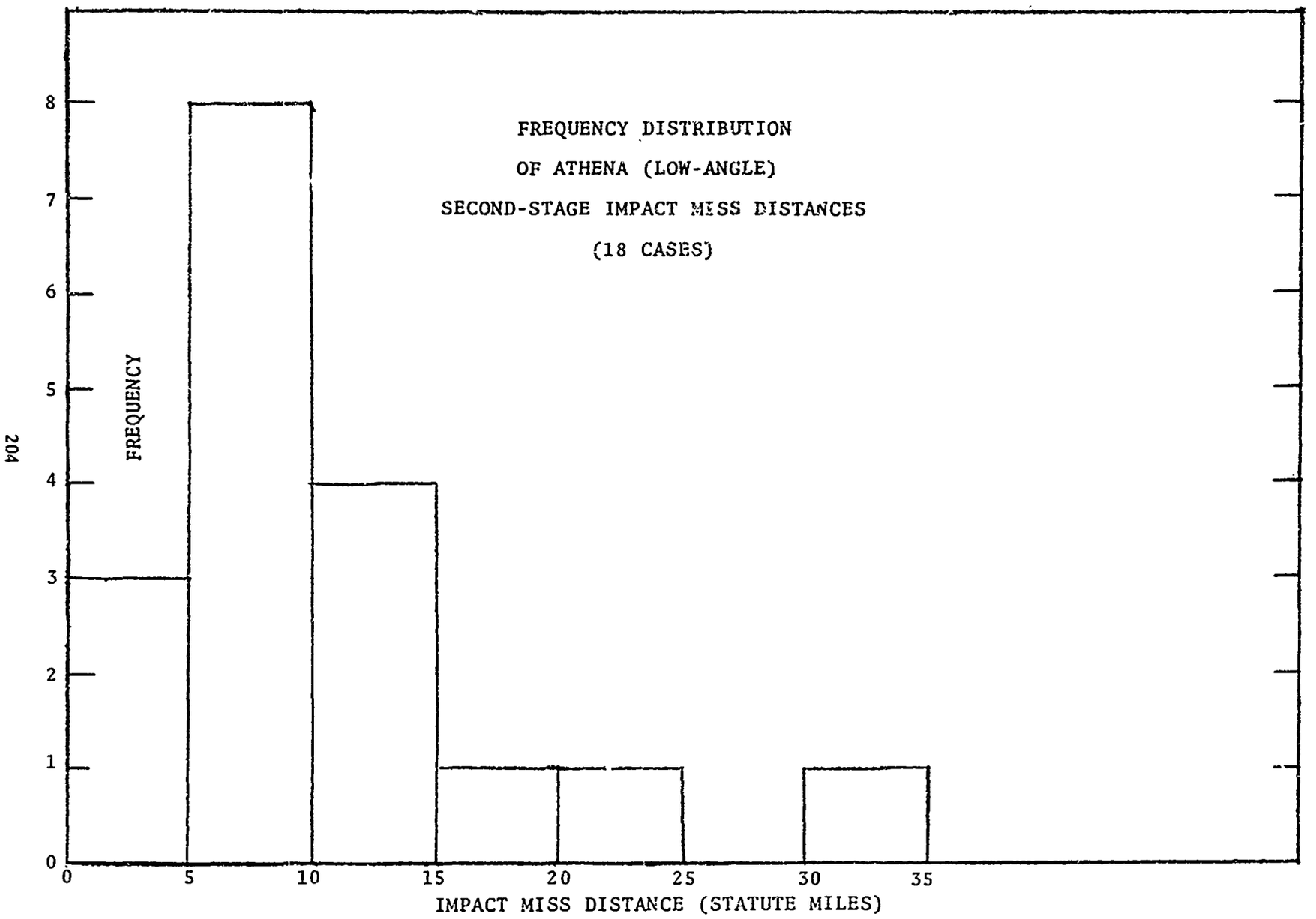
FREQUENCY DISTRIBUTION
OF ATHENA (LOW-ANGLE)
SECOND-STAGE IMPACT MISS DISTANCES
(18 CASES)
FREQUENCY
0
1
2
3
4
5
6
7
8
0
5
10
15
20
25
30
35
IMPACT MISS DISTANCE (STATUTE MILES)

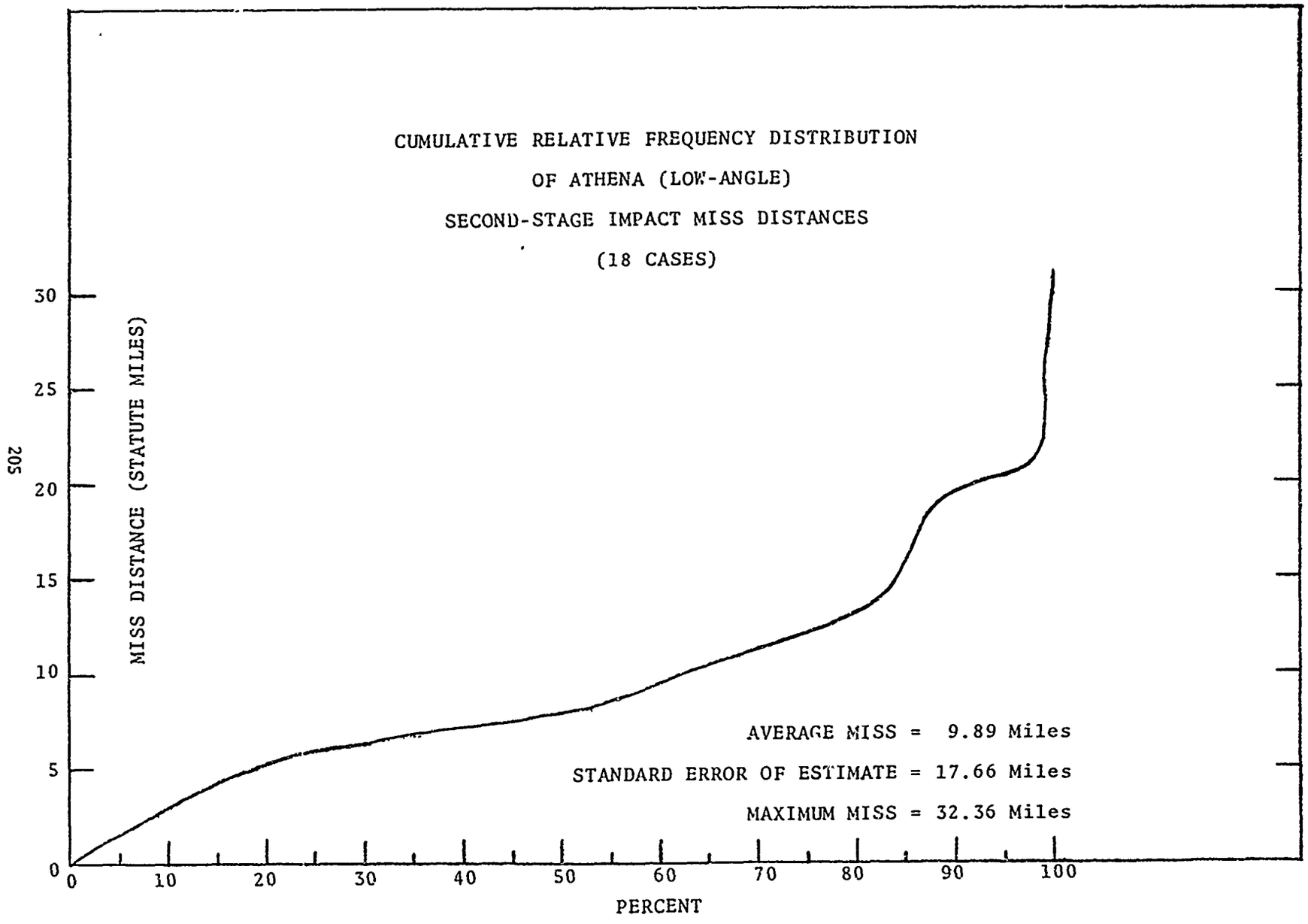
CUMULATIVE RELATIVE FREQUENCY DISTRIBUTION
OF ATHENA (LOW-ANGLE)
SECOND-STAGE IMPACT MISS DISTANCES
(18 CASES)
MISS DISTANCE (STATUTE MILES)
0
5
10
15
20
25
30
0
10
20
30
40
50
60
70
80
90
100
PERCENT
AVERAGE MISS = 9.89 Miles
STANDARD ERROR OF ESTIMATE = 17.66 Miles
MAXIMUM MISS = 32.36 Miles

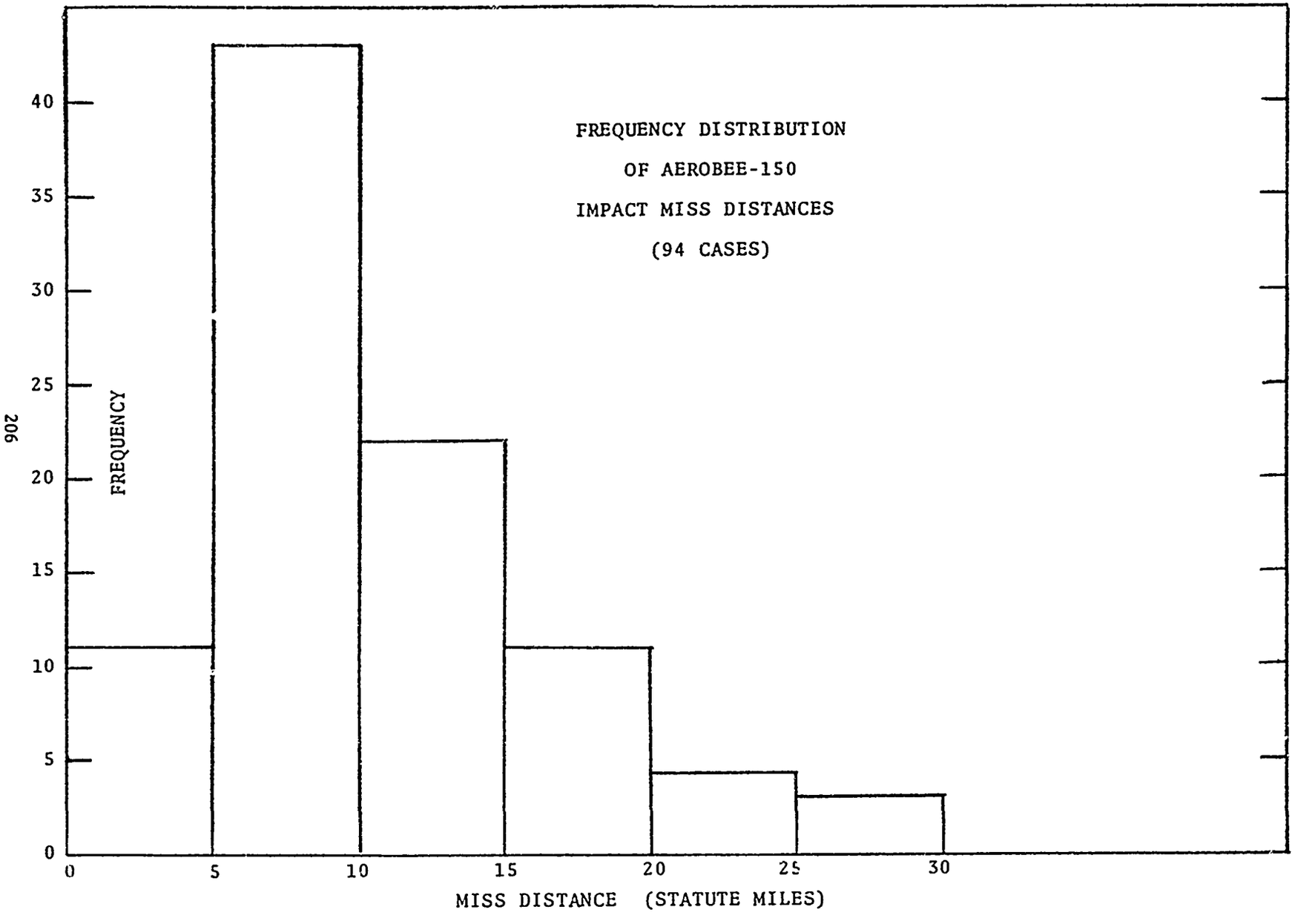
FREQUENCY DISTRIBUTION
OF AEROBEE-150
IMPACT MISS DISTANCES
(94 CASES)
FREQUENCY
206
0
5
10
15
20
25
30
35
40
0
5
10
15
20
25
30
MISS DISTANCE (STATUTE MILES)

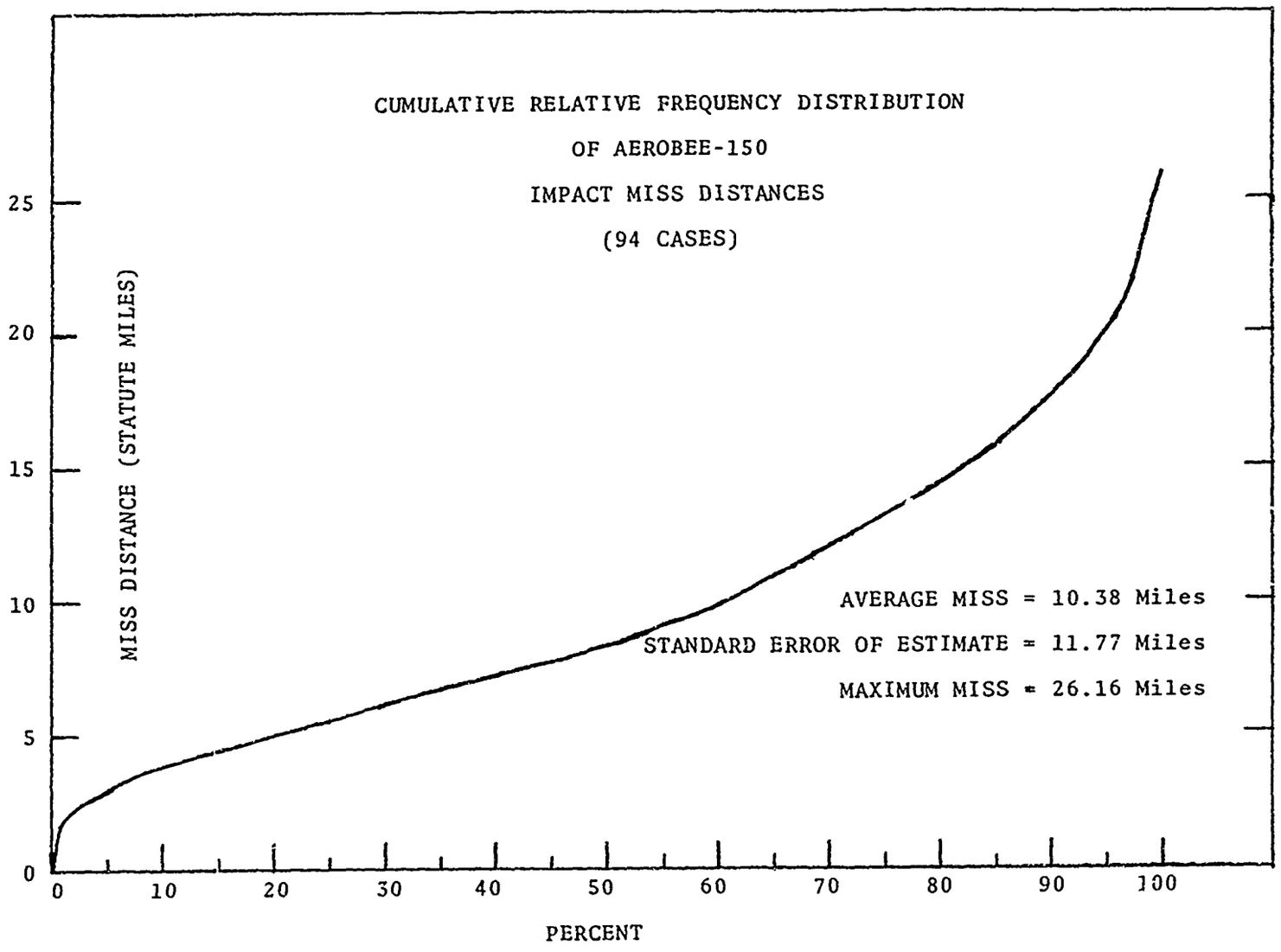
CUMULATIVE RELATIVE FREQUENCY DISTRIBUTION
OF AEROBEE-150
IMPACT MISS DISTANCES
(94 CASES)
MISS DISTANCE (STATUTE MILES)
25
20
15
10
5
0
0
10
20
30
40
50
60
70
80
90
100
PERCENT
AVERAGE MISS = 10.38 Miles
STANDARD ERROR OF ESTIMATE = 11.77 Miles
MAXIMUM MISS = 26.16 Miles

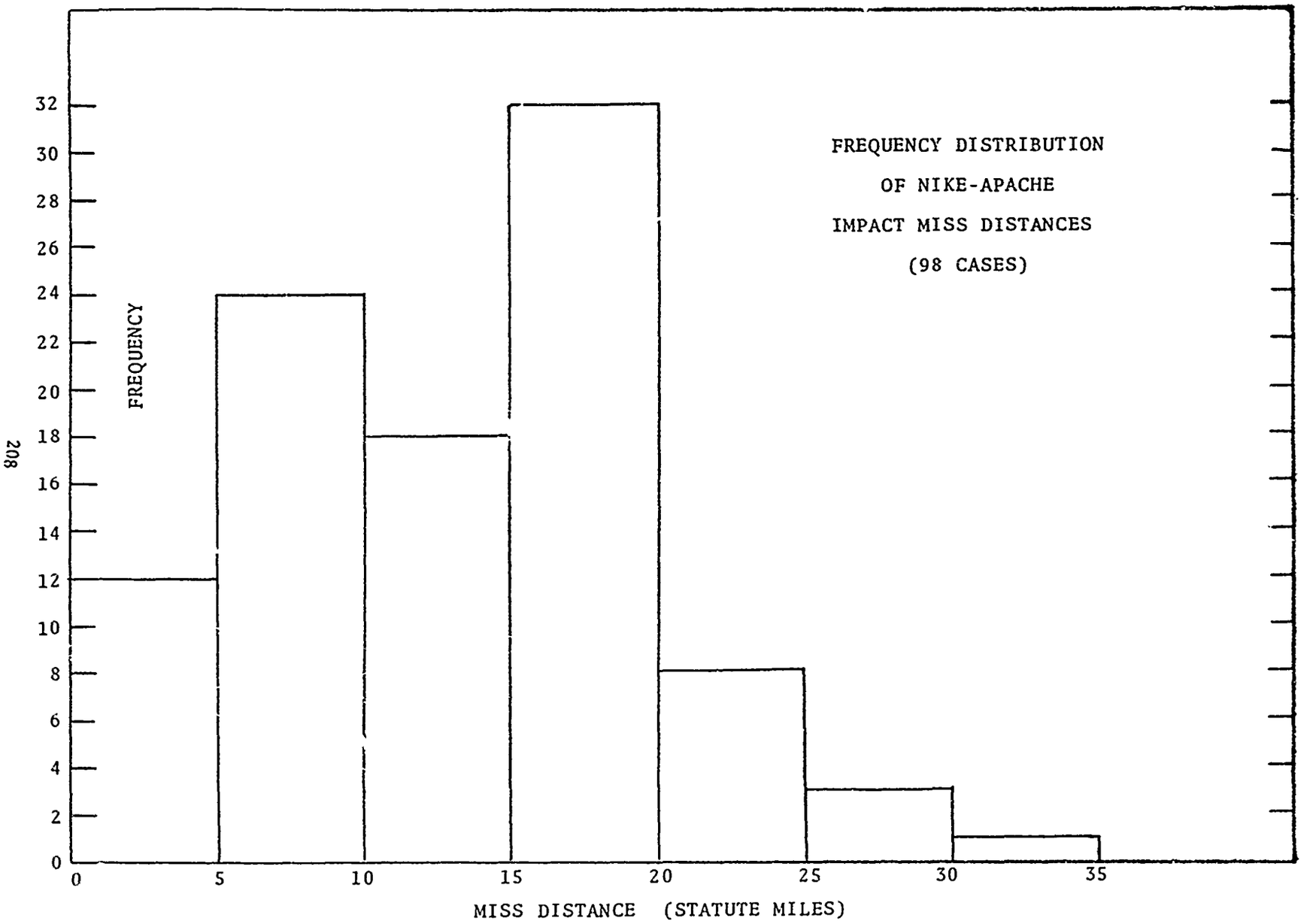
FREQUENCY DISTRIBUTION
OF NIKE-APACHE
IMPACT MISS DISTANCES
(98 CASES)
FREQUENCY
0
2
4
6
8
10
12
14
16
18
20
22
24
26
28
30
32
0
5
10
15
20
25
30
35
MISS DISTANCE (STATUTE MILES)

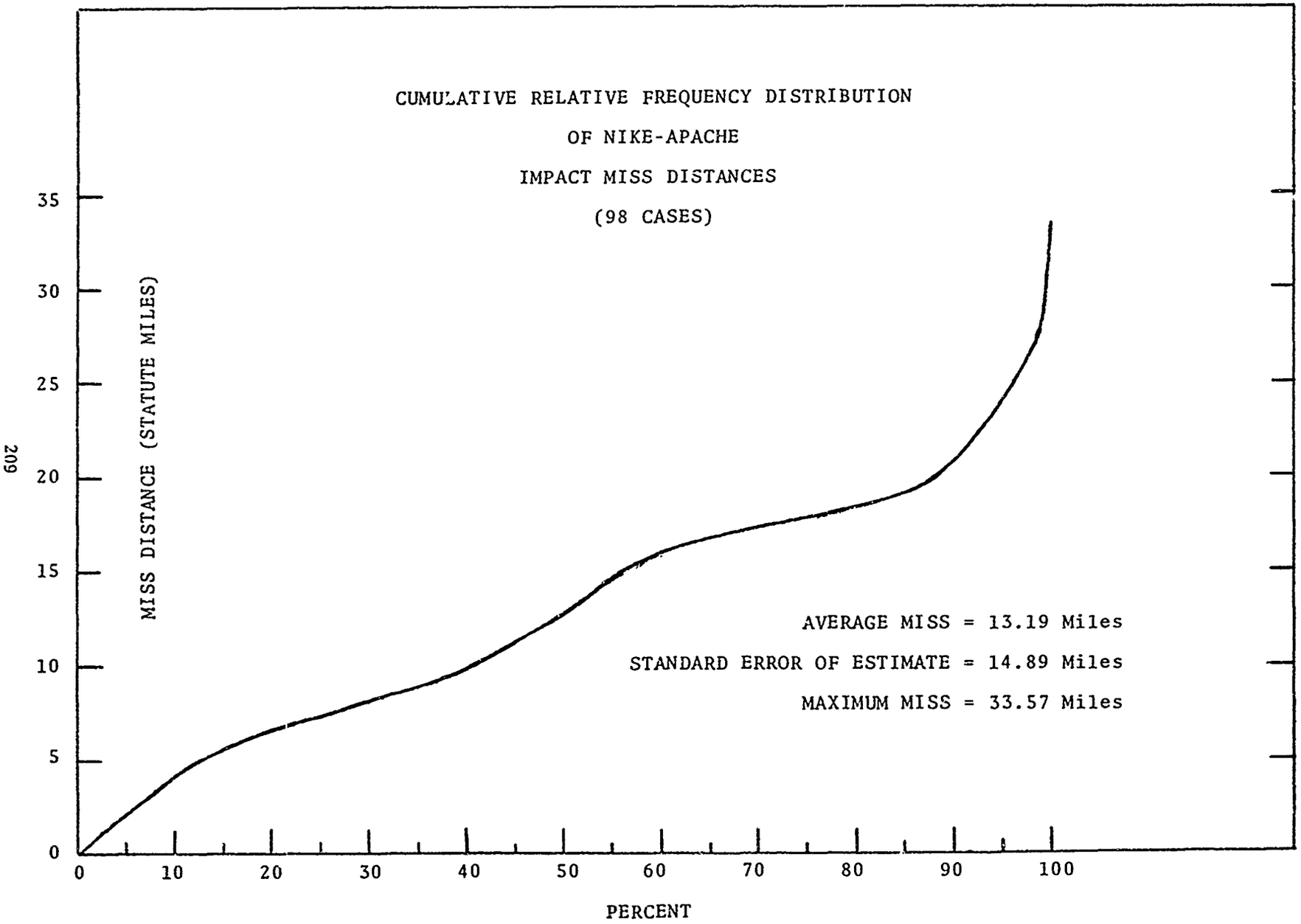
CUMULATIVE RELATIVE FREQUENCY DISTRIBUTION
OF NIKE-APACHE
IMPACT MISS DISTANCES
(98 CASES)
MISS DISTANCE (STATUTE MILES)
35
30
25
20
15
10
5
0
0
10
20
30
40
50
60
70
80
90
100
PERCENT
AVERAGE MISS = 13.19 Miles
STANDARD ERROR OF ESTIMATE = 14.89 Miles
MAXIMUM MISS = 33.57 Miles

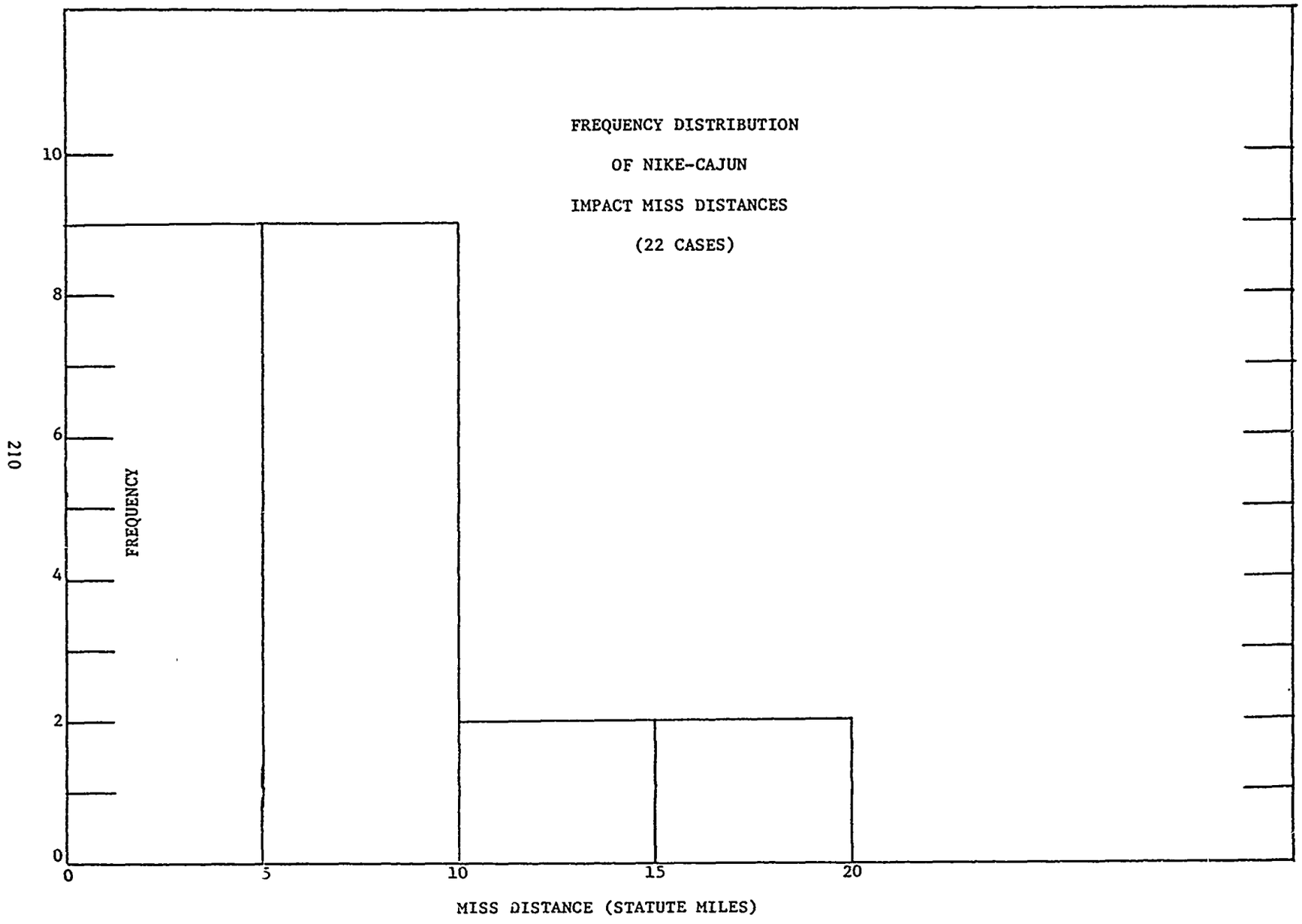
FREQUENCY DISTRIBUTION
OF NIKE-CAJUN
IMPACT MISS DISTANCES
(22 CASES)
FREQUENCY
0
2
4
6
8
10
0
5
10
15
20
MISS DISTANCE (STATUTE MILES)

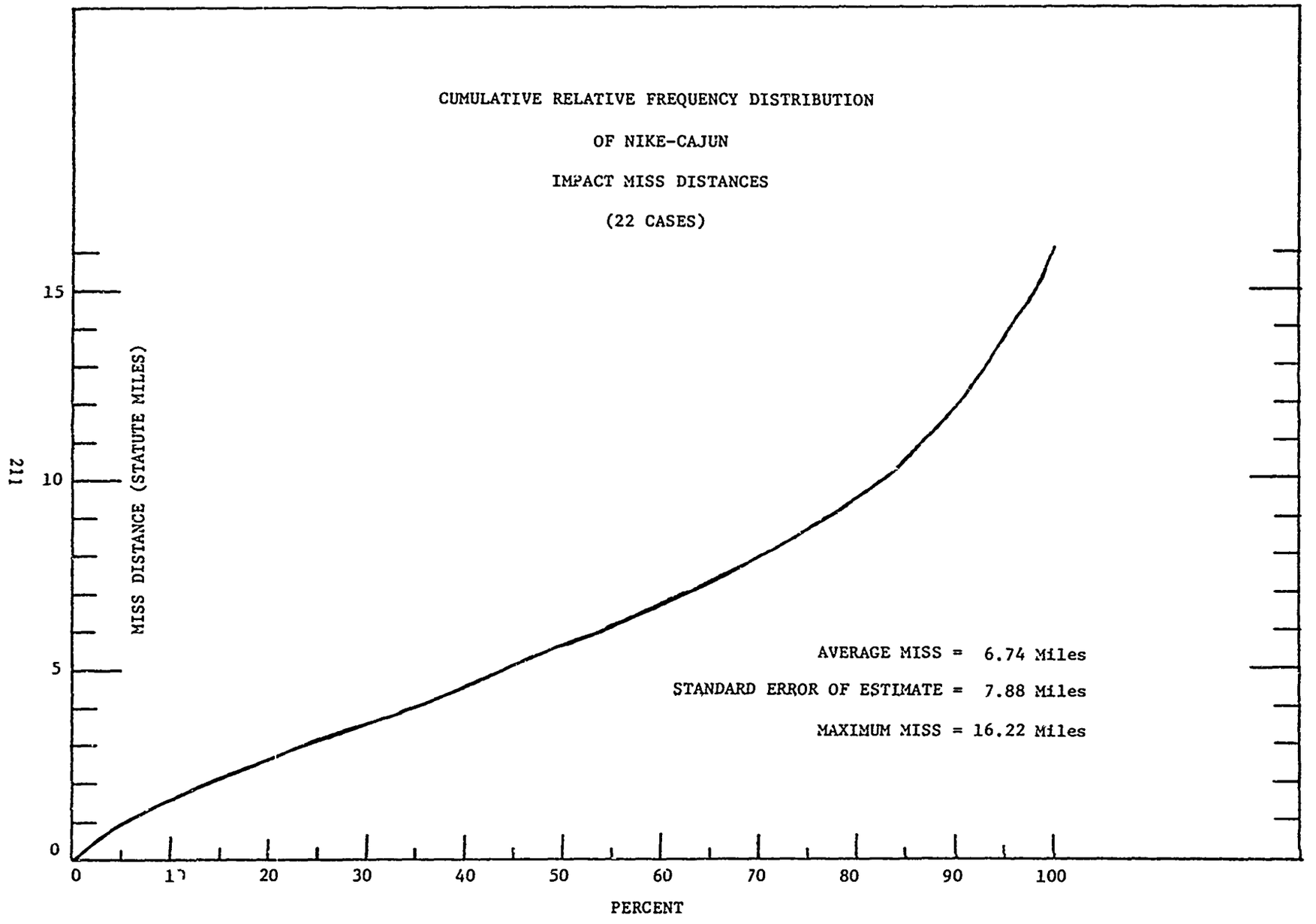
CUMULATIVE RELATIVE FREQUENCY DISTRIBUTION
OF NIKE-CAJUN
IMPACT MISS DISTANCES
(22 CASES)
MISS DISTANCE (STATUTE MILES)
0
5
10
15
0
10
20
30
40
50
60
70
80
90
100
PERCENT
AVERAGE MISS = 6.74 Miles
STANDARD ERROR OF ESTIMATE = 7.88 Miles
MAXIMUM MISS = 16.22 Miles

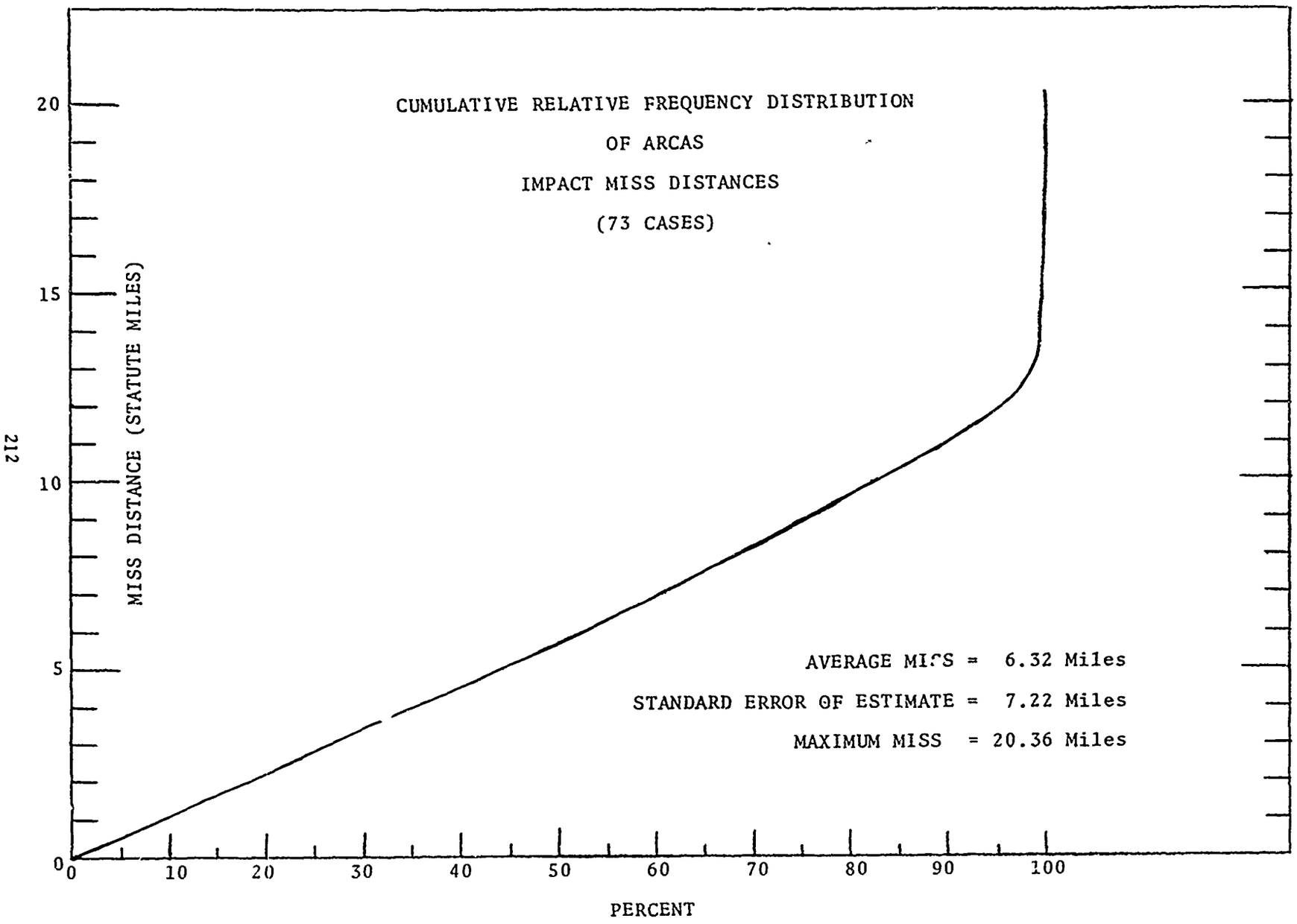
CUMULATIVE RELATIVE FREQUENCY DISTRIBUTION
OF ARCAS
IMPACT MISS DISTANCES
(73 CASES)
MISS DISTANCE (STATUTE MILES)
20
15
10
5
0
0
10
20
30
40
50
60
70
80
90
100
PERCENT
AVERAGE MISS = 6.32 Miles
STANDARD ERROR OF ESTIMATE = 7.22 Miles
MAXIMUM MISS = 20.36 Miles

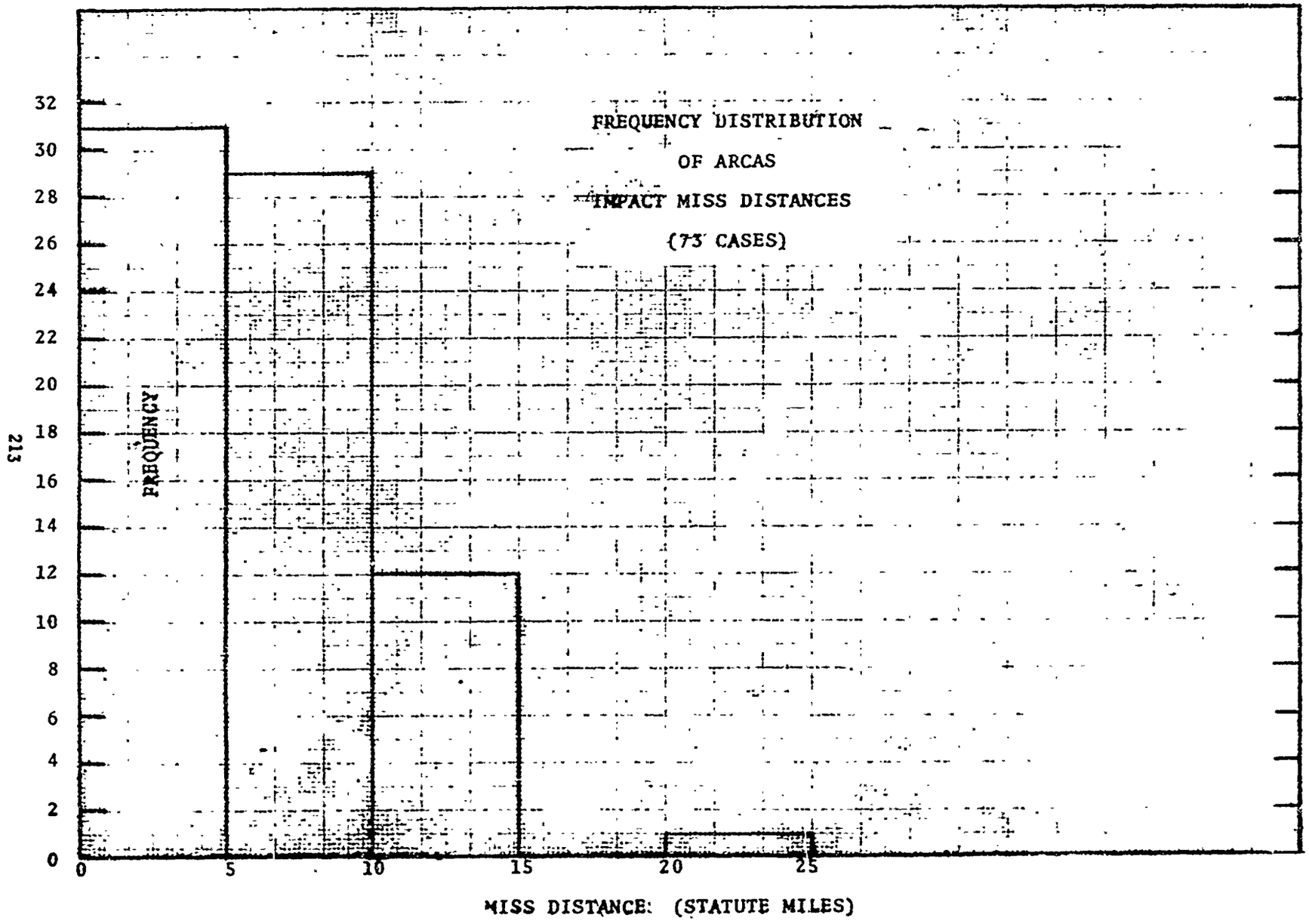
FREQUENCY DISTRIBUTION
OF ARCAS
IMPACT MISS DISTANCES
(73 CASES)
FREQUENCY
32
30
28
26
24
22
20
18
16
14
12
10
8
6
4
2
0
0
5
10
15
20
25
MISS DISTANCE (STATUTE MILES)

REFERENCES

1. Walter, Dr. Everett L., "Six Variable Ballistic Model for a Rocket," USASMSA, June 1962.

2. Duncan, Louis D., "Real Time Meteorological System for Unguided Rocket Impact Prediction," Tech Report ERDA-55, USAERDA, WSMR, N.M., July 1963.

3. Rachele, Henry and Louis D. Duncan, "Prelaunch Real-Time Impact Prediction System and Research Program for the Athena Rocket," ERDA 202, Nov. 64.

4. Duncan, Louis D. and Henry Rachele, "Real-Time Meteorological System for Firing of Unguided Rockets, ECOM 5037, February 1966.

5. Cochran, Vertis C., Edward M. D'Arcy and Florencio Ramirez, "Digital Computer Program for Five-Degree of Freedom Trajectory," ECOM 5036, March 1966.

6. Hennigh, Keith E., "Field Wind Weighting and Impact Prediction Procedure for Unguided Rockets," Physical Sciences Laboratories New Mexico State University, N.M., March 1962, for NASA Goddard Space Flight Center.

7. James, Robert L., Jr., and Ronald J. Harris, "Calculations of Wind Compensation for Launching of Unguided Rockets," NASA TN D-645, April 1961.

ACKNOWLEDGEMENTS

The author expresses his appreciation to Sp. 4 George J. Danek and Sp. 4 George W. Harmon who compiled the data and computed averages and standard errors of estimates of the impact miss distances.

RECENT SPECTRA OF ATMOSPHERIC TURBULENCE

By Niels E. Busch and Hans A. Panofsky

Atomic Energy Commission
Risö, Denmark

Pennsylvania State University*
University Park, Pa., U. S. A.

* Contribution No. 66-119 , College of Earth and Mineral Sciences

ABSTRACT

Spectra of atmospheric turbulence recently measured at various heights and sites under a variety of stability conditions have been analyzed and compared. The results are:

1. In regions over which the spectra obey -5/3 power laws, the ratio of the lateral to the longitudinal spectra shows fair agreement with the 4/3 ratio predicted by the Kolmogorov hypothesis for the inertial subrange. The vertical-longitudinal ratio has a similar tendency.

2. Dissipation rates computed from the longitudinal spectra seem to be consistent with the hypothesis that dissipation is balanced by the total production of mechanical and convective turbulent energy, provided that the turbulence is in equilibrium. In transition from rough to smooth terrain, dissipation exceeds the other terms.

3. Vertical-velocity spectra obey Monin-Obukhov similarity theory up to a height of about 50 m. Their shapes are reasonably uniform, the major change with stability being a change of scale of the wave number axis, i.e., any characteristic nondimensional wave number is a function of z/L only. This function appears to be the same as the relation between the normalized dissipation and z/L. These results are consistent with previously measured Kolmogorov constants and with measured ratios of standard deviation of vertical velocity to friction velocity. Up to about 50 m the wavelengths of maximum logarithmic spectra increase linearly with height and more slowly thereafter, up to about 300 m. The spectra in stable air above 50 m suggest the existence of a Lumley-Shur buoyant subrange.

4. Longitudinal spectra do not obey similarity theory in a number of ways. The wavelengths do not scale with height, and there may be differences between sites when the spectra are plotted in similarity coordinates.

5. Spectra over the sea seem to have relatively more energy at low frequencies than those over land.

1. Introduction

The recent years have seen a steady increase in the amount of data available concerning the detailed structure of atmospheric turbulence near the ground.

Although much remains to be done and much confusion exists with respect to the interpretation of these data, a picture of the turbulence structure in thermally stratified media is emerging. The technical difficulties connected with measurements of small scale fluctuations of atmospheric quantities are considerable and it is believed that much of the confusion arises from lack of sufficiently complete measurements of high quality.

Since its appearance in 1954, one of the most successful tools in the analysis of the mean flow in the lowest layers of the atmosphere has been the Monin-Obukhov similarity hypothesis. Several authors (for a summary see Lumley and Panofsky, 1964) have tried to apply similar reasoning to the statistics of the fluctuating flow fields in thermally stratified boundary layers, and the first indications are that although the vertical-velocity spectrum appears to obey similarity laws for reasonably small heights, the lateral and longitudinal spectra do not. Furthermore, it is known that as the height above the surface increases the similarity hypothesis breaks down also for the vertical component.

It is the primary purpose of the present paper to investigate more thoroughly to what extent similarity theory is applicable to the vertical spectra.

To this end, five sets of recent spectra were examined and compared. The sets originate from different sources and were computed from a great number of time series (or continuous records) taken in a variety of stability conditions and heights. Table 1 summarizes the most pertinent information concerning the measurements.

Table 1. Summary of observations selected for study.

Location	Round Hill	Hanford	Cedar Hill	Vancouver	Vancouver
Observer	Cramer et al.	Elderkin	Kaimal	Smith	Weiler and Burling
Type of Terrain	Tower A: smooth inhomogeneous Tower B: rough inhomogeneous	arid desert sagebrush fairly homogeneous	gently rolling countryside scattered woods	over sea	over sea
Height (m)	15, 16, 40, 46, 91	3, 6.1	46, 137, 229, 320	1.55 to 4.22	1.68 to 2.70
No. of Runs:					
Stable	11	4	52	--	3
Neutral	18	7	--	11*	--
Unstable	14	3	100	--	6
Turbulence Quantities Measured	u', v', w', T'	u', v', w'	w'	u', w'	u', w'
Type of Sensors	thermistor anemometers, bivanes, resistance thermometers	heated thermocouple wires	sonic anemometers	thrust anemometers	hot-wire anemometers
Duration of Observations (min)	60	13-134 (average 44)	20 or 40 (average 34)	32	>24
Type of Recording	digital	analogue	analogue	analogue	analogue digital
Type of Analysis	digital	analogue	digital using block averages over 1 sec	analogue	analogue
Profiles: Wind Temperature	cup anemometers resistance thermometers	cup anemometers thermocouples	Aerovanes thermocouples	cup anemometers --	cup anemometers --

* stability uncertain

2. Site properties. Experimental details and data reduction.

Round Hill. From 1960 through 1963 The Massachusetts Institute of Technology operated a field station at Round Hill near South Dartmouth in Massachusetts. The data used in this study comprise 43 sets of spectra as well as vertical heat and momentum fluxes determined directly from the fluctuation measurements. Spectra of all three velocity components were available for 5 heights (15, 16, 40, 46 and 91 m). The measurements were taken on two different towers.

Tower A (16 and 40 m) is situated about 40 m north of the shoreline of Buzzard Bay in an open area covered with grass. Several hundred meters away toward the west and northwest, the terrain changes to scattered woods. The site has been described in detail by Record and Cramer (1966) and Cramer et al. (1961).

Tower B (15, 46 and 91 m) is located about 900 m to the northwest of tower A in an area covered by brush of an average height of 1.5 m. Except for westerly directions, the site is surrounded by scattered woods (average height of about 8 m), the shortest distance to the woods being about 60 m. The topography of the site is relatively flat.

The measurements consisted of one-hour long recordings of the fluctuating wind components and temperature and were performed by use of thermistor anemometers, light bivanes and resistance thermometers. A thorough description of the instrumentation and the data-handling system can be found in Cramer et al. (1961).

The data were digitally recorded at equally spaced intervals of 1.2 seconds and analyzed numerically. The computed spectra were corrected for the influence of instrumental time-lag. Another correction was applied to correct for the fact that the original data represented deviations from 301-second moving averages. Correction

for aliasing was performed on basis of an expected -5/3 power law for the portion of the spectra above the Nyquist frequency. It was assumed that the area above this frequency had been folded once about the Nyquist frequency.

Detailed investigation of the data showed that for very small friction velocities u*, the calculated vertical momentum fluxes tended to become numerically very unstable. Hence, it was decided to discard the runs for which $u^{*2}<0.1$ $(m/sec)^2$; above this value, u^{*2} was reasonably stable. Furthermore, inspection of the data showed that in some cases the vertical heat flux computed from deviations from the mean had the opposite sign from the flux computed from deviations from a 301-second moving average. This indicates that the cospectra change sign with frequency and since the physical reason for this is not understood and it well could be a result of the numerical method used, such cases were rejected. Also rejected were runs for which the stability changed sign with height. Finally, for some runs, not all information was available.

Of the 79 runs originally available for this study, 36 were rejected for one or more of the reasons mentioned. Most of the rejected runs were taken under extreme stability conditions or during transition periods. In addition, information derived from many other runs was published by Record and Cramer (1966). Some use of these data was made in section 4.

Hanford. Elderkin (1966) reports 14 sets of wind velocity spectra for all three components measured at 3 and 6.1 m at The Battelle Northwest Laboratory, Hanford, Washington. The same report gives a complete description of the instrumentation.

The friction velocity was in each case calculated directly from the fluctuation measurements. Measurements of temperature fluctuations were not obtained; therefore, estimates of the vertical heat-flux were

not available. The thermal stability classification of the runs was obtained using gradient Richardson numbers determined from profile measurements.

A description of the site has been given by Barad et al. (1962). It is flat and fairly homogeneous desert-terrain covered with sagebrush of 1 to 2 m height interspersed with desert grasses.

The turbulence data were collected with a fast response sensor utilizing heated thermocouple wires. The data were recorded on magnetic tape and analyzed by use of analogue methods. The duration of the runs varied from 13 minutes to 134 minutes with an average duration of 44 minutes.

Cedar Hill. In August 1963 a series of vertical-velocity measurements were made on the Cedar Hill tower near Dallas, Texas. Four two-way sonic anemometers were mounted at levels 46, 137, 229 and 320 m providing simultaneous measurements of the vertical-velocity components.

A total of 40 sets of such simultaneous runs have been reported by Kaimal (1966) who also gives a description of the turbulence instrumentation and data-handling system.

The data were recorded as analogue signals on magnetic tape but later converted into time series consisting of 1-sec block averages over consecutive intervals. The analysis was carried out numerically. The spectra were corrected for the filter effect of the block averaging as well as for aliasing. The duration of the runs was 40 minutes for 28, and 20 minutes for 12 of the runs.

The only turbulence quantity measured was the vertical-velocity component; therefore, direct estimates of Reynolds stresses and heat fluxes were not available. Estimates of the frictior velocity were

obtained from the relation $\overline{w^2}/u^{*2} = 1.7$ (see section 5) and the stability was judged on the basis of gradient Richardson numbers obtained from profile measurements.

Of the 40 sets of runs reported by Kaimal only 38 are considered in this study. One set was rejected due to change of stability with height. For the other, some statistics were missing. Both sets were measured during transition periods.

A description of the tower and its instrumentation for profile measurements may be found in Gerhardt et al. (1962).

The site is described as gently-rolling countryside with scattered woods (Stevens and Gerhardt, 1959) but appears to be rather innomogeneous on a larger scale (MacCready et al., 1961).

Vancouver. Smith (1966, pp. 141-151) reports 11 measurements of the longitudinal and vertical spectra over the sea at the Spanish Banks near Vancouver, B. C. The site has been described by Pond et al. (1966), who also describes the thrust anemometer used to collect the wind data utilized in this study.

The height of measurement varied with the tide from 1.55 m to 4.22 m. The data were recorded as analogue signals on magnetic tape and the spectral analysis as well as the computation of Reynolds stresses were carried out by analogue computer. The duration of the observations was 32 minutes. Measurements of temperature fluctuations were not obtained; therefore, estimation of vertical heat-fluxes was not possible. Wind profiles were measured but not the temperature profiles. Check on the thermal stability of the atmosphere is thus not furnished.

Later, Weiler and Burling (1967) reported spectra of longitudinal and vertical-velocity components obtained at the same site but from measurements by hot-wire anemometers. Reduction of the data was similar to Smith's.

3. The ratio of one-dimensional spectra in the inertial subrange.

It is a well-known fact that one-dimensional velocity spectra measured in the atmosphere often are found to obey a -5/3 power law to much greater wavelength than can possibly be expected to lie in the inertial (Kolmogorov) subrange of the spectra. In general, the appearance of such a power-law region is taken as evidence for the existence of an inertial subrange at some higher wave numbers which may be out of the measured wave-number range, and the -5/3 region is assumed to be continuous with the truly isotropic subrange.

This extension of the Kolmogorov region is particularly important in the atmosphere because, with few exceptions, all measurements of the turbulent energy-dissipation ε have been based on measurements of energy spectra over wave-number regions for which local isotropy is doubtful.

It is a consequence of Taylor's hypothesis, the assumption of local isotropy, the incompressibility of the turbulent flow field and the Kolmogorov hypothesis that in the inertial subrange the one-dimensional velocity spectra must obey

$$\frac{S_v(n)}{S_u(n)} = \frac{S_w(n)}{S_u(n)} = \frac{4}{3} \qquad 3.1$$

where $S_v(n)$ and $S_w(n)$ denote the lateral and the vertical spectra, respectively. $S_u(n)$ is the longitudinal spectrum and n is the frequency (cycles/unit time).

If the -5/3 regions found in atmospheric spectra are simple geometrical extrapolations of the Kolmogorov regions, they, of course, must obey Eq. 3.1. Recent measurements seem to indicate that this may not be the case (R. W. Stewart, personal communication, and Elderkin, 1966), but not very much experimental evidence has so far been presented.

In order to shed some light on this problem, the Round Hill data were analyzed by plotting all spectra on double logarithmic paper. In all cases where a -5/3 power law could be distinguished, the high-frequency portion of the spectra were smoothed accordingly, and the ratios in Eq. 3.1 computed.

The results are shown in Figures 1 and 2. The abscissa is z/λ_N where z is the height of measurement, λ_N is the Nyquist wavelength, computed under the assumption of Taylor's hypothesis. Figure 1 shows the ratio of the lateral spectrum to the longitudinal spectrum. The scatter is considerable as was to be expected considering the statistical uncertainty of the spectral estimates, but for values of the abscissa greater than 2.4, the average value of the spectral ratio is 1.32 ± 0.2, indeed supporting the validity of Eq. 3.1.

Figure 2 shows the ratio of the vertical spectrum ~~and~~ the longitudinal spectrum. Clearly, the majority of the points fall below the expected value of 4/3 but there is an obvious trend towards higher values as the abscissa increases and it is apparent that for values of the abscissa larger than 5, the proper value of the ratio is approached.

This agrees with the observation that only when $z \gg \lambda_N$, the -5/3 region of the vertical-velocity spectrum is extensive and well defined.

This suggests that as the wind speed increases and less of a possible power-law region is below the Nyquist frequency, the spectra are assumed to obey a power law which, in many cases, is not quite established or maybe not existing at all.

4. Energy Dissipation and the turbulent energy budget.

The turbulent energy budget in a stationary, horizontally homogeneous flow may, with simplifications (see, e.g., Lumley and Panofsky, 1964) be written

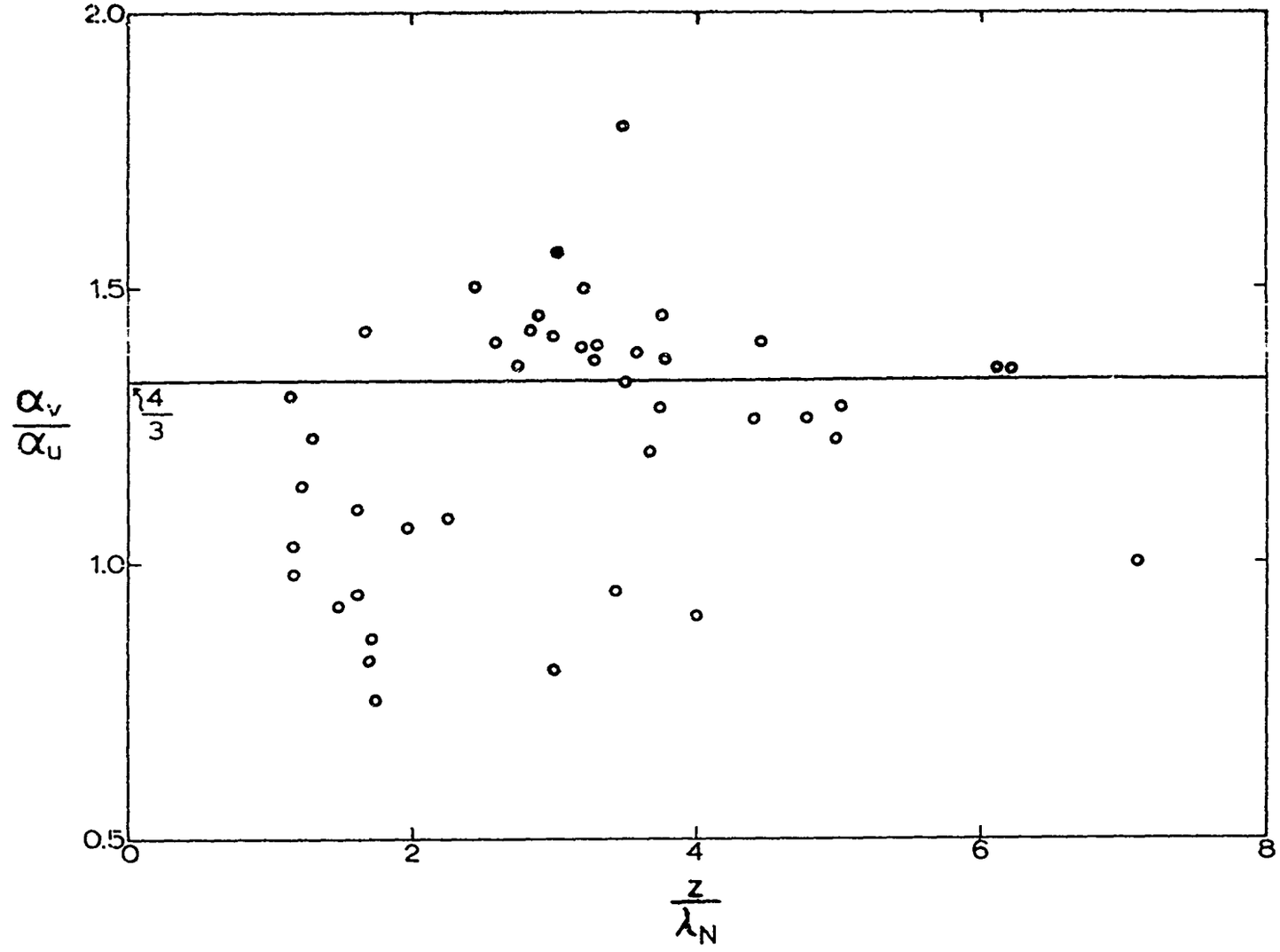

Lateral-longitudinal ratio in -5/3 region as function of ratio of height to Nyquist wavelength

Figure 1.

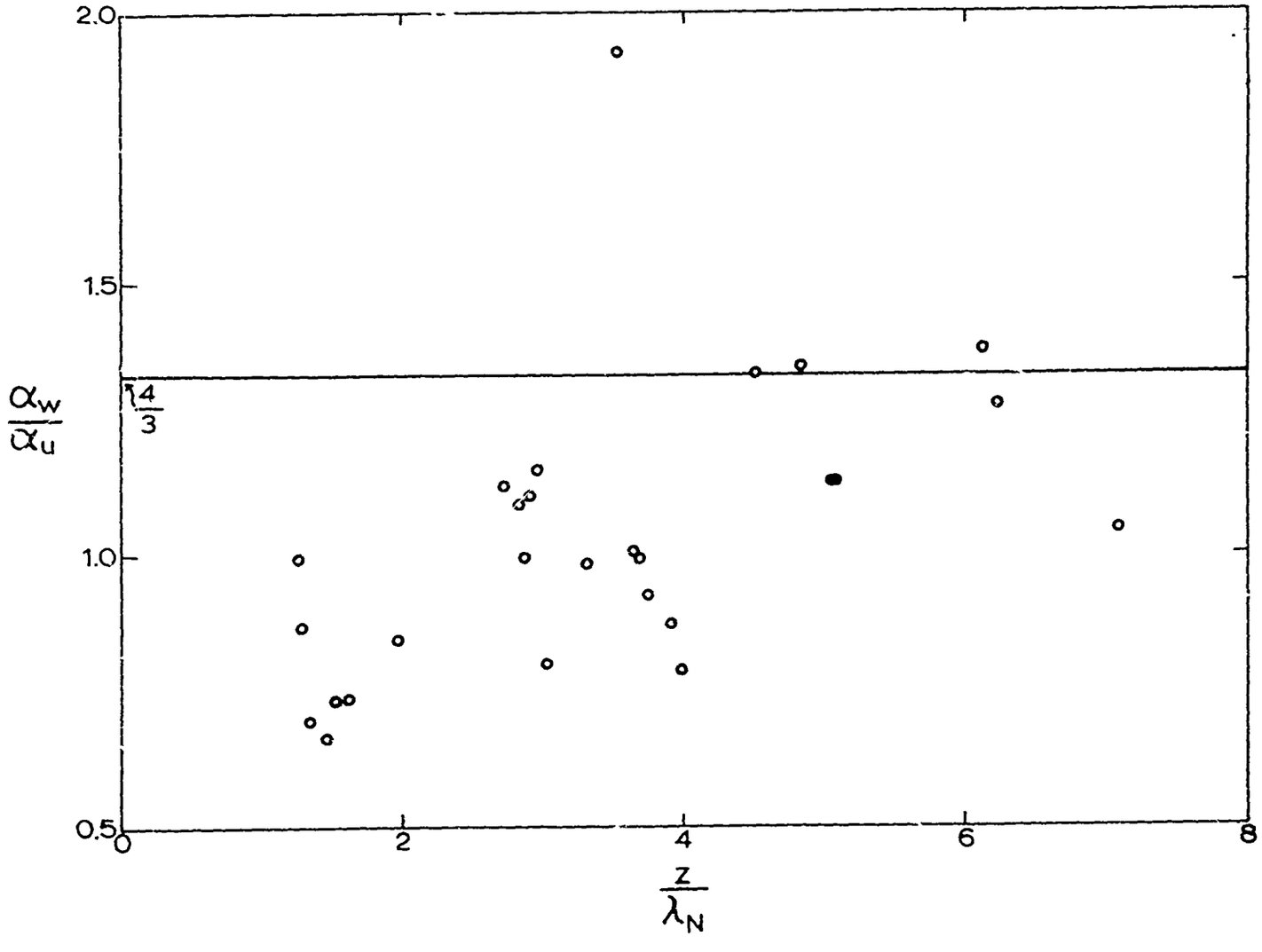

Vertical-longitudinal ratio in -5/3 region as function of ratio of height to Nyquist wavelength

Figure 2.

$$\frac{\partial E}{\partial t} = u^{*2}\frac{\partial V}{\partial z} + \overline{w'T'}\frac{g}{T} - \varepsilon - D \qquad 4.1$$

where the divergence term $D = \frac{1}{\rho}\frac{\partial}{\partial z}\overline{p'w'} + \frac{\partial}{\partial z}\overline{w'E}$

$E = u_i' u_i'$ is the instantaneous turbulent energy and the notation is standard.

Multiplication of Eq. 4.1 by (kz/u^{*3}), where $k = 0.4$ is the von Karman constant, yields

$$\frac{kz}{u^{*3}}\frac{\partial E}{\partial t} = \varphi - \frac{z}{L} - \varphi_\varepsilon - \varphi_D \qquad 4.2$$

where ϕ is the nondimensional wind shear $\frac{kz}{u^*}\frac{\partial V}{\partial z}$, L the Monin-Obukhov stability length, ϕ_ε the dimensionless dissipation rate, and ϕ_D the nondimensional divergence of the vertical energy flux. Two kinds of simplifications of Eq. 4.2 have been suggested: Lumley and Panofsky (1964) quote observations leading to the hypothesis that dissipation equals production of mechanical energy only, so that:

$$\phi = \phi_\varepsilon \qquad 4.3$$

On the other hand, many authors make the assumption that dissipation equals the sum of buoyant and mechanical energy production:

$$\phi - \frac{z}{L} = \phi_\varepsilon \qquad 4.4$$

In order to examine whether either of these hypotheses is applicable to the energy equation, 28 longitudinal spectra, all exhibiting extended and marked -5/3 power laws, were selected from the Round Hill data. The dissipation rate was estimated from the Kolmogorov expression for the inertial subrange using a universal constant equal to 0.146 corresponding to the constant used by Record and Cramer (1966)

in the structure function and in close agreement with the constant published by Pond et al. (1966).

The dimensionless dissipation rates are shown plotted versus the stability parameter z/L in Figure 3.

Also plotted in the figure are the results obtained by Record and Cramer (1966), which had been obtained from different runs at the same site. These estimates of ε which have been corrected with a factor of 2.18 were obtained from the Kolmogorov expression for the structure function. It can be shown theoretically that, due to uncorrected instrumental lag, their values must be much too small (Busch, 1967). Values of the friction velocities for the data reported by Record and Cramer were available to the present authors but the individual spectra were not. The correction factor 2.18 was determined as the average ratio ~~between the~~ of ε determined from the corrected spectra ~~and~~ & ε estimated from the uncorrected structure function using the present set of data.

As is seen from Figure 3, the two sets of data points agree very well. For $z/L \leq 0$ the average of the corrected Record and Cramer data (44 points) is 0.97 as compared to an average of 1.07 for the new data (22 points) giving a total average of 1.00. The fact that ϕ_ε is so nearly equal to one is intuitively interpreted as a confirmation of the numerical value of the Kolmogorov constant used.

Within the accuracy of the measurements and the stability range covered no tendency for ϕ_ε to vary with stability can be detected for $z/L \leq 0$.

The solid line in Figure 3 provides a test of the hypothesis implied by Eq. 4.4 On the unstable side, $\phi(z/L)$ was obtained from the excellent observations by Swinbank (1964).

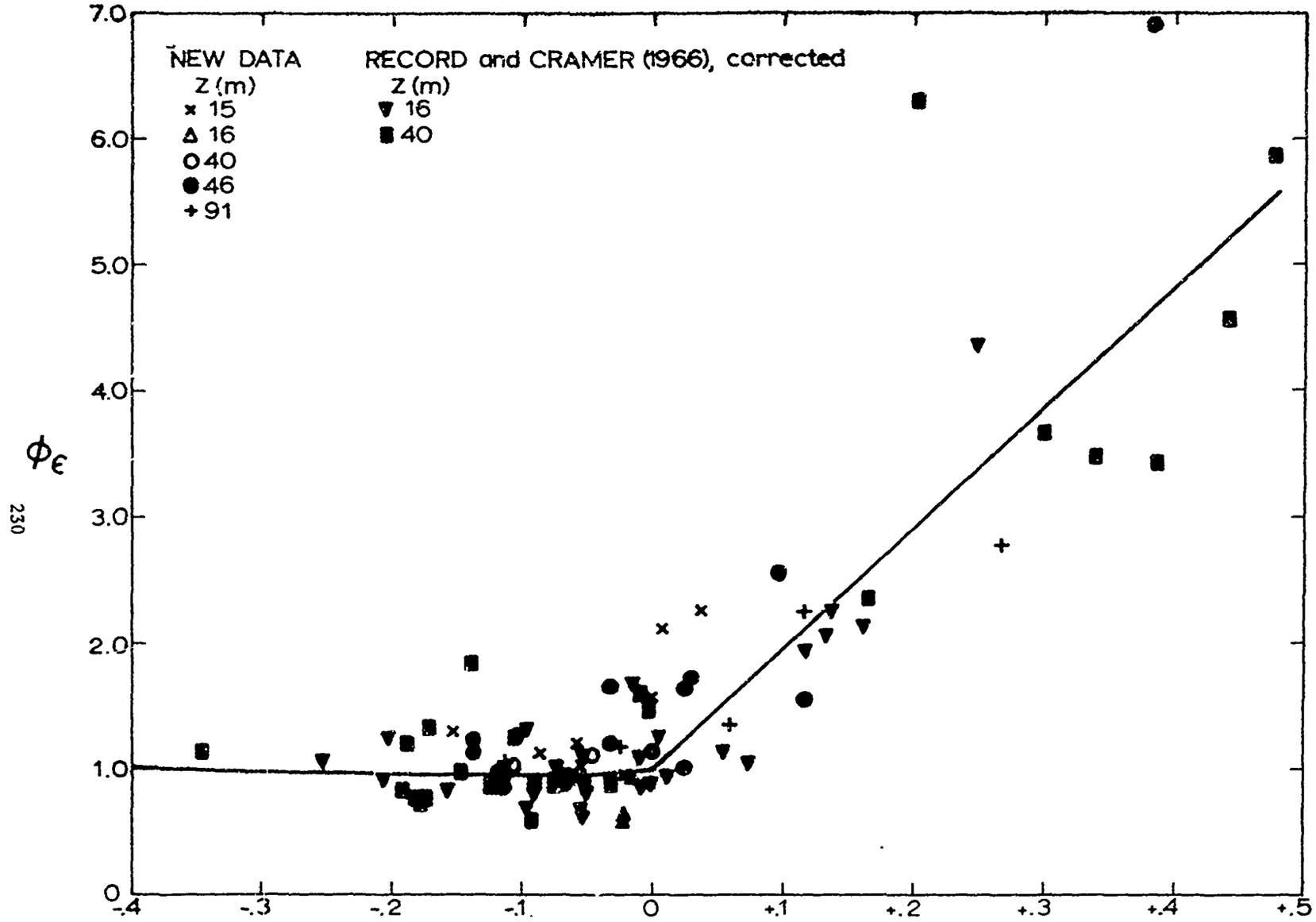

Figure 3. ϕ_ε as function of a/L. Solid line indicates theoretical estimate from energy equation

On the stable side, $\phi(z/L)$ was estimated according to an analysis by McVehil (1964) which resulted in:

$$\phi = 1 + 7 \frac{z}{L} \frac{K_m}{K_h} \qquad 4.5$$

Calculations from the Round Hill data of the ratio K_h/K_m of the turbulent diffusivities for heat and momentum, respectively, showed little dependence of the ratio on stability in stable air and gave an average ratio of 0.67 in neutral and stable air, thus yielding

$$\phi - \frac{z}{L} = 1 + 9.5\frac{z}{L} \qquad 4.6$$

This line fits the data in Figure 3 relatively well. One would, therefore, be tempted to postulate that at all heights

$$\phi_\varepsilon = \phi - \frac{z}{L} \qquad 4.7$$

i.e., that the dissipation equals the total production of mechanically and thermally produced turbulent energy.

This conclusion, however, is correct only if it can be assumed that the values of $\varphi = (kz/u^*)(dV/dz)$ at Round Hill have the same properties as those in Australia. Figure 4 presents a test of this assumption. The solid line is based on Swinbank's data (for unstable air and on McVehil's results for stable air). Apparently, the observations on tower B are in satisfactory agreement with Swinbank's; but those from tower A are systematically too small by a factor of almost two. This difference can be understood most easily from the fact that tower B is influenced by more or less homogeneously rough terrain, and the turbulence there is in equilibrium, whereas tower A is set in a clearing. In particular, at 16 m on tower A, the air is accelerating and the turbulence within it is decreasing.

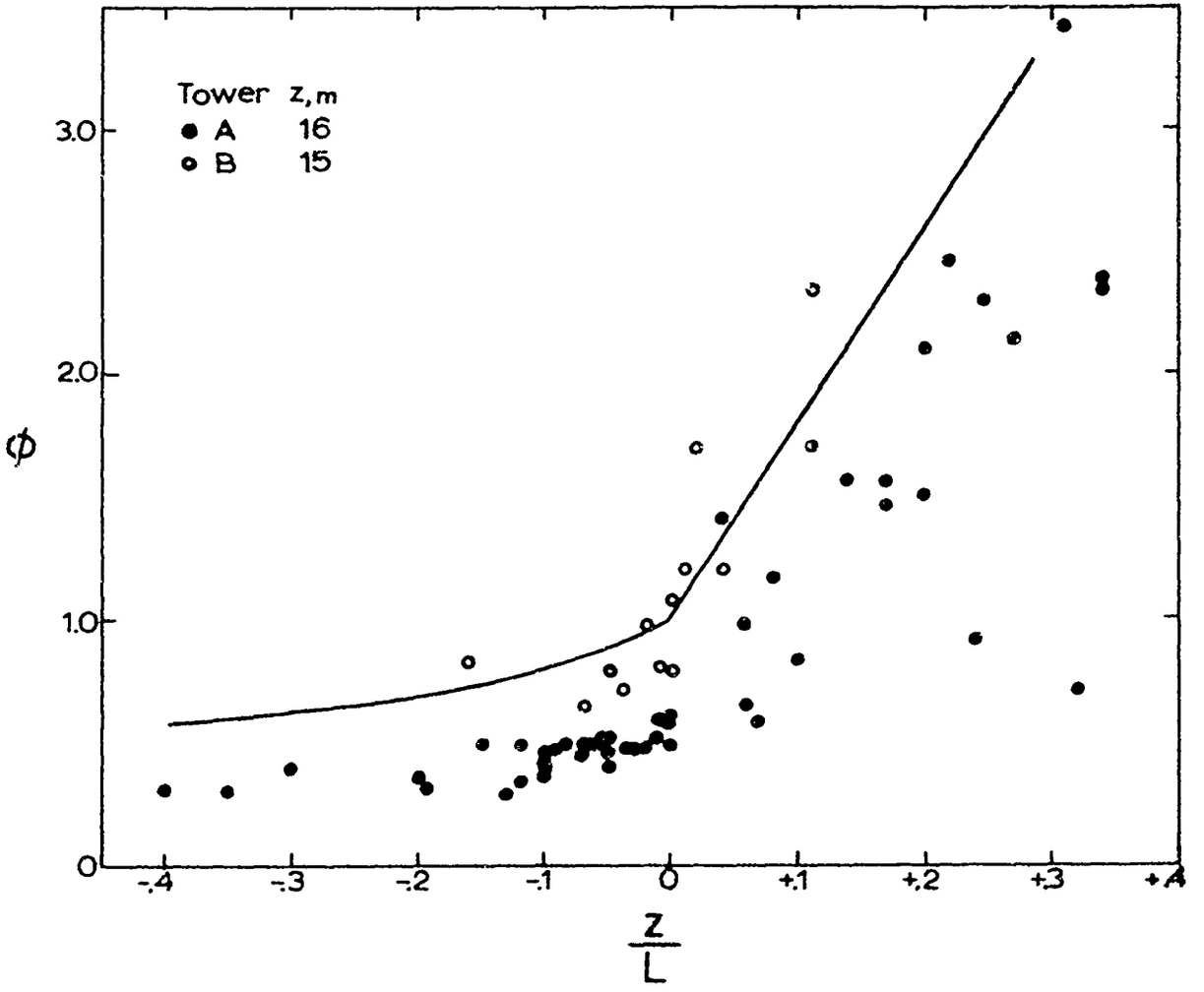

Figure 4. Nondimensional wind shear as function of z/L. Solid line represents Keyps equation best fitting Australian data

We might tentatively suggest therefore, that Eq. 4.4, which expresses a local balance between production and dissipation of turbulent energy, is valid over homogeneous terrain; but in accelerating air, dissipation far exceeds production, so that turbulence in a given parcel of air is decreasing. This is in agreement with measurements reported by Hess and Panofsky (1966).

It might be worth noting that, if the above interpretation is correct, the nondimensional wind shear in accelerating air acts as though von Kármán's constant were increased to a value as large as 0.8.

5. Characteristics of low-level vertical-velocity spectra over land.

Figures 5, 6 and 7 show logarithmic vertical-velocity spectra, normalized by the square of the friction velocity, $nS_w(n)/u^{*2}$, as function of the non-dimensional frequency $f = nz/V$. The separate figures show the relationships at the three land sites, Round Hill, Hanford and Cedar Hill, respectively.

For the Round Hill data, neutral runs were defined as those for which z/L was between -0.05 and +0.05. Runs with larger negative or positive Richardson numbers were classified as unstable and stable, respectively. At Cedar Hill, no truly neutral periods occurred. During the dawn and dusk transition periods, the sign of the stability changed with height. Such cases were eliminated and the rest classified as either stable or unstable.

In all cases, individual spectrum estimates were plotted in similarity coordinates for each stability class separately; each graph then contained the results of many independent runs. Although there was, of course, some scatter on each graph, lines could be drawn on each by eye without much difficulty. Only these subjectively fitted lines are shown in the figures.

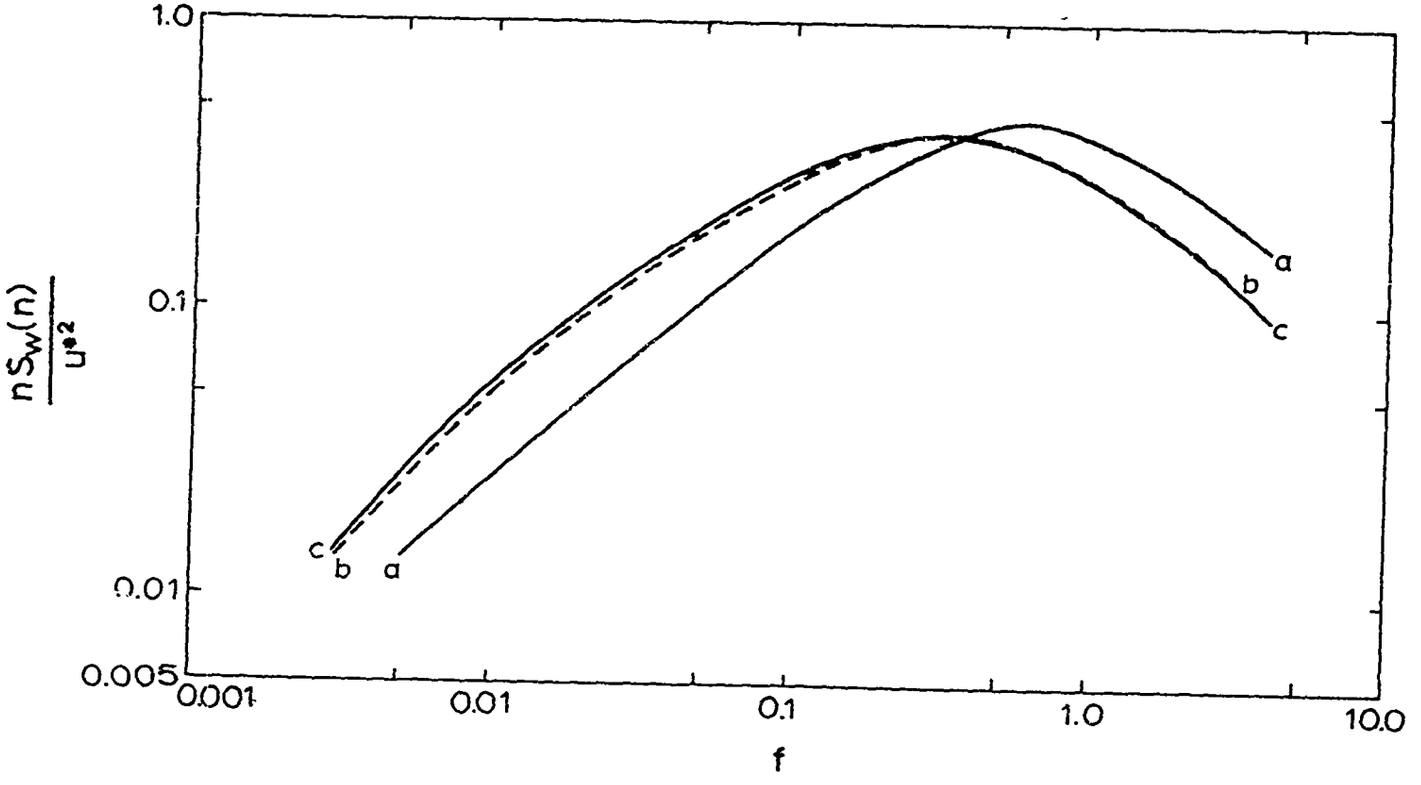

Smoothed and averaged spectra of vertical velocity at heights 15 to 91 m, Round Hill.
a: stable ($+0.420 \geq z/L \geq +0.058$);
b: neutral ($+0.050 \geq z/L \geq -0.050$);
c: unstable ($-0.051 \geq z/L \geq -1.119$)

Figure 5.

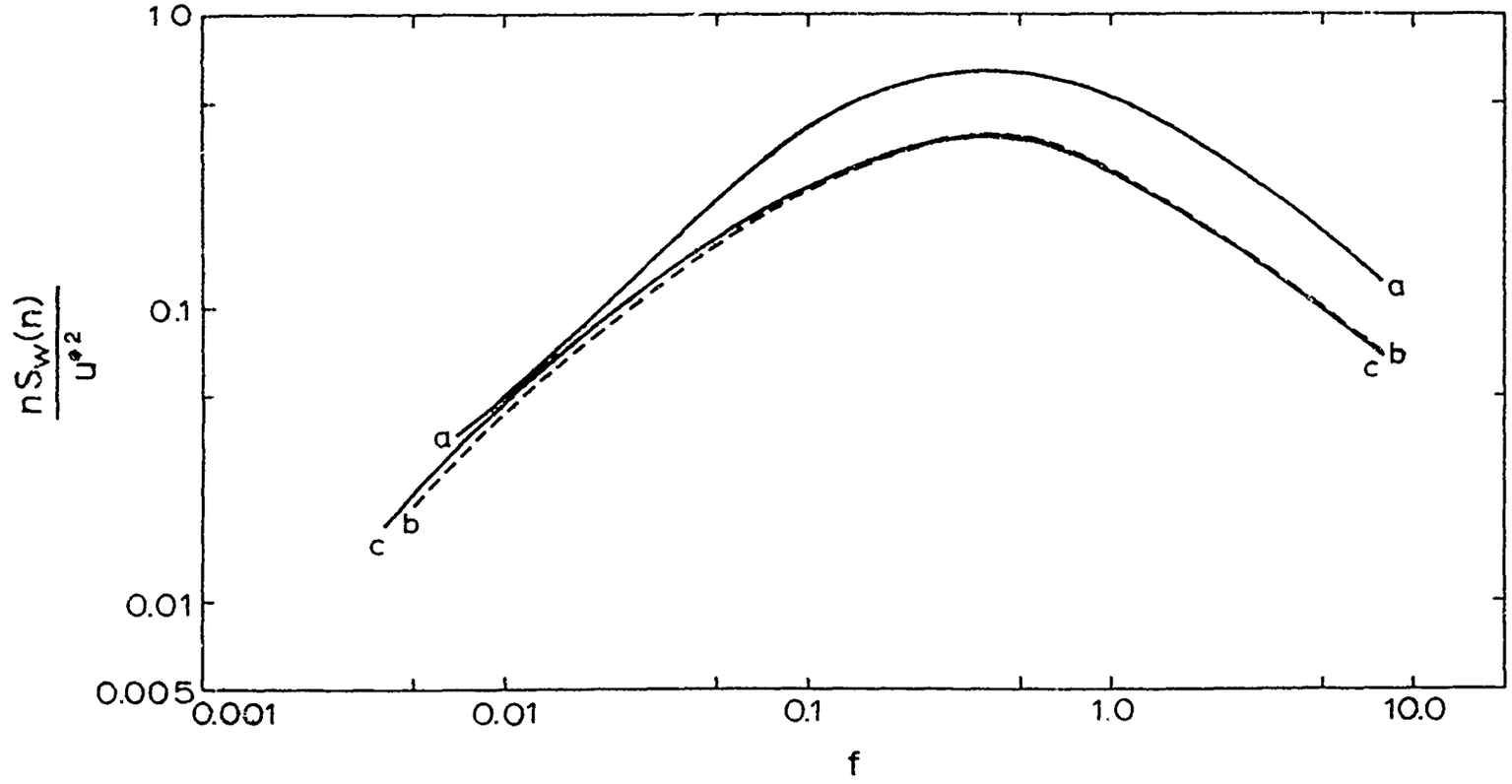

Smoothed and averaged spectra of vertical velocity at heights 3 and 6.1 m, Hanford.
a: stable (+0.18≥Ri≥+0.01);
b: neutral (0≥Ri≥-0.03);
c: unstable (-0.04≥Ri≥-0.16)

Figure 6.

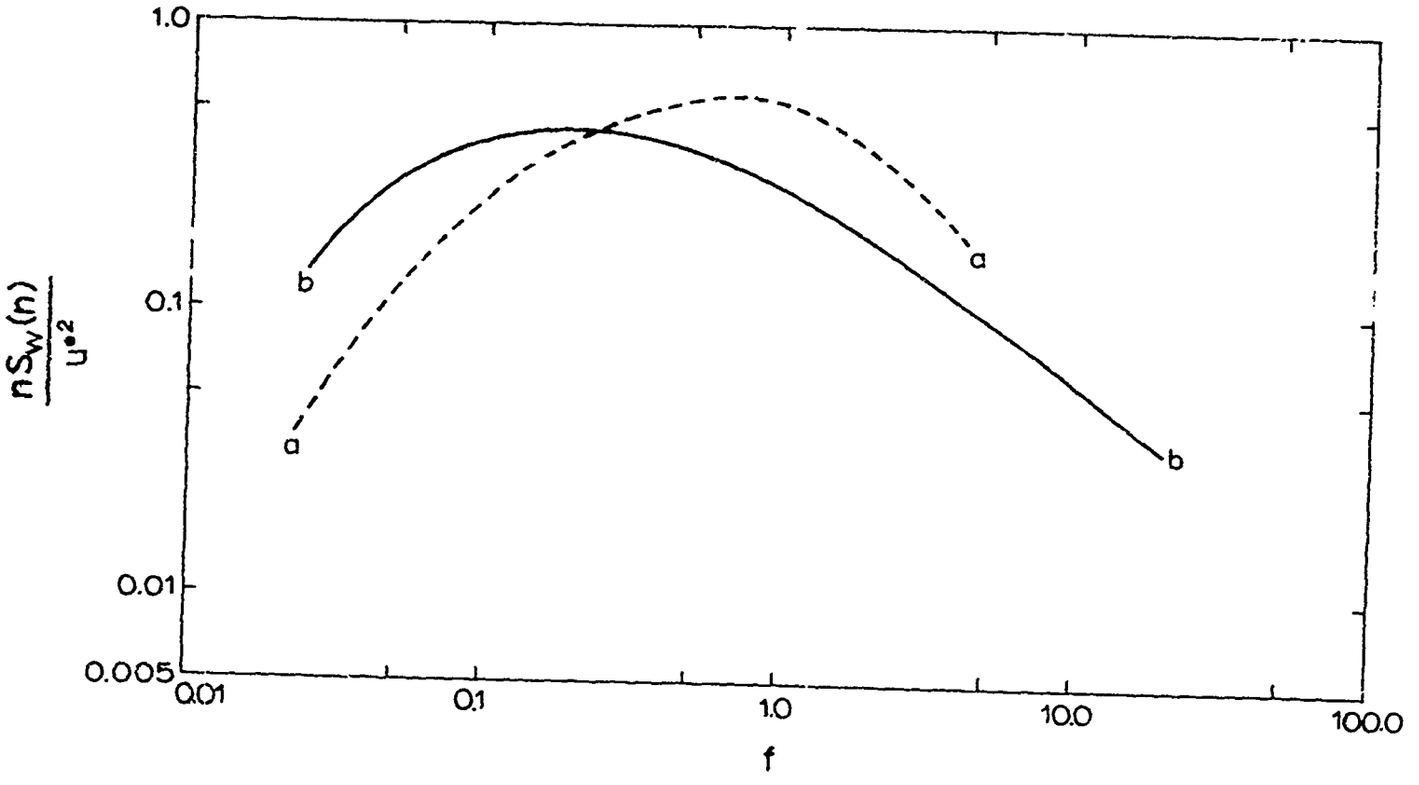

Smoothed and averaged spectra of vertical velocity at height 46 m, Cedar Hill.

a: stable ($+0.10 \geq Ri \geq +0.02$);
b: unstable ($-0.08 \geq Ri \geq -60.89$)

Figure 7.

There is considerable similarity among the shapes of all the spectra. Also, the maximum ordinate of the logarithmic spectra in similarity coordinates is about the same in all cases, namely 0.4 to 0.6. The value of f at the maximum and the high-frequency portion does not change significantly from the neutral to the unstable cases. This latter result was to be expected from the behavior of the inertial subrange described in the last section. Similarly, the very slight increase of low-frequency energy with decreasing stability is presumably not significant. As we proceed from neutral to stable conditions, there is a definite shift of the whole spectrum toward higher frequencies, with no essential change of shape.

In view of the considerable number of available spectra from Round Hill, these were originally divided into a larger number of stability categories; they essentially showed an orderly progression from the most stable to the neutral in the manner indicated by the three categories shown in the figures, and no significant change with stability under unstable conditions.

Figure 8 brings together spectra from the three sites under similar (unstable) conditions. Also included is a laboratory spectrum obtained by Bradshaw (1967) with zero pressure gradient in the "inner" boundary layer. The agreement among the atmospheric spectra is fairly good in spite of the completely different character of the terrain. Even the laboratory spectrum fits quite well.

On the same graph is shown a curve constructed from the expression:

$$nS_w(n)/u^{*2} = \frac{1.075\ f/f_m}{1 + 1.5\ (f/f_m)}^{5/3} \qquad 5.1$$

Here, f_m is the f value at the maximum. The constant in the numerator is chosen in such a way that the computed value of $nS_w(n)/u^{*2}$ is equal

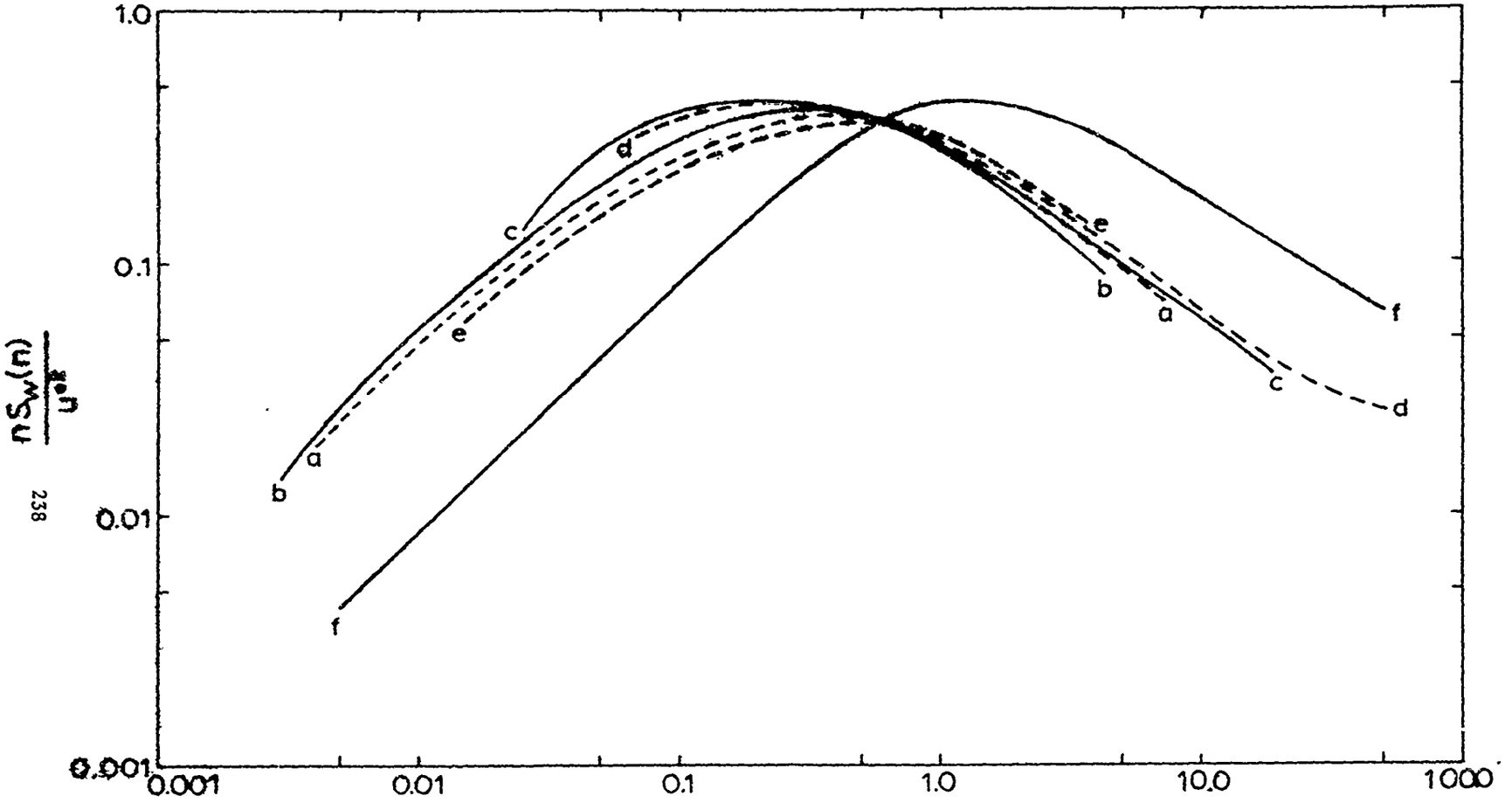

Comparison of vertical-velocity spectra in unstable air. f
a: Hanford, 3 and 6.1 m;
b: Round Hill, 15 to 91 m;
c: Cedar Hill, 46 m;
d: Cedar Hill, 137 m;
e: laboratory spectrum from Bradshaw (1967);
f: curve constructed from empirical formula with arbitrary f_m

Figure 8.

to 0.43 at $f = f_m$. Apparently, the fit is reasonably good, with f_m around 0.32, in neutral and unstable air, although the energy at low wave numbers is systematically underestimated.

Since the shapes of the vertical-velocity spectra over land appear to be nearly invariant with z/L, it is here recommended to use Eq. 5.1 under all stability conditions and at heights up to 50 m, but allow f_m to vary with z/L. The relationship between f_m and z/L will be developed later from the properties of the inertial subrange.

The consistency of Eq. 5.1 with published data can be tested in several ways. For example, if we integrate Eq. 5.1 over all frequencies, we find that $\sigma_w^2/u^{*2} = 1.67$, independent of f_m, and therefore independent of stability. This result is quite consistent with recent direct measurements of this ratio, such as those by Mordukhovich and Tsvang (1966) with sonic anemometers. Also Prasad, in an unpublished summary of observations from many sites, comes to a similar conclusion: the ratio σ_w^2/u^{*2} is about 1.7 for stable, neutral and unstable air up to $-z/L = 0.5$.

Another comparison of the properties of Eq. 5.1 with independent observations can be made by considering the inertial subrange ($f \gg 1$). For large f, the equation then gives a relation between f_m and the "universal" constant b_A in the one-dimensional lateral spectrum $\mathcal{P}$:

$$b = 0.388(f_m/\phi_\varepsilon)^{2/3} \qquad 5.2$$

Under neutral conditions, ϕ_ε is unity and f_m about 0.32. This gives 0.182 for the universal constant b when wave number is measured in cycles per unit length, and 0.62 when k is measured in radians per unit length. If we consider that the ratio of lateral to longitudinal constants is 4/3, this result is in good agreement with the numerical value of the longitudinal constant supported by the preceding section,

and with previously published values (see, e.g., Pond et al. 1966). Thus, the numerical consequences of Eq. 5.1 are in good agreement with independent measurements.

Because b is a universal constant, Eq. 5.2 predicts the variation of f_m with stability:

$$f_m = 0.32\phi_\varepsilon(z/L) \qquad 5.3$$

Since we saw in the preceding section that ϕ_ε does not vary significantly from neutral to unstable air (within the stability range covered in this study), Eq. 5.3 suggests that f_m varies little on the unstable side, in agreement with observations. On the other hand, f_m increases rapidly with increasing stability.

By a combination of Equations 5.1 and 5.3, we can now construct a complete algebraic model which permits the estimation of spectra of vertical motions up to about 50 m:

$$\frac{nS_w(n)}{u^{*2}} = \frac{3.36\ f/\phi_\varepsilon}{1 + (3.98\ f/\phi_\varepsilon)^{5/3}} \qquad 5.4$$

Since u* can be fairly well estimated from wind, Richardson number and roughness (see Panofsky, 1963), Eq. 5.4 relates the spectrum to wind, roughness, height, stability and frequency. For most practical purposes, ϕ_ε can be taken as unity in unstable air In stable air, ϕ_ε is given by Equations 4.6 and 4.7.

One of the consequences of Eq. 5.3 and the statement that $\sigma_w^2/u^{*2} = 1.67$ is that the dissipation can be calculated from relatively slow-response measurements through the relation:

$$\varepsilon = 3.62\ \sigma_w^3 k_m \qquad 5.5$$

where k_m is the wave number of the spectral maximum in cycles per unit length and σ_w is the standard deviation of vertical velocity.

Although Eq. 5.1 has some useful properties, it systematically underestimates the spectrum at low frequencies. In this sense, the expression suggested by Pasquill and Butler (1964)

$$\frac{n S(n)}{u^{*2}} = \frac{A f/f_m}{(1+1.5 f/f_m)^{5/3}} \qquad 5.6$$

(where A is a constant) is superior, although it does not fit as well at high wave numbers. However, altogether it cannot be claimed that Eq. 5.1 generally provides a better fit than Eq. 5.5; in fact, one could argue that Eq. 5.5 is more satisfactory at Cedar Hill, and Eq. 5.1 at Round Hill and Hanford. It is doubtful whether any of these differences are significant.

6. The variction of vertical-velocity spectra with height.

The observations at Cedar Hill provide the opportunity to study the variation of the vertical-velocity spectra with height beyond the first 50 m where the conditions of the last section are likely to hold.

Figures 9 and 10 show average spectra $nS_w(n)$ at various heights in stable and unstable air, respectively. In unstable air, increasing height does not change much the shape of the spectra, but mainly the position. Thus, f_m begins to increase with height above 50 m.

The shape of the spectra in unstable air is still described well by Eq. 5.1 which is shown in Figure 9 for comparison. The fit is less good in the stable periods, where the energy is concentrated around higher frequencies than in unstable air. There is an indication here of a slope much larger numerically than 2/3. A possible explanation is the existence of a buoyant subrange for f>>1, where the slope may be of order -2, as suggested by Lumley (1964).

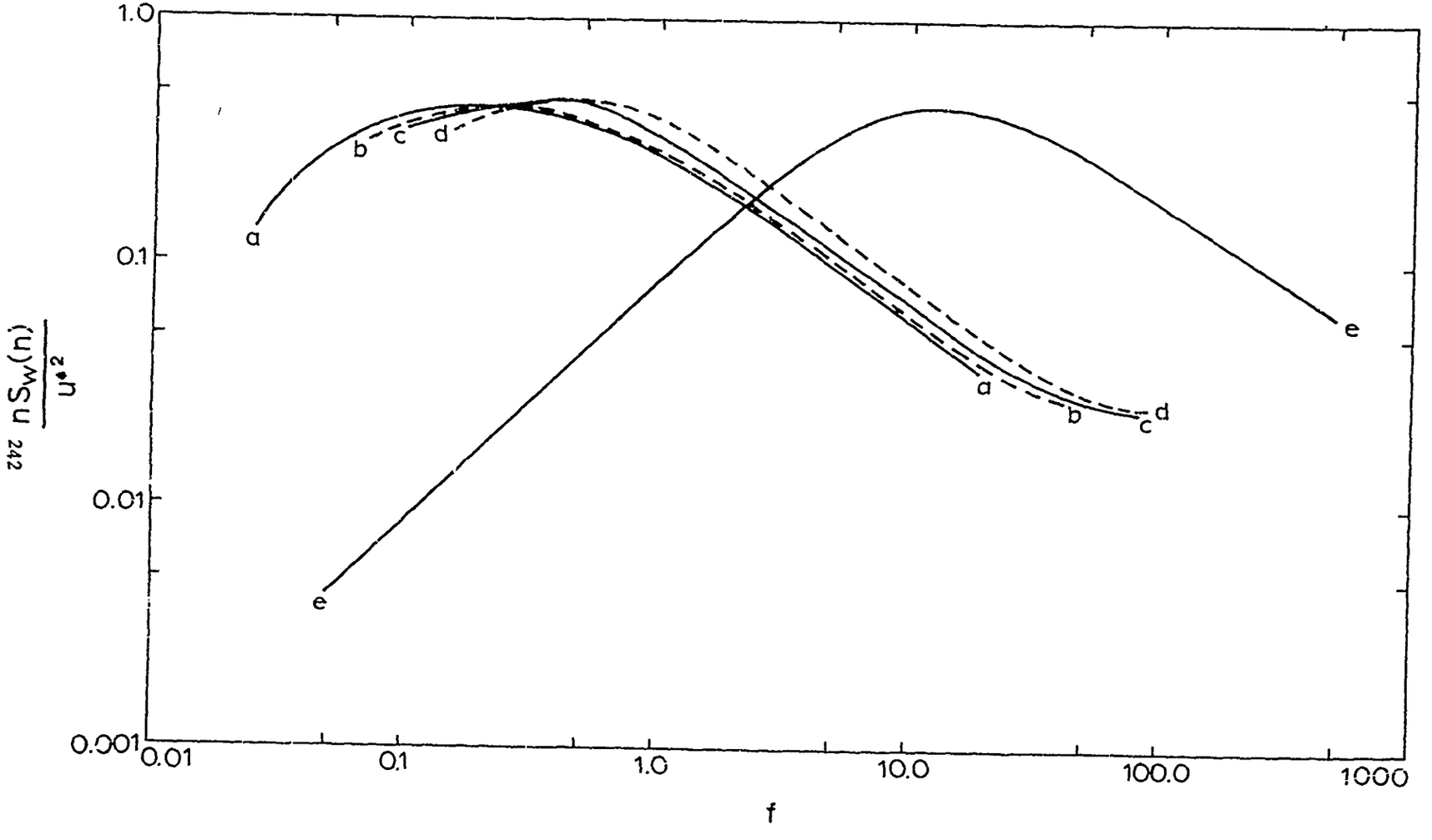

Figure 9. Variation of vertical-velocity spectra with height in unstable air at Cedar Hill. a: 46 m; b: 137 m; c: 229 m; d: 320 m; e: constructed from empirical formula with arbitrary f_m

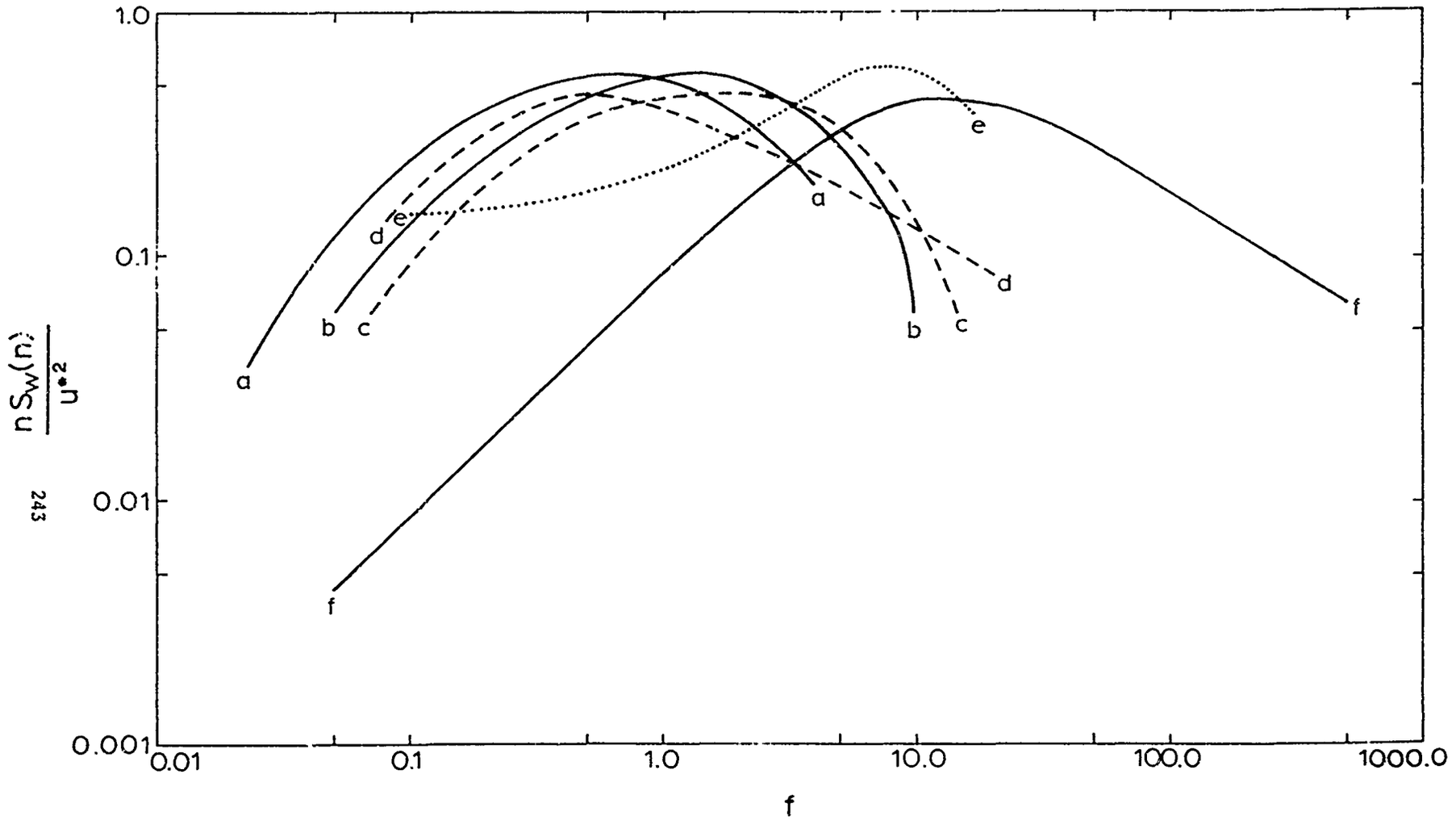

Figure 10. Variation of vertical-velocity spectra with height in stable air at Cedar Hill. a: 46 m; b: 137 m; c: 229 m; d: 320 m, high frequency peak; e: 320 m, low-frequency peak; f: constructed from empirical formula with arbitrary f_m

At 320 m the spectra fall into two families, so that two curves have been drawn for that height. In one family, the principal peak occurs at a high frequency, consistent with lower levels. The other has peaks around a wavelength of 600 m which have been ascribed to gravity waves by Kaimal and Izumi (1965).

The variation of the wavelength at the maxima of the logarithmic spectra is further illustrated by Figure 11. This figure also contains maximum wavelengths at low levels inferred from the spectra described in the last section.

The lower portion of the line constructed for unstable conditions implies that $f_m = .25$. The observed value at Round Hill was, as mentioned, probably somewhat higher ($f_m = .32$), but the difference is not believed to be significant.

The figure illustrates again that, in general, "eddies" in stable air have shorter wavelengths than those in unstable air. The increase with height which, in agreement with similarity theory, is linear at first, later becomes smaller. Above 200 m, it reaches a maximum, or perhaps a constant value. The observations are not sufficiently accurate to distinguish between these two possibilities. This variation of wavelength with height is similar to that of "mixing length" needed to describe the wind distribution in the planetary boundary layer (Blackadar, 1962).

Two separate points are indicated for the position of the maximum in stable air at 320 m, reflecting the common occurrence of two distinct peaks. As mentioned before, the long-wave peak at this level is ascribed to gravity waves.

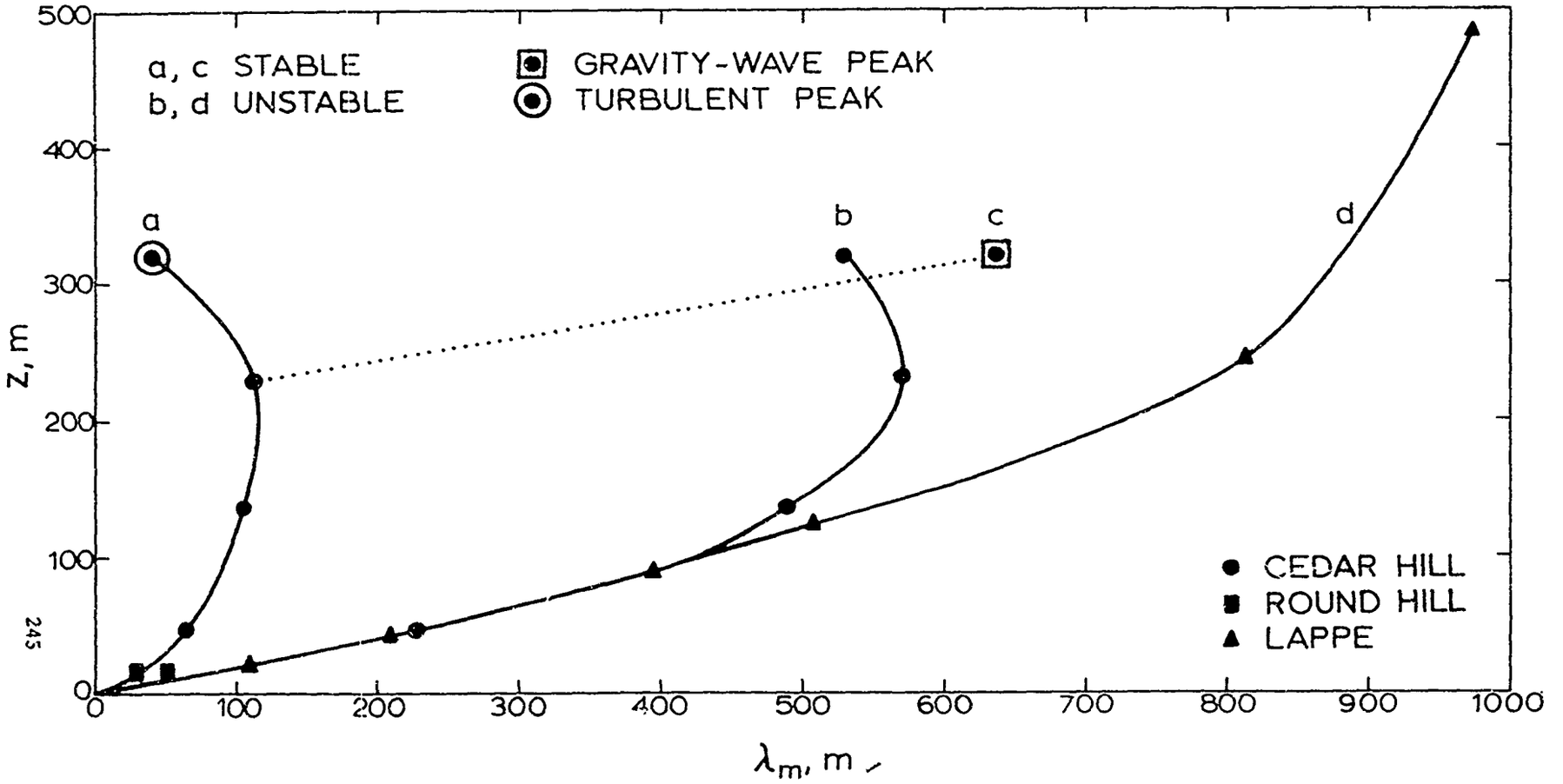

Variation of maximum wavelength of logarithmic vertical-velocity spectra

Figure 11

Figure 11 also shows the variation of peak wavelengths with height taken from Lumley and Panofsky (1964), based on airplane measurements made in unusually fast winds under the direction of Lappe et al. (1959). These observations were made in unstable air so that the resemblance between that curve and the corresponding curve for Cedar Hill below 50 m is not surprising. Exact equivalence above 50 m is not to be expected because the distribution of maximum wavelengths with height above the surface layer probably is governed by factors not considered here, such as the geostrophic wind and the Coriolis parameter (see Blackadar, 1962).

7. Spectra of the longitudinal wind component over land.

Spectra of the longitudinal wind component, even in the surface boundary layer, cannot be summarized as simply as those of the vertical component. Observations from many sites have already been brought together by Berman (1965), and the material under discussion here will not add significantly to his results, particularly since no such observations were made at Cedar Hill.

The high-frequency portions of the longitudinal spectra have already been discussed in section 4, where they were shown to be in good agreement with the postulates of the theory of the inertial subrange.

Figures 12-14 show smoothed, eye-average spectra of the longitudinal components under varying stability conditions at Round Hill, and Figure 15 indicates the same type of information for the spectra at Hanford. The results are quite confusing in that the spectra appear not only to vary with stability, but also with height, and even from one tower to the other at Round Hill.

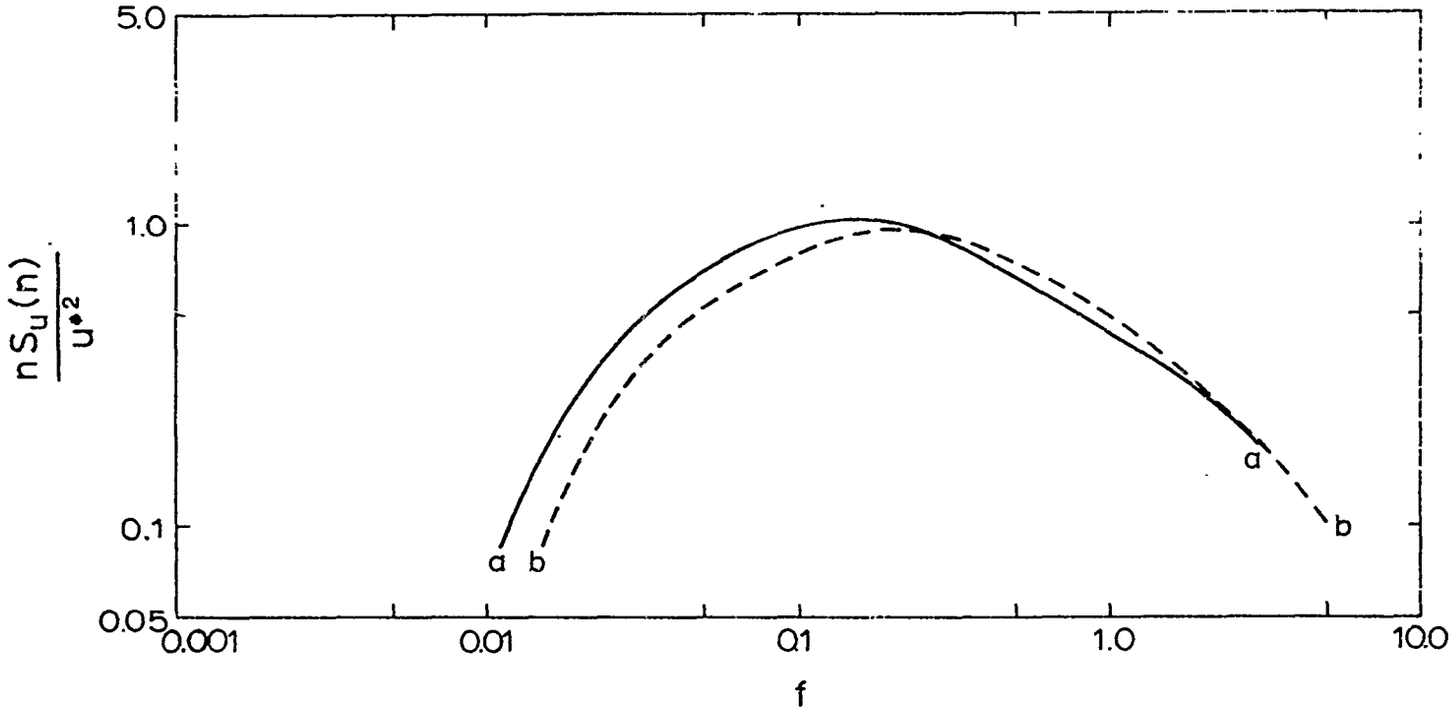

Smoothed and averaged spectra of longitudinal velocity in stable air at tower B, Round Hill. a: 46 m; b: 91 m

Figure 12.

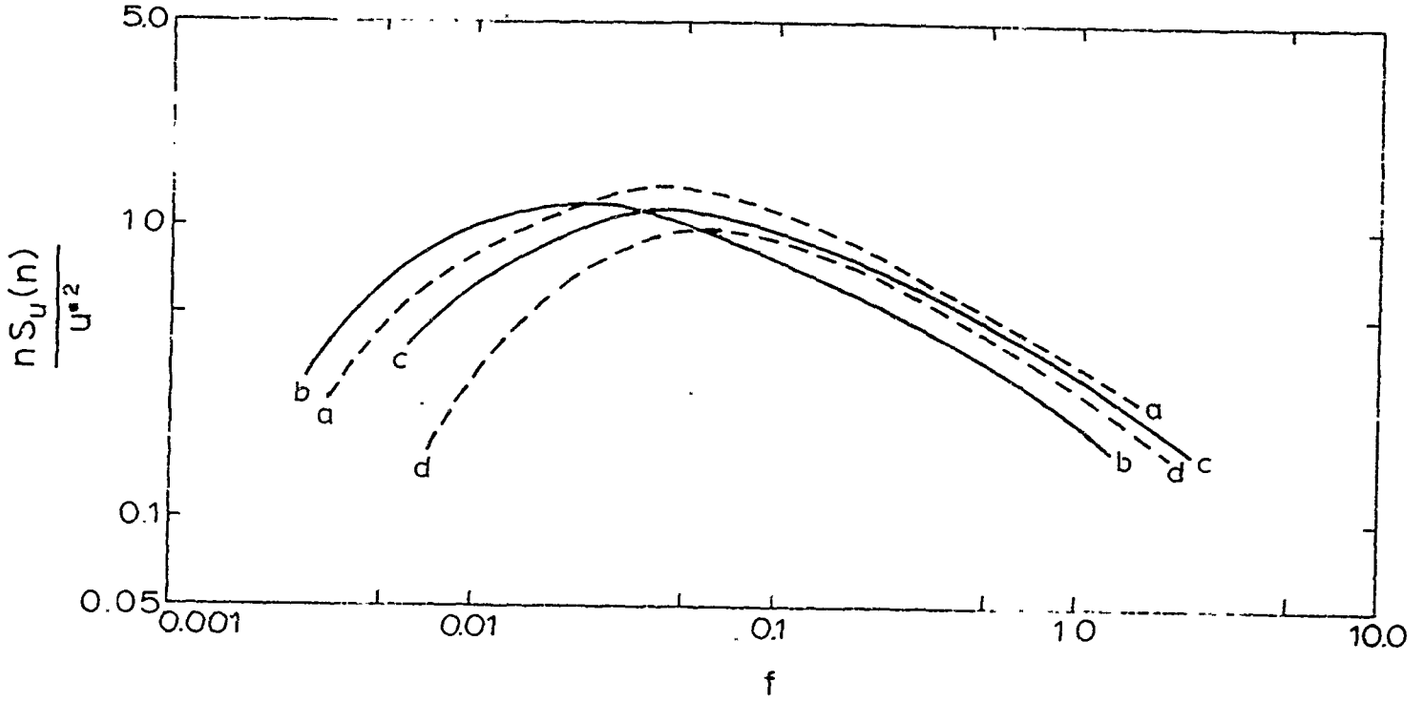

Smoothed and averaged spectra of longitudinal velocity in neutral air at Round Hill. a: 15 m, tower B; b: 16 m, tower A; c: 40 m, tower A; d: 46 m, tower B

Figure 13.

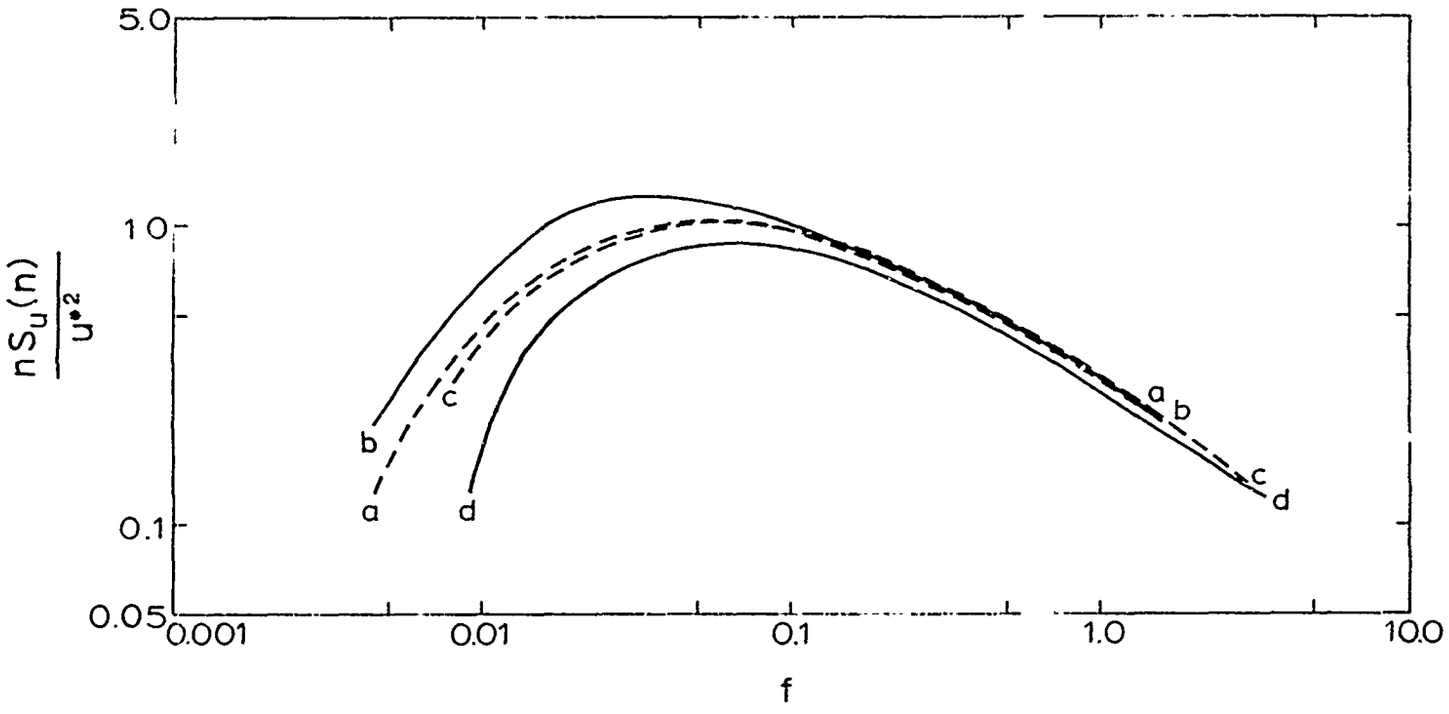

Smoothed and averaged spectra of longitudinal velocity in unstable air at Round Hill. a: 15 m, tower B; b: 16 m, tower A; c: 40 m, tower A; d: 46 m, tower B

Figure 14.

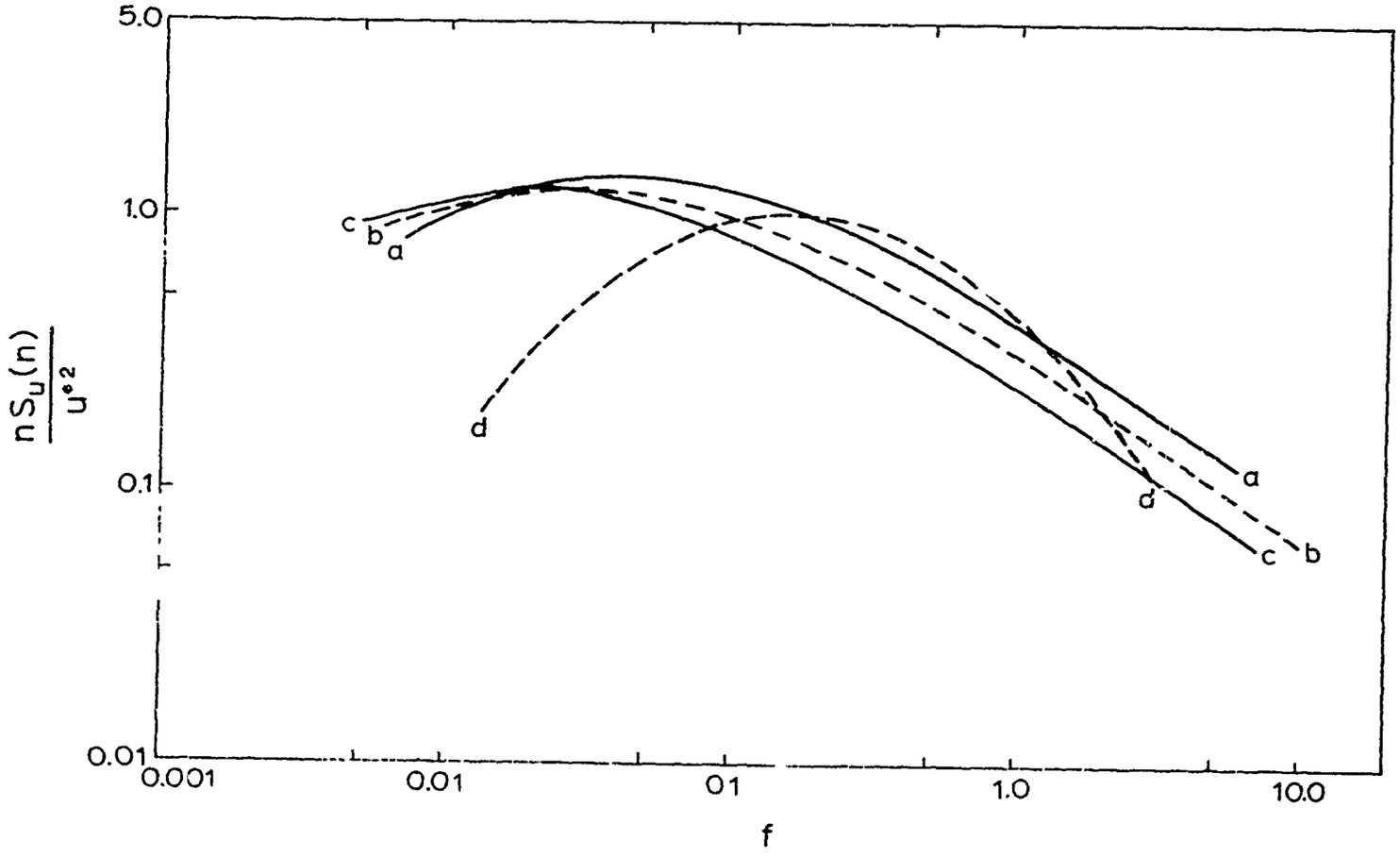

Figure 15. Smoothed and averaged spectra of longitudinal velocity at Hanford. a: stable; b: neutral; c: unstable; d: laboratory spectrum from Bradshaw (1967)

In order to make the effects of the various observing conditions clearer, Table 2 summarizes values of f_m for all plotted curves, and also compares them with estimates by Berman in neutral air. The table shows, primarily, that f_m increases with height at all locations, as it did for Berman's observations. This is an important way in which the longitudinal spectra disagree with similarity theory. The agreement between the new spectra and Berman's values of f_m is fair. The increase of the scale of turbulence with decreasing stability (which is usually reported) is just barely indicated by the present data.

There is, however, an unexplained difference between the present and Berman's nondimensional spectra: the numerical values of the ordinates of the present set average about 30% lower than Berman's. This difference may be due to inaccuracies of the stresses used to normalize Berman's data; in most cases, these stresses had to be estimated from rather uncertain drag coefficients.

A laboratory boundary layer spectrum of the u component from Bradshaw (1967) is also entered in Figure 15. Clearly, the low frequency portions of the u spectra vary strongly between sites and between atmosphere and laboratory, an indication of the failure of similarity at low frequencies.

Table 2. Characteristics of f_m in the u spectra.

	Hanford			Berman
Height	Stable	Neutral	Unstable	Neutral
3-6 m	.04	.03	.02	.02

	Tower A, Round Hill			Berman
Height	Stable	Neutral	Unstable	Neutral
16 m		.025	.04	.04
40 m		.04	.06	.08

	Tower B, Round Hill			Berman
Height	Stable	Neutral	Unstable	Neutral
15 m		.04	.06	.04
46 m	.15	.06	.06	.08
91 m	.20			.13

8. Comparison of spectra near the ground over land and sea.

Figure 16 compares longitudinal and vertical spectra over land and sea. All observations represent ~~neutral~~ unstable conditions. The land data come from Hanford and Round Hill and the water data from Vancouver. All curves are eye-averages over many individual runs.

The peak value of f for the vertical spectra over land and sea is nearly the same; but the "water" spectra are somewhat wider. The high-frequency portions of Smith's "water" spectra are probably unreliable, since they lead to an untenably high value of the universal constant in the inertial subrange; the uncertainty of these observations at high frequencies is further confirmed by R. W. Stewart (personal communication). However, there seems to be little doubt about the relatively large amount of energy at low frequencies in the over-water spectra.

A comparison of the longitudinal spectra over land and water also shows that the over-water spectra contain significantly more energy than the over-land spectra at low frequencies. The reasons for these differences are so far quite speculative. R. W. Stewart suggests that, over the sea, there exist large rolls with horizontal axes nearly parallel to the wind which drift slowly past the observer. There is some evidence for such rolls from the wind records.

Over land, these rolls should be generated also, but are either broken up or "frozen in" by the terrain. In either case, they would contribute no energy to the low-frequency longitudinal and vertical velocity fluctuations over land.

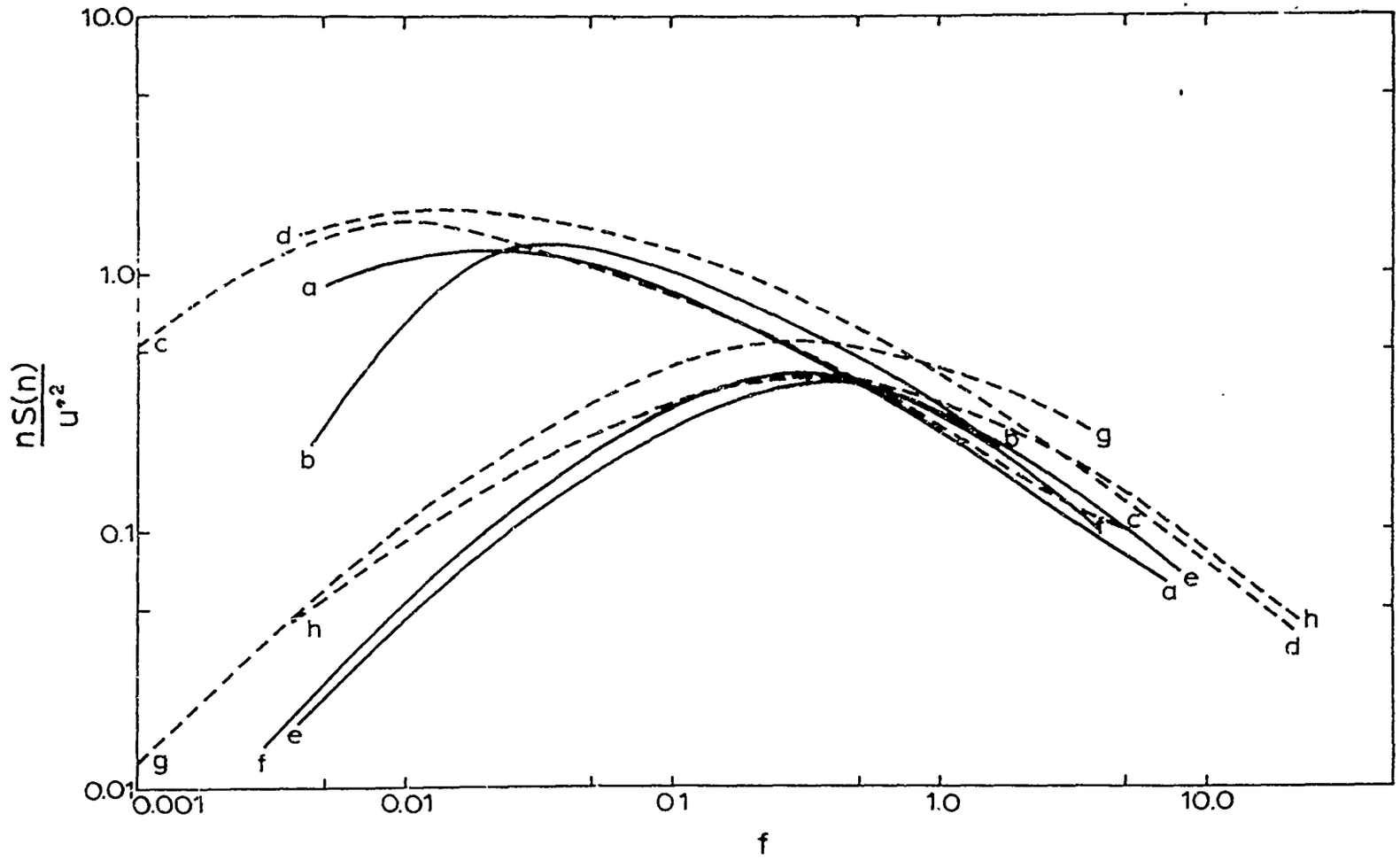

Comparison of spectra over land and sea. Longitudinal velocity, a: Hanford; b: Round Hill; c: over sea near Vancouver (Smith); d: over sea near Vancouver (Weiler and Burling). Vertical velocity, e: Hanford; f: Round Hill; g: over sea near Vancouver (Smith); h: over sea near Vancouver (Weiler and Burling)

Figure 16.

Concluding remarks

In summary, vertical-velocity spectra below 50 m obey similarity theory well (the normalized spectra varying only with z/L, but not with height or terrain), with a possible anomaly over water. Above 50 m, the spectra shift toward larger f = nz/V.

Longitudinal spectra do not obey similarity theory at low frequencies, a fact which also influences the behavior of the maximum of the spectra.

REFERENCES

Barad, M. L. and J. J. Fuquay (Ed.s), 1962: Geophys. Res. Paper No. 73, AFCRL-62-251(1), Hanford Doc. No. HW-71400-Vol. 1.

Berman, S., 1965: Quart. J. R. Met. Soc., 91, p. 302.

Blackadar, A. K., 1962: J. Geophys. Res., 67, p. 3095.

Bradshaw, P., 1967: Euromech Colloquium, Southampton, England, 1967.

Busch, N. E., 1967: (The influence of instrumental lag on estimates of energy dissipation from structure functions), to be published.

Cramer, H. E., F. A. Record, J. E. Tillman and H. C. Vaughan, 1961: Annual Report under Contract No. DA-36-039-SC-80209, Department of Meteorology, Mass. Inst. of Tech.

Elderkin, C. E., 1966: AEC Research and Development Report. BNWL-329, Battelle Memorial Institute/Pacific Northwest Laboratory, Hanford, Washington.

Gerhardt, J. R., W. S. Mitcham and A. W. Straiton, 1962: Proc. JRE, 50, 2263-2271.

Hess, G. D. and H. A. Panofsky, 1966: Quart. J. R. Met. Soc., 92, 277-280.

Kaimal, J., 1966: AFCRL Report No. AFCRL-66-542.

Kaimal, J. and Y. Izumi, 1965: J. Appl. Met., 4, p. 576.

Lappe, U. O., B. Davidson and C. B. Notess, 1959: Inst. Aero. Sci. Rep. No. 59-44.

Lumley, J. L., 1964: Journ. Atmos. Sci., 21, p. 99.

Lumley, J. L. and H. A. Panofsky, 1964: The Structure of Atmospheric Turbulence, Interscience Monographs and Texts in Physics and Astronomy, v. XII, John Wiley & Sons, New York, 239 + xi pp.

MacCready, Jr., P. B., T. B. Smith and M. A. Wolf, 1961: Final Report to Dugway Proving Ground, Contract DA-42-007-CML-504.

McVehil, G. E., 1964: Quart. J. R. Met. Soc., 90, 136-146.

Mordukhovich, M. I. and L. R. Tsvang, 1966: Izv. Acad. Nauk. Atm. and Ocean, 2, p. 786.

Panofsky, H. A., 1963: Quart. J. R. Met. Soc., 88, p. 85.

Pasquill, F. and H. E. Butler, 1964: Quart. J. R. Met. Soc., 90, 79-84.

REFERENCES (Continued)

Pond, S., S. D. Smith, P. E. Hamblin and R. W. Burling, 1966: J. Atmos. Sci., 23, 376-386.

Record, F. A. and H. E. Cramer, 1966: Quart. J. R. Met. Soc., 92, 519-532.

Smith, S. D., 1966: Bedford Inst. of Oceanography, Report-BIO-66-8. ~~(unpublished manuscript)~~.

Stevens, D. W. and J. R. Gerhardt, 1959: Bull. AMS, 40, 24-26.

Swinbank, W. C., 1964: Quart. J. R. Met. Soc., 89, 119-135.

Weiler, H. S. and R. W. Burling, 1967: To be published in Journ. Atmos. Sci.

BLANK PAGE

WIND VARIABILITY IN TIME AND SPACE

by

MANUEL ARMENDARIZ

and

VIRGIL D. LANG

ATMOSPHERIC SCIENCES LABORATORY
WHITE SANDS MISSILE RANGE, NEW MEXICO

ABSTRACT

Wind data gathered from three windmill-type anemometers arranged in a triangular array are compared for varying lag times and sample averaging intervals. The anemometers were placed 274 meters apart at the vertices of an equilateral triangle at a height of 19 meters, thus yielding time and space variability of wind in range and cross sense simultaneously. Included are the root mean square errors (RMSE) of direction and speed differences, tabulated values of the coefficients and exponents of an exponential equation fitted to the variability curves, and the spectrum and cross spectrum of the wind components.

INTRODUCTION

The purpose of this paper is to present the characteristics of wind variability as obtained from windmill-type anemometers mounted at a height of 19 meters above surface at the vertices of an equilateral triangle with sides of 274 meters.

Wind variability plays a major role in predicting the impact point of an unguided rocket or in predicting the diffusivity of the atmosphere. Several studies, mainly Beer et al. (1962), Hertz et al. (1965), Rachele (1962a,b), Rachele and Veith (1965), Karna et al. (1966), and Rachele and Armendariz (1967), on wind variability have been directed toward determining an optimum "simple sampling" of the wind at a given point which will best serve as a predictor for the wind at a point a given distance from the wind measurement and some time later. The term "simple sampling" means a wind averaged over a time interval. This time interval is designated in Figure 1 as Δt_1 which has various values extending from one second through 300 seconds. Delay time or lag time is depicted by Δt_2. The time interval used for verification of the wind which a rocket normally experiences in early flight is Δt_3. For the purpose of this paper Δt_3 is kept constant at 4 seconds. Wind calculated over the time interval Δt_1 at point A in Figure 1 is used as the predictor of the wind at point B a given distance away and at a later time. Differences in these wind directions and speeds are then used in the determination of the root mean square error for the wind vector.

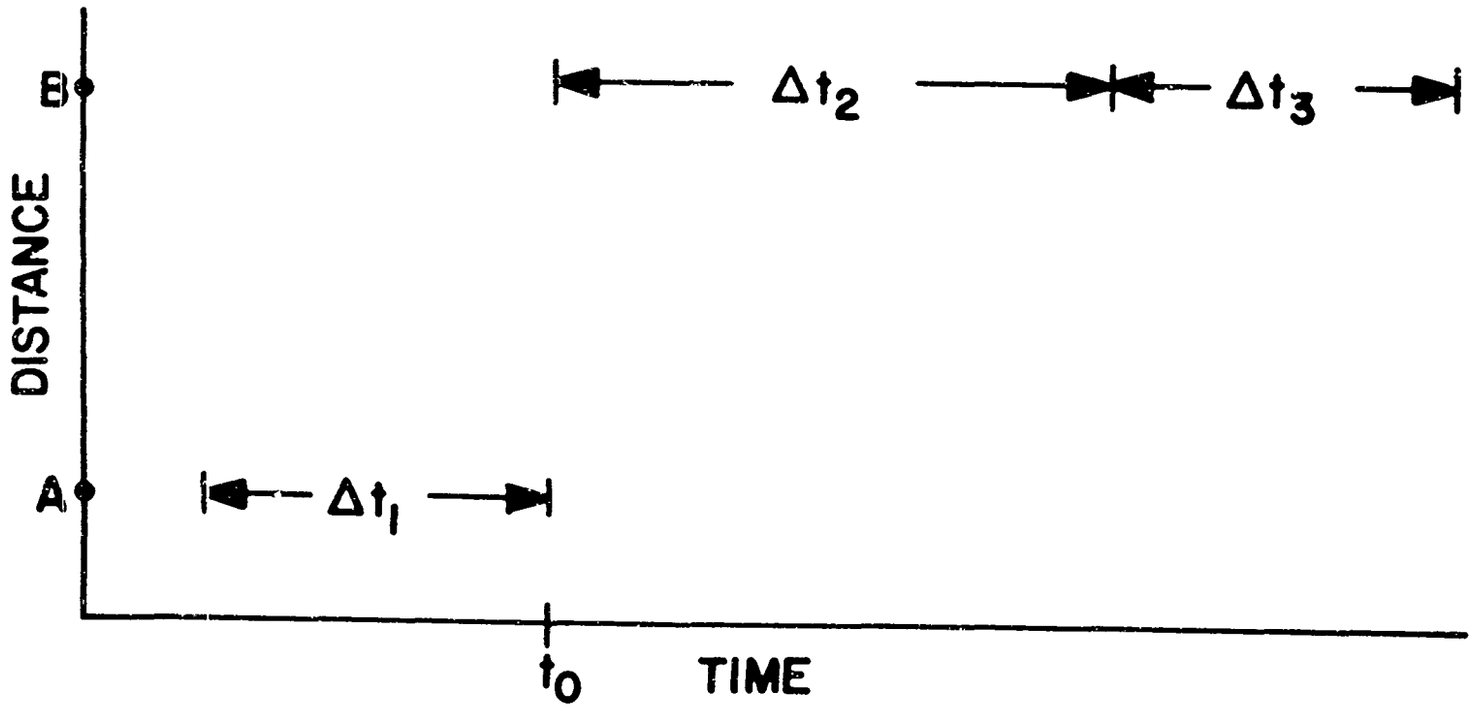

Fig. 1. Time designations: Simple sampling time (Δt_1), Lag time (Δt_2), Constant time period (Δt_3), and Nominal observational time (t_0).

Spectral analysis as well as visual observation indicated that the surface area was nonhomogeneous; however, results appear to substantiate Taylor's hypothesis. Root mean square error (RMSE) of direction differences was 10 to 20 degrees, depending on the averaging interval used when wind measurements were made along the mean wind flow, increasing to 18-25 degrees when the wind measurements were made perpendicular to the flow. The RMSE of the wind speed differences was 0.9 to 1.8 m sec^{-1} when wind measurements were along the mean flow and 1.6 to 2.2 m sec^{-1} when perpendicular to the mean flow.

Moreover, an exponential equation of the form RMSE = $a\Delta t_2^b$ was fitted to the wind data. Numerical ranges for the coefficient were 6.2 to 17.3 for direction and 1.02 to 2.64 for speed, while limiting values of the exponent were 0.01 to 0.20 and 0.01 to 0.16 for direction and speed, respectively.

SITE DESCRIPTION

White Sands Missile Range is located almost entirely within the Tularosa Basin of southcentral New Mexico. The major axis of the Basin extends northward from El Paso, Texas, approximately 215 kilometers. The Basin width is approximately 65 kilometers and elevations range from 1.2 to 1.5 kilometers MSL.

The data collection site is located in the southern extremity of the missile range. The typical terrain of the area consists of

randomly distributed hillocks or sand dunes approximately one to three meters in height sparsely covered with mesquite, greasewood, pigweed, various varieties of cacti and other desert plants.

One wind sensing instrument, designated as A_5 is located at the tower site, and another instrument, designated as T_2, is located on a pole which is 275 meters from the tower. These are situated in typical terrain with the recorder located in a building near the tower which borders on a line between A_5 and T_2. Approximate dimensions of the building are 7 x 10 x 4 meters. The third instrument, P_1, is located near the Honest John launch complex which consists of a concrete surfaced area, launcher, and various buildings which are about 200 meters to the south.

DISCUSSION AND RESULTS

Wind data were collected from the triangular array for three stability regimes in hour periods. Five one-hour observations were made. Two of the observations were made under forced convection conditions, i.e., Richardson number (Ri) approximately -0.02 and two others during free convection conditions (Ri = -0.10). The fifth observation was made under neutral conditions (Ri = 0). The wind data were collected on Esterline Angus recorders and visually read for one-second intervals at each site.

The mean wind direction was computed; from this value a decision was made as to which instrument was to be used as the predictor for the wind for downwind, crosswind, against the wind or at a point for comparison purposes. The root mean square error of the wind direction or speed differences was used as a measure of the wind variability. Symbolically,

$$RMSE = \sqrt{\frac{1}{N}\sum_{i=1}^{N}(D-\bar{D})^2},$$

where D is wind direction or speed difference between poles and/or at the same pole, but separated timewise. The bar indicates an average.

One complete set of graphs for a given stability regime is presented here. The general characteristics of the curves were similar for the other stability regimes with the differences reflected in the tables depicting the slope and intercept of an exponential fit to the data points.

The inset at the lower right hand side of Figures 2 through 9 depicts the general array of the wind sensors. The mean wind for the April data was from the wind sensor at P_1 to T_2 at 5.2 m sec^{-1}. P_1 is used as the predictor except when predicting against the wind, in which case T_2 is the predictor.

Figure 2 depicts the wind direction dispersion as a function of lag time and averaging interval at P_1. It can be seen that if the lag time is less than 60 seconds, an instantaneous (noted here as a 1-second observation) wind measurement indicates less dispersion than most of the longer samples. This is in agreement with Woodall's (1966) interpretation of the data from the United Aircraft Weather System Center. However, if the lag time is greater than 60 seconds, then a longer sampling interval yields the lesser variability which is in agreement with Rachele and Armendariz (1967). Moreover, the major part of the dispersion occurs in the first 120 seconds. This suggests that if variability is to be minimized, one must keep the lag time well below 120 seconds. Of equal importance, Figure 3 shows that the variability of wind speed has the same general characteristics as the wind direction, i.e., a sharp rise in variability up to a lag time of 120 seconds, and thence a leveling off or undulating trace.

Figures 4 and 5 depict the wind direction and speed variability from pole P_1 to T_2, i.e., along the mean wind flow. Since we have a distance separation (274 meters) as well as time, it is noted that an instantaneous reading at pole P_1 does not give a better estimate of the wind at T_2 than the longer sampling interval. It appears that a 60-second sampling interval provides a better prediction than any other sampling interval up to an approximate lag of 60 seconds, and

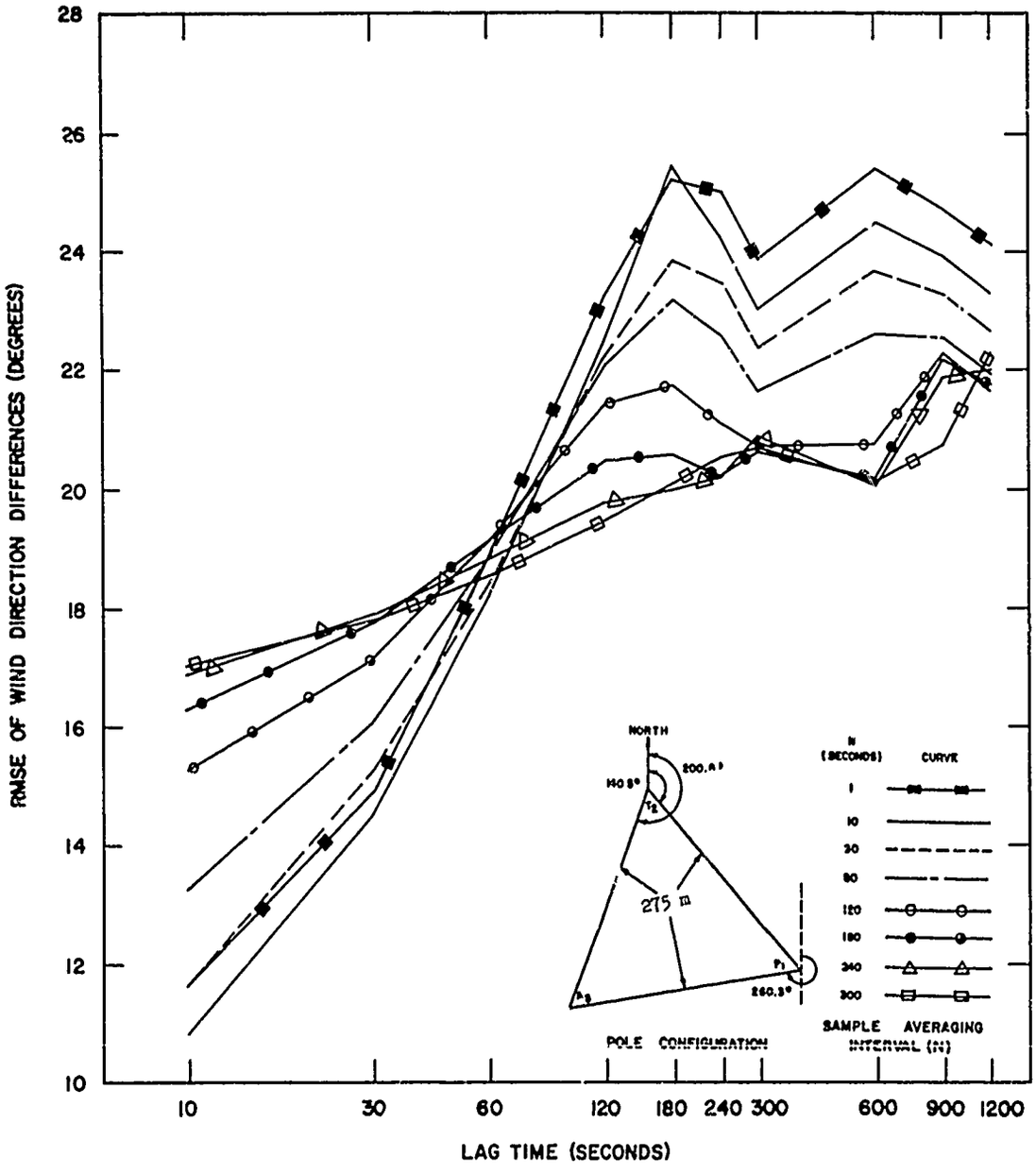

Fig. 2. Wind direction dispersion for location P_1 for varied sampling intervals and lag times. Mean wind velocity and instrumental height were 140 degrees 5.1 mps and 19 meters above the surface. Richardson number was approximately -0.1 (Free convection regime). Winds were gathered at White Sands Missile Range from 1400 to 1500 local time 28 April 1966.

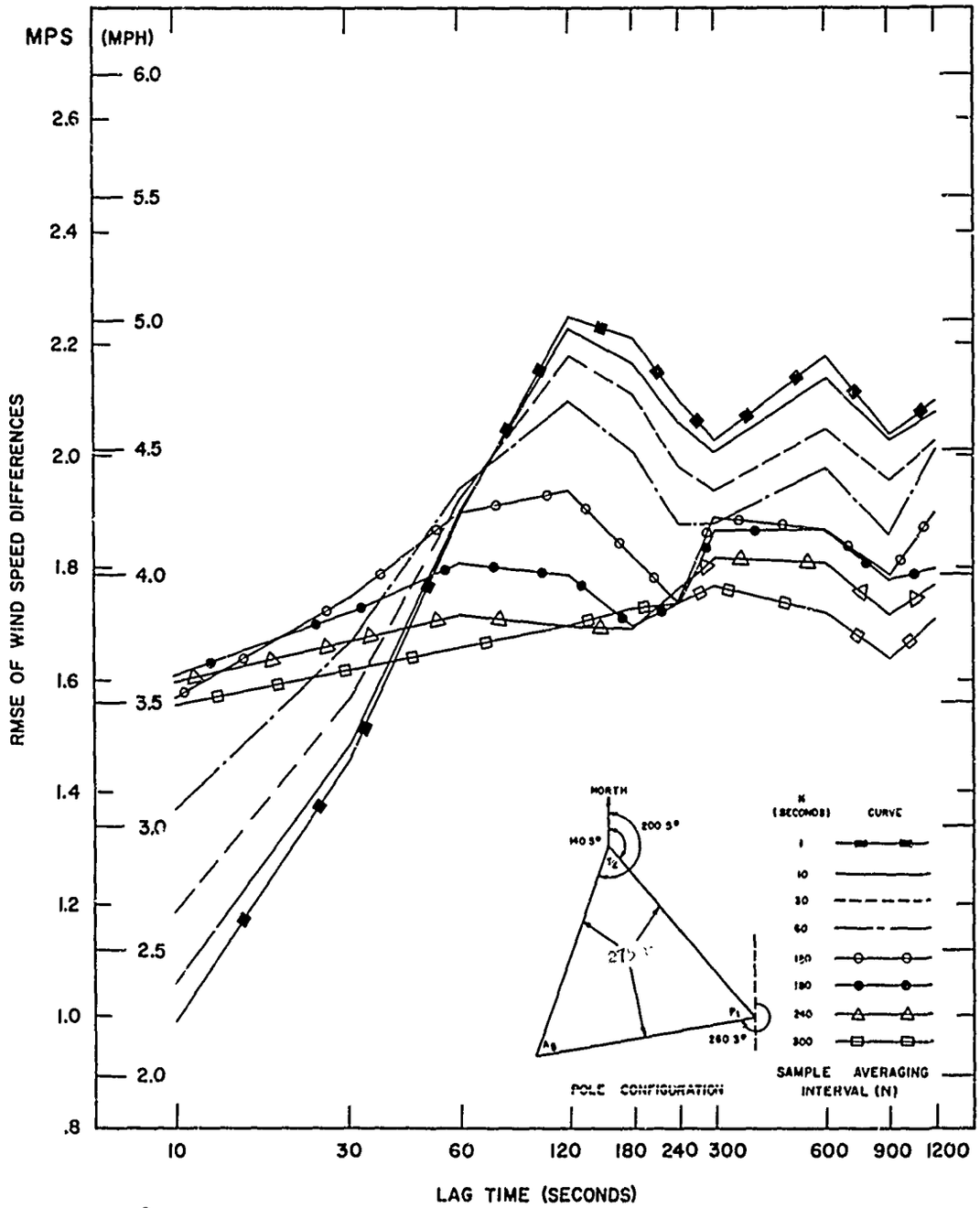

Fig. 3. Wind speed dispersion for location P_1 for varied sampling intervals and lag times. Mean wind velocity and instrumental height were 140 degrees 5.1 mps and 19 meters above the surface. Richardson number was approximately -0.1 (Free convection regime). Winds were gathered at White Sands Missile Range from 1400 to 1500 local time 28 April 1966.

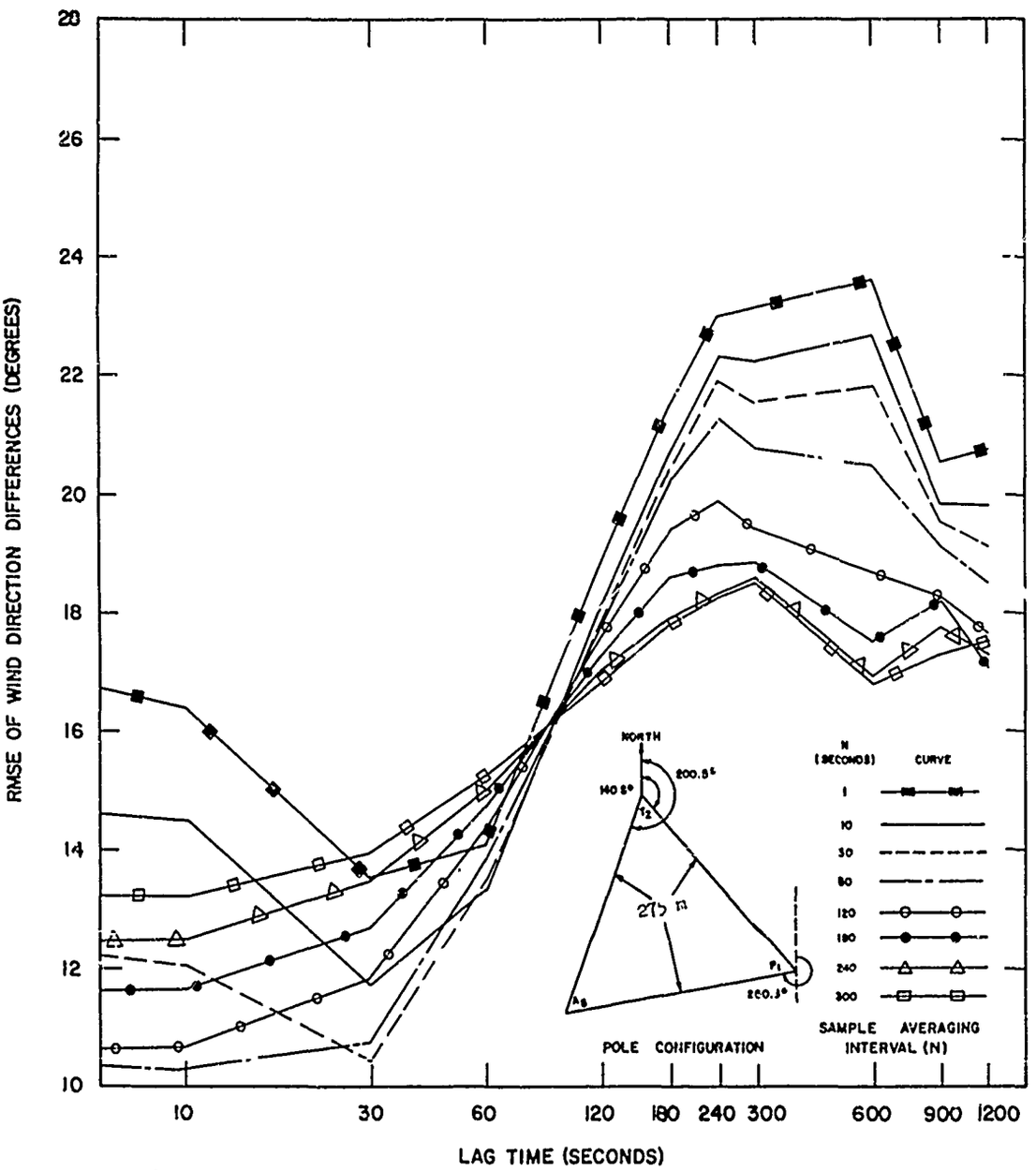

Fig. 4. Wind direction dispersion from location P_1 to location T_2 for varied sampling intervals and lag times. Mean wind velocity and instrumental height were 140 degrees 5.1 mps and 19 meters above the surface. Richardson number was approximately -0.1 (Free convection regime). Winds were gathered at White Sands Missile Range from 1400 to 1500 local time 28 April 1966.

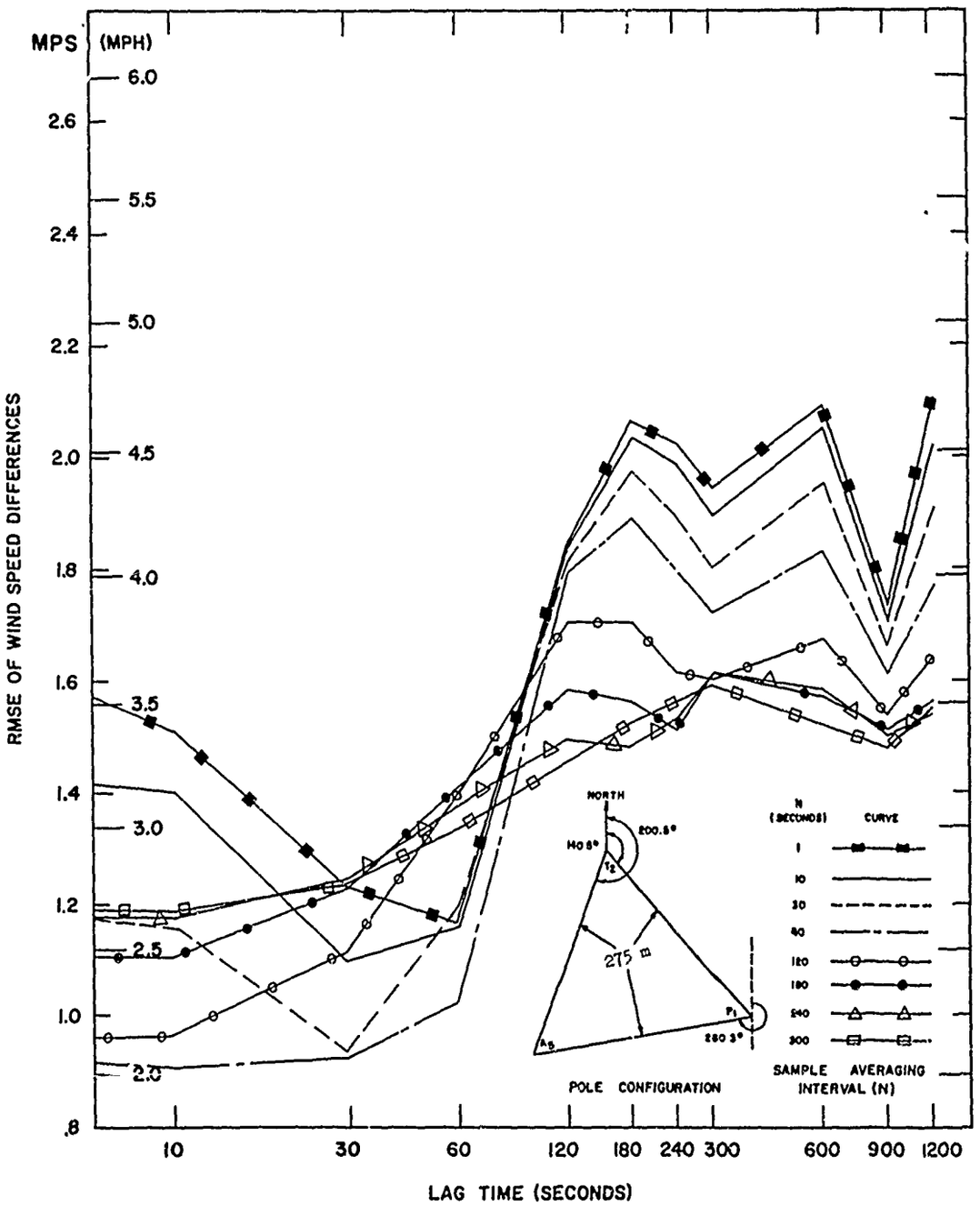

Fig. 5. Wind speed dispersion from location P_1 to location T_2 for varied sampling intervals and lag times. Mean wind velocity and instrumental height were 140 degrees 5.1 mps and 19 meters above the surface. Richardson number was approximately -0.1 (Free convection regime). Winds were gathered at White Sands Missile Range from 1400 to 1500 local time 28 April 1966.

thence the longer sampling interval of 240 or 300 seconds. Moreover, from Figures 2 to 5 it can be seen that the variability of the wind, in general, is less when predicting downwind than when the prediction is made at a point.

Figures 6 and 7 show the variability of wind when the prediction is made nearly perpendicular to the mean wind flow. It is noted that the slope of the lines for the first 120 seconds is much less than for the previous figures, indicating that the wind variability is more dependent on distance than time when predicting for a point almost perpendicular to the flow.

In Figures 8 and 9, we again see the dependence of the variability of wind on distance since the slope of the lines is relatively flat when compared to Figures 2 through 5.

In general, the best results, i.e., less variability, are found when predicting downwind as Taylor (1938) found. If we fit a least-squares line to the curves in the different figures we find that a simple exponential equation will yield a reasonable estimate of the variability. The type of equation fitted to the curves in this study was taken after Arnold and Bellucci (1957), and Bellucci (1960); that is:

$$RMSE = a\Delta t_2^b$$

where t_2 = lag time

a = intercept

b = slope.

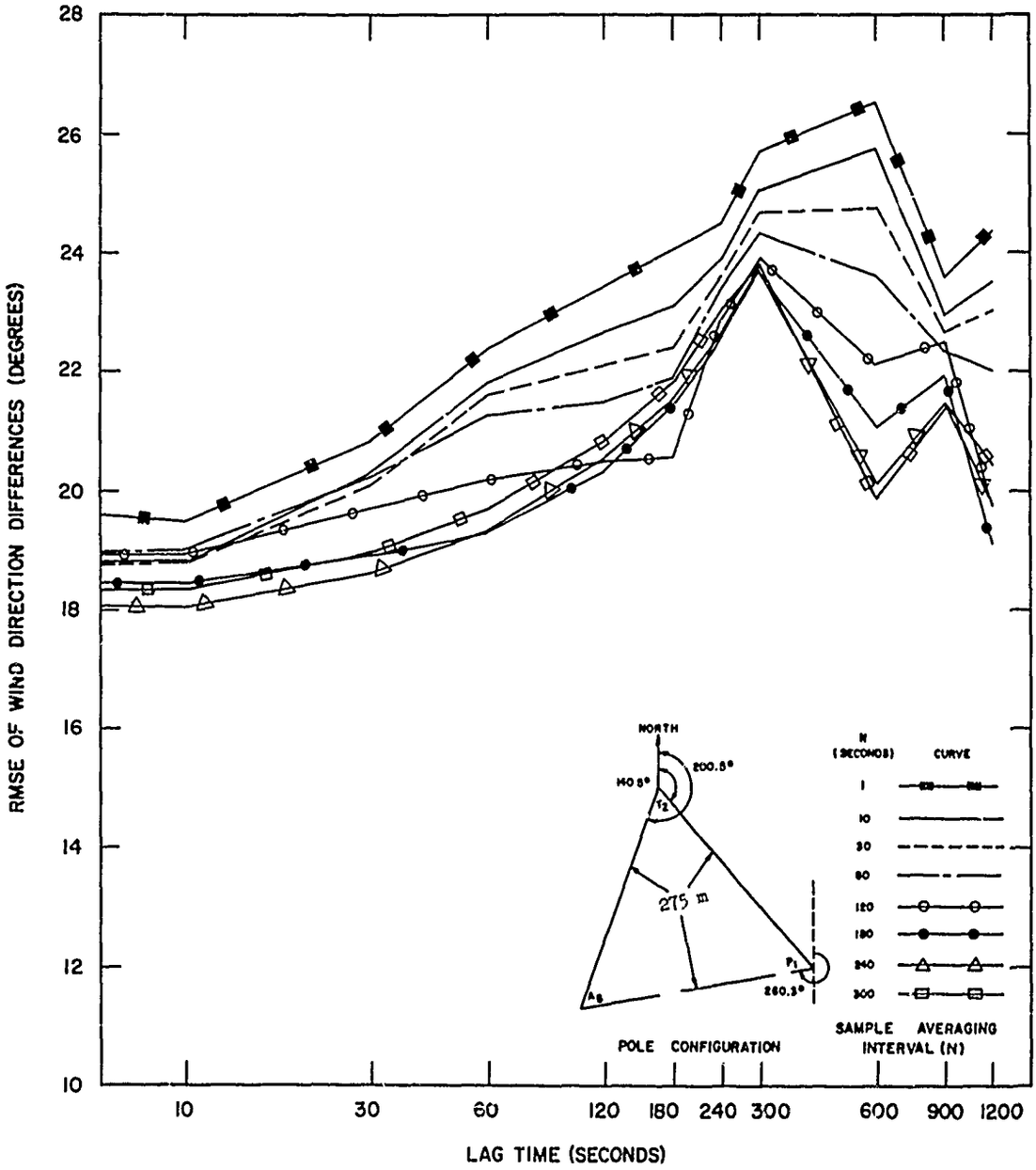

Fig. 6. Wind direction dispersion from location P_1 to location A_5 for varied sampling intervals and lag times. Mean wind velocity and instrumental height were 140 degrees 5.1 mps and 19 meters above the surface. Richardson number was approximately -0.1 (Free convection regime). Winds were gathered at White Sands Missile Range from 1400 to 1500 local time 28 April 1966.

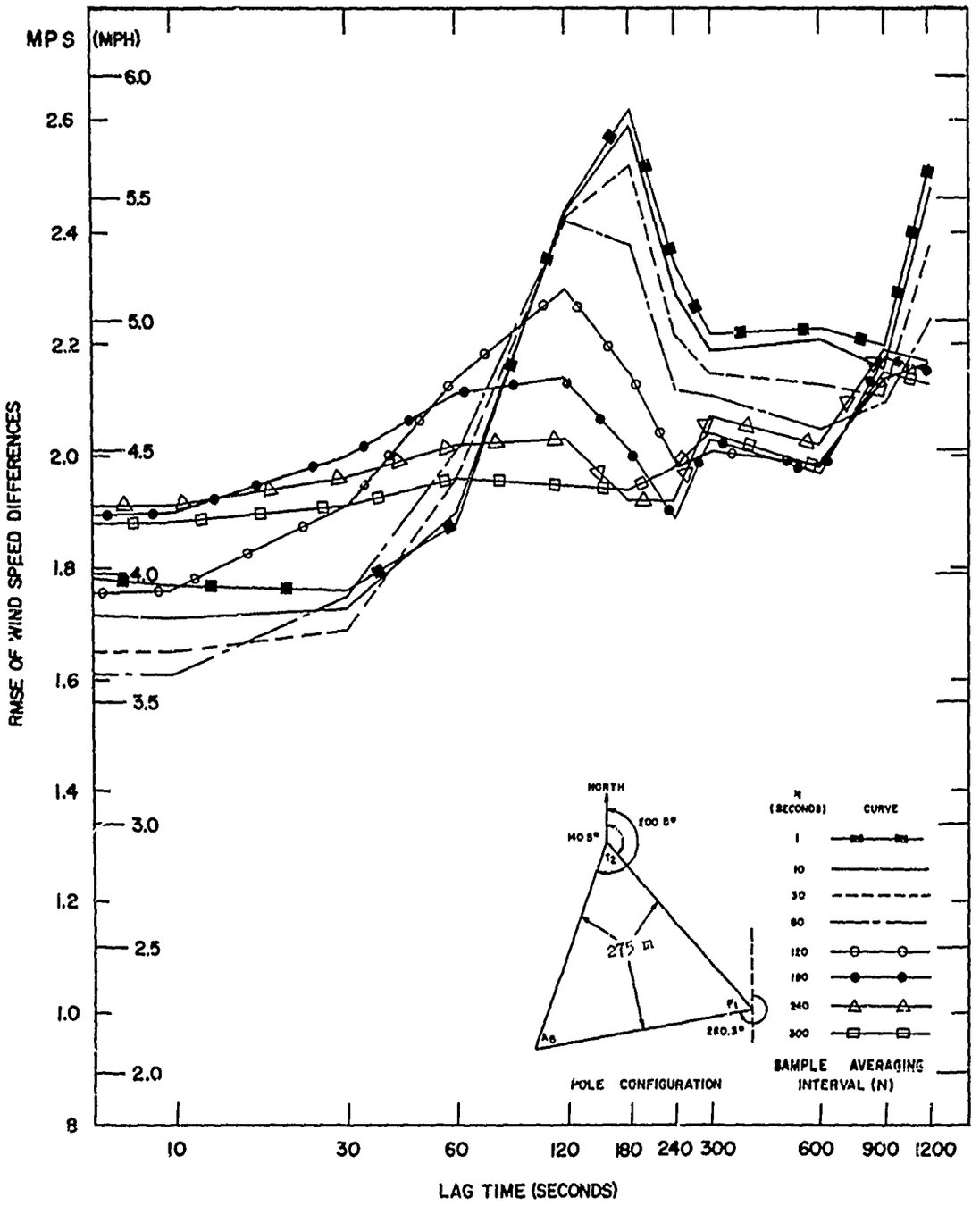

Fig. 7. Wind speed dispersion from location P_1 to location A_5 for varied sampling intervals and lag times. Mean wind velocity and instrumental height were 140 degrees 5.1 mps and 19 meters above the surface. Richardson number was approximately -0.1 (Free convection regime). Winds were gathered at White Sands Missile Range from 1400 to 1500 local time 28 April 1966.

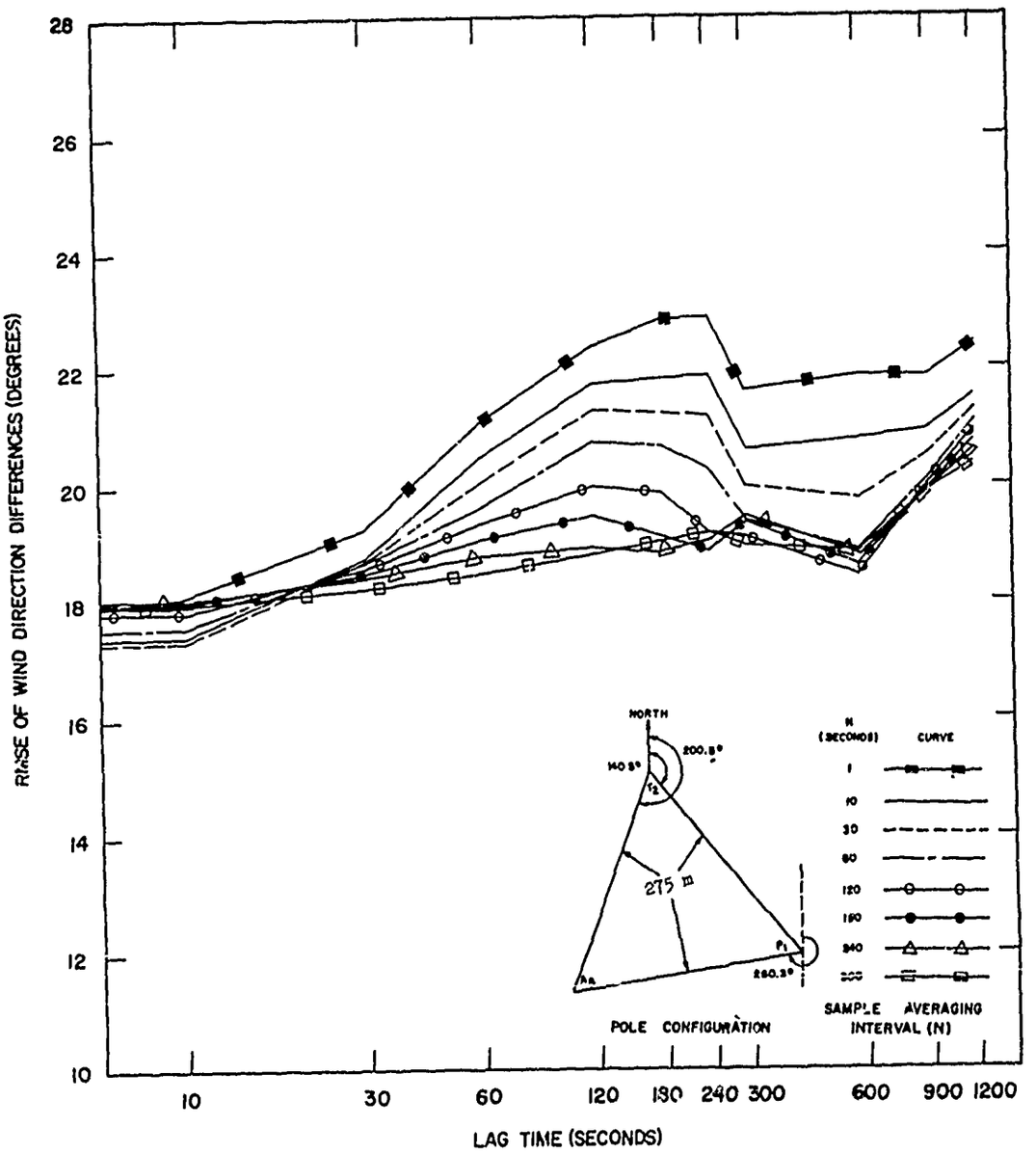

Fig. 8. Wind direction dispersion from location T_2 to location P_1 for varied sampling intervals and lag times. Mean wind velocity and instrumental height were 140 degrees 5.1 mps and 19 meters above the surface. Richardson number was approximately -0.1 (Free convection regime). Winds were gathered at White Sands Missile Range from 1400 to 1500 local time 28 April 1966.

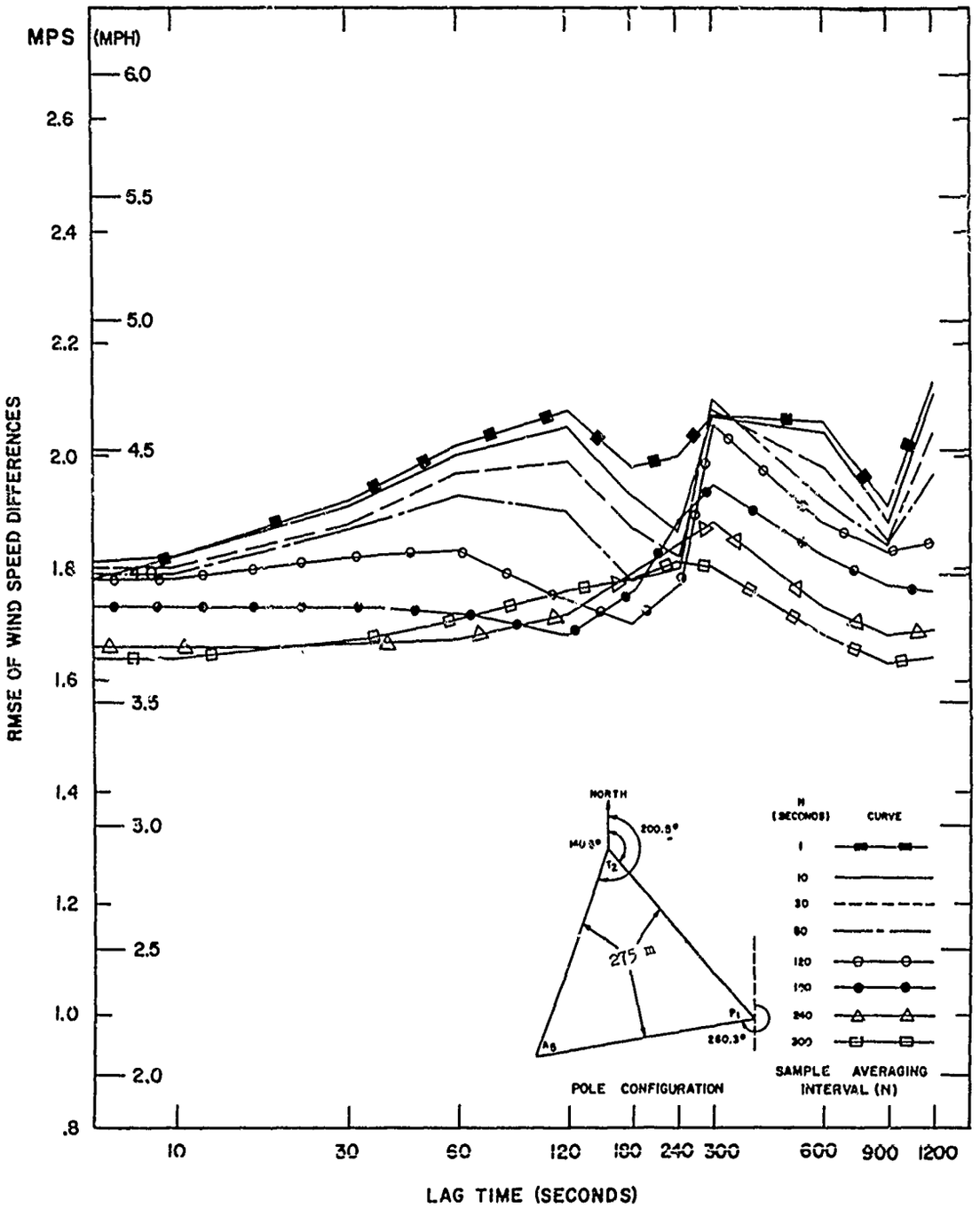

Fig. 9. Wind speed dispersion from location T_2 to location P_1 for varied sampling intervals and lag times. Mean wind velocity and instrumental height were 140 degrees 5.1 mps and 19 meters above the surface. Richardson number was approximately -0.1 (Free convection regime) Winds were gathered at White Sands Missile Range from 1400 to 1500 local time 28 April 1966.

Arnold et al. (1957), using existing upper wind data, made estimates of a and b, concluding that a reasonable value for b was 0.5 both for time and space variability, and a was approximately 1.2 m sec^{-1} for time variability, and 1.5 m sec^{-1} for space. Lenhard et al. (1963) concluded that the value for b should be 0.5; however, a was dependent on wind speed.

From Tables I and II one can see that the values of a and b for the given observations do not necessarily reflect any set pattern in relation to the stability regimes or wind speed. This may be because the mean wind direction was different for each observation, thus giving a different roughness length. The combination of different mean wind speeds, roughness lengths, and stabilities probably masks the effect of any given one of the parameters on a and b. It can be stated that if the sampling interval is increased from 1 to 300 seconds, b becomes smaller indicating less variability with lag time. Moreover, the values of b are generally much less than 0.25 as shown from the double theodolite balloon data analyzed by Bellucci (1960). This may be caused by instrumental, human, reduction, and self-induced balloon oscillation errors which would tend to distort the values of wind variability. It is also recognized that wind measurements with fixed instruments possess certain errors; however, these errors should be generally smaller than those in the double theodolite system.

TABLE I TENTATIVE VALUES OF a AND b FOR DIRECTION

	S.I.	$\bar{V}$	WIND IS SINGLE POINT a	b	ALONG a	b	AGAINST a	b	PERPENDICULAR a	b
Neutral										
9 Feb. 66	1 sec.	11.5	6.6	0.08	8.8	0.06	10.3	0.04	8.5	0.04
	300 sec		6.2	0.03	8.0	0.03	6.7	0.03	6.2	0.04
Forced Convection										
7 Feb. 66	1 sec	9.0	12.0	0.06	11.8	0.08	15.6	0.03	13.0	0.06
10 Feb. 66	1 sec	7.0	9.5	0.08	11.6	0.07	16.1	0.02	12.0	0.05
7 Feb. 66	300 sec		11.3	0.01	13.0	0.02	12.0	0.01	11.2	0.01
10 Feb. 66	300 sec		9.1	0.05	10.7	0.06	10.0	0.05	10.1	0.05
Free Convection										
21 Mar. 66	1 sec	10.0	9.2	0.11	10.0	0.10	15.1	0.04	15.1	0.03
28 Apr. 66	1 sec	5.7	7.9	0.20	11.8	0.09	17.3	0.04	16.3	0.08
21 Mar. 66	300 sec		10.4	0.04	12.1	0.03	11.2	0.03	10.3	0.03
28 Apr. 66	300 sec		15.3	0.05	11.9	0.07	17.3	0.02	16.0	0.05

$\bar{V}$ = mean wind speed (m sec^{-1}) S.I. = Sampling Interval

TABLE II TENTATIVE VALUES OF a AND b FOR SPEED

	S.I.	SINGLE POINT		WIND IS ALONG		AGAINST		PERPENDICULAR	
		a	b	a	b	a	b	a	b
Neutral									
9 Feb. 66	1 sec.	1.78	0.08	1.88	0.05	2.19	0.03	2.07	0.03
	300 sec	1.81	0.03	1.46	0.04	1.92	0.01	1.51	0.02
Forced Convection									
7 Feb. 66	1 sec.	1.97	0.13	2.36	0.07	2.40	0.06	2.29	0.04
10 Feb 66	1 sec	1.04	0.14	1.40	0.06	1.83	0.01	1.34	0.08
7 Feb. 66	300 sec.	2.53	0.04	1.92	0.04	2.64	0.03	1.89	0.04
10 Feb. 66	300 sec.	1.50	0.03	1.02	0.08	1.64	0.01	1.14	0.06
Free Convection									
21 Mar. 66	1 sec.	1.73	0.14	1.48	0.14	2.08	0.09	2.04	0.07
28 Apr. 66	1 sec	1.11	0.16	1.06	0.09	1.85	0.01	1.41	0.10
21 Mar. 66	300 sec.	2.43	0.03	2.12	0.02	2.60	0.01	2.13	0.02
28 Apr. 66	300 sec.	1.45	0.04	1.05	0.07	1.54	0.03	1.80	0.02

Figures 10 and 11 are the lateral spectra and cospectra of the April wind data. The lateral spectra indicate that the instruments were not necessarily in a homogeneous environment. The cospectra show less energy when correlations are made between poles which are along the mean flow i.e., P_1 to T_2, than when the wind is perpendicular to the poles. This substantiates Taylor's (1938) hypothesis although the area in which the data were collected is not homogeneous. Moreover, the coherence indicates that only the low frequencies, i.e., .005 cycles second^{-1} or lower, can be correlated with any degree of certainty. For example, on the wind data for April, the coherence drops from 0.78 at a frequency of 0.0017 cycles second^{-1} to 0.68 at 0.005 cycles sec^{-1}, and thence to 0.04 at 0.17 cycles second^{-1}. This is in agreement with Singer et al. (1961), and Davenport (1961), who analyzed the correlation between wind speed at different levels in terms of horizontal eddy sizes, indicating that the smaller the eddys the less correlation. Only two papers have dealt with horizontal correlation near the surface of the ground as reported by Lumley and Panofsky (1964); these are, one by Obukhov (1951), which deals with atmospheric turbulence in the inertial subrange, and Panofsky (1962), which deals with the scales of wind components at a height of 2 meters over smooth terrain, mainly at O'Neill, Nebraska. Panofsky also found a rapid drop in the coherence as a function of decreasing eddy size.

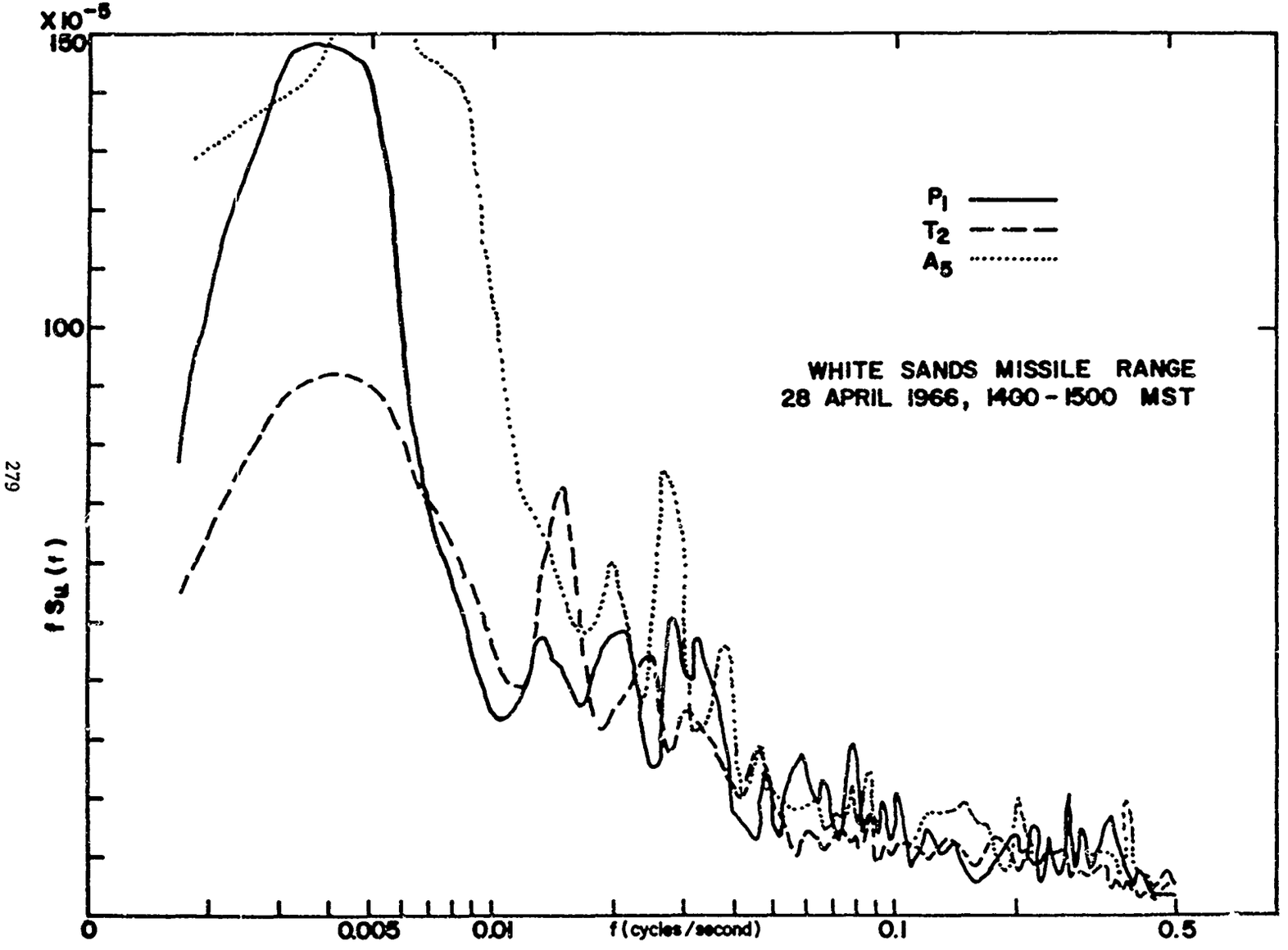

FIG. 10. LATERAL SPECTRA OF THE WIND AT EACH SITE.

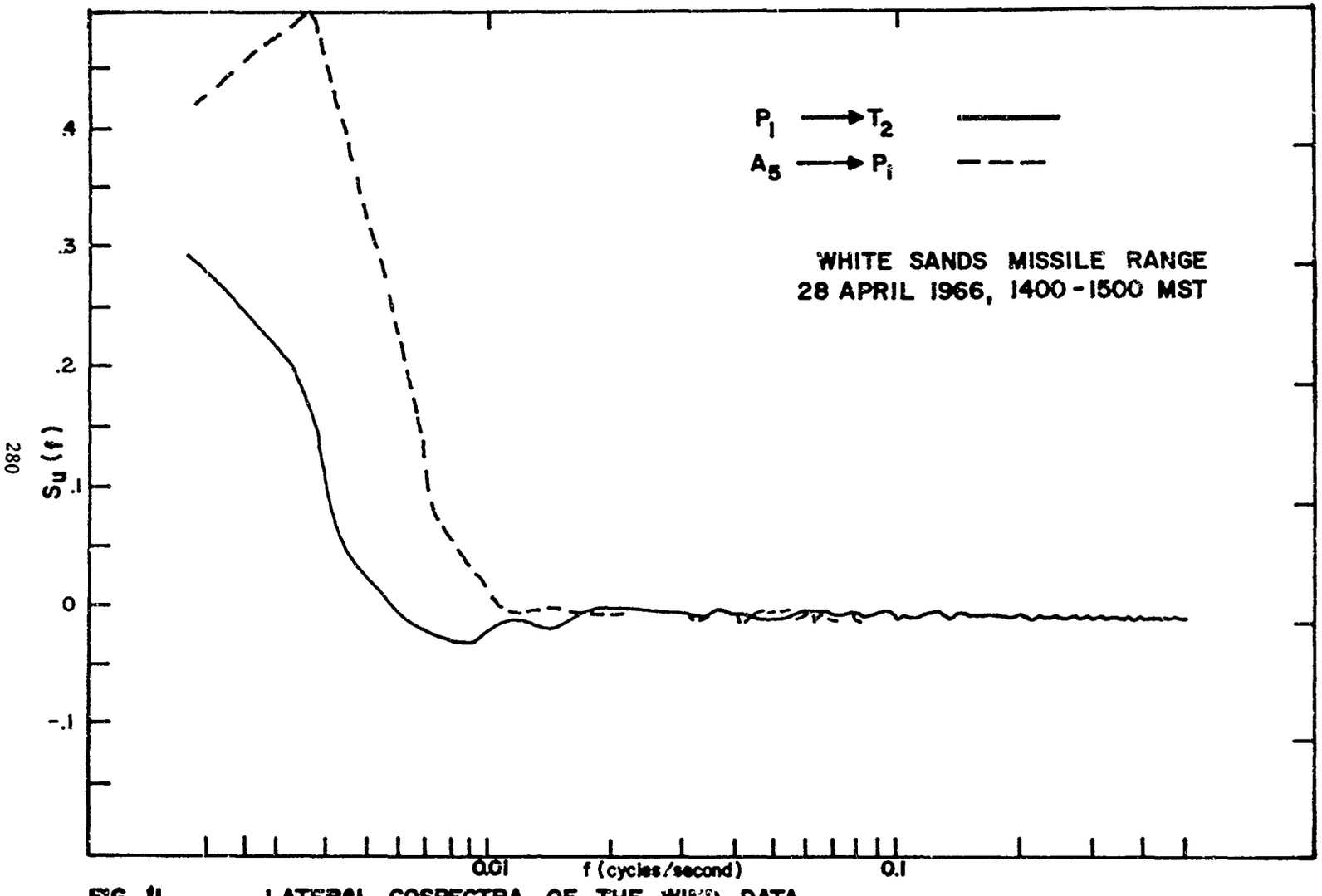

FIG. 11. LATERAL COSPECTRA OF THE WIND DATA.

CONCLUSION

It is concluded that to minimize wind variability one must have instruments which will insure that the data are readily available, keeping the delay time between measurement and usage to a minimum, preferably under 60 seconds. For lag times less than 60 seconds, an averaged wind over approximately 60 seconds will yield better results, i.e., less variability, when distance and time are involved; however, an instantaneous reading is best when predicting at the same point the measurement is made. In general, a longer sampling interval is best when the delay time exceeds 60 seconds.

The coherence between poles separated by 274 meters at White Sands Missile Range drops quite rapidly, indicating the lack of coherence for frequencies higher than approximately .005 cycles second^{-1}. Moreover, using a proper sampling interval will enhance the results obtained when predicting downwind.

REFERENCES

Arnold, A., and R. Bellucci, 1957: "Variability of Ballistic Meteorological Parameters," U. S. Army Signal Engineering Laboratories, Ft. Monmouth, N.J., 27 pp. (copies available through DDC).

Beer, F.P., and Robert G. Sarubbi, 1962: "The Determination of the Atmospheric Parameters Influencing the Trajectory of Free Rockets," Institute of Research, Lehigh University, Bethlehem, Pa., 16 pp.

Bellucci, Raymond L., 1960: "Preliminary Estimates of Variability of Winds in the Lowest 500 Feet," U. S. Army Signal Research and Development Laboratory, Fort Monmouth, New Jersey, 20 pp.

Davenport, A. G., 1961: "The Spectrum of Horizontal Gustiness near the Ground in High Winds," Quart. J. Roy Meteor. Soc. 87, 194.

Hertz, John A., and F. P. Beer, 1965: "A Simplified Approach to the Extrapolation of Nonstationary Random Processes," Lehigh University, Bethlehem, Pa., 28 pp.

Karna, Chetan L., J. A. Hertz, and F. P. Beer, 1966: "Extrapolation in Time of the Response of Free Rockets to Random Stationary Wind Velocity Profiles," Institute of Research, Lehigh University, Bethlehem, Pa., 19 pp.

Lenhard, R. W., Arnold Court, and Henry Salmela, 1963: "Variability Shown by Hourly Soundings," J. Appl. Meteor., 2, 99-104.

Lumley, John L., and Hans A. Panofsky, 1964: The Structure of Atmospheric Turbulence, New York, John Wiley and Sons, 190-191.

Obukhov, A. M., 1951: "Investigation of the Microstructure of the Wind in the Atmosphere near the Surface," Izvestia ANSSR Geophys. Ser. 1951, No. 3, 49.

Panofsky, H. A., 1962: "Scale Analysis of Atmospheric Turbulence at 2 Meters," Quart. J. Roy. Meteor. Soc., 88, 57.

Rachele, Henry, 1962a: "Surface Wind Sampling Periods for Unguided Rocket Impact Prediction," MM-458, U.S. Army Electronics Research and Development Activity, White Sands Missile Range, New Mexico, 30 pp. (copies available through DDC).

Rachele, Henry, 1962b: "Surface Wind Model for Unguided Rockets Using Spectrum and Cross Spectrum Techniques," U. S. Army Electronics Research and Development Activity, White Sands Missile Range, New Mexico, 24 pp. (copies available through DDC).

Rachele, Henry, and Daniel R. Veith, 1965: "Surface Wind Sampling for Unguided Rocket Impact Prediction," ERDA-255, U. S. Army Electronics Research and Development Activity, White Sands Missile Range, New Mexico, 54 pp. (copies available through DDC).

Rachele, Henry, and Manuel Armendariz, 1967: "Surface Wind Sampling for Unguided Rocket Impact Prediction," J. Appl. Meteor., 6, 516-518.

Singer, I. A., and Constance M. Nagle, 1961: "A Study of the Wind Profile in the Lowest 400 Feet of the Atmosphere," Progress Rep. No. 8, Contract No. R-65-8-99812 SC-04-91, Brookhaven National Laboratory, 21 pp.

Taylor, G.I., 1938: "The Spectrum of Turbulence," Proc. Roy. Soc., A164, 476.

Woodall, Merle P., 1966: "On the Concept of a Weather Observation," Bull Amer. Meteor. Soc., 47 No. 2, 111-113.

WIND PROFILES AND SHEAR DERIVED FROM SMOKE TRAILS

by

MANUEL ARMENDARIZ

and

LAURENCE J. RIDER

ATMOSPHERIC SCIENCES LABORATORY
WHITE SANDS MISSILE RANGE, NEW MEXICO

and

GERALD C. GILL
UNIVERSITY OF MICHIGAN

ABSTRACT

Simultaneous smoke trails from rockets launched 900 feet apart are examined for space and time variability and shear. The maximum height of the profile was 3000 feet and the minimum approximately 600 feet. Spacewise results obtained indicate that wind speed differences are generally less than 2.0 ft sec^{-1} and direction differences less than 5.0 degrees, except that under light wind conditions the direction differences were much larger. Timewise, wind variability was generally less than 2.0 ft sec^{-1} and 5.0 degrees for time lags up to 36 seconds.

Wind shear calculated from these profiles substantiates the exponential relationship between the shear and layer thickness previously found at White Sands Missile Range and Cape Kennedy. The value of the exponent, 0.57 for the mean shear and 0.35 for the mean maximum shear, agrees with previous findings.

INTRODUCTION

Detailed and accurate wind profiles to heights of 3000 feet above the ground are virtually nonexistent. Anemometers placed on tower structures have yielded wind data to approximately 1500 feet. However, there is a lack of mobility of these towers, they are costly, and winds resulting from these structure are subject to a sheltering effect (see Gill et al. 1966, Cermak and Horn, 1968).

The tracking of balloons with sophisticated instrumentation such as the FPS 16 (see Scoggins 1962) or cinetheodolite (see Armendariz et al., 1966) has resulted in detailed wind profiles to the heights desired, i.e., 3000 feet or higher. These wind profiles include various errors such as self-induced balloon oscillations (see Armendariz and Rachele 1967, Scoggins 1964, 1965 and Mac Cready, 1965) instrumental noise, and failure of the balloon to respond adequately to wind shears. Moreover, the wind profile obtained is not necessarily a vertical profile over a point since the balloon necessarily drifts with the wind. Also, in computing wind shear from these wind data, it is recognized that a time differential exists for any scale of shear interval used. That is, the wind shear reported is a function of the shear interval and the time it took the balloon to pass through the layer.

In May 1966, the Atmospheric Sciences Office at White Sands Missile Range undertook a study of obtaining the wind profile to 3000 feet above the ground utilizing smoke trail techniques. A contract

was awarded the University of Michigan and on 19 December 1966 a series of rocket firings was made at White Sands Missile Range.

The purpose of this paper is to show the resulting wind profiles and wind shear for two smoke trails generated and photographed simultaneously. The smoke trails were initially 900 feet apart. Photographs of the smoke trails were taken every 2.0 seconds after the rocket was fired. The rocket used for these firings was the Cricket, which is fully described in previous reports by Gill et al. (1963, 1967). Moreover, the techniques and/or equipment used to generate the smoke trails and to reduce the data are adequately described in papers by Tolefson et al. (1961), Cooke (1962), and Gill et al. (1967) who cite wind accuracies at any given point as approximately $\pm$ 0.2 ft sec^{-1} when position data is used for time intervals over 6 seconds. The site where the smoke trails were generated is relatively flat as can be seen from Figure 1.

DISCUSSION

Figure 1 depicts the smoke trail photographed at discrete time intervals to emphasize the changes in the profile. In the 0 sec frame the smoke trail has not reached its maximum height, but by the 6 sec frame the trail is up to 3200 feet. Differentiation of lateral and longitudinal components between frames at specific heights yields the wind velocity at each height used. It was noted from careful examination of the different frames that the smoke trail could be picked up

Figure 1. Smoke trails obtained at White Sands Missile Range, New Mexico. December 19, 1966 at 0900 MST.

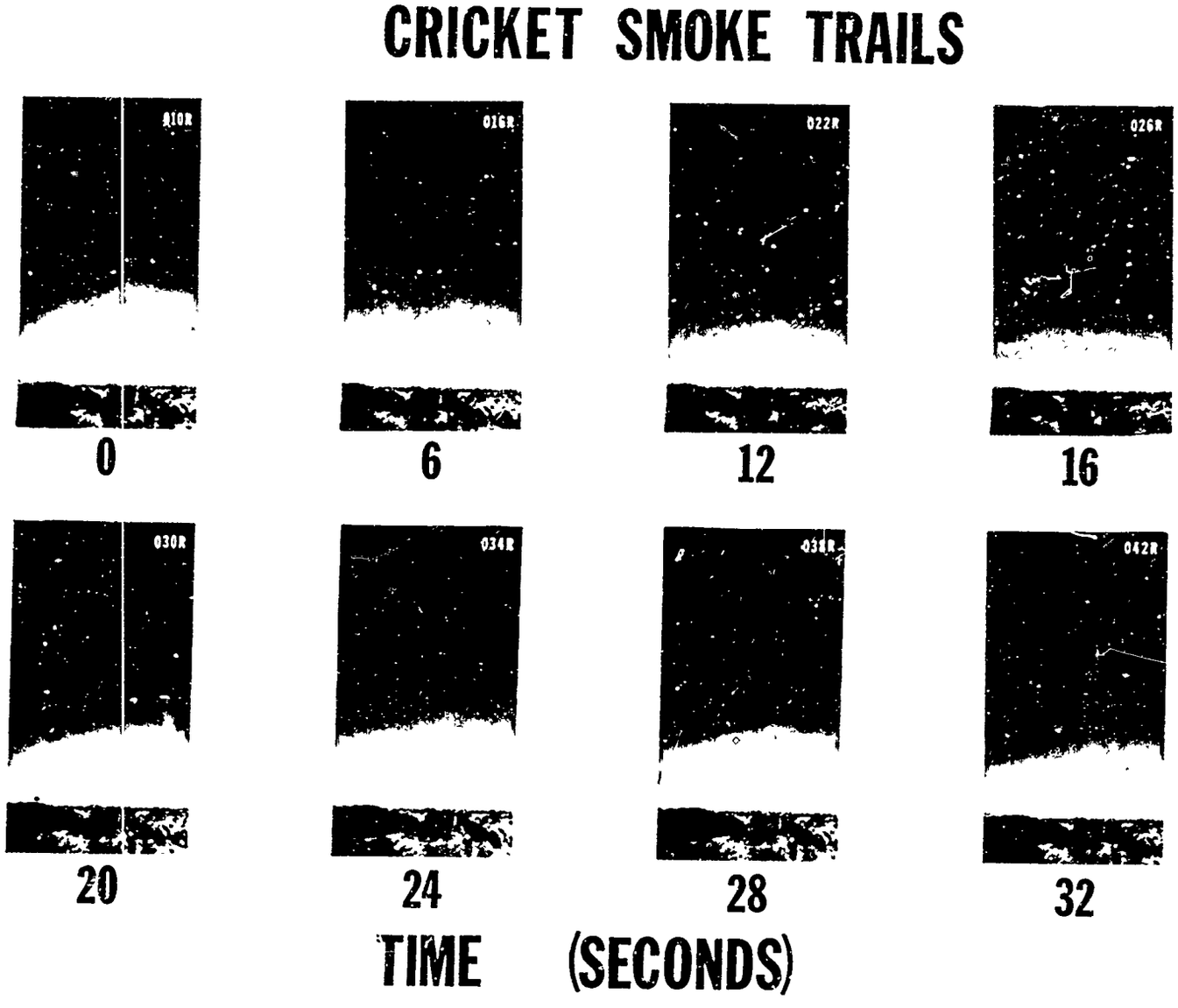

as low as 50 feet above the ground at the beginning but because of the turbulent structure of the lower atmosphere 15 seconds later it was visible only from 500 feet up. Also it can be seen that the two trails in the first frame (0 time) are 900 feet apart and in the successive frames are drifting apart particularly near the shear which is seen at approximately 2000 feet above the ground.

Figure 2 shows the wind profiles as computed from the two smoke trails. Each profile was generated by differentiating the point measurements of the lateral and longitudinal components each 200 feet in height for time intervals from 3 to 9 seconds, 9 to 15 seconds, 15 to 27 seconds and 27 to 51 seconds. Data reduction was purposely geared to read the position data at 200 feet height intervals. The wind components were than transformed to wind direction and speed and assigned to the mid-time interval, i.e., the data for the profile from 3 to 9 seconds was assigned a time of t_o+3, t_o time being 3 seconds after the rocket was fired and the data from 9 to 15 seconds was t_o+9. It can be seen that both profiles show the same general characteristics with slight deviations in speed generally less than 2.0 ft sec^{-1} and 5.0 degrees. These deviations are probably due to the distance separation of the profiles. The first profile at t_o+3 shows large deviations in the wind velocity. The profile at t_o was not clearly visible in the photograph as can be seen from Figure 1 and as a consequence position data, in this case, would not be as accurate as in the other frames.

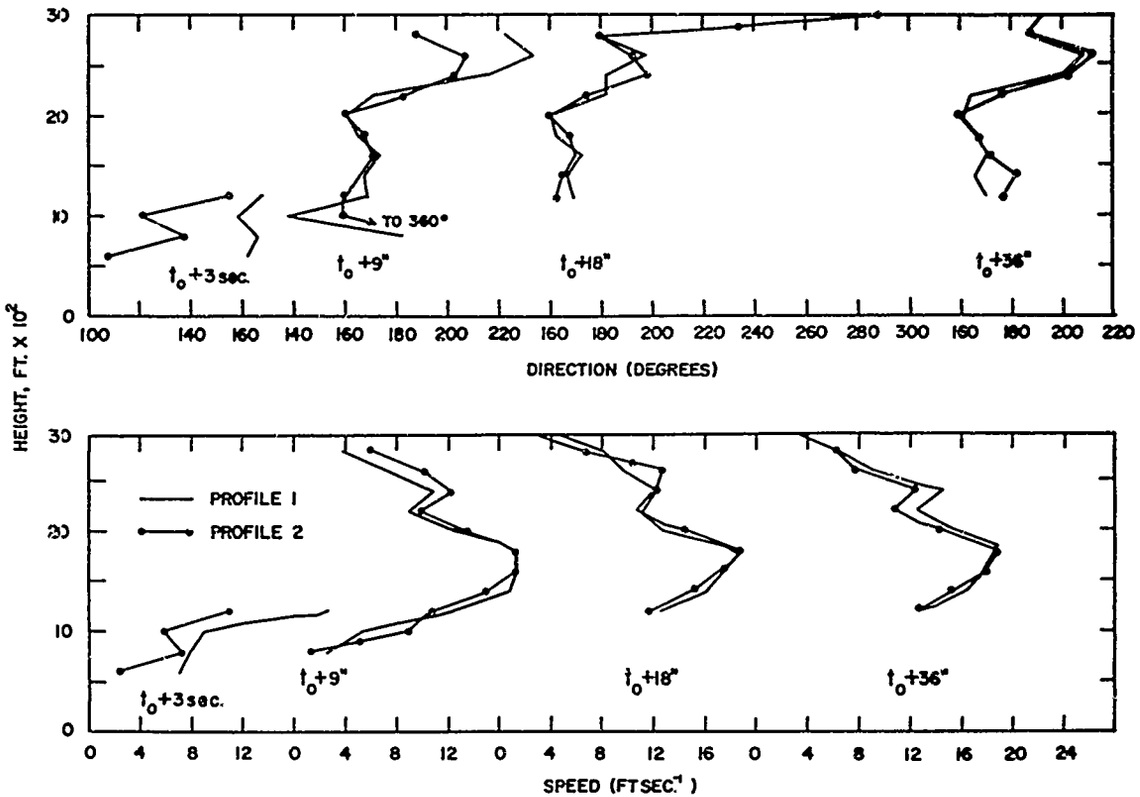

FIGURE 2. DISTANCE VARIATION OF WIND PROFILES DERIVED FROM SMOKE TRAILS AT TWO LOCATIONS SEPARATED BY 900 FEET AT WHITE SANDS MISSILE RANGE. DEC.19,1966,0900 MST.

The large wind shear which is visible in Figure 1 can easily be seen in Figure 2 at a height of approximately 2000 feet where the wind direction shifts from southeast to southwest and the speed decreases.

Again in Figure 3 we note the similarity of the wind profiles timewise and distancewise It can be seen that deviations in the profiles timewise are of the same order of magnitude as the viations due to distance.

The magnitude of the vector shear (γ) was calculated from the profiles,

where γ = the difference in wind velocity at two levels and has units of ft sec^{-1},

It was found that there was no significant difference in γ between the two profiles with the exception that Profile 2 generally showed slightly less shear than Profile 1. For example, the shear for a 200-foot layer was 4.2 ft sec^{-1} for Profile 1 and 3.8 ft sec^{-1} for Profile 2 for a difference of 0.4 ft sec^{-1} for the 200-foot layer. The 800-foot layer shear showed a difference of 1.2 ft sec^{-1}. Maximum shears calculated ranged from 9.8 ft sec^{-1} for the 200-foot layer to 18.8 ft sec^{-1} for the 1000-foot layer. The mean maximum vector shear and the mean vector shear ($\bar{\gamma}$) are plotted as a function of layer thickness in Figure 4. A least squares line is drawn to the data points substantiating previous findings by Essenwanger (1963), Essenwanger and Billions (1965), and Armendariz and Rider (1966) who determined that an

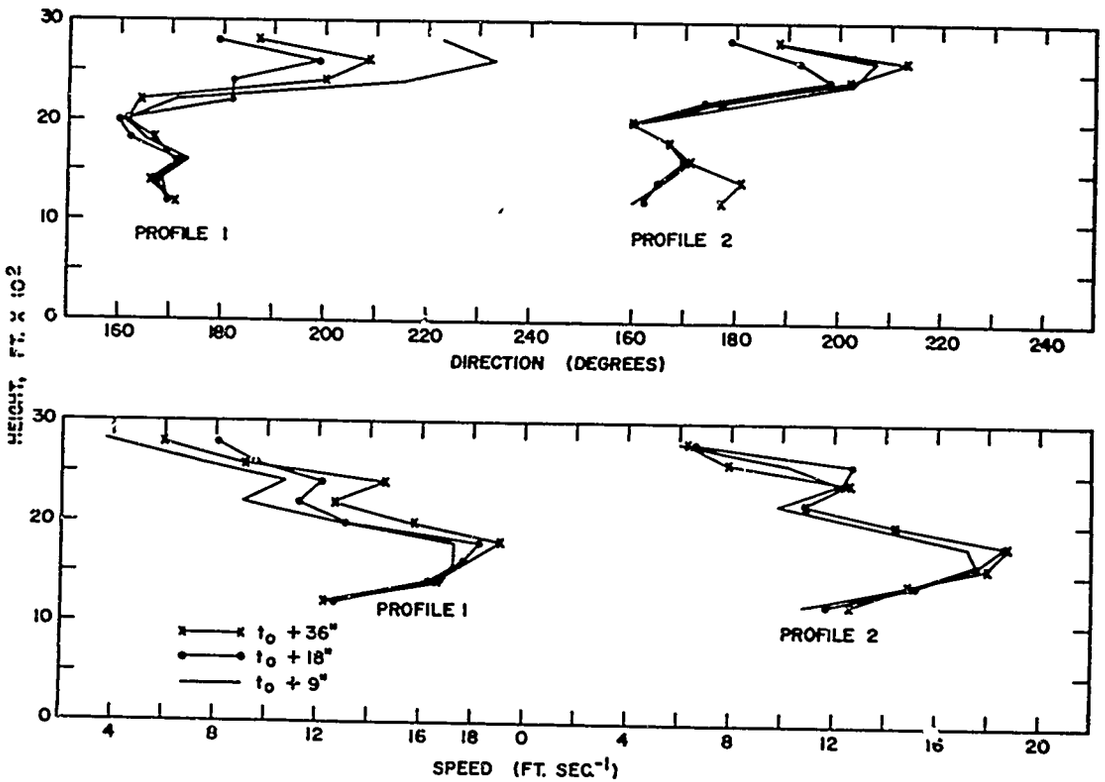

FIGURE 3. TIME VARIATION OF WIND PROFILES DERIVED FROM SMOKE TRAILS AT TWO LOCATIONS SEPARATED BY 900 FEET AT WHITE SANDS MISSILE RANGE. DEC. 19, 1966, 0900 MST.

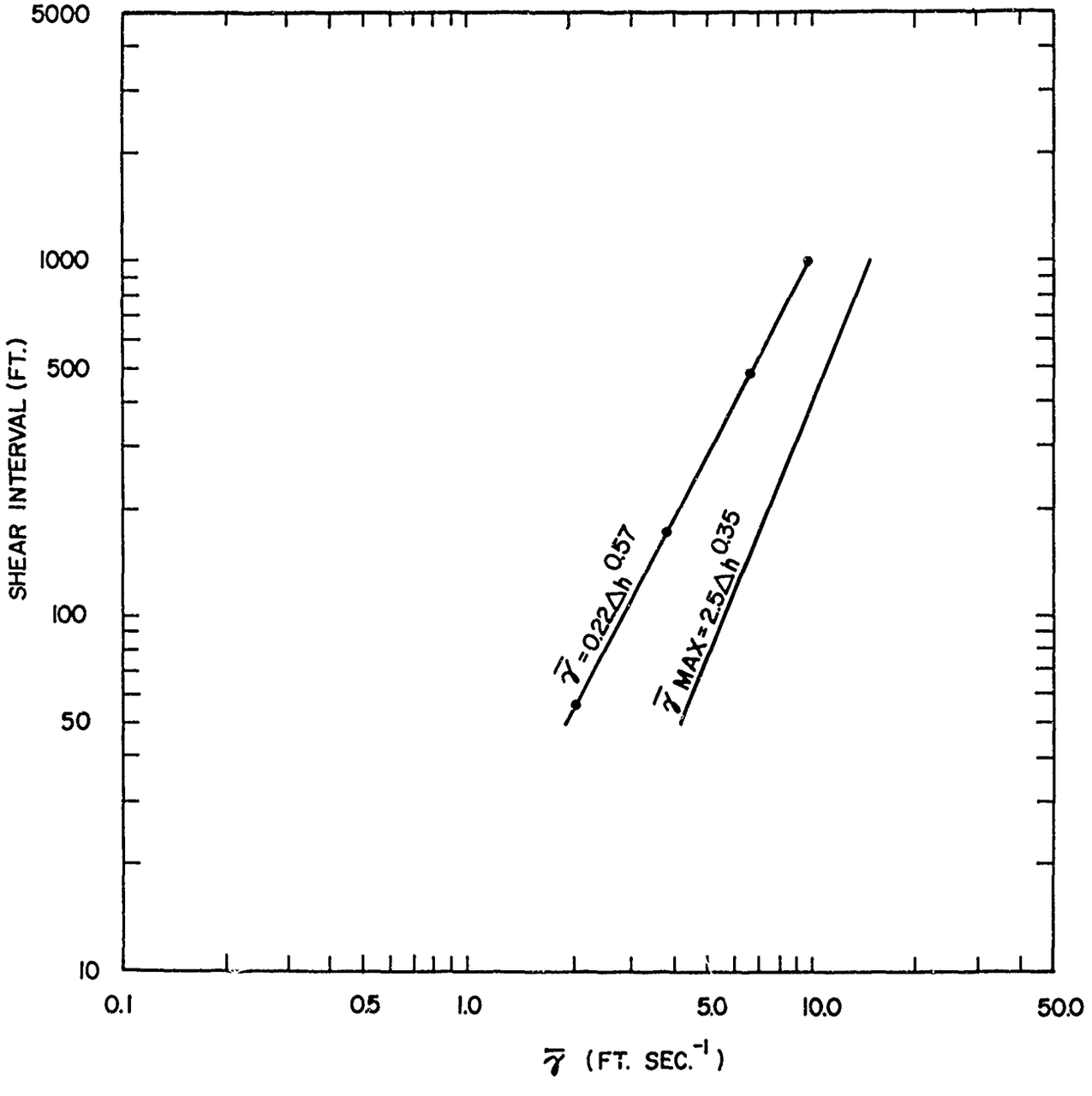

Figure 4. Relationship Between Layer Thickness (Δh) and Shear ($\bar{\gamma}$)

exponential relationship existed between layer thickness and the shear. Moreover, from their studies they concluded that the value of the exponent for mean shears should be approximately 0.5 and for the mean maximum shear 0.33. These values compare favorably with those found from the smoke trail as can be seen from Figure 4 where the exponent values were 0.57 for mean shear and 0.35 for the mean maximum shear. It should be stated that because of the accuracy with which the position data can be determined it is possible to use the smoke trail to compute shears for layers less than 200 feet thick and possibly as small as 25 feet. The limiting factor is the high cost of obtaining data every 25 feet while maintaining the accuracy of 0.2 ft sec^{-1} over a 6 sec interval.

CONCLUSION

It has been shown from these data that wind profiles derived from smoke trails and separated by a distance of 900 feet over relatively flat terrain show slight variations which are generally less than 2.0 ft sec^{-1} and 5.0 degrees. Moreover, the wind variability as a function of time, up to 36 seconds, was found to be of the same order of magnitude.

Also, it was shown, that the magnitude of the vector wind shear is exponentially related to the shear interval. The value of the exponent is 0.57 for the mean shear and 0.35 for the mean maximum shear, substantiating previous findings at White Sands Missile Range and Cape Kennedy.

REFERENCES

Armendariz, Manuel and Henry Rachele, 1967: "Determination of a Representative Wind Profile from Balloon Data," J. Geophys. Res., 72, 2997-3006.

Armendariz, Manuel and Laurence J. Rider, 1966: "Wind Shear for Small Thickness Layers," J. Appl. Meteor., 5, 810-815.

Cermak, J. E. and J. D. Horn, 1968: "The Tower Shadow Effect," To be published 1968 in J. Geophy. Res.

Cooke, T. H., 1962: "A Smoke-trail Technique ofr Measuring Winds," Quart. J. Roy. Meteor. Soc., 88, 82-88.

Essenwanger, O., 1963: "On the Derivation of Frequency Distributions of Vector Wind Shear Values for Small Shear Intervals," Geofis. Pura Appl., 56, 216-224.

Essenwanger, O., and N. Billions, 1965: "On Wind Shear Distributions for Smaller Shear Intervals. Report TP-65-4, U. S. Army Missile Command, Redstone Arsenal, Ala., AD-446 161, 28 pp.

Gill, Gerald C., Dugene W. Bierly and Jal N. Kerawalla, 1963: "An Inexpensive Rocket Technique for Obtaining Low Level Wind Profiles," J. Appl. Meteor., 2, 457-462.

Gill, G. C., L. E. Olsson, and M. Suda, 1966: "Errors in Measurements of Wind Speed and Direction Made with Tower or Stack Mounted Instruments," University of Michigan, Rpt. No. 06973-1-P, 89 pp.

Gill, Gerald C., A. W. Stohrer and T. Sweeney 1967: "A Smoke Rocket Technique for Daytime Wind Measurements to Three Thousand Feet. Paper Presented at the Unguided Rocket Ballistics Meteorology Conference at New Mexico State University 31 Oct. to 2 Nov. 1967.

MacCready, Paul B., Jr., 1965: "Comparison of Some Balloon Techniques," J. Appl. Meteor., 4, 504-508.

Scoggins, James R., 1962: "An Evaluation of Detail Wind Data as Measured by the FPS-16 Radar/Spherical Balloon Technique," NASA MTP-Aero 62-38.

Scoggins, James R., 1964: "Aerodynamics of Spherical Balloon Wind Sensors," J. Geophys. Res., 69, 591-598.

Scoggins, James R., 1965: "Spherical Balloon Wind Sensor Behavior," J. Appl. Meteor., 4, 139-145.

Tolefson, Harold B., and Robert M. Henry, 1961: "A Method of Obtaining Detailed Wind Shear Measurements for Application to Dynamic Response Problems of Missile Systems," J. Geophys. Res., 66, 2849-2862.

WIND SPEED STATISTICS ALONG A HYPOTHETICAL MISSILE TRAJECTORY DOWNWIND OF A SINUSOIDAL MODEL HILL

by

Erich J. Plate*, Paul Baer**

and

F. F. Yeh***

ABSTRACT

The wind field is investigated which is encountered by a missile traveling along a hypothetical trajectory downwind of a two-dimensional hill. Reasons are given for studying this situation in a wind tunnel. The problem is reduced to the determination of turbulence spectra and of joint probabilities for the joint occurrence of two velocities simultaneously along the trajectory set by mean flow condition.

The experimental part is concerned with measurements of profiles of mean velocities and turbulent intensities and with the determination of turbulence data for evaluating spectra and joint probability distributions. The information contained in the turbulence spectra is discussed. An example of a joint probability determination is given and some preliminary conclusions are drawn.

---

* Associate Professor, Civil Engineering Department, Colorado State University, Fort Collins, Colorado.
** Research Physicist, USA Ballistic Research Laboratories, Aberdeen Proving Ground, Maryland.
*** Graduate Student, Civil Engineering Department, Colorado State University, Fort Collins, Colorado.

INTRODUCTION

One of the major problems in predicting the target hitting capabilities of unguided rocket propelled missiles flying in the atmospheric boundary layer is the interaction between the missile and the turbulent wind field along its flight path. In the analysis of missile weapon systems, especially those used in short range (0-1 km) applications, predicting target hit probability caused by gust winds, involves prior knowledge of the wind field along the missile's trajectory. In the language of probability theory, we can formulate this problem as follows: if the trajectory of a missile is given by a deterministic curve determined by mean-wind conditions, we must find the probability distribution of the perturbations of the trajectory end point if the missile encounters random velocity fluctuations during its travel along the trajectory. The fluctuations influence the flight path in two ways. Vibrations, caused by the gust spectrum might occur, and the missile might be deflected from its course by large velocity fluctuations. For obtaining instantaneous wind measurements to calculate trajectories in a turbulent wind field, the present experimental study was undertaken. We chose the wind field which exists in the wake downwind of a two-dimensional obstruction with air flow separation at the downwind slope. The sinusoidal obstruction used in this study represents the model of a ridge. The wind field which exists in the wake of a ridge is of interest in military combat applications since ridges have been used as part of a defensive line against an attacking force. If missile launchers are emplaced along a ridge, the target impact dispersion of missiles caused

by the turbulent winds on the lee side of the ridge will play a considerable role in battlefield strategy.

A full account of this wind field is difficult to obtain in the field. The number of data points at which wind speed information is required is large, and the variability of wind speeds in natural environments would require elaborate and costly experimental equipment. Therefore, it was suggested to study the wind fields that might be encountered downwind of a sinusoidally shaped hill in the controlled environment of a laboratory where many needed data can be taken one after another instead of simultaneously, and where the reliability of measuring instruments and data analysis equipment has reached a high level.

The crucial problem in applying laboratory results for practical applications in a natural environment is the question of scaling laboratory conditions up to field dimensions. For flows of undisturbed boundary layers, such as the wind along a boundary of constant roughness over a long fetch, the modeling has been achieved beyond reasonable doubt by scaling according to the ratio of the roughness heights, and by keeping the shear velocities constant. With these conditions met, both the mean velocity conditions and the turbulence structure are approximately scaled. For a boundary layer flow which is disturbed by a sharp edged obstacle, Plate and Lin (1965) have presented an argument, based on the boundary layer integral momentum equation, that the same parameters together with the drag coefficient of the obstacle (as referred to some convenient velocity, such as the geostrophic wind velocity), suffice to model the mean velocity field. As far as the turbulence structure is concerned, no equivalent conclusions are as yet forthcoming, but some work by Plate and Lin (1966) has pointed at the

possibility that the modeling of the dissipation number is an additional requirement. Moreover, no conclusions have yet been reached on how the turbulence structure would be affected if this number is not modeled accurately. Work is in progress on this point at Colorado State University. It is reasonable to suspect that modeling requirements will result in a scale factor for the dissipation rates which does not differ very much from that for the mean velocity.

With this assumption made, translation of laboratory data to field data is a simple problem, provided that the drag coefficient of the obstruction can be estimated. The procedure would be to determine the roughness length and the geometrical pattern of the natural situation, and then to prepare a scale model of it in the laboratory, setting the roughness length in the laboratory at a convenient level by artificial roughening of the wind tunnel boundary. As long as the dimensions of the obstruction are such that it lies well within the lowest 1000 to 2000 ft of the atmosphere, and as long as the wind velocity is such that the gross Richardson number of the prototype is not essentially different from zero, and as long as the model is sharp edged, so that the separation line is fixed, the condition in the laboratory should be similar to that in the field if:

$$\left(\frac{h}{z_o}\right)_{\text{model}} = \left(\frac{h}{z_o}\right)_{\text{field}} \qquad (1)$$

In this equation, h is the height of the obstruction and z_o is the roughness height.

For an obstacle which is not sharp edged, such that the separation line moves with change in velocity, the Reynolds number affects the drag coefficient, and compensations will have to be made for this effect. A

possibility exists in artificially tripping the boundary layer on the obstruction so as to induce turbulence locally and fix the boundary layer separation line. However, such refinements have not been used in this study, which is intended to furnish qualitative information rather than quantitative design data and, in that case, it is unnecessary to substantiate the small improvements in similarity which can be had by artificially inducing separation on the model hill. Thus, the problem of scaling need not concern us in this study, especially since a comparison with field data is not possible at this time. We shall, therefore, formulate our problem in more detail without regard to scaling.

THEORETICAL CONSIDERATIONS

The techniques for using spectra to calculate vibrations of an in-flight missile shall not be discussed in this paper. We shall, however, provide the experimental information on gust spectra.

The problem of evaluating the instantaneous missile trajectory is approached in the following way. Let the trajectory of a missile be given as shown in Fig. 1 for our problem. Then on its travel along the trajectory the missile encounters mean velocities and a sequence of gusts, both described by a velocity vector $\vec{v}(\vec{s};t)$, where t is the time of flight, and $\vec{s}$ is the position vector of the trajectory. The velocity vector consists of a mean velocity $\bar{\vec{v}}(\vec{s})$ and a fluctuation in velocity $\vec{v}'(\vec{s};t)$. The position vector consists of a position vector $\bar{\vec{s}}$ corresponding to an absence of all velocity fluctuations (i.e., the trajectory in mean wind only) and a small deviation $\vec{s} - \bar{\vec{s}}$ due to the sequence of fluctuating velocities which the missile has encountered during the time t .

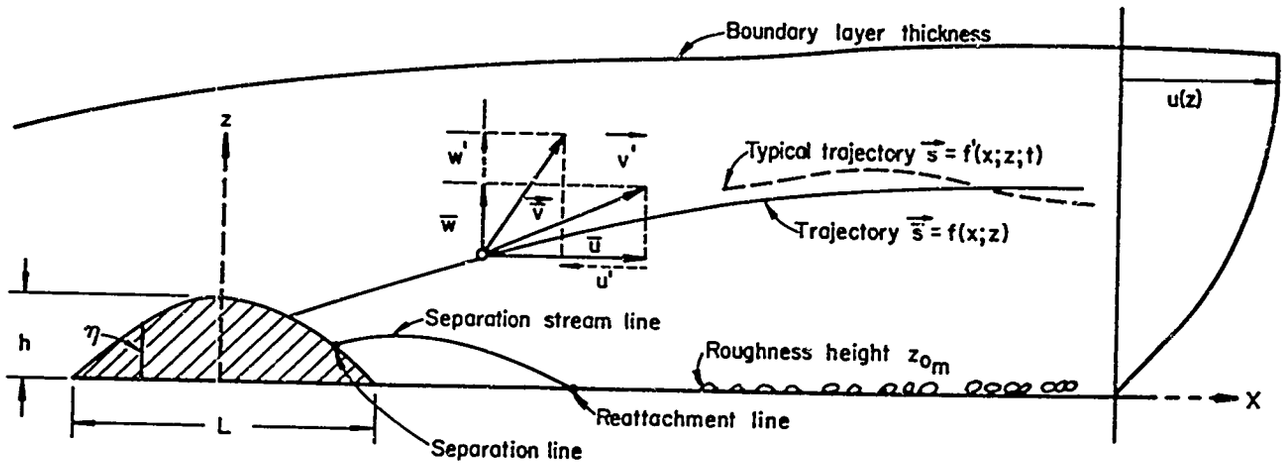

Fig. 1 Definition Sketch

Now, let the travel time until impact be equal to t_i and the end point of the mean wind trajectory be located at x_e. Then due to the sequency of fluctuations encountered during its flight, the missile has encountered total deviations x_e' from the target distance x_e. Due to the random nature of the fluctuations encountered, the x_e' will also be randomly distributed. The probability distribution of the quantity x_e' is the desired quantity of the study. To calculate it, it is required to evaluate a large number of fluctuating trajectories from start to impact.

The aerodynamic or meteorologic problem associated with this probability distribution is to make available the velocity distribution $\vec{v}$ as function of space and time - a problem which cannot be handled analytically or experimentally. A number of assumptions must, therefore, be made to simplify the analysis.

The first assumption is that the distance of the particular trajectory from the mean trajectory calculated on the basis of the mean wind distribution is small, so that

$$\vec{v}(\vec{s};t) \approx \vec{v}(\vec{s};t) \quad . \tag{2}$$

In this manner, it is no longer necessary to consider the whole space but one can concentrate on the single trajectory. Obviously, the validity of this assumption depends both on the relative magnitude of $\vec{v}'$ with respect to $\vec{v}$, and on the characteristics of the missile, and will have to be tested each time.

The second assumption concerns the time distrubution. We assume that the missile travels much faster than the velocity fluctuates, so that

$$\vec{v}(\vec{s};t) \approx \vec{v}(\vec{s};t_o) \tag{3}$$

where t_o denotes the start time. This assumption implies that during the flight time the relation holds:

$$\vec{v}'(\vec{s};t)\vec{v}'(\vec{s};t_o) \approx \vec{v}'(\vec{s};t_o)\vec{v}'(\vec{s};t_o)$$

or that, in the average for n different starting gimes t_o:

$$\frac{1}{n}\sum_{i=1}^{n}\vec{v}'(\vec{s};t)\vec{v}'(\vec{s};t_{oi}) \approx \frac{1}{n}\sum_{i=1}^{n}(\vec{v}'(\vec{s};t_{oi}))^2 .$$

If the flow is stationary, and if the ergodic hypothesis is valid, then we can restate this requirement as:

$$R_\tau \approx 1 \tag{4}$$

where

R_τ is the autocorrelation function defined by:

$$R_\tau = R(t_x - t_o) = \frac{1}{T}\int_o^T \frac{\vec{v}'(\vec{s};t_o + (t_x - t_o))\cdot\vec{v}'(\vec{s};t_o)dt_o}{\overline{v'^2}(\vec{s},t_o)} \tag{4a}$$

where

T is an observation time taken long enough to ensure a stable average, and

$t_x - t_o$ is the time during which the missile has traveled from x_o to x^*.

$$R_\tau \approx 1 - \frac{(t_x - t_o)^2}{\tau_E'^2}$$

where τ_E' is the microscale of the turbulence. The scale τ_E' can be replaced to a good approximation by the scale τ_E of the u'-component of the turbulence

---

*To convert actual travel times to model travel times, the scaling law $(\frac{tu^*}{z_o})_{model} = (\frac{tu^*}{z_o})_{field}$ must be used, which, for $u^*_{model} = u^*_{field}$ reduces to $t_m = t_{field}\frac{z_{o\ model}}{z_{o\ field}}$.

$$\tau_E^{-2} = \frac{1}{2\overline{u'^2}} \left(\frac{\partial u'}{\partial t}\right)^2 \Bigg|_{t=0} \qquad (5)$$

Consequently, it follows that $t_x - t_o << \tau_E$ for the assumption Eq. 3 to be valid.

We base our calculations on assumptions Eq. 2 and Eq. 3, and, thus, we have reduced the meteorological aspects of the problem to finding simultaneous instantaneous velocity distributions along the mean trajectory $\bar{x}$. To avoid the implied necessity of determining velocities simultaneously at many different points, we adopt the following probabilistic specification of the velocity field.

The basic quantity is the velocity probability density function (pdf) $p_o(u')$ of the fluctuating velocity in the horizontal direction at $x = x_o$. With this function known, we then find (for a two-dimensional flow) the conditional probability density $p_o(w'|u')$, (cpdf), i.e., the probability density distribution for the vertical velocity component w' in the event that a velocity u' has occurred whose magnitude lies between $u' \pm \Delta u'$. The pdf for a certain vector $\vec{v}' = u'\vec{i} + v'\vec{j} + w'\vec{k}$ to occur is then given by the joint probability density function for the three quantities u', v', w'

$$p(\vec{v}') = p(u') \cdot p(w'|u') \cdot p(v'|u'w') \; . \qquad (6)$$

where $p(v'|u'w')$ denotes the cpdf of v' to occur while both u' and w' have already occurred.

The evaluation of Eq. 6 requires the measurements of jpdf's of three variables, a task which is considered too tedious for practical applications. We, therefore, invoke the assumption that there exists no statistical relation between u' and v'. One condition for this requirement to be satisfied is that the time average product $\overline{u'v'} = 0$,

which must be satisfied because of the homogeneity of the turbulence in planes parallel to the ground. This conditions is, however, only necessary and not sufficient, and can, therefore, give a justification only to a first approximation. With the assumption of statistical independence involved we obtain:

$$p(v'|u'w') = p(v') \tag{7}$$

and thus:

$$p(\vec{v}') = p(u') \cdot p(w'|u') \cdot p(v') \tag{8}$$

Equation 8 is the pdf for finding a certain vector $\vec{v}$ at a certain point x. Consequently, at each point x_i we find the pdf for the vector v_i' to occur given by

$$p(\vec{v}_i) = p(u_i') \cdot p(v_i') \cdot p(w_i'|u_i') \tag{9}$$

Now, to calculate the velocity field simultaneously for all points along the trajectory, it is necessary to connect probability distributions between points. For this purpose, the trajectory is cut into a number of intervals which are a distance $\Delta x = x_{i+1} - x_i$ apart. The velocity is assumed constant and equal to the value

$$\vec{v}_i' = u_i'\vec{i} + v_i'\vec{j} + w_i'\vec{k}$$

in each interval, from which the trajectory between x_i and x_{i+1} is calculated. The probability of occurrence of this vector $\vec{v}_i'$ is given by Eq. 9.

In order to obtain cpdf's for other points along a trajectory when the pdf for x_o is given, it is necessary to determine cpdf's of the form:

$$p(u_i'|u_{i-1}', u_{i-2}, u_{i-3}\cdots\cdots u_o) \tag{10}$$

which can only be evaluated by simultaneous measurements along all points of the trajectory. With the cpdf defined by Eq. 10, it is then possible to calculate the joint probability density function

$$p(\vec{v}_{i+1}|\vec{v}_i) = p(\vec{v}_i) \cdot p(\vec{v}_{i+1}, \vec{v}_i) \tag{11}$$

where $p(\vec{v}_i)$ is given by Eq. 9. For obtaining the cpdf $p(\vec{v}_{i+1}|\vec{v}_i)$ certain further assumptions are needed. We shall consider these plausible special cases.

1. Consider first the assumption that $p(\vec{v}_{i+1})$ and $p(\vec{v}_i)$ are statistically independent. This condition corresponds to velocities which vary comparatively rapidly along the trajectory, in the sense that $R_x = 0$ where R_x is the spatial correlation coefficient obtained from the definition

$$R_x = R(x_{i+1} - x_i) = \frac{1}{\Delta x} \int_{x_i}^{x_{i+1}} \frac{\vec{v}'(t_o, x-x_i)\vec{v}'(t_o, x_i)dx}{\sqrt{\overline{v'^2(t_o,x_i)}} \cdot \sqrt{\overline{v'^2(t_o,x_{i+1})}}} \tag{12}$$

However, the assumption of rapidly varying velocities is in contradiction to the assumption of a velocity vector which is constant throughout the travel interval Δx, unless Δx is chosen in such a way that a meaningful relation between it and the space integral scale $\mathcal{J}_s$ exists, where:

$$\mathcal{J}_s = \int_{x_i}^{\infty} R_x dx \tag{13}$$

Also, in order to be of influence on the flight pattern, $\mathcal{J}_s$ must be large compared to the length dimension L of the missile, such that a condition for the validity of this assumption might be defined as:

$$\Delta x \ll \mathcal{J}_s \qquad \text{and} \qquad \frac{L}{\mathcal{J}_s} \ll 1 \quad \text{say} \quad <0.1 \tag{14}$$

Under these circumstances, Eq. 11 reduces to

$$p(\vec{v}_{i+1}, \vec{v}_i) = p(\vec{v}_i) \cdot p(\vec{v}_{i+1}) \tag{15}$$

where both $p(\vec{v}_i)$ and $p(\vec{v}_{i+1})$ are given by Eq. 9. This equation can be evaluated conveniently.

2. As a second possibility, we considered the condition

$$\mathcal{J}_s > x_e - x_o$$

in which case the correlation coefficient defined by Eq. 12 assumes a value very near to 1. This implies that the velocities $\vec{v}'(t_o, x_i)$ and $\vec{v}'(t_c, x_{i+1})$ are very nearly proportional, so that

$$\vec{v}'(t_o, x_{i+1}) \approx a\vec{v}\,(t_o, x_i) \tag{16}$$

where a is a (vector) constant. Furthermore, the jpdf defined by Eq. 11 becomes:

$$p(\vec{v}_{i+1}, \vec{v}_i) = p(\vec{v}_i) \tag{17}$$

because the cpdf $p(\vec{v}_{i+1} | \vec{v}_i) \approx 1$. With this result, an instantaneous trajectory is constructed by joining $\vec{v}'(x_o)$ with corresponding velocities at other points x_i first and finding the corresponding end points x_e which have a probability density function given by that of the $\vec{v}'(x_o)$ values.

3. The assumption of 1 and 2 bracket the possibilities for the probability density function of the impact distance x_e. An intermediate method, based on the assumption that the eddy structure of the turbulence is highly elongated, (as is usually the case in turbulent flows) would combine assumptions of independence of the motions perpendicular to the mean wind direction with an assumption of functional dependency of the

components in the wind direction along the trajectory. With this assumption, the cpdf in Eq. 11 becomes:

$$p(\vec{v}'_{i+1}|\vec{v}'_i) = p(u'_{i+1}|u'_i) \cdot p(v'_{i+1}) \cdot p(w'_{i+1}|u'_{i+1}) \quad . \tag{18}$$

For actual calculations, it might be desirable to employ any or all three methods outlined, and to determine the most likely distributions of x_e by considering both the statistics of the wind field as expressed through correlations or spectra, and the calculated probability distributions. Calculations of this nature will be presented elsewhere. In the present paper, we shall demonstrate some measurements of the cpdf required for evaluating Eq. 9 and Eqs. 15, 17, or 18.

EQUIPMENT AND PROCEDURES

The experiments were performed in the U.S. Army Meteorological Wind Tunnel in the Fluid Dynamics and Diffusion Laboratory of Colorado State University. This facility is shown in Fig. 2. It is a recirculating wind tunnel with an 88 ft long test section with an 8 x 8 ft^2 cross section. For the experiments of this study, the model hill was placed at a distance of approximately 40 ft downstream from the inlet where the undisturbed boundary layer, stimulated by large roughness elements in the inlet region of the test section, had an undisturbed thickness of about 24 inches. The model hill consisted of a plexiglass section with a shape η given by

$$\eta = h \cos \frac{\pi x}{L} \quad \text{for} \quad -\frac{\pi}{2} \leq \frac{x}{L} \leq \frac{\pi}{2} \tag{19}$$

where the base width L = 20 in. and the height h = 4 in. The velocity outisde of the undisturbed boundary layer was 30 fps. The mean velocity

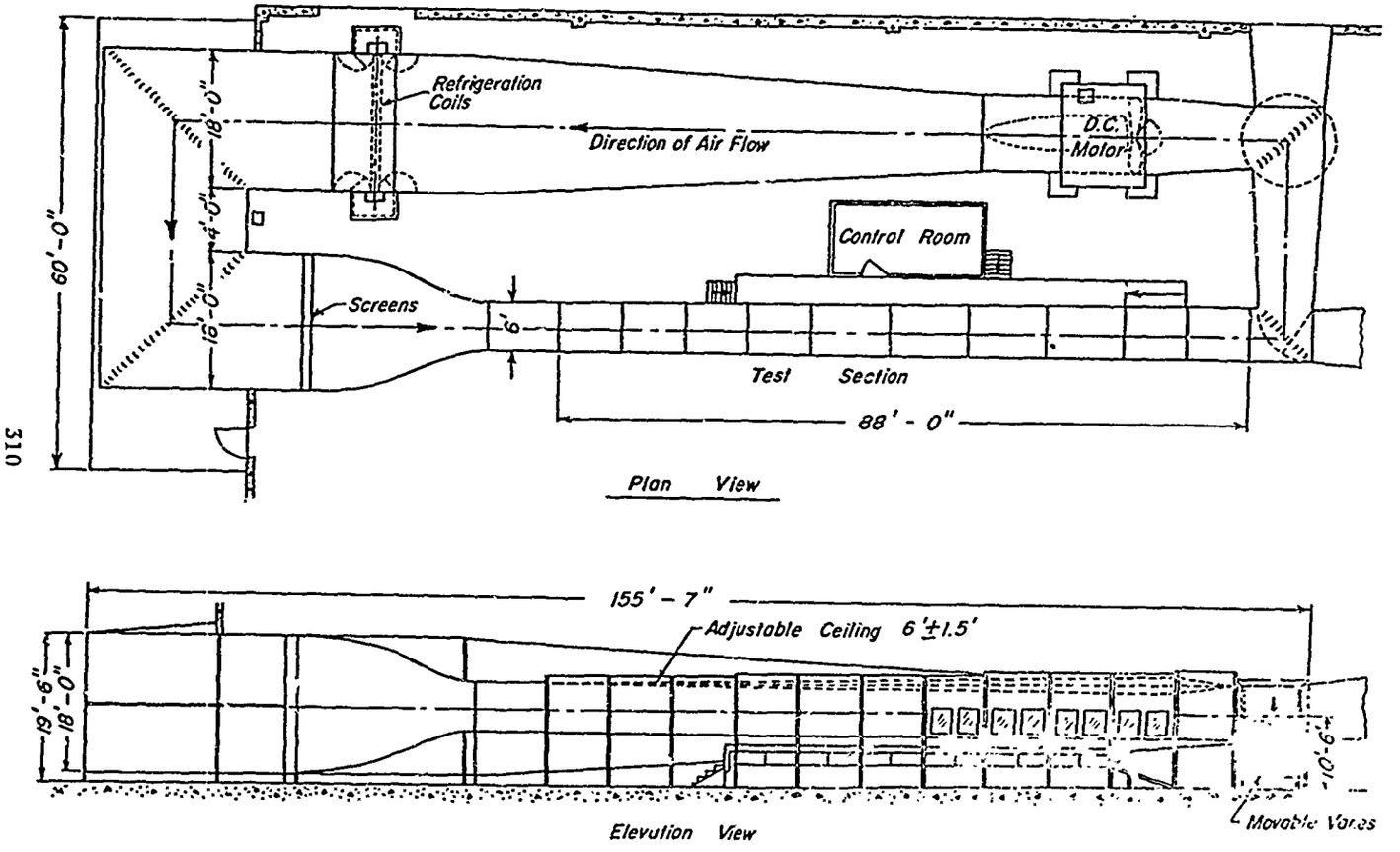

Fig. 2 LARGE WIND TUNNEL

was measured both with pitot tubes and with hot-wire anemometers. Velocities were measured by taking continuous profiles, by mounting the pitot tube on a movable carriage and connecting it to a pressure transducer and then recording position vs. transducer output on an x-y-plotter. In the region of high velocity gradients with large fluctuations in velocity it was considered more appropriate to take the data by plotting velocity (or dynamic pressure) data against time on an x-y-plotter and obtain time averages graphically.

Since the static pressure in the neighborhood of the hill changes quite rapidly with distance, the total and static pressures were measured separately. Pitot-static tube readings were then corrected for the effect of the pressure gradient.

The turbulence data given in this study were taken with either a single wire hot-wire anemometer of the constant resistance type which was held perpendicular to the direction of flow. Or they were taken with crossed wires of a two-channel constant resistance hot-wire anemometer. From the crossed wires, instantaneous signals proportional to the u' and and the v' -component were determined by suitable instantaneous adding and subtracting of hot wire signals, according to well known techniques (Hinze (1959)).

Spectra of the u'-component of the turbulence signal was obtained by means of a Bruel and Kjaer Spectrum Analyser (Type B & K), with occasional cross checks against results from a Technical Products Wave form Analyser (Type TP 627). The former has a proportional band width, passive filter system, while the latter works with active constant bandwidth filters.

Probability distribution and joint probability distributions were measured with a set of Technical Products probability densit· analysers (Type TP 647) coupled together so that the one provided the gate for the joint probability distributions obtained from the other.

THE EXPERIMENTAL RESULTS

The experimental work on this project was conducted in three phases. these were:

1. Measurements of the mean wind vertical velocity profiles and turbulent intensities at selected points on the lee side of a sinusoidal hill using the Army Wind Tunnel. This work has been reported by Plate and Lin (1965)

2. Determination of theoretical missile trajectories, if the missiles were fired from the lee side of a scaled-up version of the two-dimensional hill.

3. Determination in the wind tunnel of the characteristics of the wind field at selected points along the scaled-down missile trajectories.

A fourth phase, not reported in this paper, will be the response of the missile to the experimental wind fields determined in phase 3.

a. Determination of Missile Trajectories

This work was conducted at the USA Ballistic Research Laboratories using the laboratories computing facilities and a six degree of freedom multi-stage rocket trajectory program.

The missile used in this study was a hypothetical gun launched two-stage anti-tank missile. The gun launched the missile at 1200 f/s. After a short delay, a booster section ignited, the thrust from which accelerated the missile to a velocity of 2100 f/s. At that point, a sustainer motor ignited, the thrust from which, kept the missile at a

constant velocity until it reached a position about 1 km from the launcher. In computer simulations, this missile was shown to have a steady cross wind sensitivity of 0.36 mils, angular deflection per ft/sec of cross wind.

For the simulation study, the two-dimensional hill used in the tunnel was scaled up by a factor of 1200 to a ridge 400 ft high by 2000 ft long. It was then assumed that missile launchers were emplaced at the base of the ridge; half way up the ridge, and at the top of the ridge. All the launchers were pointed at targets on the lee side of the ridge, the targets being 1 km from the launcher sites.

The trajectories of missiles were simulated first for the no wind case and then for the case of the steady wind flowing over the ridge by interpolating in the data from Plate and Lin (1965).

The missile trajectory data from these simulations were then sent to Colorado State University to be used in further experimental work. The characteristics of the wind fields along one of the trajectories, shown in Fig. 3, generated in the above study, is reported in this paper.

b. Mean Velocities and Turbulent Intensities

Along points on the trajectory shown in Fig. 3, and on a number of important points in the flow field, which are also indicated in Fig. 3, the turbulent quantities u', v' and w' were measured and recorded on magnetic tape.

Mean velocity distributions are shown in Fig. 4. The solid lines indicate velocities measured with a pitot static tube, while the dashed lines refer to hot-wire measurements. On the whole, the agreement between the two sets is good, even without any corrections for turbulence. The small deviations might just as well be due to drift in the hot-wire characteristics, which could never be fully eliminated.

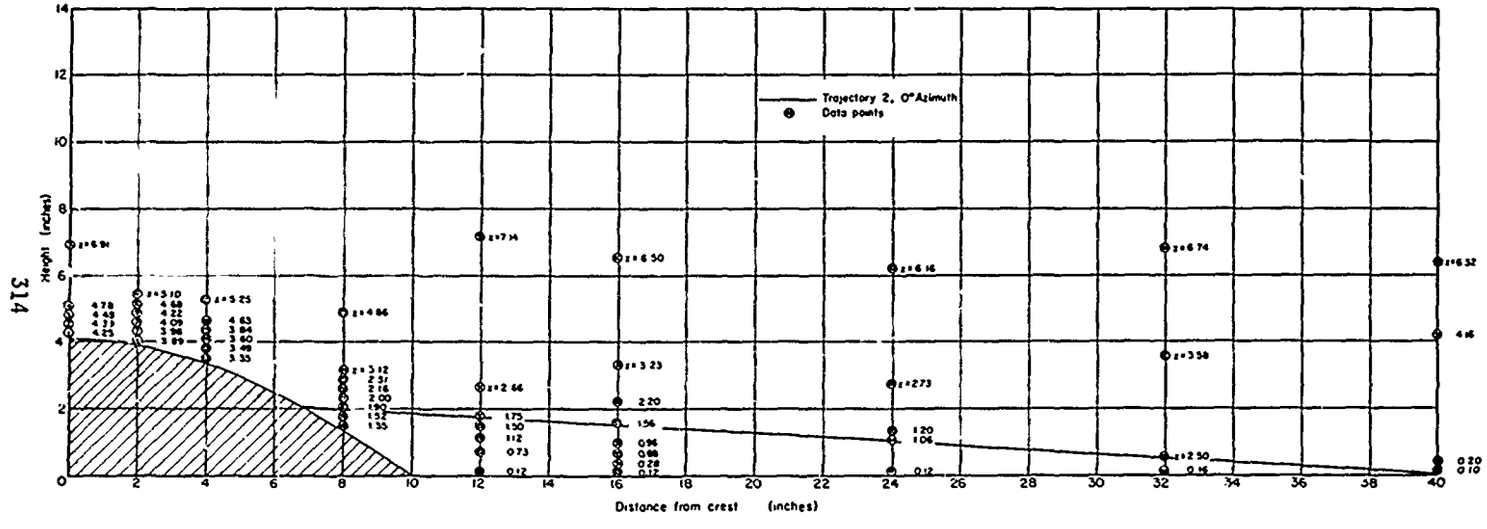

Fig. 3 Location of test points

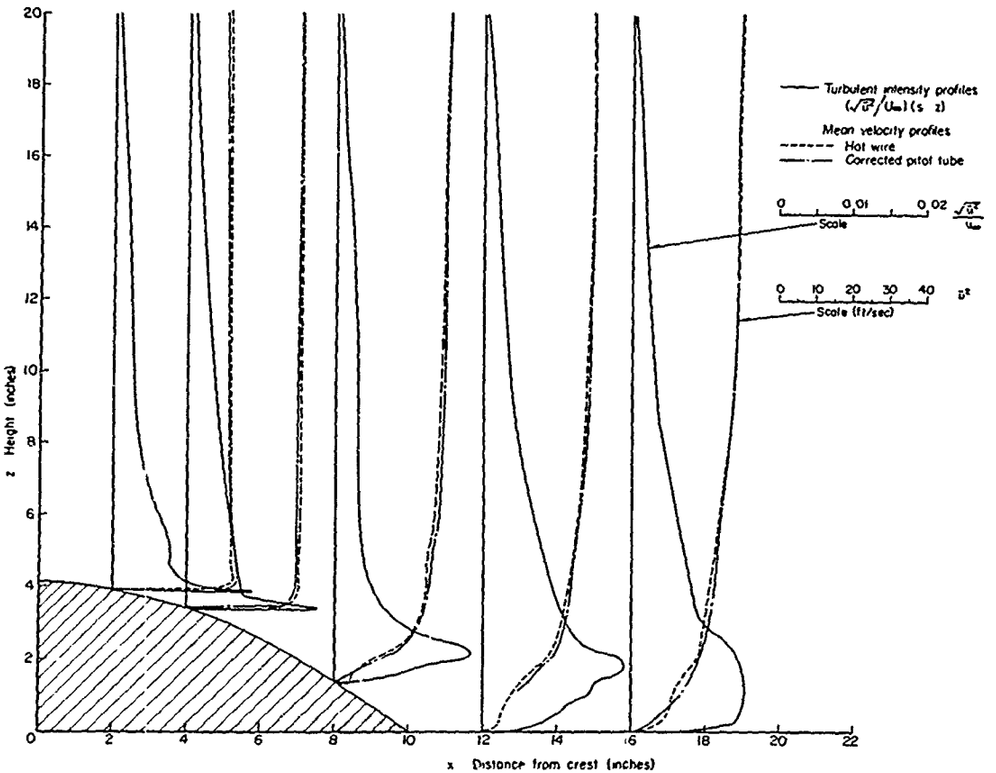

Fig. 4 Mean velocity and turbulent intensity distribution

Characteristic of the flow field is the strongly accelerated flow above the crest of the model, which gives rise to the velocity maximum, and the very sharp velocity gradients in the neighborhood of the separation streamline. These velocity gradients interact with the turbulent shear stress to cause a large increase in the amount of turbulent energy of the flow. This is evident in the turbulent intensity profiles which were also plotted in Fig. 4. These have a strongly peaked appearance, and it is easily shown that the peak occurs in the neighborhood of the separation streamline, at least for short distances from the separation point on the hill slope.

Underneath the separation streamline, the flow gradually decreases, reaches zero and reverses sign. This can be inferred from the fact that the discharge across any vertical section underneath the separation streamline must be zero. The experimental data, on the other hand, fail to show this trend. This is due to the fact that the pitot tube cannot measure any backflows, while the hotwire cannot distinguish directions. Future work will be directed towards exploration of the flow field in this region; in the present study it is seen that the trajectory does not reach into it.

c. Turbulence Spectra

Turbulence spectra were evaluated for all points indicated in Fig. 3. However, only the spectra of two vertical sections are shown in Figs. 5 and 6. The signal is plotted in the form $\overline{e'^2}$ vs. f. Here $\overline{e'^2}$ is the energy density, per Hz, of the electrical signal from the hot wire as passed through the filter of center frequency f of the spectrum analyzer. It differs from the energy level of the turbulent

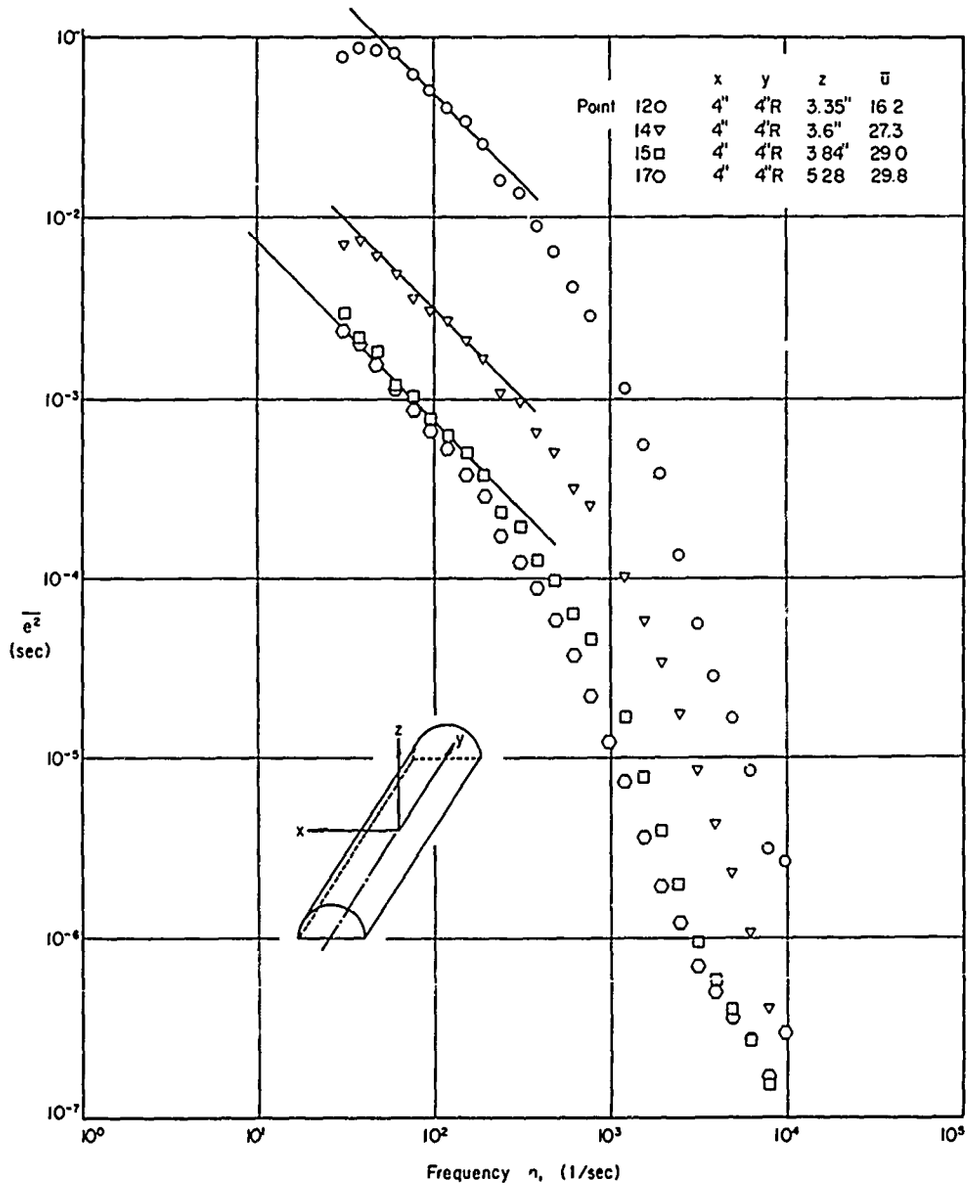

Fig. 5 Turbulent spectra of the u' component at x = 4"

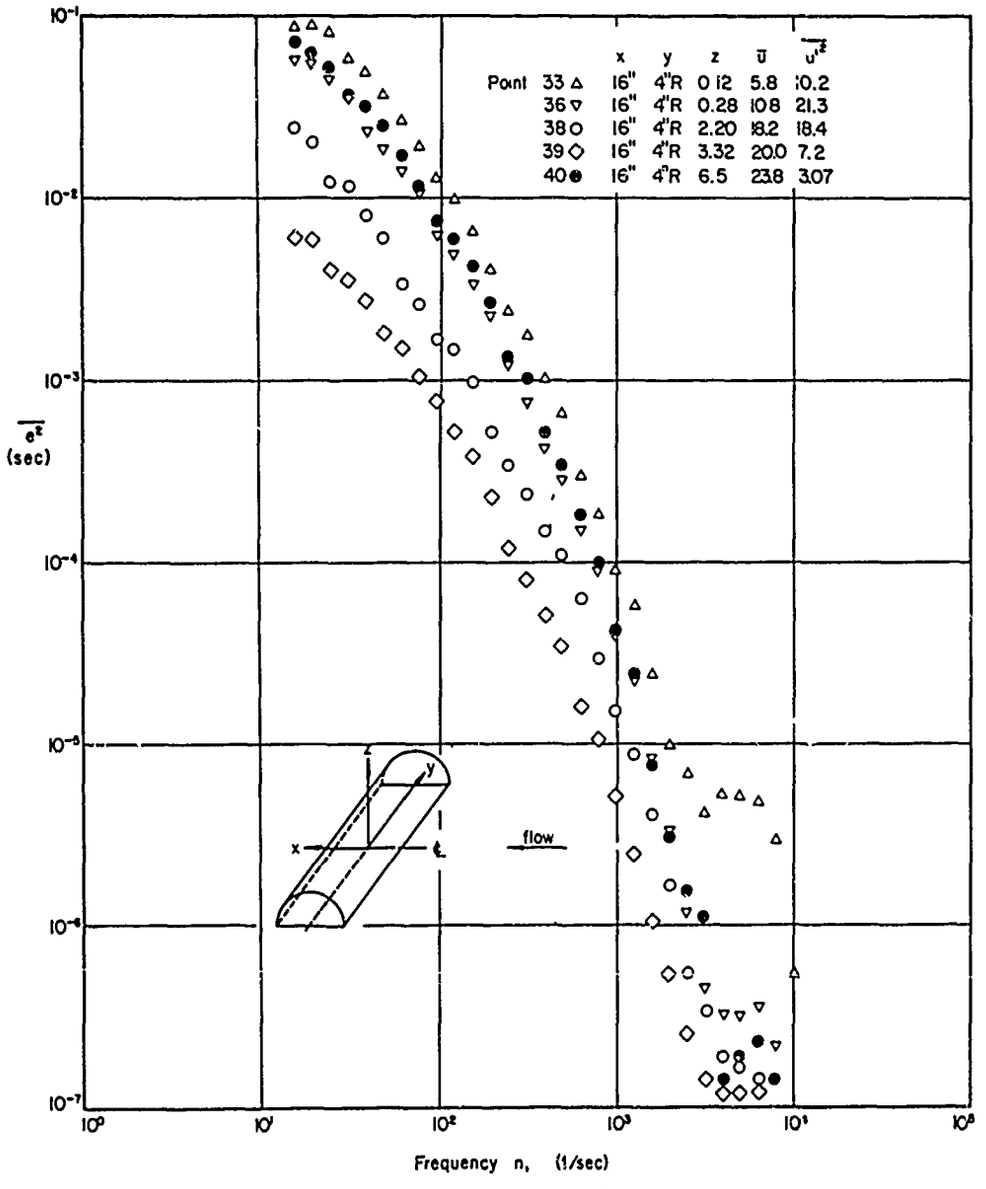

Fig. 6 Turbulent spectra of the u' component at x = 16"

motion by a calibration factor given by the square of the slope of the calibration curve u vs. e of the hot-wire anemometer.

In the low frequency range, we notice a strikingly different spectrum shape close to the hill crest as compared to the results at 16 inches downstream. At short vertical distances from the wall, the data close to the crest (Fig. 5) indicate a much slower dropp-off with frequency than the set of data shown in Fig. 6. In fact, there seems to exist a well developed region, between 40 and 200 cps, in which the energy level decreases almost linearly. This behavior is characteristics of strong interactions between mean flow and turbulence, i.e., of a flow when a large amount of turbulence generation due to large velocity gradient takes place. This behavior is not typical for other boundary layer flows of the U.S. Army Wind tunnel.

Due to strong noise levels of the magnetic tape recorders, the part of the spectra corresponding to frequencies above 2000 Hz is not usable. For large frequencies, but below 2000 Hz, the shape of the spectrum is the same for all data. In fact, if the spectrum is plotted in the similarity form of the universal equilibrium law of Kolmogoroff, we find that the shape is identical for all data, and they collapse on a single curve. This is illustrated in Figs. 7 and 8, in which the data of Figs. 5 and 6 have been replotted in dimensionless form:

$$\phi\left(\frac{k}{k_s}\right) = Bf(n) \quad . \tag{20}$$

ϕ is the non-dimensional spectral density, $f(n)$ is the measured spectral density at frequency n, and B is a conversion factor:

$$B = \frac{\overline{u'^2}\tilde{u}}{2\pi\varepsilon^{1/4}\nu^{5/4}} \tag{21}$$

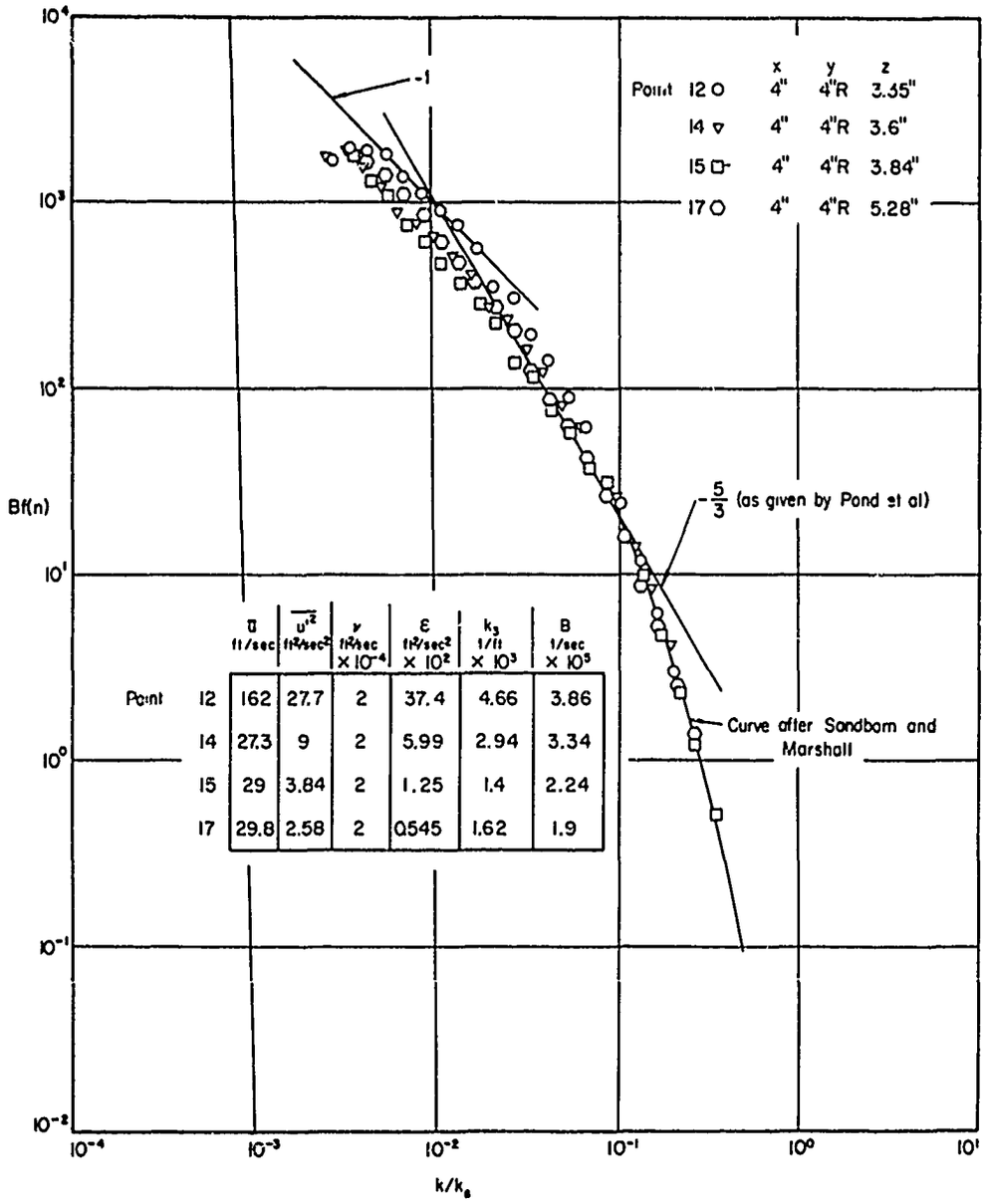

Fig. 7 Non dimensional spectra at x = 4"

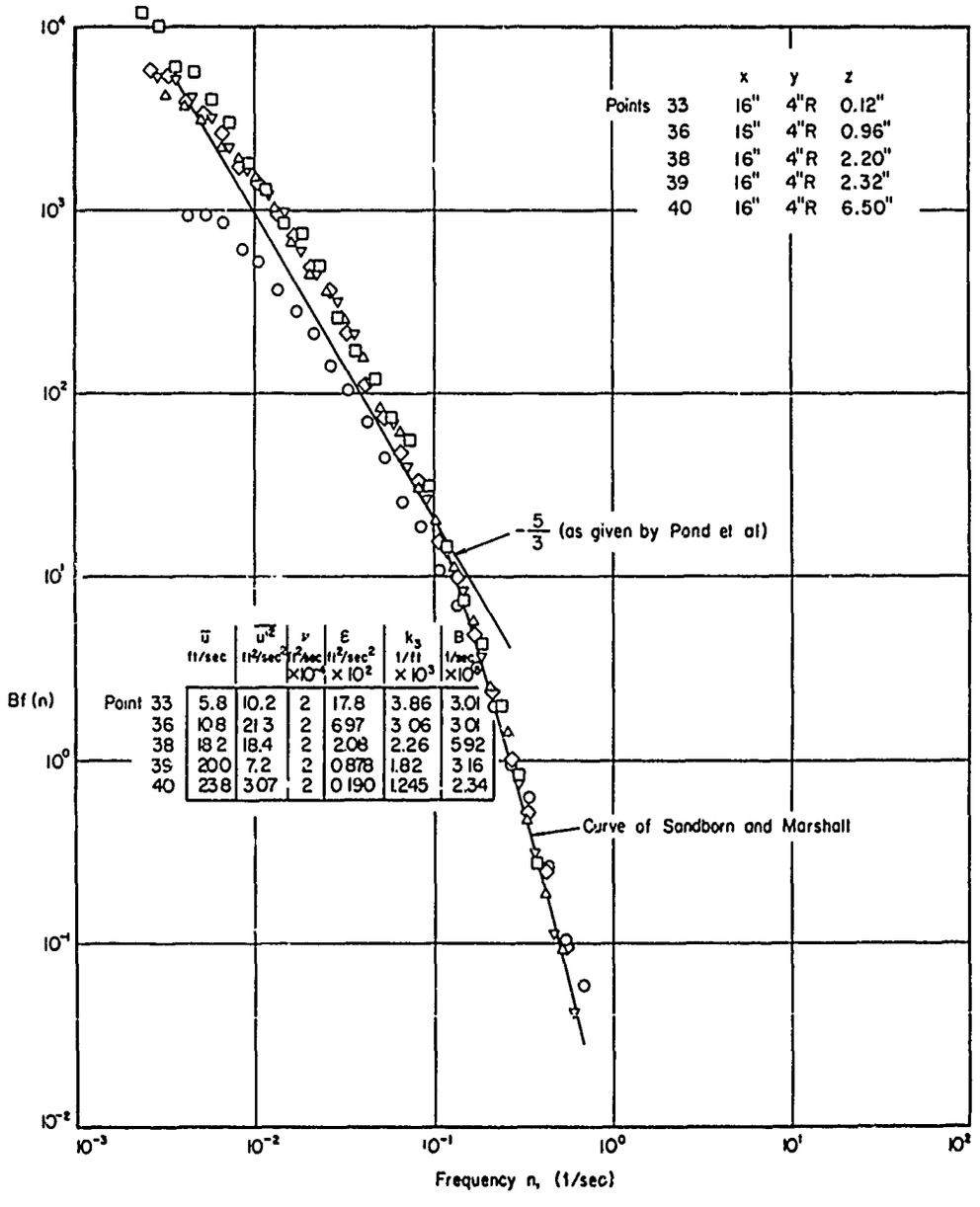

Fig. 8 Non dimensional spectra at x = 16"

Furthermore, k_s is the reference wave number based on the dissipation ε :

$$k_s = (\varepsilon \nu^{-3})^{1/4} \tag{22}$$

As an estimate for the dissipation ε we have used the isotropic relationship:

$$\varepsilon = 15\ \nu \overline{\left(\frac{\partial u'}{\partial x}\right)^2} = 15\nu\ \overline{u^{-2}}\ \overline{\left(\frac{\partial u'}{\partial t}\right)^2} \tag{23}$$

as well as the equivalent form

$$\varepsilon = 15\ \overline{u'^2} \int_0^\infty k^2 f(k)\,dk \tag{24}$$

where k is the wave number

$$k = \frac{2\pi n}{\overline{u}} \tag{25}$$

and $\overline{u}$ is the mean velocity, as before. Both methods yielded identical results for ε .

In Figs. 7 and 8 we have also indicated the -5/3 law of the inertial subrange and the universal shape of the high frequency and of the turbulence spectrum, in the form given by Sandborn and Marshall (1963). It is surprising to see that the high frequency end of the spectrum in the highly disturbed boundary layer of our case is presented exactly by the high frequency shape of the undisturbed turbulence in a boundary layer along a flat plate. Since Sandborn and Marshall have demonstrated the perfect agreement of their spectra with experimental results obtained in wind over ocean waves by Pond, et al, (1963), it becomes more and more evident that this range of the spectrum is a universal feature of all turbulent flows.

But the same conclusion cannot be drawn for the turbulence spectrum in the inertial subrange. It is held that here a spectrum law of the form is valid

$$B \cdot f(n) = K\left(\frac{k^{-5/3}}{k_s}\right) \tag{26}$$

where K is a universal constant, about 0.46 . Very near the crest of the model hill, this "constant" is well enough verified, but at larger distances downstream, in the region which derives its turbulence from the initially strong gradients in mean velocity across the separation stream line, the "constant" seems to be substantially higher. At 16" (Fig. 8) downstream from the hill crest, the best fitting -5/3 law has a constant K of about 0.35. It should be noted that in the velocity region where this is found the turbulence level decreases rapidly with distance, indicating that the amount of energy generated locally is lower than that dissipated, i.e., the ratio of dissipation to generation

$$D = \frac{\varepsilon}{\overline{u'w'}\,\frac{\partial u}{\partial y}} \tag{27}$$

in this region is greater than one. This result thus is in qualitative agreement with a result of Margolis and Lumley (`54). It has as yet, however, not been shown that a universal relation exists between K and D . Experiments are at present underway at Colorado State University to investigate this point. That D might also be an important quantity in modeling of atmospheric turbulence has been pointed out by Plat ` and Lin (1966).

The low frequency end of the spectrum is governed by the process of energy extraction from the mean flow and depends, therefore, on the local velocity field. Similarity forms can, therefore, not be expected

for the whole spectrum. But the eddies associated with the low frequency end of the spectrum input cause the most important dynamic effect on a missile during its flight. Work is therefore in progress at CSU on relations between the low frequency end of the spectrum and the local mean velocity field.

d. Probability Distributions

Two different sets of probability distributions are given for three points along the trajectory, namely at $x = 12"$, $x = 24"$, and $x = 32"$. These are probability densities of the u' and of the w' component, and joint probability densities

$$p(w',u') = p(-\infty \leq w' \leq +\infty;\ u_1 \leq u' \leq u_2)$$

where u_1 and u_2 are a distance of $0.2\ \overline{u'^2}$ apart. One notices with amazement the strong skewness of the probability distributions $p(u')$ and $p(w')$ shown in Figs. 9 to 11. Also, the probability distributions $p(w')$ are in both cases much more peaked than the $p(u')$ distributions.

The joint probability density distributions shown in Figs. 12 to 14 also show skewness. There is a definite tendency of large positive velocity fluctuations in the x-direction to be associated with large negative velocity fluctuations in the z-direction. This conclusion of an association of directed velocity fluctuation is, of course, an indication of an order in the random motion, which arises from the generation of turbulent shear stresses. The turbulent shear stresses require that in the mean the product $\overline{u'w'}$ has to be negative and non-zero.

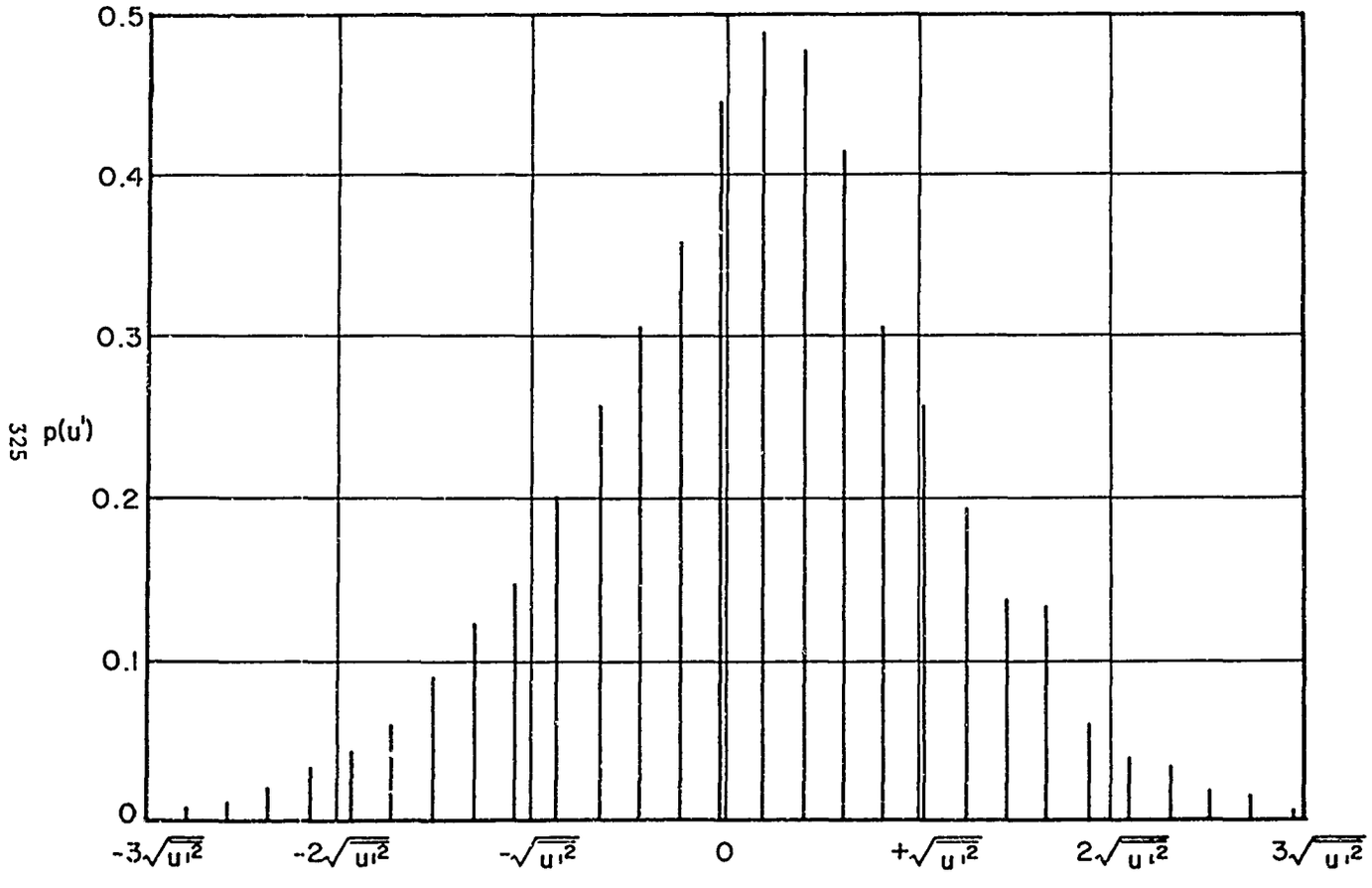

Fig. 9 Probability distribution $p(u')$ at $x = 4''$

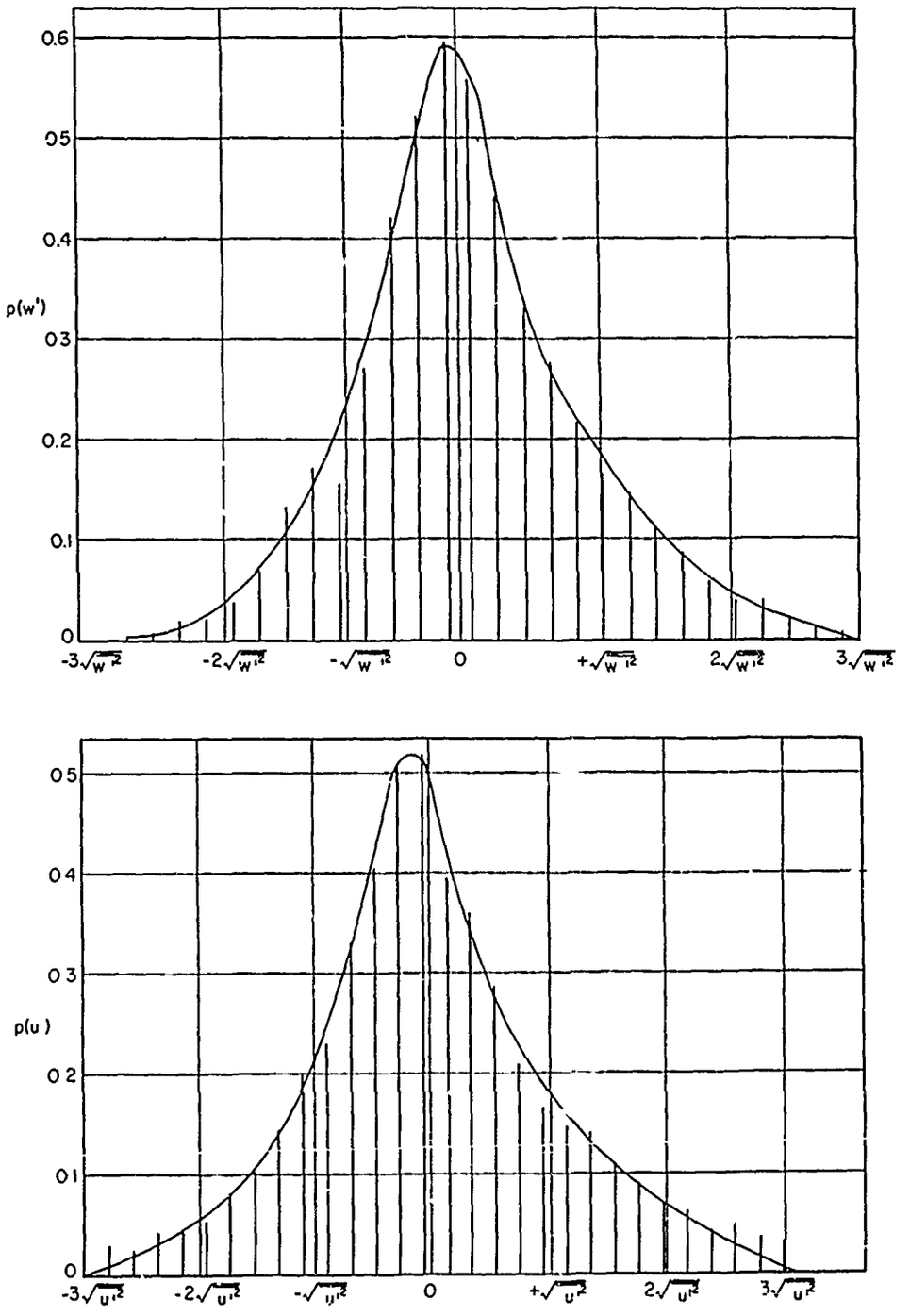

Fig. 10 Probability density distribution p(w') and p(u') at x = 12"

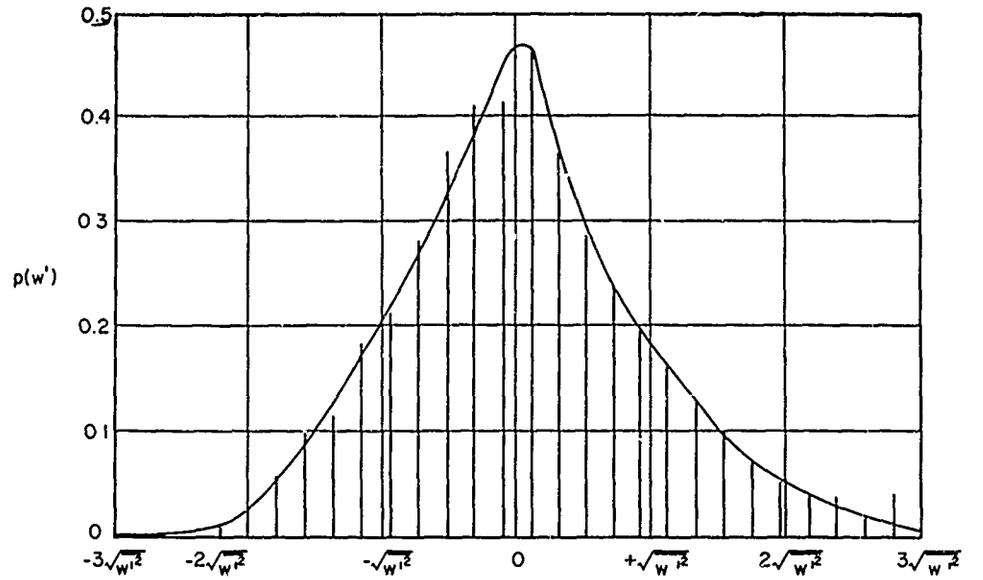

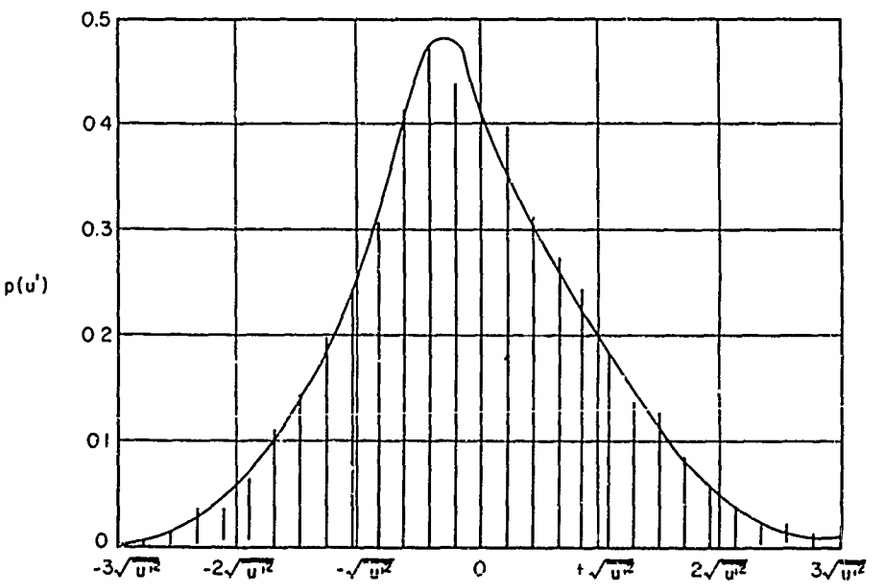

Fig. 11 Probability density distribution p(w') and p(u') at x = 24"

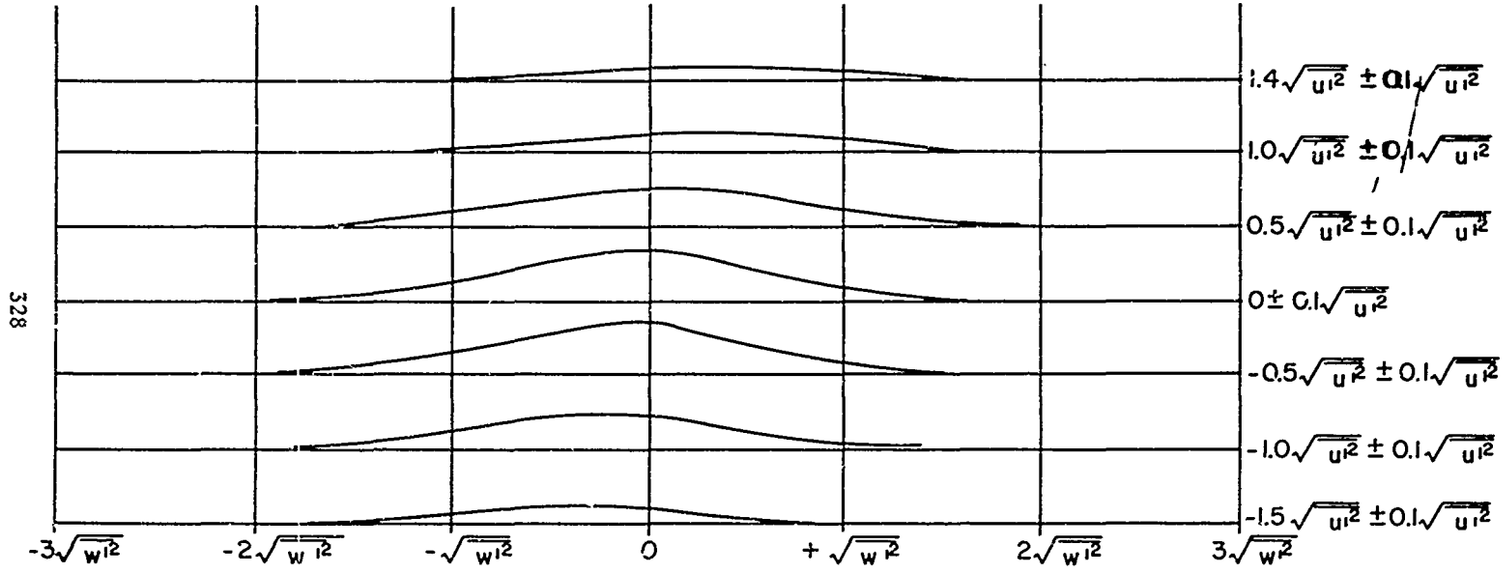

Fig. 12 Joint probability density distribution $p(w', u')$ at $x = 32''$

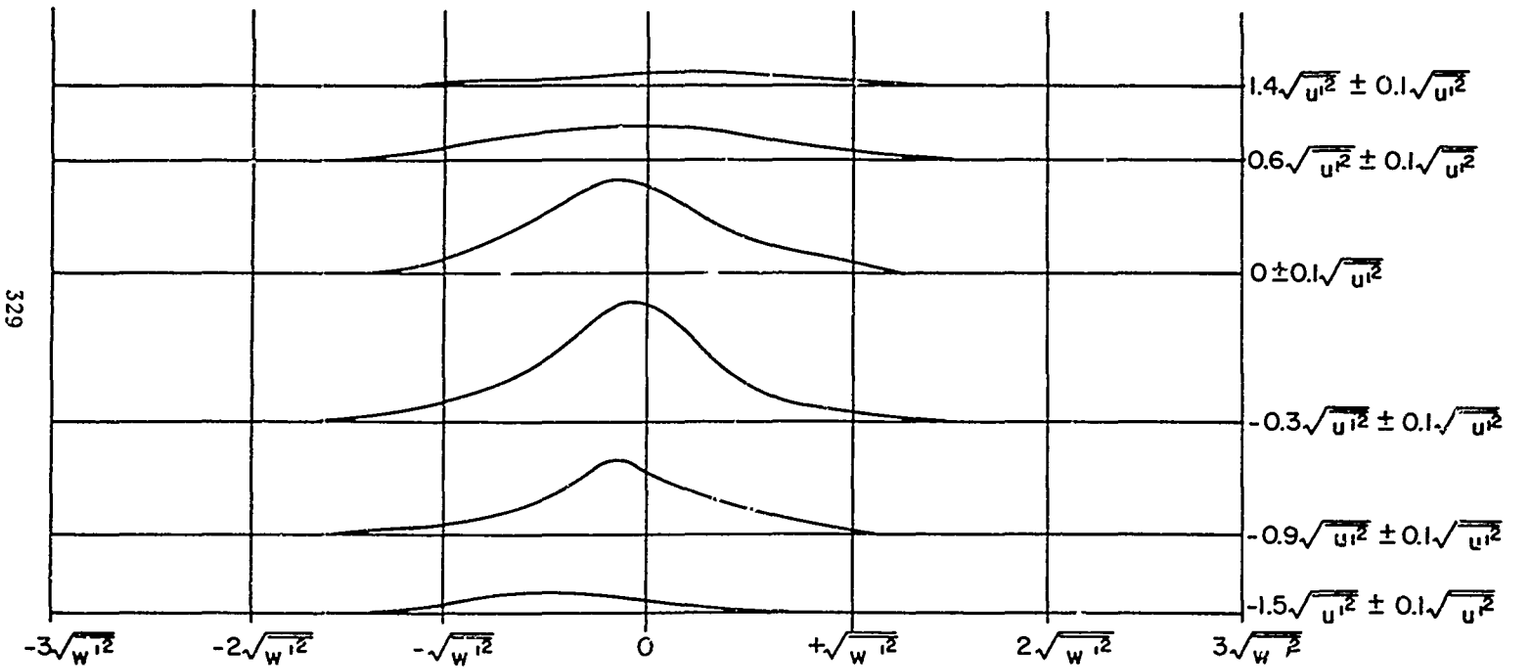

Fig. 13 Joint probability density distribution $p(w', u')$ at $x = 12''$

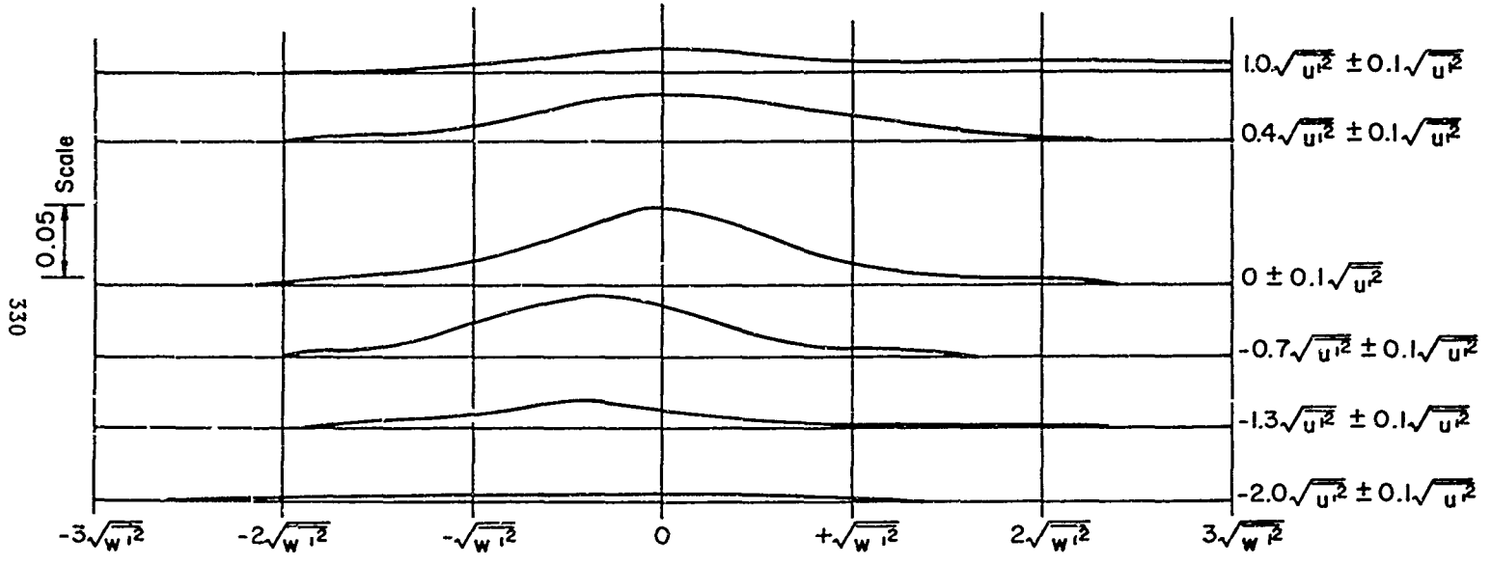

Fig. 14 Joint probability density distributions $p(w';u')$ at $x = 24''$

SUMMARY

In this paper we have derived a probabilistic description of the fluctuating velocity field along a hypothetical missile trajectory. By means of time scale arguments, it was shown that the problem of determining the velocity field everywhere can be reduced to determinations of the probability density distribution of $p(u')$ and the joint probability density distributions $p(w_i' u_i')$, $p(v', u_i')$ and $p(u_i, u_{i-1}')$. The shapes of joint distribution functions were determined for a few points along a trajectory located downwind of a model hill of sinusoidal shape.

Also, the spectra along this trajectory were given and discussed in the light of turbulence theory. Universal curves were found for the highest frequencies, but the inertial subrange was not found to possess a universal Kolmogoroff constant.

ACKNOWLEDGMENTS

Financial support for this study was obtained through U.S. Army Grant DA-AMC-28-043-65-G20. The help of Messrs. R. Kung and P. Su in taking and analyzing the experimental data is greatly appreciated.

REFERENCES

Hinze, J.O., "Turbulence" McGraw-Hill, New York, New York, 1959.

Margolis, D.P. and J.L. Lumley, "Curved turbulent mixing layer." Physics of Fluids, Vol. 8, pp. 1775-1784, 1965.

Plate, E.J. and C.Y. Lin, "The velocity field downstream from a two-dimensional model hill." Final Report, Part I, to U.S. Army Materiel Agency under Contract DA-AMC-36-039-63-G7, Civil Engineering Report No. CER65-14, Colorado State University, Fort Collins, Colorado, 1965.

Plate, E.J. and T.C. Lin, "Laboratory studies of mean velocity distributions in a thermally stratified boundary layer." Fluid Mechanics Paper No. 5, Colorado State University, Fort Collins, Colorado, 1966.

Pond, S., R.W. Stewart and R.W. Burling, "Turbulence spectra in the wind over waves." Journal of Atmospheric Sciences, Vol. 20, pp. 319-324, 1963.

Sandborn, V.A. and R.D. Marshall, "Local isotropy in wind tunnel turbulence." Technical Report CER65-71, for U.S. Army Grant No. DA-AMC-28-043-64-G9, Civil Engineering Department, Colorado State University, Fort Collins, Colorado, 1965.

LOW LEVEL WIND STUDY

by

M. D. Freeman

1. INTRODUCTION:

Low level winds are a major factor affecting the thrust portion of an unguided rocket trajectory. In the Honest John & Little John rocket systems, low level wind correction data are normally determined by use of AN/MMQ-1 series wind measuring sets. Tests were conducted at Fort Sill, Oklahoma, in the fall of 1966 to determine the reliability of the AN/MMQ-1B when used to measure incident wind and to determine the best method for predicitng low level wind at time of fire. The hand-held anemometer ML-433 was also tested to determine the feasibility of using it as a back-up device for the AN/MMQ-1B wind measuring set.

2. WIND MEASURING DEVICES:

a. The AN/MMQ-1B wind measuring set (windset) consists of a fifty-foot collapsible mast, a transmitter, and an indicator. The mast is extended hydraulically to a maximum length of fifty feet, 1 inch and is mounted on a M101 trailer. The mast is initially oriented parallel to the line of fire. The transmitter contains an impeller-driven generator with an output of six volts dc at 1000 rpm. The output of the impeller is fed through sine-cosine potentiometers mounted inside the vertical support housing of the transmitter to the indicator box. The indicator contains circuitry which provides readout of the input voltage on range and cross wind meters. The meters are calibrated in miles per hour and range from 0-25 or 0-50 mph depending on the setting of a scaling switch.

Two other switches on the AN/MMQ-1B are of interest, the AVER 'DIRECT READING switch and the MINUTES switch. The AVERAGE/DIRECT READING switch allows the operator to select either a reading of the direct wind or a reading of the average wind. The MINUTES switch determines the length of the averaging interval. This interval may be 1/2, 1, 2, 3, or 5 minutes. In the circuit the MINUTES switch selects a specific capacitor which averages the output of the transmitter for the indicated interval. Thus a moving or sliding average of the incident wind is read on the range and cross wind meters. Low level wind components, relative to the line of fire, are converted to launcher corrections by use of an appropriate firing table.

b. The ML-433 anemometer used in the study consists of a compass graduated in 400 mil increments mounted in a velometer which measures wind velocity in knots and is graduated in 0.2 knot increments on the 0-8 knot scale In operation the anemometer is held at eye level and rotated until the scribe line on the wind vane coincides with the alignment pin on the body of the anemometer. The direction of the wind is read from the compass. The velocity of the wind is obtained from the meter mounted in the anemometer.

3. METHOD OF STUDY:

a. On 1 September the first test of the AN/MMQ-1B was conducted. This test consisted primarily of subjecting the windset to non-standard physical operating conditions representative of field use and observing the results. Extreme lengths of field wire were inserted between the transmitter and the indicator, connections were purposely interchanged, and other tests of this type were conducted.

b. On 3 November 1966, the second and major test of the study was held. At 0800 hours two AN/MMQ-1B windsets and two ML-433 anemometers were taken to the test site. The site was a physical training field. Ground cover consisted of short grass (3-4 inches). The field covered a level area approximately 200 meters by 200 meters. The nearest buildings were located 600 meters east of the test site. Small rolling hills and open plain extended to the North, South, and West of the site. The M101 trailers containing the windsets were placed approximately 15 meters apart in the center of the field on an East-West line. Both anemometers were placed about 10 meters south of the windsets on the perpendicular bisector of the line joining them. The windsets and anemometers had been in use by troops of the 2d Battalion, 30th Artillery, for live rocket firings. Troops of the 2d/30th supported the field test. Prior to actual use, both windsets were calibrated by the U. S. Army Artillery Board using a Wind Simulator Set. This set calibrates both the transmitter and indicator. During the calibration one of the transmitters was shown to have a defective cosine potentiometer and had to be replaced. Calibration was completed at 1000 hours. At this time the windsets were erected. The ML-433 anemometers were not tested for calibration error. Both devices had been giving reliable results in the field and readings matched closely. The windsets were ready for operation at 1130 hours. However, there was no measurable wind at this time (the AN/MMQ-1B cannot measure wind speed less than 1 mile per hour). A light and variable wind began at 1345 hours and persisted throughout the remainder of the test. Readings were made using the 1/2 and 1 minute average positions and the direct reading position on the windsets. All anemometer readings were direct.

c. At present low level wind corrections are determined by use of the windset or pilot balloon. When these methods are not available the zero line of the met message is used. Two techniques for applying the low level wind corrections have been developed. The recurring technique requires that the rocket firing wait until the previously measured wind recurs within $\pm$ 1 mph per component. The predicted technique uses a five minute average of the wind to predict the wind at a predetermined time of fire. This average must end at least two minutes before the time of fire so that corrections may be made to the launcher azimuth and deflection. The five minute average used may be one reading with the MINUTE switch in the five minute position or the mean of five readings with the switch in the one minute position. Of all Honest John/Little John firings in 1966, 17% used the recurring technique with the windsets, 9% used either pilot balloon or zero line of the met message, and 74% used the predicted technique with the windset. For this study the predicted technique was tested.

d. A comparison of a five minute average with a 1 1/2 minute average of wind was made using both average and direct readings from the windset and direct readings from the anemometer. The data were collected in two sets of measurements, both sets being recorded with each windset and each anemometer being read by a different individual. During the first set, the windsets were in the one minute average mode and during the second set the windsets were in the 1/2 minute average mode.

e. Designating the assumed rocket firing time as T = 0, then at T - 7 minutes, an initial reading of anemometers was recorded and one minute

later both windset and anemometers readings were recorded, the procedure being repeated for a total of 5 readings per windset and 6 readings per anemometer. This same procedure was used in the second set of measurements except that the initial reading was at T - 3 1/2 minutes, the averaging interval was 1/2 minute, and only 3 readings per windset and 4 readings per anemometer were taken. For this test, time of fire of the rocket was assumed to be two minutes after the last wind measuring device reading. At T - 1/2 minute, at T = 0, and at T + 1/2 minute, readings were again taken of the incident wind by all four instruments, with the windsets in the direct reading mode.

f. The total number of readings for each windset was 30 in the 1 minute average mode (5 readings per trial for 6 trials), 48 in the 1/2 minute average mode (3 readings per trial for 16 trials), and 66 in the direct mode (3 readings per trial for 22 trials). The total number of readings for each anemometer was 36 for the 1 minute series (6 readings, 6 trials), 64 for the 1/2 minute series (4 readings, 16 trials), and 66 for the direct series (3 readings, 22 trials).

4. DATA REDUCTION:

a. Data reduction was accomplished in two phases by the CDC G-15 computer located in the Gunnery Department, U. S. Army Artillery & Missile School, Fort Sill, Oklahoma. Programs were written which were used in both phases. In the first phase, these programs:

(1) Resolved individual anemometer readings into components, converting from azimuth in mils and speed in knots to range and cross wind in miles per hour. (The ML-433 compass is marked every 22 1/2 degrees and labeled every 45 degrees with the letters N, NE, E, SE, S, SW, W, and NW. Anemeometer readings were converted mentally at the time of reading to the nearest 100 mils and recorded as such during the test).

(2) Converted direct anemometer readings into equivalent one minute or one-half minute averages corresponding to the windset readings for the same time interval.

(3) Calculated two values of standard wind:

(a) Case I wind - standard wind (W_s) is the average of the two AN/MMQ-1B windset readings, i.e.,

$$W_s = \frac{W_1 + W_2}{2} \quad \text{cross/range}$$

(b) Case II wind - standard wind (W_s) is the average of the two AN/MMQ-1B and the two ML-433 readings, i.e.,

$$W_s = \frac{W_1 + W_2 + A_1 + A_2}{4} \quad \text{cross/range}$$

where W_1 = Output of windset number 36

W_2 = Output of windset number 10

A_1 = Output of anemometer number 52

A_2 = Output of anemometer number 27

(4) Calculated average and standard deviation of measured wind from standard wind (range and cross wind components). Standard wind is taken to be the Case I and Case II averages, using the 1 minute or 1/2 minute average readings. Measured wind values are range and cross wind components at T - 6, T - 5, T - 4, T - 3, and T - 2 minutes for the 1 minute series and components at T - 3, T - 2 1/2, and T - 2 minutes for the 1/2 minute series.

(a) Deviation (ΔW_m) = Standard Wind (W_s) - Measured Wind (W_m)

(b) Average Deviation ($\overline{\Delta W_m}$) = $(W_s - W_m)/N$

N = 30 for 1 minute average series

N = 48 for 1/2 minute average series

(c) Standard Deviation (σ_m) = $\sqrt{\frac{\Sigma(\Delta W_m)^2 - N(\overline{\Delta W_m})^2}{N}}$

(5) Calculated average and standard deviation of predicted wind from standard wind. Standard wind is taken to be be Case I and Case II averages, using the direct readings at T - 1/2, T = 0, and T + 1/2 minutes. Predicted wind is the mean wind for each 5 or 3 1/2 minute period (cf paragraph 3c).

(a) Deviation (ΔW_p) = Standard Wind (W_s) - Predicted Wind (W_p)

(b) Average Deviation ($\overline{\Delta W_p}$) = $(W_s - W_p)/N$

N = 18 for the 1 minute average series

N = 48 for the 1/2 minute average series

(c) Standard Deviation (σ_p) = $\sqrt{\frac{\Sigma(\Delta W_p)^2 - N(\overline{\Delta W_p})^2}{N}}$

b. In the second phase of the data reduction, range and cross wind deviations were combined in order to obtain a single measure of instrument precision. Average and standard deviations were calculated as in the first phase of the data reduction. In this phase, however, N = 60 for the 1 minute average series, and N = 96 for the 1/2 minute average series.

5. PRESENTATION OF DATA:

a. Range wind (R) and cross wind (X) values are in miles per hour.

b. TABLE I. Average deviation of measured wind from standard wind for each device.

DEVICE	CASE I WIND				CASE II WIND			
	1/2 MIN AV		1 MIN AV		1/2 MIN AV		1 MIN AV	
	X	R	X	R	X	R	X	R
AVERAGE DEVIATION:								
W1	*	*	*	*	-0.1	0.1	-0.4	-0.1
W2	-0.3	0.1	-0.4	0.1	0.4	-0.1	0.4	-0.5
A1	-0.4	0.1	-0.2	0.5	-0.3	0.1	-0.2	0.2
A2	0.2	0.0	0.2	0.7	0.0	0.0	0.2	0.4
STANDARD DEVIATION:								
W1	*	*	*	*	0.6	0.6	0.4	0.4
W2	0.6	0.4	0.1	0.3	1.0	0.6	0.4	0.6
A1	1.0	0.7	0.9	0.6	0.6	0.4	0.6	0.3
A2	1.2	0.7	0.9	0.7	0.6	0.4	0.4	0.4

*For Case I wind, (W1 + W2)/2, W1 values are redundant.

c. The wind measuring devices were also tested to determine their effectiveness in predicting wind at time of fire and time of fire $\pm$ 1/2 minute. The direct readings made at T - 1/2, T + 0, and T + 1/2 minutes were averaged and Case I and Case II values of standard wind determined. By calculating average and standard deviations of the predicted wind from standard wind, the effect of allowing the actual time of fire to vary $\pm$ 1/2 minute from the desired time of fire could be examined. Predicted wind was taken to be the mean of the 1/2 or 1 minute average readings taken up to 2 minutes prior to desired time of fire. (Two minutes is the

minimum time normally allotted to make corrections to the rocket launcher and was determined from actual firings.)

(1) TABLE 2. Deviation of predicted wind from standard wind at T - 1/2 minute.

DEVICE	CASE I WIND				CASE II WIND			
	1/2 MIN AV		1 MIN AV		1/2 MIN AV		1 MIN AV	
	X	R	X	R	X	R	X	R
AVERAGE DEVIATION:								
W1	-2.9	1.0	0.1	1.0	-2.4	0.3	0.5	0.9
W2	-2.2	0.6	1.1	0.7	-2.0	0.1	1.5	0.6
A1	-0.9	0.4	0.4	1.6	-0.6	-0.4	0.8	1.6
A2	-0.5	-0.3	0.9	1.8	1.8	-0.6	1.3	1.7
STANDARD DEVIATION:								
W1	1.9	1.9	2.8	3.0	1.8	0.9	3.1	3.0
W2	2.5	1.8	2.7	2.7	1.8	0.9	3.0	2.8
A1	2.5	2.4	2.5	2.5	1.9	1.6	2.8	2.7
A2	2.8	2.7	2.8	3.0	3.0	1.8	3.1	2.8

(2) TABLE 3. Deviation of predicted wind from standard wind at T = 0 minutes.

DEVICE	CASE I WIND				CASE II WIND			
	1/2 MIN AV		1 MIN AV		1/2 MIN AV		1 MIN AV	
	X	R	X	R	X	R	X	R
AVERAGE DEVIATION:								
W1	-2.5	0.5	0.7	0.4	-2.2	0.5	0.8	0.7
W2	-2.1	0.3	1.6	0.0	-1.8	0.3	1.7	0.3
A1	-0.6	-0.2	0.9	1.0	-0.3	-0.2	1.0	1.3
A2	-0.4	-0.3	1.4	1.2	-0.1	-0.4	1.5	1.4
STANDARD DEVIATION:								
W1	2.7	1.3	1.9	3.0	2.1	1.3	2.1	2.8
W2	2.4	1.2	1.9	2.5	2.1	1.3	1.9	2.5
A1	2.1	1.8	1.8	2.7	1.8	1.6	1.8	2.5
A2	2.2	1.8	2.1	3.1	1.9	1.8	2.1	3.0

(3) TABLE 4. Deviation of predicted wind from standard wind at T + 1/2 minute.

DEVICE	CASE I WIND				CASE II WIND			
	1/2 MIN AV		1 MIN AV		1/2 MIN AV		1 MIN AV	
	X	R	X	R	X	R	X	R
AVERAGE DEVIATION:								
W1	-2.6	0.6	-0.8	-0.1	-2.2	0.5	-0.1	-0.0
W2	-2.2	0.4	0.1	-0.5	-1.8	0.3	0.8	-0.3
A1	-0.7	-0.1	-0.5	0.4	-0.4	-0.2	0.1	0.5
A2	-0.5	-0.2	-0.0	0.6	-0.1	-0.3	0.6	0.7
STANDARD DEVIATION:								
W1	2.4	1.5	1.6	4.0	1.9	1.3	1.9	3.8
W2	2.5	1.5	1.6	3.8	2.1	1.2	1.9	3.6
A1	2.4	1.8	1.5	3.7	1.9	1.6	1.9	3.6
A2	2.5	1.8	1.3	3.8	2.1	1.8	1.6	3.8

(4) TABLE 5. Deviation of predicted wind from standard wind for all devices combined.

TIME	CASE I WIND				CASE II WIND			
	1/2 MIN AV		1 MIN AV		1/2 MIN AV		1 MIN AV	
	X	R	X	R	X	R	X	R
AVERAGE DEVIATION:								
T - 1/2	-1.6	0.4	0.6	1.3	1.3	-0.1	1.0	1.2
T = 0	-1.4	0.1	1.1	0.6	-1.1	0.1	1.2	0.9
T + 1/2	-1.5	0.2	-0.3	0.4	-1.2	0.1	0.3	0.2
STANDARD DEVIATION:								
T - 1/2	4.9	4.5	5.4	5.6	3.7	2.7	6.0	5.6
T = 0	4.7	3.1	3.9	5.6	3.9	3.0	3.9	5.4
T + 1/2	4.9	3.3	3.0	7.7	4.0	3.0	3.7	7.4

d. To derive an overall measure of device precision, range and cross wind components were treated as items of the same set. This process yields one total average and standard deviation value for each wind measuring device at each averaging interval.

e. TABLE 6. Total deviation of each device when used to measure wind.

DEVICE	CASE I WIND		CASE II WIND	
	1/2 MIN AV	1 MIN AV	1/2 MIN AV	1 MIN AV
AVERAGE DEVIATION:				
W1	*	*	-0.0	-0.1
W2	-0.0	-0.1	0.3	0.1
A1	-0.1	0.1	-0.2	-0.3
A2	-0.1	0.4	0.0	0.2
STANDARD DEVIATION:				
W1	*	*	0.6	0.6
W2	0.6	0.4	0.9	0.4
A1	1.0	0.9	0.6	0.6
A2	1.0	0.9	0.6	0.4

* For Case I wind $(W1 + W2)/2$, W1 values are redundant.

f. Appendix 1 contains a tabulation of the data obtained from the test.

6. DISCUSSION:

a. In Table 1, Case II wind ($W_t = \frac{W1 + W2 + A1 + A2}{4}$) gives the best value of standard wind for calculation of statistics. In Case II, the average deviation ranges from -0.3 mph to 0.4 mph for the 1 minute average. The standard deviation ranges from 0.0 mph to 0.6 mph for the 1/2 minute average and from 0.2 to 0.6 for the 1 minute average. The windsets were calibrated before the test to within the $\pm$ 1 mph inherent limits. The windsets had also been used in the field for tactical rocket firings.

The results shown in Table 1 verify the accuracy and precision of the AN/MMQ-1B Wind Measuring Set when used to measure incident wind. The ML-433 anemometers also exhibit the same degree of accuracy with standard deviation no greater than 0.6 mph. The results were obtained ignoring wind profiles. The ML-433 readings were made at approximately six feet above the ground; the AN/MMQ-1B readings were made at approximately 50 feet above the ground. Apparent lack of profile may be due to the light and variable nature of the wind during the test. Prior to more tests with higher level winds, results suggest that the ML-433 would prove valuable as a back-up device for the AN/MMQ-1B windset (conversion of the ML-433 azimuth and velocity output to range and cross wind can be accomplished by use of graphs or tables.)

b. The average deviation of predicted wind from standard wind at T = 0 (Table 4), ranges from -1.4 mph to 1.2 mph, the standard deviation ranges from 3.0 mph to 5.6 mph, deviations at T $\pm$ 1/2 minutes are slightly greater with a maximum standard deviation of 7.7 mph for T + 1/2 minute. Due to the variable nature of the wind experienced during the test, all predicted wind deviations are much larger than those obtained for wind measurement only. The close agreement among T - 1/2, T = 0, and T + 1/2 minute predictions indicate that the actual time of fire may be varied $\pm$ 1/2 minute without degrading the accuracy of the low level wind corrections.

c. Table 6 supports the conclusions based on Table 1 that each device does measure wind as accurately as inherent limitations allow. Due to combining range and cross wind deviations into one set, sample size is doubled and validity of statistical processes used increased. Standard

deviation ranges from 0.4 mph to 1.0 mph. Average deviation ranges from -0.3 mph to 0.4 mph.

7. CONCLUSIONS:

a. That portion of the test designed to evaluate the use of a 1 1/2 minute average interval instead of the presently used 5 minute average interval yielded the following conclusions:

(1) There was no significantly greater deviation in measured wind from standard wind when the shorter averaging interval was used.

(2) Deviation of predicted wind from standard wind was large in both the 5 and the 1 1/2 minute average interval, but there was no significant difference between the two intervals.

(3) For low level winds of a light and variable nature (velocity less than 10 mph), three 1/2 - minute averages may be used to determine the value of the predicted wind at time of fire.

(4) A study by Rachele and Armendariz (1967) concludes that lag time (the interval between the time the last data sample was taken and firing of a rocket) " . . must be made small as possible and the sampling interval 'comparatively' large."[1] Thus, more data are needed to confirm or deny the conclusion reached in 7 (a3).

b. For that portion of the test designed to evaluate the wind measuring devices as predictors of wind at time of fire $\pm$ 1/2 these conclusions are reached:

(1) Actual time of fire can vary $\pm$ 1/2 minute from desired time of fire without seriously affecting the reliability of the low level wind corrections made to the launcher.

(2) Use of the ML-433 anemometer, in conjunction with the AN/MMQ-1B Wind Measuring Set, to determine the value of predicted wind at T = 0 can increase the reliability of this value and, hence, any launcher corrections made.

c. The overall standard deviation for the AN/MMQ-1B windsets tested (when measuring incident wind) was 1.3 mph.

d. The standard deviation for the ML-433 anemometers tested (when measuring incident wind) was 1.2 mph.

e. (In c and d above, Case II wind was used and 1/2 minute and 1 minute averaging intervals were combined.)

f. The standard deviations in wind as predicted by the devices are given below. (Case II wind was used for calculations).

	T - 1/2	T = 0	T + 1/2
AN/MMQ-1B:	4.9 mph	4.6 mph	5.0 mph
ML-433:	4.3 mph	4.4 mph	4 6 mph

(Overall system standard deviations were calculated from the following formula:

$$\sigma_{(total)} = \sqrt{\sigma_1^2 + \sigma_2^2 + \sigma_3^2 + \ldots}$$, σ_i = standard deviation of subset),

[1] Henry Rachele and Manuel Armendariz. "Surface Wind Sampling for Unguided Rocket Impact Prediction"., revised form 7 March 1967. Journal of Applied Meteorology, Vol. 6, No. 3, June, 1967. Boston: American Meteorological Society.

APPENDIX I

DATA Obtained During Low Level

Wind Test II on 3 November 1966

(All windset values are averages as given by the average switch on the windset. All anemometers values are averages as calculated by the data reduction program.)

READINGS(T=FIRE)		WINDSETS				ANEMOMETERS			
		W1		W2		A1		A2	
1346 hrs		X	R	X	R	X	R	X	R
AVERAGE:	T-3	-3.0	3.0	-3.0	3.0	-3.9	2.4	-1.3	5.4
	T-2.5	-2.0	2.0	-2.0	2.0	-2.4	1.6	-1.4	3.1
	T-2	-1.5	1.0	-1.5	2.0	- .4	.4	- .1	1.1
DIRECT:	T-.5	-1.5	1.0	-4.0	.5	-2.1	.9	-2.1	.9
	T=0	-3.0	1.0	-3.5	1.0	-3.5	.0	-4.6	.0
	T+.5	-3.0	1.0	-4.0	1.0	-2.1	.9	-2.1	.9
1352 hrs									
AVERAGE:	T-3	-4.0	.0	-4.0	1.0	-2.7	.8	-3.1	1.5
	T-2.5	-2.5	- .5	-3.0	1.0	-1.1	.1	-1.6	.7
	T-2	-3.0	- .5	-4.0	.0	-2.3	- .4	-2.3	- .2
DIRECT:	T-.5	-7.0	.0	-7.0	2.0	-4.6	.0	-6.6	-2.0
	T=0	-5.0	-1.0	-4.0	1.0	-4.6	.5	-5.7	- .6
	T+.5	-5.0	-1.0	-5.0	-1.0	-2.3	.2	-4.6	- .5
1420 hrs									
AVERAGE:	T-3	-5.0	.5	-5.0	3.0	-4.5	.6	-5.7	.9
	T-2.5	-4.5	.0	-4.0	2.0	-4.0	.2	-5.2	.2
	T-2	-4.0	.0	-4.5	1.5	-3.9	.9	-4.5	.7
DIRECT:	T-.5	-5.0	.0	-5.0	1.0	-4.5	.9	-6.9	.7
	T=0	-4.0	.0	-5.5	.5	-6.9	.7	.0	.0
	T+.5	-5.5	-1.0	-7.0	-1.0	-3.4	.3	-5.6	1.1
1426 hrs									
AVERAGE:	T-3	-4.0	-2.5	-4.0	-1.0	-2.2	-1.9	-3.6	-1.8
	T-2.5	-3.5	-3.0	-3.5	-1.5	-3.6	-2.8	-4.5	-2.6
	T-2	-3.5	-3.0	-3.5	-1.5	-3.3	-2.2	-4.5	-2.6
DIRECT:	T-.5	-2.0	-2.0	-1.0	-1.5	-1.0	- .6	-2.3	- .4
	T=0	.0	.0	-1.0	- .5	- .7	- .9	-1.3	-3.2
	T+.5	.0	.0	-1.0	.0	.0	.0	- .8	- .8

READINGS (T=FIRE)		WINDSETS				ANEMOMETERS			
		W1		W2		A1		A2	
		X	R	X	R	X	R	X	R
1526 hrs									
	T-3	-5.0	6.0	-6.0	5.0	-4.7	5.0	-4.6	5.9
	T-2.5	-4.0	6.0	-5.0	5.0	-3.1	3.4	-3.9	4.3
AVERAGE:	T-2	-3.5	5.0	-4.0	4.0	-3.5	4.6	-4.3	4.7
	T-.5	-7.0	3.5	-6.0	4.0	-5.3	4.4	-5.7	3.8
DIRECT:	T=0	-7.0	2.5	.0	3.0	-7.1	3.8	-7.7	2.3
	T+.5	-6.5	3.0	-6.0	4.0	-3.8	2.6	-3.8	2.6
1530 hrs									
	T-3	-4.0	3.0	-5.0	5.0	-5.5	4.1	-6.2	4.1
	T-2.5	-4.0	4.0	-5.5	4.0	-6.2	4.2	-6.7	4.5
AVERAGE:	T-2	-5.0	3.5	-7.0	4.0	-6.9	5.1	-7.2	4.7
	T-.5	-5.0	2.0	-7.0	4.0	-4.1	2.2	-5.8	.0
DIRECT:	T=0	-9.0	3.0	- .0	4.0	-6.7	4.5	-6.7	4.5
	T+.5	-9.0	2.5	-8.0	4.0	-6.7	4.5	-7.4	3.1
1535 hrs									
	T-3	-6.0	2.0	-6.0	2.0	-5.5	1.7	-6.0	1.8
AVERAGE:	T-2.5	-5.0	1.0	-6.0	1.0	-4.4	1.1	-5.5	1.1
	T-2	-5.0	.0	-1.0	1.0	-4.0	.4	-6.3	.7
	T-.5	-9.0	2.5	- .0	2.0	-6.9	.7	-6.9	.0
DIRECT:	T=0	-9.0	3.0	- .0	2.0	-7.7	5.1	-8.5	3.5
	T+.5	-8.0	2.5	-9.0	2.0	-7.4	3.1	-6.4	2.6
1540 hrs									
	T-3	-7.0	3.0	-8.0	3.0	-6.1	3.3	-6.6	3.5
AVERAGE:	T-2.5	-7.0	3.0	-8.0	3.0	-5.4	3.3	-6.4	3.8
	T-2	-6.5	2.0	-7.5	2.5	-4.9	3.0	-6.9	2.6
	T-.5	-6.0	3.0	-6.0	3.5	-3.3	1.0	-4.5	.9
DIRECT:	T=0	-5.0	4.0	-5.0	4.0	-4.8	3.2	-4.8	3.2
	T+.5	-5.0	3.5	-6.0	4.0	-3.3	3.3	-3.2	4.8

READINGS (T-FIRE)		WINDSETS				ANEMOMETERS			
		W1		W2		A1		A2	
1545 hrs		X	R	X	R	X	R	X	R
	T-3	-5.0	5.0	-7.0	3.0	-4.1	4.1	-4.3	2.7
	T-2.5	-4.5	4.0	-6.0	4.0	-4.0	4.9	-4.9	4.9
AVERAGE:	T-2	-4.5	3.5	-6.0	3.5	-4.8	4.8	-6.4	4.6
	T-.5	-7.0	3.0	-7.0	3.0	-6.6	2.0	-6.8	1.3
DIRECT:	T=0	-8.0	1.5	-6.0	2.5	-4.8	3.2	-6.4	2.6
	T+.5	-7.0	1.5	-5.0	2.0	-7.7	2.3	-6.9	.7
1550 hrs									
	T-3	-7.0	4.0	-8.0	3.0	-5.3	2.2	-5.4	4.7
	T-2.5	-6.0	3.5	-7.0	3.5	-5.8	2.4	-5.4	4.7
AVERAGE:	T-2	-5.5	3.5	-6.0	3.0	-5.1	2.6	-5.4	3.1
	T-.5	-6.0	3.0	-5.0	4.0	-1.9	1.3	-3.2	1.3
DIRECT:	T=0	-5.5	4.0	-6.0	4.0	-4.1	4.1	-3.3	3.3
	T+.5	-7.0	5.0	-7.0	5.0	-4.8	3.2	-6.4	2.6
1555 hrs									
	T-3	-7.0	3.0	-9.0	3.0	-7.1	3.8	-7.4	3.1
AVERAGE:	T-2.5	-7.0	1.0	- .0	1.5	-8.2	2.4	-8.8	2.7
	T-2	-7.0	-1.0	- .0	.0	-9.1	.4	-9.0	- .0
	T-.5	-7.5	.0	-9.0	-1.0	-6.9	.0	-8.1	.0
DIRECT:	T=0	-7.0	.0	-7.0	1.0	-9.2	.0	-9.2	.0
	T+.5	-5.0	2.5	.0	2.0	-5.6	1.1	-5.7	.6
1600 hrs									
	T-3	-7.5	.0	-1.0	3.0	-7.9	1.3	-6.6	1.3
AVERAGE:	T-2.5	-7.5	3.5	-9.0	3.0	-7.5	3.9	-6.9	2.9
	T-2	-7.5	3.0	-8.0	3.0	-7.5	3.9	-7.6	2.7
	T-.5	-7.0	2.0	-6.0	3.0	-4.8	3.2	-4.4	3.7
DIRECT:	T=0	-7.0	2.0	-7.0	3.0	-5.5	1.7	-6.6	2.0
	T+.5	-7.5	2.0	-8.0	4.0	-5.5	1.7	-6.6	2.0

READINGS (T-FIRE)		WINDSETS				ANEMOMETERS			
		W1		W2		A1		A2	
		X	R	X	R	X	R	X	R
1605 hrs									
AVERAGE:	T-3	-5.0	2.0	-6.0	2.0	-5.2	- .2	-4.6	- .2
	T-2.5	-5.0	2.0	-6.5	2.5	-6.6	1.5	-5.5	1.3
	T-2	-5.5	2.0	-7.0	2.0	-7.7	2.3	-7.1	2.1
DIRECT:	T-.5	-6.0	3.0	-5.5	3.5	-4.4	3.7	-4.8	3.2
	T=0	-4.0	2.5	-4.5	3.0	-3.3	3.3	-3.6	2.9
	T+.5	-6.5	2.5	-6.0	2.0	-5.3	2.2	-6.1	3.3
1610 hrs									
AVERAGE:	T-3	-6.0	5.0	-6.0	2.5	-4.7	2.2	-4.2	2.9
	T-2.5	-6.0	3.5	-7.0	2.0	-6.4	2.5	-4.8	2.9
	T-2	-6.0	2.5	-7.5	2.0	-7.7	2.3	-6.7	1.6
DIRECT:	T-.5	-8.5	1.0	-8.0	1.0	-6.9	.7	-8.0	.8
	T=0	-7.5	- .5	-7.5	- .5	-4.6	.5	-5.6	1.1
	T+.5	-8.0	1.0	-8.0	-1.0	-6.9	- .7	-6.9	.0
1615 hrs									
AVERAGE:	T-3	-6.0	.0	-7.0	1.0	-4.0	.0	-5.2	- .1
	T-2.5	-5.5	.0	-7.0	1.0	-5.8	.0	-6.9	- .3
	T-2	-6.0	.0	-7.0	.0	-6.9	.0	-7.5	.0
DIRECT:	T-.5	-6.0	.0	-6.0	2.0	-6.9	.7	-5.6	1.1
	T=0	-6.0	1.0	-5.0	1.0	-3.5	.0	-4.6	.5
	T+.5	-5.0	1.0	-6.0	1.5	-6.8	1.3	-6.6	2.0
1620 hrs									
AVERAGE:	T-3	-6.0	1.5	-6.0	.5	-3.9	.5	-3.7	- .7
	T-2.5	-4.5	.0	-5.0	1.0	-3.4	- .3	-3.2	- .8
	T-2	-5.0	.5	-6.0	1.0	-4.4	.9	-4.8	1.8
DIRECT:	T-.5	-5.5	1.0	-6.0	.5	-3.3	1.0	-4.6	.0
	T=0	-4.0	.5	-5.5	.5	-2.3	.2	-4.6	.0
	T+.5	-4.5	.5	-4.5	1.0	-3.4	- .3	-4.6	.0

READINGS(T=FIRE)		WINDSETS				ANEMOMETERS			
		W1		W2		A1		A2	
1356 hrs		X	R	X	R	X	R	X	R
	T-6	-5.0	3.0	-6.0	3.0	-4.8	1.8	-5.6	.8
	T-5	-4.0	2.5	-5.0	2.5	-4.3	1.8	-5.0	1.3
AVERAGE:	T-4	-3.0	2.5	-4.0	3.0	-2.6	1.3	-4.8	1.8
	T-3	-3.0	2.0	-3.5	3.0	-2.6	1.1	-4.1	2.0
	T-2	-3.0	1.5	-4.0	2.5	-3.1	1.4	-4.4	1.2
	T-.5	-1.5	2.0	-1.5	2.0	- .8	.8	-1.6	1.6
DIRECT:	T=0	-1.0	1.0	-1.0	1.0	-1.9	1.3	-2.2	2.7
	T+.5	-5.0	.0	-7.0	.5	-3.2	1.3	-5.8	.0
1405 hrs									
	T-6	-4.5	1.0	-5.0	2.0	-4.9	- .4	-4.8	-1.1
	T-5	-4.0	3.0	-5.0	2.5	-5.6	1.3	-5.4	.8
AVERAGE:	T-4	-4.0	1.5	-5.0	2.0	-6.2	1.0	-6.0	.9
	T-3	-5.0	1.0	-6.0	2.0	-6.2	1.0	-6.2	1.0
	T-2	-4.0	.5	-5.0	1.5	-4.5	1.0	-5.1	.8
	T-.5	-3.5	1.0	-3.5	1.0	.0	.0	.0	.0
DIRECT:	T=0	-2.0	1.5	-3.0	2.5	-2.0	1.1	-1.5	1.8
	T+.5	-4.5	-2.0	-4.0	-1.0	-2.3	.4	-2.7	2.2
1435 hrs									
	T-6	-3.0	2.0	-4.0	2.0	-3.1	1.5	-2.7	2.8
	T-5	-4.0	1.5	-4.5	1.5	-2.5	1.4	-2.4	2.2
AVERAGE:	T-4	-3.0	1.5	-4.0	1.5	-3.4	.7	-4.5	.7
	T-3	-3.5	1.0	-4.0	1.0	-4.5	.9	-5.2	.0
	T-2	-3.5	1.0	-4.5	.0	-3.2	.1	-4.0	- .2
	T-.5	-1.0	.0	-1.0	-1.0	.0	.0	- .8	- .8
DIRECT:	T=0	-1.0	-1.0	-4.0	-3.0	-1.0	- .5	-2.0	-1.1
	T+.5	-4.0	-3.0	-4.0	-3.0	-5.3	-4.4	-4.4	-3.7

READINGS (T=FIRE)		WINDSETS				ANEMOMETERS			
		W1		W2		A1		A2	
		X	R	X	R	X	R	X	R
1444 hrs									
AVERAGE:	T-6	-3.0	-3.0	-4.0	-1.0	-3.5	-3.8	-3.5	-4.5
	T-5	-4.0	-2.0	-6.0	-1.0	-4.0	-1.1	-4.5	-2.0
	T-4	-4.0	-1.0	-5.0	- .5	-4.0	.2	-5.0	- .7
	T-3	-3.0	.0	-4.0	.0	-1.7	- .0	-2.2	- .6
	T-2	-1.0	.0	-1.5	.0	- .6	.1	- .6	.1
DIRECT:	T-.5	.0	.0	-5.0	1.0	-4.6	.0	-6.9	.0
	T=0	-3.0	.0	-2.0	.5	-3.4	.7	-3.4	.7
	T+.5	-2.0	.0	-3.0	.5	.0	.0	.0	.0
1455 hrs									
AVERAGE:	T-6	-3.5	-1.5	-4.0	.0	-3.7	-1.6	-4.0	-2.2
	T-5	-4.0	-4.0	-4.5	-1.5	-3.9	-3.3	-4.3	-3.5
	T-4	-3.0	-3.0	-4.0	-2.0	-4.6	-3.1	-4.2	-3.8
	T-3	-3.5	-3.0	-5.0	-2.0	-6.1	-1.8	-5.2	-2.4
	T-2	-4.0	- .5	-6.0	.0	-6.7	- .3	-6.6	-1.3
DIRECT:	T-.5	-8.5	3.0	-8.0	4.0	-7.7	2.3	-7.7	2.3
	T=0	-6.5	2.0	-6.0	2.5	-6.4	2.6	-6.4	2.6
	T+.5	-6.0	2.0	-7.0	3.0	-5.3	2.2	-5.3	2.2
1505 hrs									
AVERAGE:	T-6	-6.0	2.0	-7.0	1.5	-4.9	1.4	-6.1	1.8
	T-5	-4.5	3.5	-5.0	2.5	-4.3	1.8	-5.4	1.9
	T-4	-5.0	4.0	-6.5	3.0	-4.8	3.1	-5.8	3.7
	T-3	-5.0	5.0	-6.0	4.0	-4.0	3.3	-5.5	4.2
	T-2	-6.0	5.0	-7.0	4.5	-4.9	4.0	-4.3	4.5
DIRECT:	T-.5	-5.0	4.5	-6.0	6.0	-3.1	7.4	-1.6	7.9
	T=0	-4.5	4.0	-4.0	5.0	-4.1	4.1	-1.3	6.8
	T+.5	-5.0	6.0	-5.0	6.0	-2.2	5.3	-3.3	6.1

BLANK PAGE

The Nondimensional Wind Shear over Heterogeneous Terrain

E. Peterson and H. A. Panofsky

The nondimensional wind shear, $\phi = (0.4z/u^*)\ (\partial V/\partial z)$ plays a basic role in the application of Monin-Obukhov similarity theory. Here u^* is the friction velocity, V the wind speed, z the height. In unstable air, ~~the~~ ϕ ~~behavior~~ as function of Richardson number is quite well determined by:

$$\phi = (1 - 18\ Ri)^{-1/4} \qquad 1$$

This equation fits well independent data from the Antarctic, from O'Neill, Nebraska, from Kerang, Australia, and elsewhere. Because, however, the variation of the Richardson number with height is not known a priori, Eq. 1 does not really specify the wind profile. This can be done only if ϕ is given as function of z/L. Unfortunately, there are relatively few published data over uniform terrain, including both good wind profiles and accurate estimates of the heat flux. The only generally available set of data of this type is that published by Swinbank (1964). Even here, the friction velocity was not measured directly and is somewhat uncertain. Also, no observations were taken in stable air. Businger (unpublished), after careful evaluation of these data, suggests that an equation of the form:

$$\phi = (1 - 18\ z/L)^{-1/4} \qquad 2$$

fits these data well. This form has the advantage over other forms (e.g., the Keyps equation), that it can be integrated with respect to height in terms of elementary functions, thus yielding an explicit expression for the wind profile in unstable air.

For the stable side, we only have the analysis by McVehil (1964), who suggests:

$$\phi = 1 + 7\ (K_m/K_h)(z/L) \qquad 3$$

Making use of the fact that at Round Hill, K_h/K_m in stable air is about 0.7, we suggest here, for stable air, the expression:

$$\phi = 1 + 10\ z/L \qquad 4$$

Actually, there is some doubt whether the nondimensional wind shear is uniquely determined by z/L in stable air, since radiation becomes relatively important. Some recent data obtained by Haugen and others over flat terrain in Kansas (unpublished) suggest that Equation 3 fits reasonably well.

The Round Hill data have the advantage over all the other published material that all ingredients have been measured independently; on the other hand, the terrain is complex. Figure 1 shows the nondimensional wind shear as function of z/L, for both towers A and B. The same figure also shows, as solid line, the predictions according to Equations 2 and 4. Clearly, the line well fits the observations from tower B. This tower is affected by relatively homogeneous terrain.

More interestingly, though, the data from 16m, tower A, definitely do not agree with the theory. Even in the limit of neutral air, the nondimensional wind shear is not unity. Yet, the values of ϕ appear to be proportional to the corresponding values on tower B. It is as though von Kármán's constant at 16m on tower A was a little above 0.7.

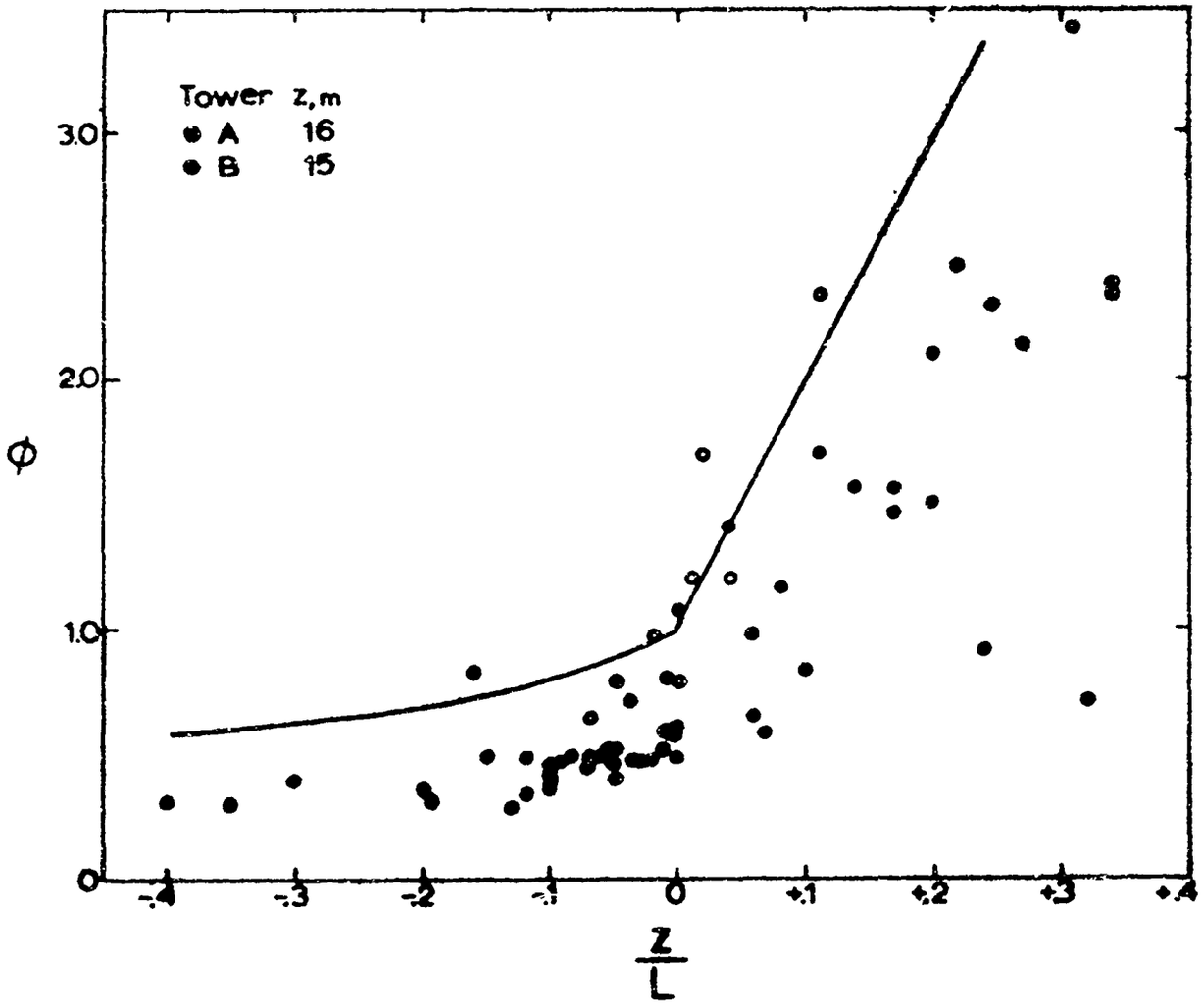
Tower z,m
A 16
B 15
3.0
2.0
1.0
0
Φ
-.4
-.3
-.2
-.1
0
+.1
+.2
+.3
+.4
z/L

For a possible explanation of this peculiar behavior, it should be noted that the 16m level on tower A is in a transition zone between smooth and rough terrain. The portion of the tower below 16m is definitely governed by the conditions over the smooth grass, whereas the air much above 16m has not yet come in contact with the smooth terrain. Right at 16m, the wind shear is that characteristic of small roughness, whereas the Reynolds stress is representative of the brush. This is why ϕ came out smaller than it does for air in equilibrium. In other words, as air flows from rough to smooth terrain, there is an acceleration immediately next to the ground. This decreases the wind shear. The reduced wind shear decreases the rate of mechanical energy production, so that, for a while, dissipation of energy exceeds production. In this state, the energy itself, and therefore u* are at first relatively large (compared to the wind shear), so that ϕ is small. As the flow over the smooth terrain continues, the dissipation reduces energy and friction velocity and produces a new equilibrium in which ϕ again approaches the usual characteristics.

A numerical experiment is being performed on the basis of the following equations:

$$V \frac{\partial V}{\partial x} = \frac{\partial u^{*2}}{\partial x} \qquad 5$$

$$V \frac{\partial E}{\partial x} = u^{*2} \frac{\partial V}{\partial z} - \varepsilon \qquad 6$$

where E is eddy energy and ε dissipation, assumed to be proportional to $E^{3/2}/z$. Also, E was assumed to be proportional to u^{*2}, with the factor of proportionality determined empirically. Numberical integration of 5 and 6 leads to encouraging results, showing that $\phi<1$ in the accelerating air. Also the slope of the interface between "rough" and "smooth" air is realistic.

"A Method to Compute the Effects of Wind on the Dispersion of a Vertically Launched Rocket"

by

Robert L. Ammons
Atlantic Research Corporation
Missile Systems Division
3333 Harbor Boulevard
Costa Mesa, California

and

Charles P. Hoult
Air Force Cambridge Research Laboratories
L. G. Hanscom Field
Bedford, Massachusetts

ABSTRACT

This paper describes a rational approach to the estimation of a standard deviation in ballistic wind which can be used in the analysis of the impact point dispersion of vertically launched rockets. It is assumed that errors in the rocket response model and errors due to wind measurements not being made along the rocket flight path do not contribute significantly to dispersion. Random errors in wind measurements and the effect of a time delay between wind measurement and flight are considered important.

The approach used is to calculate the variance in ballistic wind. The result requires that the inter level wind error covariance matrix be known. When this, the wind weighting factor and the unit wind effects are known, a rational estimate of wind effect on dispersion may be made.

The wind error functions for Fort Churchill, Green River and White Sands have been computed from actual firing day meteorology, multiplied by a typical wind weighting factor form. The data thus reflect the measurement errors, time delays and meteorology actually encountered in service.

These data have been examined for their distribution. It is shown that the ballistic wind errors are approximately normally distributed. As is already well known, this leads to a nongaussian distribution for the impact points.

1.0 INTRODUCTION

The estimation of impact point dispersion of near-vertically launched rockets must include an allowance for the uncertainty of winds as a consequence of the significant effect of winds on the trajectory.

In the past, no one technique for the estimation of impact point dispersion due to wind uncertainty has been agreed to either among the various National Ranges, or among the numerous users of these ranges.

It is hoped that the following discussion will present a rational approach to the solution of this problem.

2.0 BACKGROUND

The effect of winds on the trajectory of near-vertically fired rocket vehicles is well known, and estimated through classical dynamic simulation techniques.

The method usually employed is to estimate the effect of wind in any altitude layer on the rocket vehicle trajectory (wind is resolved into two components, one normal to the plane of the trajectory, and one in this plane) and then to combine these effects into an altitude dependent "wind-weighting" function, f(h), which represents the fraction of total vehicle response which has occurred in a uniform wind field up to an altitude h. The ratio of impact point displacement to wind velocity, for a uniform wind field, is called the "unit wind effect". These two functions, the wind weighting function and the unit wind effect are then used to predict the effect of winds measured prior to launch on the impact point.

The estimation of impact point dispersion due to winds is quite another matter. The "classical technique" has been to simply "guess" at the standard deviation of the mean wind velocity, and then to consider the product of this standard deviation and the unit wind effect as a range or cross-range impact point uncertainty. The further assumption that the wind uncertainty is normally distributed with a mean of zero allows the same assumptions to be employed in combining dispersion due to wind uncertainty with other factors (i.e. thrust misalignment, pointing errors, mass imbalance and uncertainty, etc.).

This combination usually assumes that range and cross-range uncertainties are all normally distributed with means of zero, and no inter-dependence (either between separate effects or between orthogonal components of any given effect). The combination thus results in a bi-variate normal distribution for total impact-point dispersion.

The purpose of this paper is not to question the combinatorial techniques (albeit this is long overdue) but rather to suggest a more rational approach to the estimation of impact point dispersion due to wind uncertainties.

Dispersion of near-vertically fired rocket vehicles due to wind can be grouped into several classes, (the restriction to a near-vertical trajectory allows several simplifying assumptions):

CLASS I

a) Uncertainties in the magnitude of measured winds due to both random and bias measurement errors.

b) Uncertainties in the magnitude of the winds due to the time difference between measurement and actual flight through the wind field.

c) Uncertainties in the magnitude of measured winds due to the different space location of the measured and the encountered wind fields.

CLASS II

d) Variations in the rocket vehicle response caused by pertubations such as thrust misalignment and mass imbalance.

e) Variations in the rocket vehicle response caused by numerical uncertainties in vehicle mass, total impulse, etc.

CLASS III

f) Uncertainties in the effect of winds on the rocket vehicle due to errors in or simplifications of the dynamic model.

The Class III uncertainties, those due to errors or simplifications

of the rocket dynamic model are certainly dependent upon the magnitude of the wind (if the rocket did not encounter a wind field, an erroneous response model would make no difference) and upon the nature of the response model errors.

Estimation of the distribution of this class of error can only be based on statistical studies of the behavior of rocket vehicles during actual flight testing. A classic example of this is the Atmospheric Sciences Laboratory (ERDA) revision of the Aerobee dynamic model based upon statistical studies of impact point dispersion from actual flight tests.[1]*

A theoretical estimate of this effect would have been predicated upon the assumption that a less erroneous model existed, which would obviate the need for inclusion of the effect.

It should be evident that the inclusion of a Class III error in the prediction of impact point dispersion is unjustifiable. Class III errors can only be used to reconcile a difference between predicted and measured dispersion.

The Class II effects, those due to interdependence between one type of uncertainty and another should be treated during the process of combination of the various impact point uncertainties, rather than as separate factors. The techniques are known and need not be pursued here. The reader is referred to any of several excellent texts on the subject.[2]-[6]

The fact that Class II effects are generally of a second order nature justifies their exclusion from most classical dispersion analyses.

We are left therefore, with the problem of defining a suitable technique for the estimation of the magnitude and distribution of the Class I errors, those resulting from measurement uncertainties and space-time variability of the wind field.

* Numbers in parenthesis refer to references at end of paper.

3.0 MATHEMATICAL MODEL

In order to present a rational technique for the estimation of impact point dispersion due to wind uncertainty, it is necessary to construct a mathematical model which lends itself to determination of the magnitude and distribution of the impact point uncertainty of a specific rocket vehicle due to Class I wind errors. These are summarised below as:

a) Measurement Errors
b) Time Variability
c) Space Variability

Our intent is to examine the nature of the effect of these three uncertainties on the impact point dispersion of a near-vertically fired rocket.

The above objective leads to one simplification of the problem, i.e. if the uncertainties can be expressed as functions of altitude, the employment of the wind weighting function applicable to a specific rocket will reduce our uncertainty to non-altitude dependent vectors, commonly referred to as "ballistic wind" errors.

Thus, given a wind weighting function

$$F_w = f(h),$$

where F_w is the percentage of total wind effect to altitude h experienced by the rocket in a uniform wind field, and given the wind uncertainty

$$v_w = V(h),$$

as a function of altitude, the uncertainty in one component of ballistic wind can be found by integrating the function

$$X_i = \int_0^H V(h) \left(\frac{df(h)}{dh}\right) dh \quad ,$$

where X_i is the ith ballistic wind uncertainty sample function. This integration is performed by the method of finite differences, by utilizing the approximate summation

$$X_i = \sum_{j=1}^{m} v_{w_{ij}} \Delta F_{w_j} \quad ,$$

where the altitude range $0 < h < H$ is divided into m intervals (usually determined for approximately equal intervals of ΔF_{w_j}) and the summation performed utilizing average wind velocities in these intervals.

It is assumed that the two components of error are uncorrelated. The chief justification at this point for this assumption is the fact that the two components of the mean wind at a constant altitude are uncorrelated.(7)

In the altitude range where the magnitude of the derivative $\frac{df(h)}{dh}$ is relatively high the interval $\Delta h = h_j - h_{j-1}$ should be considerably less than the yaw wave-length of the rocket vehicle to avoid appreciable Class III errors.

If a number, n, of samples of the ballistic wind error, X_i, are available, then the mean of this sample population is

$$E(X_i) = \frac{1}{n} \sum_{i=1}^{n} \left(\sum_{j=1}^{m} v_{w_{ij}} \Delta F_{w_j} \right) \quad ,$$

and the unbiased variance of the sample is

$$\text{Var}\,(X_i) = \frac{1}{n-1}\sum_{i=1}^{n}\left(X_i - E(X_i)\right)^2 \text{ , or}$$

$$\text{Var}\,(X_i) = \frac{1}{n-1}\left[\sum_{i=1}^{n} X_i^2 - n\left(E(X_i)\right)^2\right]$$

When processing large amounts of data, it is frequently more convenient to express the variance in terms of the covariance, λ. Thus

$$\sum_{i=1}^{n} X_i^2 = \sum_{i=1}^{n}\left(\sum_{j=1}^{m} v_{w_{ij}}\,\Delta F_{w_j}\right)^2 \text{ , or}$$

$$\sum_{i=1}^{n} X_i^2 = \sum_{i=1}^{n}\left[2\sum_{k=1}^{m}\left(v_{w_{ik}}\,\Delta F_{w_k}\right)\sum_{L=1}^{m}\left(v_{w_{iL}}\,\Delta F_{w_L}\right) - \sum_{j=1}^{m}\left(v_{w_{ij}}\,\Delta F_{w_j}\right)^2\right]$$

which can be simplified by making use of the Kronecker delta function, δ_{kL}, which equals 1 or 0 according as $k = L$ or $k \neq L$, and by interchanging the order of summation to yield

$$\sum_{i=1}^{n} X_i^2 = \sum_{k=1}^{m}\sum_{L=1}^{m}\left[\left(2-\delta_{kL}\right)\sum_{i=1}^{n}\left(v_{w_{ik}}\,v_{w_{iL}}\,\Delta F_{w_k}\,\Delta F_{w_L}\right)\right].$$

The function

$$\lambda_{kL}\,(v_{w_i}) = \frac{1}{n}\sum_{i=1}^{n}\left(v_{w_{ik}}\,v_{w_{iL}}\right)$$

yields the covariance matrix of v_{w_i}. This can be substituted in the relationship for $\sum X_i^2$, resulting in

$$\sum_{i=1}^{n} X_i^2 = n\sum_{k=1}^{m}\sum_{L=1}^{m}\left[\left(\lambda_{kL}\,\Delta F_{w_k}\,\Delta F_{w_L}\right)\left(2 - \delta_{kL}\right)\right],$$

which, when substituted into the relationship for Var (X_i) yields

$$\text{Var}\,(X_i) = \frac{n}{n-1} \sum_{k=1}^{m} \sum_{L=1}^{m} \left[\left(\lambda_{kL} \; \Delta F_{w_k} \; \Delta F_{w_L} \right) \left(2 - \delta_{kL} \right) \right]$$

$$- \frac{1}{(n)\,(n-1)} \left(\sum_{i=1}^{n} \sum_{j=1}^{m} v_{w_{ij}} \, \Delta F_{w_j} \right)^2$$

If n samples of the wind uncertainty v_{w_i} are available, then the best estimate of the standard deviation, S_x, of the ballistic wind error, X_i, is simply

$$S_x = \sqrt{\text{Var}\,(X_i)}$$

Once the mean and covariance matrix,

$$\frac{1}{n} \sum_{i=1}^{n} v_{w_i} \quad \text{and} \quad \lambda_{kL} \left(v_{w_i} \right) \quad \text{are}$$

determined for a given range as a function of time of day and season, the standard deviation in ballistic wind can be estimated for any particular rocket, provided the wind weighting function $F_w = f(h)$ for that rocket is known.

There are several problems associated with the analysis of the Class I errors. First, we must devise a method of computing an ensemble set of v_w which includes these errors properly combined. Second, is the statistical distribution of the individual effects and of their combination.

The proposed method of obtaining an ensemble of v_w is to take repeated soundings of the wind field with pilot balloons. Each sounding will yield a wind profile V (h). The proposed model for the error is

$$v_{w_{ij}} = V_{i(t=t_i,\ h=h_j)} - V_{i-k(t=t_i - \Delta t,\ h=h_j)}.$$

We next show that this will deal with all Class I errors which are likely to be seen in practice. First, the type Ic errors which are insignificant, because the horizontal difference between balloon position and rocket flight path contributes little to variability in the mean wind field. Next, we recall that wind velocity is obtained from balloon position by a numerical differentiation process which removes bias errors in position while amplifying random position errors. It should be noted that this will not be true for other types of wind sensors.

Finally, the random measurement and time delay errors are assumed statistically independent, and considering the process leading to a predicted wind profile, are additive. Since the mean of the sum of two random variables is the sum of the individual means, with a similar remark holding for the variance of a sum when independence occurs, it follows that the statistical operations performed on $v_{w_{ij}}$ will yield the desired result, with exception that the elements of the covariance matrix will all be larger than their true values by an amount equal to the variance of the random measurement errors. This error can be subtracted from λ_{ij} if wind data appropriate for the determination of the measurement errors (discussed later) is available. If not, the raw result will yield slightly conservative numerical answers.

The remarks appropriate to the distribution of $v_{w_{ij}}$ are that central limit theorem reasoning would lead us to expect that the distribution will not be far from normal. Both of the primary error effects will

approach the case of the addition of many small effects, and the addition of the two will further tend to normalize $v_{w_{ij}}$.

A final question of philosophy must be considered. This calculation will apply to two distinctly different practical problems. The first is the problem of computing the dispersion for a specific rocket which will be launched from a given range (including an existing meteorological system) at a specific launch time; the whole process subject to weather restrictions typically imposed by the rocket or its payload mission. In this case we should go to the available launch meteorological histories and form $v_{w_{ij}}$ as the difference between the last pre-flight balloon winds used for impact prediction and the first post-flight winds used for flight time wind profile information.

The second problem is that of obtaining data for the design and operation of meteorological systems used for the support of rocket flights. Here it is frequently useful to know how much of $v_{w_{ij}}$ is due to time delay and how much is random measurement noise. A series of balloon runs at fixed time intervals will yield means and covariances as a function of time delay. The result is that the dispersion for various rockets can be found under various meteorological conditions and time delays, and appropriate judgements formed.

The result for random measurement noise alone is that corresponding to zero time delay. That is, the balloon series should involve multiple simultaneous balloon launchings. As discussed earlier, it is desirable to make this experiment in order to remove an error in $_{kL}$ which would otherwise arise.

Subject to the foregoing qualifications we have arrived at a technique for determining our combined Class I error function.

4.0 NUMERICAL EXAMPLE AND RESULTS

The foregoing logic and mathematical model have been employed in analyzing some of the wind data gathered at three specific ranges, i.e., White Sands Missile Range, N. M.; Churchill Research Range, Ft. Churchill, Manitoba; Utah Test Facility, Green River, Utah.

Wind data was taken from Meteorological Data reports for actual firings of several missiles, including: Aerobee, Athena, Astrobee, Nike-Apache, Nike-Cajun.

Because of a scarcity of such data, no definite conclusions can be drawn, however, as an example of the numerical method results are presented. All ballistic winds represent measured winds as presented in the source data (see Table 1) and employ a wind weighting function for the Aerobee rocket (Figure 1). Ballistic winds were determined for both range and cross-range wind components, which were then treated as two separate populations, and combined into one population. The two components can be grouped if there is no appreciable correlation between the range and cross-range components of the change in ballistic wind over the sampling interval Δt.

TABLE 1
LIST OF REPORTS FROM WHICH DATA WERE TAKEN

U.S. Army Electronics Research and Development Activity, Meteorological Data Reports:

ERDA-204 Nike-Apache Speedball II (Round Nr. 59 SN 26), 24 Sept 1964
by H. M. Richart

ERDA-205 Nike-Apache Speedball II (Round Nr. 60 SN 27), 30 Sept 1964
by H. M. Richart and J. M. Sharpe

ERDA-209 Nike-Apache Speedball II (Round Nr. 61 SN 28), 1 Oct 1964
By J. M. Sharpe and H. M. Richart

ERDA-301 Aerobee NASA 4.128 UA, 15 July 1965
by Marjorie McLardie Hoidale

ERDA-357 Nike-Cajun Nicap/1 Rockets
Round No. 022 and 023, 20 July 1965
Round no. 024, 21 July 1965
Round no. 027 and 028, 23 July 1965
by Gordon L. Dunaway

ERDA-334 Aerobee AF 3.375, 21 July 1965
by Marjorie McLardie Hoidale

ERDA-341 Aerobee AE3.519 (AF 125-3), 12 Aug 1965
by Marjorie McLardie Hoidale

ERDA-347 Aerobee NASA 4.147 CG, 22 Sept 1965
by Marjorie McLardie Hoidale

ERDA-348 Aerobee AB 3.722 (S/N AF 114-3), 24 Sept 1965
by Marjorie McLardie Hoidale

ERDA-349 Aerobee NASA 4.150 GA-GI-GB, 28 Sept 1965
by Marjorie McLardie Hoidale

ERDA-350 Aerobee NASA 4.121 CG, 30 Sept 1965
by Marjorie McLardie Hoidale

ERDA-352 Aerobee NB 3.184 (S/N 96-3), 4 Oct 1965
by Marjorie McLardie Hoidale

ERDA-332 Athena Flight No. 015, 16 July 1965
by Harold M. Richart

ERDA-333 Athena Flight No. 016, 20 July 1965
by Harold M. Richart

ERDA-335 Athena Flight No. 017, 26 July 1965, and
Athena Flight No. 018, 27 July 1965
by Harold M. Richart

ERDA-336 Athena Flight No. 019, 31 July 1965
by Harold M. Richart

Table 1, cont'd.

USAERDA, Meteorological Data Reports, Cont'd.	
ERDA-337	Athena Flight No. 020, 2 Aug 1965 by Gordon L. Dunaway
ERDA-339	Athena Flight No. 021, 6 Aug 1965, and Athena Flight No. 022, 7 Aug 1965 by Gordon L. Dunaway
ERDA-340	Athena Flight No. 023, 20 Aug 1965, and Athena Flight No. 024, 20 Aug 1965 by Len E. Carter
ERDA-365	Athena Flight No. 032, 5 Nov 1965 by Len E. Carter
UNITED STATES ARMY ELECTRONICS COMMAND, Atmospheric Sciences Laboratory, Meteorological Data Reports:	
DR-45	Nike-Apache Photometric (SR-034), 13 June 1966 by Gordon L. Dunaway
DR-62	Nike-Apache STV (SR-033), 21 July 1966 by Len E. Carter
DR-66	Aerobee AF 3.525, 22 July 1966 by Marjorie McLardie Hoidale
PAN AMERICAN WORLD AIRWAYS, INC., Churchill Research Range Impact Prediction Data:	
	Aerobee 150, Test No. 246.6 Al 199-6L, OD No. 199, 14 Dec 1966
	Aerobee 150, Test No. 244.6 Al 274-1L, OD No. 274, 27 Nov 1966

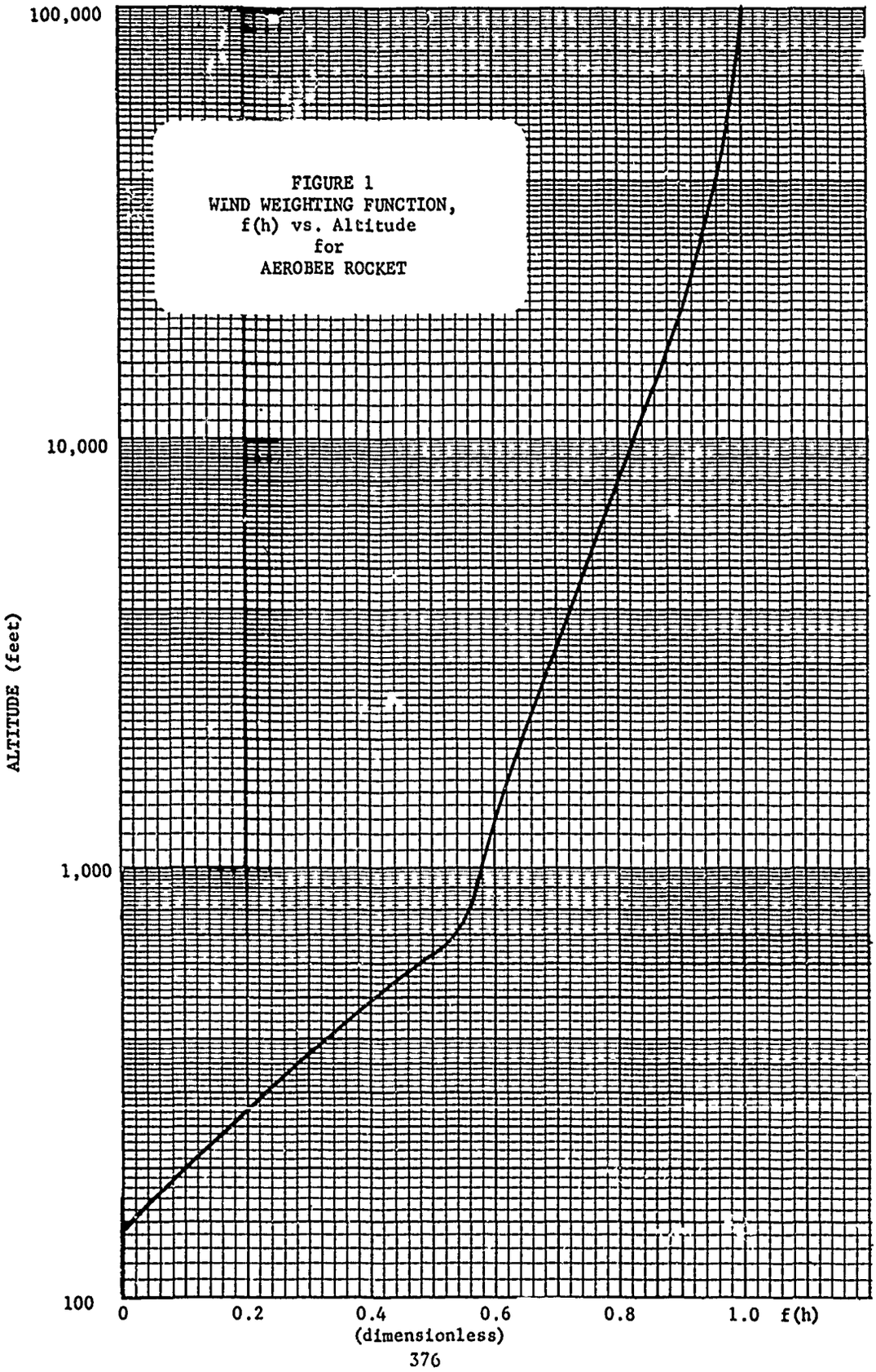

FIGURE 1
WIND WEIGHTING FUNCTION,
f(h) vs. Altitude
for
AEROBEE ROCKET

Table 2 shows the number of range days on which samples of wind were taken, by range and season**, for day and night measurements.

TABLE 2 - NUMBER OF RANGE DAYS* SAMPLED

Range	WSMR			FT. CHURCHILL			GREEN RIVER			ALL		
Season	Day	Night	Total	Day	Night	Total	Day	Night	Total	Day	Night	Total
Spring	0	0	0	0	1	1	0	0	0	0	1	1
Summer	9	1	10	0	0	0	0	10	10	9	11	20
Fall	5	3	8	0	0	0	0	1	1	5	4	9
Winter	0	0	0	0	1	1	0	0	0	0	1	1
All	14	4	18	0	2	2	0	11	11	14	17	31

* A range day is defined as any interval over which a ries of wind measurements has been made.

Each of the range days shown in Table 2 resulted in several (up to 25) measurements of wind data, however these measurements were in general neither equally spaced nor at time intervals approaching the lag between measurement and encounter of the wind field.

** The definition of such concepts as "season" and "day or night" is of necessity an arbitrary one.

As an example of the effect of time lag on the uncertainty of ballistic wind errors, the auto-correlation function, $\Phi(\tau)$, has been determined for a series of wind measurements at Green River on 26-27 July 1965 (the only range day on which sufficient data were available) and is presented in Figure 2. The auto correlation function of a time series is defined as:

$$\Phi(\tau) = \frac{\mathrm{COV}[X_t, X_{t+\tau}]}{\left[\mathrm{VAR}\, X_t \;\; \mathrm{VAR}\, X_{t+\tau}\right]^{1/2}} \quad , \text{ or}$$

$$\Phi(\tau) = \frac{\sum (X_t)(X_{t+\tau})}{\sqrt{\left[n\sum X_t^2 - \left(\sum X_t\right)^2\right]\left[n\sum X_{t+\tau}^2 - \left(\sum X_{t+\tau}\right)^2\right]}} \quad ,$$

Where n is the number of distinct pairs which can be formed from the series with a time difference τ. Thus, $\phi(\tau)$ is essentially a coefficient resulting from a regression analysis of a series of time based measurements on itself. For zero time lag ($\tau = 0$) the coefficient equals 1.0, and for increasing lag the coefficient usually approaches zero (unless successive terms of the series can be represented by a linear or periodic function of time). From Figure 2 it can be seen that the auto-correlation function can be approximated by an exponentially damped Cosine function:

$$\Phi(\tau) = e^{-\frac{c\tau}{p}} \cos\left(2\pi\frac{\tau}{p}\right) \quad ,$$

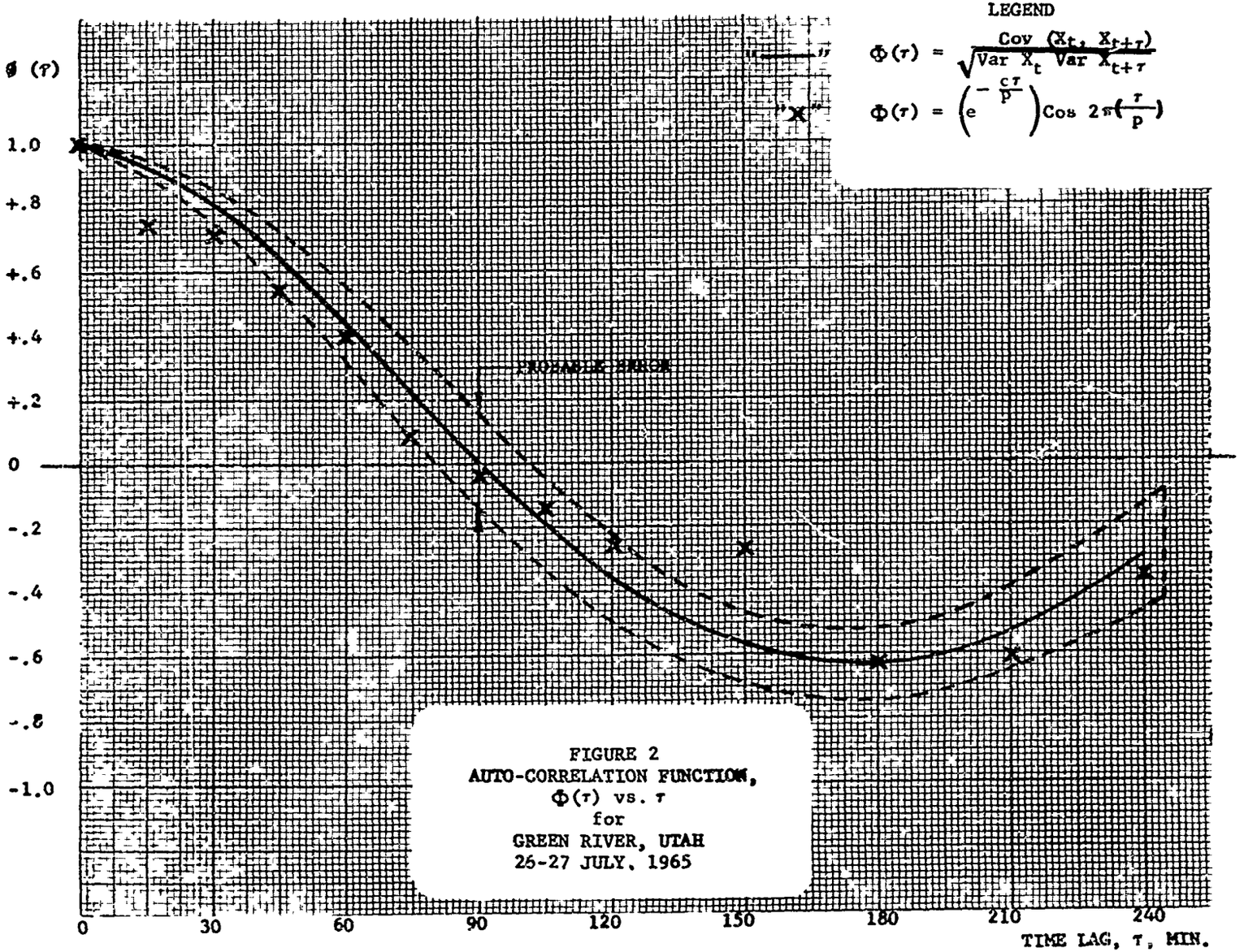

FIGURE 2
AUTO-CORRELATION FUNCTION,
$\Phi(\tau)$ vs. τ
for
GREEN RIVER, UTAH
26-27 JULY, 1965

which implies that the ballistic wind is a periodic function (with a period of approximately 6 hours) and that the effect of increasing time lag, τ, results in less and less correlation (after one cycle the maximum value of $\phi(\tau)$ has decreased to 0.40, and after two cycles to 0.16).

Thus the importance of time lag cannot be overstressed. As a consequence, the wind data presented for most range days is not useable until the sampling interval begins to approach the actual time lag between measurement and encounter of a wind field. This qualification restricted the number of pairs for each range day to those determined very close to the firing time, when the time interval, Δt, usually approaches 10 minutes for the lower, most significant levels. The technique employed was to select ballistic wind differences $(X_t - X_{t-\Delta t})$ determined from pre- and post-flight measurements of low level winds, and to employ the most current upper winds.

In cases where only a few samples were available, as indicated in Table 2, no determination of statistical parameters was attempted. These data were employed, however, in the range, season, and day-night totals. The results are shown in Table 3, which includes the number of samples N, the standard deviation s, determined by the method presented in Section 3.0, and the coefficients of skewness and kurtosis for the samples, plus the value of students "t" determined for the hypothesis that the sample had a mean of zero.

TABLE 3 STANDARD DEVIATIONS FOR BALLISTIC WIND ERRORS

RANGE	SEASON		DAY			NIGHT			BOTH		
			N-S	E-W	Both	N-S	E-W	Both	N-S	E-W	Both
WSMR	SUMMER	n	9	9	18				10	10	20
		s	1.47	2.04	1.73				1.39	2.36	1.91
		γ_1	0.31	-0.67	-0.46				0.36	-0.51	-0.60
		β_2	3.16	3.15	3.59				3.52	2.31	3.33
		t	0.3	0.5	0.6				0.4	1.0	1.0
	FALL	n	5	5	10				8	8	16
		s	1.72	1.68	1.69				2.33	1.49	1.94
		γ_1	0.30	0.62	0.41				0.28	-0.07	-0.06
		β_2	1.40	2.13	1.82				1.89	1.88	2.09
		t	1.4	0	1.0				0.4	1.0	0.2
	ALL SEASONS	n	14	14	28	4	4	8	18	18	36
		s	1.61	1.86	1.73	1.32	3.01	2.37	1.81	2.06	1.91
		γ_1	0.37	-0.46	-0.19	0.38	-1.00	-0.09	0.25	-0.75	0.34
		β_2	2.60	3.32	3.35	2.00	2.21	1.69	2.60	3.07	2.92
		t	0.7	0.4	0.1	3.0	0.1	1.3	0.5	0.4	0.7
GREEN RIVER	SUMMER	n				10	10	20	10	10	20
		s				1.70	0.84	1.40	1.70	0.84	1.40
		γ_1				0.13	0.26	0.70	0.13	0.26	0.70
		β_2				3.40	3.30	4.35	3.40	3.30	4.35
		t				1.4	0.9	0.8	1.4	0.9	0.8
	ALL SEASONS	n				11	11	22	11	11	22
		s				1.62	0.81	1.33	1.62	0.81	1.33
		γ_1				0.15	0.14	0.70	0.15	0.14	0.70
		β_2				3.74	3.44	4.71	3.74	3.44	4.71
		t				1.5	0.8	0.9	1.5	0.8	0.9
ALL RANGES	SUMMER	n	9	9	18	11	11	22	20	20	40
		s	1.47	2.04	1.73	1.64	1.54	1.69	1.58	1.74	1.70
		γ_1	0.31	-0.67	-0.46	0.28	-1.52	0.36	0.35	-0.79	0.35
		β_2	3.16	3.15	3.59	3.55	5.29	4.94	3.43	3.89	4.19
		t	0.3	0.5	0.6	1.3	1.3	0	0.8	1.4	0.5
	FALL	n	5	5	10	4	4	8	9	9	18
		s	1.72	1.68	1.69	1.42	0.86	1.52	2.20	1.40	1.82
		γ_1	0.30	0.62	0.41	0.18	0.30	-0.42	0.14	0.01	-0.12
		β_2	1.40	2.13	1.82	1.29	1.53	2.06	2.00	2.09	2.34
		t	1.4	0	1.0	1.4	2.4	0	0.3	1.0	0.3
	ALL SEASONS	n	14	14	28	17	17	34	31	31	62
		s	1.61	1.86	1.73	2.17	1.66	1.90	1.92	1.73	1.81
		γ_1	0.37	-0.46	-0.19	-0.28	-0.99	-0.56	-0.23	-0.73	-0.43
		β_2	2.60	3.32	3.35	2.84	4.55	3.47	3.17	3.88	3.51
		t	0.7	0.4	0.1	0.4	0	0.4	0	0.3	0.2

In addition to the results shown in Table 3, the 31 pairs of measurements representing the total for all ranges, all seasons, day or night, were analyzed to determine if any appreciable correlation could be found between orthogonal components. The sample correlation coefficient of r =-0.20 does not indicate any significant dependence of one component on the other. Therefore the two populations of 31 values were grouped into a single population of 62 samples in order to examine the population distribution. This sample population had a mean of -.05 ft/sec and a standard deviation of 1.813 ft/sec.

A "t" test based on the hypothesis that the population mean was zero indicated an 80% confidence level that this could be the case. The sample population had a coefficient of skewness, γ_1, equal to -0.43 (normal population equal zero) and a coefficient of kurtosis, β_2, equal to 3.51 (normal population equal 3.0).

Figure 3 is a cumulative frequency histogram of the 62 values of X_i, and includes a plot of a normal curve having a mean of zero and the same standard deviation as the sample population. Also shown is a plot of a hypothetical cumulative distribution determined by an approximate expansion utilizing Edgeworths Series.[8] Figure 4 is a frequency histogram for this same sample, and Figure 5 shows the Probability density functions for the sample population and for the

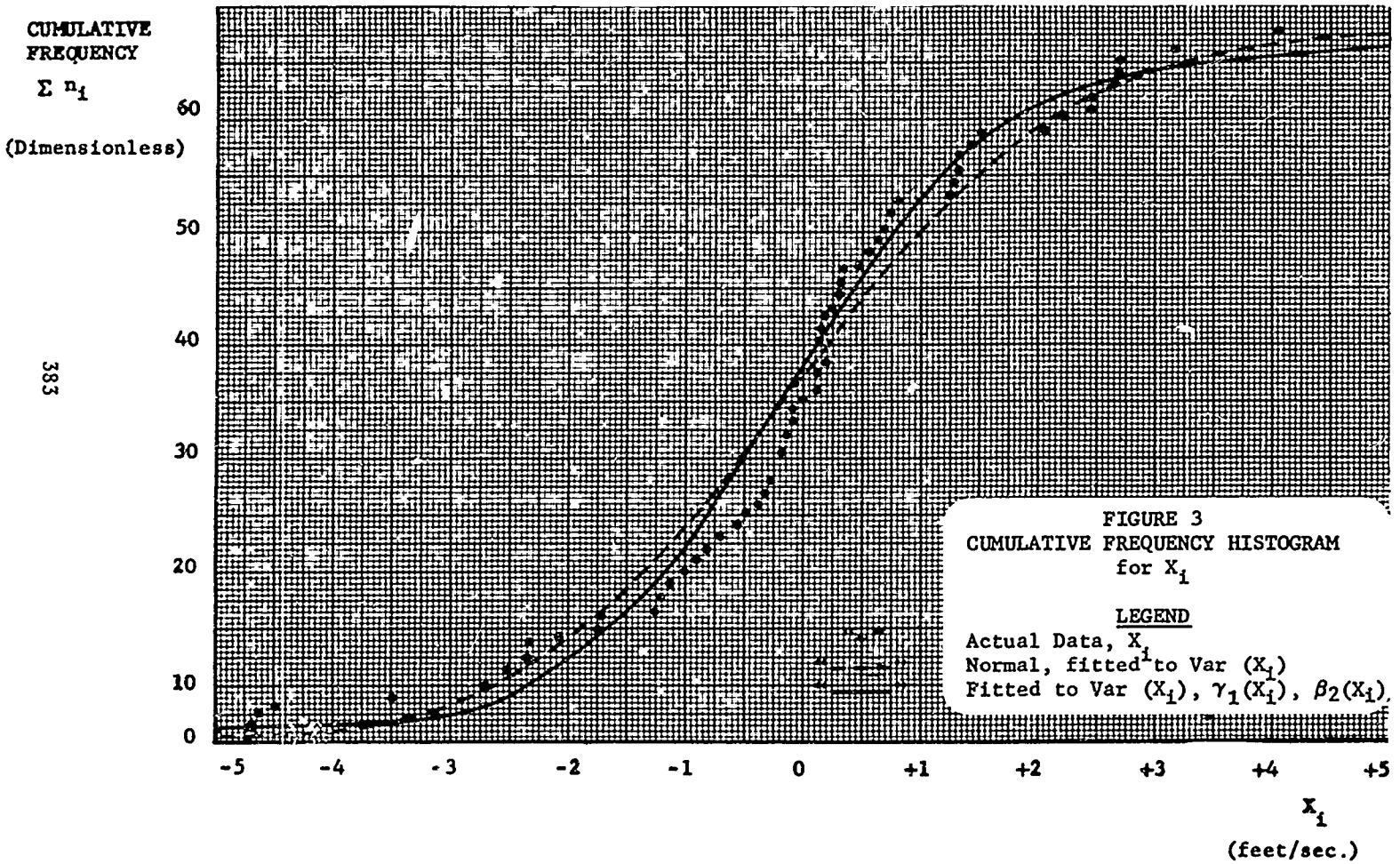

FIGURE 3
CUMULATIVE FREQUENCY HISTOGRAM
for X_i

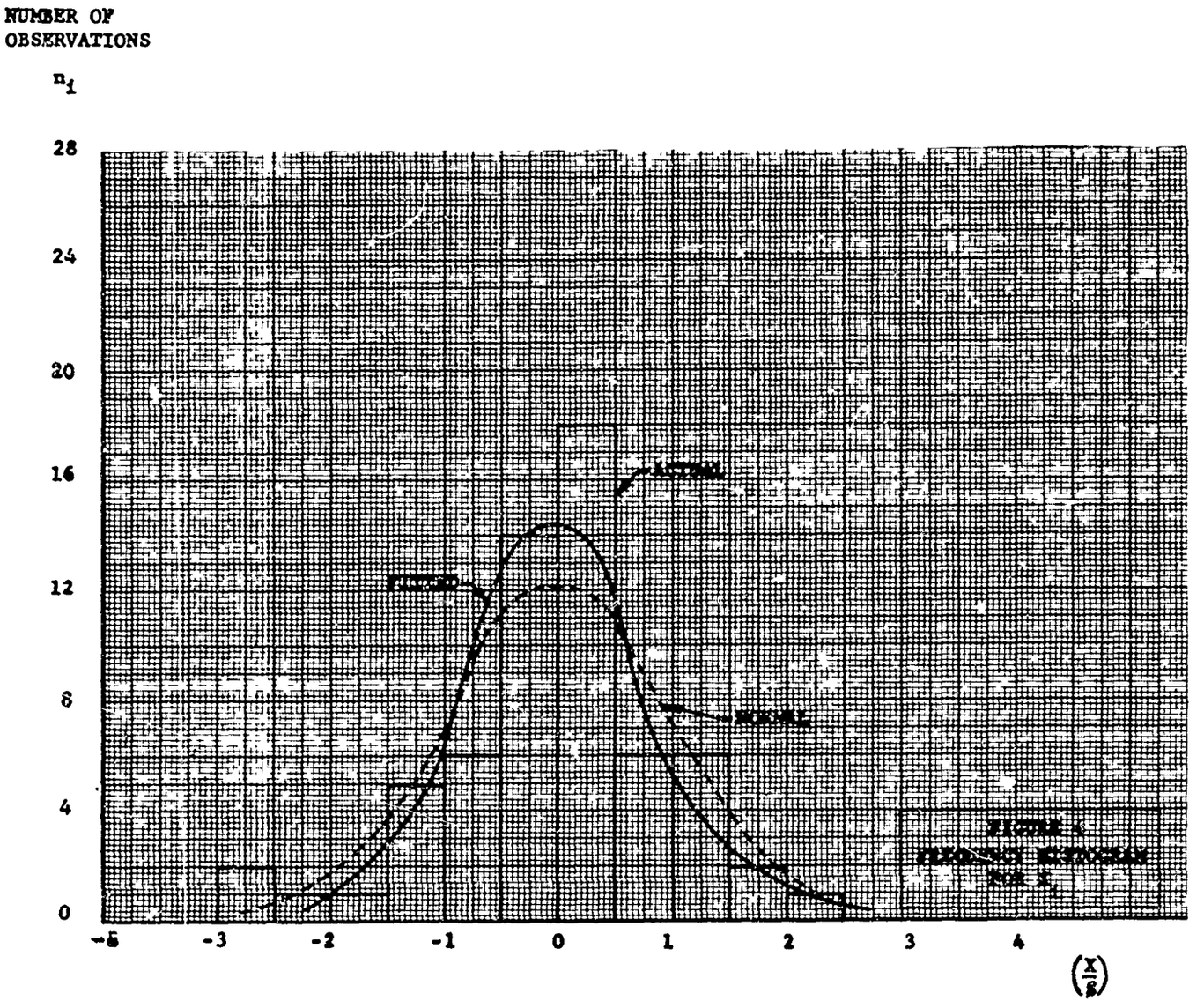
NUMBER OF
OBSERVATIONS
n_i
28
24
20
16
12
8
4
0
-5
-3
-2
-1
0
1
2
3
4
$\left(\frac{X}{\sigma}\right)$

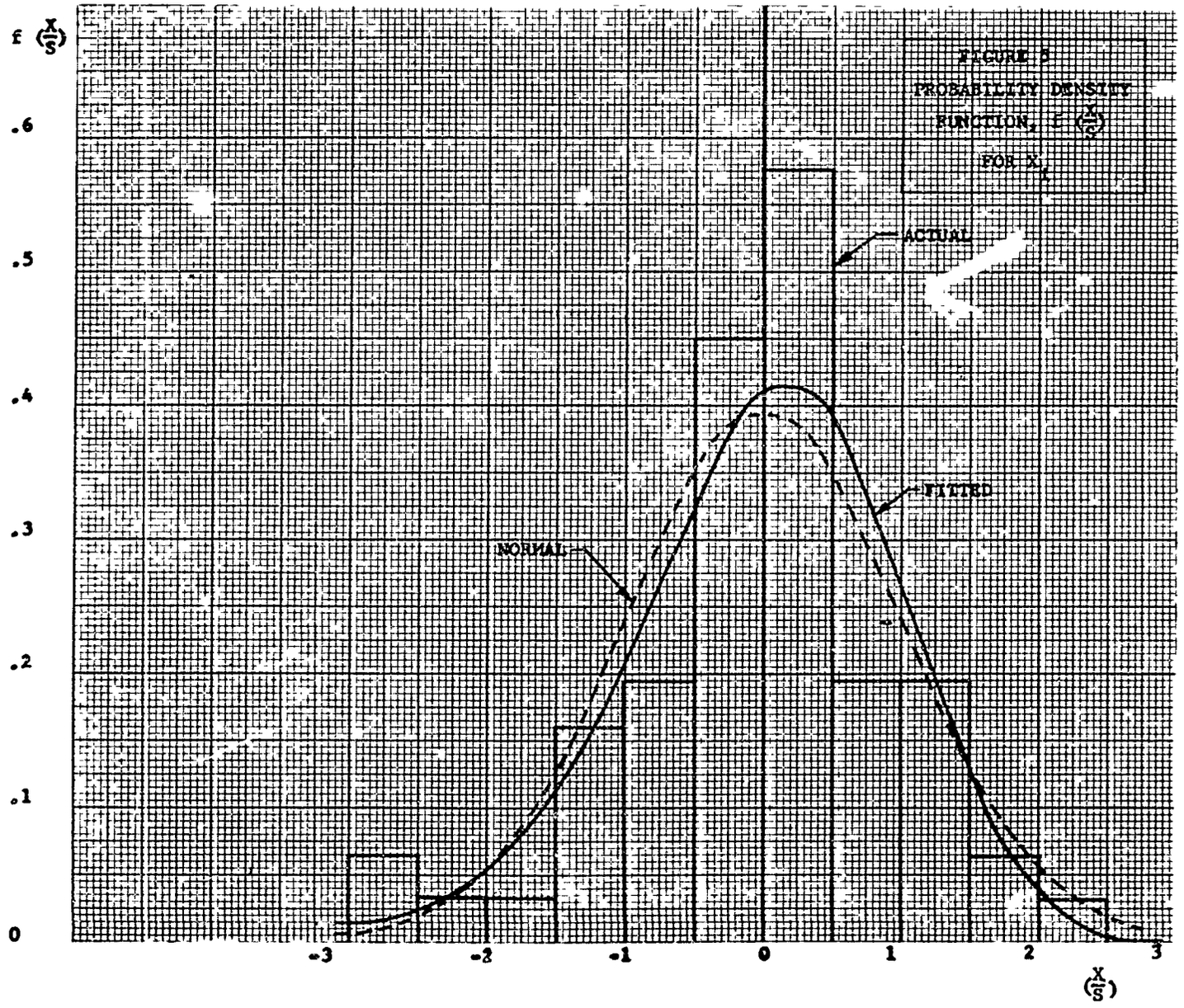

FIGURE 5
PROBABILITY DENSITY FUNCTION, f (X/S) FOR X_1

normal and approximate functions.

The sample population was subjected to a Chi Square (χ^2) test[9] based on the hypothesis that it was taken from one of four actual populations:

(1) A normal population, $\phi\left(\frac{x}{s}\right)$ with a mean of zero and variance equal to the sample.

(2) A fitted population, $f_1\left(\frac{x}{s}\right)$, having the same mean, variance, and coefficient of skewness as the sample.

(3) A fitted population, $f_2\left(\frac{x}{s}\right)$, having the same mean, variance, and coefficient of kurtosis as the sample.

(4) A fitted population, $f_3\left(\frac{x}{s}\right)$, having the same mean, variance, and coefficients of skewness and kurtosis as the sample.

The results are summarized in Table 4.

TABLE 4, RESULTS OF χ^2 TESTS

POPULATION	χ^2	CONFIDENCE LEVEL
Normal, $\Psi(\frac{x}{s})$, $S^2=3.29$	9.7	$\epsilon < 0.3$
Fitted, $f_1(\frac{x}{s})$, $m=-.05$, $S^2=3.29$, $\gamma_1=-.43$	5.0	$\epsilon < 0.7$
Fitted, $f_2(\frac{x}{s})$, $m=-.05$, $S^2=3.29$, $\beta_2=3.51$	11.6	$\epsilon < 0.2$
Fitted, $f_3(\frac{x}{s})$, $m=-.05$, $S^2=3.29$, $\gamma_1=-.43, \beta_2=3.51$	6.6	$\epsilon < 0.5$

These results do not indicate with a sufficiently high confidence level that any of the hypotheses can be rejected (except possibly the f_2 distribution) and thus, our sample may well have come from a normal or from the f_1 or f_3 distributions.

Although the sample population differs somewhat from a normal distribution, the authors feel that more data, representing more equally spaced time samples, in large enough quantities to allow processing by range, season, and time of day, should rectify these small discrepancies.

5.0 CONCLUSIONS

In Section 3 it was shown that if the Class I errors are each normally distributed, then by the central limit theorem, their sum will be normally distributed. This sum, if it truly represents random errors must have a mean of zero.

Section 4 showed the results of an analysis on some 31 pairs of time separated ballistic wind determinations, with the conclusion that the population formed by 62 orthogonal components could have a mean of zero and be normally distributed.

Because of a lack of data, it was not possible to arrive at similar results by range, season, and time of day.

The authors feel that the techniques described in the foregoing sections do indeed result in a rational, statistically valid model of the ballistic wind uncertainty due to measurement errors and space-time variation of the wind field.

We would like to address an appeal to the attendees of this conference for more data. If sufficient wind data can be gathered for the various ranges, then in addition to a final verification of the validity of the technique, further analysis will result in a summary report including mean wind errors and covariance matrixes for the various ranges studied, broken down by season, time of day, and measurement-encounter lag.

REFERENCES

(1) Duncan, L. D. and R. J. Ensey, November 1964: "Six Degree of Freedom Digital Simulation Model for Unguided Fin-Stabilized Rockets". ERDA-196, Environmental Sciences Directorate, United States Army Electronics Research and Development Activity, White Sands Missile Range, Nex Mexico.

(2) Hoel, Paul G., (1962): "Introduction to Mathematical Statistics" published by John Wiley & Sons, Inc.

(3) Anderson, T. W., (1958): "An Introduction to Multivariate Statistical Analysis" published by John Wiley & Sons, Inc.

(4) Cramer, H., (1946): "Mathematical Methods of Statistics" Princeton University Press.

(5) Fieller, E. C., T. Lewis, and E. S. Pearson (1955): "Correlated Random Normal Deviates" Cambridge University Press

(6) Mood, A. M., (1950): "Introduction to the Theory of Statistics" McGraw-Hill Book Company.

(7) Valley, S. L., Editor (1965): "Handbook of Geophysics and Space Environments" Air Force Cambridge Research Laboratories, Office of Aerospace Research, USAF.

(8) Burington, R. S. and D. C. May (1953): "Handbook of Probability and Statistics with Tables" Handbook Publishers, Inc.

(9) Panofsky, H. A. and G. W. Brier (1963): "Some Applications of Statistics to Meteorology" Pennsylvania State University.

ON NONPARAMETRIC TESTING OF THE NATURE OF CERTAIN TIME SERIES

By

Walter B. Miller
and
Henry Rachele

ABSTRACT

Nonparametric tests were adapted and used to determine if a given set of samples from a time series is stationary, τ-dependent and Markov.

Results obtained from analyzing (testing) a number sequence generated by a random number generator and sets of wind speed and direction data collected at White Sands Missile Range are presented.

INTRODUCTION

Many studies in meteorological research require that meaningful inferences be drawn from time sequential data. The field of mathematics concerned with such inferences is generally referred to as time series analysis or, more generally, stochastic processes. The most general stochastic process is simply an indexed family of random variables. Such generalities will not be considered here since little can be said of such broad families. Instead, the processes considered will be stationary or differ from stationarity in prescribed manners. The key features of stationary time series which are of interest are the ergodic properties. In a stationary time series each random variable in the aggregate has the same mean and variance, hence one may speak of the mean and variance of the time series itself. Ergodicity enables one to estimate these parameters by use of a realization of the time series, i.e., the actual observation of the values of the process.

In general, the time series studied will be continuous, but the experimentor may only observe the process at a finite number of points. An observation at a time t_0 then may be considered as a sample of size one of the random variable indexed by t_0. The samples $X_1, X_2, \ldots, X_n$ taken at time $t_1, t_2, \ldots, t_n$, however, do not in general constitute a sample of size n of some random variable. The main feature of a sample, independence, is lacking. If the stochastic process, call it $\{X_t\}_{t\in T}$, is ergodic in first and second means, and $t_{i+1}-t_i = h$ for each i among 1, 2, ..., n, the random variables $\frac{1}{n}\sum_{i=1}^{n} X_i$ and $\frac{1}{n-k}\sum_{i=1}^{n-k}(X_i-\mu)(X_{i+k}-\mu)$ ha expected values μ and $B(kh)$, where μ is the mean of $\{X_t\}_{t\in T}$ and $B(kh)$ the value of the autocovariance function at $t = kh$. The variance of $\frac{1}{n}\sum_{i=1}^{n} X_i$ is not in general $\frac{\sigma^2}{n}$, but an involved expression of various values of the autocovariance function,

hence is not available without further information. If $\{X_t\}_{t\in T}$ is not stationary, recall that mean and variance for the process are not even defined.

Among the many types of time series of interest, two classes possess unusually pleasant characteristics. In each case these features are related to the form of the autocovariance function. The first is the τ-dependent process. Intuitively, a τ-dependent process is one in which events occurring τ units of time apart are independent. Such processes have autocovariance functions which are zero for any $t \geq \tau$. The second type has autocovariance function $B(t) = \sigma^2 a^{-|t|}$, where σ^2 is the variance of the process and $|a| < 1$. Time series possessing such an autocovariance function are of a type called Markov processes and have very simple prediction characteristics. In each of the above classes, ergodicity may be demonstrated, and in the first case, if random variables of separation greater than τ are taken, the result is a sample in the statistical sense with all resultant properties.

The purpose of this report is to make known some of the tests devised and performed to determine if a given set of samples from a time series may indicate that the series is one of the above forms and results of applying these tests to some meteorological data. It is believed by the authors that the results of the tests are of a nature to warrant further study along these lines.

DISCUSSION - PART I

Definitions and Theorems:

Let $\{X_t\}_{t\in R}$ be given, where R is the real numbers and X_t is a random variable for each $t\in R$. If $E(X_t) = \mu$, and $\text{Var}(X_t) = \sigma^2$ for all $t\in R$, $\{X_t\}_{t\in R}$ will be called weakly stationary. If X_t is normal for each t, $\{X_t\}_{t\in R}$ will be called a normal process or normal time series. For the purpose of this report we will make the following definition.

Definition 1: Let $\{X_t\}_{t\in R}$ be a random process. An n-tuple $\{X_1, X_2, \ldots, X_n\}$ will be called an h-sample of length n if

for each i among 1, 2, ..., n, X_i is a sample of the random variable X_{t_i} and $t_{i+1} - t_i = h$.

For a given h-sample $\{X_1, X_2, \ldots, X_n\}$, the following random variables will be defined:

$$(1) \quad \tilde{X} = \frac{1}{n} \sum_{i=1}^{n} X_i,$$

$$(2) \quad \tilde{B}(k, h) = \frac{1}{n} \sum_{i=1}^{n-k} (X_i - \tilde{X})(X_{i+k} - \tilde{X}).$$

The random variable $\tilde{X}$ will be called the average of the h-sample and $\tilde{B}(k, h)$ the kth lagged product of the h-sample.

Interest will now be centered on a special type of weakly stationary process, the description of which is the context of the following definition.

Definition 2: Let $\{X_t\}_{t\in R}$ be weakly stationary. This process is said to be τ-dependent if and only if for any $h \geq \tau$, $B(h) = E[(X_t - E(X_t))(X_{t+h} - E(X_{t+h}))] = 0$.

The properties of interest concerning τ-dependent time series are well known and are stated here without proof.

Theorem 1: Let $\{X_t\}_{t\in R}$ be a τ-dependent time series, and suppose $E(X_t) = \mu$, and $\mathrm{Var}(X_t) = \sigma^2$ for all $t\in R$. If $\{X_1, X_2, \ldots, X_n\}$ is an h-sample of length n for $h \geq J$, then $\{X_1, X_2, \ldots, X_n\}$ is also a sample of size n of a random variable with mean μ and variance σ^2, and $\tilde{X}$ is an estimator of μ with variance σ^2/n and $\tilde{B}(0, h)$ is an estimator of σ^2. In particular, one may use $\tilde{X}$ to estimate μ and know that the variance of $\tilde{X}$ is no greater than $\frac{\sigma^2}{n}$.

If $\{X_1, X_2, \ldots, X_n\}$ is an h-sample of length n of a τ-dependent process, a run test [1] may be employed to test the hypothesis $h \geq \tau$ against the alternative that it is not, i.e., $h < \tau$. As a run test is nonparametric in nature, this test does not depend on the distribution of the $\{X_i\}_{i=1}^{n}$.

In general, the nature of the h-sample will not be known. In this case, if a run test is employed and the result is negative, one of three following conditions may hold.

(1) $\{X_1, X_2, \ldots, X_n\}$ is an h-sample of a non-stationary process.

(2) $\{X_1, X_2, \ldots, X_n\}$ is an h-sample of a stationary process which is not τ-dependent.

(3) $\{X_1, X_2, \ldots, X_n\}$ is a τ-dependent process with $\tau < h$.

If a run test is employed and the results are positive, one may conclude,

(1) $\{X_1, X_2, \ldots, X_n\}$ is τ-dependent for some $\tau < h$,

(2) $\{X_1, X_2, \ldots, X_n\}$ is stationary and $B(h) = 0$,

(3) $\{X_1, X_2, \ldots, X_n\}$ constitutes a sample yet $\{X_t\}_{t\in T}$ is nonstationary.

Considering the negative case first, and avoiding conditions (1) and (2), one may resolve conditions (3) by first taking an h-sample, then a 2h-sample and so on until finally an mh sample is taken. If all tests are negative, no information is gained other than a possible lower bound for τ. If, on the other hand, for $j < m$, one has predominately all tests negative, and for $j \geq m$, all tests positive, then one might conclude that $\{X_1, X_2, \ldots, X_m\}$ is τ-dependent for some $(j-1)h < \tau \leq jh$.

In practical situations, it would be nearly impossible to take the required samples for such a procedure; thus, the following scheme will be considered. Suppose an h-sample of length n of a process $\{X_t\}_{t\in T}$ is taken for the smallest value

of h allowed by the sampling device, and large n. It is observed that this h-sample of length n also gives rise to a 2h-sample of length [n/2], a 3h-sample of length [n/3], and finally an (n-1)h-sample of length 2. One may then perform a run test on the h-sample, then the 2h-sample, etc. Since the normal approximation used in the run tests indicates use of sample of length $n \geq 20$, the sequence of run tests will be terminated at the $[\frac{n}{21}]$h-sample which will be of length at least 20. If $T_1, T_2, \ldots, T_m$ is the sequence of tests performed with $m = [\frac{n}{21}]$, it is clear they are not independent, and an exact probability statement is not immediate. Nonetheless, this procedure was given preliminary tests with a random number generator and also for wind speed and direction data taken at the 200-ft tower at White Sands Missile Range [2].

Data Analysis

The results are listed as follows. Using a 5% significance level for each test, a (-) is recorded if the test rejects the hypothesis of randomness and (+) if it fails to reject. The tests are written as a sequence of plus and minus signs for ascending values of the sample interval, hence ----- +++++++ would indicate negative results for the h-sample, 2h-sample, on to the-5h sample, and positive for the 6h-sample through the 12h-sample. The results of one set of these preliminary tests are shown in Table I. It is noted from the results column that positive results are obtained for the 1h to 7h-samples and except for spurious negatives, which as yet are unexplained, remain positive for all samples computed (36h). Hence, a reasonable conclusion may be that the data tested are τ-dependent for 30 sec $\leq \tau \leq$ 35 sec. On the strength of these results, it was concluded that further consideration of the problem would be justified. Of the approaches listed below, (a) and (b) are considered in this paper.

Specifically, the following was considered:

(a) Random processes were devised using numbers obtained from a random number generator [3] which are τ-dependent for various values of τ and tested by the previously mentioned methods.

TABLE I

Run test results for determination of τ using data collected from White Sands Missile Range Research Tower on 12 February 1958. Data consist of one hour of speed observations (5-second visual means).

M	Sample Length	Expected Number of Runs	Observed Number of Runs	Results
1	720	361	129	-
2	360	181	103	-
3	240	121	77	-
4	180	91	66	-
5	144	73	60	-
6	120	61	52	-
7	102	52	46	+
8	90	46	46	+
9	80	41	48	+
10	72	37	46	+
11	64	33	37	+
12	60	31	34	+
13	54	28	29	+
14	50	26	31	+
15	48	25	24	+
16	44	23	19	+
17	42	22	23	+
18	40	21	20	+
19	36	19	11	-
20	36	19	17	+
21	34	18	15	+
22	32	17	17	+
23	30	16	17	+
24	30	16	11	-
25	28	15	16	+
26	26	14	11	+
27	26	14	13	+
28	24	13	11	+
29	24	13	13	+
30	24	13	15	+
31	22	12	13	+
32	22	12	12	+
33	20	11	10	+
34	20	11	7	-
35	20	11	13	+
36	20	11	11	+

Let $X_1, X_2, \ldots, X_N$ be a sample of size N of a normal random variable with mean 0 and variance 1. For k = 0, 1, 2, ..., m; m $\leq$ N, the following sequences of random variables may be defined. Let $Y_{0,j} = X_j$ and for k > 0 let

$Y_{k,j} = \frac{1}{\sqrt{k}} \sum_{j=1}^{k} X_{j+i}$. Observe that for any value of j and k

$E(Y_{k,j}) = 0$, $\mathrm{Var}(Y_{k,j}) = 1$. It follows that for each k among

0, 1, ..., m, $\{Y_{k,j}\}_{j=1}^{N-k}$ may be considered a weakly stationary process. Observe also that $B_k(\ell) = E(Y_{k,j}\, Y_{k,j+\ell}) =$

$$E\left(\frac{1}{\sqrt{k}} \sum_{i=1}^{k} X_{j+i} \frac{1}{\sqrt{k}} \sum_{i=1}^{k} Y_{j+\ell+i}\right) = \frac{1}{k} \sum_{r=1}^{k} \sum_{s=1}^{k} E(X_{j+r}\, X_{j+\ell+s}).$$

It is clear that if $\ell \geq k$, $B(\ell) = 0$, and if $\ell < k$, then $B(\ell) > 0$. It follows that $\{Y_{k,j}\}_{j=1}^{N-k}$ is k-dependent. The random number generator [3] was employed to determine a sample $X_1, X_2, \ldots, X_n$, and the sequences $\{Y_{k,j}\}_{j=1}^{N}$ were calculated in the obvious manner. It would be encouraging if the sequence of tests previously described gave results with these data of the form

\+ + + + + +
\- + + + + +
\- - + + + +
\- - - + + +
\- - - - + +

In reality the results of the tests performed are given in Table II, and may be summarized as follows: as expected, for the initial set of random numbers, τ is probably less than h. For the second set of numbers which were deliberately generated so that $\tau \leq 2h$ the test was effective. This was also true, except for a decrease in sensitivity above 4h for each succ sive set of data, i.e., for $\tau \leq 3h$, 4h, 5h, 6h, 7h. However, negative results appear occasionally where positive results were expected. The reason for this, as yet, is unresolved although it was found that the "power spectrum" of the random data was not flat. This result may be due to the way in which the spectral estimates are computed or to the nature of the

TABLE II a

Run test to determine τ using data generated by a random number generator. Seven hundred and twenty random numbers were used.

M	Sample Length	Expected Number of Runs	Observed Number of Runs	Results
1	720	361	363	+
2	360	181	191	+
3	240	121	115	+
4	180	91	89	+
5	144	73	73	+
6	120	61	65	+
7	102	52	42	-
8	90	46	39	+
9	80	41	43	+
10	72	37	40	+
11	64	33	32	+
12	60	31	36	+
13	54	28	21	-
14	50	26	28	+
15	48	25	23	+
16	44	23	27	+
17	42	22	22	+
18	40	21	21	+
19	36	19	16	+
20	36	19	17	+
21	34	18	10	-
22	32	17	15	+
23	30	16	13	+
24	30	16	15	+
25	28	15	16	+
26	26	14	12	+
27	26	14	12	+
28	24	13	11	+
29	24	13	17	+
30	24	13	7	-
31	22	12	10	+
32	22	12	16	+
33	20	11	10	+
34	20	11	10	+
35	20	11	12	+
36	20	11	9	+

TABLE II b

Run test to determine τ using data generated by a random number generator. Seven hundred and twenty random numbers were used to generate a 1h dependent set of numbers.

M	Sample Length	Expected Number of Runs	Observed Number of Runs	Results
1	718	360	267	-
2	358	180	189	+
3	238	120	117	+
4	178	90	97	+
5	142	72	79	+
6	118	60	67	+
7	102	52	48	+
8	88	45	50	+
9	78	40	46	+
10	70	36	37	+
11	64	33	26	-
12	58	30	27	+
13	54	28	29	+
14	50	26	27	+
15	46	24	30	+
16	44	23	29	+
17	42	22	18	+
18	38	20	17	+
19	36	19	13	-
20	34	18	17	+
21	34	18	20	+
22	32	17	14	+
23	30	16	13	+
24	28	15	17	+
25	28	15	12	+
26	26	14	14	+
27	26	14	15	+
28	24	13	16	+
29	24	13	11	+
30	22	12	12	+
31	22	12	10	+
32	22	12	10	+
33	20	11	16	+
34	20	11	12	+
35	20	11	15	+

TABLE II c

Run test to determine τ using data generated by a random number generator. Seven hundred and twenty random numbers were used to generate a 2h dependent set of numbers.

M	Sample Length	Expected Value	Observed Value	Results
1	718	360	197	-
2	358	180	141	-
3	238	120	121	+
4	178	90	86	+
5	142	72	67	+
6	118	60	56	+
7	102	52	60	+
8	88	45	46	+
9	78	40	42	+
10	70	36	35	+
11	64	33	36	+
12	58	30	21	-
13	54	28	27	+
14	50	26	27	+
15	46	24	28	+
16	44	23	27	+
17	42	22	18	+
18	38	20	17	+
19	36	19	17	+
20	34	18	15	+
21	34	18	18	+
22	32	17	13	+
23	30	16	17	+
24	28	15	15	+
25	28	15	18	+
26	26	14	14	+
27	26	14	16	+
28	24	13	16	+
29	24	13	15	+
30	22	12	11	+
31	22	12	14	+
32	22	12	10	+
33	20	11	14	+
34	20	11	9	+
35	20	11	15	+

TABLE II d

Run test to determine τ using data generated by a random number generator. Seven hundred and twenty random numbers were used to generate a 3h dependent set of numbers.

M	Sample Length	Expected Number	Observed Number	Results
1	716	359	179	-
2	358	180	123	-
3	238	120	93	-
4	178	90	93	+
5	142	72	76	+
6	118	60	52	+
7	102	52	60	+
8	88	45	52	+
9	78	40	46	+
10	70	36	39	+
11	64	33	42	+
12	58	30	29	+
13	54	28	31	+
14	50	26	29	+
15	46	24	26	+
16	44	23	31	+
17	42	22	18	+
18	38	20	17	+
19	36	19	13	-
20	34	18	17	+
21	34	18	20	+
22	32	17	15	+
23	30	16	13	+
24	28	15	14	+
25	28	15	20	+
26	26	14	10	+
27	26	14	14	+
28	24	13	16	+
29	24	13	13	+
30	22	12	11	+
31	22	12	10	+
32	22	12	14	+
33	20	11	12	-
34	20	11	7	-
35	20	11	13	+

TABLE II e

Run test to determine τ using data generated by a random number generator. Seven hundred and twenty random numbers were used to generate a 4h dependent set of numbers.

M	Sample Length	Expected Value	Observed Value	Results
1	716	359	155	-
2	358	180	105	-
3	238	120	73	-
4	178	90	73	-
5	142	72	77	+
6	118	60	55	+
7	102	52	58	+
8	88	45	52	+
9	78	40	38	+
10	70	36	37	+
11	66	33	38	+
12	58	30	29	+
13	54	28	35	+
14	50	26	29	+
15	46	24	24	+
16	44	23	29	+
17	42	22	18	+
18	38	20	19	+
19	36	19	13	-
20	34	18	15	+
21	34	18	20	+
22	32	17	21	+
23	30	16	14	+
24	28	15	12	+
25	28	15	20	+
26	26	14	10	+
27	26	14	18	+
28	24	13	17	+
29	24	13	10	+
30	22	12	10	+
31	22	12	14	+
32	22	12	12	+
33	20	11	12	+
34	20	11	8	+
35	20	11	11	+

"random" numbers generated. This series of tests was then repeated using 4000 points, instead of 720, giving no appreciable difference in results.

(b) Additional nonparametric tests were sought which when performed gave rise to a more nearly independent sequence of tests. The most promising of these are the Hill and Trough Test [4], and the Sen Test [5]. To date only one of these, the Hill and Trough Test, has been used by the authors for analyzing data; therefore, it alone will be discussed in this paper.

Briefly, the Hill and Trough test is a nonparametric test which is based on the occurrence of triples of points in which the middle point is either greater or less than those on the ends. A discussion of this test may be found in section [21.43] of [4].

Results of using this test on the random data, par (a) above, and 12 February 1958 speed data are shown in Tables III and IV.

As with the run test, the results of this method were very encouraging; however, the run test results, in general, were somewhat stronger.

(c) Sequences of tests were studied which were aimed at making precise probability statements. Results to date are limited and hence will not be presented in this paper.

Discussion Part II

From the results in the previous section, there is evidence that the time series representing wind speed and direction at a given point are stationary and may have autocovariance function of the form $B(t) = \sigma^2 e^{-\alpha|t|}$, $\alpha > 0$, or $\sigma^2 a^{|t|}$, $0 \leq a < 1$. In this case, the processes in question would appear to be τ-dependent, the value of τ depending on the size of α, or a.

It is, therefore, of interest to ascertain whether or not a given h-sample $\{X_1, X_2, \ldots, X_n\}$ is from a stationary process with autocovariance function $B(t) = C_1 a^{|t|}$.

TABLE III a

Hill and Trough test to determine τ using data generated by a random number generator. Seven hundred and twenty random numbers were used.

M	Sample Length	Expected Value	Observed Value	Result
1	720	478	463	+
2	360	238	245	+
3	240	158	151	+
4	180	118	114	+
5	144	94	95	+
6	120	78	69	-
7	102	66	61	+
8	90	58	57	+
9	80	52	56	+
10	72	46	54	+
11	64	41	44	+
12	60	38	38	+
13	54	34	33	+
14	50	32	27	-
15	48	30	34	+
16	44	28	27	+
17	42	26	24	+
18	40	25	27	+
19	36	22	27	+
20	36	22	21	+
21	34	21	22	+
22	32	20	19	+
23	30	18	17	+
24	30	18	19	+
25	28	17	18	+
26	26	16	13	+
27	26	16	18	+
28	24	14	14	+
29	24	14	17	+
30	24	14	16	+
31	22	13	13	+
32	22	13	16	+
33	20	12	13	+
34	20	12	12	+
35	20	12	13	+
36	20	12	13	+

TABLE III b

Hill and Trough test to determine τ using data generated by a random number generator. Seven hundred and twenty random numbers were used to generate a 1h dependent set of numbers.

M	Sample Length	Expected Value	Observed Value	Result
1	718	478	369	-
2	358	237	240	+
3	238	157	163	+
4	178	117	117	+
5	142	93	93	+
6	118	77	76	+
7	102	66	68	+
8	88	57	54	+
9	78	50	54	+
10	70	45	42	+
11	64	41	41	+
12	58	37	37	+
13	54	34	32	+
14	50	32	31	+
15	46	29	34	+
16	44	28	29	+
17	42	26	25	+
18	38	24	18	-
19	36	22	22	+
20	34	21	22	+
21	34	21	20	+
22	32	20	21	+
23	30	18	23	+
24	28	17	15	+
25	28	17	18	+
26	26	16	15	+
27	26	16	15	+
28	24	14	16	+
29	24	14	16	+
30	22	13	13	+
31	22	13	15	+
32	22	13	12	+
33	20	12	14	+
34	20	12	16	+
35	20	12	14	+

TABLE III c

Hill and Trough test to determine τ using data generated by a random number generator. Seven hundred and twenty random numbers were used to generate a 2h dependent set of numbers.

M	Sample Length	Expected Value	Observed Value	Result
1	718	477	359	0
2	358	237	220	0
3	238	157	153	+
4	178	117	118	+
5	142	93	86	+
6	118	77	81	+
7	102	66	68	+
8	88	57	58	+
9	78	50	50	+
10	70	45	49	+
11	64	41	46	+
12	58	37	35	+
13	54	34	37	+
14	50	32	33	+
15	46	29	32	+
16	44	28	31	+
17	42	26	29	+
18	38	24	18	-
19	36	22	22	+
20	34	21	23	+
21	34	22	24	+
22	32	20	19	+
23	30	18	19	+
24	28	17	18	+
25	28	17	20	+
26	26	16	15	+
27	26	16	18	+
28	24	14	14	+
29	24	14	17	+
30	22	13	13	+
31	22	13	14	+
32	22	13	13	+
33	20	12	12	+
34	20	12	14	+
35	20	12	16	+

TABLE III d

Hill and Trough test to determine τ using data generated by a random number generator. Seven hundred and twenty random numbers were used to generate a 3h dependent set of numbers.

M	Sample Length	Expected Value	Observed Value	Result
1	716	476	369	-
2	358	237	281	-
3	238	157	143	-
4	178	117	111	+
5	142	93	88	+
6	118	77	75	+
7	102	66	66	+
8	88	57	58	+
9	78	50	54	+
10	70	45	47	+
11	64	41	47	+
12	58	37	37	+
13	54	34	41	+
14	50	32	33	+
15	46	29	34	+
16	44	28	30	+
17	42	26	23	+
18	38	24	22	+
19	36	22	22	+
20	34	21	21	+
21	34	21	28	+
22	32	20	21	+
23	30	18	17	+
24	28	17	18	+
25	28	17	19	+
26	26	16	12	-
27	26	16	16	+
28	24	14	15	+
29	24	14	18	+
30	22	13	12	+
31	22	13	11	+
32	22	13	14	+
33	20	12	12	+
34	20	12	12	+
35	20	12	1[illegible]	+

TABLE III e

Hill and Trough test to determine τ using data generated by a random number generator. Seven hundred and twenty random numbers were used to generate a 4h dependent set of numbers.

M	Sample Length	Expected Value	Observed Value	Result
1	716	476	359	-
2	358	237	181	-
3	238	157	129	-
4	178	117	105	-
5	142	93	87	+
6	118	77	74	+
7	102	66	64	+
8	88	57	58	+
9	78	50	53	+
10	70	45	50	+
11	66	41	44	+
12	58	37	35	+
13	54	34	39	+
14	50	32	33	+
15	46	29	30	+
16	44	28	30	+
17	42	26	27	+
18	38	24	22	+
19	36	22	22	+
20	34	21	16	-
21	34	21	22	+
22	32	20	19	+
23	30	18	19	+
24	28	17	17	+
25	28	17	19	+
26	26	16	11	-
27	26	16	19	+
28	24	14	17	+
29	24	14	13	+
30	22	13	10	-
31	22	13	13	+
32	22	13	16	+
33	20	12	11	+
34	20	12	15	+
35	20	12	12	+

TABLE IV a

Results of Markov tests using data collected from White Sands Missile Range Research Tower, 7 March 1958. Data consist of one hour of observations (5-second visual means). The one-tail limit, F test, is 43 at 95% confidence level. Computed values (in parentheses) are given for each level.

	MARKOV TEST RESULTS		ESTIMATED SPECTRAL CHARACTERISTIC FOR EXTRAPOLATION	
LEVEL	SPEED	DIRECTION	SPEED	DIRECTION
1	reject (41)	accept (48)		.661
2	accept (47)	accept (67)	.532	.828
3	accept (46)	accept (60)	.535	.824
4	reject (42)	accept (56)		.768
5	reject (31)	accept (58)		.682
6	reject (32)	accept (57)		.713
7	reject (38)	accept (62)		.690
8	reject (40)	accept (59)		.742
9	reject (36)	accept (55)		.700

TABLE IV b

Results of Markov tests using wind data collected from White Sands Missile Range Research Tower, 13 February 1958. Data consist of one hour of observations (5-second visual means). The one-tail limit, F test, is 43 at 95% confidence level. Computed values (in parentheses) are given for each level.

	MARKOV TEST RESULTS		ESTIMATED SPECTRAL CHARACTERISTIC FOR EXTRAPOLATION	
LEVEL	SPEED	DIRECTION	SPEED	DIRECTION
1	reject (39)	accept (50)		.637
2	reject (25)	reject (23)		
3	reject (33)	reject (18)		
4	reject (23)	reject (21)		
5	reject (27)	reject (31)		
6	reject (33)	reject (21)		
7	reject (23)	reject (34)		
8	reject (19)	reject (22)		
9	reject (25)	reject (38)		

Consider the random variables

$$\tilde{X} = \frac{1}{n} \sum_{i=1}^{n} X_i,$$

$$B(k, h) = \frac{1}{n-k} \sum_{i=1}^{n-k} (X_i - \tilde{X})(X_{i+k} - \tilde{X}).$$

Under certain conditions, a sufficient one being r-dependence, $\tilde{X}$ may be taken as an estimate of the mean of the time series and $B(k, h)$ the value of the autocovariance function B at kh. Then

$B(1, h), B(2, h), \ldots, B(n-1, h)$ are all estimates, generally with increasingly poor accuracy, of $B(h), B(2h), \ldots, B((n-1)h)$.

It may be observed that for any value of k not exceeding $n-2$, $\frac{B(k+1)h)}{B(kh)} = a^h$. Consider the random variable $A(k, h) = \frac{B(k+1, h)}{B(k, h)}$. It would be enlightening if, under the hypothesis that $\{X_1, X_2, \ldots, X_n\}$ is an h-sample of a normal process with autocovariance $B(t) = C_1 a^{|t|}$, one could prove that for any $k \leq n-1$, $A(k, h)$ has expected value a^h, and a distribution perhaps similar to the F-distribution.

To study this problem, speed and direction data were used to compute $A(k, h)$ for $h = 5$ seconds, $n = 720$, $k = 700$. A run test on the median was performed. As a run test is more sensitive to location than shape, one might expect that a run test would fail to detect trends in the variance of the $A(k, h)$ but should detect trends in the mean. Only the results of the speed data for 7 March 1958 are presented in this report. The results of this test are included in Table IV. The fact that in a number of cases tested the run test did not call for rejection is reason to consider seriously the possibility that $A(k, h)$ can be of the nature mentioned earlier and that the nature of certain low altitude winds may be described

as a process with autocovariance function $B(t) = C_1 a^{|t|}$. This latter fact would be of considerable importance in prediction, in that the process is Markov, and the spectral characteristic for extrapolation being quite simple could possibly be estimated by use of the median.

CONCLUSION

Results from the preliminary studies presented in this report are very encouraging. It is believed that these tests can be used effectively in studying meteorological data for determination of stationarity, τ-dependence, and Markov characteristics.

REFERENCES

1. Brunk, H. D., An Introduction to Mathematical Statistics, Ginn and Company, 1960.

2. Rachele, Henry and M. E. McLardie, "The White Sands Missile Geophysics Research Tower," Special Report 7, U. S. Army Signal Missile Support Agency, White Sands Missile Range, New Mexico. July 1957.

3. Lee, Robert P., "A Program For Random Number Generation," Internal Report Atmospheric Sciences Laboratory, White Sands Missile Range, New Mexico. July 1966.

4. Kendall, Maurice G., The Advanced Theory of Statistics, Vol. II, Hafner Publishing Company, New York, 1951.

5. Sen, P. K., "Some Non-parametric Tests For M-Dependent Time Series," J. Amer. Stat. Assoc., 60, 309, March 1965.

A TECHNIQUE FOR PREDICTING NONLINEAR WIND COMPENSATION OF BALLISTIC ROCKET SYSTEMS*

G. G. Wilson
Staff Member, Aero-Thermodynamics Department
Sandia Laboratory, Albuquerque, New Mexico

ABSTRACT

Factors affecting the nonlinearities associated with wind compensation of ballistic rocket systems are discussed. A linear wind compensation method, used by Sandia Laboratory since 1959, is presented and extended to account for nonlinear effects. Comparisons between the two methods are made to show expected improvements in accuracy.

*This work was supported by the United States Atomic Energy Commission.

LIST OF SYMBOLS

D	Deflection, meters
h	Altitude, meters
R	Range, meters
R_N	Nominal range, meters
V	Ballistic wind velocity, meters per second
V_N	Normal component of ballistic wind, meters per second
V_P	Parallel component of ballistic wind, meters per second
X	Distance along X-axis, meters
Y	Distance along Y-axis, meters
Δ	Denotes incremental quantity
$\frac{\Delta R}{\Delta \theta}$	Change in range due to a change in elevation angle, meters per degree
η	Azimuth angle, degrees
η_o	Nominal azimuth angle, degrees
θ	Elevation angle, degrees
θ_o	Nominal elevation angle, degrees
λ	Ballistic wind direction, degrees

SUMMARY

A theoretical development of wind compensation equations is presented and discussed. The coefficients in the equations are assumed to be a function of the ballistic wind magnitude and direction, and the change in launch elevation angle. The proposed method of uniquely defining and determining the coefficients is evaluated through the use of a digital six-degree-of-freedom trajectory program that incorporates the physical, aerodynamic, thrust, and fuel flow characteristics of a typical ballistic rocket system.

The launcher set-correction technique is evaluated by assuming values of the ballistic wind and its direction. These values are used to determine from the launcher set chart the azimuth and elevation corrections required to compensate for the ballistic wind. Fourteen six-degree-of-freedom trajectories were computed to evaluate the proposed correction technique. These trajectories, using two magnitudes of ballistic wind impinging on the rocket system from seven different directions, show that the flight path of the rocket is corrected to within a maximum error of 3 mils, based on the slant range, for the ballistic wind environments tested. Fourteen comparison trajectories, using azimuth and elevation corrections determined from linear coefficients, give a maximum error of 19 mils.

A TECHNIQUE FOR PREDICTING NONLINEAR WIND COMPENSATION OF BALLISTIC ROCKET SYSTEMS

Introduction

Statistical variations in ballistic rocket parameters that cause deviation from the nominal trajectory have been of increasing concern to the ballistician as the altitude and range of rocket systems have increased. It is necessary from a range safety point of view that the impact point of each stage and its related hardware be accurately predicted. Also, accurate impact prediction is desirable to facilitate airborne and surface vessel payload recovery and data acquisition. More recently, scientific experimenters have required greater accuracy of payload placement at a designated point in space. To assist in the attainment of these goals, this paper presents a linear wind compensation method* used very successfully by Sandia Laboratory since 1959. The linear technique is extended to account for all nonlinear effects, regardless of their origin.

Development of Equations

The equations being developed assume that the altitude-wind profile obtained near the time of launch is effectively reduced by a wind-weighting system to a ballistic wind of magnitude, V, that is blowing at

*The original equations using linear (or constant) coefficients were developed by Mr. H. A. Wente, Staff Member, Aero-Thermodynamics Department, Sandia Laboratory.

an angle, λ. The right-hand orthogonal axis system used to describe the physical quantities is located at the launch point on the earth with the X-axis northward, the Y-axis eastward, and the Z-axis downward. All angles are measured by the right-hand rule from the X-axis, with the exception of the elevation angle, θ, which is measured positive-upward from the X, Y-plane. Three coordinates are required to fully specify the position of the vehicle in space at any given time. Instead of using the X, Y, Z coordinates, three generalized coordinates: elevation angle, θ, deflection from the corrected azimuth, D, and range, R, are used to specify the vehicle location.

Figure 1 shows the projection of ballistic rocket trajectories onto the X, Y-plane. When no ballistic wind is present, the range, R, for a new launcher setting located at azimuth angle, η, and elevation ange, θ, may be obtained by

$$R = R_N + \left(\frac{\Delta R}{\Delta \theta}\right) \cdot \Delta\theta, \tag{1}$$

where R_N and θ_o are the nominal range and nominal elevation angle, respectively ($\Delta\theta = \theta - \theta_o$). The quantity $\Delta R/\Delta\theta$ is negative for a positive $\Delta\theta$ at large elevation angles.*

When a ballistic wind acts on the system, as shown in Figure 2, the launcher must be moved through incremental changes in azimuth and elevation angles to compensate for the wind. The correct changes will cause the vehicle to pass through the nominal aiming point, A. Expressions for ΔD and ΔR are obtained from Figure 2 and combined with Equation (1) to give

$$\Delta D = - R_N \sin \Delta\eta, \tag{2}$$

and

$$\Delta R = R_N (\cos \Delta\eta - 1) - \left(\frac{\Delta R}{\Delta \theta}\right) \cdot \Delta\theta. \tag{3}$$

*For elevation angles below the maximum range elevation angle, $(\Delta R/\Delta\theta)$ changes sign.

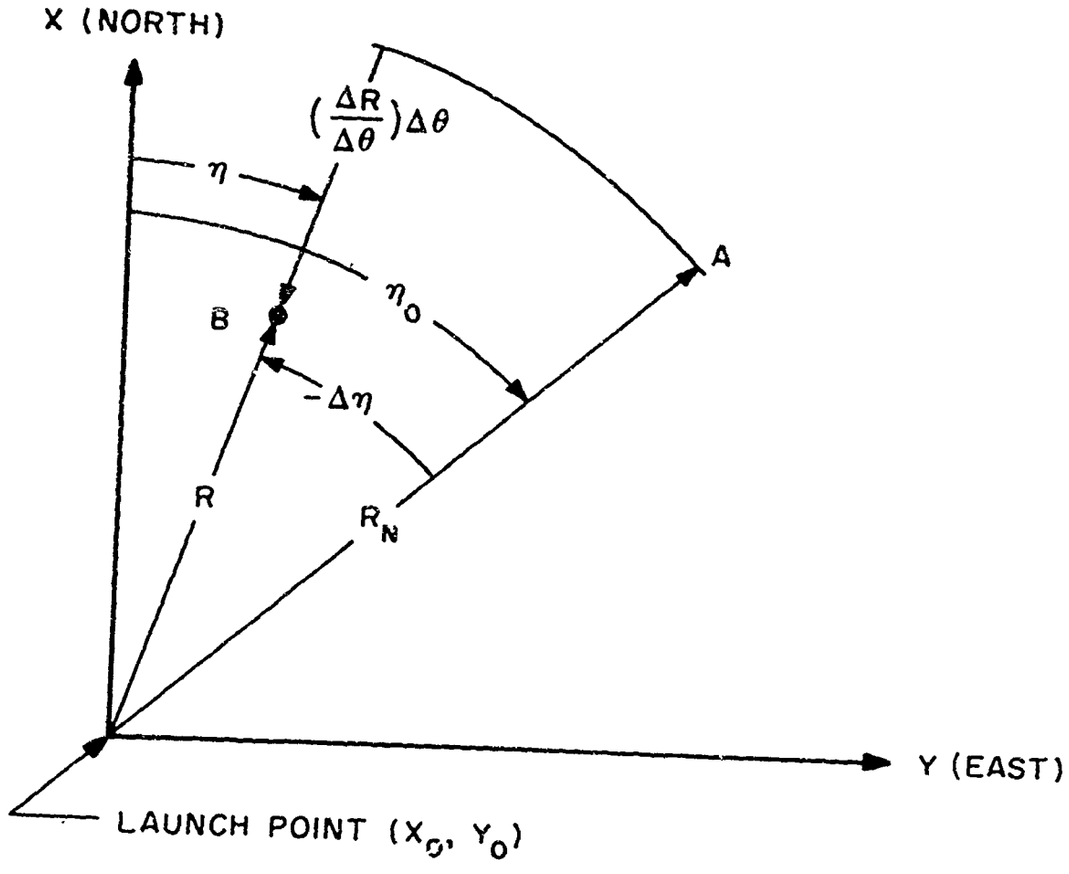

FIG. 1 – SCHEMATIC OF ROCKET TRAJECTORIES FOR NO WIND CONDITION

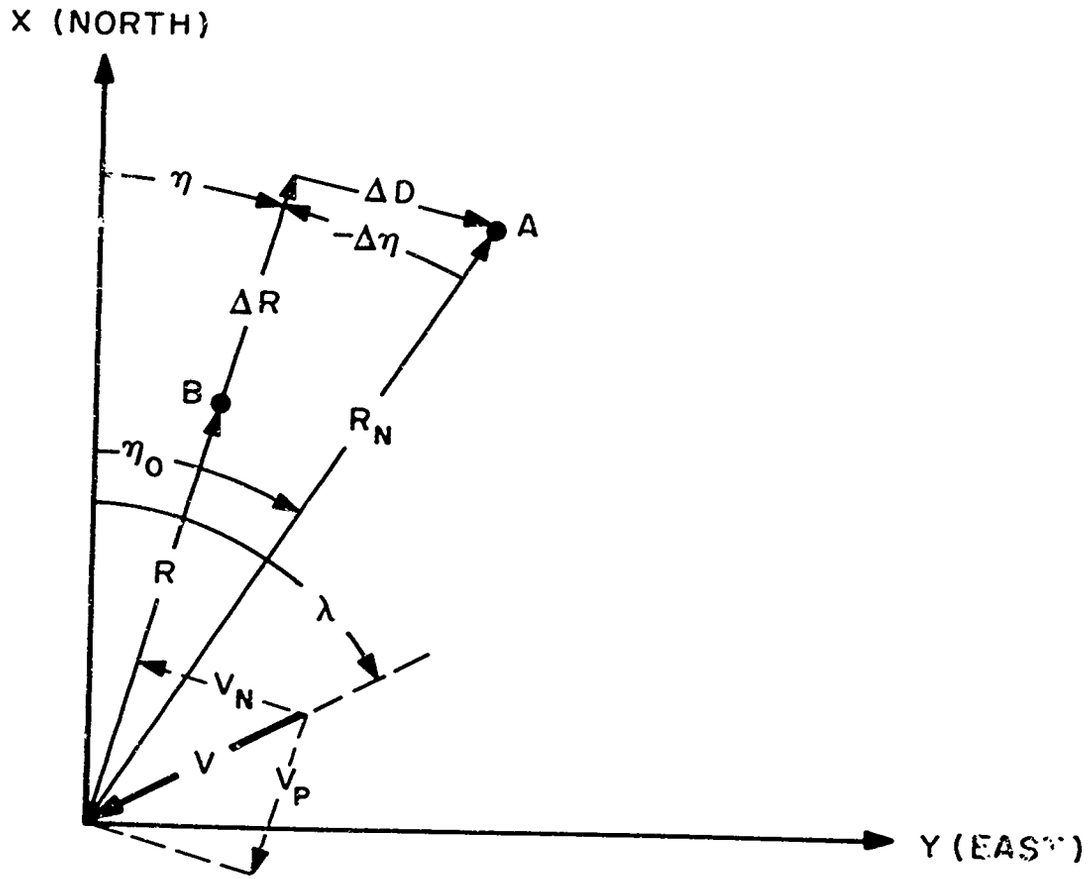

FIG. 2 - SCHEMATIC OF ROCKET TRAJECTORIES FOR A BALLISTIC WIND IMPINGING ON THE ROCKET SYSTEM

To determine ΔR and ΔD, it is necessary to consider these quantities as functions of Δ and the ballistic wind components V_N and V_P, which are the normal and parallel components, respectively. Figures 3 and 4 show range and deflection variations with ballistic wind components for a given elevation angle. These figures show range and deflection for a typical ballistic, fin-stabilized rocket system. For a vehicle launched at high elevation angles, having large launch accelerations and comparatively linear aerodynamics, the curves in these figures tend to coalesce and approach the same slope about the origin for small changes in elevation angle. Under these conditions the changes in range and deflection can be assumed to be independent of normal and parallel ballistic wind components, respectively. The expressions for ΔR and ΔD can then be written

$$\Delta R = \left(\frac{\partial R}{\partial V_P}\right) \cdot V_P = \left(\frac{\partial R}{\partial V}\right) \cdot V \cdot \cos(\lambda - \eta_o - \Delta\eta) \qquad (4)$$

and

$$\Delta D = \left(\frac{\partial D}{\partial V_N}\right) \cdot V_N = \left(\frac{\partial D}{\partial V}\right) \cdot V \cdot \sin(\lambda - \eta_o - \Delta\eta). \qquad (5)$$

The subscript notation has been dropped for convenience and the expressions for V_N and V_P are obtained from Figure 2. Equations (3) and (4), and (2) and (5) are combined to yield

$$\left(\frac{\partial R}{\partial V}\right) \cdot V \cdot \cos(\lambda - \eta_o - \Delta\eta) = R_N (\cos \Delta\eta - 1) - \left(\frac{\partial R}{\partial \theta}\right) \cdot \Delta\theta \,, \qquad (6)$$

and

$$\left(\frac{\partial D}{\partial V}\right) \cdot V \cdot \sin(\lambda - \eta_o - \Delta\eta) = - R_N \sin \Delta\eta. \qquad (7)$$

Equations (6) and (7) contain the four unknowns λ, $\Delta\eta$, $\Delta\theta$, and V. It is possible to assume values of two of the unknowns and solve for the remaining unknowns. For launcher set chart construction, values of $\Delta\theta$

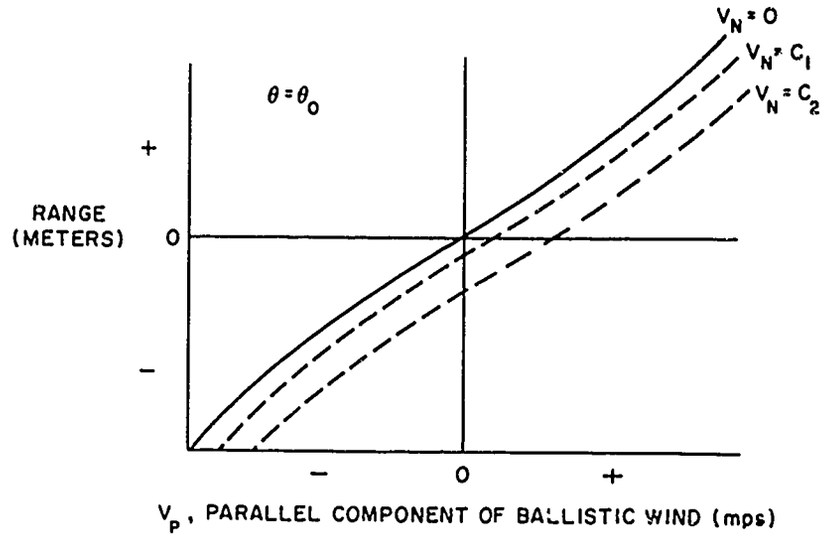

FIG. 3 – VARIATION OF RANGE WITH BALLISTIC WIND COMPONENTS

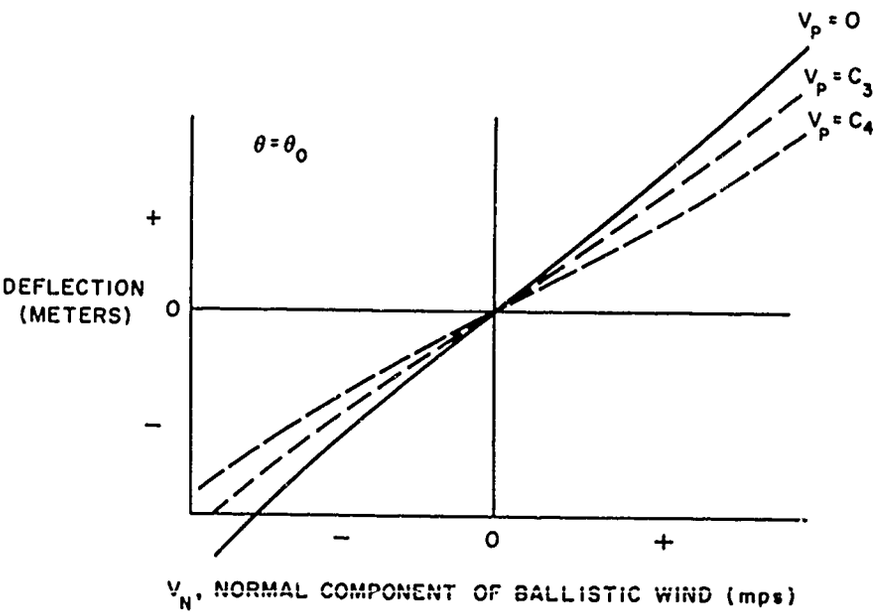

FIG. 4 - VARIATION OF DEFLECTION WITH BALLISTIC WIND COMPONENTS

15

and $\Delta\eta$ are assumed and the equations are solved for λ and V. Polar coordinates are used to locate λ and V along the angular and radial coordinates, respectively. Lines of constant $\Delta\eta$ and $\Delta\theta$ are constructed graphically to facilitate locating the correct launcher setting, as shown in Figure 5. The equations can be programmed on relatively small digital computers to aid in determining launcher settings at the launch site. The value of the ballistic wind and its direction are known and the equations are solved for the wind compensation settings, $\Delta\theta$ and $\Delta\eta$.

The impact point of any portion of the rocket system may be determined from Figure 2 by summing the components in the X and Y directions to give

$$X = X_o + (R \dot{+} \Delta R) \cos \eta - \Delta D \sin \eta \tag{8}$$

and

$$Y = Y_o + (R + \Delta R) \sin \eta + \Delta D \cos \eta . \tag{9}$$

Substitution for the expressions in these equations gives

$$X = X_o + \left[\left(\frac{\partial R}{\partial \theta}\right) \cdot \Delta\theta + R_N\right] \cos \eta + \left[\left(\frac{\partial R}{\partial V}\right) \cdot V \cdot \cos (\lambda - \eta_o - \Delta\eta)\right] \cos \eta$$

$$- \left[\left(\frac{\partial D}{\partial V}\right) \cdot V \cdot \sin (\lambda - \eta_o - \Delta\eta)\right] \sin \eta, \tag{10}$$

and

$$Y = Y_o + \left[\left(\frac{\partial R}{\partial \theta}\right) \cdot \Delta\theta + R_N\right] \sin \eta + \left[\left(\frac{\partial R}{\partial V}\right) \cdot V \cos (\lambda - \eta_o - \Delta\eta)\right] \sin \eta$$

$$+ \left[\left(\frac{\partial D}{\partial V}\right) \cdot V \cdot \sin (\lambda - \eta_o - \Delta\eta)\right] \cos \eta . \tag{11}$$

The appropriate values of the constants and coefficients are provided for each stage or component part to yield its respective impact location.

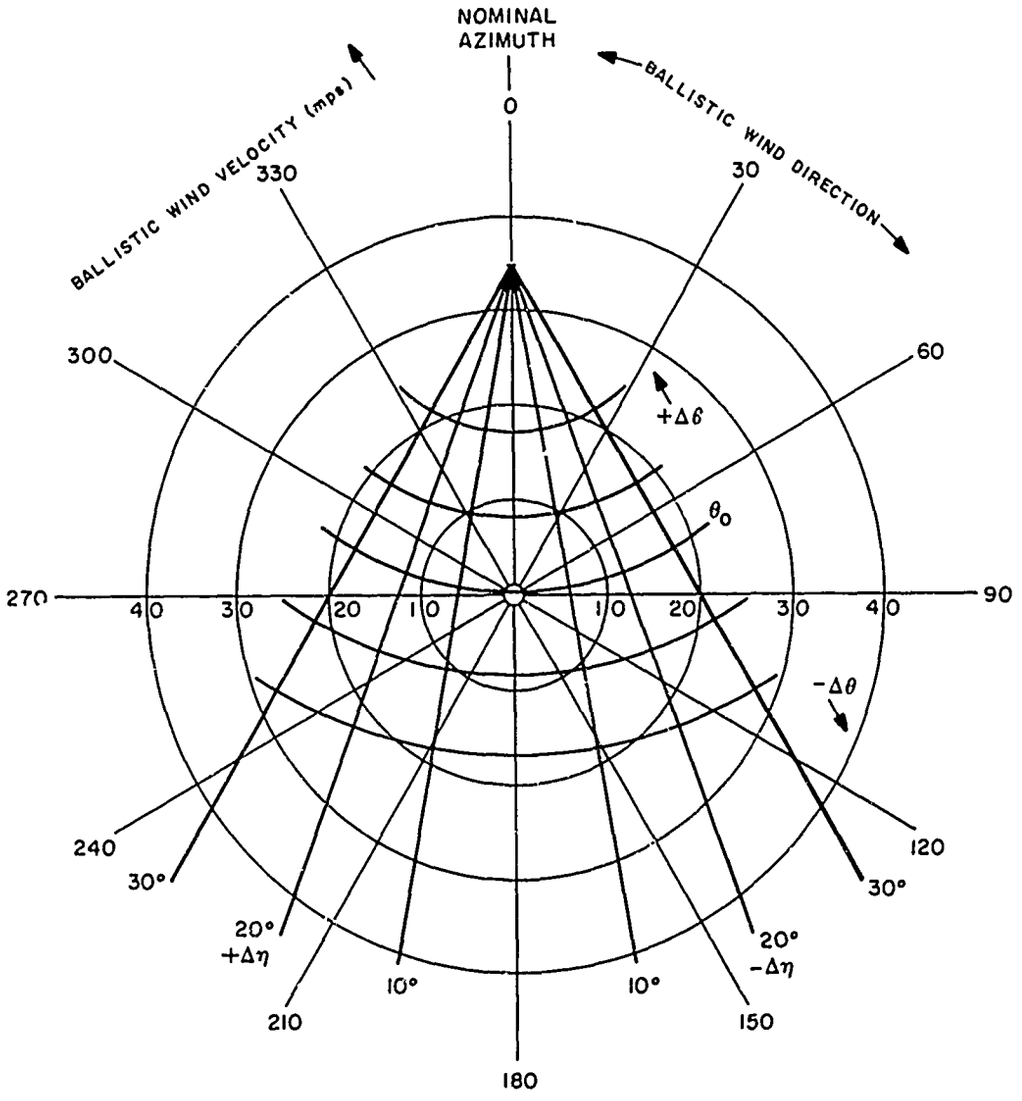

FIG. 5 - LAUNCHER SET CHART BASED ON LINEAR COEFFICIENTS

When the rocket system is accelerating slowly and/or has a low velocity at launch, the changes in range and deflection are not linear. The assumption that these changes are independent of the ballistic wind components is not valid, and the resulting large changes in elevation angle cause changes in the slopes of Figures 3 and 4. Nonlinear aerodynamic coefficients and all other nonlinear phenomena help compound the nonlinearity associated with these figures. If accurate wind compensation is to be realized, these nonlinearities must be fully accounted for.

One method of accounting for the nonlinearities is to use a six-degree-of-freedom digital computer program to determine ΔR and ΔD in Figure 2. If the computer program incorporates a rotating oblate-spheroid earth, along with the vehicle's aerodynamic, physical, thrust, and fuel flow characteristics, then all the nonlinear effects are incorporated in the determination of ΔR and ΔD. It is then possible to determine these changes in range and deflection as functions of the ballistic wind components and changes in elevation angle.

Equations (2) and (3) retain their original form where ΔD and ΔR are written

$$\Delta D = f_1 (V_N, V_P, \Delta\theta), \tag{12}$$

and

$$\Delta R = f_2 (V_N, V_P, \Delta\theta), \tag{13}$$

to show functional dependence. It should also be noted that $(\Delta R/\Delta\theta)$ in Equation (1) must show functional dependence on $\Delta\theta$ for moderate-to-large changes in elevation angle.

Equations (12) and (13) are equated to Equations (2) and (3) to provide two equations in the two unknowns, $\Delta\theta$ and $\Delta\eta$, and must be solved simultaneously. These equations do not represent an explicit

closed-form solution as was obtained in Equations (6) and (7). Solution of these equations requires that an iterative technique be used and proceeds in the following manner:

1. Assume incremental values of λ and V.
2. For an assumed value of V, compute V_P and V_N using Equations (4) and (5), assuming $\Delta\eta = 0$.
3. For $\Delta\theta = 0°$, and the computed values of V_P and V_N, find $\Delta R/\Delta\theta$, $\Delta R(V_P, V_N, \Delta\theta)$, and $\Delta D(V_P, V_N, \Delta\theta)$.
4. Use Equation (12) to compute $\Delta\eta$.
5. Use Equation (13) to compute $\Delta\theta$ using the value of $\Delta\eta$ from Step (4).
6. Recompute V_P and V_N using the results of Step (4).
7. Using the results of Steps (5) and (6), find new values $\Delta R/\Delta\theta$, $\Delta R(V_P, V_N, \Delta\theta)$, and $\Delta D(V_P, V_N, \Delta\theta)$.
8. Repeat Steps (4) and (5).
9. Continue the iteration procedure till convergence occurs for both $\Delta\theta$ and $\Delta\eta$.

A launcher set chart can be graphically constructed by plotting $\Delta\theta$ as a function of $\Delta\eta$. Lines of constant $\lambda - \eta_o$ and constant V are located on the chart to form a grid that aids in locating the proper launcher correction.

The nonlinear wind compensation method was evaluated using a typical rocket system. A six-degree-of-freedom program[1] incorporating the aerodynamic, mass, thrust, and fuel flow characteristics of the vehicle was used to determine ΔR, ΔD, and $\Delta\lambda/\Delta\theta$ as

functions of the ballistic wind components and changes in elevation angle. A Fortran IV program, containing the necessary two- and four-dimensional tables needed to describe accurately the coefficients, was used to solve Equations (12) and (13). The results of the computations and the launcher set chart are shown in Figure 6.

Ballistic wind velocities of 4.572 and 9.144 meters per second for impingement angles of 0, 30, 60, 90, 120, 150 and 180 degrees were selected for evaluation purposes. The corresponding azimuth and elevation angle corrections, along with the appropriate ballistic wind components, were used in the six-degree-of-freedom trajectory program and evaluated at 87.0 seconds trajectory time. This is the time the rocket system reaches the aiming point in space for a no-wind condition. The results of the fourteen trajectories were compared with the nominal trajectory. The maximum error at the target point is 238.1 meters or 3 mils* based on the slant range distance from launch to aiming point.

For comparison purposes, fourteen trajectories were computed using azimuth and elevation angle corrections based on linear coefficients and the same ballistic wind velocities. These results were compared to the nominal trajectory. The maximum error at the target point is 1551.7 meters or 19 mils.

Concluding Remarks

Evaluation of the correction technique validates the basic launcher set correction equations, and shows that the coefficients in the equation, which incorporate the vehicle characteristics, can be accurately determined as functions of the ballistic wind velocity components and changes in elevation angle.

---

*Mil error = Miss distance x 1000/Slant range

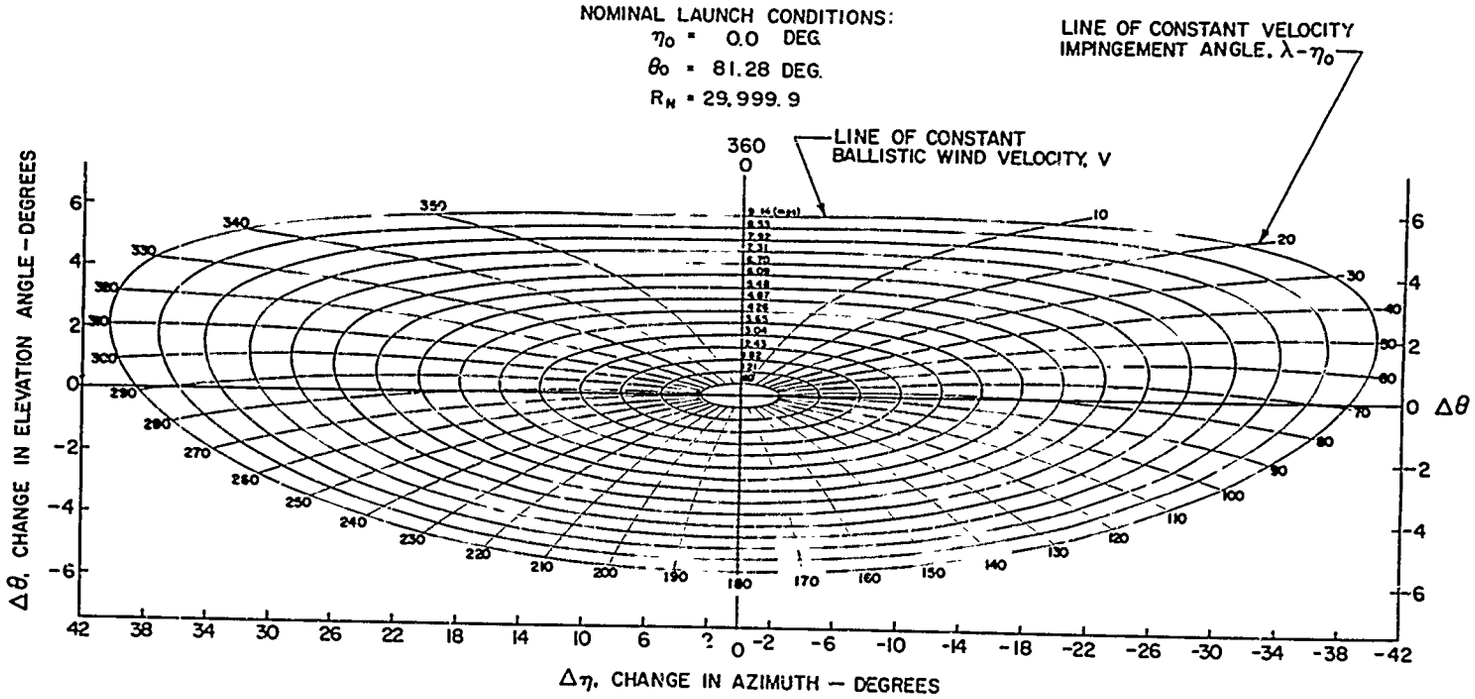

FIG. 6-LAUNCHER SET CHART FOR A TYPICAL BALLISTIC ROCKET SYSTEM

The 3 mil error using nonlinear coefficients is a significant improvement over the 19 mil error using linear coefficients for the low-launch velocity of the typical rocket system considered. Rocket systems having large accelerations and velocities at launch would not show the same improvement in accuracy, but would maintain the same degree of accuracy.

Inaccuracies encountered during reduction of the altitude-wind profile to a ballistic wind have not been evaluated. This particular source of error should not be overlooked when applying any wind-compensation method.

REFERENCE

1. "Six-Degree-of-Freedom Flight-Path Study Generalized Computer Program," FDL-TDR-64-1, Air Force Flight Dynamics Laboratory, Wright-Patterson Air Force Base, Ohio, October 1964.

PROJECT TWINKLE*

R. E. Gardner
Staff Member, Aero-Thermodynamics Department
Sandia Laboratory, Albuquerque, New Mexico

ABSTRACT

A series of upper atmosphere experiments was conducted by Sandia Laboratory, using Apache-Dart and Tomahawk-Dart rocket systems. The primary purpose of the experiments was to provide insight into the phenomenon of starlight scintillation. A discussion of the rocket development and experimental programs, with primary emphasis on the aerodynamic characteristics of the rocket and parachute systems, is presented.

*This work was supported by the United States Atomic Energy Commission.

SUMMARY

Atmospheric causes of starlight scintillation (twinkling) were investigated by Sandia Laboratory at its Tonopah Test Range, Tonopah, Nevada. The investigation involved two series of experiments, using Apache-Dart and Tomahawk-Dart rocket systems to deliver payloads to apogee altitudes of 63,000 and 150,000 ft, respectively. At apogee a parachute was deployed to lower the payload to the ground. A tracking telescope at the impact target detected, measured, and recorded the intensity of a light located on the nose of the descending rocket payload. This paper presents the aerodynamics and ballistics of the rocket systems and parachutes and a brief discussion of the light-intensity data.

PROJECT TWINKLE

Introduction

The scintillation or twinkling of a star may be defined as intensity fluctuations of the star's image, and until recently, not too much was known about this phenomenon. The most widely accepted explanation is that scintillation is caused by atmospheric turbulence resulting in small-scale fluctuations in the refraction and/or diffraction index of the atmosphere. A similar phenomenon occurs with radio frequency waves.

In 1963, Sandia Laboratory started a series of experiments intended to provide more insight into the phenomenon of light scintillation (see Hudson[1]). The experiments consisted essentially of lofting a high-intensity light source to altitudes of 50,000 to 150,000 feet by a rocket system, and then lowering the light source to the ground by a parachute. During descent, the light intensity was measured and recorded on the ground. This paper discusses the aeroballistic development of the rocket and parachute systems along with a brief discussion of the light-intensity data. A detailed analysis will be reported shortly by Pepper and Gardner.[2]

Test Facilities

Sandia's Tonopah Test Range was the site selected for performing the experiment. The launch facilities for this range are located approximately 35 miles southeast of Tonopah, Nevada, and 135 miles northwest of Las Vegas, Nevada.

Figure 1 is a sketch of the test range. The rocket launch facilities are located at Station 9 on the sketch. At Station 14 is located the Contraves cinetheodolite (a tracking telescope) which was selected to record light-intensity data. For the experimental operation, cameras were removed from the telescope, and it was refitted with a photomultiplier tube. The output from the tube was amplified and recorded on magnetic tape. Station 14 is located 35,200 feet downrange from the launcher, on an azimuth of 145°. It was felt that, for a successful experiment, the light source must be kept as close to being directly overhead of the telescope as possible. Thus, Station 14 became the impact target for the rocket launches.

Phase I. Apache-Dart Launches

For the first series of tests, an Apache rocket motor was selected[3] to boost a 6-inch diameter Dart (i.e., inert vehicle) second stage, which carried the payload. The Apache motor burns for 6.44 seconds and has an average thrust of 4748 pounds. Figure 2 is a sketch of the system. The boosted Dart configuration was selected over a single-stage rocket because it provides a simple method of separating the payload from the booster; this allows the parachute to be deployed from the rear of the Dart. The total weight of the Dart was 72 pounds, and the weight of the entire vehicle at the time of launch was 322 pounds.

The payload consisted of batteries, a parachute, a 500-watt lamp in the nose, a small rear lamp for tracking during the ascent portion of the trajectory, and a timer for deploying the parachute, blowing off the nose, and turning on the lights. There was no telemetry on board.

The rocket system was launched from a small rail launcher which provided 2-1/2 feet of guidance. The fins on both the Dart and the Apache booster were set at zero incidence angle; however, the vehicle did roll

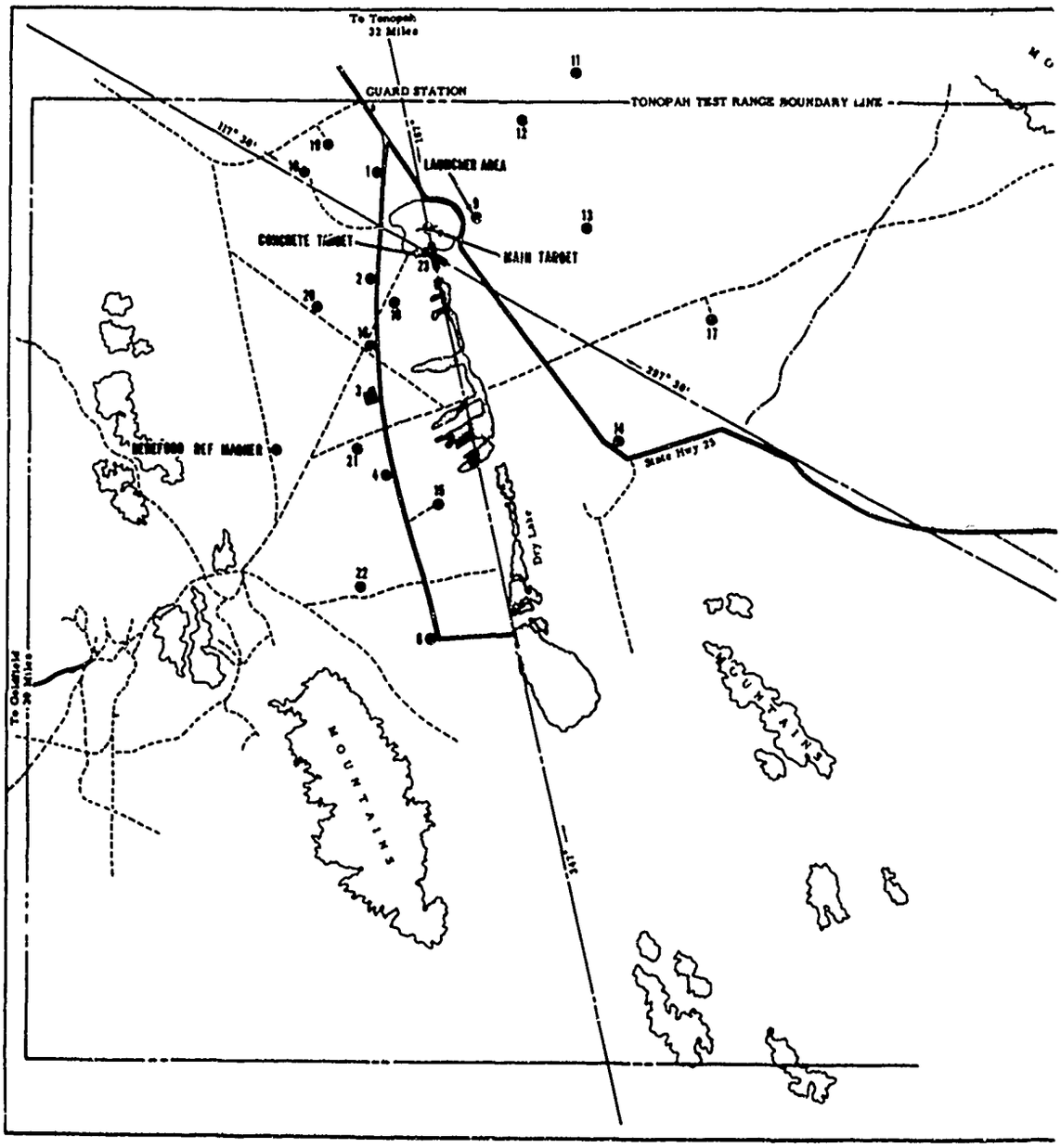

FIG. 1a - TONOPAH TEST RANGE

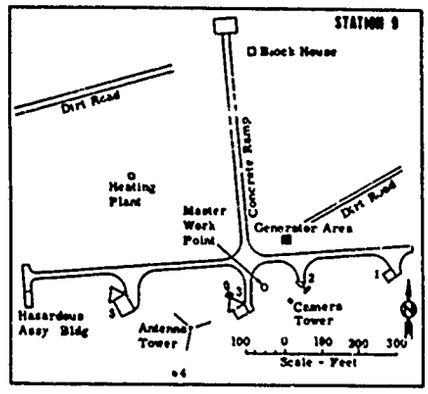

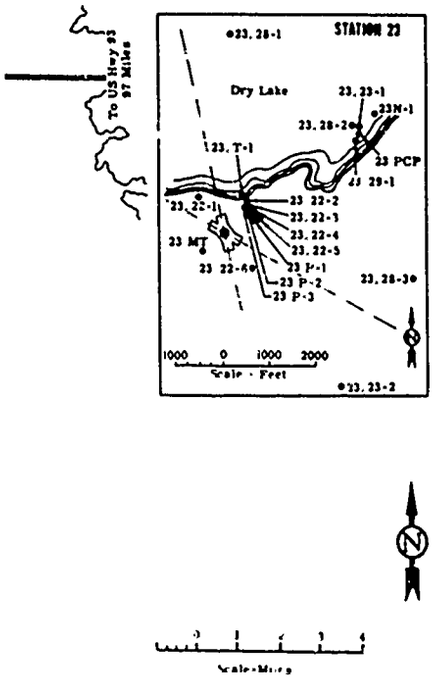

STATION	INSTRUMENTATION	GRID COORDINATES		
		Easting	Northing	Elevation (MSL)
Main Target Hereford Reference Marker		E483,002.94 480,947.01	N1,138,085.06 1,000,195.29	5331.44 5857.07
1	Ashania, T-33 Radar	475,555.12	1,133,445.42	5307.487
2,1	M-45	474,461.62	1,120,089.12	5319.460
2,2	ME-16	474,399.83	1,119,835.42	5395.559
3	Ashania, Control, Metro, Telemetry Receiving	474,550.04	1,105,717.23	5536.014
4	ME-19, Ashania, SCR 584 Radar	476,968.53	1,094,702.93	5573.212
6	LA-34	483,266.46	1,073,079.75	5592.820
9 Launcher Area	Rocket Launchers, Blockhouse, Cameras, Assembly Building	480,413.02	1,127,072.94	5349.060
Launcher No. 1	Launcher	480,760.84	1,127,102.30	5345.73
Launcher No. 2	Launcher	480,513.88	1,127,078.17	5350.58
Launcher No. 3	Launcher	480,329.30	1,127,039.81	5346.27
Launcher No. 4	Launcher	480,172.35	1,126,868.33	5342.32
Launcher No. 5	Launcher	480,013.72	1,127,052.01	5345.91
10	MIDOT	486,250.48	1,133,804.56	5333.80
11	MIDOT	502,189.58	1,145,355.08	5612.65
12 (approximate)	Contraves	494,511.00	1,139,284.00	5465.00
13 (approximate)	Contraves	502,532.00	1,125,683.00	5484.00
14 (approximate)	Contraves	500,902.00	1,000,350.00	5492.00
15	MIDOT	482,811.33	1,089,288.38	5499.80
16,1 (approximate)	M-45	474,627.00	1,100,281.00	5479.00
16,2 (approximate)	ME-16	474,627.00	1,100,281.00	5479.00
17 (approximate)	Contraves	519,835.00	1,114,515.00	5660.00
18	Metro	477,700.13	1,118,486.51	5383.54
19 (approximate)	Contraves	468,072.00	1,136,436.00	5311.00
20 (approximate)	Contraves	467,937.00	1,118,937.00	5452.00
21 (approximate)	Contraves	472,819.00	1,097,948.00	5647.00
22 (approximate)	Contraves	475,183.00	1,079,758.00	5822.00
23	Concrete Target	482,835.26	1,122,484.43	5335.02
23,22-1	CZR-1	482,548.28	1,123,490.16	5336.45
23,22-2	CZR-1	483,296.33	1,123,109.91	5336.45
23,22-3	CZR-1	483,382.95	1,122,998.02	5336.43
23,22-4	CZR-1	483,469.60	1,122,886.13	5336.39
23,22-5	CZR-1	483,556.23	1,122,774.38	5336.39
23,22-6	CZR-1	483,382.45	1,121,777.21	5339.87
23,23-1	Photo-Sonic 70 mm	485,639.25	1,124,655.83	5337.78
23,23-2	Photo-Sonic 70 mm	485,251.04	1,119,363.41	5347.98
23,23-3	Photo-Sonic 70 mm			
23,28-1	Flight Analyser	482,968.38	1,126,566.61	5337.06
23,28-2	Flight Analyser	485,530.71	1,124,697.66	5337.04
23,28-3	Flight Analyser	486,820.36	1,121,571.37	5348.14
23,29-1	Profile Plotter	485,657.71	1,124,511.04	5338.96
23N-1	M-45	485,994.08	1,124,930.68	5342.58
23P-1 (approximate)	High Speed Tracking Camera	483,290.00	1,123,010.00	5335.00
23P-2 (approximate)	High Speed Tracking Camera	483,380.00	1,122,900.00	5335.00
23P-3 (approximate)	High Speed Tracking Camera	483,460.00	1,122,780.00	5335.00
23T-1	Telemetry			
23PCP	Contr[illegible]			
23MT	Metro Tower			

FIG. 1b - COORDINATES OF TONOPAH TEST RANGE INSTRUMENTATION

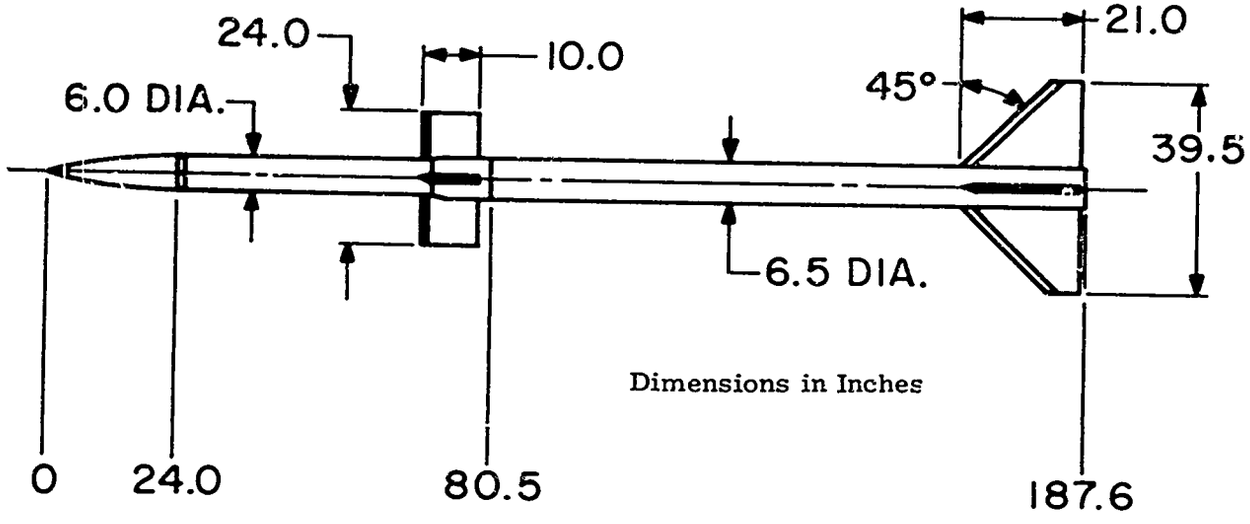

FIG. 2 - APACHE-DART ROCKET SYSTEM

somewhat, because of manufacturing tolerances and induced effects. Figure 3 shows altitude, range, and velocity, as a function of time from launch of the system. The nominal no-wind launch elevation angle of the system was 74 degrees. The launcher was adjusted, however, to compensate for wind effects on the rocket during ascent, and on the parachute during descent.

The Dart attained an apogee altitude of 63,000 feet. At the time of apogee, the parachute was deployed, nose cone ejected, forward light turned on, and rear light turned off. Figure 4 is a sketch of the Dart descending on the 4-foot guide-surface parachute.

A total of eight Apache-Dart rockets were flown. The first two were for the development of the vehicle, parachute, and payload. The remaining six were for performance of the twinkling experiment. Good data were obtained on five of these flights; the one failure was attributed to a timer malfunction, since the parachute was not deployed and the lamp was not turned on.

Phase II. Tomahawk 9-Inch Dart Launcher

Following analysis of the experimental data, a second series of experiments was initiated to determine if there were any twinkling effects caused by the atmosphere at altitudes up to 120,000 feet, to measure small fluctuations in atmospheric pressure and temperature, and to correlate these variations with the observed twinkling.

A Tomahawk TE-416 motor was selected to boost a 9-inch diameter Dart second stage. The Tomahawk motor, which burns for approximately 8.9 seconds, has an average thrust of 10,855 pounds. Although the Dart payload weighed 285 pounds, the rocket system was more than adequately powered for the apogee altitude and impact range requirements. In order to restrain performance of the system, the interstage adapter was

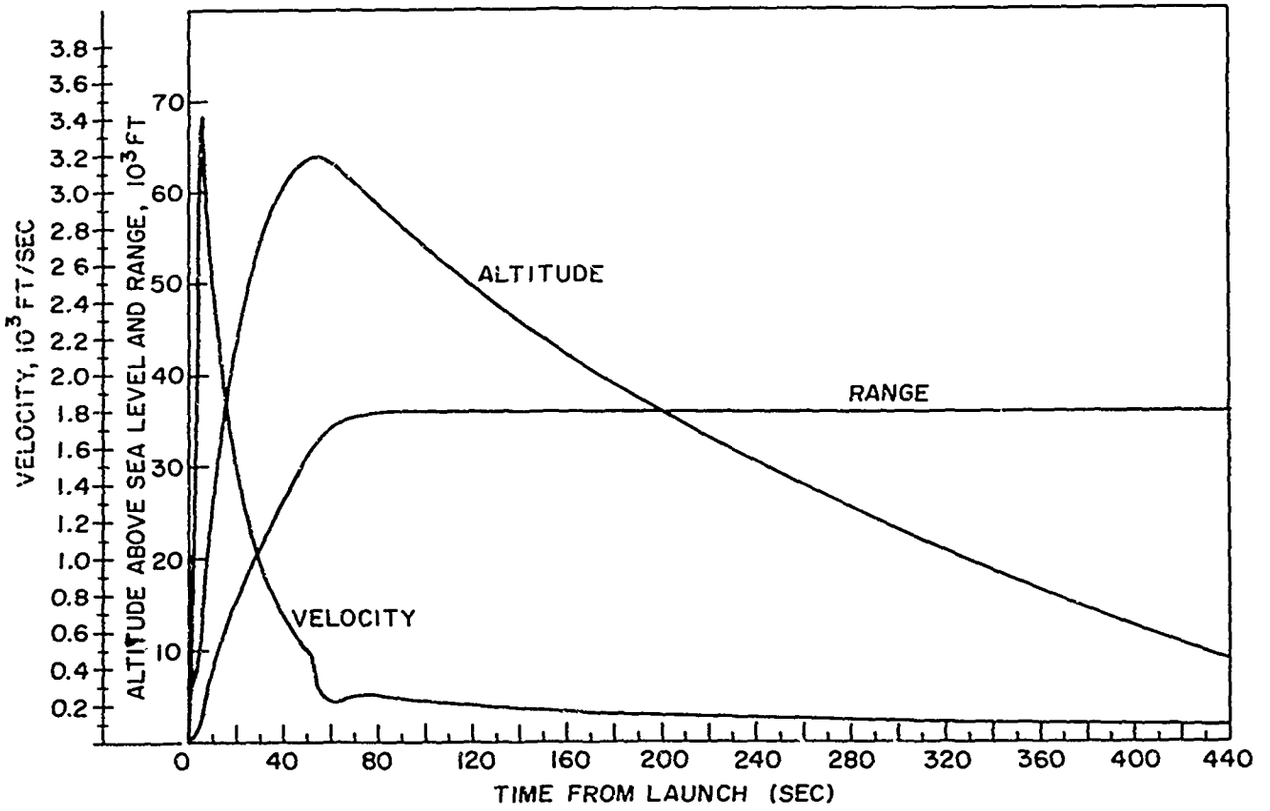

FIG. 3 - CHARACTERISTICS OF THE APACHE-DART TRAJECTORY, AS A FUNCTION OF TIME FROM LAUNCH

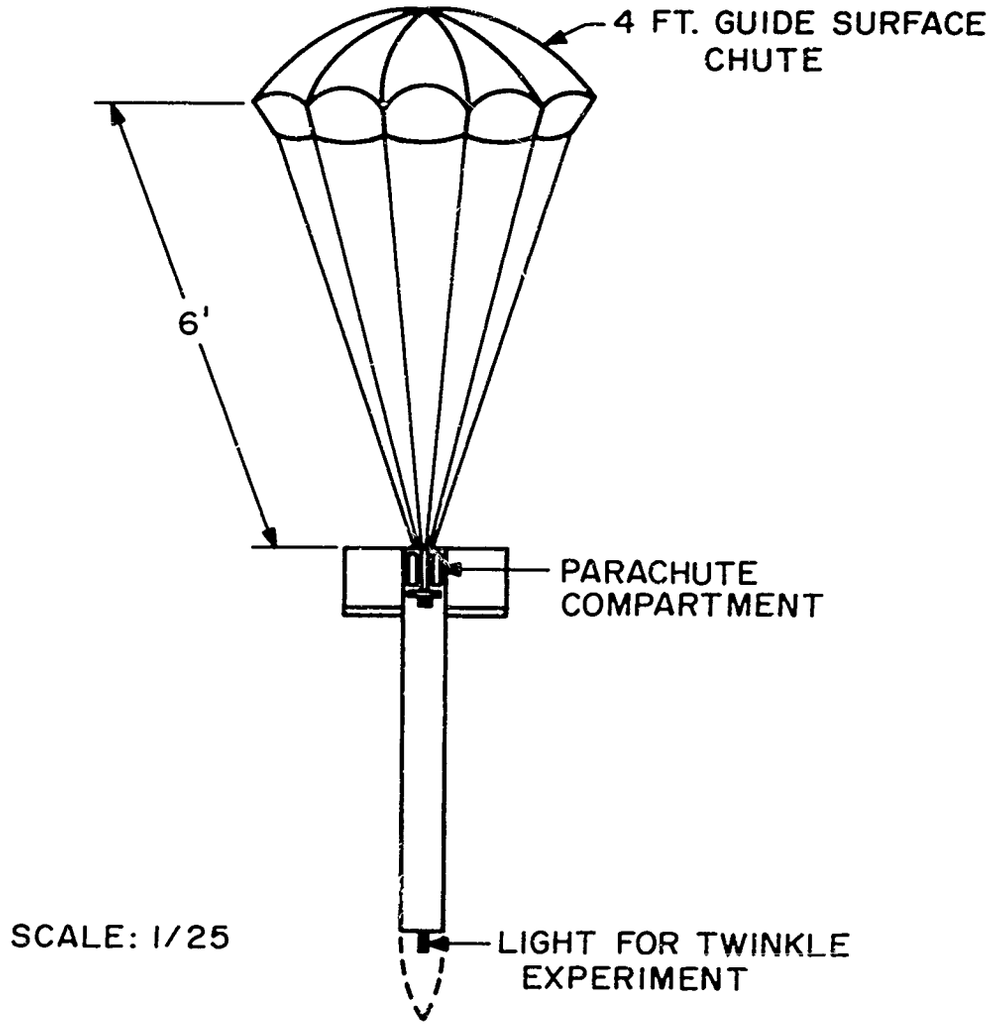

FIG. 4 - APACHE-DART PARACHUTE SYSTEM

designed so that it could be ballasted to adjust the performance of the system. For all the flights, the interstage adapter weighed 110 pounds, approximately 90 pounds of which was ballast. Without this ballast, the apogee altitude attainable with this system would have been about 100,000 feet higher than the desired maximum of 150,000 feet.

The payload consisted of batteries, parachute, 650-watt lamp in the nose, small rear lamp for tracking during the ascent portion of the trajectory, telemetry system, strain gage pressure transducer, thermistors, microphones for measurement of very small pressure changes, and high-frequency-response gages for measurement of small temperature changes.

Figure 5 is a sketch of the Tomahawk–Dart system, and Figure 6 shows the system on a launcher. This rail launcher provided 10-1/2 feet of guidance for the system. The complete rocket system weighed 934 pounds at the time of launch.

The booster fins were the same as those used on Sandia's Nike-Tomahawk-9-inch, Darthawk (a Tomahawk with a 6-1/2-inch-diameter Dart payload), and single-stage Tomahawk rocket systems. The booster fin incidence angle was adjustable to provide any angle up to ±30 minutes. The Dart fins were set at a zero incidence angle and the booster fins at an incidence angle of 14 mirutes per fin, providing a roll rate at motor burnout of 1.7 revolutions per second. As soon as the Dart separated, its roll rate quickly decreased to less than 0.2 revolution per second. The low roll rate of the Dart was selected in order to avoid problems which might be encountered if the parachute were deployed at a time of rapid rolling.

This system was also launched at Tonopah Test Range, at the same target as in the Apache-Dart series. Figure 7 shows the altitude, range, and velocity as a function of time from launch. The nominal no-wind launch elevation angle was 86 degrees. The launcher was adjusted to compensate for wind effects on the rocket during ascent and on the parachute during descent.

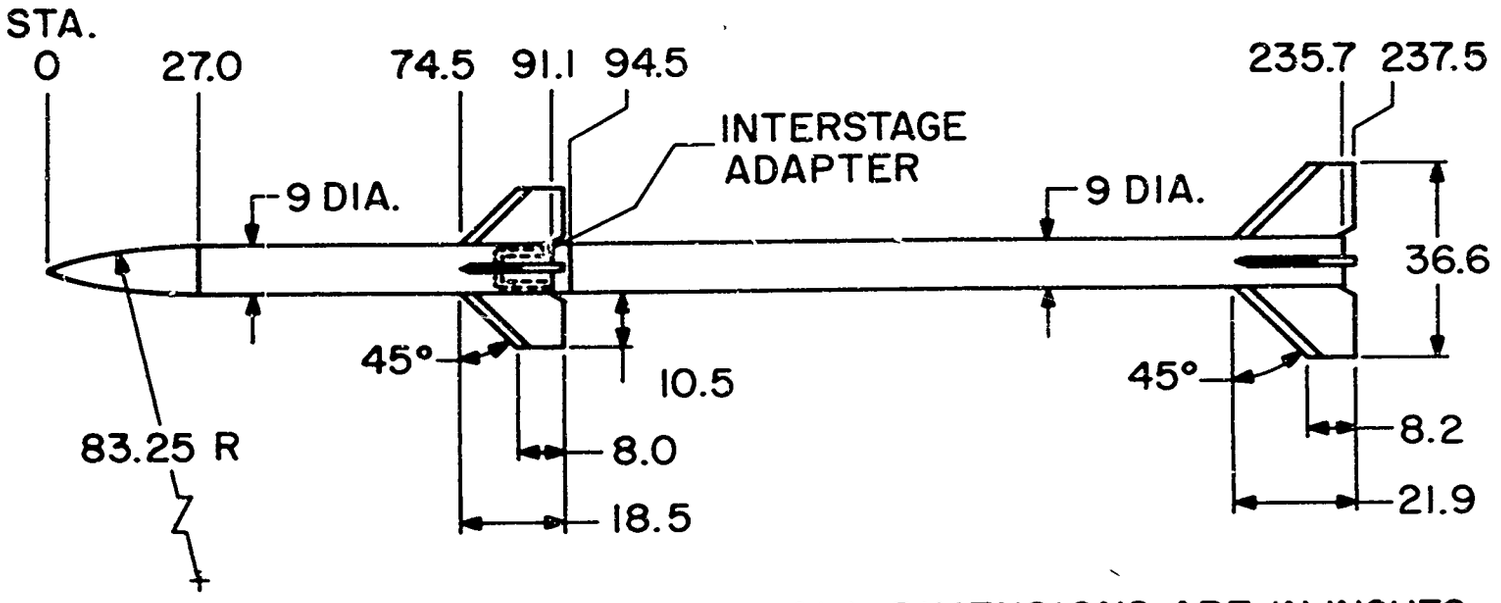

442

FIG. 5 - TOMAHAWK - 9-INCH DART

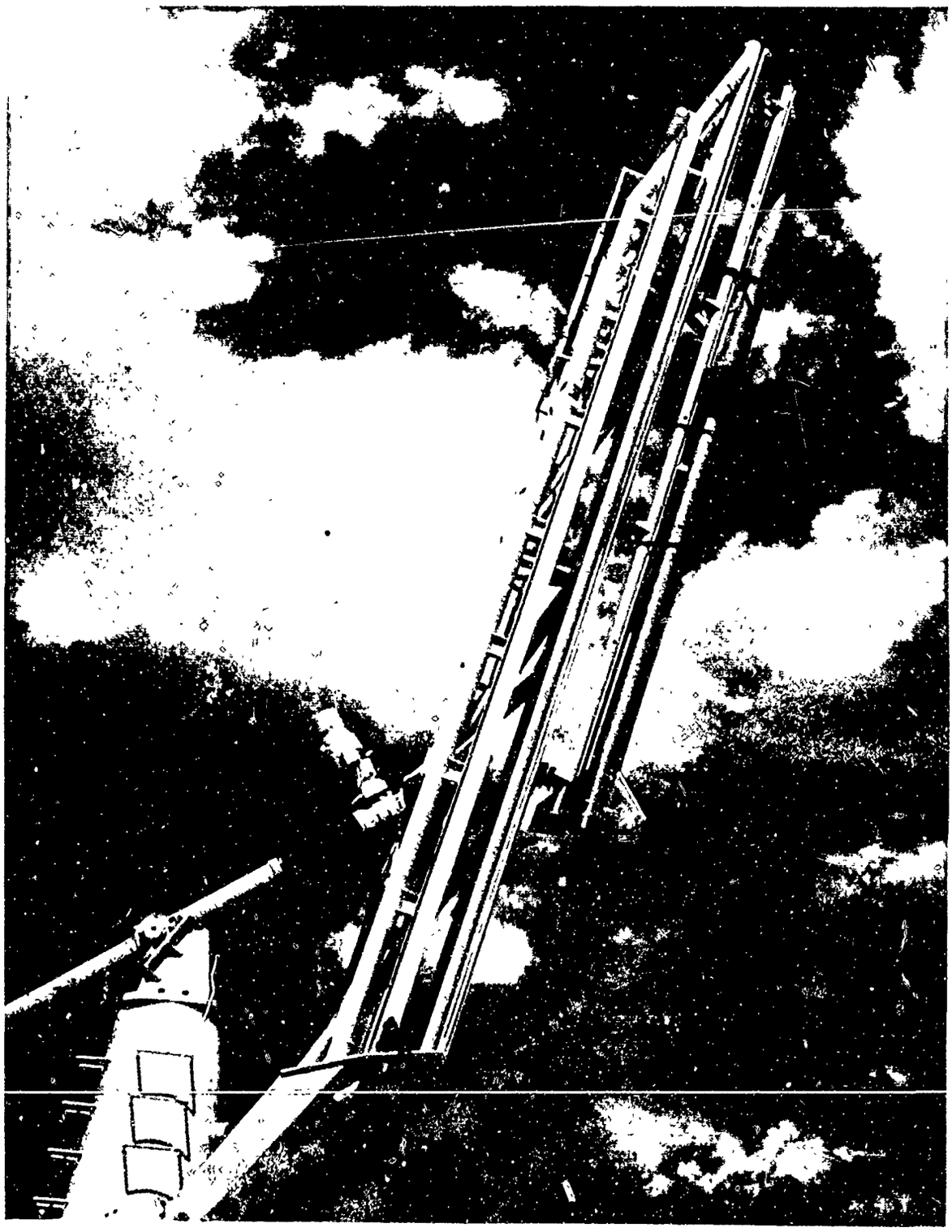

FIG. 6-TOMAHAWK-9-INCH DART ON LAUNCHER

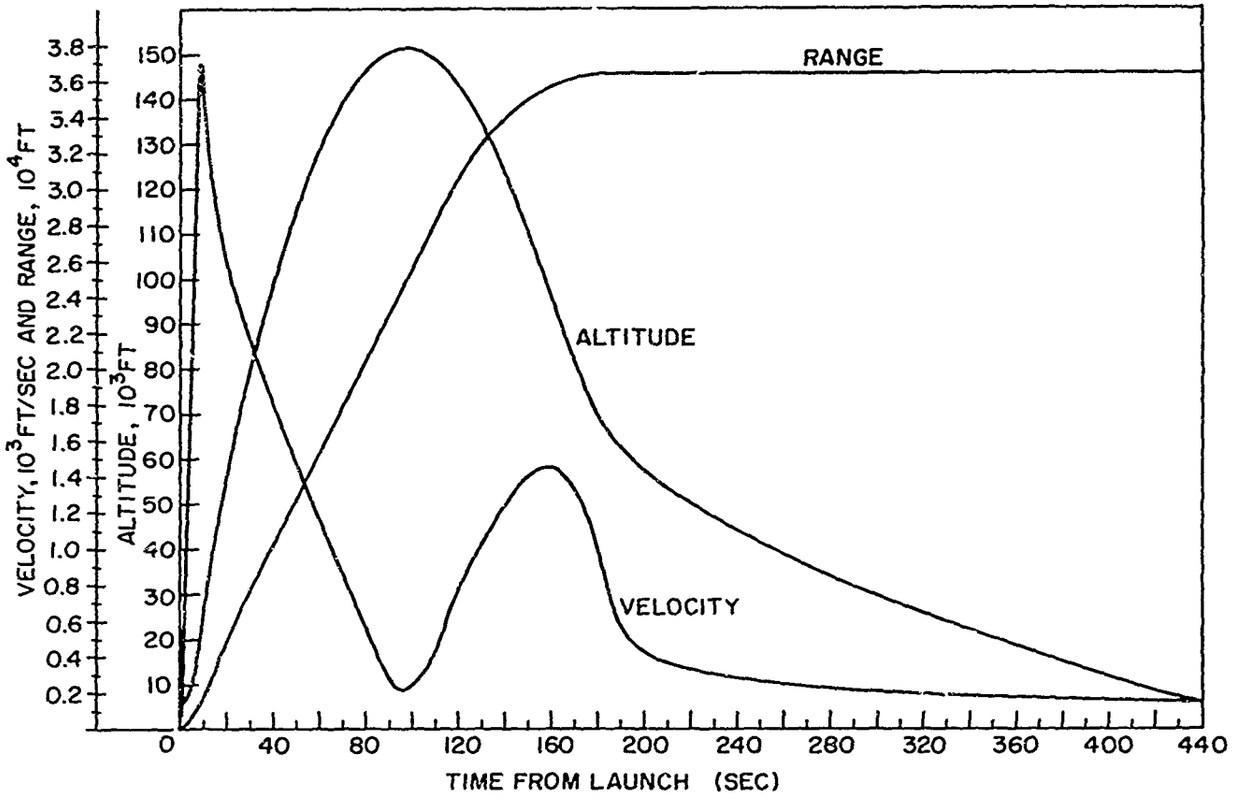

FIG. 7 - CHARACTERISTICS OF THE TOMAHAWK - 9-INCH DART TRAJECTORY, AS A FUNCTION OF TIME FROM LAUNCH

The nose cone was ejected from the vehicle at the time of apogee. At an altitude of 143,000 feet, and 120 seconds after launch, the high-intensity lamp was turned on, and the 6-foot guide-surface parachute was deployed. As can be seen in Figure 7, the parachute was effective even at altitudes as high as 140,000 feet. The system reached a maximum velocity during descent of 1450 feet per second, at an altitude of 99,000 feet.

Figure 8 is a sketch of the vehicle descending with the parachute deployed. A unique feature of this parachute was a polyethylene torus, installed in a nylon sleeve, which was sewed to the skirt of the guide-surface chute before packing. Sealed in the torus were a few drops of water at atmospheric pressure. At the time of parachute deployment, the torus inflated immediately, as the water within the torus vaporized until the pressure of the vapor within the compartment equaled the corresponding vapor pressure of water at the temperature of the water in the compartment.

There were four flights of the Tomahawk 9-inch Dart. The first two were for development of the vehicle, the parachute, and the instrumentation systems. The last two were for the purpose of obtaining experimental data. All flights were completely successful, and good scientific data were obtained on the last two flights.

Wind Compensation

Compensating for wind effects was accomplished in the same manner for both the Apache-Dart and the Tomahawk-Dart and was done in two steps. The first step involved compensating for drift of the parachute; it was assumed that the vehicle, with parachute deployed, would drift at the same velocity as the local wind velocity as the vehicle fell through the atmosphere in the region from 70,000 feet to the ground. In the case of the Tomahawk-Dart vehicle, it was assumed that the wind had no effect on the parachute at altitudes above 70,000 feet. This introduces some small

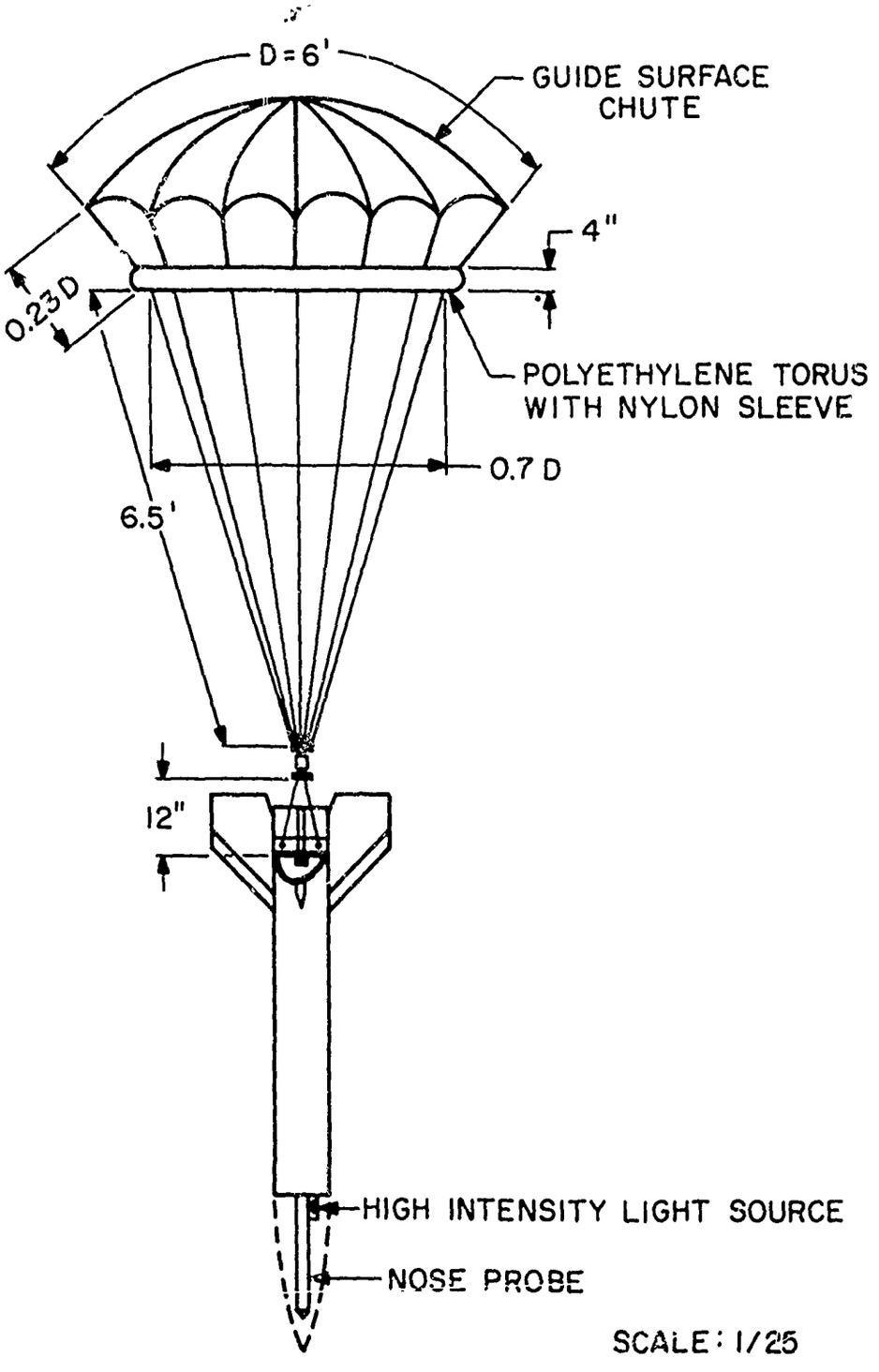

FIG. 8 - TOMAHAWK - DART PARACHUTE SYSTEM

errors, but was accepted because it is difficult to get good data on winds above 70,000 feet by the standard methods of radar tracking of balloons at the test range. The atmosphere was assumed to be divided into altitude layers of 5000 feet. A parachute drift factor, D_i, equal to the amount of time the vehicle spent in the ith altitude zone, was computed for each altitude layer.. By taking the sum of the east-west components of wind, times their respective drift factors, $\sum_{o}^{n} V_{W_i} D_i$, and by summing the north-south wind components times their respective drift factors, the location at which the descending vehicle should be when it is at 70,000 feet, in order to impact at the tracking telescope (Station 14), was calculated. By using the results from a series of previously computed theoretical trajectories, the nominal launcher elevation angle, azimuth angle, and the vehicle impact point in case of parachute failure were calculated.

The second step of the wind compensation procedure involved calculating the effects of wind on the rocket as it ascends through the atmosphere. The theory involved in the method is described in Reference 3. Based on the wind profile obtained by means of radar tracking of balloons, a weighted-average wind (ballistic wind) is calculated. Two wind sensitivity factors, $\partial R/\partial V_{BW}$ and $\partial D/\partial V_{BW}$, which are the unit ballistic wind effect on impact range and impact deflection, respectively, are then utilized linearly to determine the final launcher setting. This portion of the wind compensation procedure had been previously programmed for a CDC-160A computer. For Project Twinkle, the first step of the procedure was done by hand calculations, requiring approximately five minutes for computations. The results were then fed into the computer, which gave the final launcher setting.

Concluding Remarks

The results of the first phase of the twinkling experiments are discussed by Hudson[1] who concludes, based on data from the Apache-Dart launches, that a "twinkling layer" in the atmosphere exists. Approximately 80 percent of the starlight scintillation occurs in this layer, with about 10 percent caused by the atmosphere above and 10 percent caused by the atmosphere below, the layer. The height of the layer corresponds roughly to the tropopause. Data from the second series of experiments have not as yet been completely reduced. However, a first look at the data also indicates that the twinkling layer is located at the tropopause, and that associated with this layer are measurable temperature fluctuations of the order of a few hundredths of a degree centigrade.

REFERENCES

1. Hudson, C. C., "Experimental Evidence of a Twinkling Layer in the Earth's Atmosphere," Nature, Vol. 207, No. 4994, pp 247-249, July 17, 1965.

2. Pepper, W. B. and Gardner, R. E., Rocket and Parachute Systems Design and Performance for Project Twinkle, (to be published).

3. Rocket and Recovery Systems Division 9324, Aeroballistic Design and Flight Results of the Sandia Nike-Apache Rocket Systems, Sandia Corporation, SC-4773(RR), April 1966.

Computer Applications to Wind Weighting and Their Limitations

by

Philip A. Sollow, Technical Specialist
Aerothermodynamics Department
Space-General Plant, Aerojet-General Corporation

ABSTRACT

The currently employed wind weighting methods are reviewed and the inaccuracies inherent in this system are discussed. Examples are presented of a number of different wind weighting curves derived for the same vehicle without violating the accepted concepts of deriving these curves. It is shown that these same inaccuracies exist in the use of ballistic factors. A method of using the contemporary technique with improved accuracy is discussed and approaches which show promise of major improvement in the accuracy of wind weighting are presented.

A measured wind profile includes both steady winds and turbulent winds. Wind weighting is properly done for the steady winds, but not for the turbulent winds which change rapidly with time. It is shown that the measured wind profile may be reduced to the steady wind profile through appropriate filtering. A method of determining the dispersion due to turbulent wind from the power spectrum of this wind is discussed, and a sample determination is presented. It is shown that, if the measured wind profile is not filtered, it is advantageous to make launcher setting corrections which are smaller than those called for by wind weighting.

SYMBOLS AND NOMENCLATURE

A	Deflection of impact point due to sinusoidal wind associated with a_λ	(feet)
a_λ	Amplitude of sinusoidal wind of wavelength λ	(feet/second)
B	Deflection of impact point due to launcher adjustment	(feet)
b_λ	Amplitude of cosinusoidal wind of wavelength λ	(feet/second)
C_A	Aerodynamics axial force coefficient	
C_{m_q}	Aerodynamic damping coefficient	(1/radians)
C_{m_α}	Aerodynamic static pitching moment coefficient slope	(1/radians)
C_{N_α}	Aerodynamic normal force coefficient slope	(1/radians)
d	Aerodynamic reference length	(feet)
dw/dh	Wind shear	[(feet/second)per unit altitude]
H	Altitude for negligible wind effect on impact point	(feet)
h	Altitude	(feet)
K	Proportionality constant (B/A)	
$K(a_\lambda)$	Value of K appropriate to wind velocity amplitude associated with a_λ to effect minimum dispersion	
$K(b_\lambda)$	Value of K appropriate to wind velocity amplitude associated with b_λ to effect minimum dispersion	
$K'(\lambda)$	Ratio of steady wind speed amplitude to total wind speed amplitude for the wind of wavelength λ	
M	Aerodynamic pitching moment	(lb-ft)
m	Mass	(slugs)

N	Aerodynamic normal force	(pounds)
Q	Dynamic pressure	(pounds/ft^2)
q	Pitch rate	(radians/second)
$\vec{\Delta R}$	Vector change in impact point	(feet)
$R^2(W,O)$	Square of the dispersion of the impact point per unit wind velocity squared at wave number W	[meters per (meter/second)^2]
S	Aerodynamic reference area	(feet^2)
SWF	Shear weighting factor	
T	Thrust	(pounds)
ΔT	Time interval	(seconds)
V	Velocity	(feet/second)
V_B	Ballistic wind velocity	(feet/second)
V_λ	Amplitude of wind of wavelength λ	(feet/second)
W	Wave number	(cycles/400 0 meters)
WWF	Wind weighting factor	
X	Aerodynamic axial force	(pounds)
α	Angle of attack	(radians)
γ	Elevation of velocity vector	(radians)
δ	Dispersion distance	(feet)
θ	Elevation of longitudinal body axis	(radians)
λ	Wind Wavelength	(feet/cycle)

ρ	Ambient air density	(slugs/ft^3)
σ	Standard deviation	(various units)
σ_{a_λ}	Standard deviation of impact point due to wind associated with a_λ	(feet)
σ_y	Standard deviation of impact point assuming isotropic impact point response to winds	(meters)

I. INTRODUCTION

The rather general term "wind weighting" encompasses all the knowledge and skills necessary to fire an unguided vehicle to a selected point in the presence of arbitrary winds. The point which is selected may be at impact, apogee, or some other point which is considered significant. In any case, the requisite wind weighting techniques will be much the same. The necessity for wind weighting derives from several sources: A primary one in the field of sounding rockets is range safety. For most combinations of vehicle and launch site, realizable wind profiles can alter the flight path of the vehicle sufficiently to carry it far beyond the confines of the allowable impact area if no wind corrections are performed. A second condition, which sometimes arises when scientific payloads are flown, is a requirement that the vehicle pass through some given position during the flight. The necessity for wind weighting for unguided artillery rockets is obvious.

Computer Applications to Wind
Weighting and Their Limitations

It is an unhappy fact of life that no present technique of wind weighting is wholly without fault, and there is good reason to believe that none will be. There are, however, specific flaws in the present methods which may be identified and thus there is a concrete basis for expecting that an improvement in the techniques may be made.

II. DISCUSSION

There are several general steps in the wind weighting procedure, in each of which errors will arise. The sequence which is employed in the field is to first measure the winds, then interpret the acquired data, and finally to calculate the launcher alignment necessary to reach the desired point in the presence of the measured winds. This final step invariably involves the use, either directly or indirectly, of trajectories calculated through the use of a digital computer.

The first step, the measurement of the winds, is accomplished by a number of techniques which all have a common basis, i.e., the observation of the displacement of some object due to the action of the wind. All of the present methods are prone to inaccuracies in the measurement of the displacement magnitude and have a response threshold, i.e., winds below some level of magnitude or duration are not observed. Also, they all measure winds which are displaced timewise, and usually

positionwise, from the actual flight. Although the wind profile may be measured during the flight, this data is obviously of no benefit in determining launcher alignment. Thus, the best situation which might be hoped for is to make optimum use of the wind measurements made prior to launch. The presence of a response threshold, for the wind measuring devices, which causes them to fail to record winds of small magnitude is a cause of some inaccuracy; however, the failure of the equipment to measure winds of short duration will be shown not to affect the wind weighting accuracy appreciably.

It is common practice in aircraft load analyses to separate the total wind profile into two components, termed steady or quasi-steady wind, and turbulent wind. There does not appear to be any strict definition of the appropriate interface between these, but there are some general conventions regarding the difference. Considering the total wind profile to be represented by a Fourier Series which is periodic in altitude, the short wavelength winds are considered turbulent and the long wavelengths steady. Additionally, the steady winds are considered to be predictable to a reasonable degree of accuracy for several hours on the basis of prior measurements while the turbulent winds are not considered reasonably predictable even for a period of several seconds. It may be seen that these conventionalizations do not allow for a middle ground where winds are neither

wholly steady nor wholly turbulent. If the conventionalized situation did indeed exist, it would be simple to make a single measurement of the wind profile prior to launch, perform a Fourier analysis of the profile, throw out all of the frequencies defined as turbulence and perform the rest of the wind weighting procedure with the remaining winds which would be "steady" and therefore extrapolable in time. Unfortunately, this happy situation does not exist, and it is necessary to define a filter which is wavelength dependent to separate the steady from the turbulent winds. It is not immediately apparent that the use of such a filter would be beneficial in wind weighting. However, consideration of several alternatives makes its desirability more clear. In the first we assume that the wind may be separated into "classical" steady and turbulent components. Assume for the moment that the deflection of the impact point due to some wind profile is isotropic and varies linearly with the effective amplitude of the profile (say the equivalent Ballistic Wind, which will be discussed later). Then, due to the turbulent wind profile at the time of flight, there will be a deflection of the impact point $\Delta\vec{R}_2$. Let us now assume that the total wind profile is measured just prior to flight and an adjustment made to the launcher setting based on this profile. This adjustment includes an allowance for the deflection of the impact point due to the turbulent wind profile at the time of the wind measurement. Denote

this deflection $\Delta\vec{R}_1$. Now, at the time of flight, the turbulent wind profile has changed, so that there is a deflection of the impact point of $\Delta\vec{R}_2$ due to the turbulent wind at the time of flight plus a deflection of the impact point of $-\Delta\vec{R}_1$ due to the absence of the turbulent wind for which allowance was made when adjusting the tower. Since the two wholly turbulent wind profiles are, by definition, statistically independent, the magnitude of the expected dispersion, at the 1σ probability level, is seen to be $(\Delta R_1^2 + \Delta R_2^2)^{\frac{1}{2}}$ which is obviously greater (41.4% greater on the average) than the dispersion (ΔR_2) which would have resulted if the measured turbulent winds were completely disregarded. We may consider another approach to the wind weighting procedure. In this approach, a number of soundings are made sequentially, prior to launch, and the mean of the measured wind profiles is determined. This has the effect of filtering out the non-steady (turbulent) portion of the wind profile and would at first seem a reasonable solution. However, if a number of soundings, N, are performed at intervals ΔT, with the last one being made at launch time (as a limiting case), the mean wind which was determined would be the most likely wind at a time $(N-1)\Delta T/2$ before launch. For a reasonable number of soundings (to provide a reliable estimate of the mean), and with the slow rising balloons which are usually employed for wind soundings, the time for which the mean wind was pertinent could be quite a while prior to the actual time of launch.

Thus it may be seen that a loss of currency is inherent in the use of the mean profile, although the desired filtering is effected, i.e., the variable portion of the wind profile is discounted. It should be noted that as the number of soundings increases, the time $(N-1)\Delta T/2$ also increases and the procedure would tend to show increasingly more of the wind profile to be turbulent, since the variability of even the longest wavelength (most nearly steady) winds would increase with the length of time over which the soundings were performed. What is obviously desired is a filter which may be applied to the most current wind profile to predict the launcher alignment which would cause minimum dispersion. It appears that such a filter may be determined from a number of soundings made at equally spaced time intervals.

Let us assume that a number of wind soundings, N+1, are made of the atmosphere at time intervals ΔT. We will next assume that the wind profile is represented by a Fourier Series in each of two orthogonal directions. Then, along a given azimuth, the horizontal wind of wavelength λ is represented by:

$$V_\lambda = a_\lambda \sin (2\pi h/\lambda) + b_\lambda \cos (2\pi h/\lambda) \qquad (1)$$

Let us take one of the coefficients, say a_λ, and consider the effect of its time variation on dispersion. Assume that, for a given

magnitude of a_λ, there would be a displacement of the impact point of A if a rocket were flown at the time of the sounding. We will further assume, for convenience of analysis that A varies linearly with a_λ. (This is not quite the case, although this type of assumption is quite often made in wind weighting analyses).

If a rocket were flown at the time of the $n+1^{th}$ sounding, the wind component represented by a_λ would cause a displacement of the impact point of A_{n+1}. If the launcher had been adjusted to give a deflection of the impact point of B_{n+1} in an attempt to compensate for the effect of a_λ, the dispersion of the impact point from its desired position would be

$$\delta_{n+1} = A_{n+1} - B_{n+1} \tag{2}$$

Let us assume that the correction B_{n+1} was made to be proportional to the nth value of A, that is:

$$B_{n+1} = K A_n \tag{3}$$

Then the dispersion is obviously,

$$\delta_{n+1} = A_{n+1} - K A_n \tag{4}$$

If at the time of each of the N+1 soundings, except for the first, a rocket was fired from a launcher which had been adjusted according to Eq. (3), the variance of the impact point, i.e., the square of the 1σ dispersion, would be:

$$\sigma^2_{a_\lambda} = \frac{\sum_{n=1}^{N} (A_{n+1} - K A_n)^2}{(N-1)} \tag{5}$$

Differentiating Eq. (5) with respect to K yields:

$$\frac{d\sigma^2_{a_\lambda}}{d K} = \frac{\sum_{n=1}^{N} [2K A_n^2 - 2 (A_{n+1} A_n)]}{(N-1)} \tag{6}$$

The dispersion due to a_λ is minimized by setting $\frac{d\sigma^2_{a_\lambda}}{d K}$ equal to zero and solving for K:

$$K = \frac{\sum_{n=1}^{N} (A_{n+1} A_n)}{\sum_{n=1}^{N} A_n^2} \tag{7}$$

This procedure may be repeated for each wind wavelength, for both a_λ and b_λ, and in the two orthogonal directions into which the wind profiles were resolved. It may be seen that this produces a filter in which $K(a_\lambda)$, $K(b_\lambda)$ represent the proportionate part of the total magnitude of each a_λ, b_λ which is to be considered steady and therefore to be compensated for in the launcher setting.

To achieve a reasonably accurate representation of the measured wind profiles with a Fourier Series, it is necessary that such singularities as embedded jets be removed, prior to fitting the series, and

handled separately. At least for the jet stream, considerable empirical data is available to define its variability. For other singularities, additional study will be necessary.

It should be noted that the development above assumed a fixed interval ΔT between the soundings. It is implicit in this that if the filter were applied to a wind profile measured $\Delta T'$ before a launch, it would be strictly applicable only if $\Delta T = \Delta T'$. However, the filter could be evaluated for several values of ΔT, and filters for arbitrary $\Delta T'$ determined empirically. Since the rate of ascent of a typical sounding rocket is considerably higher than that of a meteorological balloon, a vehicle launched at some given ΔT after a sounding was made would pass through successively higher altitudes increasingly earlier than would a balloon released at the time of launch. Thus, for any given a_λ, or b_λ, the appropriate value of K would tend to increase with altitude. At any altitude, h, the appropriate K would be the one for

$$\Delta T = \Delta T_{launch} - (T_h - T'_h) \tag{8}$$

where ΔT_{launch} is the time interval from the release of the balloon on which the tower settings are based to the time of vehicle launch, T_h is the time required for the balloon to reach altitude h, and T'_h is the time required for the vehicle to reach h. It is, of course, rather likely that the filter varies slowly with ΔT, in which case it might be

possible to define a filter which was accurate over a reasonable range of ΔT, hence the application of Eq. (8) might not be necessary.

It is not apparent from any of the above that the filter is stationary in time, i.e., that it could for instance be evaluated on one day and used several days later. However, it is to be expected that the filter would be variant only with differing synoptic scale conditions (such as lapse rate) and that the filter could be evaluated as a function of these conditions so that it would then become quasi-stationary. At this time, this correlation remains undefined.

Reference (1) presents the power spectra for both the total wind and what is designated as the turbulent wind for 13 soundings made above Cape Kennedy for an altitude range of 1 to 10 km. A filter for separating the turbulent wind from the total wind is presented in that reference. However, no time factor (ΔT) is stated and it is indicated that the selection of the filter was somewhat arbitrary. At any rate, this filter is reproduced here as Figure 1, since it serves to exhibit the general shape expected if the analysis presented above were to be made. It should be noted that this filter was computed to filter speed profiles rather than velocity profiles so that the factor $K'(\lambda)$ shown as the ordinate is not exactly equivalent to the $K(a_\lambda)$, $K(b_\lambda)$ discussed above. Figures 2 and 3 show, respectively, the mean total wind power spectrum and mean turbulent wind power spectrum derived from the 13 soundings for which data were presented in Reference (1).

FIGURE 1

$K'(\lambda)$, RATIO OF STEADY TO TOTAL WIND SPEED VERSUS WIND WAVELENGTH, λ

AFTER SCOGGINS (REF. 1)

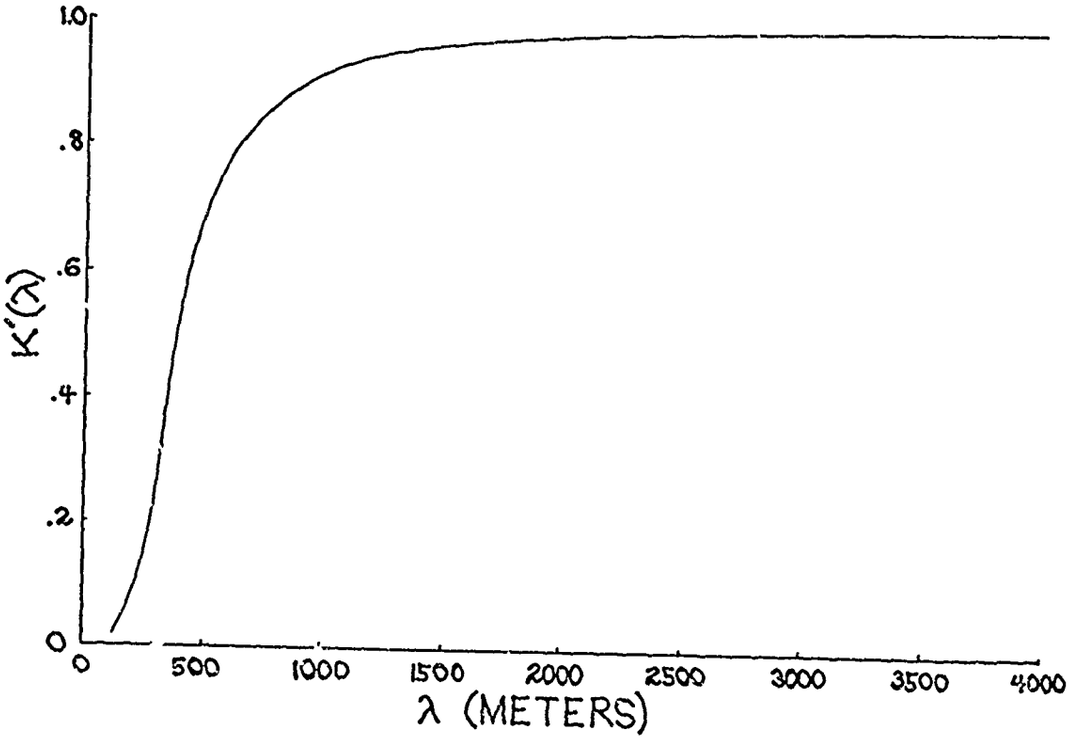

FIGURE 2
TOTAL WIND POWER SPECTRUM

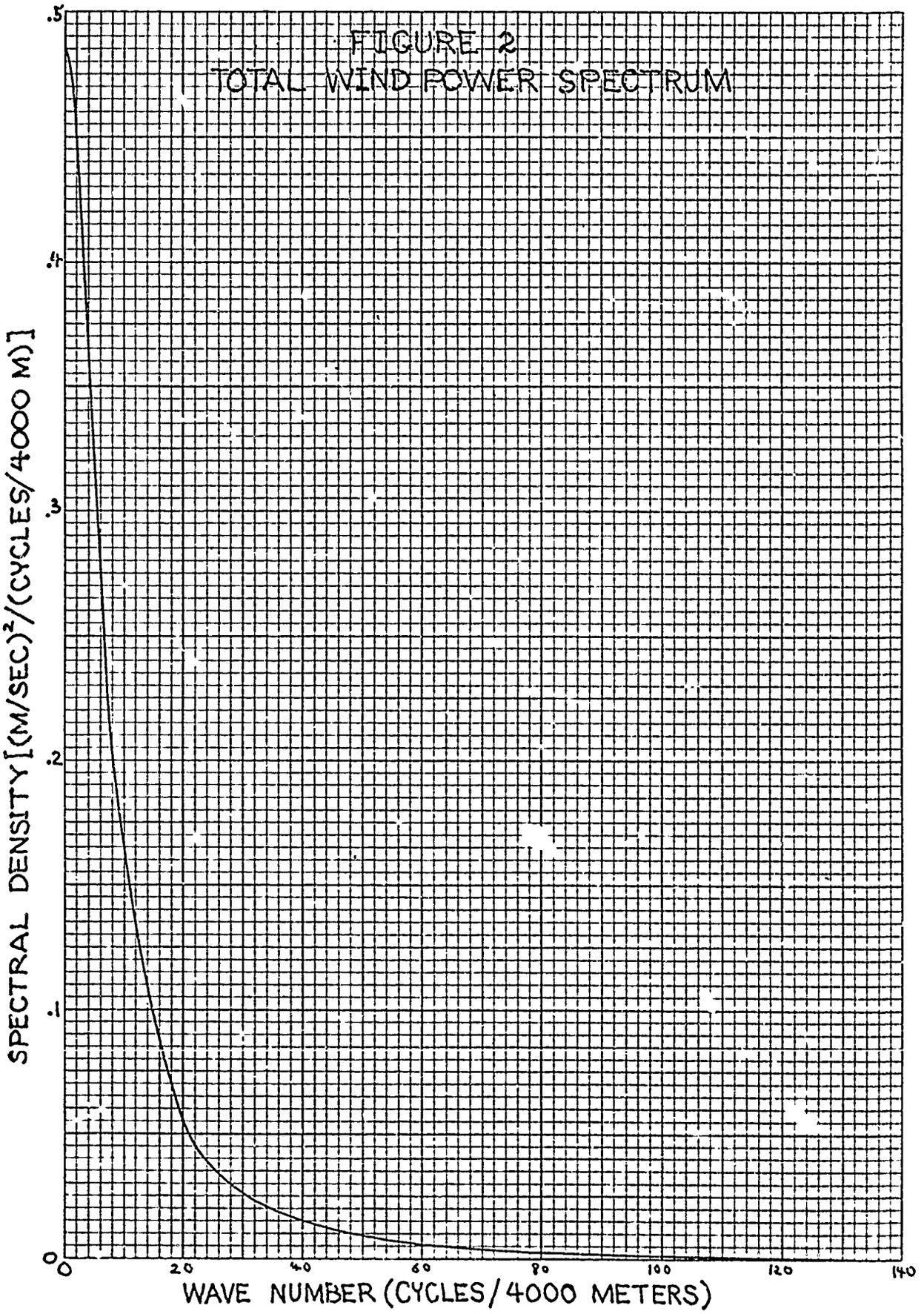

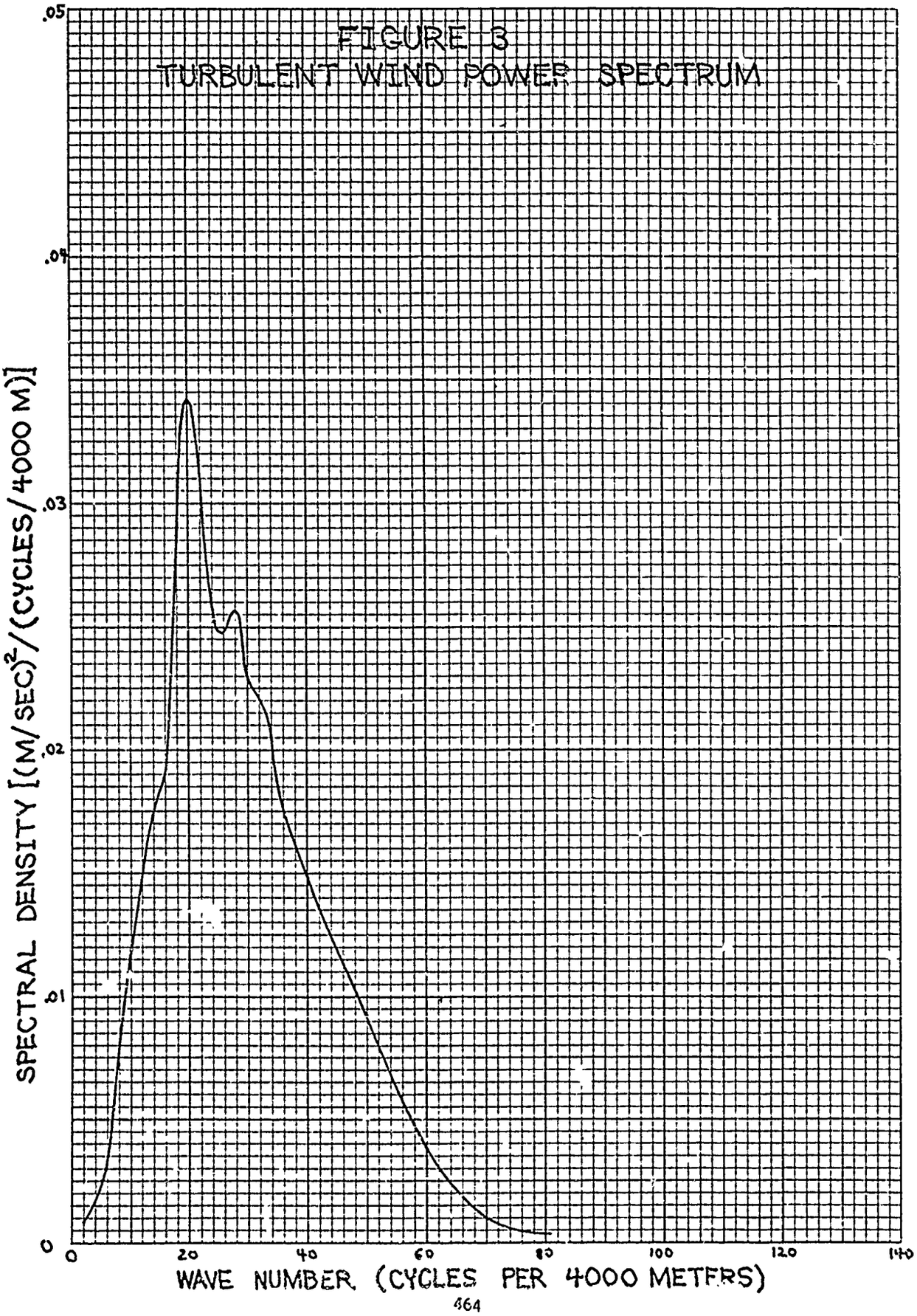
FIGURE 3
TURBULENT WIND POWER SPECTRUM
SPECTRAL DENSITY [(M/SEC)²/(CYCLES/4000 M)]
.05
.04
.03
.02
.01
0
0
20
40
60
80
100
120
140
WAVE NUMBER (CYCLES PER 4000 METERS)

Computer Applications to Wind
Weighting and Their Limitations

In the course of determining the dispersion of a small artillery rocket, the author had the opportunity of evaluating the relative magnitudes of the dispersion due to the steady wind spectrum (assuming no wind weighting) and the turbulent spectrum. Although this type of vehicle will present wind response characteristics which are quite different from those exhibited by sounding rockets, these data are of interest since they give some indication of the importance of the wind filter described above. The spectra shown in Figures 2 and 3 were chosen for this analysis. The results are approximate since it was necessary to make several concessions to expediency. It was assumed that the total wind spectrum was horizontally isotropic and that the turbulent spectrum was three dimensionally isotropic. It was also assumed that the dispersion due to wind of any one frequency was linearly proportional to the amplitude of the wind at that frequency and that the vector dispersions due to different wind frequencies were statistically independent. The following analysis serves to relate the dispersion due to wind to the power spectrum of the wind:

For an input-output relationship which may be characterized as linear, the relationship could be represented by an integral, i.e., we could write

$$y(h) = \int_0^h f(h,\eta)x(\eta)d\eta \qquad (9)$$

where y(h) is the output, x(h) is the input, and $f(h,\eta)$ is an appropriate weighting function for the operation. The variance of y(h) (taken as an ensemble average at fixed h) may then be found as

$$\sigma_y^2(h) = \int_0^h f(h,\eta_1)d\eta_1 \int_0^h f(h,\eta_2)\ \gamma_{xx}(\eta_1,\eta_2)d\eta_n \qquad (10)$$

where $\gamma_{xx}(\eta_1,\eta_2)$ is the auto-covariance function of x. Assuming x(h) to be stationary with respect to h, $\gamma_{xx}(\eta_1,\eta_2)$ is related to the power spectrum of x, $G_{xx}(\frac{2\pi}{\lambda})$, by

$$\gamma_{xx}(\eta_1,\eta_2) = \int_0^\infty G_{xx}(\tfrac{2\pi}{\lambda})\cos\ [2\pi \tfrac{\eta_2-\eta_1}{\lambda}]\ d(\tfrac{2\pi}{\lambda}) \qquad (11)$$

so we have

$$\sigma_y^2(h) = \int_0^\infty G_{xx}(\tfrac{2\pi}{\lambda})\ d(\tfrac{2\pi}{\lambda}) \int_0^h f(h,\eta_1)d\eta_1 \int_0^h f(h,\eta_2)\ \cos\ [2\pi \tfrac{\eta_2-\eta_1}{\lambda}]d\eta_2 \qquad (12)$$

$$= \int_0^\infty G_{xx}(\tfrac{2\pi}{\lambda})\ d(\tfrac{2\pi}{\lambda}) \int_0^h f(h,\eta_1)d\eta_1 \int_0^h f(h,\eta_2)\ [\cos(2\pi \tfrac{\eta_2}{\lambda})\ \cos(2\pi \tfrac{\eta_1}{\lambda}) + \sin(2\pi \tfrac{\eta_2}{\lambda})\ \sin(2\pi \tfrac{\eta_1}{\lambda})]\ d\eta_2 \qquad (13)$$

$$\sigma_y^2(h) = \int_0^\infty G_{xx}(\tfrac{2\pi}{\lambda})[\Theta_1^2(\lambda,h) + \Theta_2^2(\lambda,h)]\ d(\tfrac{2\pi}{\lambda}) \qquad (14)$$

where $\Theta_1(\lambda,h)$ and $\Theta_2(\lambda,h)$ are, respectively, the responses (at h) to cosine and sine wave inputs, (i.e.x's) both with wavelength λ.

The variable of integration in the above development is frequency. However, the power spectrum and the dispersion response function may also be written in terms of wave number, with the variable of integration then becoming wave number. The variance $\sigma_y^2(h)$ is evaluated at impact, i.e., h = 0, when the responses to the wave inputs are defined for this position. The 1σ dispersion is simply $\sigma_y(0)$, the square root of the variance. The form in which Eq. (14) was employed is:

$$\sigma_y^2(0) = \int_0^\infty G'_{xx}(W)\,[R^2(W,0)]\,dW \qquad (15)$$

where $G'_{xx}(W)$ is the power spectrum in terms of wave number, W, as given in Figures 2 and 3, and $R^2(W,0)$ is the sum of the squares of the dispersion responses (at h=0) to the cosine and sine wave inputs. A number of six-degree-of-freedom trajectories were computed with sinusoidal (zero wind velocity at ground level) and cosinusoidal (maximum wind velocity at ground level) in-range unit horizontal winds at different frequencies. Differencing the impact range in each of these trajectories from the zero wind range yielded the dispersion per unit magnitude wind for each wave considered. From these data, $R^2(W,0)$ was computed for each wavelength considered, and a curve fitted through the points to yield $R^2(W,0)$ as a function of W. Figure 4 shows a normalized curve of this function, i.e., $R^2(W,0)/R^2(0,0)$ is plotted

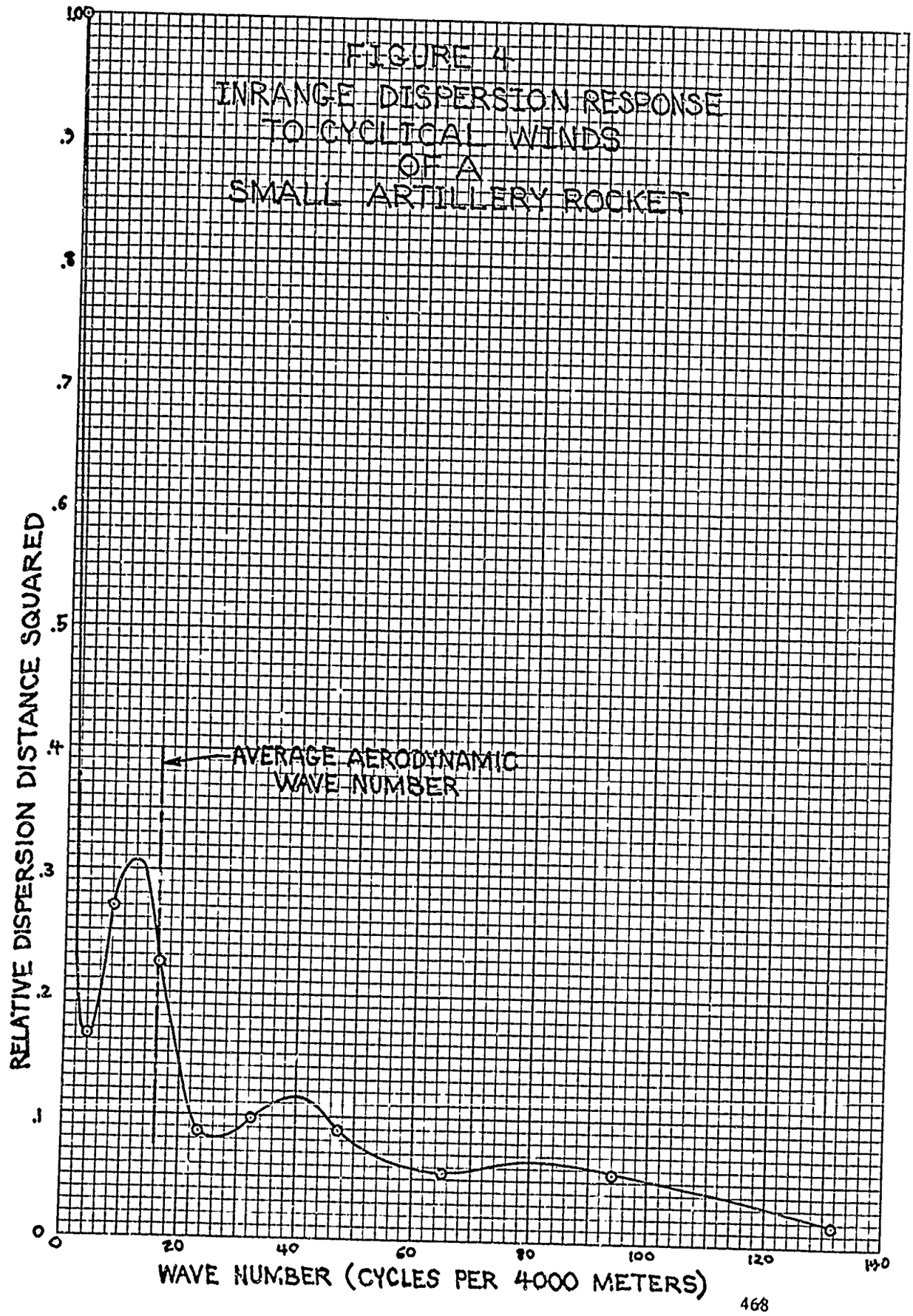
FIGURE 4
INRANGE DISPERSION RESPONSE
TO CYCLICAL WINDS
OF A
SMALL ARTILLERY ROCKET
RELATIVE DISPERSION DISTANCE SQUARED
AVERAGE AERODYNAMIC
WAVE NUMBER
WAVE NUMBER (CYCLES PER 4000 METERS)
0
.1
.2
.3
.4
.5
.6
.7
.8
.9
1.00
0
20
40
60
80
100
120
140

versus W. Also shown are the values of this function which represent the computed trajectories, and the wave number equivalent to the aerodynamic wavelength of the vehicle during burning. Since an artillery rocket was being investigated, the trajectories were computed for a low quadrant elevation of 32°, rather than at a superelevation characteristic of sounding rockets. Since the flight path was so far from vertical, it was decided to consider the turbulent wind spectrum as representing wind normal to the flight path rather than parallel to the ground. Simple arithmetic manipulation made the data of Figure 4 applicable to this condition. To evaluate the dispersion magnitude, Eq. (15) was integrated numerically for both the total wind spectrum, Fig. 2, and the turbulent spectrum, Fig. 3 to evaluate, respectively, $\sigma_{y\,(total)}^{2}(0)$ and $\sigma_{y\,(turbulent)}^{2}(0)$. Since the dispersion components due to different frequencies of wind were considered statistically independent, it was possible to evaluate the variance of the impact point due to steady wind as:

$$\sigma_{y\,(steady)}^{2}(0) = \sigma_{y\,(total)}^{2}(0) - \sigma_{y\,(turbulent)}^{2}(0) \quad (16)$$

(The variances which were calculated were pertinent only to inplane dispersion and additional manipulation was necessary to determine the crosswind dispersion component). The ratio of the inrange dispersion due to turbulent wind, $\sigma_{y(turbulent)}(0)$, to the inrange dispersion due

to steady wind, $\sigma_{y(steady)}(0)$ was found to be 0.433 which shows that a large proportion of the total wind profile represents turbulence, and failure to properly filter the measured wind data may lead to large increases in dispersion.

Once a selection has been made of the wind profile which will be assumed to exist at the time of flight, it is next required that the launcher alignment which will cause the vehicle to fly to or through the desired position in the presence of this wind be established. There are basically two methods of attempting to achieve this objective. One method is to compute a number of trajectories which include this wind profile, with the launcher alignment being changed between trajectories so that the correct launcher alignment is achieved by an iterative procedure. A second method involves the use of functions relating the tower alignment and the wind profile which have been generated a priori by calculating a number of trajectories which include an ordered set of winds. This second method may or may not be an iterative procedure. In general, the objections which may be lodged against the first method is that a relatively large scale computer is required and some immediacy of the wind data is lost due to the time involved in computing the trajectories. Also, the iterative procedure usually involves the application, in some form, of the second method. The objection which may be made to the second one is that there is an inherent loss of

accuracy since it is not possible to have precomputed trajectories for all possible wind profiles, and the measured wind profile must be related by approximation to some other profile for which data is available.

It was mentioned above, in discussing the artillery rocket dispersion evaluation, that a wind response function was calculated in terms of the response of the impact point to sinusoidal and cosinusoidal unit winds. It was also pointed out, in discussing the wind filter, that a wind profile could be represented by a Fourier Series. It is apparent that here is one approach to a method of relating flight path deflection to a measured wind profile without resorting to the computation of trajectories for that particular profile. Of course this approach still assumes linearities which do not necessarily exist. The much more common approach, at this time, involves the use of Wind Weighting Curves and Ballistic Factors. A Ballistic Factor is a measure of the perturbation to the flight path caused by a wind which is constant in magnitude and direction and acts throughout a flight. A wind with these properties is termed a Ballistic Wind. Usually, the Ballistic Factor is given in terms of the displacement of the impact point per unit Ballistic Wind. A Wind Weighting Curve is used to relate a specific wind profile to an equivalent Ballistic Wind. The relationship is such that

$$V_B = \int_0^H V(h) \frac{d(WWF)}{dh} dh \qquad (17)$$

where V(h) is the horizontal wind velocity at altitude h, (WWF) is the Wind Weighting Factor, H is an altitude at which winds may be considered to no longer affect the flight path of the vehicle, and V_B is the equivalent ballistic wind. The supposition is that if a wind profile is measured and separated into two orthogonal components (usually in-range and cross-range) and Eq. (17) is applied, two orthogonal Ballistic Winds will be evaluated which cause the same displacement of the impact point as does the measured profile. This displacement is usually evaluated by multiplying each of the Ballistic Winds by the appropriate Ballistic Factor. This Ballistic Factor will vary appreciably with quadrant elevation, wind velocity, and wind azimuth relative to the launcher azimuth. In field application, a nominal launcher alignment is selected on the basis of impact point location or the location of some other significant point in the trajectory. This launcher alignment is selected without regard to winds. The displacement of the trajectory due to the measured wind profile is then calculated as described above. A new launcher alignment is next calculated which corrects for this displacement. Since this new alignment would have associated with it a different set of Ballistic Factors and would require a different

resolution of the wind profile into in-range and cross-range components, it is usually necessary to iterate for the launcher alignment several times. Non-iterative methods are available, but inherent in them are the same error sources as in the more common iterative method.

It is common practice to accept a single wind weighting curve for a given vehicle, and to assume that it applies for all quadrant elevations and all Ballistic Wind magnitudes. Figure 5 shows a number of different Wind Weighting Factors, all of which, unhappily, are for the same vehicle, and all of which were calculated in what might be considered a standard manner. The most common method of determining Wind Weighting Curves (the term used to designate a plot of Wind Weighting Factor versus altitude) is to compute a number of trajectories with headwinds of a constant magnitude from the ground up to different altitudes. The ratio of the deflection of the impact point (some other pertinent point might of course be used) due to wind up to a given altitude to the deflections due to a Ballistic Wind of the same magnitude is the Wind Weighting Factor at that altitude. It is not a major extension of this to assume that the Wind Weighting Curve could also be calculated by computing trajectories which included winds of constant magnitude acting everywhere above different selected altitudes. Using this approach, the Wind Weighting Factor at any altitude would then be one minus the ratio of the displacement of the impact point due to a constant wind

above that altitude to the displacement due to a Ballistic Wind of the same magnitude. The Wind Weighting Curves of Figure 5 which were calculated in this manner are designated "Inverse Method." Considering the extreme curves shown, the usual and the "Inverse Method" curves for a 50 ft/second headwind and an 87° quadrant elevation, the former indicates a 32% greater deflection of the impact point for a constant wind below 1000 feet than does the latter. In comparison, only a 2% difference in the indicated deflection occurs when the equivalent curves for a 10 ft/sec headwind are employed. Obviously, this indicates that the use of a single Wind Weighting Curve is more correct when wind magnitudes are small, rather than that the curve should be evaluated for small wind magnitudes and used with any measured winds. It may be seen from Figure 5 that, even for a 10 ft/second wind, there is a 10% difference in the Wind Weighting Factor at 1000 feet when the curves for 80° and 87° quadrant elevation are compared. Obviously, even for small wind magnitudes, the Wind Weighting Curve must be a function of quadrant elevation. So far, only the Wind Weighting Curve for in-range headwinds has been discussed. It is apparent, from the variants of this curve which are possible with different quadrant elevations and velocities, that adding the azimuth between the wind plane and the trajectory plane as a variable would result in even more different Wind Weighting Curves. An additional complication is immediately

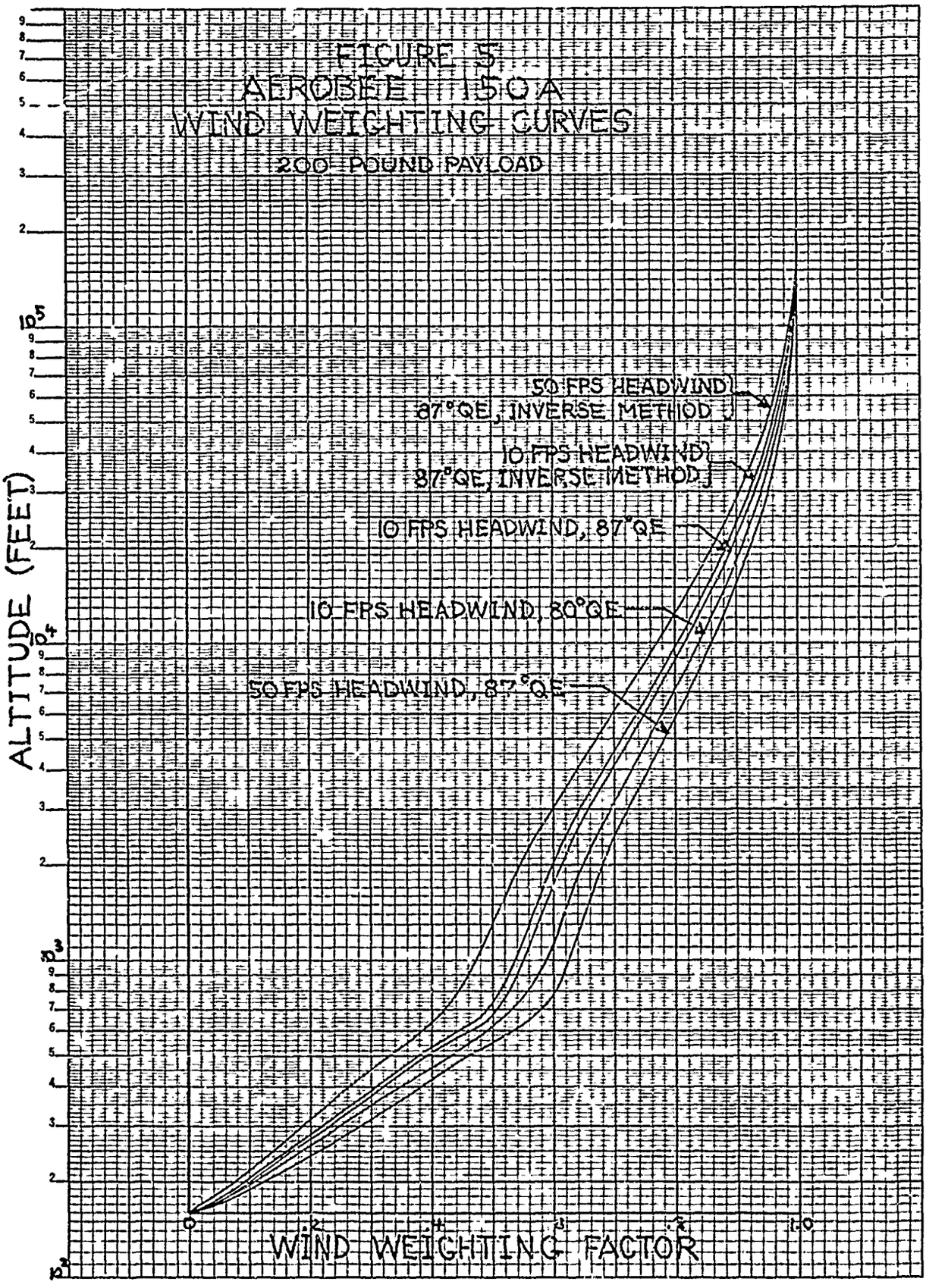
FIGURE 5
AEROBEE 150A
WIND WEIGHTING CURVES
200 POUND PAYLOAD
50 FPS HEADWIND
87°QE, INVERSE METHOD
10 FPS HEADWIND
87°QE, INVERSE METHOD
10 FPS HEADWIND, 87°QE
10 FPS HEADWIND, 80°QE
50 FPS HEADWIND, 87°QE
ALTITUDE (FEET)
WIND WEIGHTING FACTOR

obvious: Unless the wind profile is entirely in the plane of the launcher(or simply planar with any azimuth for a vertical launch) the trajectory will be rotated about a vertical axis by the wind so that the apportionment between in-range and cross-range winds would change with altitude. Thus, the selection of the appropriate Wind Weighting Curves becomes doubly difficult. It is apparent that this same effect makes the use of Ballistic Factors suspect. It may be seen from Eq. (17) that the incremental displacement of the impact point due to a wind at some altitude, h, is proportional to d(WWF)/dh at h. Comparing two Wind Weighting Curves in Figure 5 which are evaluated using the same method and the same wind velocity but different quadrant elevations, it may be seen that the slopes of the curves, i.e., d(WWF)/dh, differ at any given h. It is apparent that this difference must be due to the difference in the flight path elevation at h. In general, this flight path angle would be a function of both the launcher elevation and the entire wind profile below h. Consideration of even a nominal trajectory with no wind shows the flight path angle at any altitude to be somewhat non-linearly related to the flight path angle at some previous time. It must thus be expected that the WWF at h will be a non-linear function of both the launcher elevation and the wind profile below h. Two courses appear open, short of using a complete trajectory simulation, each of which would result in an improvement in accuracy.

The simpler approach, although inherently less accurate, is to accept the use of Ballistic Factors and Wind Weighting Curves, with their attendent inaccuracies, but to base the corrections on deviations from a nominal trajectory which includes the mean range wind profile rather than zero wind. This has the effect of reducing, on the average, the magnitude of winds for which wind weighting must be done, and therefore of reducing the magnitude of the errors involved in the use of the Ballistic Factors and Wind Weighting Curves. If this approach is used in conjunction with the filtered wind profile discussed earlier, it appears that the method would result in a considerable improvement in accuracy.

The second method requires considerably more analysis to establish the correction parameters and requires also a somewhat larger scale computer facility in the field. However, both the size of the computer and the amount of computing required at the launch site should be considerably less than those required to calculate the vehicle trajectory. This method is not exact, but appears to overcome some of the disadvantages of the use of Wind Weighting Factors and Ballistic Factors in that local wind amplitudes are individually accounted for. The method uses a representation of the wind profile as a set of layers in each of which the wind is treated as a sharp edged gust. This simulation does not duplicate the actual flight path of the vehicle,

which would in actuality experience a distribution of wind shears with few, if any, sharp edged gusts. However, it is felt that the total rotation of the velocity vector between launch and burnout is well reproduced (with the exception of a response to velocity distribution along the body, which will be discussed presently.) Let us consider the dynamics of a vehicle passing through a gust of finite thickness. The significant point to bear in mind is that the vehicle responds to the transverse velocity discontinuities which are encountered both when entering and leaving the gust. When the vehicle first enters the gust (the vehicle will here be considered as having a zero length) it experiences an angle of attack, and therefore begins to rotate into the wind if it is stable (which a sounding rocket would be expected to be). As the vehicle rotates, the thrust, axial force, and normal force vectors rotate with it. This causes a rotation of the velocity vector from the path it would follow if the gust were absent. Since the vehicle will have finite moment of inertia, finite aerodynamic restoring moment, and finite aerodynamic and jet damping coefficients, the response of the body axis to entering the gust layer will be approximately a damped sinusoidal motion. The corresponding motion of the velocity vector will also be a damped sinusoid but will differ from the body axis motion both in amplitude and phase. Upon leaving the gust, the vehicle again encounters a discontinuity in the lateral velocity, but in the opposite

direction from the discontinuity encountered when entering the gust. Damped sinusoidal motions of the body and the velocity axis again occur. The flight path at some distance above the gust may be seen to be a function of the response of the vehicle to both entering and leaving the gust. If a wind profile model is to be built up of a number of layered gusts, it is obvious that the total effect of both boundaries of each gust must be represented. It is also obvious that if the method is to work, it must be possible to replace a given gust layer with two thinner gust layers and still calculate the same total effect on the impact point. There is a manner in which the total effect on the flight path due to a gust may be represented within the confines of that gust so that this superposition is possible. It is common with sounding rockets that after the vehicle has reached final burnout the effect of wind on the impact point is negligible. Also, the variation in the vehicle position at burnout due to flying through different wind profiles affects dispersion negligibly if the burnout velocity vector is assumed fixed in azimuth, elevation, and magnitude. Therefore, the effect of winds on the flight path may be defined in terms of their effect on the burnout velocity vector orientation (horizontal winds usually have a negligible effect on burnout velocity at fixed burnout velocity vector orientation) and the impact point may be closely predicted on the basis of the orientation of the burnout velocity vector. Now, let

us first assume that a number of trajectories have been computed, for the vehicle in question, with various launcher elevations and without any wind or other perturbations. Assume that these trajectories have been computed from launch to impact so that the impact point may be defined as a function of the orientation of the velocity vector at burnout and the velocity vector orientation at burnout may be represented as a function of the velocity vector orientation at any earlier time. Next, let us assume that a trajectory is computed from launch to burnout which includes a gust layer of some selected velocity and azimuth relative to the launcher azimuth. Some launcher elevation is arbitrarily selected, as is the layer thickness. Once the velocity vector elevation and azimuth at burnout are known, the nominal (zero wind) trajectories may be consulted, and the velocity vector elevation and azimuth of a nominal trajectory, at the altitude corresponding to the top of the gust layer, which would give the same burnout velocity vector elevation and azimuth may be determined. Also known, from the trajectory computed with the gust, are the velocity vector azimuth and elevation as the vehicle enters the gust, and the velocity and azimuth of the gust and its thickness. Thus, if it is assumed that the entire dynamic responses to both faces of the gust are confined within the gust, i.e., the vehicle leaves the gust with the velocity vector orientation determined from the nominal trajectory with the same velocity

vector orientation at burnout, a relationship is found between the flight path azimuth and elevation at the bottom of the gust, the velocity and azimuth of the gust, and the effective flight path azimuth and elevation at the top of the gust. If a number of similar trajectories are computed with varying launcher elevation, gust velocity, and gust azimuth, a set of relationships may be built up for the wind layer which relate the effective velocity vector orientation at the top of the gust to that at the bottom in terms of the velocity and azimuth of the gust. It is apparent that the flight path from launch to burnout may be divided into a number of altitude bands, and the above procedure repeated for each band, thus generating a set of relationships between the velocity vector orientations entering and leaving each of the contiguous layers in terms of the gust velocity and azimuth in each layer. It is obvious that, when considering the gust azimuths, it is the relative azimuth angle between the wind vector and either the entering or leaving velocity vector that is important. Now, an assumption must be made which will not be rigorously proven: that when several gust layers are combined, the appropriate velocity vector orientation to assume when entering each layer is the effective (from the no-wind nominal trajectories) orientation when leaving the previous one. Since all of the dynamic response to both sides of each gust is accounted for by the use of this effective orientation, this seems a valid assumption.

The error involved is small and is associated with the difference in angle of attack due to the edge of the gust when this angle is calculated using the actual versus the effective flight path orientation. (It is probable that for artillery rockets with depressed trajectories this error would be significant.) A distinguishing feature of this approach to wind weighting is that it may be non-iterative. Consider that the relationship between the velocity vector orientations when entering and leaving a gust and the gust velocity and azimuth may be used to solve for the effective vehicle velocity azimuth and elevation at the bottom of the gust given the vehicle velocity azimuth and elevation at the top of the gust and the velocity of the gust and its azimuth relative to the vehicle velocity vector at the top of the gust. As pointed out earlier, variations in the position of the vehicle at burnout, with fixed burnout velocity vector azimuth and elevation, do not significantly affect the impact point. Thus, once the desired impact point is selected, the burnout velocity vector orientation is defined and, with the measured (and filtered) wind profile resolved into layered gusts, the flight path may be calculated by working downward through the gust layers starting with the desired azimuth and elevation of the burnout velocity vector. If the gust layers are disposed so that the bottom of the lowest layer is at the altitude of the launcher exit, the final values of vehicle velocity azimuth and elevation calculated will be, identically, the required launcher setting.

We may finally turn our attention to the subject of the response of the vehicle to a wind velocity distribution along the body. Obviously, this velocity distribution may take several forms: a shear distribution, the edge of a gust passing along the body, or various curvilinear distributions. The one which is treated here is the shear distribution along the body. It has been common practice to ignore the effect of these wind distributions when computing wind response trajectories. It may be shown that these effects are actually of quite significant magnitude. Since trajectory programs commonly define the relative wind vector as the one extant at the center of gravity, the attendant shear distribution would consist of a velocity normal to the longitudinal axis of the vehicle with a zero amplitude at the center of gravity and increasing linearly in amplitude with increasing distance from this point. The direction of this transverse velocity would naturally be of opposite sign forward and aft of the c.g. It may be seen that this distribution is identical to that due to a pitch or yaw rate. This suggests that the aerodynamic pitch damping coefficient may be pressed into service to represent the moment about the c.g. due to a wind shear. The moment due to a pitch rate, q, is given by:

$$M = C_{m_q} \left(\frac{qd}{2V}\right) QSd \qquad (18)$$

The transverse velocity at a point on the vehicle at a distance ℓ forward of the c.g. is $q\ell$ (feet/second when q is in radians/second and ℓ is in feet).

For a wind shear $\frac{dw}{dh}$, the transverse velocity at the same position, ℓ, is $\ell(dw/dh)$ (feet/second when dw/dh is in feet per second per foot) when the vehicle is vertical, and $\ell(dw/dh)$ sin θ for a body elevation of θ. It may be seen that the dw/dh sin θ may be substituted directly for q, yielding a moment due to wind shear of:

$$M = C_{m_q} \left(\frac{\frac{dw}{dh} d}{2V} \right) QSd \sin \theta \qquad (19)$$

This term could be added to the moment equations in a trajectory program, thus improving the simulation of the wind response of a vehicle. It is also possible to derive a Shear Weighting Curve which is comparable to a Wind Weighting Curve and a Ballistic Shear Factor which serves a purpose equivalent to a Ballistic Factor. This will be illustrated for the case of small coplanar wind shears and a vertical flight. This particular case is of somewhat limited usefulness, but serves to demonstrate the effect of the wind shear distribution along the body on the trajectory.

We first write two of the equations of motion of a vehicle flying a planar trajectory above a flat earth with no wind:

$$\dot{V} = \frac{(T-X)}{m} \cos \alpha - \frac{N}{m} \sin \alpha - g \sin \gamma \qquad (20)$$

$$V\dot{\gamma} = \frac{(T-X) \sin \alpha}{m} + \frac{N \cos \alpha}{m} - g \cos \gamma \qquad (21)$$

where V is the velocity of the vehicle along the flight path, γ is the elevation of the velocity vector, α is the angle of attack (positive when the elevation of the body axis is greater than γ), m is the mass of the vehicle, T is the thrust, X is the aerodynamic axial force, N is the aerodynamic normal force, and g is the acceleration due to gravity. The moment equation has been omitted since α will later be defined in terms of the wind shear. Differentiating Eq. (21) with respect to α yields:

$$\frac{\partial \dot{\gamma}}{\partial \alpha} = \frac{(T-X)}{mV} \cos \alpha - \frac{dA}{d\alpha} \frac{\sin \alpha}{mV} - \frac{N}{mV} \sin \alpha + \frac{\cos \alpha}{mV} \left(\frac{dN}{d\alpha}\right) \qquad (22)$$

Assuming α to be very small, and N to be equal to $\alpha(dN/d\alpha)$, Eq. (22) becomes

$$\frac{\partial \dot{\gamma}}{\partial \alpha} = \frac{(T-X)}{mV} + \left(\frac{dN}{d\alpha}\right) \frac{(1-\alpha^2)}{mV} = \frac{(T-X)}{mV} + \frac{C_{N_\alpha} \rho VS}{2m} \qquad (23)$$

Note that the g cos γ term of Eq. (21) was ignored, limiting the validity of Eq. (23) to vertical flight. For vertical flight at small α, sin θ in Eq. (19) is approximately equal to 1.0, and assuming that the vehicle flies in a trim condition such that the aerodynamic restoring moment balances the moment due to wind shear distribution, we may determine the angle of attack by:

$$\alpha = - \frac{C_{m_q}}{C_{m_\alpha}} \left[\frac{(dw/dh)\, d}{2V}\right] \qquad (24)$$

Eq. (23) may be written as:

$$d\dot{\gamma} = -\left[\frac{T}{mV} + \frac{(C_A - C_{N_\alpha})\ \rho\ VS}{2m}\right] d\alpha \qquad (25)$$

Assuming that, in the absence of wind shear $\alpha = 0$, we may combine Eq. (24) and (25) to yield:

$$\dot{\gamma} = -\left[\frac{T}{Q} + (C_{N_\alpha} - C_A)\ S\right] \frac{\rho d}{4m} \left(\frac{C_{m_q}}{C_{m_\alpha}}\right) \left(\frac{dw}{dh}\right) \qquad (26)$$

The change in flight path angle, at time τ, per unit wind shear is then:

$$\frac{d\gamma}{d(dw/dh)} = -\int_0^\tau \left\{\frac{T}{Q} + (C_{N_\alpha} - C_A)S\right\} \frac{\rho d}{4m} \left(\frac{C_{m_q}}{C_{m_\alpha}}\right) dt \qquad (27)$$

This equation is easily integrated numerically if a reference trajectory is available. If τ is set equal to the time at which the wind shear distribution has a negligible effect on the trajectory and the resultant value of $d\gamma/d(dw/dh)$ is multiplied by $d(\text{range})/d\gamma$, the product is the Ballistic Shear Factor. The ratio of $d\gamma/d(dw/dh)$ at some intermediate τ to the value at the τ for negligible effect is the Shear Weighting Factor, SWF. A Ballistic Shear may be determined by:

$$\left(\frac{dw}{dh}\right)_B = \int_0^H \frac{dw}{dh}(h)\ \frac{d(SWF)}{dh}\ dh \qquad (28)$$

where time τ has been replaced by the equivalent altitude, h, as the independent variable, and H is the altitude for negligible effect of wind shear distribution. This equation is completely analogous to Eq. (17). Multiplying the Ballistic Shear by the Ballistic Shear Factor yields the change in range due to the wind shear distribution.

A sample computation has been made for an Aerobee 350 with a 408 pound net payload. No vertical trajectories were available, so data was taken from a trajectory with an 84° launcher elevation. This does not result in any unduly large errors, particularly for a sample case as limited in application as is this one. It was found that $H = h_{burnout}$ accounted for effectively all of the wind shear distribution effect. The Ballistic Shear Factor was found to be 0.624 Nautical Miles per ft/second wind shear per 1000 feet altitude. Figure 6 shows the Shear Weighting Curve. Reference (2) reports the probability of occurrence of wind shears of varying lengths and magnitudes as a function of altitude. Choosing a 1σ probability level, and a 3000 foot shear layer starting at the top of the tower, the shear is found to be $dw/dh = 4.5$ (ft/sec) per 1000 ft. From Figure 6, this is found to result in an impact point displacement of 1.1 NM. It may be seen that the dispersion due to wind shear through a complete wind profile may easily be non-negligible.

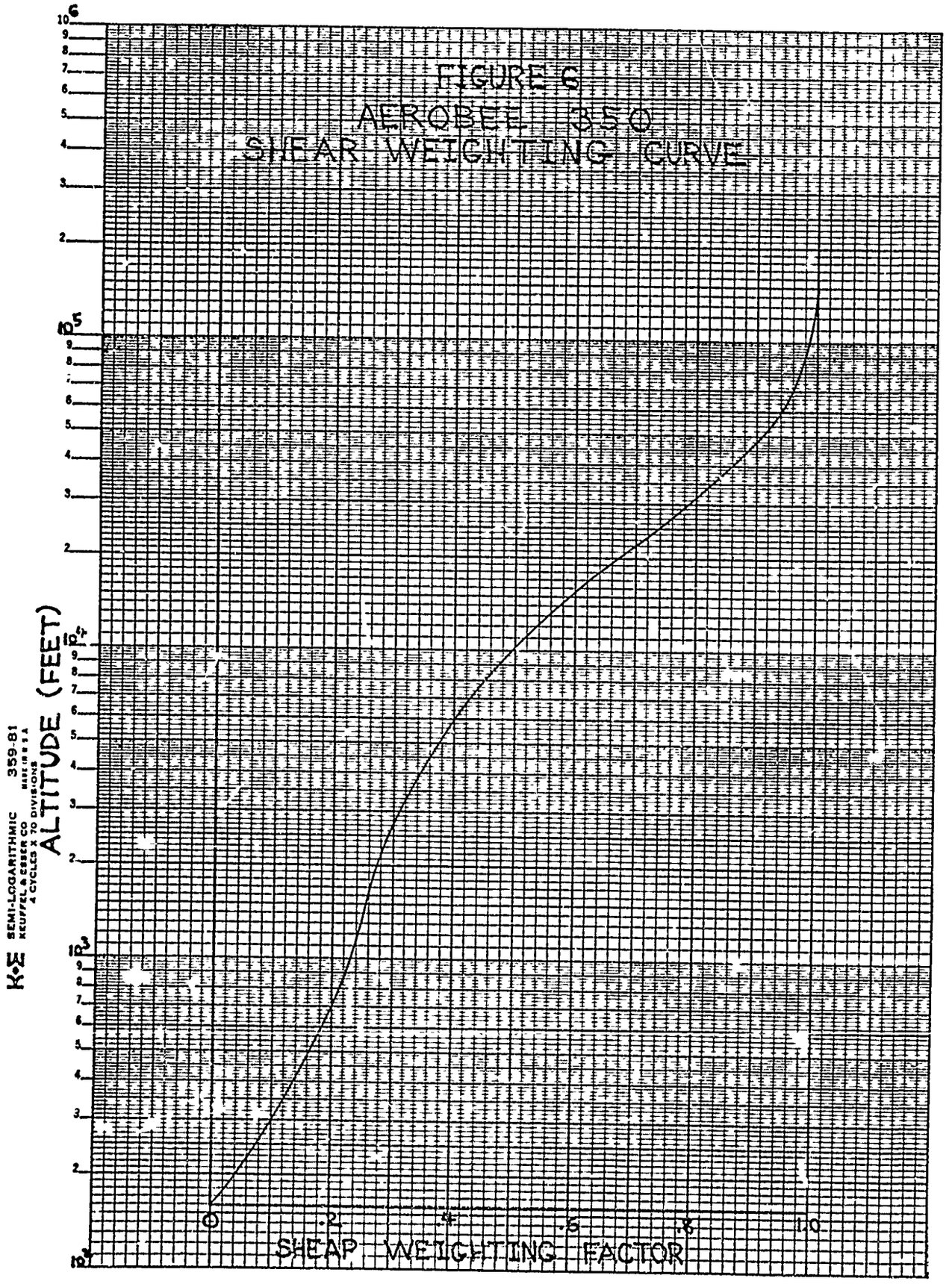
FIGURE 6
AEROBEE 350
SHEAR WEIGHTING CURVE
ALTITUDE (FEET)
SHEAR WEIGHTING FACTOR
0
.2
.4
.6
.8
1.0
K&E 359-81
SEMI-LOGARITHMIC
KEUFFEL & ESSER CO
4 CYCLES X 70 DIVISIONS

CONCLUSIONS

We have seen a number of places in the total wind weighting procedure where our present methods are less accurate than what is presently achievable, and far less accurate than what is ultimately possible. Several points have been touched on in this paper, but none have been carried to their limits. There are no doubt many other areas in which improvement of the wind weighting procedures may be made. As the range and apogee performance of sounding rockets improves, and as a burgeoning population closes in on the available test ranges, the need to minimize the dispersion of sounding rockets increases. It has been shown that improvements in the wind weighting procedure will contribute to this evermore necessary dispersion reduction.

The recommended procedure for relating the wind profile to the requisite launcher orientation using a gust distribution needs to be tested, both analytically and in the field. This testing would have to go far beyond comparison with the current Wind Weighting Factor/ Ballistic Factor approach, since that comparison would show only that the two procedures yielded different answers.

The dispersion due to wind shear distributions along the vehicle has been shown not to be negligible. However, only the simplest example of a non-computer-trajectory-oriented approach has been presented. The analysis needs to be extended to the general case of

variable vehicle velocity vector orientation and generalized wind velocity distribution along the body and melded with, at one accuracy level the Wind Weighting Curve and Ballistic Factor procedure, and at the next level of accuracy with the gust distribution weighting approach. It is apparent that the least difficult application is the addition of this effect to computer trajectory programs, which are in the last analysis our most accurate means of determining the response of a rocket to a particular wind profile.

REFERENCES:

1. J.R. Scoggins; "Preliminary Study of Atmospheric Turbulence Above Cape Canaveral, Florida"; MTP-AERO-63-10; George C. Marshall Space Flight Center; 1 Feb. '63.

2. N. Dvoskin, N. Sissenwine; "Evaluation of AN/GMD-2 Wind Shear Data for Development of Missile Design Criteria"; #99; Air Force Cambridge Research Center; April 1958.

DISCRETE RECURSIVE ESTIMATION: AN OPTIMUM AUTOMATED DATA PROCESSING TECHNIQUE FOR MULTI-ELECTRONIC TRACKING SYSTEMS

by

Maceo T. Scott

Mathematician, Processing Sciences Division
Analysis and Computation Directorate
White Sands Missile Range, New Mexico

SUMMARY

Automation of range instrumentation data handling and the improvement of information recovery quality from simultaneous tracking instruments are problems always in need of updating. An approach to solving some of these problems through judicious selection of mathematical techniques are herein presented.

This study seeks to show how optimal estimation and recursive procedures are being utilized at several stages in a single pass computer program to accomplish the following:

1. Correct for instrumentation system and geodesy errors through optimal transformations.
2. Provide an inherent data editing procedure.
3. Provide best estimates of the trajectory and the dynamic variables.
4. Provide covariance matrices of the tracking instrument observation errors and recovery of the errors for each of the instruments.

The results appear as a set of optimum trajectory parameters which are delivered in final report form. The time consumed to handle the total processing of N-Radar Stations is approximately 1 1/2 minutes of Direct Coupled System (DCS) machine time per minute of flight time and hence make these techniques highly attractive for operations that involve the processing of large quantities of electronic tracking data on a timely basis.

INTRODUCTION

The modern approach to solving problems through automated means is to combine ingenuity and scientific purpose with the powerful computation procedures at our command. This viewpoint and the desire to improve matters over the past, motivates the scientific organization of a procedure for efficient manipulation of data governed by more advanced mathematical principles and the pressing need to faithfully represent information with

its timely delivery. With a philosophy developed around these points, the realization of the full potential of the mathematical and computational tools will lead the way to the automation and improvement of scientific data processing.

The purpose of this paper is to illustrate a single pass processing strategy that can be obtained from a single pass N-station radar reduction procedure. This procedure is a direct consequence of a long standing motivation to utilize simultaneous electronic tracking data in a single pass from the original recording of real-time data.

The computer program utilizes the techniques of discrete recursive estimation. The basic recursive estimation scheme utilized in this program is due to R. E. Kalman.*

The major advantages of this program are as follows:

1. Provides self-calibration and optimization of transformed instrumentation data.

2. Has an inherent editing procedure.

3. Provide the covariance matrix of the error associated with the optimal estimates.

One of the first important procedures to the automation process was to set into motion the long standing range capability to capture all data in real-time on a single tape and thus eliminate the former necessity to

1. Handle individual on-site digital tapes.

2. Rely upon courier service for delivery of data.

3. To eliminate the potentially time consuming radar data conversion process in converting from an incompatible tape to a computer compatible digital tape, and

4. To eliminate the time correlation step among a number of on-site radar tapes.

THE GENERALIZED PROCESSING APPROACH

One of the fundamental concepts that lies at the basis of an understanding, is that the processing procedures are no longer at the mercy of nonadaptive, open-loop systems. Furthermore, since the procedures are optimum, the human analyst can no longer compete with his visual inspection techniques.

---

*Kalman, R. (1961), "New Methods and Results in Linear Prediction and Filtering Theory," Tech. Report 61-1 R.I.A.S., Baltimore, Md.

For example, Figure 1 shows in structure a typical open-loop process where each step is an entirety unto itself.

In this kind of procedure there can be no inherent automatic correction or adaptive control capability. In order to obtain results which "appear right" to the data analyst, the procedures usually break down into a human oriented run-look-run sequence motivated by an insufficient guarantee that all is well at any stage of the process. This by its very nature eliminates its consideration from a mathematical optimization and automated process.

The significant features of the new method is illustrated in Figure 2. Here we are attempting to illustrate the overall structure of the entire, single pass information delivery procedure. In the strategy of these procedures extensive use is made of a mathematical model of each of the particular processes that we are attempting to optimize.

It is significant at this time to mention that this approach laid the foundation for improvements in systems control work and impact prediction techniques. This has been mainly due to the successful application of a more powerful mathematical tool which transcends other techniques of the past but includes them as special cases of the general theory. These new procedures are self-correcting, dynamic and optimum for each stage of filtering and hence there is no need to consider drastic program changes or new schemes for each mission. The matrix representations for each function within a filter are extremely compact and the programming efforts are minimized since the computing system is already prepared to manipulate matrices. The behavior of data is easier to trace and diagnose once the theory and mechanics of the recursive estimation procedure are known. With a number of these matrix packages accumulated for different functions within a filter, the ability to respond to new requirements comes with increasing facility and the job of connecting the packages through appropriate logic is easier to satisfy.

The only other consideration when going to these methods is that the individuals must become more aware of the instrument characteristics and flight process, as well as the mathematical procedures in the program, than in the past.

For it is only when these factors can be integrated under a common understanding can major processing problems be addressed and solved as a more complete system.

GENERAL DESCRIPTION OF THE AUTOMATED DATA PROCESSING PROCEDURE(RADARS)*

We assume that n-radars are tracking a single target and they are being simultaneously strobed. The data is recorded in real-time and playbacks are made depending upon computer availability.

---

*See diagram at the end of the section.

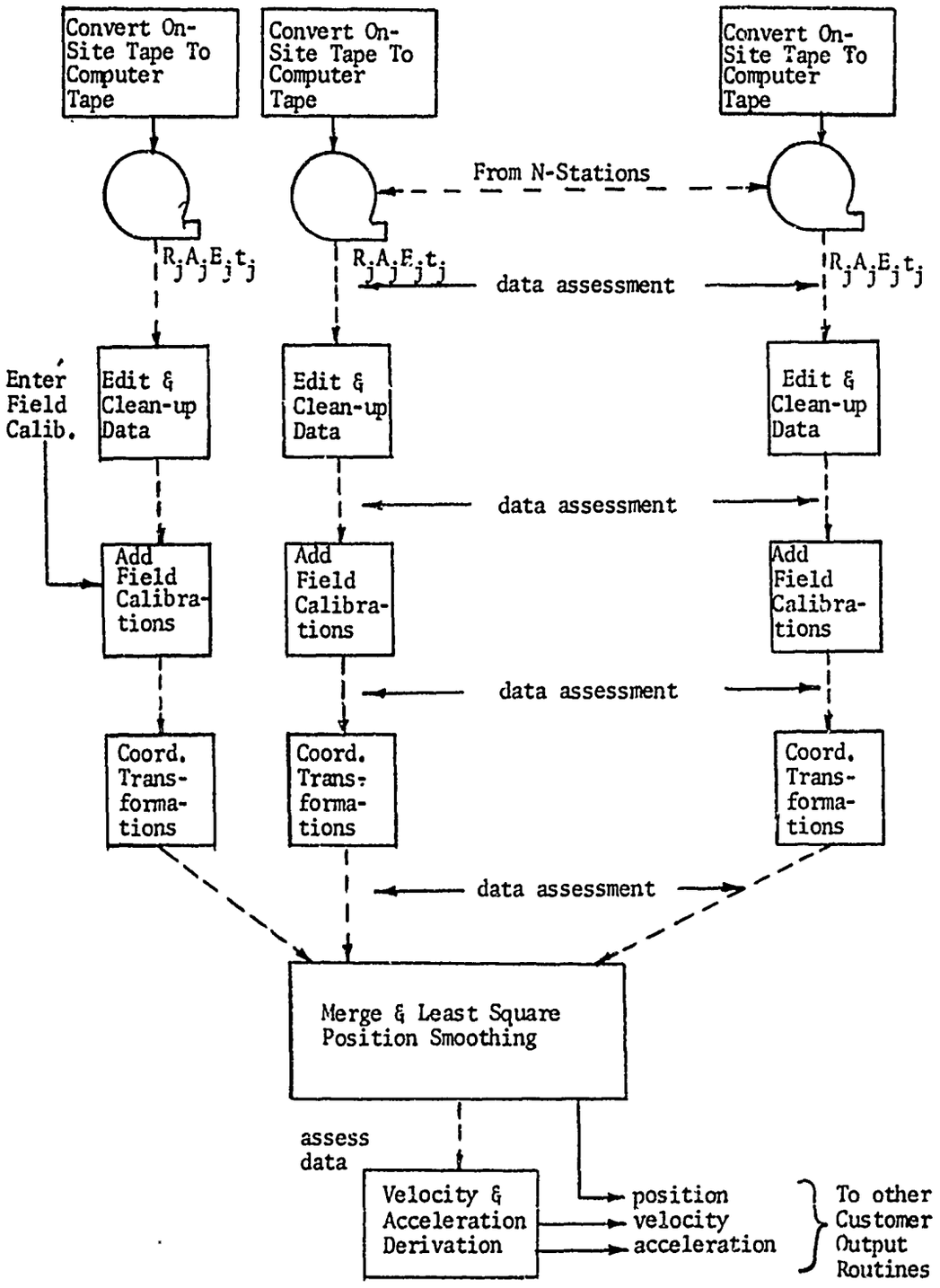
Convert On-Site Tape To Computer Tape
Convert On-Site Tape To Computer Tape
Convert On-Site Tape To Computer Tape
From N-Stations
$R_jA_jE_jt_j$
$R_jA_jE_jt_j$
$R_jA_jE_jt_j$
data assessment
Enter Field Calib.
Edit & Clean-up Data
Edit & Clean-up Data
Edit & Clean-up Data
data assessment
Add Field Calibrations
Add Field Calibrations
Add Field Calibrations
data assessment
Coord. Transformations
Coord. Transformations
Coord. Transformations
data assessment
Merge & Least Square Position Smoothing
assess data
Velocity & Acceleration Derivation
position
velocity
acceleration
To other Customer Output Routines

Figure 1

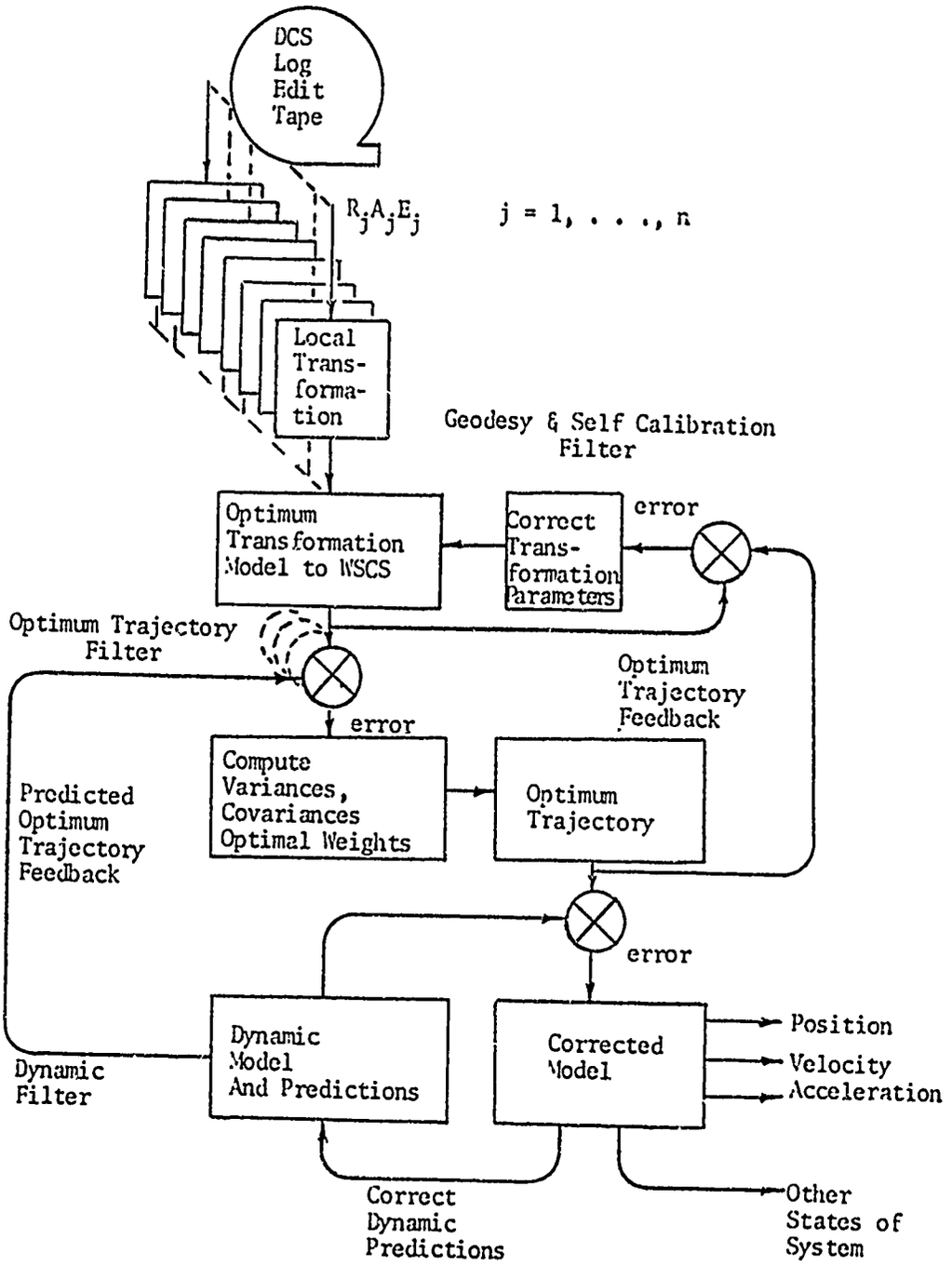
DCS
Log
Edit
Tape
$R_jA_jE_j$
j = 1, . . ., n
Local
Trans-
forma-
tion
Geodesy & Self Calibration
Filter
Optimum
Transformation
Model to WSCS
Correct
Trans-
formation
Parameters
error
Optimum Trajectory
Filter
Optimum
Trajectory
Feedback
error
Compute
Variances,
Covariances
Optimal Weights
Optimum
Trajectory
Predicted
Optimum
Trajectory
Feedback
error
Dynamic
Model
And Predictions
Corrected
Model
Position
Velocity
Acceleration
Dynamic
Filter
Correct
Dynamic
Predictions
Other
States of
System

Figure 2

Our first task is to use our optimum estimates of the radar locations and convert all data to a common frame of reference. Next, we use the optimized n-station solution filter to obtain the best estimate of the trajectory based upon all given observations. The best estimate of the trajectory based on observations is used to

(1) Provide input data to the geodesy filter and

(2) Provide input data to the dynamic filter.

The output of the geodesy filter provides optimum transformation corrections. The output of the dynamic filter provides the best estimate of the trajectory and other state variables. In addition, the optimum predicted state of the system is utilized to generate the observation covariance matrices associated with the radars. It is evident from the diagram that we have indeed developed a closed-loop data processing procedure.

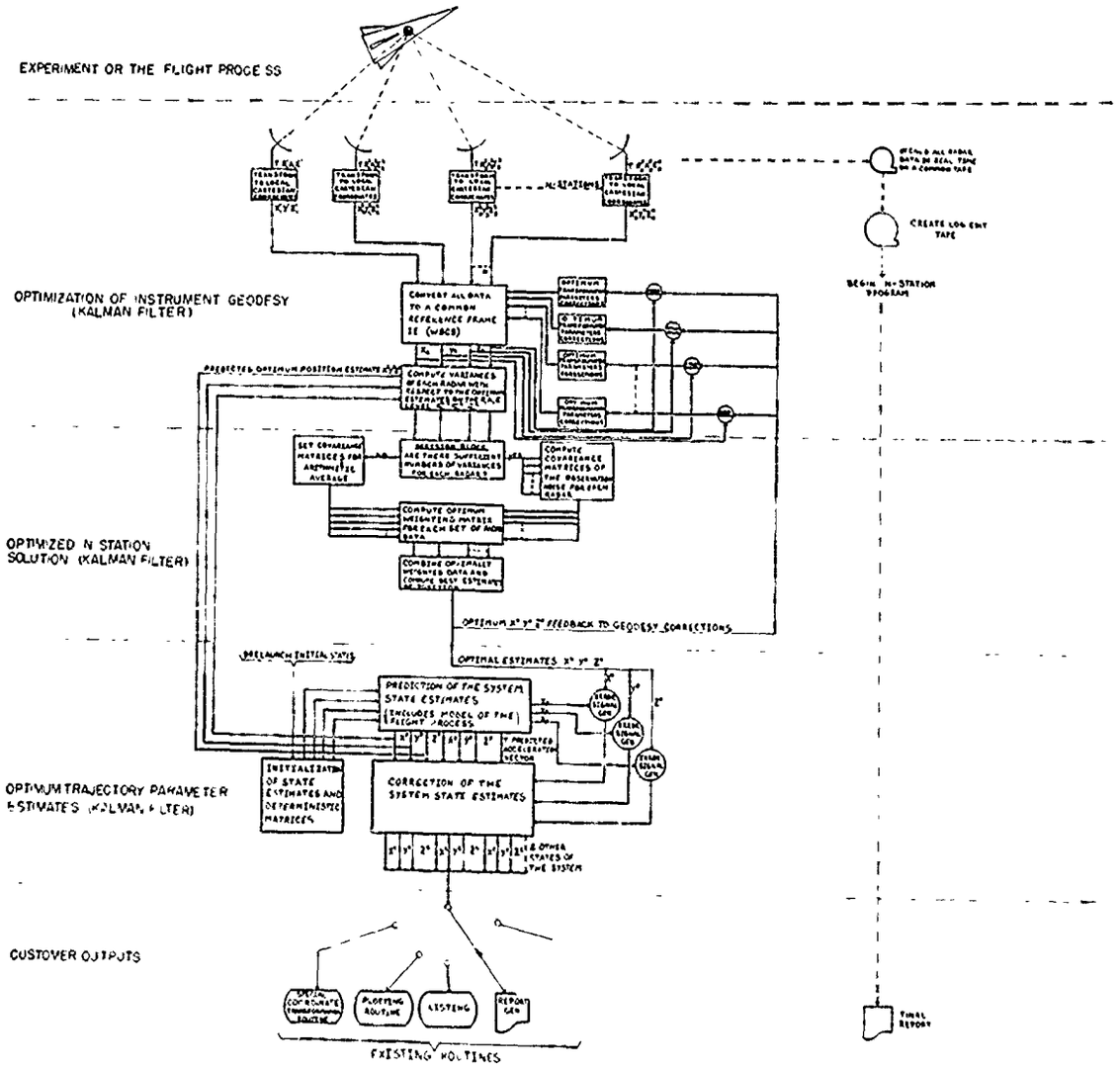
EXPERIMENT OR THE FLIGHT PROCESS
OPTIMIZATION OF INSTRUMENT GEODESY (KALMAN FILTER)
OPTIMIZED N STATION SOLUTION (KALMAN FILTER)
OPTIMUM TRAJECTORY PARAMETER ESTIMATES (KALMAN FILTER)
CUSTOVER OUTPUTS
CREATE LOG ENT TAPE
BEGIN N-STATION PROGRAM
CONVERT ALL DATA TO A COMMON REFERENCE FRAME IE (WGS)
PREDICTED OPTIMUM POSITION ESTIMATE
OPTIMUM FEEDBACK TO GEODESY CORRECTIONS
OPTIMAL ESTIMATES
PREDICTION OF THE SYSTEM STATE ESTIMATES
CORRECTION OF THE SYSTEM STATE ESTIMATES
PLOTTING ROUTINE
LISTING
REPORT GEN
FINAL REPORT
EXISTING ROUTINES

The General Formulation of the

Kalman-Bucy Filter

1. Structure of the Model

We will consider a rather general model consisting of a random process in discrete time and of observations made upon it. The structure of the model is defined by the following linear matrix equations.

(1.1) $x(k+1) = \phi(k+1,k)x(k) + u(k)$ $\qquad (k = 0, 1, 2, \ldots)$

(1.2) $z(k) = H(k)x(k) + v(k)$ $\qquad (k = 1, 2, \ldots)$

In these equations k is a discrete running index which may be identified with time in many applications. For convenience, we shall refer to such quantities as x(k) as the value of x at time k although frequently the amount of real-time elapsing between (k-1) and k is not unity and may be variable. Note also that equations (1.1) and (1.2) are indexed upward from an initial value of k = 0 and k = 1 respectively.

(1.1) and (1.2) are matrix equations containing column vectors x(k) and u(k) of dimension p, while column vectors z(k) and v(k) are dimension q. $\phi(k+1,k)$ is a square (pxp) matrix, while H(k) is a matrix of q rows and p columns.

Equation (1.1) is called the state equation. It is a first order difference equation in k relating one value of x, x(k), to the next value x(k+1). The vector x(k) represents the parameter, or state vector, whose components we will try to estimate. When the components of the state vector are time dependent, (1.1) structures their dynamical behavior. Most of the generality of the recursive model is due to the use of this equation.

The multiplicative part of the connection between x(k+1) and x(k) is provided by the transition matrices $\phi(k+1,k)$, for $k \geq 0$. They specify the dynamics of the model. The added vectors u(k), for $k \geq 0$, are driving terms (forcing function) of the difference equation.

The state equation (1.1) is a model for the true state of affairs, the true values of the state vector at time k. Equation (1.2), called the observation equation, is a model of the measurement process. z(k) represents the measurement (observation) vector whose components are the individual scalar measurements made at time k. Equation (1.2) relates these measurements to the state vector via the observation matrix H(k), for $k \geq 1$. The random measurement noise is represented by v(k), for $k \geq 1$. It should be observed that the observation equation contributes no dynamics to the model.

2. Statistics of the Model

The matrix sequences $\phi(k+1,k)$ and $H(k)$ are assumed to be specifically and deterministically given in any particular application of the model. They actually define the deterministic structure of the model. Equations (1.1) and (1.2) may be viewed as defining how the x(k) and z(k) sequences as dependent variables can be generated from the u(k) and v(k) sequences plus the initial condition x(0) as independent vectors. Since the latter vectors are random, they induce a random behavior on the x(k), z(k) sequences.

We shall assume that the u(k), v(k), x(0) populations are joint gaussian. Hence it suffices to give the first and second moment statistics of these populations. We further assume that u(k) and v(k) for each k and x(0) are mutually independent. With these assumptions, it is necessary only to specify further the statistics of each of these independent vectors. We will denote the expectation operator by E[ ] and the covariance operator by COV[ ] i.e. if for the column vector W, $E[W] = \overline{W}$, then $COV[W] = E(W - \overline{W})^T$ where ^{T} denotes matrix transportation.

Hence we have that

2.1 $E[u(k)] = 0 \qquad k \geq 0$

$E[v(k)] = 0 \qquad k \geq 0$

$E[x(0)] = \overline{x}$

2.2 $COV[u(k)] = Q(k) \qquad k > 0$

$COV[v(k)] = R(k) \qquad k \geq 0$

$COV[x(0)] = P(0)$

It should be stated that the covariance matrix sequences Q(k), R(k) of u(k), v(k) comprise the main statistical information. Although u(k) and v(k) are statistically independent, the components of u(k) or v(k) need not be independent. That is Q(k) and R(k) need not be diagonal.

3. Generalized Solution

Before beginning our discussion concerning linear best estimates of the state vector x(k), some definitions are in order.

1. x(k+1), x(k) - The state vectors which describe the state of the system at t = k+1 and t = k respectively. (px1)

2. $\phi(k+1,k)$ - A (pxp) transition matrix (deterministic) which relates the state of the system at t = k to the state of the system t = k+1.

3. u(k) - Gaussian random vector with zero mean and $E[u(j)u^T(k)] = Q(k)\delta_{jk}$.

4. z(k) - Observations at t = k. (qx1)

5. H(k) - Observation matrix (deterministic) which relates the state vector to the observations. (qxp)

6. v(k) - Gaussian random vector with zero mean and $E[v(j)v^T(k)] = R(k)\delta_{jk}$

7. x(k/k - 1) - Our best predicted estimate of the state x(k) based on observations z(1), z(2), . . ., z(k-1). (pxl)

8. x(k/k) - Our best estimate of the state x(k) based on observations z(1), z(2), . . ., z(k). (This is the corrected value) (pxl)

9. P(k/k-1) - Covariance matrix of the error associated with $\hat{x}(k/k-1)$. (pxp)

10. P(k/k) - Covariance matrix of the error associated with $\hat{x}(k/k)$. (pxp)

11. W(k) - Optimum weighting matrix $W(k) = P(k/k-1)H^T(k)[R(k)+H(k)P(k/k-1)H^T(k)]^{-1}$. (pxq)

At each instant of time k, we assume that

a. x(k/k-1)

b. P(k/k-1)

are known

We will then receive an observation z(k) [it includes measurement noise]. Our first problem then is to correct the predicted state x(k/k-1) based on the new information z(k) and obtain x(k/k).

*From the theory of the Kalman-Bucy Filter, it follows that

(1) $x(k/k) = x(k/k-1)+W(k)[z(k)-H(k)x(k/k-1)]$.

Equation (1) says that our best estimates at t = k, using all observations up to and including k, is equal to our predicted estimate plus the error (difference) between what was observed and what we claim should have been observed multiplied by some weighting factor (W(k)). The key to this equation is indeed the weighting factor. It determines how much we will alter or change our estimate of the state based on the new observation. If the elements of the matrix W(k) are;

a. Small $\Rightarrow$ that we have considerable confidence in our model.

b. Large $\Rightarrow$ that we have considerable confidence in our observation measurements.

W(k) changes with time and hopefully always is optimum. It is highly dependent upon our characterization of the measurement noise (R(k)). If R(k) = I, the elements of W(k) strictly decrease in absolute value and represent the classical least squares approach.

*See section on derivations.

Our next problem is to correct the covariance matrix for the error in the state x(k/k). Again without proof we have that

(2) $P(k/k) = [I-W(k)H(k)]P(k/k-1)$

Our correction process would be complete if W(k) and H(k) were well defined. First, H(k) is deterministic and fixed (no problem). Secondly,

(3) $W(k) = P(k/k-1)H^T(k)[R(k)+H(k)P(k/k-1)H^T(k)]^{-1}$

The procedure will be complete if we can define methods for computing

a. $x(k+1/k)$

b. $P(k+1/k)$.

It follows from equation (1) that

(4) $x(k+1/k) = \phi(k+1,k)x(k/k)+u(k)$.

Let $\dot{x}(k/k)$ represent the first time derivative of x(k/k). Moreover, assume that the state vector can be expressed in terms of its components i.e.

$$x(k/k) = \begin{bmatrix} x_1(k/k) \\ x_2(k/k) \\ \cdot \\ \cdot \\ \cdot \\ x_p(k/k) \end{bmatrix}$$

It follows that

$$\dot{x}(k/k) = \begin{bmatrix} \dot{x}_1(k/k) \\ \dot{x}_2(k/k) \\ \cdot \\ \cdot \\ \cdot \\ \dot{x}_p(k/k) \end{bmatrix}$$

Let

$$F(x(k/k)) = \frac{\partial \dot{x}(k/k)}{\partial x(k/k)}$$

Then this will give a (pxp) matrix of the form

$$F(x(k/k))_{ij} = \frac{\partial \dot{x}_i(k/k)}{\partial x_j(k/k)}$$

and

$$\phi(k+1/k) = [I+F(\hat{x}(k/k))\Delta t]$$

also

$$P(k+1/k) = \phi(k+1/k)P(k/k)\phi^T(k+1/k)+\Gamma Q(k)\Gamma^T$$

where Q(k) is the covariance matrix of u(k) and

$$\Gamma = S_{ij} \qquad \begin{matrix} i = j & \Delta t \\ i \neq j & 0. \end{matrix}$$

Derivations of Optimal Estimation Equations

The General Problem

Consider a system whose state vector $x(k)$ is described by the linear state transition equation

$$x(k+1) = \phi(k+1,k)x(k)+u(k).$$

The state of the system is related to an observable quantity, $z(k)$ by

$$z(k) = H(k)x(k)+v(k).$$

We will assume that the vector $v(k)$ is a gaussian random process with mean zero and covariance matrix $R(k)$. The special case of interest is when $u(k)$ is non-random i.e. $E[u(k)] = u(k)$ and its covariance matrix $Q(k) = 0$.

We propose to show that the optimal estimate of $x(k+1)$ given all of the past observed quantities $z(k)$, $z(k-1)$, . . . $z(0)$ is

$$x(k+1/k) = \phi^*(k+1,k)x(k/k-1)+W(k)z(k)$$

where

$$\phi^*(k+1,k) = \phi(k+1,k)-W(k)H(k)$$

and

$$W(k) = \phi(k+1,k)P(k)H^T(k)[H(k)P(k)H^T(k)+R(k)]^{-1}.$$

1 Basic Properties

1.1 The underlying principle of the optimal estimation method is that of orthogonal projection.

1.2 Let $Z(k) = [z(k), z(k-1), . . . z(0)]$ be the linear manifold of observations. Then, the optimal estimates of the gaussian random variable $x(k+1)$ is the orthogonal projection of $x(k+1)$ on $Z(k)$.

1.3 Let $E[x(k+1)/Z(k)]$ be the expected value of $x(k+1)$ given $Z(k)$ and $x(k+1/k)$ be the orthogonal projection of $x(k+1)$ onto $Z(k)$, then

$$x(k+1/k) \equiv E(x(k+1)/Z(k))$$

1.4 Consider the subspace $Z(k-1) = [z(k-1), z(k-2), . . . z(0)]$. Then

$$z(k) = Z(k-1) + Y(k)$$

where every vector in Y(k) is orthogonal to Z(k-1). If $z(k) \epsilon Z(k-1)$, then Y(k) is empty.

1.5 The state vector x(k) is described by

$$x(k+1) = \phi(k+1,k)x(k)+u(k)$$

and the state is related to the observables by

$$z(k) = H(k)x(k) + v(k).$$

1.6 We say that $\tilde{z}(k/k-1) \epsilon Y(k)$ where

$$\tilde{z}(k/k-1) = z(k)-H(k)x(k/k-1)$$

1.7 The orthogonal projection of x(k+1) on the linear manifold Y(k) is

$$E[x(k+1)/Y(k)].$$

2. Derivations

Lemma I

$$\tilde{x}(k+1/k-1) = \phi(k+1,k)\tilde{x}(k/k-1)$$

where $\tilde{x}(k+1/k-1)$ is orthogonal to z(k).

Proof:

$$\tilde{x}(k+1/k-1) = x(k+1)-x(k+1/k-1)$$

$$\tilde{x}(k+1/k-1) = x(k+1)-E[x(k+1)/Z(k-1)].$$

From 1.5 we have

$$\tilde{x}(k+1/k-1) = x(k+1)-E[\phi(k+1,k)x(k)+u(k)/Z(k-1)]$$

$\phi(k+1,k)$ is deterministic, hence we have

$$\text{(I.a)} \quad \tilde{x}(k+1/k-1) = x(k+1)-\phi(k+1,k)E[x(k)/Z(k-1)]-E[u(k)/z(k-1)]$$

By definition

$$E[x(k)/Z(k-1)] = x(k/k-1).$$

We will assume that u(k) is non-random, hence we have

$$E[u(k)/Z(k-1)] = u(k).$$

(I.a) may be written as

$$\tilde{x}(k+1/k-1) = x(k+1)-\phi(k+1,k)x(k/k-1)-u(k).$$

Again from (1.5) we have

$$\tilde{x}(k+1/k-1) = \phi(k+1,k)x(k)+u(k)-\phi(k+1,k)x(k/k-1)-u(k)$$

$$\tilde{x}(k+1/k-1) = \phi(k+1,k)[x(k)-x(k/k-1)]$$

$$\tilde{x}(k+1/k-1) = \phi(k+1,k)\tilde{x}(k/k-1) \quad \text{Q.E.D.}$$

Lemma II

$$\tilde{z}(k/k-1) = H(k)\tilde{x}(k/k-1)+v(k)$$

Proof:

By definition we have that

$$\tilde{z}(k/k-1) = z(k)-H(k)x(k/k-1)$$

$$= H(k)x(k)+v(k)-H(k)x(k/k-1)$$

$$= H(k)[x(k)-x(k/k-1)]+v(k)$$

$$= H(k)\tilde{x}(k/k-1)+v(k). \quad \text{Q.E.D.}$$

Theorem I

$$W(k) = \phi(k+1,k)P(k)H^T(k)[H(k)P(k)H^T(k)+R(k)]^{-1}$$

Proof:

By statement (1.2), we know that

$$\tilde{x}(k+1/Y(k) = x(k+1)-E[x(k+1)/Y(k)]. \tag{1.1}$$

We also know that $\tilde{z}(k/k-1)$ lies completely in $Y(k)$ and $\tilde{x}(k+1/k-1)$ is orthogonal to $Y(k)$. Hence we have that

$$0^* = E[\{x(k+1)-E[x(k+1)/Y(k)]\}\tilde{y}^T(k/k-1)] \tag{1.2}$$

We define the optimal weighting filter $W(k)$ by the equation

$$W(k)\tilde{y}(k/k-1) \equiv E[x(k+1)/Y(k)] \tag{1.3}$$

Now (1.2) becomes

$$0 = E[\{x(k+1)-W(k)\tilde{y}(k/k-1)\}\tilde{y}^T(k/k-1)] \tag{1.4}$$

*Two random vectors a and b are orthogonal if $E[ab^1] = E[ba^1] = 0$.

$x(k+1)$ may be decomposed into two orthogonal components $x(k+1/k-1)\epsilon Z(k-1)$ and $\tilde{x}(k+1/k-1)$ which is orthogonal to $Z(k-1)$. From (1.4) we have

$$0 = E[x(k+1/k-1)\tilde{y}^T(k/k-1)+\tilde{x}(k+1/k-1)\tilde{y}^T(k/k-1)-W(k)\tilde{y}(k/k-1)\tilde{y}^T(k/k-1)] \quad (1.5)$$

It is obvious that

$$E[x(k+1/k-1)\tilde{y}^T(k/k-1)] = 0$$

Hence (1.5) becomes

$$0 = E[\tilde{x}(k+1/k-1)\tilde{y}^T(k/k-1)-W(k)\tilde{y}(k/k-1)\tilde{y}^T(k/k-1)]$$

By Lemma I, we have

$$0 = E[\{\phi(k+1,k)\tilde{x}(k/k-1)\}\tilde{y}(k/k-1)-W(k)\tilde{y}(k/k-1)\tilde{y}^T(k/k-1)]$$

Using Lemma II, we have

$$0 = E[\{\phi(k+1,k)\tilde{x}(k/k-1)\}\{H(k)\tilde{x}(k/k-1)+V(k)\}^T-W(k)\{H(k)\tilde{x}(k/k-1)+V(k)\}\{H(k)\tilde{x}(k/k-1)+V(k)\}^T] \quad (1.6)$$

Expanding (1.6) we have

$$0 = E[\phi(k+1,k)\tilde{x}(k/k-1)\tilde{x}^T(k/k-1)H^T(k)+\phi(k+1,k)\tilde{x}(k/k-1)V^T(k)-W(k)\{H(k)\tilde{x}(k/k-1)\tilde{x}^T(k/k-1)H^T(k)+H(k)\tilde{x}(k/k-1)V^1(k)+V(k)\tilde{x}^1(k/k-1)H^T(k)+V(k)V^T(k)\}] \quad (1.7)$$

We observe that

$$E[\tilde{x}(k/k-1)v^T(k)] = 0$$
$$E[v(k)\tilde{x}^T(k/k-1)] = 0 \qquad \text{because they are uncorrelated.}$$

Hence we have from (1.7) that

$$0 = \phi(k+1,k)E[\tilde{x}(k/k-1)\tilde{x}^T(k/k-1)]H^T(k)-W(k)H(k)E[\tilde{x}(k/k-1)\tilde{x}^1(k/k-1)]H^T(k)+E[v(k)v^T(k)]. \quad (1.8)$$

We know that $R(k) = E[v(k)v^T(k)]$ and we define $P(k) = E[\tilde{x}(k/k-1)\tilde{x}^T(k/k-1)]$. Then (1.8) becomes

$$0 = \phi(k+1,k)P(k)H^T(k)-W(k)[H(k)P(k)H^T(k)+R(k)]$$

or

$$W(k) = \phi(k+1,k)P(k)H^T(k)[H(k)P(k)H^T(k)+R(k)]^{-1}$$

It is of some interest to note that

1. $P(k)$ is the covariance matrix of the estimation error.

2. R(k) is the covariance matrix of the measurement error.

3. H(k) is the observation matrix.

4. $\phi(k+1,k)$ is the state transition matrix.

Theorem II

$$x(k+1/k) = \phi^*(k+1,k)x(k/k-1)+u(k)+W(k)z(k)$$

Proof:

By definition

$$x(k+1/k) \equiv E[x(k+1)Z(k)] \tag{2.1}$$

The vector x(k+1/k) may be decomposed into the sum of two orthogonal components, namely

$$x(k+1/k) \equiv E[x(k+1)/Z(k-1)]+E[x(k+1)/Y(k)] \tag{2.2}$$

The first term in (2.2) is simply x(k+1/k-1), hence

$$x(k+1/k) = x(k+1/k-1)+E[x(k+1/Y(k)]. \tag{2.3}$$

We now observe that

$$x(k+1/k-1) = \phi(k+1,k)x(k/k-1)+u(k)$$

And from equation (1.3) we have that

$$E[x(k+1)/Y(k)] = W(k)\tilde{y}(k/k-1)$$

Hence equation (2.3) becomes

$$x(k+1/k) = \phi(k+1,k)x(k/k-1)+u(k)+W(k)\tilde{y}(k/k-1) \tag{2.4}$$

We know that

$$\tilde{z}(k/k-1) = z(k)-H(k)x(k/k-1)$$

Hence (2.4) becomes

$$x(k+1/k) = \phi(k+1,k)x(k/k-1)+u(k)+W(k)[z(k)-H(k)x(k/k-1)] \tag{2.5}$$

We may rewrite (2.5) by factoring as

$$x(k+1/k) = [\phi(k+1,k)-W(k)H(k)]x(k/k-1)+u(k)+W(k)z(k)$$

But $\phi^*(k+1,k) = \phi(k+1,k)-W(k)H(k)$, hence we obtain

$$x(k+1/k) = \phi^*(k+1,k)x(k/k-1)+u(k)+W(k)z(k).$$

Theorem III

$$P(k+1) = \phi(k+1,k)P(k)\phi^T(k+1,k) - \phi(k+1,k)H^T(k)[H(k)P(k)H^1(k)+R(k)]^{-1}H(k)$$
$$P(k)\phi^T(k+1,k)$$

Proof:

By definition

$$P(k+1) = E[\tilde{x}(k+1/k)\tilde{x}^T(k+1/k)]$$

We know that

$$\tilde{x}(k+1/k) = x(k+1) - x(k+1/k)$$
$$= \phi(k+1,k)x(k) + u(x) - \phi(k+1,k)x(k/k-1) - u(k) - W(k)\tilde{z}(k/k-1)$$
$$= \phi(k+1,k)[x(k) - x(k/k-1)] - W(k)\tilde{z}(k/k-1)$$
$$= \phi(k+1,k)\tilde{x}(k/k-1) - W(k)\tilde{z}(k/k-1).$$

We observe that

$$\tilde{z}(k/k-1) = H(k)\tilde{x}(k/k-1) + v(k)$$

Hence we have that

$$\tilde{x}(k+1/k) = \phi(k+1,k)\tilde{x}(k/k-1) - W(k)[H(k)\tilde{x}(k/k-1) + v(k)]$$
$$= [\phi(k+1,k) - W(k)]\tilde{x}(k/k-1) - W(k)v(k)$$
$$= \phi^*(k+1,k)\tilde{x}(k/k-1) - W(k)v(k)$$

Substitution in the original equation yields

$$P(k+1) = E[(\phi^*(k+1,k)\tilde{x}(k/k-1) - W(k)v(k))(\tilde{x}^T(k/k-1)\phi^{*1}(k+1,k) - v^T(k)W^T(k))]$$
$$= E[\phi^*(k+1,k)\tilde{x}(k/k-1)\tilde{x}^T(k/k-1)\phi^{*T}(k+1,k)] - E[\phi^*(k+1,k)\tilde{x}(k/k-1)$$
$$v^T(k)W^T(k)] - E[W(k)v(k)\tilde{x}^T(k/k-1)\phi^{*T}(k+1,k)] + E[W(k)v(k)v^T(k)W^T(k)]$$

The second and third terms are equal to zero because they are not correlated. Moreover we observe that

$$R(k) = E[v(k)v^T(k)]$$

$$P(k) = E[\tilde{x}(k/k-1)\tilde{x}^T(k/k-1)]$$

Hence we have

$$P(k+1) = \phi^*(k+1,k)P(k)\phi^{*T}(k+1,k) + W(k)R(k)W^T(k)$$

For simplicity, we will drop the matrix arguments i.e.

$$P(k+1) = \phi^* P \phi^{*T} + WRW^T$$

First we observe that

$$\phi^{*T} = \phi^T \cdot H^T W^T.$$

Hence we now have

$$\begin{aligned} P(k+1) &= \phi^* P(\phi^T - H^T W^T) + WRW^T \\ &= \phi^* P \phi^T - \phi^* P H^T W^T + WRW^T \\ &= \phi^* P \phi^T - (\phi - WH) P H^T W^T + WRW^T \\ &= \phi^* P \phi^T - \phi P H^T W^T + WHP H^T W^T + WRW^T \\ &= \phi^* P \phi^T = \phi P H^T W^T + W(HPH^T + R) W^T. \end{aligned}$$

We recall that

$$W = \phi P H^T (HPH^T + R)^{-1}$$

Hence we have that

$$\begin{aligned} P(k+1) &= \phi^* P \phi^T - \phi P H^T W^T + \phi P H^T (HPH^T + R)^{-1} (HPH^T + R) W^T \\ &= \phi^* P \phi^T - \phi P H^T W^T + \phi P H^T W^T \\ &= \phi^* P \phi^T \\ &= (\phi - WH) P \phi^T \\ &= \phi P \phi^T - WHP \phi^T \\ &= \phi P \phi^T - \phi P H^T (HPH^T + R)^{-1} HP \phi^T \end{aligned}$$

Q.E.D.

Geodesy and Self Calibration Filter*

The problem that we are concerned with is that of transforming all radar tracking data to a common frame of reference without the utilization of calibration data obtained prior to the mission. In addition, we require that this transformation be optimum relative to the loss function for locally constant parameters which is used throughout this report.

In order to insure that the parameters that we intend to optimize are linearly independent, we utilize the following transformation representation:

$$(1)\quad \begin{bmatrix} x \\ y \\ z \end{bmatrix}_c = \begin{bmatrix} a_{11} & a_{12} & a_{13} & a_{14} \\ a_{21} & a_{22} & a_{23} & a_{24} \\ a_{31} & a_{32} & a_{33} & a_{34} \end{bmatrix}_i \begin{bmatrix} x_i \\ y_i \\ z_i \\ \Delta P_i \end{bmatrix}$$

where c represents the common frame of reference and the subscripts i(i = 1, 2, . . . n) represent the data from the various trackers. It should be obvious that the only equation utilized relative to the Kalman formulation of the recursive estimation method is

$$(2)\quad z(k) = H(k)x(k/k)+v(k) \qquad k = 1, 2, \ldots n.$$

It is well known that for locally constant parameters, the optimum x(k/k) where k = 1, 2, . . . n is given by

$$(3)\quad x(k/k) = (H^T(k)R^{-1}(k)H(k))^{-1}H^T(k)R^{-1}(k)z(k)$$

For our problem, we assume that at the beginning of the mission we have optimum estimates x(k/k). As the mission progresses, we obtain additional data and pose the question as to whether or not we may improve our optimum estimates x(k/k) by utilizing the additional data. Again it should be obvious that we will require x(k/k) plus some corrections $\Delta x(k+1/k+1)$ to be optimum relative to the enlarged set of observations. The mathematical structure of the problem is as follows:

$$(4)\quad \begin{bmatrix} z(k) \\ z(k+1) \end{bmatrix} = \begin{bmatrix} H(k) \\ H(k+1) \end{bmatrix} [x(k/k)+\Delta x(k+1/k+1)]$$

where

(a) z(k+1) represents the additional observations.

---

*See block diagram at the end of the Appendix.

(b) H(k+1) represents the new observation matrix (which in general will equal H(k)).

(c) $\Delta x(k+1/k+1)$ represents the optimum corrections to the optimum estimates based upon the additional information.

The loss function associated with representation (4) is as follows:

$$(5)\quad J = ||\Delta x(k+1/k+1)||^2_{H^T(k)R^{-1}(k)H(k)} + ||H(k+1)(x(k/k)+\Delta x(k+1/k+1) - z(k+1)||^2_{R^{-1}(k+1)}$$

Now setting $\frac{\partial J}{\partial \Delta x(k+1/k+1)} = 0$ we obtain

$$(6)\quad \Delta x(k+1/k+1) = (H^T(k)R^{-1}(k)H(k)+H^T(k+1)R^{-1}(k+1)H(k+1))^{-1} H^T(k+1)R^{-1}(k+1)(z(k+1)-H(k+1)x(k/k))$$

where

$$x(k/k) = \begin{bmatrix} a_{11} \\ a_{12} \\ a_{13} \\ a_{14} \\ a_{21} \\ a_{22} \\ a_{23} \\ a_{24} \\ a_{31} \\ a_{32} \\ a_{33} \\ a_{34} \end{bmatrix} \qquad H(k) = H(k+1) = \begin{bmatrix} x_i & y_i & z_i & \Delta P_i & 0 & 0 & 0 & 0 & 0 & 0 & 0 & 0 \\ 0 & 0 & 0 & 0 & x_i & y_i & z_i & \Delta P_i & 0 & 0 & 0 & 0 \\ 0 & 0 & 0 & 0 & 0 & 0 & 0 & 0 & x_i & y_i & z_i & \Delta P_i \end{bmatrix}$$

$$z_i(k+1) = \begin{bmatrix} x_i \\ y_i \\ z_i \end{bmatrix}$$

$$\Delta x(k+1/k+1)_{ij} = (\Delta a_{ij}) \qquad i = 1, 2, 3 \qquad j = 1, 2, 3, 4$$

And hence the new optimum estimates have the representation $(a_{ij} + \Delta a_{ij})$.

Equation (6) suggests a successive improvement scheme for determining the unknown $x(k+J/k+J)$ $(J \geq 1)$ as more and more observations are made.

If we define

$$(7) \quad (H^T(k)R^{-1}(k)H_k)^{-1} = P(k)$$

$$(H^T(k)R^{-1}(k)H(k)+H^T(k+1)R^{-1}(k+1)H(k+1))^{-1} = P(k+1)$$

Then

$$(8) \quad P^{-1}(k+1) = P^{-1}(k)+H^T(k+1)R^{-1}(k+1)H(k+1)$$

and

$$(9) \quad \Delta x(k+1/k+1) = P(k+1)H^T(k+1)R^{-1}(k+1)(z(k+1)-H(k+1)x(k/k))$$

are the desired recursion formulas. Equation (9) has one major drawback - the inversion of the nxn matrix P(k+1) must be carried out at every stage. In order to circumvent this difficulty, we make use of Householder's (Penrose) matrix inversion lemma.

Lemma: If $P^{-1}(k+1) = P^{-1}(k)+H^T(k+1)R^{-1}(k+1)H(k+1)$

where P(k) and R(k) are positive definite, symmetric, and nonsingular, then P(k+1) exists and is given by

$$(10) \quad P(k+1) = P(k)-P(k)H^T(k+1)(H(k+1)P(k)H^T(k+1)+R(k+1))^{-1}H(k+1)P(k)$$

Equation (10) can take the place of equation (8). The matrix $(H(k+1)P(k)H^T(k+1)+R(k+1))$ is of dimension rxn where r is the number of new observations. Since we are at liberty to process new data either singly or a group at a time, we simply take r equal to one. Hence, the matrix inversion problem has been completely eliminated in the stagewise (recursion) correction scheme.

OPTIMIZATION OF INSTRUMENT GEODESY (KALMAN FILTER)

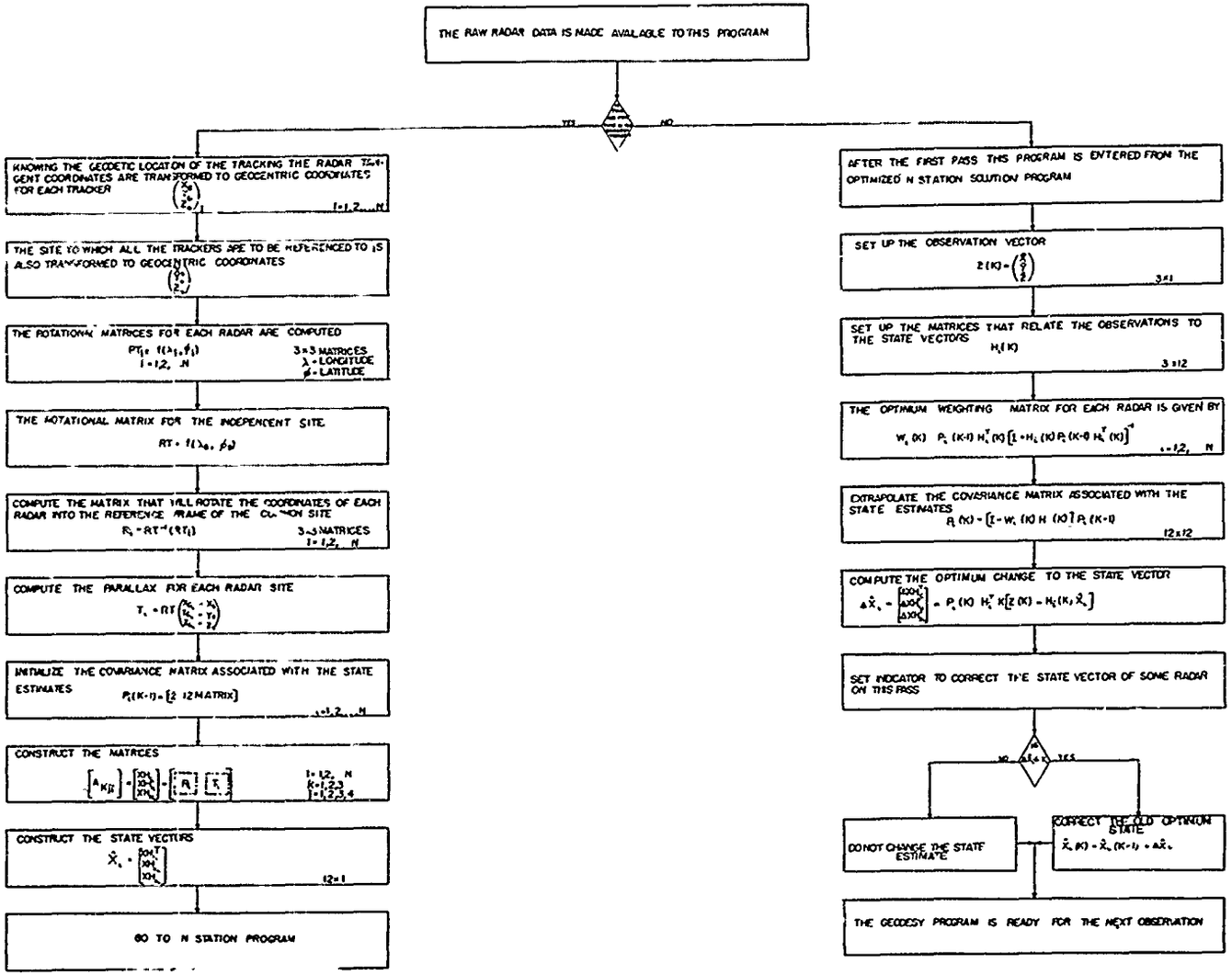

Derivation of the Best Estimate of The Trajectory Via the Use of Measurement Data*

Let us assume that at each sampling time t = k, n instruments (radars) record the approximate position $[R_j^R(k), A_j^R(k), E_j^R(k)]$ $j = 1, 2, \ldots n$ of a vehicle in space. Let us further assume that by some optimum process,** the position data can be transformed to a common rectangular Cartesian Coordinate System. At time t = k, let

$$Z_j(k) = \begin{bmatrix} x_j(k) \\ y_j(k) \\ z_j(k) \end{bmatrix} \qquad j = 1, 2, \ldots n \tag{1}$$

represent the available data. Finally, assume that the covariance matrix $R_j(k)$ for each radar is known.*** The covariance matrices are of the form

$$R_j(k) = \begin{bmatrix} \sigma_x^2 & \sigma_{xy} & \sigma_{xz} \\ \sigma_{xy} & \sigma_y^2 & \sigma_{yz} \\ \sigma_{xz} & \sigma_{yz} & \sigma_z^2 \end{bmatrix} \tag{2}$$

Now consider the observation equation developed in Appendix B i.e.

$$Z(k) = H(k)X(k)+V(k) \tag{3}$$

Since we have n such relations (one for each radar), the equation of interest must be of the form

$$Z_j(k) = H_j(k)X_j(k)+V_j(k) \qquad j = 1, 2, \ldots n \tag{4}$$

---

*See flow diagram at the end of the Appendix.

**See Appendix F for the Derivation.

***A method for approximating $R_j(k)$ is contained in the next section of this Appendix.

In matrix notation (4) would have the following form

$$\begin{bmatrix} x_j(k) \\ y_j(k) \\ z_j(k) \end{bmatrix} = \begin{bmatrix} 1 & 0 & 0 \\ 0 & 1 & 0 \\ 0 & 0 & 1 \end{bmatrix} \begin{bmatrix} x(k) \\ y(k) \\ z(k) \end{bmatrix} + \begin{bmatrix} \Delta x_j(k) \\ \Delta y_j(k) \\ \Delta z_j(k) \end{bmatrix} \tag{5}$$

where

$x_j(k)$, $y_j(k)$, $z_j(k)$ represent the n observations

$\Delta x_j(k)$, $\Delta y_j(k)$, $\Delta z_j(k)$ represent the n measurement errors

$x(k)$, $y(k)$, $z(k)$ represent the best estimate of the trajectory point

and $H_j(k)$ is equal to the identity matrix because all of the observations are expressed in a common frame of reference.

Using the notation of equation (4) and remembering that $H_j(k)$ is equal to the identity matrix for all j and k, we define our best estimate of the trajectory by the following loss function:

$$J = \sum_{j=1}^{n} [(z_j(k)-X(k))^T R_j^{-1}(k)(z_j(k)-X(k))] \tag{6a}$$

or

$$J = \sum_{j=1}^{n} \left[\begin{bmatrix} x_j(k) \\ y_j(k) \\ z_j(k) \end{bmatrix} - \begin{bmatrix} x(k) \\ y(k) \\ z(k) \end{bmatrix} \right]^T \begin{bmatrix} \sigma^2_{x_j} & \sigma_{xy_j} & \sigma_{xz_j} \\ \sigma_{xy_j} & \sigma^2_{y_j} & \sigma_{yz_j} \\ \sigma_{xz_j} & \sigma_{yz_j} & \sigma^2_{z_j} \end{bmatrix}^{-1} \left[\begin{bmatrix} x_j(k) \\ y_j(k) \\ z_j(k) \end{bmatrix} - \begin{bmatrix} x(k) \\ y(k) \\ z(k) \end{bmatrix} \right] \tag{6b}$$

Our best estimate $\begin{bmatrix} x(k) \\ y(k) \\ z(k) \end{bmatrix}$ is optimum when J is a minimum. A necessary and sufficient condition for J to be a minimum is for $\frac{\partial J}{\partial X(k)} = 0$.

Performing the latter operation utilizing equation (6a) we obtain

$$(\sum_{j=1}^{n} R_j^{-1}(k))^{-1} X(k) = \sum_{j=1}^{n} R_j^{-1}(k) Z_j(k) \tag{7a}$$

or

$$X(k) = (\sum_{j=1}^{n} R_j^{-1}(k))^{-1} \sum_{j=1}^{n} R_j^{-1} Z_j(k) \tag{7b}$$

(7b) may be written as

$$\begin{bmatrix} x(k) \\ y(k) \\ z(k) \end{bmatrix} = \left[\sum_{j=1}^{n} R_j^{-1}(k)\right]^{-1} \sum_{j=1}^{n} R_j^{-1}(k) \begin{bmatrix} x_j(k) \\ y_j(k) \\ z_j(k) \end{bmatrix} \tag{8}$$

It should be observed that if $R_j(k)$ is the same for all j, then (8) reduces to a simple arithmetic average of the measurement data.

Derivation of $R_j(k)$.

At each sampling time, t = k, the dynamic filter provides optimum predicted estimates of what the instruments should measure. Hence, for each radar, we consider the deviation in R, A, E (from the predicted) for t = k, (k-1), (k-2), (k-3), (k-4). This information allows us to approximate a σ_R, σ_A, and σ_E for each radar. If one assumes that the measurement errors are independent, in radar coordinates the covariance matrix would be of the form

$$\begin{bmatrix} \sigma_R^2 & 0 & 0 \\ 0 & \sigma_A^2 & 0 \\ 0 & 0 & \sigma_E^2 \end{bmatrix}$$

Our problem is to derive the covariance matrix of the noise associated with $Z_j(k)$, given the covariance matrix of the radar measurement noise as follows:

$$V_j(k) = \begin{bmatrix} \Delta R_j \\ \Delta A_j \\ \Delta E_j \end{bmatrix}$$

We know that

$$x = R\cos(E)\sin$$

$$y = R\cos(E)\cos$$

$$z = R\sin(E)$$

If the deviations (ΔR_j, ΔA_j, ΔE_j) are small compared to the values R, A, and E then

$$\begin{bmatrix} \Delta X \\ \Delta Y \\ \Delta Z \end{bmatrix} = \begin{bmatrix} \frac{\partial X}{\partial(\Delta R_j)} & \frac{\partial X}{\partial(\Delta A_j)} & \frac{\partial X}{\partial(\Delta E_j)} \\ \frac{\partial Y}{\partial(\Delta R_j)} & \frac{\partial Y}{\partial(\Delta A_j)} & \frac{\partial Y}{\partial(\Delta E_j)} \\ \frac{\partial Z}{\partial(\Delta R_j)} & \frac{\partial Z}{\partial(\Delta A_j)} & \frac{\partial Z}{\partial(\Delta E_j)} \end{bmatrix} \begin{bmatrix} \Delta R_j \\ \Delta A_j \\ \Delta E_j \end{bmatrix}$$

or

$$\begin{bmatrix} \Delta X \\ \Delta Y \\ \Delta Z \end{bmatrix} = T \begin{bmatrix} \Delta R_j \\ \Delta A_j \\ \Delta E_j \end{bmatrix}$$

If the covariance matrix of the errors in radar measurements, denoted $\bar{R}_j(k)$ is given by

$$\bar{R}_j(k) = \begin{bmatrix} \sigma^2_{R_j} & 0 & 0 \\ 0 & \sigma^2_{A_j} & 0 \\ 0 & 0 & \sigma^2_{E_j} \end{bmatrix}$$

where

$\sigma^2_{R_j}$ = variance of noise in range measurement for the $j^{\underline{th}}$ radar

$\sigma^2_{A_j}$ = variance of noise in azimuth measurement for the $j^{\underline{th}}$ radar

$\sigma^2_{E_j}$ = variance of noise in elevation measurement for the $j^{\underline{th}}$ radar

Then, provided that the measurement errors ΔR_j, ΔA_j, and ΔE_j are small compared to the actual values of R, A, and E, the desired covariance matrix $R_j(k)$ is determined as

$$R_j(k) = E\left[\left[T\begin{pmatrix}\Delta R_j\\ \Delta A_j\\ \Delta E_j\end{pmatrix}\right]\left[T\begin{pmatrix}\Delta R_j\\ \Delta A_j\\ \Delta E_j\end{pmatrix}\right]^T\right] \qquad (1)$$

If we let

$$\Delta_j = \begin{bmatrix}\Delta R_j\\ \Delta A_j\\ \Delta E_j\end{bmatrix}$$

Then, manipulating equation (1) we have

$$\begin{aligned} R_j(k) &= E[T\Delta_j(T\Delta_j)^T] \\ &= E[T\Delta_j\Delta_j^T T^T] \\ &= TE[\Delta_j\Delta_j^T]T^T \\ &= T\bar{R}_j(k)\ T \end{aligned}$$

OPTIMIZED N-STATION SOLUTION (KALMAN FILTER)

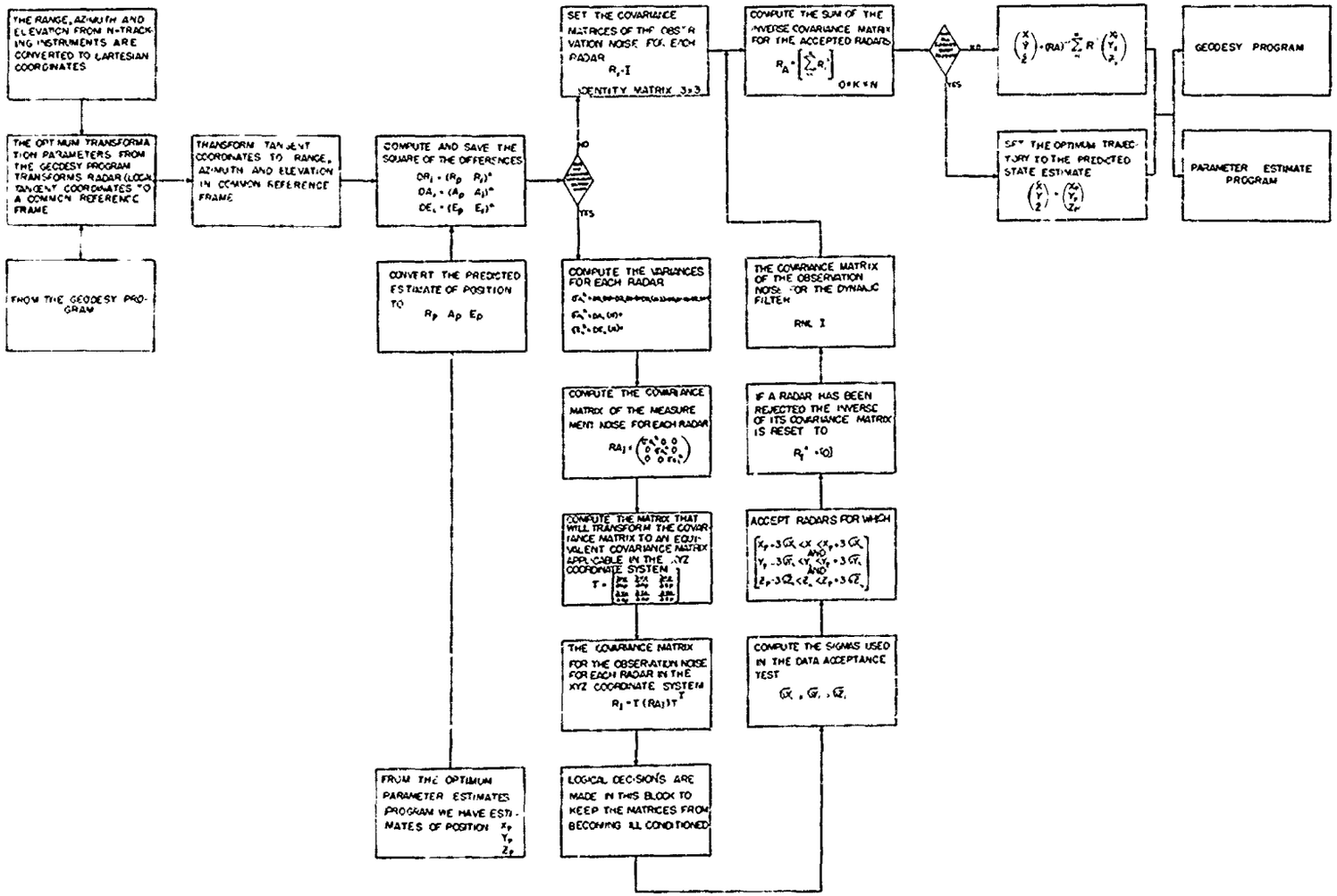

Dynamic Filter for the Generation of Optimum Trajectory Parameters*

Characteristic to any system of measurements are errors in the measuring devices. The radars used in missile tracking contain errors of this type. For some time, the Processing Sciences Division of the Analysis and Computation Directorate has been concerned with the study of how to better approximate the data associated with a radar signal which is corrupted with noise. Hence, we seek to develop a digital filter which will correct for the errors in these measurements. Furthermore, we would like for the filter to yield optimum estimates of the missile's trajectory, in particular, the rectangular cartesian coordinates of position, velocity and acceleration.

The structure of the filter which we will develop is completely compatible with the Kalman-Bucy filter described in Appendix (B). Thus, our filter will be a recursive filter and it will be optimum in the sense defined in Appendix (B).

Figure (1) illustrates the general approach utilized by the Kalman-Bucy filter. It is this approach which we will use in approximating the solution to our problem.

In this Appendix we are concerned mainly with illustrating how we applied the methods of Appendix (B). We will also present the mathematical structure and computational procedure of the filter, and render physical interpretation to pertinent mathematical expressions. For the sake of clarity and communication between appendices we will use the same notation in our mathematical expressions; hence the definitions given on pages (3) and (4) of Appendix (B) will also apply in this section.

In constructing our filter we assume the only real-time observations (measurements) made are radar position data (R, A, E). We will attempt to construct the simplest filter which will generate the desired optimal estimates of the trajectory.

From Appendix (B), we know there are certain steps that we must follow. For convenience we will summarize these steps.

(1) We start by assuming we know what the state of the system will be at time = k, denoted in vector form by x(k/k-1) and the covariance matrix P(k/k-1).

(2) Make an observation (R^r, A^r, E^r) denoted in vector form yz(k) with associated covariance R(k).

(3) Correct the state of the system x(k/k) and its covariance matrix P(k/k).

---

*See Flow Diagram at the end of the Appendix.

(4) Propagate the state estimate and covariance matrix to time t = k+1 to obtain x(k+1/k) and P(k+1/k).

(5) We return to step (1), advance time and await our next measurement.

Specifically, our problem may be defined as follows:

(1) Construct a mathematical model which will allow us to propagate the state of the system from time k to k+1.

(2) Construct the deterministic matrices utilized by the Kalman-Bucy filter.

PROBLEM FORMULATION

We will now apply the general equations of Appendix (B) to the specific problem of interest. Let (x, y, z) represent the rectangular cartesian position coordinates of the vehicle being tracked and ($\dot{x}$, $\dot{y}$, $\dot{z}$) the respective first time derivatives of the position coordinates. Let A_t represent the acceleration or deceleration of the missile acting along the velocity vector.

We represent the state of the system x(k) as a (7x1) matrix or state vector having components x_i where i = 1, 2, . . . 7. Furthermore we claim that x(k) may be represented as follows:

$$x(k) = \begin{bmatrix} x_1 \\ x_2 \\ x_3 \\ x_4 \\ x_5 \\ x_6 \\ x_7 \end{bmatrix} = \begin{bmatrix} x \\ y \\ z \\ \dot{x} \\ \dot{y} \\ \dot{z} \\ A_t \end{bmatrix}$$

Now, assume that we have at time = k a predicted value x(k/k-1) and its covariance matrix P(k/k-1) for the state of the system x(k).

From Appendix (B) we have the mathematical tools which we need to construct our filter. We know that at time = k the equations below will correct the state of the system x(k/k) and the covariance matrix P(k/k).

(1) $x(k/k) = x(k/k-1)+W(k)[z(k)-H(k)x(k/k-1)]$

(2) $P(k/k) = [I-W(k)H(k)]P(k/k-1)$

where

(3) $W(k) = P(k/k-1)H^T(k)[R(k)+H(k)P(k/k-1)H^T(k)]^{-1}$

We also know that we can predict what the state of the system should be at time k+1 and the covariance matrix associated with errors in this prediction via the equations.

(4) $x(k+1/k) = \phi(k+1,k)x(k/k)+B(k)u(k)$

(5) $P(k+1/k) = \phi(k+1,k)P(k/k)\phi^T(k+1,k)+\Gamma Q(k)\Gamma^T$

At time = k we receive a measurement R^r, A^r, E^r from the tracker (radar). These three measurements define the observation vector with components (R^r, A^r, E^r). In state vector form

$$z(k) = \begin{bmatrix} R^r \\ A^r \\ E^r \end{bmatrix} \qquad (3x1)$$

However for our filter we prefer to utilize the observation data in rectangular coordinates. Hence for filter utilization, we define z(k) to be of the form

$$z(k) = \begin{bmatrix} x \\ y \\ z \end{bmatrix}$$

where

$x = R^r\cos(E^r)\sin(A^r)$

$y = R^r\cos(E^r)\cos(A^r)$

$z = R^r\sin(E^r)$

Before we can correct the state of the system through equation (1) above, we need to define and construct several matrices. We note that equation (1) calls for a matrix H(k).

Appendix (B) defines the equation

$z(k) = H(k)x(k)+V(k)$

From this equation we see that H(k) must be a matrix which relates the state of the system to what is being observed. Hence, we have that

$$\begin{bmatrix} x \\ y \\ z \end{bmatrix} = H(k) \begin{bmatrix} x \\ y \\ z \\ \dot{x} \\ \dot{y} \\ \dot{z} \\ \Lambda_t \end{bmatrix} + V(k)$$

This implies that H(k) is a 3x7 matrix of the form

$$H(k) = \begin{bmatrix} 1 & 0 & 0 & 0 & 0 & 0 & 0 \\ 0 & 1 & 0 & 0 & 0 & 0 & 0 \\ 0 & 0 & 1 & 0 & 0 & 0 & 0 \end{bmatrix}$$

for all k i.e. it is independent of time.

We also need the so-called optimum weighting matrix W(k) in equation (1). W(k) is given by equation (3) that we need only to define and construct the matrix R(k) which will allow us to compute W(k) and in turn correct the state estimate through equation (1).

From the relation equation

$$z(k) = H(k)x(k)+V(k)$$

we note that V(k) is a (3x1) vector. It is the vector associated with the observation noise of the tracker i.e. for each k there exists an error in the tracking data, namely

$$V(k) = \begin{bmatrix} \Delta R(k) \\ \Delta A(k) \\ \Delta E(k) \end{bmatrix}$$

We will assume that the (arithmetic mean of V(k)) expected value (E[V(k)]) is equal to zero and that the errors are independent. The covariance matrix of V(k) is defined as follows:

$$E[V(k)V(k)^T] = \begin{bmatrix} \sigma_R^2 & 0 & 0 \\ 0 & \sigma_A^2 & 0 \\ 0 & 0 & \sigma_E^2 \end{bmatrix}$$

Hence we are assuming that the observation noise has the following character:

1. The component are statistically independent.
2. The expected value equals zero.
3. The noise is Gaussian
4. The noise is white i.e. uncorrelated.

The characterization of the observation noise i.e. the construction of its covariance matrix would be complete of it was expressed in the (x, y, z) reference frame.

We know that

$x = R^r\cos(E^r)\sin(A^r)$.

$y = R^r\cos(E^r)\cos(A^r)$.

$z = R^r\sin(E^r)$,

If the deviations (ΔR, ΔA, ΔE) from the trajectory are small compared to the values of R^r, A^r, and E^r, then

$$\begin{bmatrix} \Delta x \\ \Delta y \\ \Delta z \end{bmatrix} = \begin{bmatrix} \frac{\partial x}{\partial(\Delta R)} & \frac{\partial x}{\partial(\Delta A)} & \frac{\partial x}{\partial(\Delta E)} \\ \frac{\partial y}{\partial(\Delta R)} & \frac{\partial y}{\partial(\Delta A)} & \frac{\partial y}{\partial(\Delta E)} \\ \frac{\partial z}{\partial(\Delta R)} & \frac{\partial z}{\partial(\Delta A)} & \frac{\partial z}{\partial(\Delta E)} \end{bmatrix} \begin{bmatrix} \Delta R \\ \Delta A \\ \Delta E \end{bmatrix}$$

or

$$\begin{bmatrix} \Delta x \\ \Delta y \\ \Delta z \end{bmatrix} = \tilde{T} \begin{bmatrix} \Delta R \\ \Delta A \\ \Delta E \end{bmatrix}$$

$\tilde{T}$ may be evaluated using (1), hence we have that

$$\tilde{T} = \begin{bmatrix} \cos(E^r)\sin(A^r) & R\cos(E^r)\cos(A^r) & -R\sin(E^r)\sin(A^r) \\ \cos(E^r)\sin(A^r) & -R\cos(E^r)\sin(A^r) & -R\sin(E^r)\sin(A^r) \\ \sin(E^r) & 0 & R\cos(E^r) \end{bmatrix}$$

It can be shown that the desired covariance matrix (R(k) on the x, y, z level) is given by

$$R(k) = \tilde{T} \begin{bmatrix} \sigma_R^2 & 0 & 0 \\ 0 & \sigma_A^2 & 0 \\ 0 & 0 & \sigma_E^2 \end{bmatrix} \tilde{T}^T.$$

$\hat{x}(k/k-1)$ represent our best estimate of

$$\begin{bmatrix} x \\ y \\ z \\ \dot{x} \\ \dot{y} \\ \dot{z} \\ A_t \end{bmatrix}$$

at time t = k based on all observations up to and including time t = k-1. These are our best predicted estimates. Initial values must be furnished. If the radar begins tracking when the vehicle is on the launcher and if the (x_L, y_L, z_L) position of the launcher with respect to the radar is known, then a suitable set of initial conditions would be

$$x(k/k-1) = \begin{bmatrix} x_L \\ y_L \\ z_L \\ 0 \\ 0 \\ 0 \\ 0 \end{bmatrix}$$

$\hat{x}(k/k)$ represents our (best) optimum estimates of

$$\begin{bmatrix} x \\ y \\ z \\ \dot{x} \\ \dot{y} \\ \dot{z} \\ A_t \end{bmatrix}$$

At time t = k based on all observations up to and including time t = k. This is the output we seek from our filter. No initialization is required on the part of the user.

P(k/k-1) is actually the covariance matrix of the error associated with $\hat{x}(k/k-1)$. This matrix must be initialized i.e. P(1/0) must be defined. A representative set of values is as follows

$$P(k/k-1) = \begin{bmatrix} 5000 & 0 & 0 & 0 & 0 & 0 & 0 \\ 0 & 5000 & 0 & 0 & 0 & 0 & 0 \\ 0 & 0 & 5000 & 0 & 0 & 0 & 0 \\ 0 & 0 & 0 & 2000 & 0 & 0 & 0 \\ 0 & 0 & 0 & 0 & 2000 & 0 & 0 \\ 0 & 0 & 0 & 0 & 0 & 2000 & 0 \\ 0 & 0 & 0 & 0 & 0 & 0 & 750 \end{bmatrix}$$

It is acceptable to assume that the errors associated with our initial estimates are independent and the magnitude of the variances are given by the above numbers. It should be noted that the filter is highly insensitive to the initial values of this matrix. P(k/k) is the covariance matrix of the error associated with our optimum estimate of the state $\hat{x}(k/k)$.

The single most important quantity associated with the filter is the so-called optimum weighting matrix (W(k)). For each observation, we have an estimate of what the observation should be. The difference between the estimate and observation defines the error signal. The matrix W(k) then utilized this error signal and our predicted estimate $\hat{x}(k/k-1)$ to compute the optimum estimate $\ddot{x}(k/k)$. Hence it is obvious that maximum care must be given in the indirect construction of W(k). This completes our correction problem.

The procedure will be complete if we define and construct the matrices needed in the equations.

(4) $x(k+1/k) = \phi(k+1,k)x(k/k)+B(k)u(k)$

(5) $P(k+1/k) = \phi(k+1,k)P(k/k)\phi^{T}(k+1,k)+rQ(k)r^{T}$

Our immediate task is to construct the transition matrix $\phi(k+1,k)$ which will propagate the state from time k to k+1. We make use of the following basic equations of motion in constructing $\phi(k+1,k)$.

(6) $\ddot{x} = T(\dot{x}/V)$

(7) $\ddot{y} = T(\dot{y}/V)$

(8) $\ddot{z} = T(\dot{z}/V)-G$

where x, y, z are the cartesian coordinates of missile position.

G = gravitational acceleration

$V = \sqrt{\dot{x}^2+\dot{y}^2+\dot{z}^2}$

T = represents the acceleration or deceleration of the missile acting along the velocity vector.

From Appendix (B) we have that

$\phi(k+1,k) = [I+F(\hat{x}(k/k))\Delta t]$

where

$$I = \begin{bmatrix} 1 & 0 & 0 & 0 & 0 & 0 & 0 \\ 0 & 1 & 0 & 0 & 0 & 0 & 0 \\ 0 & 0 & 1 & 0 & 0 & 0 & 0 \\ 0 & 0 & 0 & 1 & 0 & 0 & 0 \\ 0 & 0 & 0 & 0 & 1 & 0 & 0 \\ 0 & 0 & 0 & 0 & 0 & 1 & 0 \\ 0 & 0 & 0 & 0 & 0 & 0 & 1 \end{bmatrix}$$

Previously we expressed the state vector in terms of its components. It had the form

$$\hat{x}(k/k) = \begin{bmatrix} x_1(k/k) \\ x_2(k/k) \\ x_3(k/k) \\ x_4(k/k) \\ x_5(k/k) \\ x_6(k/k) \\ x_7(k/k) \end{bmatrix}$$

It follows that the first time derivative $\dot{\hat{x}}(k/k)$ of $\hat{x}(k/k)$ can be expressed as

$$\dot{\hat{x}}(k/k) \begin{bmatrix} \dot{x}_1 \\ \dot{x}_2 \\ \dot{x}_3 \\ \dot{x}_4 \\ \dot{x}_5 \\ \dot{x}_6 \\ \dot{x}_7 \end{bmatrix} = \begin{bmatrix} x_4(k/k) \\ x_5(k/k) \\ x_6(k/k) \\ [x_7(k/k)][x_4(k/k)]/V(k) \\ [x_7(k/k)][x_5(k/k)]/V(k) \\ [x_7(k/k)][x_6(k/k)]/V(k) \\ 0. \end{bmatrix}$$

where

$$V(k) = \sqrt{[x_4(k/k)]^2+[x_5(k/k)]^2+[x_6(k/k)]^2}$$

Hence for our problem, using the definition F(x(k/k)) in Appendix (B) we have

$$F(x(k/k))_{ij} = \begin{bmatrix} \frac{\partial \dot{x}_1}{\partial x_1} & \frac{\partial \dot{x}_2}{\partial x_1} & \frac{\partial \dot{x}_3}{\partial x_1} & \frac{\partial \dot{x}_4}{\partial x_1} & \frac{\partial \dot{x}_5}{\partial x_1} & \frac{\partial \dot{x}_6}{\partial x_1} & \frac{\partial \dot{x}_7}{\partial x_1} \\ \frac{\partial \dot{x}_1}{\partial x_2} & \frac{\partial \dot{x}_2}{\partial x_2} & \frac{\partial \dot{x}_3}{\partial x_2} & \frac{\partial \dot{x}_4}{\partial x_2} & \frac{\partial \dot{x}_5}{\partial x_2} & \frac{\partial \dot{x}_6}{\partial x_2} & \frac{\partial \dot{x}_7}{\partial x_2} \\ \frac{\partial \dot{x}_1}{\partial x_3} & \frac{\partial \dot{x}_2}{\partial x_3} & \frac{\partial \dot{x}_3}{\partial x_3} & \frac{\partial \dot{x}_4}{\partial x_3} & \frac{\partial \dot{x}_5}{\partial x_3} & \frac{\partial \dot{x}_6}{\partial x_3} & \frac{\partial \dot{x}_7}{\partial x_3} \\ \frac{\partial \dot{x}_1}{\partial x_4} & \frac{\partial \dot{x}_2}{\partial x_4} & \frac{\partial \dot{x}_3}{\partial x_4} & \frac{\partial \dot{x}_4}{\partial x_4} & \frac{\partial \dot{x}_5}{\partial x_4} & \frac{\partial \dot{x}_6}{\partial x_4} & \frac{\partial \dot{x}_7}{\partial x_4} \\ \frac{\partial \dot{x}_1}{\partial x_5} & \frac{\partial \dot{x}_2}{\partial x_5} & \frac{\partial \dot{x}_3}{\partial x_5} & \frac{\partial \dot{x}_4}{\partial x_5} & \frac{\partial \dot{x}_5}{\partial x_5} & \frac{\partial \dot{x}_6}{\partial x_5} & \frac{\partial \dot{x}_7}{\partial x_5} \\ \frac{\partial \dot{x}_1}{\partial x_6} & \frac{\partial \dot{x}_2}{\partial x_6} & \frac{\partial \dot{x}_3}{\partial x_6} & \frac{\partial \dot{x}_4}{\partial x_6} & \frac{\partial \dot{x}_5}{\partial x_6} & \frac{\partial \dot{x}_6}{\partial x_6} & \frac{\partial \dot{x}_7}{\partial x_6} \\ \frac{\partial \dot{x}_1}{\partial x_7} & \frac{\partial \dot{x}_2}{\partial x_7} & \frac{\partial \dot{x}_3}{\partial x_7} & \frac{\partial \dot{x}_4}{\partial x_7} & \frac{\partial \dot{x}_5}{\partial x_7} & \frac{\partial \dot{x}_6}{\partial x_7} & \frac{\partial \dot{x}_7}{\partial x_7} \end{bmatrix}$$

$j=1,2,\ldots 7$

$i=1,2,\ldots 7$

therefore

$$F = \begin{bmatrix} 0 & 0 & 0 & 1 & 0 & 0 & 0 \\ 0 & 0 & 0 & 0 & 1 & 0 & 0 \\ 0 & 0 & 0 & 0 & 0 & 1 & 0 \\ 0 & 0 & 0 & x_7(V^2-x_4^2)/V^3 & -x_7x_4x_5/V^3 & -x_7x_4x_6/V^3 & x_4/V \\ 0 & 0 & 0 & -x_7x_4x_5/V^3 & x_7(V^2-x_5^2)/V^3 & -x_7x_5x_6/V^3 & x_5/V \\ 0 & 0 & 0 & -x_7x_4x_6/V^3 & -x_7x_5x_6/V^3 & x_7(V^2-x_6^2)/V^3 & x_6/V \\ 0 & 0 & 0 & 0 & 0 & 0 & 0 \end{bmatrix}$$

and Δt is the sampling interval. Hence $\phi(k+1/k)$ becomes

$$\phi(k+1,k) = \begin{bmatrix} 1 & 0 & 0 & \Delta t & 0 & 0 & 0 \\ 0 & 1 & 0 & 0 & \Delta t & 0 & 0 \\ 0 & 0 & 1 & 0 & 0 & \Delta t & 0 \\ 0 & 0 & 0 & 1+F(x(k/k))_{44}\Delta t & F(x(k/k))_{45}\Delta t & F(x(k/k))_{46}\Delta t & 0 \\ 0 & 0 & 0 & F(x(k/k))_{54}\Delta t & 1+F(x(k/k))_{55}\Delta t & F(x(k/k))_{56}\Delta t & 0 \\ 0 & 0 & 0 & F(x(k/k))_{64}\Delta t & F(x(k/k))_{65}\Delta t & 1+F(x(k/k))_{66}\Delta t & 0 \\ 0 & 0 & 0 & 0 & 0 & 0 & 1 \end{bmatrix}$$

We let $u(k) = T$, which represents our estimate of tangential acceleration, and only requires an initial value since it is a component of the state vector.

Since B(k) is deterministic and must properly project T onto $\hat{x}(k)$, we define it as a (7x1) matrix having the following form:

$$B(k) = \begin{bmatrix} \frac{\Delta t^2}{2} & \frac{x_4}{V(k)} \\ \frac{\Delta t^2}{2} & \frac{x_5}{V(k)} \\ \frac{\Delta t^2}{2} & \frac{x_6}{V(k)} \\ \Delta t & \frac{x_4}{V(k)} \\ \Delta t & \frac{x_5}{V(k)} \\ \Delta t & \frac{x_6}{V(k)} \\ 0 & \end{bmatrix}$$

Finally we need to compute P(k+1/k). Again since

$$P(k+1/k) = \phi(k+1)P(k/k)\phi^T(k+1/k) = \Gamma Q(k)\Gamma^T$$

we define two additional matrices which are independent of time. Γ a (7x7) matrix defined as the random forcing function distribution matrix.

$$\Gamma = \begin{bmatrix} \Delta t & 0 & 0 & 0 & 0 & 0 & 0 \\ 0 & \Delta t & 0 & 0 & 0 & 0 & 0 \\ 0 & 0 & \Delta t & 0 & 0 & 0 & 0 \\ 0 & 0 & 0 & \Delta t & 0 & 0 & 0 \\ 0 & 0 & 0 & 0 & \Delta t & 0 & 0 \\ 0 & 0 & 0 & 0 & 0 & \Delta t & 0 \\ 0 & 0 & 0 & 0 & 0 & 0 & \Delta t \end{bmatrix}$$

and Q(k) which is the covariance matrix of random forcing function

$$Q(k) = \begin{bmatrix} 500 & 0 & 0 & 0 & 0 & 0 & 0 \\ 0 & 500 & 0 & 0 & 0 & 0 & 0 \\ 0 & 0 & 500 & 0 & 0 & 0 & 0 \\ 0 & 0 & 0 & 500 & 0 & 0 & 0 \\ 0 & 0 & 0 & 0 & 500 & 0 & 0 \\ 0 & 0 & 0 & 0 & 0 & 500 & 0 \\ 0 & 0 & 0 & 0 & 0 & 0 & 500 \end{bmatrix}$$

This latter matrix may also be changed depending upon known characteristics of the system. The Q(k) matrix allows us to determine the maximum amount of confidence we will place in our optimum estimates $\hat{x}(k/k)$, since P(k/k) is the covariance matrix of the error associated with our optimum estimates. Q(k) states that I will always assume that at least this much error exists in the optimum estimates. Q(k) may be changed at the discretion of the user. Hence we have

$$P(k+1/k) = \phi(k+1,k)P(k/k)\phi^{T}(k+1,k)+\Gamma Q(k)\Gamma^{T}$$

which completes the recursive estimation method.

It is obvious that P(k+1/k) replaces P(k/k-1), x(k/k-1) is replaced by x(k+1/k) and we begin the computations again starting with equation (1). Finally, only the numbered equations are utilized by the filter.

OPTIMUM TRAJECTORY PARAMETER ESTIMATES (KALMAN FILTER)

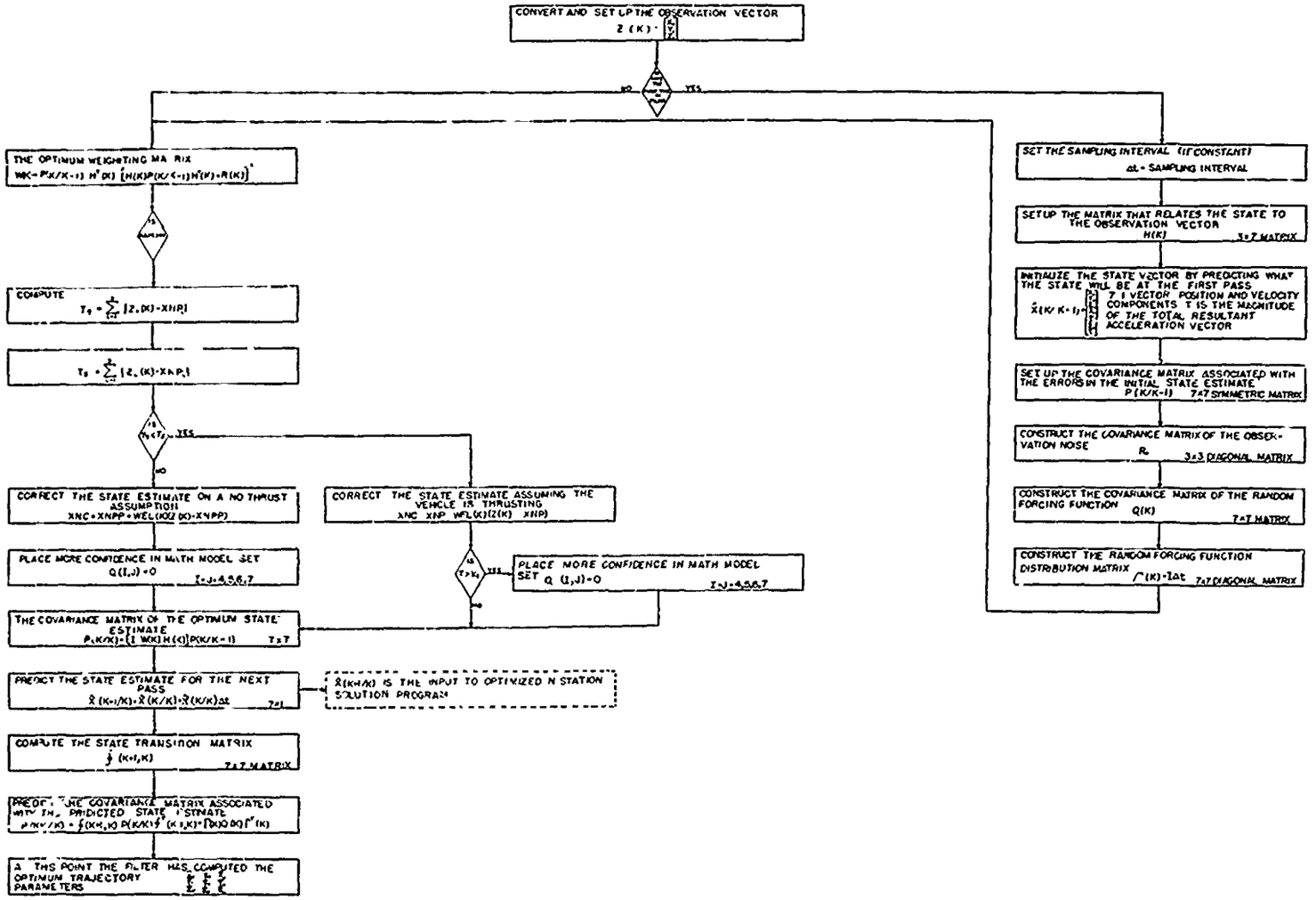

COMPUTATION OF MEAN WIND SPEED FROM BALLOON TRACK

by

LOUIS D. DUNCAN

and

BERNARD F. ENGEBOS

ABSTRACT

It is shown that the mean wind through a given altitude layer can be determined from balloon tracking data without computing wind values for individual points. The assumptions involved in the procedure are similar to the assumption made in numerical differentiation techniques, i.e., the position can be approximated by a polynomial.

INTRODUCTION

Standard techniques to obtain wind data above the level at which a fixed instrument (i.e., an anemometer) is feasible employ the observation of balloons. As the balloon ascends, its position is observed (tracked) by an instrument such as a theodolite, GMD, radar, etc. Sufficient tracking information is obtained to determine the position of the balloon at discrete time periods.

To determine the wind velocity one usually numerically differentiates the position data and assumes that the horizontal component of the wind is equal (at least in magnitude) to the horizontal component of the balloon velocity. The amount of sophistication involved in the numerical differentiation techniques depends, to a large extent, on the amount and frequency of the data.

A real-time meteorological system has been developed by the Atmospheric Sciences Office at White Sands Missile Range, New Mexico. This system includes a semi-automatic pilot balloon tracking system which automatically samples three manually operated theodolites at the rate of one sample per second. These data are reduced to obtain balloon position at the rate of one point per second.

Once one has obtained wind values at various altitudes, the mean over a given altitude layer can be computed as a simple average. This paper discusses a technique for computing this mean which does not require the computation of the individual wind values.

DISCUSSION

Throughout this paper an underlying coordinate system (x, y, z, t) will be understood. This system is such that (x, y, z) is a right-hand orthogonal system with z vertical, x, y horizontal, and t time.

The motion of the balloon can be expressed by a functional relationship (x, y, z) = f(t). The component motions are expressed functionally by x = X(t), y = Y(t), and z = Z(t). Since f(t) represents the motion of a physical body, it is a continuous function. It will be assumed that f(t) is almost everywhere differentiable. Now X(t), Y(t), and Z(t) are necessarily continuous and almost everywhere differentiable. Suppose it is desired to compute $\bar{\dot{X}}$ for $t_1 \leq t \leq t_2$.

Then

$$\bar{\dot{X}} = \frac{1}{t_2 - t_1} \int_{t_1}^{t_2} \dot{X}(t)dt = [X(t_2) - X(t_1)]/(t_2 - t_1) \tag{1}$$

Similarly one obtains

$$\bar{\dot{Y}} = [Y(t_2) - Y(t_1)]/(t_2 - t_1) \tag{2}$$

and

$$\bar{\dot{Z}} = [Z(t_2) - Z(t_1)]/(t_2 - t_1). \tag{3}$$

Therefore, if one can determine the functions X(t), Y(t), and Z(t), then it is easy to compute the mean speeds. Unfortunately, it is

usually difficult, it not impossible, to determine these functions. The standard technique is to assume that the function can be approximated sufficiently close by a polynomial of order n and then use a curve fit technique to determine the coefficients of the polynomial. Most numerical differentiation techniques employ similar assumptions.

Henceforth, we shall assume that time (t) is equally spaced and centered about its mean. Let $X(t) = A_n t^n + A_{n-1} t^{n-1} + \ldots + A_1 t + A_o$ $n = 1, 2, 3, 4$. By using a least square fit to the data, one can simplify equation (1) for various values of n [the degree of the polynomial, X(t)] to obtain

$$(4^1) \quad \bar{X} = A_1 \qquad n = 1$$

$$(4^2) \quad \bar{X} = A_1 \qquad n = 2.$$

$$(4^3) \quad \bar{X} = A_3 t_2^2 + A_1 \qquad n = 3.$$

$$(4^4) \quad \bar{X} = A_3 t_2^2 + A_1 \qquad n = 4.$$

It can be shown that for n odd, n and n + 1 yield the same equation. Substituting the least squares estimates for A_1 and A_3 in equations (4^1) and (4^3) one obtains, after simplification

$$(5^1) \quad \bar{X} = (12\,\Sigma tx)/N(N^2 - 1)$$

and

$$(5^3) \quad \bar{X} = \left\{\frac{[140(3N^2-7)\Sigma tx - 2800\Sigma t^3 x]t_2^2 + 140(3N^2-7)\Sigma t^3 x - 25(3N^4-18N+31)\Sigma tx}{N(N^2 - 1)(N^2 - 9)(4 - N^2)}\right\}$$

where N is the number of points in the interval.

EVALUATION OF THE TECHNIQUE

The procedure outlined above was programmed for an electronic digital computer, and several balloon tracks were analyzed. Several different altitude layers were used. For each layer, equations (5^1) and 5^3) were computed, and in each case the accuracy of the curve fit was computed. Based upon the data analyzed to date, there appears to be no significant differences among the results from the two equations.

BLANK PAGE

BLUE GOOSE WIND CORRECTION ANALYSIS

Urban H. DeH. Lynch, Captain, USAF

ABSTRACT

This report contains the techniques to develop accurate wind compensation for unguided vehicles. This work was performed under Contract AF29(601)-6311 by Space Systems Incorporated in conjunction with the Air Force Weapons Laboratory as a requirement for a new sounding rocket named the Blue Goose. Analytical results for arbitrary wind profiles indicate that the technique can correct the trajectory to within 0.2 degree dispersion. Inherent in the quoted trajectory accuracy is the need for accurate wind tunnel data (to include high angle of attack aerodynamics at low Mach number) for the vehicle and a proven six-degree-of-freedom trajectory calculation.

SECTION I

INTRODUCTION

Space Systems Incorporated (SSI), City of Industry, Los Angeles, California, under supervision of the Air Force Weapons Laboratory was responsible for the design and development of a highly accurate unguided sounding rocket called the Blue Goose Vehicle. During the development of the vehicle, a wind weighting technique was derived that proved to be very accurate (0.2 degree trajectory dispersion). Most of the original analysis was done by Mr. Bruce Bohi of SSI. The author checked Mr. Bohi's analysis, determined the accuracy of the technique, and used it in the field. Because the technique proved to be accurate, the author felt the work worthy of documentation. That documentation follows.

SECTION II

CONCEPTS

1. Vehicle Concepts

The Blue Goose (BG) vehicle concepts were definitely an outgrowth of its mission: To design and build an unguided booster vehicle capable of carrying payloads of the 2,500-pound class to altitudes around 100,000 feet with an accuracy of 19 mils while maintaining a velocity of 4,000 ft/sec.

At first examination, the mission specifications of "unguided" and "19 mils" (coupled with other performance specifications) sound mutually exclusive. Indeed the specifications were mutually exclusive without advancing the state of the art of unguided vehicle rocketry.

The following general problem areas were defined after six-degree-of-freedom trajectory analysis and dispersion studies:

(1) The vehicle must be wind insensitive and have an accurate wind weighting analysis.

(2) Thrust misalignment effects must be held to an absolute minimum.

(3) The launcher must be very stable and have a high degree of pointing accuracy.

(4) Vehicle nominal quadrant elevation (Q.E.) must be corrected for propellant temperature and final vehicle buildup weight.

The above general problem areas led to specific solutions which were in part completely new concepts in unguided vehicle rocketry and in part a high degree of refinement of standard concepts. The specific solutions were as follows:

a. Wind insensitive vehicle.

(1) Low static margin at lift-off (6 inches).

(2) High acceleration at lift-off (14 g).

b. Accurate wind weighting (0.2 degree trajectory dispersion).

(1) Wind tunnel analysis to pick the best vehicle configuration and to get high angle of attack aerodynamic data at low Mach number.

(2) Computer six-degree trajectory analysis to devise very accurate wind weighting techniques.

c. Thrust misalignment effects.

(1) Close configurational control on thrust lines of all motors to make thrust misalignment an absolute minimum at lift-off.

(2) Spin vehicle on launcher prior to ignition and zero length launch.

d. Launcher with a high degree of pointing accuracy. Responsibility of DASA Project 9.5.

e. Corrections in Q.E. for propellant temperature and final weight. Computer six-degree trajectory analysis to provice Q.E. corrections for perturbations in vehicle nominal weight and propellant temperature.

Only the wind weighting problem is discussed in this report.

2. Wind Weighting Concepts

a. Wind Insensitive Vehicle

The vehicle design was made as wind insensitive as possible so as to minimize the effects of variable launch winds on trajectory. As already mentioned, this was accomplished by low static margin and high acceleration at lift-off. Confidence in the low static margin was achieved by accurate wind tunnel testing and vehicle ballasting. The high acceleration at lift-off (14 g) was achieved by auxiliary booster motors. Figures 2 and 3 of the appendix are the elevation and azimuth correction curves for the final vehicle configuration. Note the wind sensitivity of the vehicle: For a 40-ft/sec headwind the elevation correction is approximately 2.9 degrees: for a 40-ft/sec sidewind the azimuth correction is approximately 10.5 degrees.

b. Solution Concepts

The wind weighting problem has historically been solved by solving the following two problems: derive elevation and azimuth correction curves for wind profiles of constant magnitude and constant but arbitrary direction; derive a method to reduce the actual wind profile to a wind profile of constant magnitude and direction. Each problem will be discussed in turn.

(1) Azimuth and Elevation Correction Curves

The azimuth and elevation correction curves (see Figures 2 and 3 of the appendix) indicate how to reaim the vehicle for any wind profile of constant magnitude and direction. The accuracy to which this can be done depends upon the trajectory simulation and the technique used to reduce the trajectory data.

The trajectory simulation used in this report was a six-degree-of-freedom digital computer calculation employing an oblate, spheroidal, rotating earth model and complete wind tunnel aerodynamics to include high-angle aerodynamics at low Mach number. The high-angle aerodynamics was necessary for an accurate simulation of wind effect since high angles of attack (70°, etc.) exist at lift-off.

The technique used to reduce the basic trajectory data to azimuth and elevation correction curves is an adaptation of the "James method" outlined in NASA TND 645.* In TND 645 the main physical constraint used to develop the correction curves is the no-wind attitude of the vehicle at an altitude where wind no longer appreciably affects the vehicle. This technique is constructed so that the vehicle in the presence of winds will have the same attitude, at the altitude where wind no longer appreciably affects the vehicle, as the no-wind nominal trajectory. Since the requirement for the Blue Goose vehicle was to hit a fixed target in space, the physical constraint used to reduce the trajectory data was the target position. In other words, the azimuth and elevation correction curves allow one to reaim the vehicle so that a fixed spatial target is hit. This constraint was used since controlling the attitude at a particular altitude does not necessarily control the position at that altitude. The choice of physical constraint is purely arbitrary and depends solely on the requirements for the trajectory. The detailed technique of going from the basic trajectory data to the correction curves is explained in the appendix.

(2) Wind Profile to Ballistic Wind

The azimuth and elevation curves allow one to correct the trajectory for the effects of a constant wind profile of constant but arbitrary direction. Unfortunately, though, the winds are not that cooperative. One must have a technique to reduce an arbitrary wind profile to a wind of constant magnitude and direction that has the same effect on the vehicle as the arbitrary wind

*James, Robert L., and Ronald J. Harris, Calculation of Wind Compensation for Launching Unguided Rockets, April 1961.

profile. This wind of constant magnitude and direction is called the "ballistic wind." The technique of going from an arbitrary wind profile to a ballistic wind is called "wind weighting." It is here that this report radically differs from others on the subject.

Common assumptions made at this point in the analysis are

(a) Wind effect is linear with wind velocity at a given altitude.

(b) Head, tail, and side winds have the same effect on the vehicle.

These assumptions are only true for that portion of the flight that has angles of attack in the linear aerodynamic range. These assumptions generally do not hold at lift-off because the vehicle is moving slowly. Since most of the wind effect on unguided vehicles occurs in the first portion of the flight, the above assumptions can lead to considerable error. The magnitude of this error is a function of the specific vehicle; whether or not one accepts this error depends on the desired accuracy of the trajectory.

The results of assumptions (a) and (b) are wind weighting factors that are independent of wind velocity and wind direction at all altitudes. The appendix shows in detail how to correct for the nonlinear aerodynamic effect in weighting the vehicle for wind. In general, the results of including nonlinear aerodynamics are wind weighting factors that are not only a function of altitude, but also a function of wind direction and wind velocity in the lower altitudes.

SECTION III

ANALYTICAL RESULTS

At this point, the wind compensation analysis is complete except for an analytical check to determine the trajectory accuracy of the technique. This analytical check is best performed through the six-degree trajectory simulation by assuming arbitrary wind profiles that have been corrected by the wind compensation technique. A myriad of the calculations were made at AFWL, the results of which appear in table I. Table I reveals that a conservative estimate of the target error is about 400 feet. Since the target is approximately 120,000 feet from launch, this results in a trajectory accuracy of approximately 0.2 degree.

Table I

WIND WEIGHTING ACCURACY

Wind condition	Ballistic wind		Aiming		Miss distance	
	V_{WBE}(ft/sec)	θ_{WBE}(°)	QE (°)	Az (°)	ΔN (ft)	ΔCR (ft)
C	40	180	73.94	181	+100	-100
C	40	0	67.68	179.15	-100	-330
C	40	270	70.70	169.60	- 20	-125
C	40	225	73.08	172.39	+ 50	+100
C	18.03	303.68	70.012	176.64	- 10	+110
C	17.81	56.22	69.848	183.089	- 60	0
C	31.63	108.43	71.055	187.898	+ 60	+110
C	29.80	150.334	72.483	184.61	+ 90	- 70
P	11.76	37.750	69.960	181.418	-150	0
P	34.78	37.866	68.406	184.195	-400	-210
P	34.47	141.725	72.530	186.689	- 20	-100
P	34.47	218.275	72.918	174.584	+470	+150
P	34.82	322.183	68.685	174.824	+260	+330

C - constant

P - profile

ΔN - normal to nominal trajectory in pitch plane

ΔCR - normal to nominal trajectory in yaw plane

SECTION IV

MET PROGRAM

1. Met Program, Eglin AFB

Closely associated with the wind weighting technique is, obviously, the technique for obtaining the winds at launch. The wind weighting technique, no matter how accurate, is useless unless one obtains accurate up-to-date launch winds. For this reason, AFWL, in coordination with Detachment #10 of the Sixth Weather Wing, Eglin AFB, developed a met program which exhausted their wind-measuring capabilities. The wind-measuring program is best portrayed in graphical form and supplemented with a table of events. The figure on the following page and table II show these data. The main constraint in designing the figure is the time it takes for a wind balloon to rise a given height (~1,000 ft/min).

2. Calculation Technique for Wind Weighting

When one examines the wind-weighting technique and the number of calculations that must be made to arrive at an accurate answer, it becomes obvious that hand calculation of any form during the countdown is too long and cumbersome. For this reason, the wind-weighting technique was stored in a computer. Ballistics Division, Eglin AFB, programmed the wind-weighting technique on their LGP-30. Linear interpolation was used and the data for the program came from the appendix of the contractor's final report. The data in the appendix were plotted on large graphs and the data used in the computer program were picked off the large graphs in sufficient quantity to permit linear interpolation to be accurate.

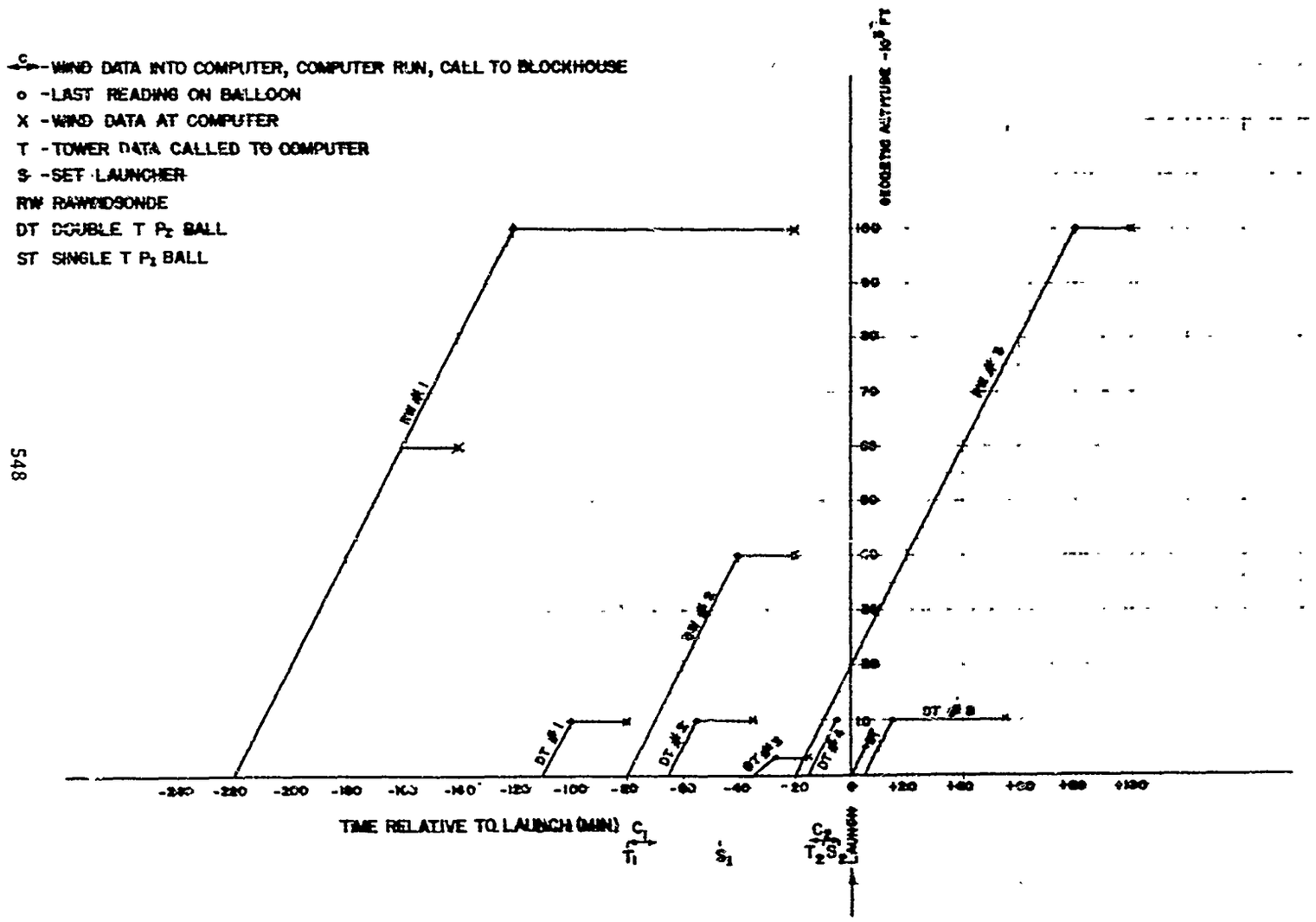
C--WIND DATA INTO COMPUTER, COMPUTER RUN, CALL TO BLOCKHOUSE
o -LAST READING ON BALLOON
X -WIND DATA AT COMPUTER
T -TOWER DATA CALLED TO COMPUTER
S -SET LAUNCHER
RW RAWINSONDE
DT DOUBLE T P2 BALL
ST SINGLE T P1 BALL
RW #1
RW #2
RW #3
DT #1
DT #2
DT #3
DT #4
DT #5
ST
-240 -220 -200 -180 -160 -140 -120 -100 -80 -60 -40 -20 0 +20 +40 +60 +80 +100
TIME RELATIVE TO LAUNCH (MIN)
C1
T1
S1
C2
T2
S2
LAUNCH

Table II

TABLE OF EVENTS (Eglin Wind System)

Time relative to launch (min)	Event
-220	Launch RW #1
-140	Call in first 60K of RW #1
-110	Launch DT #1
- 80	DT #1 called to computer
	T_1 called to computer
	Launch RW #2
- 70	Launcher settings
- 65	Launch DT #2
- 47	Set launcher #1
- 35	Call in DT #2
	Launch DT #3
- 20	Call in 40-60K layer RW #1
	Launch RW #3
	Call in RW #2
- 15	Call in DT #3
	Launch DT #4
- 10	Call in T_2
- 5	Launcher settings
	Set launcher #2
0	Launch vehicle
	Launch ST
+ 5	Launch DT #5
+ 55	Call in DT #4, ST and DT #5
+100	Call in RW #3

SECTION V

FLIGHT RESULTS

The Blue Goose Vehicle System was flight-tested at Eglin AFB, Florida, on 5 February 1966. A launcher failure occurred, however, changing the nominal flight path of the vehicle. The mode of the failure was one that apparently caused initial pitch and yaw rates to the vehicle. Fastax film of the lift-off (1,000 frames/sec) indicated that the vehicle was pitching down at a rate of 2°/sec, thereby appreciably changing (trajectory 3° lower) what was to be the nominal trajectory.

To check the accuracy of the vehicle performance, a new nominal trajectory was calculated which was the same calculation as was done for the planned flight except the initial pitch rate was changed from zero to the measured value 2.08°/sec. The actual measured flight path was then compared to this new nominal trajectory. The miss distance at the target was 800 feet which is approximately 0.4-degree trajectory dispersion. This strongly suggests that the vehicle was performing as designed when one includes the effects of the launcher failure.

For completeness, the measured wind data are presented in table III. The prelaunch winds used for the launch and the post-launch winds are shown in table IV.

Table III

MEASURED WIND DATA

Alt layer	RW #1	DT #1	T #1	RW #2	DT #2	DT #3A	DT #3B	T #2	DT #4	ST #1	T_{launch}	DT #5	RW #3
53 - 60			10/005°					*5/030°			6/355°		
60 - 80			11/003°					*6/030°			6/360°		
80 - 100			12/005°					*6/040°			6/360°		
100 - 130		7/012°	11/030°		10/360°	8/038°	8/010°	*8/040°	7/012°	8/010°	6/015°	4/016°	
130 - 160		7/013°			10/360°	8/038°	* 8/010°		7/012°	8/010°		4/017°	
160 - 200		7/014°			10/360°	8/037°	* 8/010°		7/014°	8/010°		4/020°	
200 - 400		8/017°			10/360°	9/034°	* 8/005°		8/016°	8/010°		3/025°	
400 - 700		9/020°			10/005°	8/025°	*10/360°		7/019°	8/010°		4/031°	
700 -1000		8/020°			13/360°	6/012°	*11/005°		8/019°	10/010°		5/034°	
1 - 2 K		7/357°		8/350°	11/360°	9/020°	* 7/350°		10/355°	10/015°		4/026°	8 /354 °
2 - 3 K		11/002°		9/360°	8/353°	6/360°	* 6/340°		10/354°	12/010°		6/010°	10 /347 °
3 - 4 K		13/360°		10/350°	11/353°	*9/350°			10/351°	14/360°		7/353°	10 5/342 °
4 - 5 K		10/356°		10/330°	13/349°	*7/346°			9/355°	10/360°		10/360°	9 /331.5°
5 - 7.5K	18/300°	10/317°		12/330°	* 9/306°				10/312°			8/300°	11.5/314.5°
7.5- 10 K	17/330°	18/315°		17/330°	*16/329°				14/302°			16/310°	21 /306 °
10 - 15 K	26/320°			*29/310°									31 /300 °
15 - 20 K	40/310°			*42/300°									43 /301 °
20 - 30 K	49/300°			*48/300°									48.5/296 °
30 - 40 K	65/290°			*64/280°									64 /278 °
40 - 60 K	*62/290°												61 /278 °
60 - 100 K	*30/270°												29 /263 °

Winds: knots and degrees from true North

*Winds to be used for final launch setting

Table IV

WIND DATA USED

Alt layer	Measured prelaunch winds used	Measured post launch winds
53 - 60	5/030°	6 /355°
60 - 80	6/030°	6 /360°
80 - 100	6/040°	6 /360°
100 - 130	8/040°	6 /015°
130 - 160	8/010°	8 /010°
160 - 200	8/010°	8 /010°
200 - 400	8/005°	8 /010°
400 - 700	10/360°	8 /010°
700 -1000	11/005°	10 /010°
1 - 2 K	7/350°	10 /015°
2 - 3 K	6/340°	12 /010°
3 - 4 K	9/350°	14 /360°
4 - 5 K	7/346°	10 /360°
5 - 7.5K	9/306°	10 /312°
7.5- 10 K	16/329°	15 /306°
10 - 15 K	29/310°	31 /300°
15 - 20 K	42/300°	43 /301°
20 - 30 K	48/300°	48.5/296°
30 - 40 K	64/280°	64 /278°
40 - 60 K	62/290°	61 /278°
60 - 100 K	30/270°	29 /263°
QE	69.53°	69.45°
AZ	176.49°	176.53°

SECTION VI

CONCLUSIONS

Analytical calculations and measured flight results indicate that the Blue Goose Wind Correction Analysis was very successful. One must keep in mind, however, that each vehicle is a special case. The Blue Goose had comprehensive wind-tunnel testing, a special wind-insensitive design, and a detailed met program backed up by a computer. Everything possible was done to minimize the effects of a variable wind between prelaunch and launch. The application of the Blue Goose Wind Correction Analysis to other unguided vehicles is recommended, but one must realize that the final trajectory accuracy is very much vehicle-dependent.

APPENDIX

WIND CORRECTION ANALYSIS
BLUE GOOSE

PREPARED BY		REPORT NO. 8006-10
CHECKED BY		PAGE NO. ii
DATE		

ABSTRACT

Engineering data necessary for the launcher correction of the Blue Goose for measured winds are presented.

FORM 7

LIST OF SYMBOLS

V_W	Wind velocity, ft/sec
Θ_W	Direction from which wind is blowing, degrees from true north (Θ_W for a wind from the east is $+90^\circ$).
L	Geodetic altitude above mean sea level, ft.
V_{W_H}, V_{W_C}, V_{W_T}	Wind velocity components from head, crosswind, and tail directions, respectively, ft/sec.
$\bar{V}_{W_H}$, $\bar{V}_{W_C}$, $\bar{V}_{W_T}$	Average wind velocity components across an altitude layer, from head, crosswind, and tail directions, respectively, ft/sec.
f_W	Value of wind weighting factor at any altitude f_W = displacement due to wind from launch to the noted altitude divided by displacement due to wind from launch to 100,000 feet computed using linear aerodynamics.
Δf_W	Difference in wind weighting factor across an altitude layer.
$V_{W_{BH}}$, $V_{W_{BC}}$, $V_{W_{BT}}$	Ballistic wind velocity components in head, crosswind, and tail directions, respectively, ft/sec.
$U.W.E._{L-HW}$, $U.W.E._{L-CW}$	$U.W.E._{L-TW}$ displacement at test altitude due to a unit wind acting from launch to 100,000 ft in head, crosswind, and tail directions, respectively, ft/ft/sec.
ΔR_{HW}, ΔR_{TW}	Displacement in range at test altitude due to head or tail winds, ft.
CR_{CW}	Displacement in cross-range at test altitude due to a crosswind. Cross-range is measured perpendicular to the nominal azimuth. A displacement to the right of the trajectory is positive, ft.

FORM 1

$V_{W_{BE-H}}$, $V_{W_{BE-C}}$, $V_{W_{BE-T}}$	Effective ballistic wind component velocities, ft/sec.
$C_{m_{\alpha\text{-launch}}}$	Pitching moment coefficient at vehicle launch. 1/deg $C_{m_{\alpha\text{-launch}}}$ = .222 times center of pressure position minus center of gravity position divided by 31. Reference center of pressure is at station 256.14.
$V_{W_{BE}}$, $\theta_{W_{BE}}$	Velocity and direction of the effective ballistic wind vector. Ft/sec and degrees true.
$\sigma_{L\,nom}$	Nominal launcher azimuth, degrees from true north (an easterly launch gives + 90°).
$\gamma_{L\,nom}$	Norminal launcher elevation, degrees above horizontal.
$\sigma_{L\,set}$, $\sigma_{L\,set}$	Launcher settings in azimuth and elevation after compensation for wind, degrees true and degrees

INTRODUCTION

Space Systems, Inc., under Contract AF29(601)-6311 for the Air Force Weapons Laboratory has the responsibility for the design of the Blue Goose missile. In order for this missile to meet its targeting objectives, it is necessary to measure and compensate for measured winds at launch time. This study presents the engineering data necessary to accomplish this task.

The nominal trajectory for the Blue Goose missile requires traversing a test point in space. The nominal coordinates of this test point with reference to a geodetic earth are an altitude of 98,502 feet, a range of 65,293 feet, and a cross-range of zero. When launched fron. Eglin Air Force Base with pad coordinates of 30.394635 degrees north latitude, 86.716446 west longitude, the test point location is at a latitude of 30.0484 north latitude and the nominal pad longitude. The initial altitude of the vehicle center of gravity on the pad is 53 feet. When the vehicle is launched no wind at an elevation angle of 70.634 degrees and an azimuth of 180.042 degrees true, the Blue Goose vehicle will attain the required test point 44.975 seconds after the start of Castor ignition. Procedures and data are provided for weighting the measured winds and correcting the launcher elevation and azimuth settings to achieve the above trajectory.

DATA USAGE

The following steps are necessary to convert a measured wind profile into a corrected launcher setting:

1. Conversion to wind components

   The raw wind profile data consisting of velocity, V_W, and direction, ~~Θ_W~~, versus altitude above mean sea level, h, is broken into components parallel, V_{W_H}, V_{W_T}, and perpendicular V_{W_C} to the nominal launcher azimuth. For the Eglin launching, this corresponds to north-south and east-west components. The average value of each wind component, $\bar{V}_{W_H}$, $\bar{V}_{W_T}$, and $\bar{V}_{W_C}$ is determined for each of the altitude layers shown in Table 3.

2. Weighting of wind

   The wind weighting factor increments, Δf_W, for layers below 200 feet altitude are read from Table 2 as a function of the average wind velocity component, $\bar{V}_{W_H}$, $\bar{V}_{W_T}$, and $\bar{V}_{W_C}$. It is necessary to distinguish between head and tail winds for this purpose. The wind weighting factor increments, Δf W, for altitudes above 200 feet are read from Table 3. These data are also plotted in Figure 1. These are independent of wind velocity and direction.

   The wind is then weighted by multiplying the average wind component, $\bar{V}_{W_H}$, $\bar{V}_{W_T}$, $\bar{V}_{W_C}$, by the weighting factor increment, Δf W.

   Thus,

$$V_{W_{BH}} = \sum_{L=0}^{L=100K} \Delta f_W \times \bar{V}_{W_H}$$

$$V_{W_{BC}} = \sum_{L=0}^{L=100K} \Delta f_W \times \bar{V}_{W_C}$$

$$V_{W_{BT}} = \sum_{L=0}^{L=100K} \Delta f_W \times \bar{V}_{W_T}$$

Note that when $\bar{V}_{W_H}$ exist, $\bar{V}_{W_T}$ is zero and vice versa.

3. Obtain linearized displacements

Table 6 is entered using the weighted wind components determined in Step 2 and the linear aerodynamics unit wind effects, $U.W.E._{L-HW}$, $U.W.E._{L-TW}$, $U.W.E._{L-CW}$, are obtained. The linearized displacements are then computed using the below equations:

$$\Delta R_{HW} = V_{W_{BH}} \times U.W.E._{L-HW}$$

$$CR_{CW} = V_{W_{BC}} \times U.W.E._{L-CW}$$

$$\Delta R_{TW} = V_{W_{BT}} \times U.W.E._{L-TW}$$

4. Convert to effective ballistic wind

Table 5 is entered using the linearized displacements obtained in Step 3 and the effective ballistic wind components are read, $V_{W_{BE-H}}$, $V_{W_{BE-C}}$, and $V_{W_{BE-T}}$. These are interpolated as a function of the launch pitching moment coefficient, $C_{m_\alpha\text{-launch}}$. $C_{m_\alpha\text{-launch}}$ is determined from measurements made during the vehicle buildup and will be supplied shortly before launch time. It is a constant and if desired, Table 5 can be manually interpolated and only the data has the applicable $C_{m_\alpha\text{-launch}}$ inserted into the computer.

The net head or tail ballistic wind component is then computed.

$$V_{W_{BE-HT}} = V_{W_{BEH}} - V_{W_{BET}}$$

The total ballistic wind velocity is then computed as the root-sum-square of the components.

$$V_{W_{BE}} = \sqrt{(V_{W_{BE-HT}})^2 + (V_{W_{BE-C}})^2}$$

The direction with respect to the vehicle nominal azimuth is computed

$$\psi_W = \sigma_{W_{BE}} - \sigma_{L\,nom} = \text{TAN}^{-1} \frac{V_{W_{BE-C}}}{V_{W_{BE-HT}}}$$

The following sign convention has been used for the enclosed data:

$\sigma_{W_{BE}} - \sigma_{Lnom}$	Wind Condition
0	Headwind
+90	Wind from right side of vehicle
180	Vehicle tailwind
-90	Wind from left side of vehicle

561

5. Compute launcher correction

The charts shown on Figures 2 and 3 and in Table 7 were computed for $\sigma_{L\,nom}$ = 180 degrees true and $\gamma_{L\,nom}$ = 70.634 degrees above the horizon. Determine $\Theta_{W_{BE}}$ from $\Theta_{W_{BE}} = \Theta_{W_{BE}} \sigma_{L\,nom}$ + 180 degrees. Enter Table 7 using $\Theta_{W_{BE}}$ and $V_{W_{BE}}$ and read $\gamma_{L\,set}$ and $\sigma_{L\,set}$.

Note if it is desired to use Table 7 for some other nominal azimuth than 180°, the following changes will accomplish this. Convert the Θ_W scale to $\Theta_W - \sigma_{L\,nom}$ by subtracting 180°. Convert the $\sigma_{L\,set}$ ordinate to $\sigma_{L\,set} - \sigma_{L\,nom}$ by subtracting 180°. The chart can then be used as is for any other nominal azimuth. New data must be computed if a different nominal elevation is required.

The following general information applies to the enclosed tables. Data for the calculated points are presented. Additional points may be necessary to maintain accuracy depending on the intepolation scheme used in the computer program. Selection of data points to be input and the interpolation scheme is left to the programmer. Plots of Tables 3 and 7 are enclosed to facilitate this operation. Most data is presented to three decimal places to facilitate taking additional data points. Two place accuracy is sufficient for the enclosed tables.

Tables 1 and 4 are not used directly in the computation. They are included for reference purposes. Table 1 presents wind velocities at which the angle of attack exceeds five degrees at various altitude points. These data indicate the point at which nonlinearities arise in the wind effect data. Table 4 shows the unit wind effects used in the deviation of the wind weighting data of Tables 2 and 3.

DATA DERIVATION (GENERAL)* (R)

Digital computer trajectories using constant winds to various altitudes were run using both linear and nonlinear aerodynamic coefficients. The displacements at test altitude either in-range or in cross-range under the influence of wind using linear aerodynamic coefficients were used as the reference value. These data are presented in Table 4. The ratio of the wind effect between launch and any given altitude to the above reference value was taken as the wind weighting factor for that altitude. At altitudes below 200 feet the wind weighting factor varied with wind velocity. This effect was calculated based on linear extrapolation of the reference value with wind velocity and resulting data are presented in Table 3. It was also found that the total displacement at test altitude when using linear aerodynamics was proportional to wind velocity. Data showing this effect are presented in Table 6.

Digital computer trajectories using nonlinear aerodynamic coefficients were also computed. The displacement at test altitude versus wind velocity was calculated for three launcher center of gravity positions; the resulting data are presented in Table 5.

The launcher correction charts presented in Table 7 were derived using methods outlined in NASA TN D-645 and SSI Memo 8006-AS-10-29-64.

*For procedures employed, see pages 24 and on in this appendix. (R)

TABLE 1

WIND VELOCITY FOR FIVE DEGREE ANGLE OF ATTACK VERSUS ALTITUDE

Reference Only

H Altitude Ft. Above M.S.L.	V_{W_5} Wind Velocity at Which $\alpha = 5^\circ$	
53	1.24	
60	7.21	
80	14.30	
100	18.50	
130	23.30	
160	27.30	
200	32.00	End of test
216	33.60	Reference only
281	39.26	Reference only

IF V_W is greater than V_{W_5}, α is greater than 5°.

IF V_W is less than V_{W_5}, α is less than 5°.

PREPARED BY		REPORT NO. 8006-10
CHECKED BY		PAGE NO. 8
DATE		

TABLE 2

WIND WEIGHTING FACTORS FOR ALTITUDE LAYERS VERSUS WIND VELOCITY

Δ_H Altitude Layer Ft.	V_W Wind Velocity Feet/Sec	Δf_W Per Cent
For Headwinds		
53-60	0	.540
↓	10	2.854
	20	3.707
	30	3.910
	40	4.028
60-80	0	2.386
↓	10.76	2.386
	20	5.864
	30	7.740
	40	8.879
80-100	0	1.709
↓	14.3	1.709
	20	3.236
	30	5.25
	40	6.865
100-130	0	1.980
↓	18.5	1.980
	20.0	3.114
	30.0	5.300
	40.0	6.806
130-160	0	1.693
↓	23.30	1.693
	40.0	4.923
160-200	0	2.496
↓	27.30	2.496
	40.0	4.258

FORM 7

PREPARED BY		REPORT NO. 8006-10
CHECKED BY		PAGE NO. 9
DATE		

TABLE 2--Continued

Δ H Altitude Layer Ft.	V_W Wind Velocity Feet/Sec	Δf_W Per Cent	
For Crosswinds			
53-60	0	.540	
↓	10	2.061	
	20	2.800	
	30	3.140	
↓	40	3.386	
60-80	0	2.018	
↓	10.76	2.018	
	20	5.232	
	30	7.350	
↓	40	8.521	
80-100	0	1.355	
↓	16.4	1.355	
	20	2.147	
	30	3.862	
↓	40	5.200	
100-130	0	1.738	
↓	20.9	1.738	
	30	3.041	
↓	40	4.685	
130-160	0	1.919	
↓	25.3	1.919	
	30	2.644	(R)
↓	40	3.855	(R)
160-200	0	3.082	
↓	29.6	3.082	
	40.0	3.899	

FORM 1

TABLE 2--Continued

Δ H Altitude Layer Ft.	V_W Wind Velocity Feet/Sec.	Δf_W Per Cent
For Tailwinds		
53-60	0	.540
↓	10	1.496
	20	2.321
	30	2.780
↓	40	2.912
60-80	0	1.051
↓	10.76	1.051
	20	3.599
	30	5.30
↓	40	6.262
80-100	0	1.790
↓	18.5	1.790
	20	1.929
	30	3.370
↓	40	4.447
100-130	0	1.714
↓	23.30	1.714
	30	2.85
↓	40	4.249
130-160	0	1.718
↓	27.30	1.718
	[illegible]	2.538
160-200	[illegible]	2.781
↓	32.0	2.781
	40.0	2.424

FORM 7

PREPARED BY		REPORT NO. 8006-10
CHECKED BY		PAGE NO. 11
DATE		

TABLE 3

LINEAR AERODYNAMICS WIND WEIGHTING FACTOR VERSUS ALTITUDE

H Altitude Ft. Above M.S.L.	$\mathcal{F}_{W_n}$ Per Cent	Altitude Layer Ft.	$\Delta \mathcal{F}_{W_n}$ Per Cent
53	0.0	-	-
60	0.540	53-60	.540
80	2.227	60-80	1.687
100	3.582	80-100	1.355
130	5.120	100-130	1.538
160	7.039	130-160	1.919
200	10.121	160-200	3.082
400	17.118	200-400	6.997
700	23.320	400-700	6.202
1,000	28.336	700-1000	5.016
2,000	36.679	1K-2K	8.343
3,000	50.896	2K-3K	14.217
4,000	58.339	3K-4K	7.443
5,000	62.324	4K-5K	3.985
7,500	72.597	5K-7.5K	10.273
10,000	78.359	7.5K-10K	5.762
15,000	86.124	10K-15K	7.765
20,000	90.781	15K-20K	4.657
30,000	95.606	20K-30K	4.825
40,000	98.223	30K-40K	2.617
60,000	99.909	40K-60K	1.686
100,000	100.000	60K-100K	.091

For Reference Only

FORM 1

PREPARED BY		REPORT NO. 8006-10
CHECKED BY		PAGE NO. 12
DATE		

TABLE 4

UNIT WIND EFFECT FOR LINEAR AERODYNAMICS
Reference Only

ψ_W^* Wind Direction From Vehicle Deg.		$U.W.E._L$ Unit Wind Effect Ft/Ft/Sec
0	= headwind	290.82 in-range
90 or 270	= crosswind	245.08 in cross-range
180	= tailwind	281.50 in-range

$$^*\psi_W = \sigma_W - \sigma_{L_{nom}}$$

FORM 7

PREPARED BY		REPORT NO. 8006-10
CHECKED BY		PAGE NO. 13
DATE		

TABLE 5

DISPLACEMENT VERSUS EFFECTIVE
BALLISTIC WIND VELOCITY
(For Headwinds)

C_{m_α} -launch 1/Deg	ΔR_{HW} Displacement In Range Ft.	$V_{W_{BE-H}}$ Effective Ballistic Wind Velocity Ft/Sec.
-.0385	0	0
↓	3007	10
↓	6472	20
↓	10645	30
↓	15227	40
-.0099	-929	0
↓	1684	10
↓	4694	20
↓	8519	30
↓	12718	40
-.0672	639	0
↓	3970	10
↓	7809	20
↓	12280	30
↓	17189	40

FORM 1

PREPARED BY		REPORT NO. 8006-10
CHECKED BY		PAGE NO. 14
DATE		

TABLE 5--Continued

(For Crosswinds)

$C_{m_{\alpha}}$ -launch 1/Deg	CR_{CW} Displacement In Crossrange Ft.	$V_{W_{BE-C}}$ Effective Ballistic Wind Velocity Ft/Sec.
-.0385	0	0
↓	2501	10
	5248	20
	8369	30
	11813	40
-.0099	-119	0
↓	2055	10
	4442	20
	7327	30
	10510	40
-.0672	62	0
↓	2823	10
	5855	20
	9206	30
	12903	40

Form 1

TABLE 5--Continued

(For Tailwinds)

$C_{m_{\alpha}}$ -launch 1/Deg	ΔR_{TW} Displacement In Range Ft.	$V_{W_{BE-T}}$ Effective Ballistic Wind Velocity Ft/Sec.
-.0385	0	0
↓	2859	10
	5832	20
	9017	30
	12420	40
-.0099	929	0
↓	3391	10
	5952	20
	8835	30
	11915	40
-.0672	639	0
↓	2530	10
	5826	20
	9232	30
	12872	40

PREPARED BY		REPORT NO. 8006-10
CHECKED BY		PAGE NO. 16
DATE		

TABLE 6

LINEAR AERODYNAMICS UNIT WIND EFFECT
VERSUS BALLISTIC WIND
VELOCITY

$V_{W_{BH}}$ $V_{W_{BC}}$ $V_{W_{BT}}$ Ballistic Wind Velocity Ft/Sec	U.W.E.$_{L\text{-}H.W,\ CW,\ TW}$ Unit Wind Effect Ft/Ft/Sec	
For headwinds	$\Psi_W = 0$	
0	287.10	U.W.E.$_{L\text{-}HW}$
10	290.82	
20	294.76	
30	298.85	
40	303.03	
For crosswinds	$\Psi_W = 90, 270$	
0	244.45	U.W.E.$_{L\text{-}CW}$
10	245.08	
20	245.78	
30	246.72	
40	248.26	
For tailwinds	$\Psi_W = 180$	
0	282.56	U.W.E.$_{L\text{-}TW}$
10	281.50	
20	280.33	
30	278.82	
40	276.04	

FORM 7

PREPARED BY		REPORT NO. 8006-10
CHECKED BY		PAGE NO. 17
DATE		

TABLE 7

CALCULATED LAUNCHER CORRECTION CHART POINTS

$V_{W_{BE}}$ Effective Ballistic Wind Velocity Ft/Sec	$\Theta_{W_{BE}}$ Effective Ballistic Wind Direction Degrees True	$\gamma_{L_{set}}$ Launcher Elevation Setting Degrees	$\sigma_{L_{set}}$ Launcher Azimuth Setting Degrees True
0	All	70.634	180.042
10.0	359.877	69.967	179.877
	23.230	69.996	180.730
	46.478	70.127	181.478
	69.507	70.332	182.007
	92.240	70.589	182.240
	114.627	70.850	182.127
	136.708	71.080	181.708
	158.534	71.247	181.034
	180.207	71.320	180.207
	201.857	71.293	179.357
	223.612	71.167	178.612
	245.583	70.960	178.083
	267.851	70.712	177.851
	290.459	70.446	177.959
	313.373	70.213	178.373
	336.551	70.044	179.051

FORM 7

PREPARED BY		REPORT NO 8006-10
CHECKED BY		PAGE NO 18
DATE		

TABLE 7--Continued

$V_{W_{BE}}$	$\Phi_{W_{BE}}$	$\gamma_{L_{set}}$	$\sigma_{L_{set}}$
20	359.684	69.262	179.684
	23.958	69.322	181.458
	48.021	69.595	183.021
	71.648	70.038	184.148
	94.652	70.575	184.652
	116.942	71.127	184.442
	138.565	71.605	183.565
	159.640	71.946	182.140
	180.405	72.098	180.405
	201.120	72.045	178.620
	222.049	71.789	177.049
	243.433	71.367	175.933
	265.444	70.839	175.444
	288.172	70.279	175.672
	311.652	69.876	176.652
	334.468	69.421	177.968

FORM 1

PREPARED BY		REPORT NO. 8006-10
CHECKED BY		PAGE NO. 19
DATE		

TABLE 7--Continued

$V_{W_{BE}}$	$\Theta_{W_{BE}}$	$\gamma_{L_{set}}$	$\sigma_{L_{set}}$
30	359.455	68.502	179.455
	24.760	68.593	182.260
	49.757	69.024	184.757
	74.071	69.736	186.571
	97.399	70.602	187.399
	119.586	71.480	187.086
	140.664	72.185 (R)	185.664
	160.906	72.753	183.406
	200.301	72.909	177.801
	180.646	72.991	180.646
	220.292	72.519	175.292
	240.997	71.873	173.497
	262.728	71.037	172.728
	285.577	70.146	173.077
	309.503	69.344	174.503
	334.243	68.765	176.743

FORM 7

TABLE I--Continued

$V_{W_{BE}}$	$\Theta_{W_{BE}}$	$\gamma_{L_{set}}$	$\sigma_{L_{set}}$
40	359.177	67.679	179.177
	25.621	67.803	183.121
	51.690	68.429	186.690
	76.789	69.448	189.289
	100.419	70.674	190.419
	122.436	71.901	189.936
	142.929	72.925	187.929
	162.232	73.623	184.732
	180.896	73.947	180.896
	199.447	73.840	176.947
	218.424	73.328	173.424
	238.341	72.452	170.841
	259.727	71.305	169.727
	282.667	70.055	170.167
	307.198	68.905	172.198
	332.855	68.070	175.355

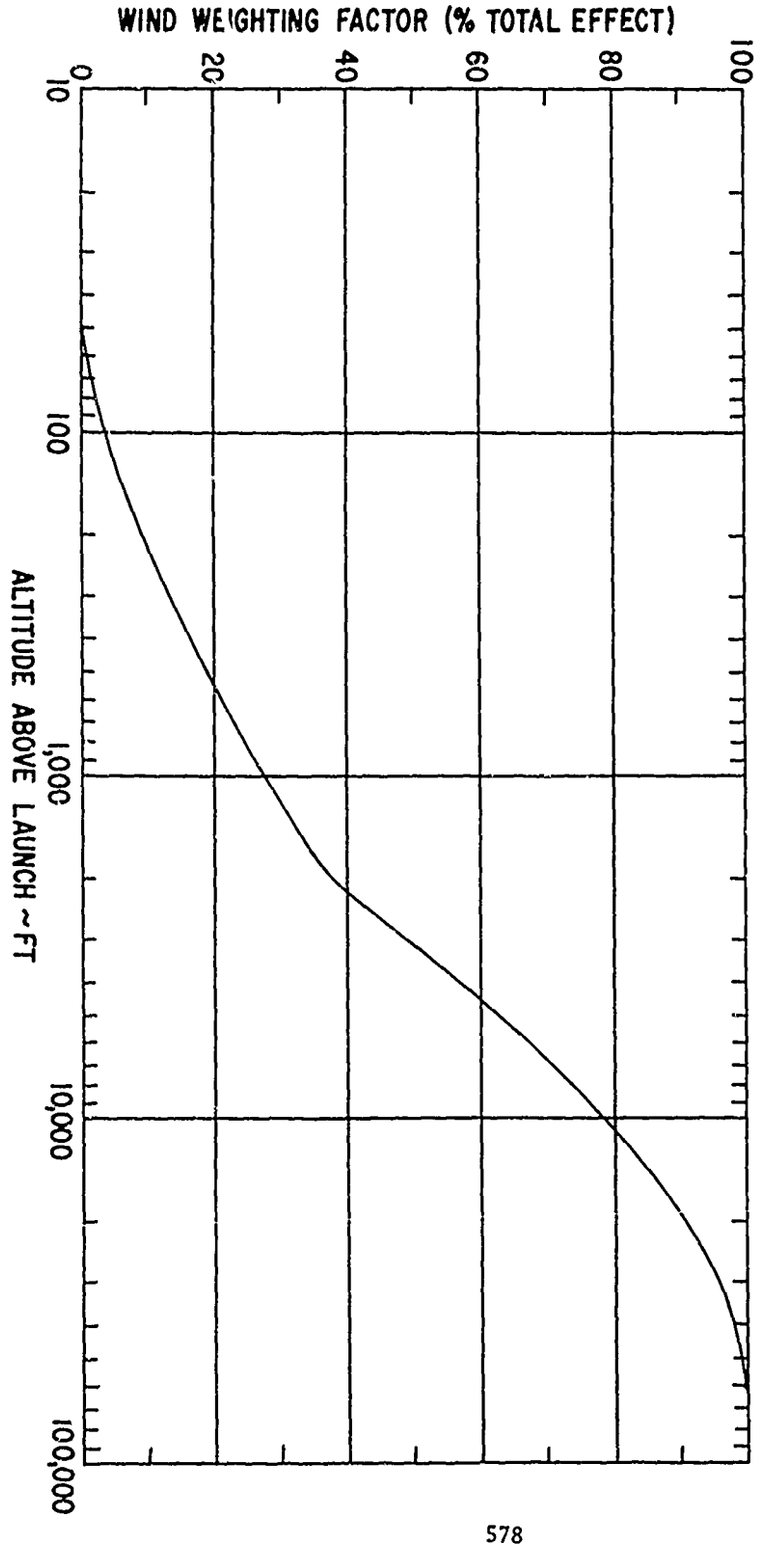

Figure 1. Linear Aerodynamics Wind Weighting Factor versus Altitude

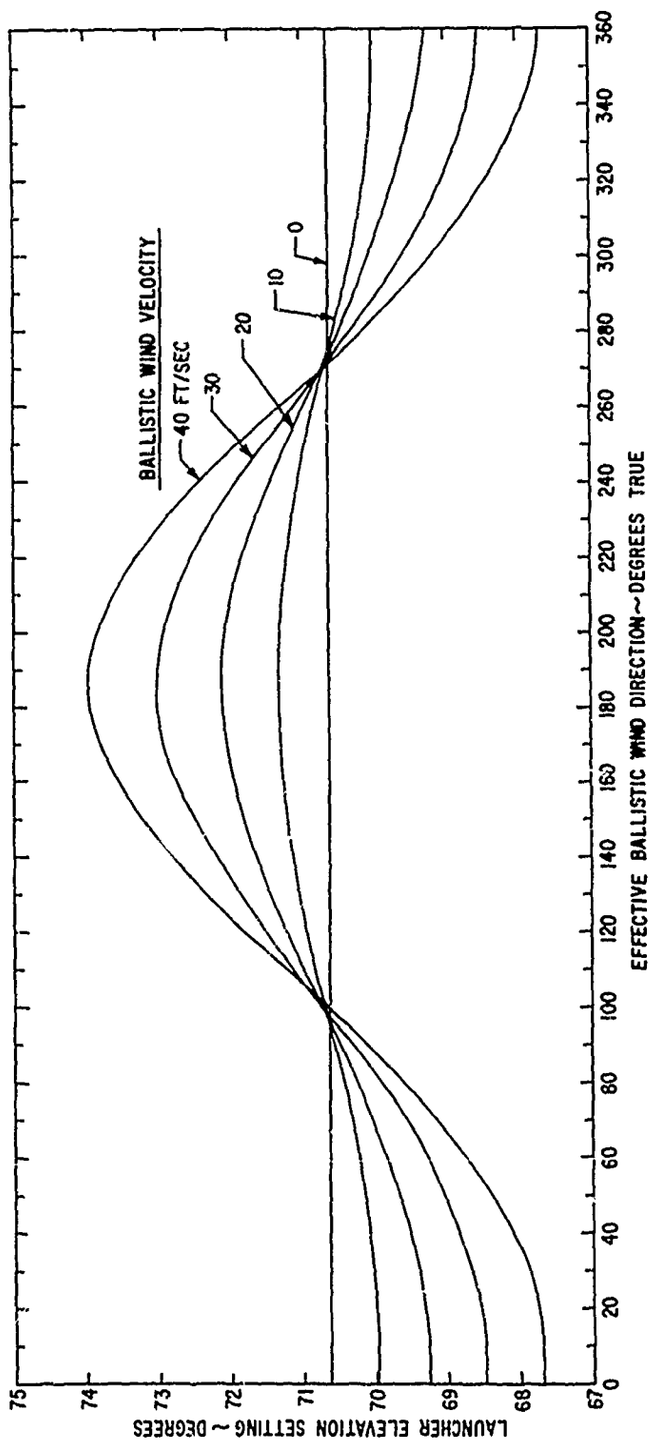

Figure 2. Launcher Correction Chart (Elevation for Ballistic Winds)

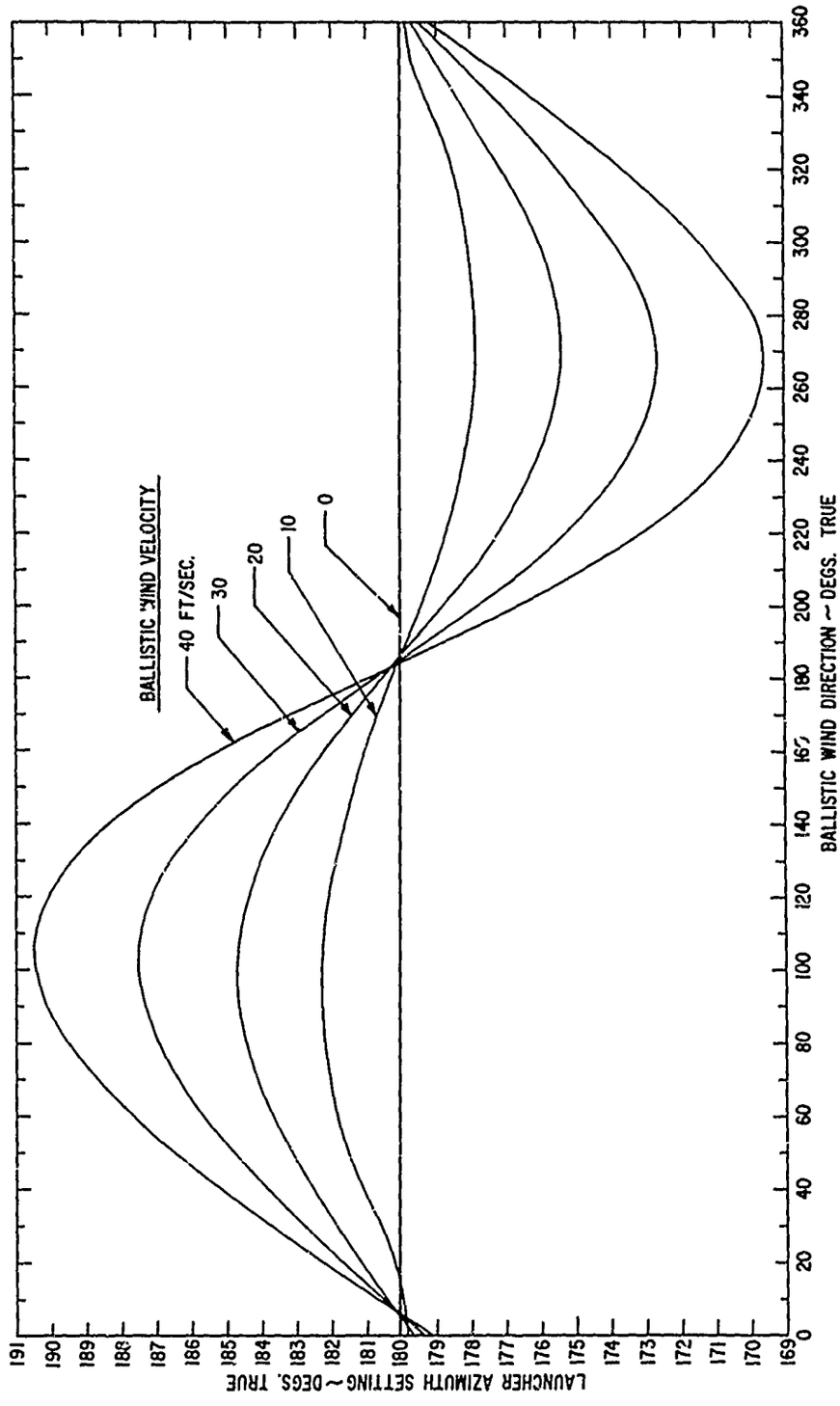

Figure 3. Launcher Correction Chart (Azimuth for Ballistic Wind)

PROCEDURES FOR DERIVATION OF DATA FROM COMPUTER RUNS

This section describes the step-by-step procedures employed to obtain the tabular data in this report from digital computer runs. The computer runs are also briefly described.

GENERAL DESCRIPTION OF COMPUTER RUNS

Two series of computer runs were necessary. The run schedule for both sets is shown in Table 8. The 400 series runs were used to determine the wind weighting data and the 500 series were used to determine the launcher correction charts.

All runs were made from launch at 53 feet of altitude to the test point altitude. Differences in range and cross-range from nominal at the test point altitude were used as input data for determination of wind weighting and launcher correction charts.

All runs used a nominal vehicle weight of 15,478 pounds, a nominal temperature of 77°F, and nominal mass property data. All runs used the "Aero-Ballistic Axes System" with six degrees-of-freedom. This system of reference axes pitches and yaws with the vehicle body but does not roll with it. The effects of spin are accounted for by treating the vehicle as a non-rolling body which has on board a spinning rotor with exactly the same mass properties as the vehicle. Spin rate of the rotor, is specified versus time from a nominal six degree-of-freedom body axes run.

Aerodynamic coefficients used were referenced to body axes and were obtained from the Basic Data Summary. The term "nonlinear aerodynamics" refers to the exact coefficients taken from the Basic Data Summary. In the low subsonic region, both normal force and pitching moment coefficient were nonlinear with respect to angle of attack above five degrees. The term "linear aerodynamics" refers to coefficients extrapolated linearly with angle of attack beyond five degrees. The coefficients slopes between zero and five degrees angle of attack are the same for both "linear" and "nonlinear" aerodynamics and are also the slopes used in the extrapolation of the "linear aerodynamics" data.

For convenience, the significant data from each run was entered on a form similar to that shown in Table 9.

COMPUTATION OF DATA IN TABLE 1, WIND VELOCITY FOR FIVE DEGREE ANGLE OF ATTACK VERSUS ALTITUDE

Vehicle velocity versus altitude data were taken from a nominal trajectory. The wind velocity required from the side wind direction to produce a five degree angle of attack was computed from

$$\text{Wind Velocity} = \tan 5^{\circ} \times \text{Vehicle Velocity}$$

COMPUTATIONS FOR TABLE 2, WIND WEIGHTING FACTORS FOR ALTITUDE LAYERS VERSUS WIND VELOCITY

Data from computer runs 434 through 487 were used. These runs all contained nonlinear aerodynamics and nominal elevation and azimuth launch angles. Constant wind values of different velocities, directions, and altitude coverage were input. In addition, certain data from the

nominal computer run, 500, and linear aero runs, 422, 423, and 424 were used.

The computer data were entered on a form identical to Table 10.

A synopsis of input data and operations is given below. Columns not listed are blank.

Column No.	Entry Description	Source
1	Run number	Run schedule
2	V_W, wind velocity, ft/sec	Computer run
3	ψ_W, wind direction from veh. deg.	Computer run
4	h_W, wind cutoff altitude, ft	Computer run
6	RD))N, range at test point, ft	Computer run
7	Δ RD, change in range with respect to nominal test point range, ft	Col 6--nominal RD))N
8	YD))F, cross-range at test point, ft	Computer run
9	ΔYD, change in cross-range with respect to nominal cross-range	Col. 8--nominal YD))F
11	Δ YD 100 per cent, cross-range for a cross-wind over entire altitude range using linear aerodynamics Note: ΔYD 100 per cent for a 20 ft/sec wind is twice Δ YD 100 per cent for a 10 ft/sec wind	Computer run No. 422

Column No.	Entry Description	Source
13	$f$wn, cross-wind weighting factor for altitude layer from launch to altitude listed in Col. 4, no units	Col 9/Col 11
15	Δ RD 100 per cent, change in range for a head (tail) wind over entire altitude range using linear aerodynamics. Note: Δ RD 100 per cent also extrapolated linearly with wind velocity like Δ YD 100 per cent	Computer run 423 for headwinds; 424 for tailwinds
17	$f$wn, head (tail) wind weighting factor for altitude layer from launch to altitude listed in Col. 4, no units	Col 7/ Col 15
19	Δ fw, change in wind weighting factor across the altitude layer listed in Col. 20, no units	Col. 13 for higher altitude minus Col. 13 for lower. Also computed using Col. 15
20	ΔH, altitude layer used in computing fw	

After the computations of Table 10 were completed, the results of Col. 19 Δ fw, were plotted versus wind velocity, V_W, Col. 2. One curve is required for each altitude layer, ΔH, Col. 20, and each wind direction $_W$, Col. 3. A nonlinear curve results which has a break point near the wind velocity giving five degrees angle of attack. The required number of wind weighting factor, Δ fw, versus wind velocity, V_W, points were read off the plot and entered in Table 2.

COMPUTATIONS FOR TABLE 3, LINEAR AERODYNAMICS WIND WEIGHTING FACTOR VERSUS ALTITUDE

These computations are identical to those used for Table 2, except as follows: (a)all computer runs use linear aerodynamics, (b) the runs used are 400 through 422, (c) the computation of wind weighting factors were again accomplished using Table 10, except that only wind weighting factors for the cross-range direction were computed.

COMPUTATIONS FOR TABLE 4, UNIT WIND EFFECT FOR LINEAR AERODYNAMICS

Data from runs 422, 423, and 424 were used. These runs were made with linear aerodynamics and constant 10 ft/sec cross-head and tail winds, respectively. The wind field extends from launch to test point altitude. The change in range or cross-range between these runs and the nominal, run 500, were divided by the wind velocity to determine the linear unit wind effect, $U.W.E._L$.

COMPUTATIONS FOR TABLE 5, DISPLACEMENT VERSUS EFFECTIVE BALLISTIC WIND VELOCITY

All computer runs used nonlinear aerodynamics and constant wind fields from launch to test point altitude. Data for the nominal C_{M_α}-LAUNCH was taken from runs 500 through 508 through 540. Data for the other

values of C_{M} -LAUNCH were taken from runs 304 through 317.

Differences in range and cross-range at test altitude between wind and no wind cases were computed. These displacements were tabulated against the respective wind input. Since constant wind fields were used in the runs, these winds represent effective ballistic winds and are tabulated as such.

Displacements noted for all $C_{M\alpha}$-LAUNCH cases are referenced to the same test point coordinator. Note that an off nominal $C_{M\alpha}$-LAUNCH run with no wind input misses the test point.

COMPUTATIONS FOR TABLE 6, LINEAR AERODYNAMICS UNIT WIND EFFECT VERSUS BALLISTIC WIND VELOCITY

Computer data was generated by the nominal run number 500, and runs 422 through 433. All runs, except the nominal, used aerodynamics and constant wind fields from launch to test point altitude. The displacements at test altitude were computed for Table 5, and divided by the wind velocity to obtain the linear aerodynamic Unit Wind Effect, $U.W.E._{L}$.

COMPUTATIONS FOR TABLE 7, CALCULATED LAUNCHER CORRECTION CHART POINTS

These computations consist of two basic sections, those for elevation correction and those for azimuth correction.

Elevation Correction

The relationship between head or tail wind and launch elevation angle is first determined. The rate of change of test point range (i.e., range at test point altitude) was determined from computer runs 300 through 302.

These runs all used nonlinear aerodynamics and no wind. From these, the nominal launch angle was determined and the nominal trajectory, run 500, was performed.

Then computer runs were made using various head and tail wind velocities while retaining the nominal launch elevation angle. These are runs 501 through 508.

The results of runs 301, 302, and 501 through 508 were plotted on Figure 3. From this figure, estimates were made of the launch angle required to obtain test point range for a given wind input. Trajectories were then computed using these launch angles and the results were also plotted on Figure 3. These were numbered runs 509 through 524, and lines of constant wind drawn. From Figure 3, the precise launch angle required to hit the test point could be read for each head and tail wind velocity. Since the constant wind lines were very linear, interpolation was used to determine launch angle values rather than curve reading.

The above data were then entered in Table 11. The entries were as follows:

TABLE 11

Column No.	Entry Description	Source
1	Line No.	Consecutive
2	V_W, wind velocity used in computer run at nominal launch angle, ft/sec (e.g. 10 ft/sec for run 501)	Run schedule
3	ψ_W, wind direction from vehicle azimuth, deg	Run schedule
5	RW, range at nominal test altitude for computer run with minimal launch angle, ft (e.g., 68, 302.4 ft for run 501)	Computer run
6	Δ R, difference in test point range between lines, ft	Col. 5, line A Col. 5, line B

Column No.	Entry Description	Source
7	$\gamma_{L_{SET}}$ launch angle required to correct to nominal test point range for wind of Col. 2 and 3	Figure 3
8	$\Delta\gamma$, difference in $\gamma_{L_{SET}}$ between lines, deg	Col. 7, line A Col. 7, line B
9	$\Delta R/\Delta\gamma$, rate of change of test point range with launch angle, ft/deg	Col. 6/Col. 8

These data were also plotted on Figure 4 to assure that linear interpolation was accurate. The data in Table 11 permits one to correct the launch elevation angle for any constant wind if the change in test point range is known.

Azimuth Correction

Digital computer trajectories were calculated with wind inputs of various velocities and directions. These runs all used constant wind fields, nonlinear aerodynamics and the nominal launch elevation angle. These are runs 525 through 562, 566 through 583, and 500 through 508. Data from these runs were entered in Table 12 and the corresponding azimuth and elevation corrections computed.

Since the above computer runs all use the nominal elevation angle and some wind input, they will pierce the test altitude plane at a different range than the nominal. Denote this range as R_W. The cross-range, measured perpendicular to the nominal azimuth line, at R_W will be designated CR_W. The cross-range at the test point is zero. When the range at test altitude is nominal, this range and any cross-range from

this point will be denoted R_N and CR_N, respectively. Since each trajectory with wind will be corrected in elevation so that R_N is attained at the test altitude, the azimuth correction must be based on CR_N and R_N, not on the raw computer data which gives CR_W and R_W. The test point altitude will be designated H_N. H_N is a constant. The trajectory arc length from launch to test point is given the symbol S'. S will denote the chord of the arc length,

$$S = \sqrt{H^2 + R^2}$$

For the wind field under consideration, CR/S' can be taken as constant. Since the trajectory is only slightly curved, CR/S is proportional to CR/S'.

Now $$S_N^2 = R_N^2 + H_N^2$$

$$S_W^2 = R_W^2 + H_N^2$$

and $$S_W = S_N \sqrt{\frac{R_W^2 + H_N^2}{R_N^2 + H_N^2}}$$

Also $$\frac{CR_N}{S_N} = \frac{CR_W}{S_W}$$

Now the change in azimuth is denoted ΔAZ and

$$\sin \Delta AZ = \frac{CR_N}{R_N}$$

$$\text{Therefore: } \Delta \sin AZ = \frac{CR_W}{R_N} \times \sqrt{\frac{R_N^2 + H_N^2}{R_W^2 + H_N^2}}$$

$$\text{and} \quad \sin \Delta AZ = \frac{CR_W}{R_N} \sqrt{\frac{1 + \left(\frac{H_N}{R_N}\right)^2}{\frac{R_W^2}{R_N} + \frac{H_N^2}{R_N}}}$$

Now, $(H_N/R_N)^2 = 2.275745$ using $H_N = 98,502$ ft

and $R_N = 65,295.5$ ft.

$$\text{Therefore: } \sin \Delta AZ = \frac{CR_W}{65,295.5} \sqrt{\frac{3.275745}{\frac{R_W^2}{65,295.5} + 2.275745}}$$

This equation will be used to compute the corrected change in azimuth in Table 12, a description of which is as follows:

TABLE 12

Column No.	Entry Description	Source
1	Run number	Run schedule
2	$V_{W_{BE}}$, wind velocity used in run and effective ballistic wind velocity (ft/sec)	Computer run
3	Ψ_W, wind direction from vehicle launch azimuth, deg	Computer run
4	Line of Table 11 which contains applicable nominal data	---
5	R_W, range at nominal test altitude using nominal launch angle and wind input, ft	Computer run
6	R_W-R_N, difference in range between computer run and applicable nominal from Table 11	Col. 5 Col. 5 nom. (Table 11)
7	γ_{nom}, nominal elevation angle from Table 11, deg	Col. 7 (Table 11)
8	$\Delta\gamma$, change in launch angle required to attain nominal test range, deg	Interpolated from Table 11
9	$\gamma_{L_{SET}}$, required launch angle to compensate for wind, deg	Col. 7 + Col. 8
11	CR_W, cross-range at R_W, ft	Computer run
12 thru 18	Computations to obtain Δ AZ per equation (A)	---
20	$\Theta_{W_{BE}}$, effective ballistic wind direction, degrees true	Col. 3 + Col. 18 + 180°
21	$\sigma_{L_{SET}}$, launcher azimuth setting, degrees true	180° + Col. 18

The results of Columns 2, 9, 20, and 21 constitute Table 7.

TABLE 8
400 SERIES WIND WEIGHTING RUNS

Run No.	Program	V_W	Ψ_W	Wind H_{max}	Errors and Remarks All W.W. Runs Use Nom OE
400	A-B axis	10	90	60	Linear aero. runs Initial veh. alt. = 53 ft.
402				80	
404				100	
405				130	
406				160	
407				200	
408				400	
409				700	
410				1K	
411				2K	
412				3K	
413				4K	
414				5K	
415				7.5K	
416				10K	
417				15K	
418				20K	
419				30K	
420				40K	
421				60K	
422				100K	U.W.E.$_L$ cross-wind @ 10 fps
423			0		" head wind
424			180		" tail wind
425		20	0		" H.W. 20 fps
426			90		C.W.
427			180		T.W.
428		40	0		H.W. 40 fps
429			90		C.W.
430			180		T.W.
431	Res. for	30	0		
432			90		
433			180		

Runs 400-433 Linear Aero.

TABLE 8--Continued

Run No.	Program	V_W	Θ_W	Wind H_{max}	Errors and Remarks All W. W. Runs Use Nom QE
434	A-B axis	10	90	60	Nonlinear aero runs
435				80	
436				200	
437			0	60	
438				80	
439				200	
440			180	60	
441				80	
442				200	
443		20	90	60	
444				80	
445				100	
446				130	
447				200	
448			0	60	
449				80	
450				100	
451				130	
452				200	
453			180	60	
454				80	
455				100	
456				130	
457				200	
458		40	90	60	
459				80	
460				100	
461				130	
462				160	
463				200	
464			0	60	
465				80	
466				100	
467				130	

TABLE 8--Continued

Run No.	Program	V_W	Θ_W	Wind H_{max}	Errors and Remarks
468	A-B axis	40	0	160	Nonlinear aero. runs
469		↓	↓	200	
470		40	180	60	
471				80	
472				100	
473				130	
474				160	
475				200	
476		30	90	60	
477				180	
478				100	
479				130	
480				160	
481		35		200	
482		10	0	100	
483		↓	180	↓	
484		10	0	130	
485		↓	180	↓	
486		20	0	160	
487		↓	180	↓	

TABLE 8--Continued
500 SERIES LAUNCHER SETTING CHARTS

Run No.	Program	QE	V_W	Ψ_W	Errors and Remarks
500	A-B axes	70.634	0	-	Nominal --AB axes-
501			10	0	All winds thru
502			20	0	test point
503			30	0	nonlinear aero
504			40	0	nominal WT, temp
505			10	180	and c.g.
506			20		
507			30		
508			40		
509		71.4	10	0	
510		71.0	10	0	
511		69.9	10	180	
512		70.2	10	180	
513		72.15	20	0	
514		71.50		0	
515		69.10		180	
516		69.70		180	
517		73.00	30	0	
518		72.00		0	
519		68.20		180	
520		69.20		180	
521		74.00	40	0	
522		73.00		0	
523		67.20		180	
524		68.20		180	
525		70.634	10	22.5	
526			20		
527			30		
528			40		
529			10	45	
530			20		
531			30		
532			40		
533			10	67.5	

TABLE 8--Continued

Run No.	Program	QE	V_W	Ψ_W	Errors and Remarks
534	A-B axes	70.634	20	67.5	
535			30		
536			40		
537			10	90	
538			20		
539			30		
540			40		
541			10	112.5	
542			20		
543			30		
544			40		
545			10	135	
546			20		
547			30		
548			40		
549			10	157.5	
550			20		
551			30		
552			40		
553			20	-22.5	
554			40		
555			20	-45	
556			40		
557			10	-90	
558			20		
559			30		
560			40		
561			20	-135	
562			40		
563		71.305	40	259.727	Check run σ_L = 169.727
564		71.293	10	201.857	" σ_L = 179.357
565		69.344	30	309.503	" σ_L = 174.503

TABLE 8--Continued

Run No.	V_W	ψ_W	Similar to Run
566	10	22.5	525
567	30	↓	527
568	10	-45	529
569	30	↓	531
570	10	-135	545
571	30	↓	547
572	10	-67.5	533
573	20	↓	534
574	30	↓	535
575	40	↓	536
576	10	-112.5	541
577	20	↓	542
578	30	↓	543
579	40	↓	544
580	10	-157.5	549
581	20	↓	550
582	30	↓	551
583	40	↓	552

TABLE 9

PAGE NO INTERPOLATED DATA

①	②	③	④	⑤	⑥	⑦	⑧	⑨	⑩	⑪	⑫	⑬	⑭	⑮	⑯	⑰	⑱	⑲	⑳	㉑
										Test Conditions										
RUN NO.	REMARKS			γ_L LAUNCH ANGLE	σ_L LAUNCH AZIMUTH		V_w FT/SEC	Θ_w DEGS. TRUE		TIME COL. 1,1. SECS.	HGC)F 5,1 FT.	RD))N 1,4 FT.	XD))F 4,3 FT.	YD))F 5,3 LAT. FT.	PHIGD 3,1 LONG. DEG.	THL)D 4,1 DEG.	GAMDD 5,4 DEG.	t	HGC)F	RD))N

508

NON LINEAR AERO RUNS – W.W.
TABLE 10

REPORT NO 5006-10

PAGE NO 42

① RUN NO	② V_ω	③ ψ_ω	④ h_ω	⑤	⑥ RDIN RANGE FT.	⑦ ΔR_D ⑥-NOM	⑧ YDIN CROSS RANGE	⑨ ΔY_D ⑧-NOM	⑩	⑪ ΔY_D 100%	⑫	⑬ f_{w_m} ⑨/⑩	⑭	⑮ ΔR_D 100%	⑯	⑰ f_{w_n} ⑰/⑮	⑱	⑲ Δf_ω $f_{w_n} - f_{w_{n-1}}$	⑳ ΔH	㉑
500 (NOM.)	0	–	–		65295	0	-47.78	0		245049				2908.2	N.W.					
434	10	90	60				2.782	50.512		245085		.02061						.02061	53-60	CROSS
435	"	"	80				52.195	99.975		"		.04079						.02018	60-80	
436	"	"	100				247.816	295.576		"		.12160								
437	10	0	60		65378.5	83.0								2908.2	"	.07854		.07854	53-60	NOAD
438	"	"	130		65497.9	152.4								"		.10240		.02386	60-80	"
439	"	"	200		65666.8	371.3								"		.13767		.01709	80-100	"
ETC.																				

Form 4

REPORT NO 8006-10

PAGE NO 43

TABLE II

① Line No.	② V_w	③ $\psi_N = \theta_N$ on Run Sched.	④ Line for Nominal Data	⑤ Range at Nom. Test Alt. γ_L=26.63°	⑥ ΔR	⑦ θ_L set Launch Angle to Corr. to Nom. Test Range	⑧ $\Delta\theta$	⑨ $\frac{\Delta R_{TD}}{\Delta \theta_L}$ Ft/Deg	⑩	⑪ C_{RN} Yds	⑫ $\frac{⑪}{65295.5}$	⑬ $\frac{⑪^2}{2.276748}$ +	⑭ $\frac{3.276748}{⑬}$	⑮ $\sqrt{⑭}$	⑯ $\frac{⑪}{65295.5}$	⑰ $\sin\Delta A_{TD} = ⑯ \times ⑮$	⑱ $\Delta A_{TD} = \sin^{-1}⑰$	⑲	⑳ $\theta_w - \theta_{Nom}$ ⑤ + ⑱	㉑ θ_L set $\theta_w + 180° + ⑱$
1	40	0		80522.5		Linear interpol. 73.347		47929		-1099.61	1.233202	3.276748	.862826	.928884	-.0240538	-.015442	+.896		+.896	180.896
					415 820		.956													
2	30	0		75940.5		72.991		46727		-774.857	.1532636	3.628381	.902.82	.950164	7.28869×10^{-3}	.010276	+.646		-.646	180.646
					4172.7		.893													
3	20	0		71767.8		72.098		44542		-474.031		3.483819	.940271	.969677	7.28044×10^{-3}		+.405		+.405	180.405
					3463.4		.778													
4	10	0		68302.4		71.320		43832		-289.527		3.369968	1.023114	1.011532	-3.	.0036167	+.207		+.207	180.207
					3006.9		.686													
5	0	0		65295.5		70.634		42820		-97.78	1	3.276748	1	1	.13175	.13175	+.042		+.042	180.042
					2859.4		.667													
6	10	180		62436.1		69.967		42163		138.549		3.18001	.971879	.985838		.002.30	-.123		179.877	179.877
Etc																				

Form 4

REPORT NO 8006-10

PAGE NO. 44

TABLE 12

(1) LINE N	(2) V_w	(3) ψ_w	(4) LINE FOR NOM. DATA	(5) RANGE AT NOM. TEST ALT. $\gamma_L = 70.634$	(6) $R - R_{nom}$	(7) γ_{nom}	(8) $\Delta\gamma$	(9) $\gamma_{L_{SET}}$	(10)	(11) C_{EW} $YD \gg F$	(12) $\frac{(5)}{65295.5}$	(13) $(12)^2 + 2.275765$	(14) $\frac{(13)}{3.275765}$	(15) $\sqrt{(14)}$	(16) $\frac{(11)}{65295.5}$	(17) $\sin \Delta AZ$ $\frac{(16)}{(15)}$	(18) ΔAZ $-\sin^{-1}(17)$	(19)	(20) σ_{nom} (3) + (18)	(21) $\sigma_{L_{SET}}$ $180° +$ (18)
18	10	67.5	5	667246	1429.1	70.634	.326	70.960		219843			1.013509	1.006752		.033444	-1.917		65.583	178.083
19	20	•	4	68937	211.3	71.320	.047	71.367		4702.11			1.030834	1.01530		.070928	-4.067		63.433	175.933
20	30	•	4	707653	2462.9	71.320	.553	71.873		7589.9			1.033288	1.026298		.113260	-6.503		60.997	173.497
ETC -																				

Form 4

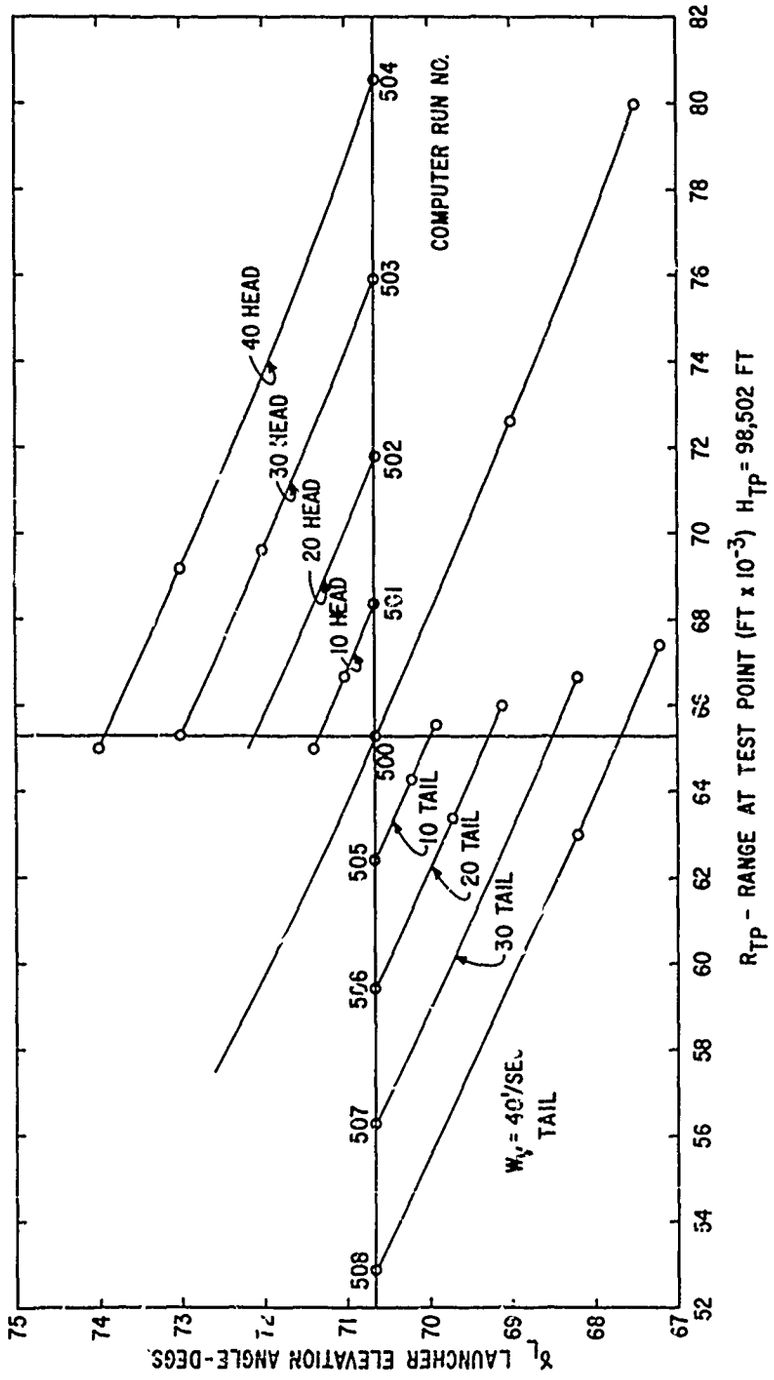
COMPUTER RUN NO.
504
503
502
501
500
505
506
507
508
40 HEAD
30 HEAD
20 HEAD
10 HEAD
10 TAIL
20 TAIL
30 TAIL
W_y = 40'/SEC TAIL
γ_L LAUNCHER ELEVATION ANGLE-DEGS
R_{TP} - RANGE AT TEST POINT (FT x 10^{-3}) H_{TP} = 98,502 FT

Figure 3

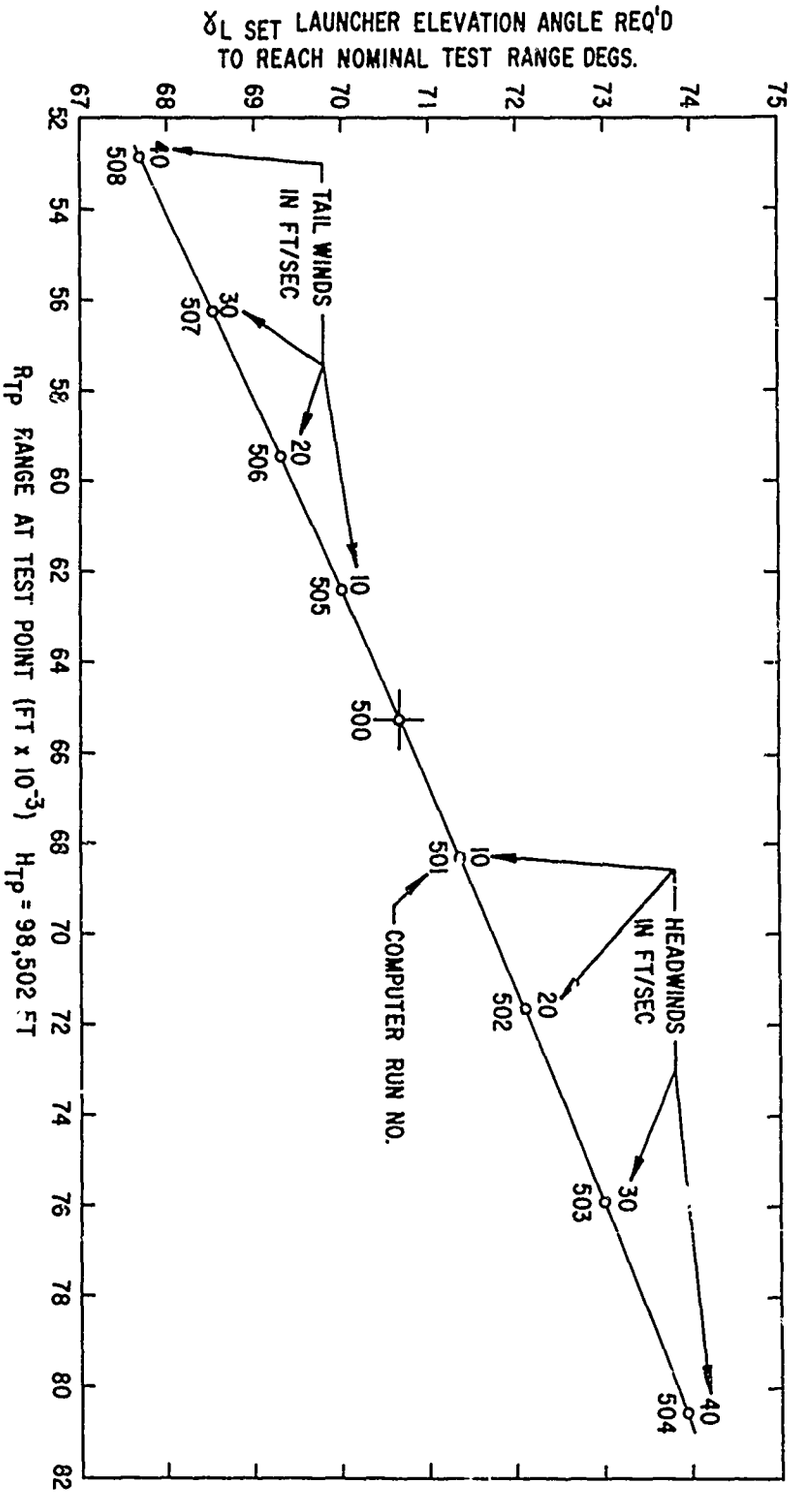
γ_L SET LAUNCHER ELEVATION ANGLE REQ'D
TO REACH NOMINAL TEST RANGE DEGS.
67
68
69
70
71
72
73
74
75
52
54
56
58
60
62
64
66
68
70
72
74
76
78
80
82
TAIL WINDS
IN FT/SEC
40
30
20
10
HEADWINDS
IN FT/SEC
10
20
30
40
COMPUTER RUN NO.
508
507
506
505
500
501
502
503
504
R_{TP} RANGE AT TEST POINT (FT x 10^{-3}) H_{TP} = 98,502 FT

Figure 4

BLANK PAGE

PRELAUNCH REAL-TIME IMPACT PREDICTION SYSTEM FOR THE AEROBEE 350 ROCKET

by

HENRY RACHELE

and

VERTIS C. COCHRAN

ATMOSPHERIC SCIENCES LABORATORY
WHITE SANDS MISSILE RANGE, NEW MEXICO

ABSTRACT

A general description is given for an improved automatic data collection and processing system for use in prelaunch impact prediction of the high altitude, highly wind-sensitive Aerobee 350 rocket.

The system differs in many respects from those presently used at White Sands Missile Range, but fundamentally is an outgrowth of previous developments incorporating recent knowledge on wind sensors and measurement techniques, statistical analyses and prediction techniques, ballistic model refinements, state-of-the-art electronics for wind measurement, and the use of complex high-speed computer programs during countdown operations.

Specifically, the major components include the use of a 500-ft. wind tower, multiple pilot balloons, GMD-4 and the FPS-16 radar for upper wind measurements. New data processing techniques include data editing procedures, wind extrapolation in time, and the reduction in time of the operational countdown period.

INTRODUCTION

The primary problem in firing unguided rockets is being able to predict the behavior of the rocket before actual firing. One of the factors that has a great influence on this behavior is the wind, since unguided rockets are fin-stabilized. Hence, they will turn into the wind during the burning phase and drift with the wind while coasting.

The problem of the wind is further complicated by variability which is difficult to measure and predict. Hence, it is concluded that the wind velocities must be measured accurately and continually up to launch time, that this information be used in rather detailed and sophisticated ballistic models, and finally that results therefrom be made available immediately to the impact predictor (ballistician).

In order to solve this problem many developments of ballistic models, wind measuring systems, and general impact prediction techniques have been going on at White Sands Missile Range for several years for both simulation studies and to provide prelaunch impact point prediction (for range safety and experiment package recovery) of unguided rockets.

The latest development of prelaunch impact prediction system at White Sands Missile Range was the Meteorological Real-Time Prediction System used in support of the Athena project. The Athena is a multiple-stage unguided rocket which travels over populated areas for a distance of 450 miles.

The need and justification of such a system was based on (1) the reduction in the number of rockets which must be "cut down" for safety reasons, (2) a decrease in the number of cancellations due to atmospheric conditions, which minimizes the cost of each firing, and (3) the maximization of the number of rockets which can be safely fired in a given time period.

This paper gives a general description of a further improved system for support of the Aerobee 350 rocket including improvements made to the 500-ft. wind tower, better balloon sensors and (T-9) radar trackers, the use of more sophisticated upper wind tracking instrumentation (GMD/4 and FPS-16 radar), mathematical and statistical data processing and wind data prediction techniques; and a recommended countdown schedule which is much shorter timewise than those used previously for similar support operations.

DISCUSSION

The real-time system for the Aerobee 350 (Fig. 1) will consist of an Automatic Wind Display on Strip Chart Recorders and a printer connected directly to the central computer at the blockhouse, a 500-ft. meteorological tower, three automatic radar (T-9) for pilot-balloon (pibal) tracking, GMD/4 and/or AN/FPS-16 radar (upper wind system), meteorological rockets for wind measurements above 100,000 feet, a data transmission system (analog and digital) and a high-speed digital computer.

REAL-TIME METEOROLOGICAL DATA SYSTEM

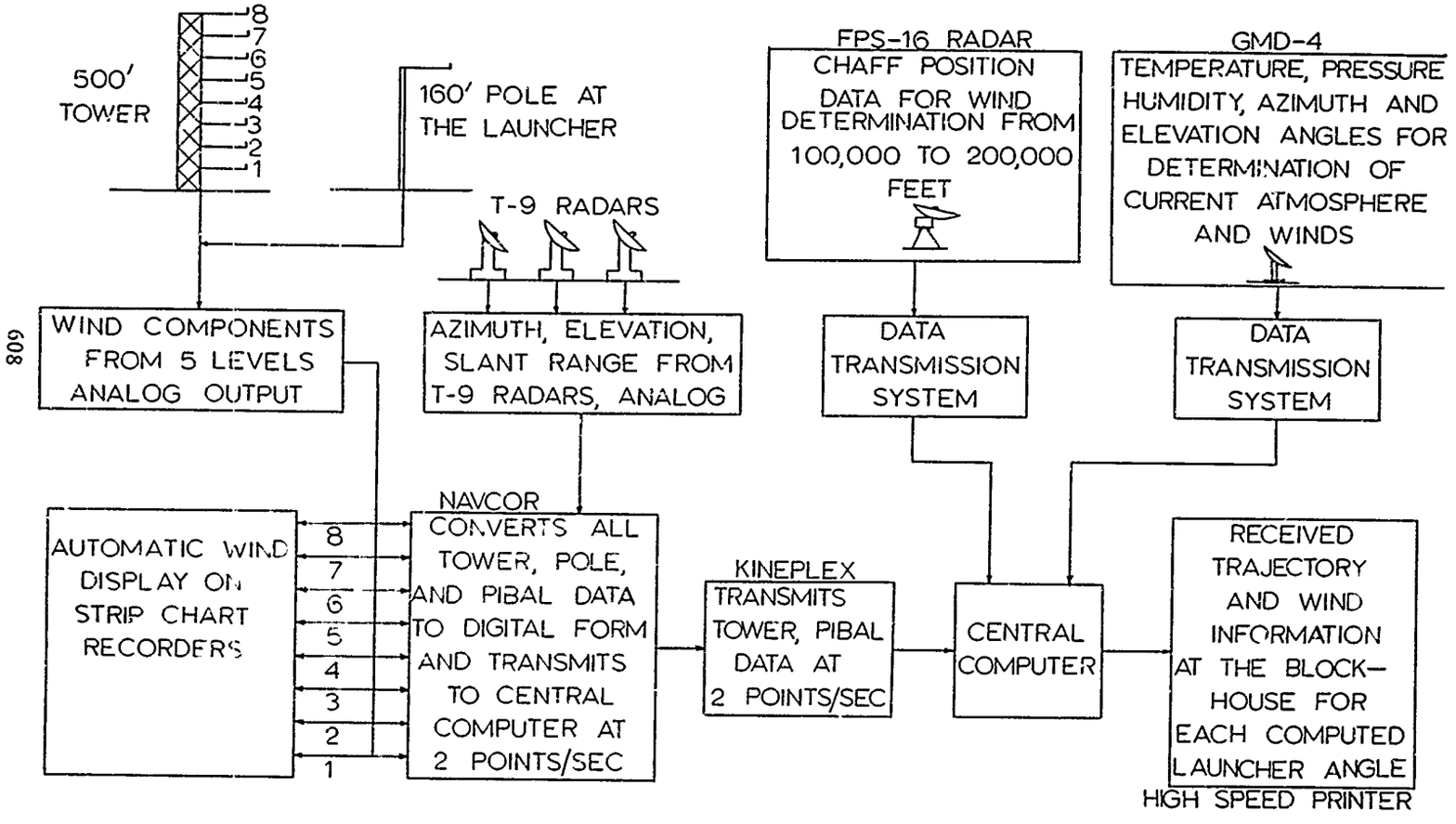

(1) The Wind Display Recorders accept wind data (analog form) from the tower. It continually and automatically displays tower wind information as components.

Since data from the tower and the T-9 trackers are in analog form, an independent feature is used at the blockhouse for digitizing the data for transmission to the digital computer. Basically it consists of NAVCOR and digital encoders.

(2) The 500-ft. tower is as near the rocket launch tower (160 feet high) as possible. The unusual aspect of the wind tower is the method used to place the wind measuring sensors in position. The technique consists of specially designed, light-weight, instrument carriages which travel up and down a face of the tower on a three-rail track and are completely controlled from the ground. The instruments, a total of eight, are mounted on 10-ft. booms affixed to the carriage. In the case of the Aerobee 350 only five instruments will be used above 160 feet. These five booms will be placed on the tower relative to a special preflight analysis made on the Aerobee 350.

The wind data from the tower, in components, are collected continuously and transmitted (analog) to the blockhouse where they are (a) displayed on strip chart recorders, and (b) digitized for transmission to the digital computer at the rate of two data frames per second.

(3) The three (T-9) radar are used for tracking pilot balloons, up to heights of 15,000 feet above the surface. During initial planning of the system an improved balloon (Jimsphere) was considered. An evaluation of both 100-gram and Jimsphere performance as wind sensors showed that for Aerobee 350 support an underinflated 100-gram balloon would be sufficient. A point of significance in this study, however, is that the Jimsphere is shown to be less erratic in aerodynamic behavior than the 100-gram balloon and the Jimsphere wind data provide more stable impact prediction results when applied to the Aerobee 350 rocket. However, the difference in impact prediction results are well within the no-wind dispersion of the rocket.

Since there are three T-9 radars, and only one is required for tracking any one balloon, it is possible to track two balloons (released six minutes apart) providing data which has six minutes time variability up to 10,000 feet.

The T-9 has a continuous and automatic readout (analog) of azimuth and elevation angles and slant range. The slant range and angle data are transmitted (analog) to the blockhouse. The data from any two of the three radar are digitized (two frames/second) and transmitted to the digital computer where they are processed and made available for ballistic computation.

(4) The GMD/4 and/or AN/FPS-16 will be used for obtaining upper wind data from 10,000 feet up to approximately 215,000 feet.

The GMD/4 accepts meteorological and ranging data, prepares it for Kineplex transmission at selected time intervals by means of a Meteorological Data Processor, Sonex Type 3703C. Tracking range is 400,000 yards with an accuracy of one yard in slant range. Accuracy of the azimuth and elevation angles is 0.01 degrees.

The FPS-16 radar was designed specifically for guided missile range instrumentation, providing highly accurate trajectory data for evaluation of missile performance. It has accuracy of 0.1 mil both azimuth and elevation, five yards rmse in range on all targets having a signal-to-noise ratio of 20 db, either skin or beacon track. Since the FPS-16 radar have been adapted for real-time data transmission, and because of the high degree of accuracy in determining the position of a balloon with time and height, and consequently the resulting wind velocities, the plan is to incorporate the real-time capability into the Aerobee 350 system. Hopefully the data processing methods used will result in mean velocity errors which are less than three feet/second.

(5) The Data Transmission System at the blockhouse has the capability of handling wind in components (five levels) from the tower, and the azimuth and elevation angles and slant range from two T-9's, all sampled at the rate of two data points per second. Because of the distance of transmission to the computer center, it is more feasible to transmit the data in digital form.

The system selected for the actual transmission is the Collins Kineplex Serial/Parallel digital Data Modern (TE-210 D-2), which is a solid state, full duplex transmitter and receiver capable of a 2400 bits-per-second data rate over a voice bandwidth channel such as wire line, cable, carrier or microwave.

(6) The principal data analysis and computations are performed by a high-speed computer which is located at WSMR main computer complex. The real-time program used will be a modification of the MARK I program (3), runs under a priority-controlled monitor which receives the input data and supervises the operations of the various data processors. The three major processors are: (1) the tower data processor; (2) the pibal processor; and (3) the launch angle processor.

The tower data processor maintains a current file of the latest N (the exact value is determined by a premission input) seconds of data from the 500-ft. tower. When instructed by the monitor, these data are edited, averaged, and the quality of these data is assessed. When poor quality data are detected at a given level, these data are replaced by extrapolations or interpolations from adjacent levels.

The pibal data processor receives the data from the T-9 radar, edits and smooths these data, and then computes the balloon's position and the wind components.

Launcher settings are determined after the completion of each pibal balloon track. These computations may also be performed at any other times by a command from the computer operator and using updated tower

or upper wind data. These launcher settings are determined by an iterative procedure. The wind profile is introduced into a ballistic model. The point of interest (usually second stage impact) is determined by numerically integrating the equations of motion. If the simulated point is not within a prestated tolerance to the desired point, a new simulation is performed using different launcher settings, and the iteration is continued until the difference between the desired and simulated points is within tolerance.

After the final launcher setting is obtained the model will also provide the impact of the instrumentation or payload.

In Figure II is shown what is felt to be an ideal countdown for the Aerobee 350.

CONCLUSION

Even though the current real-time system at WSMR is a proven system and the foundation for the Aerobee 350 system, the models and systems can never be expected to provide trajectories which agree exactly with the impact of an actual flight because of the other uncertainties in aerodynamics parameters and the general mechanics of unguided rocket systems. However, a simple fact, and an extremely important one, is that by designing and refining the ballistic models and wind measuring systems, one can minimize the impact prediction dispersion due to atmospheric effect on the rocket.

Even though it is felt that the presented countdown for the Aerobee 350 is ideal, it may be modified in any way by the project and ballistician in charge to have a successful mission. Also there is no mention of recycle time in case of extended holds since this will also be a problem to be solved by the project and ballistician in charge of the impact prediction.

COUNTDOWN SCHEDULE

TIME	PIBAL	RAOB	RAWIN	ARCAS	PERT. INFO.
Prior to T-180					GMD 1 Manual Reduction of data; ballistic comp. using weighting factors to determine likelyhood of firing.
T-180		100K			GMD/4 only - record in computer center on digital tape
T-100				215K	FPS/16 Only-record at comp. in real time
T-90					Computer declared Operational
T-75		100K			GMD/4 only
T-60					Met. check out of comp.
T-45					Met. check out complete; RAOB winds (100K) computed and stored; ARCAS winds 215-80K computed and stored
T-45	100 gr. (T-9#1) to 10,000 ft				First Impact Pred. using digital comp. and full scale model
T-39	100 gr. (T-9 #2) to 10,000 ft				
T-31	100 gr. (T-9 #1) to 15,000 ft				
T-24	100 gr. (T-9 #2) to 10,000 ft				
T-14	100 gr. (T-9 #1) to 5,000 ft.				
T-10	100 gr. (T-9 #2) to 5,000 ft				Rawin complete and stored
T-8	100 gr. (T-9 #1) to 10,000 ft				Impact prediction using full scale ballistics model
T-4	100 gr. (T-9 #2) to 5,000 ft				
T-2					Final Launcher Setting
T-1					Pert. Eq. using tower data, T-3 pibal data, and wind prediction equations

BIBLIOGRAPHY

Ballard, Harold N., "Rocketsonde Techniques for the Measurement of Temperature and Wind in the Stratosphere," ERDA-269, U. S. Army Electronics Research and Development Activity, White Sands Missile Range, New Mexico, February 1965.

Cochran, V. C., E. M. D'Arcy, and F. Ramirez, "Digital Computer Program for Five-Degree-of-Freedom Trajectory," ECOM-5036, March 1966.

Duncan, L. D. and H. Rachele, "Real-Time Meteorological System for Firing of Unguided Rockets," ECOM-5037, February 1966.

Glass, Roy I., Jr., "Missile Meteorology Tower," Bull. Amer. Meteor. Soc., September 1964.

USA ERDAW and IBM/FSD/WSMR, "Documentation of the USA ERDAW Real-Time Meteorological Software System," Mark I, Prepared by USA ERDAW and IBM/FSD/WSMR, 21 April 1965.

METEOROLOGICAL REQUIREMENTS FOR THE AEROBEE - 350

by

Edward M. D'Arcy

ABSTRACT

This report discusses the optimum wind layer thickness to be used for the Aerobee - 350. These layers should be small near the surface (close to the launcher) but can be relatively large at the top of the profile.

The need for wind data above 100,000 feet is discussed. Results show that they are needed for the Aerobee - 350.

The advisability of firing the Aerobee - 350 with a real-time met system is discussed and the conclusion reached that for best results, such a system should be used.

INTRODUCTION

For many years the Aerobee - 150 has been fired successfully at White Sands Missile Range using the field wind-weighting technique. Now, in response to the demand for higher performance rockets, the Aerobee - 350 is being considered. The 350 model is capable of placing a much heavier payload to a higher altitude than the 150. From the preliminary study it appears that the Aerobee - 350 will be a very useful research vehicle. For each new rocket brought to the range, a study must be made to determine if the missile can safely be fired at White Sands. A dispersion analysis has been performed for the Aerobee - 350 (1). Using results from that dispersion analysis, this report presents some of the meteorological requirements such as:

(1) How fine or coarse should the wind layers be to give the desired accuracy in impact?

(2) Will increased accuracy of impact prediction warrant the use of a rocket to obtain winds above 100,000 feet?

(3) Should the missile be fired with a real-time met system or will field techniques suffice?

DISCUSSION

Wind Layer Thickness

To determine the layer size to use in measuring winds for the impact prediction of the Aerobee - 350, data were obtained from

cinetheodolites at three-foot intervals from ground level to 12,000 feet. These original data were used and then averaged for layers of 24, 51, 99, 198, 498 and 999 feet. These profiles were then applied in the equations of motion (2) and checked against the three-foot layers as a standard. It can be seen from Table I that accuracy declines rapidly as the layer thickness increases. For operational simplicity one desires the least number of wind layers possible. One can see that the 51-foot layers seem to fit these conditions. Further study shows that if we start with 50-foot layers at the top of the launcher we can increase them considerably towards the top of the profile, as can be noted from the ballistic factors presented in Table II. The factors are large in the lower layers and decrease toward the top.

There were no large changes due to increased layer thickness in the profile above 15,000 ft. as can be seen from the second part of Table I. This could have been expected since from Table II one can see that by 15,000 ft., 82% of the wind weighting has taken place. The layer thickness marked Real Time is a variable layer thickness profile. Table III is a tabulation of layers compiled from this study.

Winds Above 100,000 Feet

A Rawinsonde is used to obtain wind data to an altitude of about 100,000 feet. If winds above this altitude are to be measured, a small rocket designed for this purpose must be used. Because of the expense involved in hardware and range time, it must be determined that the increased accuracy in impact prediction warrants the cost.

TABLE I

Change in Impact Due to Increase in Layer Thickness

Layer Thickness (ft)	X (ft)	Y (ft)	ΔX (ft)	ΔY (ft)
3	109676	1133293		
24	109842	1131807	166	1486
51	109342	1128266	334	5027
99	106407	1125731	3269	7562
198	95474	1122155	14202	11138
498	76223	1126785	33453	6508
999	58714	1135628	50962	2335

Above 15,000 Feet

	X(mi)	Y(mi)	ΔX(mi)	ΔY(mi)
500	201.2	398.7		
1000	201.0	398.9	.2	.2
2000	200.8	399.0	.4	.3
5000	199.3	399.9	1.9	1.2
Real Time	200.3	399.3	.8	.6

TABLE II

Ballistic Factors

Height	B.F.	Height	B.F.
4200	0	9040	.0330
4270	.1162	11040	.0467
4340	.0859	14040	.0456
4410	.0739	16540	.0259
4480	.0548	19040	.0197
4550	.0513	24040	.0281
4640	.0443	29040	.0194
4740	.0399	34040	.0143
4840	.0253	44040	.0203
4940	.0174	54040	.0133
5140	.0118	64040	.0097
5340	.0138	84040	.0114
5540	.0170	104040	.0072
5790	.0204	124040	.0053
6040	.0171	144040	.0035
6290	.0174	164040	.0021
6540	.0151	184040	.0008
7040	.0280		
8040	.0436		

TABLE III

Layers For The Aerobee - 350

(Feet MSL)

Tower	Rawinsonde
4200 - 4270	14040 - 16540
4270 - 4340	16540 - 19040
4340 - 4410	19040 - 24040
4410 - 4480	24040 - 29040
4480 - 4550	29040 - 34040
	34040 - 44040
Pibal	44040 - 54040
4550 - 4640	54040 - 64040
4640 - 4740	64040 - 84040
4740 - 4840	84040 - 104040
4840 - 4940	
4940 - 5140	Rocket
5140 - 5340	104040 - 124040
5340 - 5540	124040 - 144040
5540 - 5790	144040 - 164040
5790 - 6040	164040 - 184040
6040 - 6290	
6290 - 6540	
6540 - 7040	
7040 - 8040	
8040 - 9040	
9040 - 11040	
11040 - 14040	

Naturally, no wind data above 100,000 feet are needed for rockets that burnout at or below that altitude because the effect on a nonburning rocket, at these altitudes, is negligible. The Aerobee - 350, however, burns out between 150,000 and 175,000 feet depending on payload and launch angle. To determine whether wind data above 100,000 feet are needed, ten profiles measured during Athena firings were applied to the 500- and 150-pound payload Aerobee - 350 with a launch angle of 1° from vertical. Table IV shows that there can easily be enough displacement, especially in the 150-lb payload, to warrant the use of a rocket for upper winds.

Real-Time Launch

To launch a rocket using a real-time met system costs much more than the normal field method. This is because a high-speed computer must be utilized solely for this purpose for several hours. A dispersion analysis has been made on the Aerobee - 350 and shows it to be fairly wind sensitive. The 1σ radius, computed from theoretical data, for the 150-lb payload is about 30 miles and about 22 miles for the 500-lb payload. To compute the dispersion, changes were made in C_D, C_{n_α}, C. P., C_{m_q}, Thrust, Mass, C. G. and moment of inertia. The r.m.s. value of these changes gives the column in Table V marked "no wind". The column marked "5-mph, no wind error," shows the influence of a 5-mph wind with the changes. The 10 and 20-mph columns show what a 5-fps error in a constant base profile of 10 and 20-mph,

TABLE IV

Effect of Wind Above 100,000 Feet

500-lb Payload 1°

Wind	X (mi)	Y (mi)	ΔX (mi)	ΔY (mi)
No Wind	13.435	30.665		
B-001	9.498	30.612	3.937	.053
B-002	9.852	30.460	3.583	.205
B-003	8.347	30.317	5.088	.348
C-009	9.150	30.731	4.285	.066
D-004	9.112	30.288	4.325	.377
D-005	8.577	30.731	4.858	.066
D-006	13.125	30.480	0.310	.185
D-009	9.906	30.327	3.529	.136
D-012	10.700	30.229	2.735	.436
D-033	13.072	31.468	0.363	.803

150-lb Payload 1°

No Wind	20.852	40.192		
B-001	13.590	40.888	7.262	.696
B-002	14.300	40.285	6.552	.093
B-003	11.752	39.949	9.100	.243
C-009	13.441	40.624	7.411	.432
D-004	12.824	39.334	8.028	.858
D-005	12.324	40.820	8.528	.628
D-006	20.925	40.496	0.073	.304
D-009	14.454	39.941	6.398	.251
D-012	16.101	39.750	4.751	.442
D-033	20.008	41.789	0.844	1.597

TABLE V

Radius of 1σ Dispersion Circle
(mi)
150 lb Payload
(+) errors

Launch Angle	No Wind	5 mph No Wind Error	10 mph	20 mph
1	3.488	3.668	30.780	29.067
2	7.238	7.343	30.644	28.652
3	10.967	11.049	30.839	28.554
4	14.707	14.774	31.358	28.903
5	18.512	18.570	32.257	29.768
		(-) Errors		
1	3.588	3.598	31.161	29.547
2	7.364	7.376	31.199	29.220
3	11.106	11.114	31.475	29.266
4	14.888	14.894	32.361	29.743
5	18.699	18.704	33.060	30.632
		500 lb Payload (+) Errors		
1	2.627	2.754	23.456	21.852
2	5.352	5.426	23.284	21.381
3	8.175	8.230	23.244	21.113
4	11.008	11.052	23.506	21.280
5	13.860	13.899	24.035	21.820
		(-) Errors		
1	2.497	2.527	23.835	22.383
2	5.333	5.347	23.708	21.932
3	8.123	8.132	23.817	21.806
4	10.956	10.962	24.102	21.964
5	13.800	13.805	24.653	22.469

combined with the aerodynamic changes, can do. The large dispersion shown here would seem to necessitate the use of a real-time met system.

CONCLUSIONS

To obtain the desired accuracy and still maintain a small number of wind layers for operational simplicity, the layers should be small at the bottom and can become quite large at the top of the profile.

For the Aerobee - 350 it is advised that a rocket be used to obtain wind data above 100,000 feet for use in the impact prediction. These measured winds should go to at least 180,000 feet.

Because of the wind sensitivity of the Aerobee - 350, and the large dispersion area, it is advised that at White Sands Missile Range it be fired only using a real-time met system.

BIBLIOGRAPHY

1. D'Arcy, Edward M., "Theoretical Dispersion Analysis of the Aerobee - 350," Atmospheric Sciences Laboratory, White Sands Missile Range, New Mexico, August 1967.
2. Walter, Dr. Everett L., "Six-Variable Ballistic Model for a Rocket," Missile Meteorology Division, U. S. Army Signal Missile Support Agency, White Sands Missile Range, New Mexico, 1962.

DATA REDUCTION TECHNIQUES FOR USE ON METEOROLOGICAL DATA ABOVE 30 KILOMETERS

by

E. P. AVARA

and

B. T. MIERS

ATMOSPHERIC SCIENCES LABORATORY
WHITE SANDS MISSILE RANGE, NEW MEXICO

ABSTRACT

The FPS-16 tracking systems superimpose undesired oscillations on the real position data, resulting in rapidly fluctuating successive position points which are physically unrealistic. A linear digital filter of the form $\overline{Q}_K = \sum_{M=-58}^{M=58} W_M Q_{K+M}$ is applied separately to each component to smooth the data. The frequency response is given, and the data are corrected by a method derived by Eddy et al. (1965). Atmospheric temperature is measured by use of the STS rocketsonde, and pressure and density are calculated from these data by use of the hydrostatic and state equations.

INTRODUCTION

Atmospheric temperature, pressure, density and wind data derived from meteorological rocket soundings are used in meteorological research and for military projects requiring a knowledge of stratospheric behavior. Detailed wind profiles are often required for computing trajectories for ballistic rockets. A detailed profile of the atmospheric temperature and density structure is also needed by projects investigating re-entry problems. This paper will discuss meteorological data gathered above 30 km.

WIND DATA

Wind data derived from radar tracks of parachutes and spheres falling through the atmosphere are used as meteorological support data by several projects at White Sands Missile Range. This section will describe the filtering and correction techniques used to derive these winds.

An FPS-16 radar tracks the sensor and records its position, relative to the radar, on a magnetic tape at the rate of twenty points per second. The meteorological wind reduction technique, however, uses only every other point, or ten points per second. These position points are specified by time and three space coordinates (slant range, azimuth angle, elevation angle). A correction for refraction and earth curvature is then applied to the position points. A typical wind profile consists

of about 18,000 data points and yields wind data from 25 km to about 65 km.

As is true with any tracking system, the system itself superimposes undesired oscillations (noise) on the real position data resulting in rapidly fluctuating successive position points which are physically unrealistic. To help compensate for this feature, a linear digital filter (Equ. 1) in the form of a weighted running average over 117 points (11.7 seconds) is applied separately to each component (slant range, azimuth angle, elevation angle).

$$\overline{Q}_K = \sum_{M=-58}^{M=58} W_M Q_{K+M} \qquad (1)$$

where W_M is the value of the Mth weight, Q_{K+M} is the (K+M)th unsmoothed value of a coordinate, and $\overline{Q}_K$ is the Kth smoothed value of the coordinate. The weights are symmetrically centered about $W_O (W_N = W_{-N})$ and are shown in Figure 1. Assuming the unsmoothed coordinate values may be represented by a sum of sinusoidal oscillations of various amplitudes, phases and frequencies, a frequency response (ratio of the amplitude of a sinusoidal wave in the smoothed data to the amplitude of the same wave in the unsmoothed data) may be calculated (Equ. 2). This will give the effect of the filter on the data.

$$R(f) = \sum_{M=-58}^{M=58} W_M \cos\left(\frac{\pi f M}{5}\right) \quad \text{for } 0 \leq f \leq 5 \text{ sec}^{-1} \qquad (2)$$

where R(f) is the frequency response at frequency f. The frequency response of this filter is shown in Figure 2. The filter essentially eliminates oscillations which have frequencies greater than 0.3 sec^{-1} (periods less than three seconds). Figures 3, 4 and 5 show typical samples of the first differences in the smoothed and unsmoothed values of slant range, azimuth and elevation angles at an increment of 0.1 second.

The first and second derivatives of each coordinate are approximated by equations (3) and (4).

$$\dot{\bar{Q}}_K = 5(\bar{Q}_{K+1} - \bar{Q}_{K-1}) \tag{3}$$

$$\ddot{\bar{Q}}_K = 100(\bar{Q}_{K+1} - 2\bar{Q}_K + \bar{Q}_{K-1}) \tag{4}$$

where $\bar{Q}_K$, $\dot{\bar{Q}}_K$, and $\ddot{\bar{Q}}_K$ are the Kth values of the smoothed coordinate and its first and second derivatives, respectively. A transformation of coordinates is performed which gives position, velocity and acceleration data in terms of components oriented north-south (y), east-west (x), and normal to the surface of the earth (z). The acceleration values of each component fluctuate excessively and are physically unacceptable. Ten weights are used to filter these data and are derived from Equation 5,

$$\ddot{\bar{A}}_K = \sum_{m=0}^{9} W_M^* \ddot{A}_{K-10M} \tag{5}$$

where $\ddot{A}_K$ is the Kth value of the smoothed acceleration data, W_M^* is the Mth weight, and $\ddot{A}_{K-10M}$ is the (K-10M)th value of the unsmoothed acceleration data of one of the components. Unsmoothed values one second apart instead of a tenth of a second apart are used in the smoothing. The amplitude of the frequency response may be calculated from equations 6, 7 and 8.

$$|R^*(f)| = (C[f]^2 + S[f]^2)^{1/2} \tag{6}$$

$$C(f) = \sum_{M=0}^{9} W_M^* \cos(2\pi fM) \tag{7}$$

$$S(f) = \sum_{M=1}^{9} W_M^* \sin(2\pi fM) \tag{8}$$

for $0 \leq f \leq 0.5$ sec^{-1} where $|R^*(f)|$ is the magnitude of the frequency response at frequency f. The weights are shown in Figure 6 and $|R^*(f)|$ in Figure 7.

Another error of the system must be corrected, namely the sensor's ability to respond to the actual wind. The faster the sensor falls, the less likely it will respond to the actual wind. In other words, small-scale wind oscillations will have little effect on the sensor, while those with longer periods will be observed with greater accuracy. Therefore, the wind sensor itself becomes a time varying filter applied to the wind data. Eddy et al. (1965) designed a correction technique which theoretically eliminates this effect (Equ. 9).

$$\dot{\bar{X}}_K = \dot{X}_K - \frac{\ddot{X}_K \ddot{Z}_K}{Z_K + g} \tag{9}$$

where $\dot{\bar{X}}_K$, $\dot{X}_K$, $\ddot{X}_K$, $\dot{Z}_K$, and $\ddot{Z}_K$ are the Kth values of the east-west wind component, sensor velocity, sensor acceleration, sensor vertical velocity, and sensor vertical acceleration, respectively, and g the gravity constant. An analogous equation is also applied to the north-south component. $\dot{\bar{Z}}_K$ is always assumed to be zero. This correction technique has been experimentally verified by Kays and Olsen (1966). Typical north-south and east-west wind component profiles in final filtered and corrected form are shown in Figure 8.

TEMPERATURE, PRESSURE AND DENSITY DATA

Atmospheric temperature is the other variable measured by the meteorological rocket systems. The method of reduction, some of the characteristics of individual soundings, and the method of computation of pressure and density will be discussed in this section.

Figure 9, a typical GMD-1 receiver and TMQ-5 recorder record, shows the preflight check of recorder sensitivity and calibration, the recorder ordinate corresponding to the reference resistance, and the recorder ordinates corresponding to the values of the thermistor resistance and the reference resistance during flight (Ballard 1967). Figure 10 is typical of the temperature data transmitted by the STS-1 instrument. Some significant features of this record are (1) rocket launch accompanied by a 13°C cooling caused by an adiabatic expansion of the air within the nose cone, (2) rapid temperature rise to 80°C followed by a cooling to 70°C, (3) instrument expulsion at 73 km altitude

with apogee at 74 km, and (4) the fall rate then increased to a maximum of 325 m sec^{-1} at 69 km and then decreased to 170 m sec^{-1} at 65 km and furthered decreased to 120 m sec^{-1} at 60 km and 70 m sec^{-1} at 50 km. These fall velocities are important when a correction is applied to the data to account for aerodynamic heating. Typical temperature corrections are 6.2°C at 65 km, 3.8°C at 60 km, 2.2°C at 55 km and 1.1°C at 50 km. Electrical power dissipated across the thermistor is usually about 3μW, and the resulting temperature increase of the thermistor due to ohmic heating is less than 0.2°C (Ballard 1967). The effect of solar radiation on the thermistor is eliminated by using the lowest values of the recorder ordinates. (Clark and McCoy, 1965).

Since the temperature data are recorded on a strip chart, it is necessary to select only a few data points which are representative of the record from the infinite number available. (Work is now progressing on a method to digitize the temperature data.) Instantaneous ordinate values are chosen as data points at inflection points of the record. An ordinate tolerance of $\pm$ 2°C is imposed upon the data and is determined from the curves of recorder ordinate vs thermistor resistance vs temperature. For example an ordinate value of 60 might correspond to a temperature of - 22°C. An increase in temperature of 2°C would correspond to a thermistor resistance of 180K ohms and an ordinate value of 6.5. Therefore ordinate values selected as temperature levels in this region of the trace will vary at least 1.5 ordinates.

Pressure and density values are computed using the temperature data described above and the hydrostatic and state equations. The hydrostatic equation

$$dp = - \rho g dz \tag{10}$$

is modified by substituting from the equation of state

$$dp = - \frac{pmg}{RT'} dz \tag{11}$$

where T' is the virtual temperature. Equation (11) is then integrated with the limits p_o (a radiosonde pressure level at height Z_o) and p_1 (a desired upper pressure level corresponding to height Z_1) yielding in final form equation (13).

$$\int_{p_o}^{p_1} \frac{dp}{p} = - \frac{mg}{R} \int_{Z_o}^{Z_1} \frac{1}{T'} dz \tag{12}$$

$$p_1 = p_o \exp \frac{-g(Z_1 - Z_o)}{R' T'_M} \tag{13}$$

where $R' = \frac{R}{M}$ the gas constant for dry air and T'_M the mean virtual temperature (^oK) through the layer ($Z_1 - Z_o$) or as in this case the equally weighted mean temperature of the layer. The computation is reiterated with each succeeding calculated pressure (p_1) and height (Z_1) at the top of the layer becoming the new p_o and Z_o to the maximum height. The density is then computed using equation (14) the measured temperature (T) and the computed pressure (p) (Thiele 1961).

$$\rho = \frac{p}{R'T} \tag{14}$$

equation of state.

REFERENCES

Ballard, H. N., 1967: "The Measurement of Temperature in the Stratosphere and Mesosphere," J. Appl. Meteor., 6, 150-163.

Clark, G., and J. McCoy, 1965: "Measurement of Stratospheric Temperature," J. Appl. Meteor., 3, 365-370.

Eddy, A., C. E. Duchon, F. M. Haase, and D. R. Haragan, 1965: "Determination of Winds from Meteorological Rocketsondes," Atmospheric Sciences Group Report No. 2, College of Engineering, the University of Texas, Austin, Texas.

Kays, M. D., and R. O. Olsen, 1966: "Improved Rocketsonde Parachute-Derived Wind Profiles," Atmospheric Sciences Laboratory ECOM-5086, White Sands Missile Range, New Mexico.

Thiele, O. W., 1961: "Density and Pressure Profiles Derived from Metecrological Rocket Measurements," Missile Meteorology Division Tech Report 108, U. S. Army Signal Missile Support Agnecy, White Sands Missile Range, New Mexico.

(Illustrations not available at time of publication)